

AD-A094 767

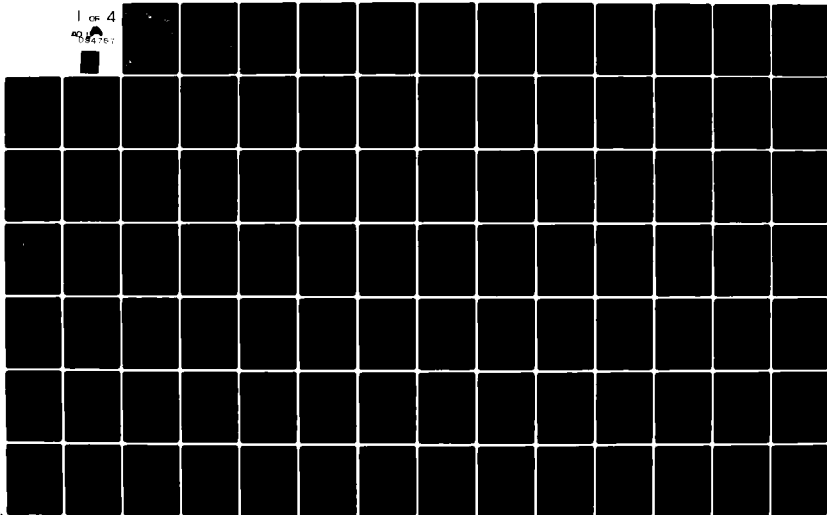
AIR FORCE INST OF TECH WRIGHT-PATTERSON AFB OH SCHOO--ETC F/6 19/5
COMPARISON OF THREE EXTENDED KALMAN FILTERS FOR AIR-TO-AIR TRAC--ETC(U)
DEC 80 W H WORSLEY
AFIT/GAE/AA/80S-2

UNCLASSIFIED

NL

1 of 4

AD-A094 767

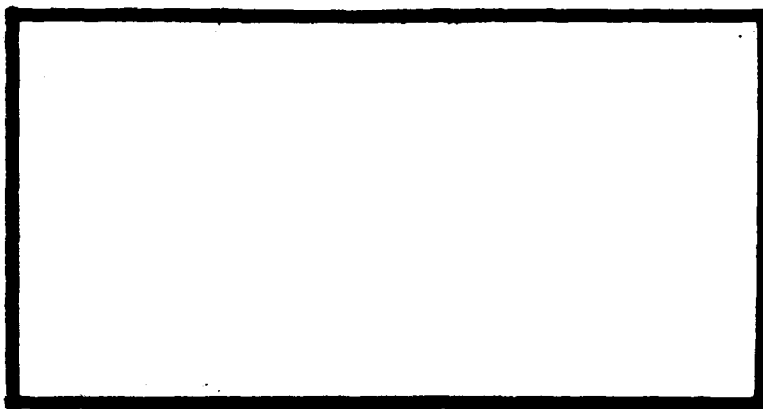


AD A094767



LEVEL II

**DTIC
ELECT
FEB 10 1981**



DOC FILE COPY

DISTRIBUTION STATEMENT A
Approved for public release;
Distribution Unlimited

**DEPARTMENT OF THE AIR FORCE
AIR UNIVERSITY (ATC)
AIR FORCE INSTITUTE OF TECHNOLOGY**

Wright-Patterson Air Force Base, Ohio

81 2 09 099

23 JAN 1981

APPROVED FOR PUBLIC RELEASE AFR 190-17.

Laurel A. Lampela

LAUREL A. LAMPELA, 2Lt, USAF
Deputy Director, Public Affairs

Air Force Institute of Technology (ATC)
Wright-Patterson AFB, OH 45433

(14) Dec 84

(9) master's thesis

Accession For	
NTIS GRA&I	<input checked="" type="checkbox"/>
DTIC TAB	<input type="checkbox"/>
Unannounced	<input type="checkbox"/>
Justification	<input type="checkbox"/>
By _____	
Distribution/	
Availability Codes	
Avail and/or	
Dist	Special
A	

(6) COMPARISON OF THREE EXTENDED
KALMAN FILTERS FOR
AIR-TO-AIR TRACKING.

DTIC
SELECTE
FEB 10 1981
S D F

(14) AFIT/GAE/AA/80S-2 (10) William H./Worsley
Capt USAF

(12) 348

Approved for public release; distribution unlimited

012225

U

AFIT/GAE/AA/80S-2

COMPARISON OF THREE EXTENDED
KALMAN FILTERS FOR
AIR-TO-AIR TRACKING

THESIS
FOR
Masters of Science

Presented to the Faculty of the School of Engineering
of the Air Force Institute of Technology

Air University
in Partial Fulfillment of the
Requirements for the Degree of
Master of Science in
Aeronautical Engineering

by

William H. Worsley, BSAE

Capt USAF

December 1980

Approved for public release; distribution unlimited

Acknowledgements

I wish to thank my Lord and my Saviour for providing strength when I was faltering during the completion of this thesis. Without His strength I would have never completed. I also want to thank my wife and daughter for the support and encouragement they both provided. Professor Peter S. Maybeck provided a great deal of guidance and acted as a sounding board for my thoughts, helping direct my work down the proper path. Without his guidance, the work would not have been completed. Also, I would like to express my appreciation to the Air Force for permitting me to attend AFIT and increase the scope of my knowledge. Finally, I would like to thank Mrs. Linda Penn, my typist, for the good work she did on typing my thesis and for the understanding she had when the going was rough.

Contents

	Page
Acknowledgements	ii
List of Figures.	v
List of Tables	ix
List of Important Symbols and Abbreviations.	x
Abstract	xii
I. Introduction	1
Background	1
Purpose and Objectives	2
Assumptions and Limitations.	3
II. System Dynamic Models.	6
Gauss-Markov Line of Sight Dynamics Model.	6
Gauss-Markov Inertial Coordinate Dynamics Model.	12
Constant Turn Rate Inertial Coordinate Dynamics Model.	18
III. Tracker Models and Measurements.	24
Tracker Model for Line of Sight Filter	24
Measurements for Line of Sight Filter.	26
Tracker Model for Inertial Filters	29
Measurements for Inertial Filters.	31
Selection of Tracker Measurement Noises.	34
IV. Extended Kalman Filter Implementation.	38
Extended Kalman Filter	38
Extended Kalman Filter for Gauss-Markov Line of Sight Model.	40
Extended Kalman Filter for Gauss-Markov Inertial Model	49
Extended Kalman Filter for Constant Turn Rate Inertial Model.	58
Selection of Parameters of Extended Kalman Filters	61
V. Method of Evaluation	65
Monte Carlo Simulation	65
Trajectory Generation and Description.	67
Measurement Update Rates	74
Variations in Measurement Noise.	74
Figures of Merit	76

Contents (Cont'd)

	Page
VI. Results	80
General Performance of the Three Filters.	80
Comparison of the Three Filters	84
Effects of Update Rate on CTRI Filter Performance	89
Effects of Variations in Measurement Noise for the CTRI Filter.	93
VII. Conclusions and Recommendations	99
Conclusions	99
Recommendations	100
Bibliography	103
Appendix A: Coordinate Transformation	104
Appendix B: Graphical Results of the Effect of Increasing Number Monte Carlo Simulations on Solution Accuracy	108
Appendix C: Graphical Results for the Gauss-Markov Line of Sight Filter.	136
Appendix D: Graphical Results for the Gauss-Markov Inertial Coordinate Filter	164
Appendix E: Graphical Results for the Constant Turn Rate Inertial Coordinate Filter.	192
Appendix F: Graphical Results of the Effect of Variations in Update Rates on the Performance of the Constant Turn Rate Inertial Coordinate Filter.	220
Appendix G: Graphical Results of the Effect of Variations in the Range Measurement Noise on the Performance of the Constant Turn Rate Inertial Coordinate Filter	248
Appendix H: Graphical Results of the Effect of Variations of the Error Angle Measurement Noises of the Performance of the Constant Turn Rate Inertial Coordinate Filter.	276
Appendix I: Graphical Results of the Effect of Variations of the Range Rate Measurement Noise on the Performance of the Constant Turn Rate Inertial Coordinate Filter.	304

VITA

List of Figures

Figure		Page
II-1	Orientation of GMLOS Filter Coordinate Frame with Respect to an Earth-Fixed Reference Frame	7
II-2	Timing Sequence for Realignment of GMLOS Filter's Coordinate Frame.	8
II-3	Relation Between Attacker's Center of Mass and the Earth-Fixed Reference Frame at the Initial Time	14
III-1	Orientation of Tracker's Coordinate System With Respect to an Earth-Fixed Reference Frame for the GMLOS Filter.	25
III-2	Measurement of Range and the Error Angles	27
III-3	Relation Between Attacker's Body Coordinate Frame and Tracker's Coordinate Frame.	30
IV-1	Orientation of GMLOS Filter's Coordinate Frame to the Earth-Fixed Reference System at Time t_i^C	48
IV-2	Timing Sequence for Extended Kalman Filter Implementation of GMLOS Filter	50
IV-3	Block Diagram for GMLOS Extended Kalman Filter.	51
IV-4	Timing Sequence for Extended Kalman Filter Implementation of GMI and CTRI Filters	56
IV-5	Block Diagram for GMI and CTRI Extended Kalman Filters.	57
V-1	Representative Output from SOFEPL Program	68
V-2	Relation Between the Earth-Fixed Coordinate Frame Used by the Trajectory Generating Program and the Attacker's Center of Gravity at the Initial Time	69
V-3	Initial Positions and Velocities for Trajectory 1 Relative to the Earth-Fixed Reference Frame.	71
V-4	Initial Positions and Velocities for Trajectory 2 Relative to the Earth-Fixed Reference Frame.	72
V-5	Initial Positions and Velocities for Trajectory 3 Relative to the Earth-Fixed Reference Frame.	73
VI-1	Performance of the Position Estimates for the CTRI Filter When Flown Against Trajectory 2 for Various Sample Periods.	90

List of Figures (Cont'd)

Figure		Page
VI-2	Performance of the Velocity Estimates for the CTRI Filter When Flown Against Trajectory 2 for Various Sample Periods. . .	91
VI-3	Performance of the Acceleration Estimates for the CTRI Filter When Flown Against Trajectory 2 for Various Sample Periods	92
A-1	Rotation About the z_A -Axis.	105
A-2	Rotation About the y_C -Axis.	107
B-1 to B-9	Performance of the Constant Turn Rate Inertial Coordinate Filter for Trajectory 2 for 5 Monte Carlo Simulations	109 to 117
B-10 to B-18	Performance of the Constant Turn Rate Inertial Coordinate Filter for Trajectory 2 for 10 Monte Carlo Simulations.	118 to 126
B-19 to B-27	Performance of the Constant Turn Rate Inertial Coordinate Filter for Trajectory 2 for 15 Monte Carlo Simulations.	127 to 135
C-1 to C-9	Performance of the Gauss-Markov Line of Sight Filter for Trajectory 1.	137 to 145
C-10 to C-18	Performance of the Gauss-Markov Line of Sight Filter for Trajectory 2.	146 to 154
C-19 to C-27	Performance of the Gauss-Markov Line of Sight Filter for Trajectory 3.	155 to 163
D-1 to D-9	Performance of the Gauss-Markov Inertial Coordinate Filter for Trajectory 1.	165 to 173
D-10 to D-18	Performance of the Gauss-Markov Inertial Coordinate Filter for Trajectory 2.	174 to 182
D-19 to D-27	Performance of the Gauss-Markov Inertial Coordinate Filter for Trajectory 3.	183 to 191
E-1 to E-9	Performance of the Constant Turn Rate Inertial Coordinate Filter for Trajectory 1.	193 to 201

List of Figures (Cont'd)

Figures		Page
E-10 to E-18	Performance of the Constant Turn Rate Inertial Coordinate Filter for Trajectory 2.	202 to 210
E-19 to E-27	Performance of the Constant Turn Rate Inertial Coordinate Filter for Trajectory 3.	211 to 219
F-1 to F-9	Performance of the Constant Turn Rate Inertial Coordinate Filter for Trajectory 2 with 0.08 Second Sample Period	221 to 229
F-10 to F-18	Performance of the Constant Turn Rate Inertial Coordinate Filter for Trajectory 2 with a 0.16 Second Sample Period . . .	230 to 238
F-19 to F-27	Performance of the Constant Turn Rate Inertial Coordinate Filter for Trajectory 2 with a 0.24 Second Sample Period . . .	239 to 247
G-1 to G-9	Performance of the Constant Turn Rate Inertial Coordinate Filter for Trajectory 2 with a Range Measurement Noise Variance of 1000 Feet ²	249 to 257
G-10 to G-18	Performance of the Constant Turn Rate Inertial Coordinate Filter for Trajectory 2 with a Range Measurement Noise Variance of 100000 Feet ²	258 to 266
G-19 to G-27	Performance of the Constant Turn Rate Inertial Coordinate Filter for Trajectory 2 with No Range Measurement.	267 to 275
H-1 to H-9	Performance of the Constant Turn Rate Inertial Coordinate Filter for Trajectory 2 with Error Angle Measurement Noise Variances of 0.00001 Radians ²	277 to 285
H-10 to H-18	Performance of the Constant Turn Rate Inertial Coordinate Filter for Trajectory 2 with Error Angle Measurement Noise Variances of 0.0001 Radians ²	286 to 294
H-19 to H-27	Performance of the Constant Turn Rate Inertial Coordinate Filter for Trajectory 2 with No Error Angle Measurements . . .	295 to 303
I-1 to I-9	Performance of the Constant Turn Rate Inertial Coordinate Filter for Trajectory 2 with a Range Rate Measurement Noise Variance of 62.5 Feet ² /Second ²	305 to 313

List of Figures (Cont'd)

Figures		Page
I-10	Performance of the Constant Turn Rate Inertial Coordinate	314
to	Filter for Trajectory 2 with a Range Rate Measurement Noise	to
I-18	Variance of 6250 Feet ² /Second ²322
I-19	Performance of the Constant Turn Rate Inertial Coordinate	323
to	Filter for Trajectory 2 with No Range Rate Measurements	to
I-27		331

List of Tables

Table	Page
III-1	Measurement Noise Variances for Tracker Models. 37
V-1	Sample Periods Investigated for Each Filter 75
V-2	Combinations of the Measurement Noise Variances Used to Evaluate Filter Sensitivity. 77
VI-1	Comparison of the Scalar Magnitudes of the Three Components of Mean Error for Position, Velocity, and Acceleration. . . 85
VI-2	Comparison of the Scalar Magnitudes of the Time Average of the Three Components of the Standard Deviation of the Errors Committed by the Filter. 86
VI-3	Effect of Variations of the Variance of the Range Rate Measurement σ_R^2 on the Performance of the CTRI Filter When Flown Against Trajectory 2 94
VI-4	Effect of Variations of the Variance of the Error Angle Measurement σ_a^2 and σ_e^2 on the Performance of the CTRI Filter When Flown Against Trajectory 2. 95
VI-5	Effect of Variations of the Variance of the Range Rate σ_R^2 on the Performance of the CTRI Filter When Flown Against Trajectory 2. 96

List of Important Symbols and Abbreviations

<u>Symbol</u>	<u>Description</u>
A	refers to attacker quantities
CTRI	constant turn rate inertial coordinate
E	expected value
GMI	Gauss-Markov inertial coordinate
GMLOS	Gauss-Markov line of sight
I	refers inertial coordinate frame as subscript or total (inertial) quantities as superscript
IMU	inertial measuring unit
K	Kalman filter gain matrix
\hat{L}	refers to estimated LOS coordinate frame
LOS	line of sight
P	filter's conditional covariance matrix
Q	descriptor of the strength of the dynamic driving noise
R	range measurement or the descriptor of the strength of the measurement noise
\dot{R}	range rate measurement
T	refers to target quantities or the transformation from one coordinate frame to a second coordinate frame (established by super and subscripts)
T/A	refers to target relative to attacker quantities
v	measurement noise with descriptor of strength R
a	error angle between the true LOS and estimated LOS
e	error angle between the true LOS and estimated LOS
t	time
\underline{x}	state vector
\underline{w}	zero mean white driving noise vector with descriptor of strength Q

List of Important Symbols and Abbreviations (Cont'd)

<u>Symbol</u>	<u>Description</u>
<u>z</u>	measurement vector
η	Euler angle
ν	Euler angle
τ	coorelation time constant
<u>ω</u>	angular velocity vector

Abstract

The performances of the extended Kalman filter implementations for three different target acceleration models that estimate target position, velocity, and acceleration states for air-to-air gunnery were compared. The models included 1) a first order zero-mean Gauss-Markov relative target acceleration model, 2) a first order zero-mean Gauss-Markov total target acceleration model, and 3) a constant turn rate target acceleration model. Measurements available to the extended Kalman filter at update were the range, range rate, and the error angles between the true line of sight and the estimated line of sight. Additional evaluations of the effect of variations in the length of the sample period and the effect of variations in the variances of the measurement noises were conducted for the extended Kalman filter using the constant turn rate target acceleration model. All evaluations were accomplished using Monte Carlo simulation techniques.

COMPARISON OF THREE EXTENDED
KALMAN FILTERS FOR
AIR-TO-AIR TRACKING

I Introduction

Background

The accurate estimation of target position, velocity, and acceleration for use in a gunsight algorithm has been a major concern for engineers working on fire control systems. From the earliest gunsights used during World War I to the operational gunsights on the present fighter aircraft, future target position has been estimated by the pilot. He has used his personal experience, developed through years of training, along with his observation of the relative target position and velocity, to determine where the target might be one bullet time of flight in the future. Therefore, performance in air-to-air gunnery has depended on how much experience and skill each pilot has in estimating future target position. For gunnery attacks where the acceleration vector of both the target and attacker were coplanar (i.e. in-plane tracking), the dependence on pilot experience and skill did not create a significant problem since the attacking pilot could "pull" the bullet stream through the target by changing only his pitch attitude. However, as the performance of aircraft increased, pilots wanted to have a gun solution available for out-of-plane tracking (snapshots) or front (nose-to-nose) attacks because the opportunity for in-plane tracking decreased with a resultant degradation of probability of hits.

In 1979 the hardware and software required for a constant gain

extended Kalman filter to estimate target relative position, velocity, and acceleration were installed in an F-106 aircraft for testing. The estimated target data were used by the gunsight algorithm to compute and display predicted target position at one bullet time of flight into the future. A second display representing the calculated bullet path at the estimated range of the target was provided. The attacking pilot then flew his aircraft so that the two displays were properly aligned to obtain a "correct" gunnery solution based on the target parameters estimated by the filter.

The constant gain extended Kalman filter used in the test was developed in a line of sight (LOS) coordinate system using a first order Gauss-Markov relative acceleration model (Ref 1:30-59). However, two additional filters have been proposed to estimate the target parameters: a first order Gauss-Markov total target acceleration model inertial coordinate (GMI) filter and a constant inertial target turn rate constant speed inertial coordinate (CTRI) filter (Ref 2).

Purpose and Objectives

The purpose of this thesis is to present a comparison of the capabilities of a first order Gauss-Markov relative target acceleration model estimated LOS coordinate frame (GMLOS) filter, a GMI filter, and a CTRI filter. Also, results for variations in update rates and measurement noise are presented for the CTRI filter.

The objectives of the research performed for this thesis were:

1. To compare the performance of the three extended Kalman filters based upon the proposed target acceleration models, when flown against three different target acceleration profiles. These profiles were chosen to represent realistic target maneuvers in an air-to-air engagement and

to insure that none of the filters had an advantage due to profile selection.

2. To investigate the sensitivity of the CTRI filter to different update rates. This filter was chosen because it was expected to have better performance than either of the other two filters; the acceleration model used for the CTRI filter more closely approximated actual target accelerations, especially accelerations with a non-zero mean characteristic.

3. To investigate the sensitivity of the CTRI filter to different values of the measurement noise (The measurements are discussed in Section II). Again, the CTRI filter was chosen since it was expected to have the best performance of the three filters (as discussed above).

Assumptions and Limitations

The systems evaluated for this thesis were nonlinear either in measurements or dynamics and measurements, and strictly linear Kalman filter propagation and update relations could not be used. Several methods for approximating a solution for filters with nonlinear dynamics and/or measurement models exist including the truncated second order filter, the Gaussian second order filter, the linearized Kalman filter, and the extended Kalman filter (Ref 3). For the filters evaluated for this thesis, the extended Kalman filter was chosen for propagation and update. This approximation was selected since it incorporated a new reference state trajectory each time new state estimates were calculated, was relatively simple when compared to either of the second order methods, and was compatible with the program used to perform the simulation (See Section V).

The coordinate frames for all three filters were assumed to be inertially space-stabilized except possibly during an instantaneous realign-

ment. For the GMLOS filter, the coordinate frame was assumed to be impulsively aligned just before the update to the estimated LOS calculated at the end of the propagation. The GMI and CTRI filters' coordinate frames were assumed to be constantly aligned with an earth-fixed (space-stabilized) reference frame.

Tracker dynamics were not included in any of the filter evaluations. It was assumed that a closed loop control system used estimated target relative position data from the filter to point the tracker along the estimated LOS without error before the measurements were made. Also, the control system was assumed to provide an inertially space-stabilized tracker during measurements.

The assumptions of a space-stabilized coordinate system between updates and a space-stabilized tracker during measurements reduced the complexity of the propagation equations. The angular velocities of the filter's coordinate frame and tracker coordinate frame did not have to be integrated to provide the transformations required; the transformations were calculated from the estimated position states of the filter. (See Section II and IV). If an inertially rotating coordinate frame for either the filter or tracker had been used, the propagation equations would have included the equations necessary to obtain the transformations. (See Ref 1 for detailed development of GMLOS filter with rotating filter and tracker coordinate frames.)

The attacker's position, inertial velocity, and inertial acceleration relative to an earth-fixed reference frame and the transformation from the attacker body frame to the same earth-fixed frame were assumed to be available from an inertial measuring unit (IMU) without error. This assumption was made since the errors in current IMUs were much smaller than

the errors expected to be committed by the filter. Also, using these data without adding measurement noise provided the best possible performance for the filter for a given set of filter parameters; the inclusion of errors in the IMU measurements would reduce the accuracy of the filter.

The earth-fixed reference frame used in the development of the models for this thesis was assumed to have its positive axes oriented in local north, east, and down (toward the center of the earth) directions. In this thesis, when position data are referenced to this frame, the position of the origin of this frame relative to the surface of the earth will be stated.

II System Dynamics Models

Gauss-Markov Line of Sight Dynamics Model

The dynamics equations for the GMLOS filter were developed based on the assumption that the filter's coordinate system was aligned with its l-axis along the estimated LOS and with zero roll orientation with respect to the local horizon (Fig II-1). Also, the filter's coordinate frame was assumed to be space-stabilized from t_i^{-r} (where the minus sign indicates time just before a measurement update and the r denotes time after a coordinate realignment) until just before the next measurement update time t_{i+1}^{-c} (where the c denotes time before a coordinate realignment). At time t_{i+1}^{-c} , an orthogonal transformation matrix between the filter's current coordinate system and the desired coordinate system with its l-axis along the estimated LOS (based on the filter's estimate of the target's position at t_{i+1}^{-c}) was calculated. Then, the filter's current coordinate frame was assumed to be instantaneously realigned along the desired coordinate frame at t_{i+1}^{-} . (See Section IV and Fig II-2)

The state vector, $\underline{x}_{\hat{L}}(t)$, chosen for the GMLOS filter was

$$\underline{x}_{\hat{L}}(t) = \begin{bmatrix} [x_{\hat{L}}^{T/A}(t)]_1 \\ [I_{x_{\hat{L}}}^{T/A}(t)]_2 \\ [I_{x_{\hat{L}}}^{T/A}(t)]_3 \\ [x_{\hat{L}}^{T/A}(t)]_4 \\ [I_{x_{\hat{L}}}^{T/A}(t)]_5 \\ [I_{x_{\hat{L}}}^{T/A}(t)]_6 \\ [x_{\hat{L}}^{T/A}(t)]_7 \\ [I_{x_{\hat{L}}}^{T/A}(t)]_8 \\ [I_{x_{\hat{L}}}^{T/A}(t)]_9 \end{bmatrix} \quad \text{(II-1)}$$

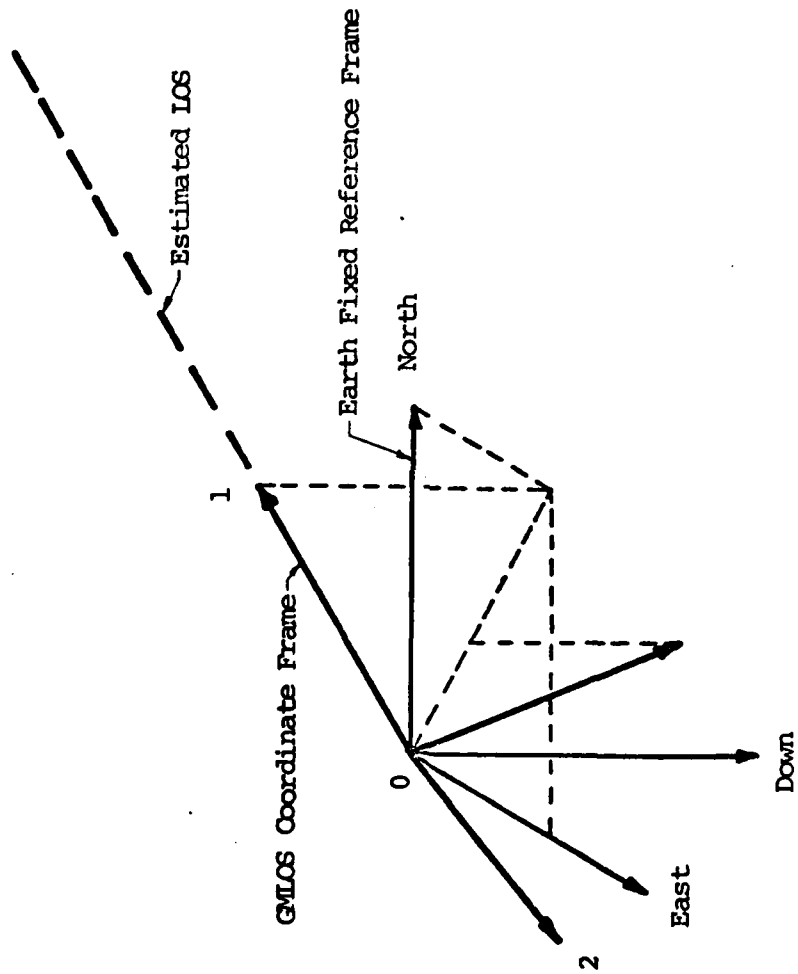
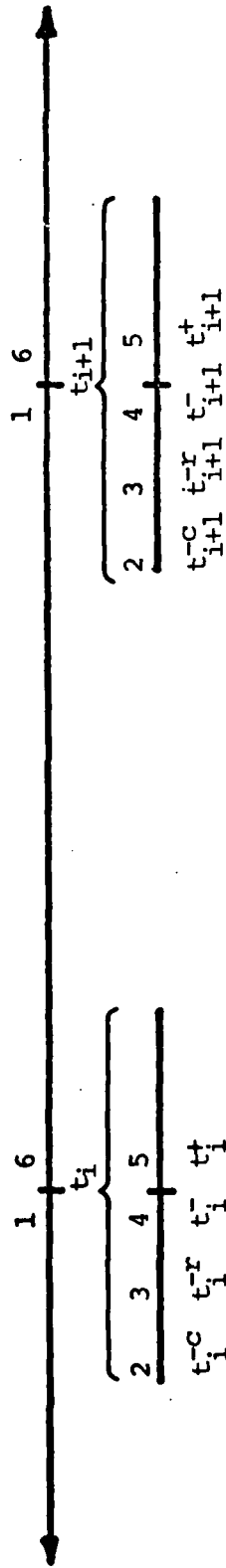


Figure II-1. Orientation of GMLOS Filter Coordinate Frame with Respect to an Earth Fixed Reference Frame



1. End of propagation.
2. Calculation of new direction cosine matrix $\hat{T}_n^C(t_i)$ to realign filter's coordinate frame.
3. Realignment of filter's coordinate frame.
4. Ready for update.
5. Update complete.
6. Start of propagation.

Figure II-2. Timing Sequence for Realignment of GMLOS Filter's Coordinate Frame

where

$$\left[x_{\hat{L}}^{T/A}(t) \right]_1,$$

$$\left[x_{\hat{L}}^{T/A}(t) \right]_4,$$

and

$$\left[x_{\hat{L}}^{T/A}(t) \right]_7 = \text{relative position of the target with respect to the attacker at time } t \text{ along the 1, 2, and 3 axes, respectively, of the filter's coordinate frame}$$

$$\left[I_{x_{\hat{L}}}^{T/A}(t) \right]_2,$$

$$\left[I_{x_{\hat{L}}}^{T/A}(t) \right]_5,$$

and

$$\left[I_{x_{\hat{L}}}^{T/A}(t) \right]_8 = \text{relative inertial velocity of the target with respect to the attacker at time } t \text{ along the 1, 2, and 3 axes, respectively, of the filter's coordinate system}$$

and

$$\left[I_{x_{\hat{L}}}^{T/A}(t) \right]_3,$$

$$\left[I_{x_{\hat{L}}}^{T/A}(t) \right]_6,$$

and

$$\left[I_{x_{\hat{L}}}^{T/A}(t) \right]_9 = \text{relative inertial acceleration of the target with respect to the attacker at time } t \text{ along the 1, 2, and 3 axes respectively, of the filter's coordinate system}$$

The superscripts I and T/A denote that the state represented a total (as seen from the inertial reference frame) relative (target with respect to the attacker) quantity. The \hat{L} subscript denotes that the state was coordinatized in the filter's coordinate frame (estimated LOS frame).

From dynamics, for an inertially space-stabilized coordinate system, the position states satisfied the differential equations

$$\left[\dot{\mathbf{x}}_{\hat{L}}^{T/A}(t) \right]_1 = \left[\mathbf{I}_{\mathbf{x}}^{T/A}(t) \right]_2 \quad (\text{II-2})$$

$$\left[\dot{\mathbf{x}}_{\hat{L}}^{T/A}(t) \right]_4 = \left[\mathbf{I}_{\mathbf{x}}^{T/A}(t) \right]_5 \quad (\text{II-3})$$

$$\left[\dot{\mathbf{x}}_{\hat{L}}^{T/A}(t) \right]_7 = \left[\mathbf{I}_{\mathbf{x}}^{T/A}(t) \right]_8 \quad (\text{II-4})$$

The velocity state differential equations were written as

$$\left[\mathbf{I}_{\dot{\mathbf{x}}}^{T/A}(t) \right]_2 = \left[\mathbf{I}_{\mathbf{x}}^{T/A}(t) \right]_3 \quad (\text{II-5})$$

$$\left[\mathbf{I}_{\dot{\mathbf{x}}}^{T/A}(t) \right]_5 = \left[\mathbf{I}_{\mathbf{x}}^{T/A}(t) \right]_6 \quad (\text{II-6})$$

$$\left[\mathbf{I}_{\dot{\mathbf{x}}}^{T/A}(t) \right]_8 = \left[\mathbf{I}_{\mathbf{x}}^{T/A}(t) \right]_9 \quad (\text{II-7})$$

Finally, a first order Gauss-Markov relative target acceleration model given by

$$\left[\mathbf{I}_{\ddot{\mathbf{x}}}^{T/A}(t) \right]_3 = -\left[\mathbf{I}_{\mathbf{x}}^{T/A}(t) \right]_3 / \tau_1 + w_1 \quad (\text{II-8})$$

$$\left[\mathbf{I}_{\ddot{\mathbf{x}}}^{T/A}(t) \right]_6 = -\left[\mathbf{I}_{\mathbf{x}}^{T/A}(t) \right]_6 / \tau_2 + w_2 \quad (\text{II-9})$$

$$\left[\mathbf{I}_{\ddot{\mathbf{x}}}^{T/A}(t) \right]_9 = -\left[\mathbf{I}_{\mathbf{x}}^{T/A}(t) \right]_9 / \tau_3 + w_3 \quad (\text{II-10})$$

where

τ_1 , τ_2 , and τ_3 = target relative acceleration
correlation time constant
along the 1, 2, and 3 axes,
respectively, of the filter's
coordinate frame

and

w_1 , w_2 , and w_3 = zero mean white Gaussian driv-
ing noise along the 1, 2, and
3 axes, respectively, of the
filter's coordinate frame account-
ing for errors between the target
relative acceleration model and
the true target relative inertial
accelerations

was selected (See Section IV for values of τ_1 , τ_2 , and τ_3 and the strengths of w_1 , w_2 , and w_3). The choice of a relative inertial acceleration model for the GMLOS filter was motivated by the fact that, if the attacker were performing in-plane tracking, the target's inertial acceleration would be nearly equal to and closely correlated with the attacker's inertial acceleration (Ref 1:15). Thus the choice of a first order Gauss-Markov relative target acceleration model was appropriate.

Note that Eqs II-2 to II-10 were not valid during the small interval t_1^c to t_1^r when the filter's coordinate frame was rotated to the new orientation calculated from the estimated target position at time t_1^c .

Now, Eqs II-2 to II-10 in state vector form were written as

$$\begin{bmatrix}
 \left[\dot{x}_{\hat{L}}^{T/A}(t) \right]_1 \\
 \left[\dot{I}_{\hat{L}}^{T/A}(t) \right]_2 \\
 \left[I_{\hat{L}}^{T/A}(t) \right]_3 \\
 \left[\dot{x}_{\hat{L}}^{T/A}(t) \right]_4 \\
 \left[I_{\hat{L}}^{T/A}(t) \right]_5 \\
 \left[\dot{I}_{\hat{L}}^{T/A}(t) \right]_6 \\
 \left[\dot{x}_{\hat{L}}^{T/A}(t) \right]_7 \\
 \left[I_{\hat{L}}^{T/A}(t) \right]_8 \\
 \left[\dot{I}_{\hat{L}}^{T/A}(t) \right]_9
 \end{bmatrix}
 =
 \begin{bmatrix}
 \left[I_{\hat{L}}^{T/A}(t) \right]_2 \\
 \left[I_{\hat{L}}^{T/A}(t) \right]_3 \\
 -\left[I_{\hat{L}}^{T/A}(t) \right]_3 / \tau_1 \\
 \left[I_{\hat{L}}^{T/A}(t) \right]_5 \\
 \left[I_{\hat{L}}^{T/A}(t) \right]_6 \\
 -\left[I_{\hat{L}}^{T/A}(t) \right]_6 / \tau_2 \\
 \left[I_{\hat{L}}^{T/A}(t) \right]_8 \\
 \left[I_{\hat{L}}^{T/A}(t) \right]_9 \\
 -\left[I_{\hat{L}}^{T/A}(t) \right]_9 / \tau_3
 \end{bmatrix}
 +
 \begin{bmatrix}
 0 \\
 0 \\
 w_1 \\
 0 \\
 0 \\
 w_2 \\
 0 \\
 0 \\
 w_3
 \end{bmatrix}
 \quad (II-11)$$

Note that Eq II-11 is in the form

$$\dot{\underline{x}} = F \underline{x} + \underline{w} \quad (II-12)$$

which is a linear stochastic differential equation.

Gauss-Markov Inertial Coordinate Dynamics Model

The dynamics model for the GMI filter expressed the relationship between the relative position of the target with respect to the attacker, the inertial target velocity, and the inertial target acceleration in an earth-fixed coordinate frame. Relative position states were chosen to keep the magnitudes of the position state estimates as small as possible. The choices of inertial target velocity and acceleration states were made to facilitate the comparison with the CTRI filter (to be discussed later) and to allow the use of a first order Gauss-Markov inertial acceleration model. The earth-fixed coordinate frame origin was located on the surface of the earth with the axes aligned in the north, east,

and down (toward the center of the earth) directions. At the start of the simulation, the center of mass of the attacker was located at an altitude h on the minus down axis (See Fig II-3). For the short time of each engagement (12 seconds), the earth-fixed coordinate system was assumed to be an inertial reference frame.

The state vector, \underline{x}_I , for the GMI filter was

$$\underline{x}_I(t) = \begin{bmatrix} [x_I^{T/A}(t)]_1 \\ [I_{x \ T}^I(t)]_2 \\ [I_{x \ T}^I(t)]_3 \\ [x_I^{T/A}(t)]_4 \\ [I_{x \ T}^I(t)]_5 \\ [I_{x \ T}^I(t)]_6 \\ [x_I^{T/A}(t)]_7 \\ [I_{x \ T}^I(t)]_8 \\ [I_{x \ T}^I(t)]_9 \end{bmatrix} \quad (\text{II-13})$$

where

$$[x_I^{T/A}(t)]_1,$$

$$[x_I^{T/A}(t)]_4,$$

and

$$[x_I^{T/A}(t)]_7 = \text{relative position of the target with respect to the attacker at time } t \text{ along the north, east, down axes, respectively, of the earth-fixed coordinate system}$$

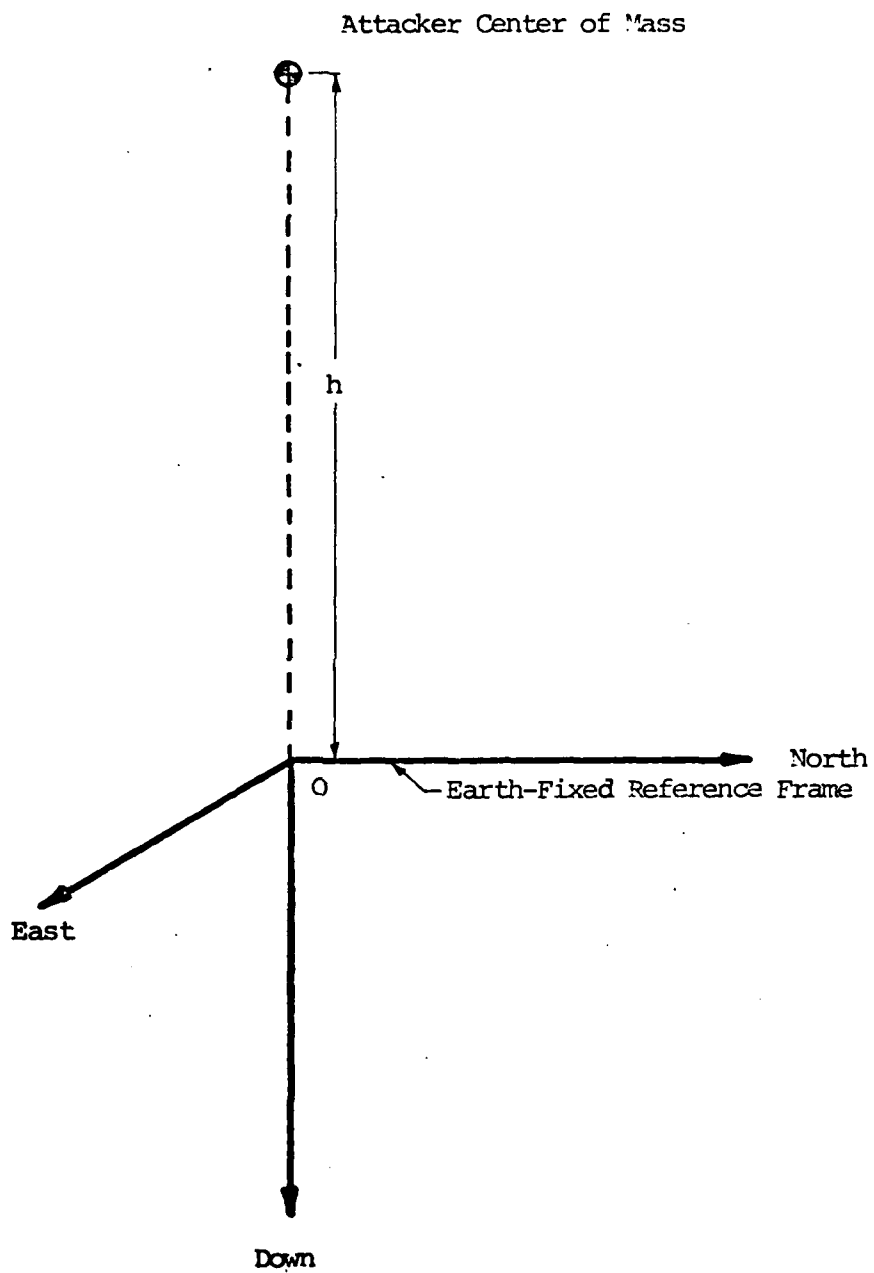


Figure II-3. Relation Between Attacker's Center of Mass and the Earth-Fixed Reference Frame at the Initial Time

$$[I_x \overset{T}{I}(t)]_2,$$

$$[I_x \overset{T}{I}(t)]_5,$$

and

$[I_x \overset{T}{I}(t)]_8$ = inertial target velocity at time t along the north, east, and down axes, respectively, of the earth-fixed coordinate system

and

$$[I_x \overset{T}{I}(t)]_3,$$

$$[I_x \overset{T}{I}(t)]_6,$$

and

$[I_x \overset{T}{I}(t)]_9$ = inertial target acceleration at time t along the north, east, and down axes, respectively, of the earth-fixed coordinate system

The superscripts I and T/A are discussed in the section on the GMLOS filter dynamics model, the superscript T denotes target quantities, and the subscript I indicates that a quantity was coordinatized in the earth-fixed (inertial) reference frame.

The differential equations for the position states were written as

$$[\overset{\cdot}{x} \overset{T/A}{I}(t)]_1 = [I_x \overset{T}{I}(t)]_2 - [I_v \overset{A}{I}(t)]_1 \quad (\text{II-14})$$

$$[\overset{\cdot}{x} \overset{T/A}{I}(t)]_4 = [I_x \overset{T}{I}(t)]_5 - [I_v \overset{A}{I}(t)]_2 \quad (\text{II-15})$$

$$[\overset{\cdot}{x} \overset{T/A}{I}(t)]_7 = [I_x \overset{T}{I}(t)]_8 - [I_v \overset{A}{I}(t)]_3 \quad (\text{II-16})$$

where

$$\left[\overset{I}{v}_I^A(t) \right]_1,$$

$$\left[\overset{I}{v}_I^A(t) \right]_2,$$

and

$$\left[\overset{I}{v}_I^A(t) \right]_3 = \text{the inertial velocity of the attacker at time } t \text{ along the north, east, down axes, respectively, of the earth-fixed coordinate system}$$

Note that the superscript A denotes attacker quantities and the superscript I and subscript I are defined above.

Now, the velocity states satisfied the differential equations

$$\left[\overset{I}{\dot{x}}_I^T(t) \right]_2 = \left[\overset{I}{x}_I^T(t) \right]_3 \quad (\text{II-17})$$

$$\left[\overset{I}{\dot{x}}_I^T(t) \right]_5 = \left[\overset{I}{x}_I^T(t) \right]_6 \quad (\text{II-18})$$

$$\left[\overset{I}{\dot{x}}_I^T(t) \right]_8 = \left[\overset{I}{x}_I^T(t) \right]_9 \quad (\text{II-19})$$

For the GM filter, the acceleration state dynamics were described

by:

$$\left[\overset{I}{\dot{x}}_I^T(t) \right]_3 = -\left[\overset{I}{x}_I^T(t) \right]_3 / \tau_1 + w_1 \quad (\text{II-20})$$

$$\left[\overset{I}{\dot{x}}_I^T(t) \right]_6 = -\left[\overset{I}{x}_I^T(t) \right]_6 / \tau_2 + w_2 \quad (\text{II-21})$$

$$\left[\overset{I}{\dot{x}}_I^T(t) \right]_9 = -\left[\overset{I}{x}_I^T(t) \right]_9 / \tau_3 + w_3 \quad (\text{II-22})$$

where

τ_1 , τ_2 , and τ_3 = target inertial acceleration correlation time constant along the north, east, down axes, respectively, of the earth-fixed coordinate frame.

and

$w_1, w_2,$ and $w_3 =$ zero mean white Gaussian driving noise along the north, east, and down axes, respectively, of the earth-fixed coordinate system accounting for errors between the target inertial acceleration model and true target inertial accelerations

(See Section IV for values for $\tau_1, \tau_2,$ and τ_3 and the strengths of $w_1, w_2,$ and w_3) The choice of the inertial target first order Gauss-Markov acceleration model was motivated by the desire to increase the filter's performance for out-of-plane tracking (snapshot or front attacks). For out-of-plane tracking, the target and attacker accelerations are only slightly correlated. This Gauss-Markov acceleration model which provides no correlation between the target and attacker accelerations was considered to be an appropriate model to use in the filter dynamics when out-of-plane tracking was anticipated.

Equations II-14 to II-22 expressed in state vector form were written

as

$$\begin{bmatrix} \left[\begin{array}{c} \dot{x}_I^{T/A}(t) \\ \dot{x}_I^T(t) \end{array} \right]_1 \\ \left[\begin{array}{c} \dot{x}_I^T(t) \\ \dot{x}_I^T(t) \end{array} \right]_2 \\ \left[\begin{array}{c} \dot{x}_I^T(t) \\ \dot{x}_I^T(t) \end{array} \right]_3 \\ \left[\begin{array}{c} \dot{x}_I^{T/A}(t) \\ \dot{x}_I^T(t) \end{array} \right]_4 \\ \left[\begin{array}{c} \dot{x}_I^T(t) \\ \dot{x}_I^T(t) \end{array} \right]_5 \\ \left[\begin{array}{c} \dot{x}_I^T(t) \\ \dot{x}_I^T(t) \end{array} \right]_6 \\ \left[\begin{array}{c} \dot{x}_I^{T/A}(t) \\ \dot{x}_I^T(t) \end{array} \right]_7 \\ \left[\begin{array}{c} \dot{x}_I^T(t) \\ \dot{x}_I^T(t) \end{array} \right]_8 \\ \left[\begin{array}{c} \dot{x}_I^T(t) \\ \dot{x}_I^T(t) \end{array} \right]_9 \end{bmatrix} = \begin{bmatrix} \left[\begin{array}{c} x_I^T(t) \\ x_I^T(t) \end{array} \right]_2 \\ \left[\begin{array}{c} x_I^T(t) \\ x_I^T(t) \end{array} \right]_3 \\ - \left[\begin{array}{c} x_I^T(t) \\ x_I^T(t) \end{array} \right]_3 / \tau_1 \\ \left[\begin{array}{c} x_I^T(t) \\ x_I^T(t) \end{array} \right]_5 \\ \left[\begin{array}{c} x_I^T(t) \\ x_I^T(t) \end{array} \right]_6 \\ - \left[\begin{array}{c} x_I^T(t) \\ x_I^T(t) \end{array} \right]_6 / \tau_2 \\ \left[\begin{array}{c} x_I^T(t) \\ x_I^T(t) \end{array} \right]_8 \\ \left[\begin{array}{c} x_I^T(t) \\ x_I^T(t) \end{array} \right]_9 \\ - \left[\begin{array}{c} x_I^T(t) \\ x_I^T(t) \end{array} \right]_9 / \tau_3 \end{bmatrix} + \begin{bmatrix} - \left[\begin{array}{c} v_I^A(t) \\ v_I^A(t) \end{array} \right]_1 \\ 0 \\ 0 \\ - \left[\begin{array}{c} v_I^A(t) \\ v_I^A(t) \end{array} \right]_2 \\ 0 \\ 0 \\ - \left[\begin{array}{c} v_I^A(t) \\ v_I^A(t) \end{array} \right]_3 \\ 0 \\ 0 \end{bmatrix} + \begin{bmatrix} 0 \\ 0 \\ w_1 \\ 0 \\ 0 \\ w_2 \\ 0 \\ 0 \\ w_3 \end{bmatrix} \quad (II-23)$$

Note that Eq II-23 is in the form

$$\dot{\underline{x}} = \underline{F} \underline{x} + \underline{u} + \underline{w} \quad (\text{II-24})$$

which is a linear stochastic differential equation.

Constant Turn Rate Inertial Coordinate Dynamics Model

The CTRI dynamics model was developed based on the assumption that the target performed a planar, constant turn rate, constant speed maneuver (Ref 2). This model more nearly represented the actual maneuvers that a target might perform during an aerial gunnery engagement than either the Gauss-Markov relative target acceleration model or Gauss-Markov total target acceleration model. As the target and attacker accelerations became more non-planar, the correlation between these accelerations was reduced. The total target acceleration modeled as a Gauss-Markov zero mean process did not represent accelerations that a target would use during an aerial engagement since this model did not account for persistent accelerations. The CTRI model used an acceleration model that did not correlate the target's and attacker's accelerations and allowed for persistent (nonzero mean) accelerations. This model eliminated the problems associated with either the GMLOS or GMI dynamic models.

Like the GMI model, the CTRI model expressed the relative positions of the target with respect to the attacker and the inertial target velocity and acceleration in an earth-fixed coordinate frame. (This coordinate frame is discussed under the GMI dynamics model). The choice of relative position was made to decrease the magnitudes of the positions while the inertial target velocity and acceleration were required to calculate explicitly the constant turn rate needed for the acceleration

model. The states used for the CTRI model were the same as for the GM model.

The position states and velocity states satisfied the differential equations given by Eqs II-14 to II-19. The difference between the GM and CTRI dynamics model was the acceleration model used to represent target maneuvers. For the CTRI model, the acceleration model was given by:

$$\left[\dot{x}_I^T(t) \right]_3 = - \left\| \underline{\omega}^T \right\|^2 \left[x_I^T(t) \right]_2 + w_1 \quad (\text{II-25})$$

$$\left[\dot{x}_I^T(t) \right]_6 = - \left\| \underline{\omega}^T \right\|^2 \left[x_I^T(t) \right]_5 + w_2 \quad (\text{II-26})$$

$$\left[\dot{x}_I^T(t) \right]_9 = - \left\| \underline{\omega}^T \right\|^2 \left[x_I^T(t) \right]_8 + w_3 \quad (\text{II-27})$$

where

w_1 , w_2 , and w_3 = driving noise on target acceleration along the north, east, and down axes, respectively, accounting for errors between the constant turn rate acceleration model and the true target inertial accelerations (See Section IV for the strength of w_1 , w_2 , and w_3)

and

$\left\| \underline{\omega}^T \right\|^2$ = the square of the magnitude of the target's inertial turn rate (to be evaluated subsequently)

Equations II-25 to II-27 were developed from the application of the Coriolis theorem written as

$$\frac{I_d}{dt} \left(\underline{I}_{V^T} \right) = \frac{T_d}{dt} \left(\underline{I}_{V^T} \right) + \left(\underline{I}_{\omega^T} \times \underline{I}_{V^T} \right) \quad (\text{II-28})$$

where \times denotes cross product and

$$\underline{I}_{V^T} = \text{inertial target velocity}$$

$$\underline{I}_{\omega^T} = \text{inertial target angular velocity}$$

and the superscripts I and T before the derivatives indicate that the derivatives are taken in the inertial reference frame and a target body frame, respectively. Now, the first term of the right hand side of Eq II-28 was zero since the target was assumed to be at a constant speed. Thus Eq II-28 became

$$\frac{I_d}{dt} \left(\underline{I}_{V^T} \right) = \left(\underline{I}_{\omega^T} \times \underline{I}_{V^T} \right) \quad (\text{II-29})$$

Now, the derivative of Eq II-29 with respect to time gave

$$\frac{I_d^2}{dt^2} \left(\underline{I}_{V^T} \right) = \frac{I_d}{dt} \left(\underline{I}_{\omega^T} \times \underline{I}_{V^T} \right) \quad (\text{II-30})$$

or, expressed in the target's body frame

$$\frac{I_d^2}{dt^2} \left(\underline{I}_{V^T} \right) = \frac{T_d}{dt} \left(\underline{I}_{\omega^T} \times \underline{I}_{V^T} \right) + \left(\underline{I}_{\omega^T} \times \left(\underline{I}_{\omega^T} \times \underline{I}_{V^T} \right) \right) \quad (\text{II-31})$$

Now, since both the target speed and angular velocity were assumed constant, the first term on the right hand side was zero and Eq II-31 became

$$\frac{I_d^2}{dt^2} \left(\underline{I}_{V^T} \right) = \left(\underline{I}_{\omega^T} \times \left(\underline{I}_{\omega^T} \times \underline{I}_{V^T} \right) \right) \quad (\text{II-32})$$

Using the relationship for a triple cross product, Eq II-32 was written as

$$\frac{d^2}{dt^2} (\underline{I}_v^T) = (\underline{I}_\omega^T \cdot \underline{I}_v^T) \underline{I}_\omega^T - (\underline{I}_\omega^T \cdot \underline{I}_\omega^T) \underline{I}_v^T \quad (\text{II-33})$$

The first term of Eq II-33 was zero since, for a planar, constant angular rate, constant velocity turn, the target's inertial velocity and angular velocity vectors are perpendicular. Thus Eq II-33 became

$$\frac{d^2}{dt^2} (\underline{I}_v^T) = - ||\underline{I}_\omega^T||^2 \underline{I}_v^T \quad (\text{II-34})$$

which was the vector equation form of Eqs II-25 to II-27.

To compute $||\underline{I}_\omega^T||^2$, the target's inertial acceleration vector, \underline{I}_a^T , was written as

$$\underline{I}_a^T = \underline{I}_\omega^T \times \underline{I}_v^T \quad (\text{II-35})$$

for a target flying at a constant speed. If the target's velocity vector was crossed into both sides of Eq II-35, then

$$\underline{I}_v^T \times \underline{I}_a^T = \underline{I}_v^T \times (\underline{I}_\omega^T \times \underline{I}_v^T) \quad (\text{II-36})$$

or, using the triple cross product relation, Eq II-36 became

$$\underline{I}_v^T \times \underline{I}_a^T = (\underline{I}_v^T \cdot \underline{I}_v^T) \underline{I}_\omega^T - (\underline{I}_v^T \cdot \underline{I}_\omega^T) \underline{I}_v^T \quad (\text{II-37})$$

Again, since the target's inertial velocity and angular velocity vectors are perpendicular for a planar constant angular rate constant velocity turn, the last term on the right hand side was zero. Rearranging Eq II-37 gave

$$\underline{I}_\omega^T = (\underline{I}_v^T \times \underline{I}_a^T) / ||\underline{I}_v^T||^2 \quad (\text{II-38})$$

Now

$$||\underline{I}_{\underline{\omega}}^T||^2 = \underline{I}_{\underline{\omega}}^T \cdot \underline{I}_{\underline{\omega}}^T \quad (\text{II-39})$$

substitution of Eq II-38 into Eq II-39 gave

$$||\underline{I}_{\underline{\omega}}^T||^2 = (\underline{I}_{\underline{v}}^T \underline{x}_{\underline{a}}^T) \cdot (\underline{I}_{\underline{v}}^T \underline{x}_{\underline{a}}^T) / ||\underline{I}_{\underline{v}}^T||^4 \quad (\text{II-40})$$

If the actual target's inertial velocity and acceleration had been known, then Eq II-40 could have been evaluated using the known values; however, only estimates of the target's inertial velocity and acceleration were available from the extended Kalman filter. Using the states defined for the CTRI filter, Eq II-40 was written as

$$\begin{aligned} ||\underline{I}_{\underline{\omega}}^T||^2 = & \left\{ \left([I_{x_I^T}(t)]_5 [I_{x_I^T}(t)]_9 - [I_{x_I^T}(t)]_6 [I_{x_I^T}(t)]_8 \right)^2 \right. \\ & + \left([I_{x_I^T}(t)]_3 [I_{x_I^T}(t)]_8 - [I_{x_I^T}(t)]_2 [I_{x_I^T}(t)]_9 \right)^2 \\ & + \left. \left([I_{x_I^T}(t)]_2 [I_{x_I^T}(t)]_6 - [I_{x_I^T}(t)]_3 [I_{x_I^T}(t)]_5 \right)^2 \right\} \\ & / \left([I_{x_I^T}(t)]_2^2 + [I_{x_I^T}(t)]_5^2 + [I_{x_I^T}(t)]_8^2 \right)^2 \quad (\text{II-41}) \end{aligned}$$

Now Eqs II-14 to II-19 and II-25 to II-27 written in state vector form were

$$\begin{bmatrix} [\dot{x}_I^{T/A}(t)]_1 \\ [I_{x_I^T}(t)]_2 \\ [I_{x_I^T}(t)]_3 \\ [\dot{x}_I^{T/A}(t)]_4 \\ [I_{x_I^T}(t)]_5 \\ [I_{x_I^T}(t)]_6 \\ [\dot{x}_I^{T/A}(t)]_7 \\ [I_{x_I^T}(t)]_8 \\ [I_{x_I^T}(t)]_9 \end{bmatrix} = \begin{bmatrix} [I_{x_I^T}(t)]_2 \\ [I_{x_I^T}(t)]_3 \\ -||\underline{I}_{\underline{\omega}}^T||^2 [I_{x_I^T}(t)]_2 \\ [I_{x_I^T}(t)]_5 \\ [I_{x_I^T}(t)]_6 \\ -||\underline{I}_{\underline{\omega}}^T||^2 [I_{x_I^T}(t)]_5 \\ [I_{x_I^T}(t)]_8 \\ [I_{x_I^T}(t)]_9 \\ -||\underline{I}_{\underline{\omega}}^T||^2 [I_{x_I^T}(t)]_8 \end{bmatrix} + \begin{bmatrix} -[I_{v_I^A}(t)]_1 \\ 0 \\ 0 \\ -[I_{v_I^A}(t)]_2 \\ 0 \\ 0 \\ -[I_{v_I^A}(t)]_3 \\ 0 \\ 0 \end{bmatrix} + \begin{bmatrix} 0 \\ 0 \\ w_1 \\ 0 \\ 0 \\ w_2 \\ 0 \\ 0 \\ w_3 \end{bmatrix} \quad (\text{II-42})$$

Since the magnitude of the target's angular velocity was a function of the state variables, Eq II-42 is a nonlinear stochastic differential equation of the form

$$\dot{\underline{x}} = \underline{f}(\underline{x}) + \underline{u} + \underline{w} \quad (\text{II-43})$$

which is properly written as an Itô stochastic differential equation

$$d\underline{x} = \underline{f}(\underline{x})dt + \underline{u}dt + d\underline{\beta}$$

where d denotes the differential and

$\underline{\beta}$ = vector Browning motion process of
diffusion Q .

III Tracker Models and Measurements

Tracker Model for Line of Sight Filter

The tracker used for the LOS filter was assumed to be inertially space-stabilized at the time of measurement t_i , with the tracker's 1-axis pointed along the estimated LOS without error. The choice of a space-stabilized tracker reduced the complexity of the dynamics model since the angular velocity of the tracker did not have to be integrated to obtain the angular orientation of the tracker. Further, the assumption that the tracker was pointed along the estimated LOS with no error eliminated the requirement to add noise to the transformation from the old tracker coordinate frame at t_i^C to the new coordinate frame at t_i^F . The 2 axis of the tracker was assumed to be parallel to the local horizon of an earth-fixed reference frame, and the origin was assumed to be located at the center of gravity cg of the attacker (See Fig III-1). The angles $\eta(t_i^C)$ and $\nu(t_i^C)$ were the Euler rotation angles, in that order, for the transformation from the earth-fixed reference frame centered at the tracker location to the tracker (estimated LOS) coordinate system. The angle $\eta(t_i^C)$ was the angle between the north axis of the earth-fixed reference frame and the projection of the estimated LOS into the north-east plane (local horizon) of the earth-fixed reference frame at time t_i^C . The angle $\nu(t_i^C)$ was the angle between the projection of the estimated LOS into the local horizon and the estimated LOS vector at time t_i^C . These two angles were not assumed to be small angles.

Tracker dynamics were not included in the filter model; a closed loop control system was assumed to move the tracker to the new position without error before the next measurement was taken. The new tracker

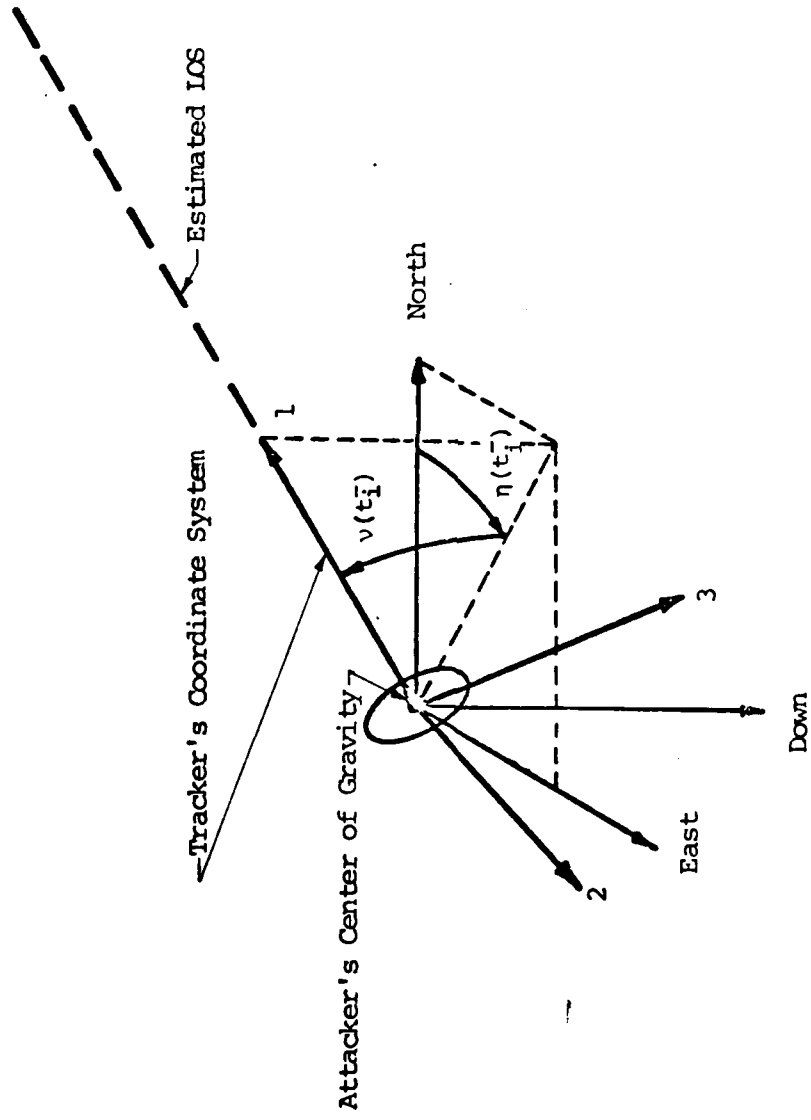


Figure III-1-1. Orientation of Tracker's Coordinate System With Respect to an Earth Fixed Reference Frame For the GLOS Filter

position at time t_i^- was calculated from the filter's estimate of the relative target position at the end of the propagation interval; $[\hat{x}_L^{T/A}(t_i^-)]_1$, $[\hat{x}_L^{T/A}(t_i^-)]_4$, and $[\hat{x}_L^{T/A}(t_i^-)]_7$. In actual implementation, the estimated position would be calculated before t_i^- . Then the tracker controller would have time to move the tracker to the new position before the measurement time t_i since the change in position for the tracker would be small for the short intervals between tracker movements. Furthermore, the actual position of the tracker relative to the filter's reference frame would be of little significance as long as the transformation from the tracker coordinate frame to the filter's coordinate frame is known, the tracker is space-stabilized during the measurement, and the target is within the field of view of the tracker.

Measurements for the Line of Sight Filter

The measurements $z(t_i)$ assumed to be available from the tracker, were the range R between the target and the attacker, the tangents of the azimuth and elevation error angles a and e , respectively, between the estimated LOS and the true LOS, and the range rate \dot{R} between the target and the attacker (See Fig III-2). Each measurement was assumed to be made by an independent device (i.e. a pulse radar for range and the tangents of the azimuth and elevation error angles and a pulse doppler radar for range rate). Note that if only a pulse radar were used, the range and range rate measurements would be corrupted by time correlated noise.

All measurements were coordinatized in the tracker coordinate frame; however, the tracker and GMLOS coordinate frames were defined identically. Therefore, the measurements $z(t_i)$ were expressed directly in terms of the states defined for the GMLOS filter in Section II. The

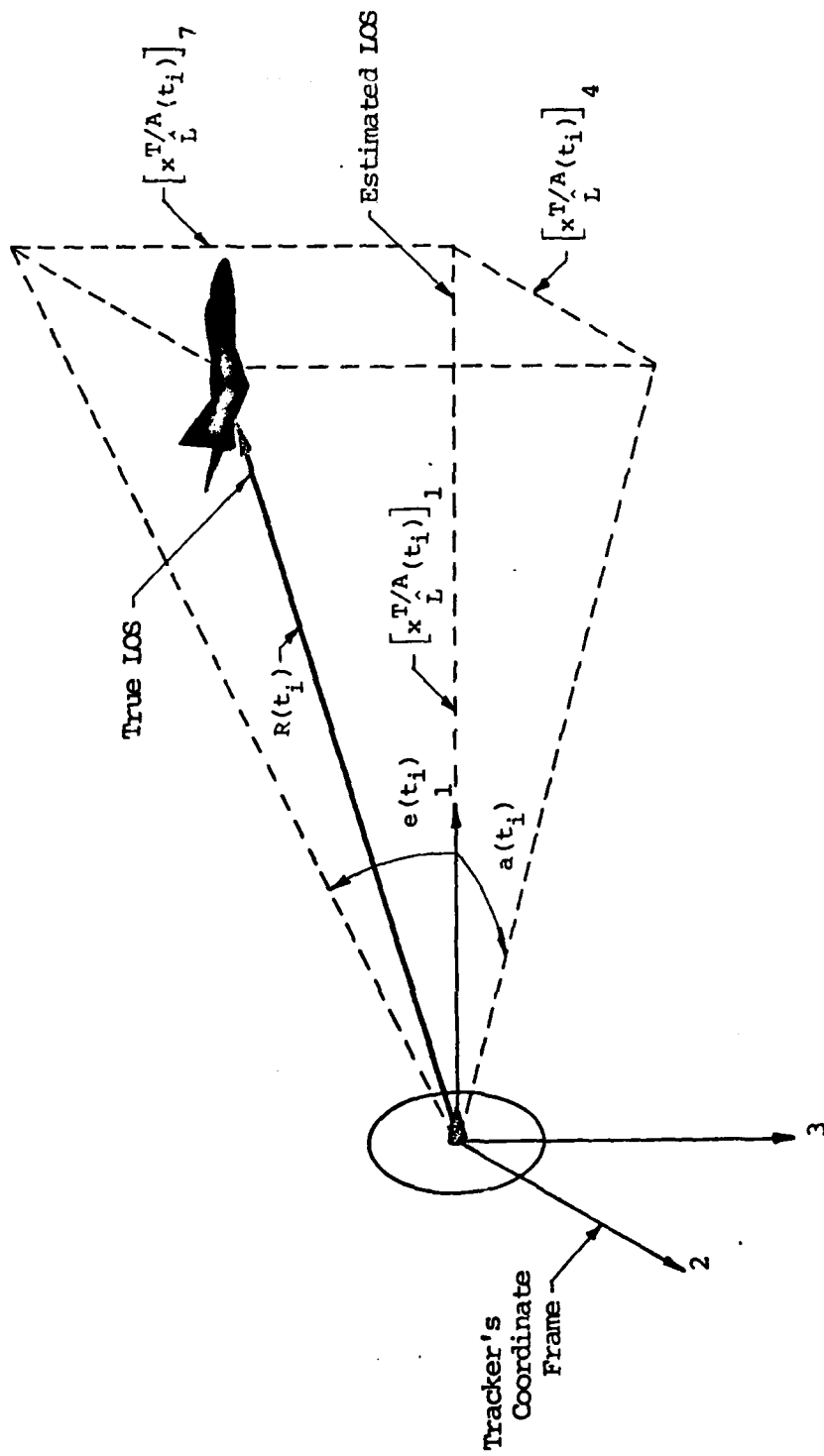


Figure III-2. Measurement of Range and the Error Angles

measurements at time t_i were defined by

$$z_1(t_i) = R(t_i) + v_1(t_i) = \left([x_{\hat{L}}^{T/A}(t_i)]_1^2 + [x_{\hat{L}}^{T/A}(t_i)]_4^2 + [x_{\hat{L}}^{T/A}(t_i)]_7^2 \right)^{1/2} + v_1(t_i) \quad (\text{III-1})$$

$$z_2(t_i) = \tan e(t_i) + v_2(t_i) = - [x_{\hat{L}}^{T/A}(t_i)]_7 / [x_{\hat{L}}^{T/A}(t_i)]_1 + v_2(t_i) \quad (\text{III-2})$$

$$z_3(t_i) = \tan a(t_i) + v_3(t_i) = [x_{\hat{L}}^{T/A}(t_i)]_4 / [x_{\hat{L}}^{T/A}(t_i)]_1 + v_3(t_i) \quad (\text{III-3})$$

$$z_4(t_i) = \dot{R}(t_i) + v_4(t_i) = \left([x_{\hat{L}}^{T/A}(t_i)]_2 [x_{\hat{L}}^{T/A}(t_i)]_1 + [x_{\hat{L}}^{T/A}(t_i)]_5 [x_{\hat{L}}^{T/A}(t_i)]_4 + [x_{\hat{L}}^{T/A}(t_i)]_8 [x_{\hat{L}}^{T/A}(t_i)]_7 \right) / \left([x_{\hat{L}}^{T/A}(t_i)]_1^2 + [x_{\hat{L}}^{T/A}(t_i)]_4^2 + [x_{\hat{L}}^{T/A}(t_i)]_7^2 \right)^{1/2} + v_4(t_i) \quad (\text{III-4})$$

where

$v_1(t_i)$ = measurement noise in range at time t_i

$v_2(t_i)$ = measurement noise in the tangent of e at time t_i

$v_3(t_i)$ = measurement noise in the tangent of a at time t_i

$v_4(t_i)$ = measurement noise in range rate at time t_i

and t_i denotes the time of the i^{th} measurement. The measurements can be written in the form

$$\underline{z}(t_i) = \underline{h}[\underline{x}(t_i)] + \underline{v}(t_i) \quad (\text{III-5})$$

which is a nonlinear measurement equation. The measurement noise $\underline{v}(t_i)$ was assumed to be zero mean white Gaussian discrete time noise with a diagonal covariance.

Tracker Model For Inertial Filters

A tracker with the same characteristics as the one for the GLOS filter was used for the inertial filters. The only difference was that the 2-axis of the tracker was assumed to be parallel to the x^b - y^b plane of the attacker body coordinate frame (See Fig III-3) instead of the north-east plane of the earth-fixed reference frame at the time of measurement t_i . The attacker body coordinate frame had the origin at the center of gravity cg of the attacker with the x^b axis out the nose, the y^b axis out the right wing, and the z^b axis down through the fuselage. The angles $\eta(t_i^c)$ and $\nu(t_i^c)$ were the Euler rotation angles, in that order, for the transformation from the attacker body axis frame to the tracker (estimated LOS) coordinate system. The angle $\eta(t_i^c)$ was the angle between the x^b axis and the projection of the estimated LOS into the x^b - y^b plane at time t_i^c . The angle $\nu(t_i^c)$ was the angle between the projection of the estimated LOS into the x^b - y^b plane and the estimated LOS vector at time t_i^c . The use of the attacker body frame for a reference for the tracker coordinate system was chosen to reduce the possibility of a singularity in the Euler angle transformation calculated by the estimator since the attacker aircraft normally would be maneuvered to keep the target within ± 90 degrees of the x^b axis. However, the transformation from the earth-fixed reference frame to the attacker body coordinate system at time t_i was required. This transformation would not be available until after time t_i if taken directly from the IMU. For this thesis, it was assumed that the errors in this coordinate transformation had only second or higher order effects on the performance of the estimator. Thus, the transformation from the earth-fixed reference system to the attacker body frame at time t_i was used without adding any measurement noise.

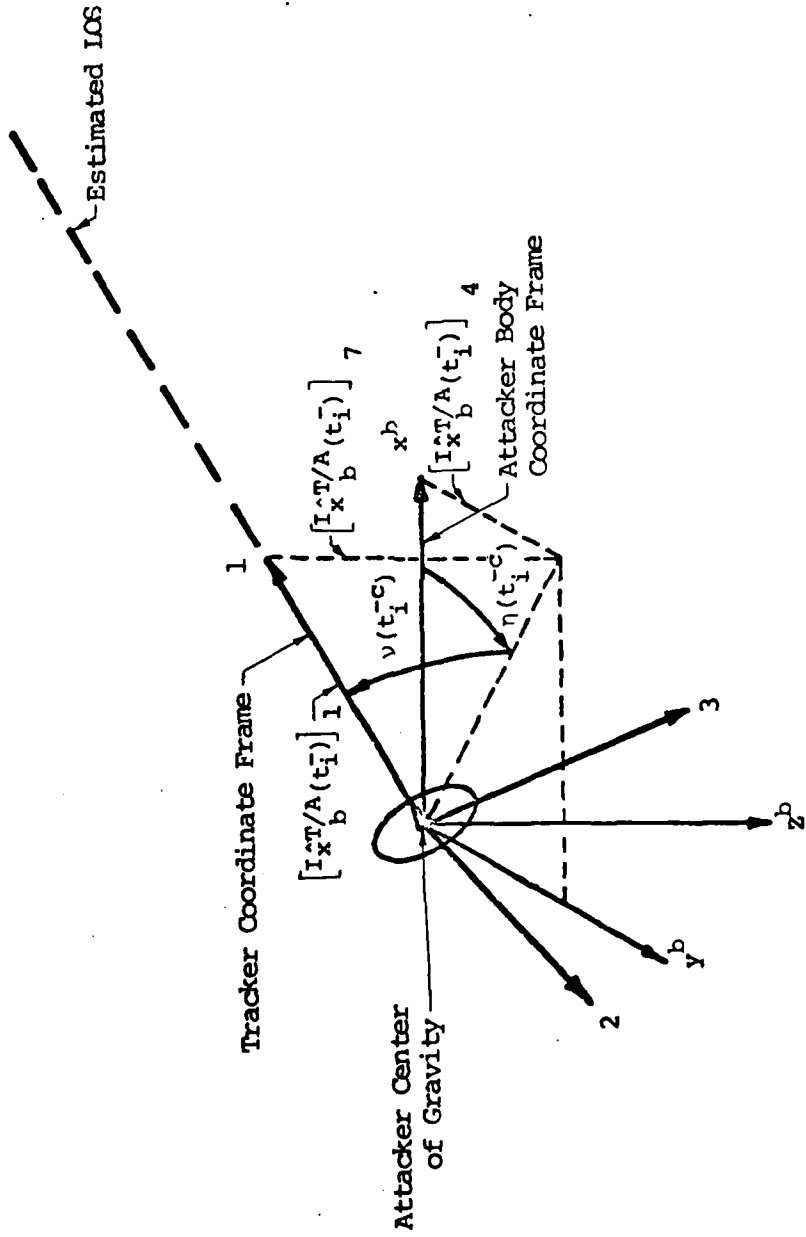


Figure III-3. Relation Between Attacker Body Coordinate Frame and Tracker Coordinate Frame

The use of the earth-fixed reference system for a reference for the tracker coordinate frame, as was done for the GMLOS filter, eliminated the need for the transformation from the earth-fixed reference frame to the attacker body axis. However, the probability of having a singularity in the Euler angle transformation calculated by the estimator was greater for this method than for the method used for the inertial filters.

Measurements For The Inertial Filters

The measurements assumed to be available from this tracker were the same as described for the GMLOS filter: range R, the tangents of the azimuth and elevation error angles α and ϵ , respectively, and the range rate \dot{R} . (See Fig III-2) As before, each measurement was assumed to be made by an independent device and was coordinatized in the tracker coordinate frame. Thus, the measurements at time t_i in the tracker coordinate frame were given by Eqs III-1 to III-4. However, the state variables for the inertial filter were defined in the inertial coordinate system.

Since

$$\underline{m}_{\hat{L}}(t_i) = T_{\hat{L}}^I(t_i) \underline{m}_I(t_i) \quad (\text{III-6})$$

where

$T_{\hat{L}}^I(t_i)$ = the transformation from an earth-fixed inertial coordinate frame to the tracker (estimated LOS) coordinate frame at time t_i

$\underline{m}_I(t_i)$ = a vector, \underline{m} , coordinatized in the earth-fixed reference frame at time t_i

$\underline{m}_{\hat{L}}(t_i)$ = vector \underline{m} coordinatized in the tracker coordinate frame at time t_i

then the measurements defined by Eqs III-1 to III-4 were written as

$$z_1(t_i) = R(t_i) + v_1(t_i) = \left(\left[x_{I}^{T/A}(t_i) \right]_1^2 + \left[x_{I}^{T/A}(t_i) \right]_4^2 + \left[x_{I}^{T/A}(t_i) \right]_7^2 \right)^{1/2} + v_1(t_i) \quad (\text{III-7})$$

$$z_2(t_i) = \tan e(t_i) + v_2(t_i) = - \left(\left[T_{L}^I(t_i) \right]_{31} \left[x_{I}^{T/A}(t_i) \right]_1 + \left[T_{L}^I(t_i) \right]_{32} \left[x_{I}^{T/A}(t_i) \right]_4 + \left[T_{L}^I(t_i) \right]_{33} \left[x_{I}^{T/A}(t_i) \right]_7 \right) / \left(\left[T_{L}^I(t_i) \right]_{11} \left[x_{I}^{T/A}(t_i) \right]_1 + \left[T_{L}^I(t_i) \right]_{12} \left[x_{I}^{T/A}(t_i) \right]_4 + \left[T_{L}^I(t_i) \right]_{13} \left[x_{I}^{T/A}(t_i) \right]_7 \right) + v_2(t_i) \quad (\text{III-8})$$

$$z_3(t_i) = \tan a(t_i) + v_3(t_i) = \left(\left[T_{L}^I(t_i) \right]_{21} \left[x_{I}^{T/A}(t_i) \right]_1 + \left[T_{L}^I(t_i) \right]_{22} \left[x_{I}^{T/A}(t_i) \right]_4 + \left[T_{L}^I(t_i) \right]_{23} \left[x_{I}^{T/A}(t_i) \right]_7 \right) / \left(\left[T_{L}^I(t_i) \right]_{11} \left[x_{I}^{T/A}(t_i) \right]_1 + \left[T_{L}^I(t_i) \right]_{12} \left[x_{I}^{T/A}(t_i) \right]_4 + \left[T_{L}^I(t_i) \right]_{13} \left[x_{I}^{T/A}(t_i) \right]_7 \right) + v_3(t_i) \quad (\text{III-9})$$

$$z_4(t_i) = \dot{R}(t_i) + v_4(t_i) = \left\{ \left(\left[I_{x^T} \right]_2 - \left[I_{v_I^A} \right]_1 \right) \left[x_{I}^{T/A}(t_i) \right]_1 + \left(\left[I_{x_I^T} \right]_5 - \left[I_{v_I^A} \right]_2 \right) \left[x_{I}^{T/A}(t_i) \right]_4 + \left(\left[I_{x_I^T} \right]_8 - \left[I_{v_I^A} \right]_3 \right) \left[x_{I}^{T/A}(t_i) \right]_7 \right\} / \left(\left[x_{I}^{T/A}(t_i) \right]_1^2 + \left[x_{I}^{T/A}(t_i) \right]_4^2 + \left[x_{I}^{T/A}(t_i) \right]_7^2 \right)^{1/2} + v_4(t_i) \quad (\text{III-10})$$

where

$T_{L}^I(t_i)_{ij}$ = the ij^{th} element of the transformation from the earth-fixed coordinate system to the tracker coordinate system at time t_i

The transformation $T_b^I(t_i)$ was calculated by transforming the relative position state estimates at time t_i to the attacker body coordinate frame using

$$\begin{bmatrix} [\hat{x}_b^{T/A}(t_i)]_1 \\ [\hat{x}_b^{T/A}(t_i)]_4 \\ [\hat{x}_b^{T/A}(t_i)]_7 \end{bmatrix} = T_b^I(t_i) \begin{bmatrix} [\hat{x}_I^{T/A}(t_i)]_1 \\ [\hat{x}_I^{T/A}(t_i)]_4 \\ [\hat{x}_I^{T/A}(t_i)]_7 \end{bmatrix} \quad (\text{III-11})$$

where

$T_b^I(t_i)$ = the transformation from the earth-fixed reference frame to the attacker body coordinate system at time t_i^{-C} assumed perfectly available from the IMU.

The subscript b denotes that a vector was coordinatized in the attacker body frame, and the ^ denotes estimated values from the filter. As discussed before, the transformation used was the true transformation available from the trajectory generating program. Then, the Euler angles $\eta(t_i^{-C})$ and $\nu(t_i^{-C})$ between the attacker's body coordinate system and the new estimated LCS based on the filter's estimate of target relative position at time t_i^{-C} (See Fig III-3) were calculated from the position vector defined by Eq III-11. These angles were assumed to be between -90 degrees and 90 degrees as discussed before. Therefore, the tangent relationships given by

$$\eta(t_i^{-C}) = \tan^{-1}([\hat{x}_b^{T/A}(t_i^{-C})]_4 / [\hat{x}_b^{T/A}(t_i^{-C})]_1) \quad (\text{III-12})$$

$$\nu(t_i^{-C}) = -\tan^{-1}([\hat{x}_b^{T/A}(t_i^{-C})]_7 / ([\hat{x}_b^{T/A}(t_i^{-C})]_1^2 + [\hat{x}_b^{T/A}(t_i^{-C})]_4^2)^{1/2}) \quad (\text{III-13})$$

were used. Once the angles $\eta(t_i^{-c})$ and $\nu(t_i^{-c})$ were calculated, the transformation $T_L^b(t_i^{-c})$ from the attacker body coordinate frame to the tracker (estimated LOS) coordinate system was found using

$$T_L^b(t_i^{-c}) = \begin{bmatrix} \text{cn}(t_i^{-c})\text{cv}(t_i^{-c}) & \text{sn}(t_i^{-c})\text{cv}(t_i^{-c}) & -\text{sv}(t_i^{-c}) \\ -\text{sn}(t_i^{-c}) & \text{cn}(t_i^{-c}) & 0 \\ \text{cn}(t_i^{-c})\text{sv}(t_i^{-c}) & \text{sn}(t_i^{-c})\text{sv}(t_i^{-c}) & \text{cv}(t_i^{-c}) \end{bmatrix} \quad (\text{III-14})$$

where s and c denote sine and cosine functions, respectively. (See Appendix A for the development of this transformation.) Finally, the transformation $T_L^I(t_i)$ required for the measurement equations was calculated from

$$T_L^I(t_i) = T_L^b(t_i^{-c})T_b^I(t_i) \quad (\text{III-15})$$

As with the tracker for the GMLOS filter, the measurements, Eqs III-7 to III-10, can be written in the form of Eq III-5, a nonlinear vector measurement equation.

Selection of Tracker Measurement Noises

The noises to be added to the true measurements were assumed to have the same statistical characterization for each tracker model since the same quantities were measured. The value of the variance of the noise for each measurement was based upon the capabilities of trackers in current fighter aircraft (Ref 4). The probability distribution of the error in the measurement was assumed to be well represented by a Gaussian distribution with a mean of zero. Also, since each measurement was made by an independent device, there were no noise cross correlations. Thus, the measurement noises were characterized by a Gaussian distribution with the properties

$$E[\underline{v}(t_i)] = 0 \quad (\text{III-16})$$

and

$$E[\underline{v}(t_i)\underline{v}^T(t_i)] = R(t_i)\delta_{ij} \quad (\text{III-17})$$

where

$$\delta_{ij} = \begin{cases} 0 & i \neq j \\ 1 & i = j \end{cases}$$

The covariances of the measurement noise $R(t_i)$ were defined by

$$R(t_i) = \begin{bmatrix} \sigma_R^2(t_i) & 0 & 0 & 0 \\ 0 & \sigma_e^2(t_i) & 0 & 0 \\ 0 & 0 & \sigma_a^2(t_i) & 0 \\ 0 & 0 & 0 & \sigma_{\dot{R}}^2(t_i) \end{bmatrix} \quad (\text{III-18})$$

The quantities $\sigma_R^2(t_i)$, $\sigma_e^2(t_i)$, $\sigma_a^2(t_i)$, and $\sigma_{\dot{R}}^2(t_i)$ were the variances of the range, tangent of the error angle e , tangent of the error angle a , and range rate measurement noises.

For the range measurement, the tracker was assumed to provide measurements with + 300 feet, which was considered a 3 sigma value. Therefore, the 1 sigma value σ_R was + 100 feet. The variance of the range measurement noise, σ_R^2 , was calculated from

$$\sigma_R^2 = (100 \text{ feet})^2 = 10000 \text{ feet}^2 \quad (\text{III-19})$$

The tracker was assumed to measure the tangent of either error angle to within + 0.030 radians (+ 1.72 degrees). Again, this was considered a 3 sigma value; the 1 sigma value σ_e or σ_a was + 0.010 radians.

Thus, the variances σ_e^2 and σ_a^2 for the measurement noise of the tangents of the error angles e and a were calculated from

$$\sigma_e^2 = (0.010)^2 = 0.0001 \quad (\text{III-20})$$

and

$$\sigma_a^2 = (0.010)^2 = 0.0001 \quad (\text{III-21})$$

Finally, the range rate measurement was assumed to be accurate within ± 75 feet per second. This gave a variance σ_R^2 for the range rate measurement noise calculated from

$$\sigma_R^2 = (25 \text{ feet/second})^2 = 625 \text{ feet}^2/\text{second}^2 \quad (\text{III-22})$$

A summary of the values for σ_R^2 , σ_e^2 , σ_a^2 , and σ_R^2 is presented in Table III-1. These values were used as the baseline for the variance of the measurement noises.

TABLE III-1

Measurement Noise Variances for Tracker Models

Measurement	Three Sigma Value for Error	Value Used in R Matrix
Range	300 feet	10000 feet ²
Tan e	0.030	0.0001
Tan a	0.030	0.0001
Range Rate	75 feet/second	625 feet ² /second ²

IV Extended Kalman Filter Implementation

Extended Kalman Filter

The extended Kalman filter approximation for the nonlinear filter was chosen since a new reference state trajectory for linearization would be used each time new state estimates were calculated, and the complexity of the solution was significantly less than other higher order methods available. The use of a new reference state trajectory for linearization provided performance that was far superior to a linearized Kalman filter since the nominal trajectory for an air-to-air tracking task was not known a priori. Further, the extended Kalman filter was compatible with a previously written simulation program used to evaluate Kalman filters (Ref 5). The equations (Ref 3) for the propagation of the state estimates and the propagation of the conditional covariance of the dynamics modeled by Eq II-43 and measurements modeled by Eq III-5 were

$$\hat{\underline{x}}(t/t_1) = \underline{f}[\hat{\underline{x}}(t/t_1)] \quad (\text{IV-1})$$

$$\hat{P}(t/t_1) = F[\hat{\underline{x}}(t/t_1)] P(t/t_1) + P(t/t_1) F[\hat{\underline{x}}(t/t_1)] + Q(t) \quad (\text{IV-2})$$

The update equations for the state estimates and conditional covariance were

$$K(t_1) = P(t_1^-) H^T[\hat{\underline{x}}(t_1^-)] \left\{ H[\hat{\underline{x}}(t_1^-)] P(t_1^-) H^T[\hat{\underline{x}}(t_1^-)] + R(t_1) \right\}^{-1} \quad (\text{IV-3})$$

$$\hat{\underline{x}}(t_1^+) = \hat{\underline{x}}(t_1^-) + K(t_1) \left\{ \underline{z}(t_1) - \underline{h}[\hat{\underline{x}}(t_1^-)] \right\} \quad (\text{IV-4})$$

$$P(t_1^+) = P(t_1^-) - K(t_1) H[\hat{\underline{x}}(t_1^-)] P(t_1^-) \quad (\text{IV-5})$$

where

$\hat{\underline{x}}(t/t_i)$ = state estimate at time t for $t \in (t_i, t_{i+1})$
based on the initial conditions $\hat{\underline{x}}(t_i/t_i) = \underline{x}(t_i^+)$,
i.e., on measurements through time t_i

$\underline{f}[\hat{\underline{x}}(t/t_i)]$ = the dynamics model as a function of
 $\hat{\underline{x}}(t/t_i)$

$P(t/t_i)$ = filter's conditional error covariance
matrix at time t based on the initial
condition $P(t_i/t_i) = P(t_i^+)$, i.e., on
measurements through time t_i

$\underline{q}(t)$ = the descriptor of the strength of the
dynamic driving noise vector, $\underline{w}(t)$, at
time t

$P(t_i^-)$ = filter's conditional covariance matrix
just before the update time t_i

$K(t_i)$ = filter's gain matrix at time t_i

$R(t_i)$ = covariance matrix of measurement noises

$\underline{z}(t_i)$ = true measurement vector at time t_i

$\underline{h}[\hat{\underline{x}}(t_i^-)]$ = measurement model vector evaluated
using $\hat{\underline{x}}(t_i^-)$

and

$$\underline{F}[\hat{\underline{x}}(t/t_i)] \triangleq \left[\frac{\partial \underline{f}(\underline{x})}{\partial \underline{x}} \right]_{\underline{x} = \hat{\underline{x}}(t/t_i)} \quad (\text{IV-6})$$

and

$$\underline{H}[\hat{\underline{x}}(t_i^-)] \triangleq \left[\frac{\partial \underline{h}(\underline{x})}{\partial \underline{x}} \right]_{\underline{x} = \hat{\underline{x}}(t_i^-)} \quad (\text{IV-7})$$

Note that the dynamic driving noise vector $\underline{w}(t)$ was assumed to be a zero mean white Gaussian noise (as described in Section II) with covariance given by

$$E [\underline{w}(t)\underline{w}^T(t+\tau)] = Q(t)\delta(\tau) \quad (IV-8)$$

Extended Kalman Filter for Gauss-Markov Line of Sight Model

The implementation of the GMLOS model in the extended Kalman filter required not only the calculation of the F and H matrices, but, also the transformation of the state estimates and the filter's conditional covariance at time t_1^C to the new filter coordinate frame calculated from the position state estimates at time t_1^C . The calculation of the F matrix for the GMLOS dynamics model (Eq II-12) was straightforward since the dynamics model described a linear stochastic system. Using Eq IV-6, the F matrix for the GMLOS dynamics model was

$$F [\hat{\underline{x}}(t/t_1)] = \begin{bmatrix} 0 & 1 & 0 & | & 0 & 0 & 0 & | & 0 & 0 & 0 \\ 0 & 0 & 1 & | & 0 & 0 & 0 & | & 0 & 0 & 0 \\ 0 & 0 & \frac{1}{\tau_1} & | & 0 & 0 & 0 & | & 0 & 0 & 0 \\ - & - & - & - & - & - & - & - & - & - & - \\ 0 & 0 & 0 & | & 0 & 1 & 0 & | & 0 & 0 & 0 \\ 0 & 0 & 0 & | & 0 & 0 & 1 & | & 0 & 0 & 0 \\ 0 & 0 & 0 & | & 0 & 0 & -\frac{1}{\tau_2} & | & 0 & 0 & 0 \\ - & - & - & - & - & - & - & - & - & - & - \\ 0 & 0 & 0 & | & 0 & 0 & 0 & | & 0 & 1 & 0 \\ 0 & 0 & 0 & | & 0 & 0 & 0 & | & 0 & 0 & 1 \\ 0 & 0 & 0 & | & 0 & 0 & 0 & | & 0 & 0 & -\frac{1}{\tau_3} \end{bmatrix} \quad (IV-9)$$

$\underline{x} = \hat{\underline{x}}(t/t_1)$

Note that the correlation time constants were assumed to be time invariant since the target's acceleration probability distribution was assumed constant with time (i.e., the target's configuration did not change during the engagement): Also, the correlation time constants were assumed to be equal since out-of-plane tracking was anticipated. (Note that when in-plane tracking is anticipated, the correlation time constants are not assumed to be equal.)

The calculation of the H matrix was more difficult since the measurement model for the GMLOS filter was nonlinear. Using Eq IV-7, the H matrix for the tracker measurement model used with the GMLOS filter (Eqs III-1 to III-4) was

$$H[\hat{\underline{x}}(t_i^-)] = \begin{bmatrix} H_1 & 0 & 0 & H_2 & 0 & 0 & H_3 & 0 & 0 \\ H_4 & 0 & 0 & 0 & 0 & 0 & H_5 & 0 & 0 \\ H_6 & 0 & 0 & H_7 & 0 & 0 & 0 & 0 & 0 \\ H_8 & H_9 & 0 & H_{10} & H_{11} & 0 & H_{12} & H_{13} & 0 \end{bmatrix} \quad (IV-10)$$

$\underline{x} = \hat{\underline{x}}(t_i^-)$

where

$$H_1 = \frac{[x_{\hat{L}}^{T/A}(t_i)]_1}{\left([x_{\hat{L}}^{T/A}(t_i)]_1^2 + [x_{\hat{L}}^{T/A}(t_i)]_4^2 + [x_{\hat{L}}^{T/A}(t_i)]_7^2 \right)^{1/2}}$$

$$H_2 = \frac{[x_{\hat{L}}^{T/A}(t_i)]_4}{\left([x_{\hat{L}}^{T/A}(t_i)]_1^2 + [x_{\hat{L}}^{T/A}(t_i)]_4^2 + [x_{\hat{L}}^{T/A}(t_i)]_7^2 \right)^{1/2}}$$

$$H_3 = \frac{[x_{\hat{L}}^{T/A}(t_i)]_7}{\left([x_{\hat{L}}^{T/A}(t_i)]_1^2 + [x_{\hat{L}}^{T/A}(t_i)]_4^2 + [x_{\hat{L}}^{T/A}(t_i)]_7^2 \right)^{1/2}}$$

$$H_4 = \frac{[x_{\hat{L}}^{T/A}(t_i)]_7}{[x_{\hat{L}}^{T/A}(t_i)]_1^2}$$

$$H_5 = -\frac{1}{[x_{\hat{L}}^{T/A}(t_i)]_1}$$

$$H_6 = -\frac{[x_{\hat{L}}^{T/A}(t_i)]_4}{[x_{\hat{L}}^{T/A}(t_i)]_1^2}$$

$$H_7 = \frac{1}{[x_{\hat{L}}^{T/A}(t_i)]_1}$$

$$H_8 = \left\{ [x_{\hat{L}}^{T/A}(t_i)]_2 \left([x_{\hat{L}}^{T/A}(t_i)]_1^2 + [x_{\hat{L}}^{T/A}(t_i)]_4^2 + [x_{\hat{L}}^{T/A}(t_i)]_7^2 \right) \right. \\ \left. - [x_{\hat{L}}^{T/A}(t_i)]_1 \left([x_{\hat{L}}^{T/A}(t_i)]_1 [x_{\hat{L}}^{T/A}(t_i)]_2 \right) \right. \\ \left. + [x_{\hat{L}}^{T/A}(t_i)]_4 [x_{\hat{L}}^{T/A}(t_i)]_5 + [x_{\hat{L}}^{T/A}(t_i)]_7 [x_{\hat{L}}^{T/A}(t_i)]_8 \right\} \\ \left. / \left([x_{\hat{L}}^{T/A}(t_i)]_1^2 + [x_{\hat{L}}^{T/A}(t_i)]_4^2 + [x_{\hat{L}}^{T/A}(t_i)]_7^2 \right)^{3/2}$$

$$H_9 = \frac{[x_{\hat{L}}^{T/A}(t_i)]_1}{\left([x_{\hat{L}}^{T/A}(t_i)]_1^2 + [x_{\hat{L}}^{T/A}(t_i)]_4^2 + [x_{\hat{L}}^{T/A}(t_i)]_7^2 \right)^{1/2}}$$

$$\begin{aligned}
H_{10} = & \left\{ \left[I_{x \hat{L}}^{T/A}(t_i) \right]_5 \left(\left[x_{\hat{L}}^{T/A}(t_i) \right]_1^2 + \left[x_{\hat{L}}^{T/A}(t_i) \right]_4^2 + \left[x_{\hat{L}}^{T/A}(t_i) \right]_7^2 \right) \right. \\
& - \left[x_{\hat{L}}^{T/A}(t_i) \right]_4 \left(\left[x_{\hat{L}}^{T/A}(t_i) \right]_1 \left[I_{x \hat{L}}^{T/A}(t_i) \right]_2 \right. \\
& \left. \left. + \left[x_{\hat{L}}^{T/A}(t_i) \right]_4 \left[I_{x \hat{L}}^{T/A}(t_i) \right]_5 + \left[x_{\hat{L}}^{T/A}(t_i) \right]_7 \left[I_{x \hat{L}}^{T/A}(t_i) \right]_8 \right) \right\} \\
& / \left(\left[x_{\hat{L}}^{T/A}(t_i) \right]_1^2 + \left[x_{\hat{L}}^{T/A}(t_i) \right]_4^2 + \left[x_{\hat{L}}^{T/A}(t_i) \right]_7^2 \right)^{3/2}
\end{aligned}$$

$$H_{11} = \frac{\left[x_{\hat{L}}^{T/A}(t_i) \right]_4}{\left(\left[x_{\hat{L}}^{T/A}(t_i) \right]_1^2 + \left[x_{\hat{L}}^{T/A}(t_i) \right]_4^2 + \left[x_{\hat{L}}^{T/A}(t_i) \right]_7^2 \right)^{1/2}}$$

$$\begin{aligned}
H_{12} = & \left\{ \left[I_{x \hat{L}}^{T/A}(t_i) \right]_8 \left(\left[x_{\hat{L}}^{T/A}(t_i) \right]_1^2 + \left[x_{\hat{L}}^{T/A}(t_i) \right]_4^2 + \left[x_{\hat{L}}^{T/A}(t_i) \right]_7^2 \right) \right. \\
& - \left[x_{\hat{L}}^{T/A}(t_i) \right]_7 \left(\left[x_{\hat{L}}^{T/A}(t_i) \right]_1 \left[I_{x \hat{L}}^{T/A}(t_i) \right]_2 \right. \\
& \left. \left. + \left[x_{\hat{L}}^{T/A}(t_i) \right]_4 \left[I_{x \hat{L}}^{T/A}(t_i) \right]_5 + \left[x_{\hat{L}}^{T/A}(t_i) \right]_7 \left[I_{x \hat{L}}^{T/A}(t_i) \right]_8 \right) \right\} \\
& / \left(\left[x_{\hat{L}}^{T/A}(t_i) \right]_1^2 + \left[x_{\hat{L}}^{T/A}(t_i) \right]_4^2 + \left[x_{\hat{L}}^{T/A}(t_i) \right]_7^2 \right)^{3/2}
\end{aligned}$$

$$H_{13} = \frac{\left[x_{\hat{L}}^{T/A}(t_i) \right]_7}{\left(\left[x_{\hat{L}}^{T/A}(t_i) \right]_1^2 + \left[x_{\hat{L}}^{T/A}(t_i) \right]_4^2 + \left[x_{\hat{L}}^{T/A}(t_i) \right]_7^2 \right)^{1/2}}$$

The transformation of the state estimates from the current filter's coordinate frame \hat{L}_C at time t_i^C to the new coordinate frame \hat{L}_n at time t_i^T based on the position state estimates at t_i^C was accomplished by

$$\hat{x}_{L_n}^{\wedge}(t_i^{-F}) = T_{L_n}^{\wedge L_c}(t_i^{-}) \hat{x}_{L_c}^{\wedge}(t_i^{-C}) \quad (IV-11)$$

where

$$T_{L_n}^{\wedge L_c}(t_i^{-}) = \begin{bmatrix} T_{11} & 0 & 0 & T_{12} & 0 & 0 & T_{13} & 0 & 0 \\ 0 & T_{11} & 0 & 0 & T_{12} & 0 & 0 & T_{13} & 0 \\ 0 & 0 & T_{11} & 0 & 0 & T_{12} & 0 & 0 & T_{13} \\ T_{21} & 0 & 0 & T_{22} & 0 & 0 & T_{23} & 0 & 0 \\ 0 & T_{21} & 0 & 0 & T_{22} & 0 & 0 & T_{23} & 0 \\ 0 & 0 & T_{21} & 0 & 0 & T_{22} & 0 & 0 & T_{23} \\ T_{31} & 0 & 0 & T_{32} & 0 & 0 & T_{33} & 0 & 0 \\ 0 & T_{31} & 0 & 0 & T_{32} & 0 & 0 & T_{33} & 0 \\ 0 & 0 & T_{31} & 0 & 0 & T_{32} & 0 & 0 & T_{33} \end{bmatrix}$$

and T_{ij} is the ij^{th} element of the transformation $T_{L_n}^{\wedge L_c}(t_i^{-})$ from the current GMLOS coordinate system to the new coordinate system. Now,

$$T_{L_n}^{\wedge L_c}(t_i^{-}) = T_{L_n}^I(t_i^{-}) T_I^{\wedge L_c}(t_i^{-}) \quad (IV-12)$$

where

$T_I^{\wedge L_c}(t_i^{-})$ = the inverse of the transformation $T_{L_n}^I(t_{i-1}^{-})$ from the earth-fixed coordinate system to the GMLOS filter's coordinate frame at time t_i^{-}

$T_{L_n}^I(t_i^-)$ = the transformation from the earth-fixed reference frame to the GMLOS coordinate frame based on the position state estimates at t_i^-

These transformations are discussed in more detail later in this section.

The filter's conditional covariance matrix $P(t_i^-)$ was transformed from the current GMLOS coordinate frame to the new frame using

$$P_{L_n}^{\wedge}(t_i^{-F}) = T_{L_n}^{\wedge L_c}(t_i^-) P_{L_c}^{\wedge}(t_i^{-C}) T_{L_n}^{\wedge L_c}(t_i^-)^T \quad (IV-13)$$

This equation was developed from the definition of the conditional covariance expressed in the current coordinate frame given by

$$P_{L_c}^{\wedge}(t_i^{-C}) = E \left\{ \left[\underline{x}_{L_c}^{\wedge}(t_i) - \hat{\underline{x}}_{L_c}^{\wedge}(t_i^{-C}) \right] \left[\underline{x}_{L_c}^{\wedge}(t_i) - \hat{\underline{x}}_{L_c}^{\wedge}(t_i^{-C}) \right]^T \right. \\ \left. \left| \underline{g}(t_{i-1}) = \underline{g}_{i-1} \right. \right\} \quad (IV-14)$$

where

$\underline{g}(t_{i-1})$ = the random vector representing the entire measurement history at time t_{i-1}

\underline{g}_{i-1} = realized measurement values at time t_{i-1} for a single trial

Likewise, the conditional covariance in the new coordinate frame was expressed as

$$P_{L_n}^{\wedge}(t_i^{-F}) = E \left\{ \left[\underline{x}_{L_n}^{\wedge}(t_i) - \hat{\underline{x}}_{L_n}^{\wedge}(t_i^{-F}) \right] \left[\underline{x}_{L_n}^{\wedge}(t_i) - \hat{\underline{x}}_{L_n}^{\wedge}(t_i^{-F}) \right]^T \right. \\ \left. \left| \underline{g}(t_{i-1}) = \underline{g}_{i-1} \right. \right\} \quad (IV-15)$$

substituting Eq IV-11 into Eq IV-15, and noting that

$$\underline{x}_{L_n}^{\wedge}(t_i) = T_{L_n}^{\wedge L_c}(t_i^-) \underline{x}_{L_c}^{\wedge}(t_i) \quad (IV-16)$$

then

$$P_{\hat{x}_{L_n}}(t_i^{-r}) = E \left\{ T_{L_n}^{\hat{L}_c}(t_i^{-r}) \left[\hat{x}_{L_c}(t_i^{-r}) - \hat{x}_{L_c}(t_i^{-c}) \right] \left[\hat{x}_{L_c}(t_i^{-r}) - \hat{x}_{L_c}(t_i^{-c}) \right]^T \right. \\ \left. T_{L_n}^{\hat{L}_c}(t_i)^T \mid \underline{z}(t_{i-1}) = \underline{z}_{i-1} \right\} \quad (IV-17)$$

Now, since the transformation $T_{L_n}^{\hat{L}_c}$ was a deterministic function of the realization \underline{z}_{i-1} , Eq IV-17 was written as

$$P_{\hat{x}_{L_n}}(t_i^{-r}) = T_{L_n}^{\hat{L}_c}(t_i^{-r}) E \left\{ \left[\hat{x}_{L_c}(t_i^{-r}) - \hat{x}_{L_c}(t_i^{-c}) \right] \left[\hat{x}_{L_c}(t_i^{-r}) - \hat{x}_{L_c}(t_i^{-c}) \right]^T \right. \\ \left. \mid \underline{z}(t_{i-1}) = \underline{z}_{i-1} \right\} T_{L_n}^{\hat{L}_c}(t_i)^T \quad (IV-18)$$

which became Eq IV-13 when Eq IV-14 was substituted into Eq IV-18.

As stated earlier, the transformation $T_{L_n}^{\hat{L}_c}(t_i^{-r})$ was calculated using Eq IV-12. Since the GMLOS filter's coordinate frame was assumed to be space-stabilized from t_{i-1}^{-r} to t_i^{-c} , the transformation $T_{I_c}^{\hat{L}_c}(t_i^{-r})$ was the inverse of the transformation $T_{I_n}^{\hat{L}_c}(t_{i-1})$, which was calculated after the impulsive rotation but before the measurement update at time t_{i-1}^{-r} . The second transformation $T_{L_n}^I(t_i^{-r})$ required to evaluate the transformation $T_{L_n}^{\hat{L}_c}(t_i^{-r})$ was calculated from the position state estimates coordinated in the earth-fixed reference system at time t_i^{-c} given by

$$\begin{bmatrix} \left[\hat{x}_{I_n}^{T/A}(t_i^{-c}) \right]_1 \\ \left[\hat{x}_{I_n}^{T/A}(t_i^{-c}) \right]_4 \\ \left[\hat{x}_{I_n}^{T/A}(t_i^{-c}) \right]_7 \end{bmatrix} = T_{I_c}^{\hat{L}_c}(t_i^{-r}) \begin{bmatrix} \left[\hat{x}_{L_c}^{T/A}(t_i^{-c}) \right]_1 \\ \left[\hat{x}_{L_c}^{T/A}(t_i^{-c}) \right]_4 \\ \left[\hat{x}_{L_c}^{T/A}(t_i^{-c}) \right]_7 \end{bmatrix} \quad (IV-19)$$

The sine and cosine of the Euler rotation angles, $\eta(t_i^-)$ from the north axis of the earth-fixed reference frame to the projection of the new LOS in the north-east plane of the earth-fixed reference frame and $\nu(t_i^-)$ from the projection of the new LOS in the north-east plane to the estimated LOS (See Fig IV-1), were calculated from

$$\sin \eta(t_i^-) = \frac{[\hat{x}_I^{T/A}(t_i^-)]_4}{\left([\hat{x}_I^{T/A}(t_i^-)]_1^2 + [\hat{x}_I^{T/A}(t_i^-)]_4^2\right)^{1/2}} \quad (\text{IV-20})$$

$$\cos \eta(t_i^-) = \frac{[\hat{x}_I^{T/A}(t_i^-)]_1}{\left([\hat{x}_I^{T/A}(t_i^-)]_1^2 + [\hat{x}_I^{T/A}(t_i^-)]_4^2\right)^{1/2}} \quad (\text{IV-21})$$

$$\sin \nu(t_i^-) = \frac{[\hat{x}_I^{T/A}(t_i^-)]_7}{\left([\hat{x}_I^{T/A}(t_i^-)]_1^2 + [\hat{x}_I^{T/A}(t_i^-)]_4^2 + [\hat{x}_I^{T/A}(t_i^-)]_7^2\right)^{1/2}} \quad (\text{IV-22})$$

$$\cos \nu(t_i^-) = \frac{\left([\hat{x}_I^{T/A}(t_i^-)]_1^2 + [\hat{x}_I^{T/A}(t_i^-)]_4^2\right)^{1/2}}{\left([\hat{x}_I^{T/A}(t_i^-)]_1^2 + [\hat{x}_I^{T/A}(t_i^-)]_4^2 + [\hat{x}_I^{T/A}(t_i^-)]_7^2\right)^{1/2}} \quad (\text{IV-23})$$

Once the sine and cosine values were calculated, the transformation

$T_{I_h}^I(t_i^-)$ was evaluated using

$$T_{I_h}^I(t_i^-) = \begin{bmatrix} \cos \eta(t_i^-) \cos \nu(t_i^-) & \sin \eta(t_i^-) \cos \nu(t_i^-) & -\sin \nu(t_i^-) \\ -\sin \eta(t_i^-) & \cos \eta(t_i^-) & 0 \\ \cos \eta(t_i^-) \sin \nu(t_i^-) & \sin \eta(t_i^-) \sin \nu(t_i^-) & \cos \nu(t_i^-) \end{bmatrix} \quad (\text{IV-24})$$

(See Appendix A for development of this transformation.)

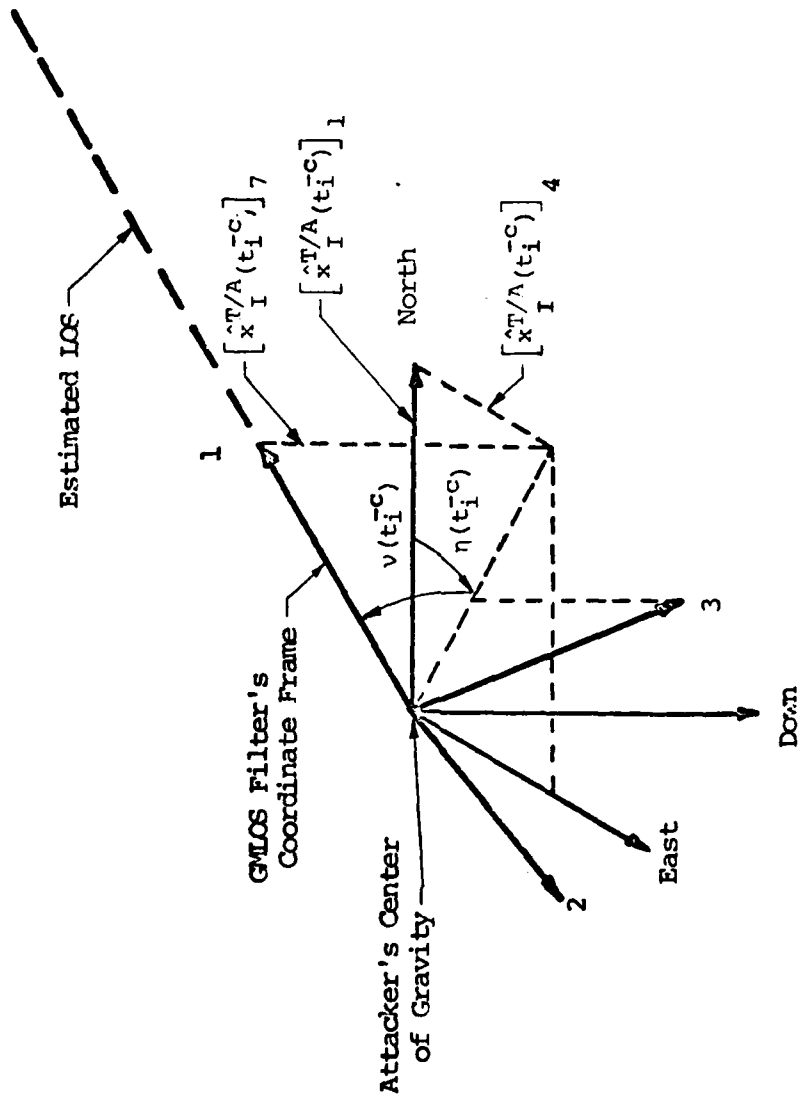


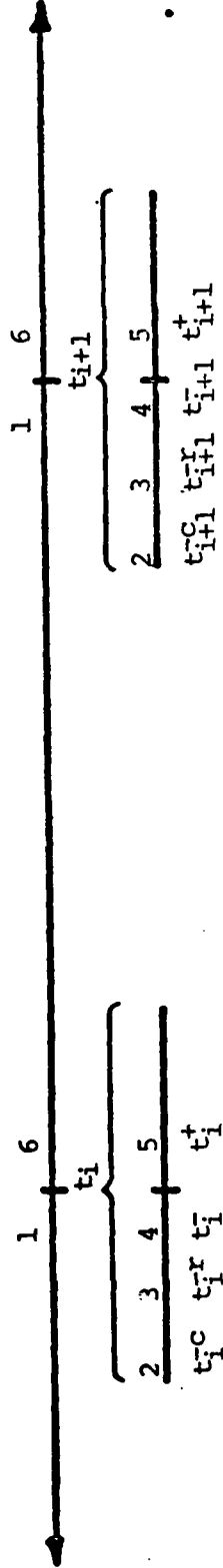
Figure IV-1. Orientation of GMLOS Filter's Coordinate Frame to the Earth-Fixed Reference System at Time t_i^c

The timing of the events for the GMLOS extended Kalman filter is shown in Fig IV-2, and the block diagram is depicted in Fig IV-3. The state estimates $\hat{x}_{L_C}(t)$ and conditional covariance $P_{L_C}(t)$ were propagated forward in time to time t_i^{-C} in the current estimated LOS coordinate frame (\hat{L}_C). At time t_i , the state estimates and conditional covariance were sampled, and the transformation $T_{L_C}^{\hat{L}_n}$ from the current estimated LOS (filter's) coordinate frame \hat{L}_C to the new estimated (filter's) coordinate frame \hat{L}_n was calculated. This transformation was used to realign the tracker, and both the state estimates and conditional covariance were expressed in the new coordinate system. Then, the estimates of the measurements were calculated from the state estimates, the Kalman filter gain $K(t_i)$ was calculated from the conditional covariance, and the conditional covariance update was performed. Finally, the measurement residuals were calculated, multiplied times the Kalman filter gain, and summed with the state estimates to generate the state estimates after the measurement update at time t_i^+ .

Extended Kalman Filter for Gauss-Markov Inertial Model

The implementation of the GMI extended Kalman filter required only the evaluation of the F and H matrices since the coordinate frame was not rotated to a new position at time t_i^+ as was the coordinate frame for the GMLOS filter. Like the GMLOS model, the calculation of the F matrix was straightforward since the dynamics were represented by a linear stochastic model. Using Eq IV-6, the F matrix for the GMI dynamics model was given by Eq IV-9. Again, the correlation time constants were assumed to be time invariant and equal since the target was assumed to have the same acceleration capability along any axis.

The calculation of the H matrix for the GMI model from Eqs III-7 to III-10 was more difficult and involved two approximations in the two



1. End of propagation
2. Calculation of new direction cosine matrix $T_{L_n}^{C}(t_i)$ to realign filter's coordinate frame and tracker's coordinate frame.
3. State estimates and filter's conditional covariance matrix transformed to new coordinate system. Tracker realigned impulsively.
4. Ready for update
5. Update complete
6. Start of propagation

Figure IV-2. Timing Sequence for Extended Kalman Filter Implementation of GMLOS Filter

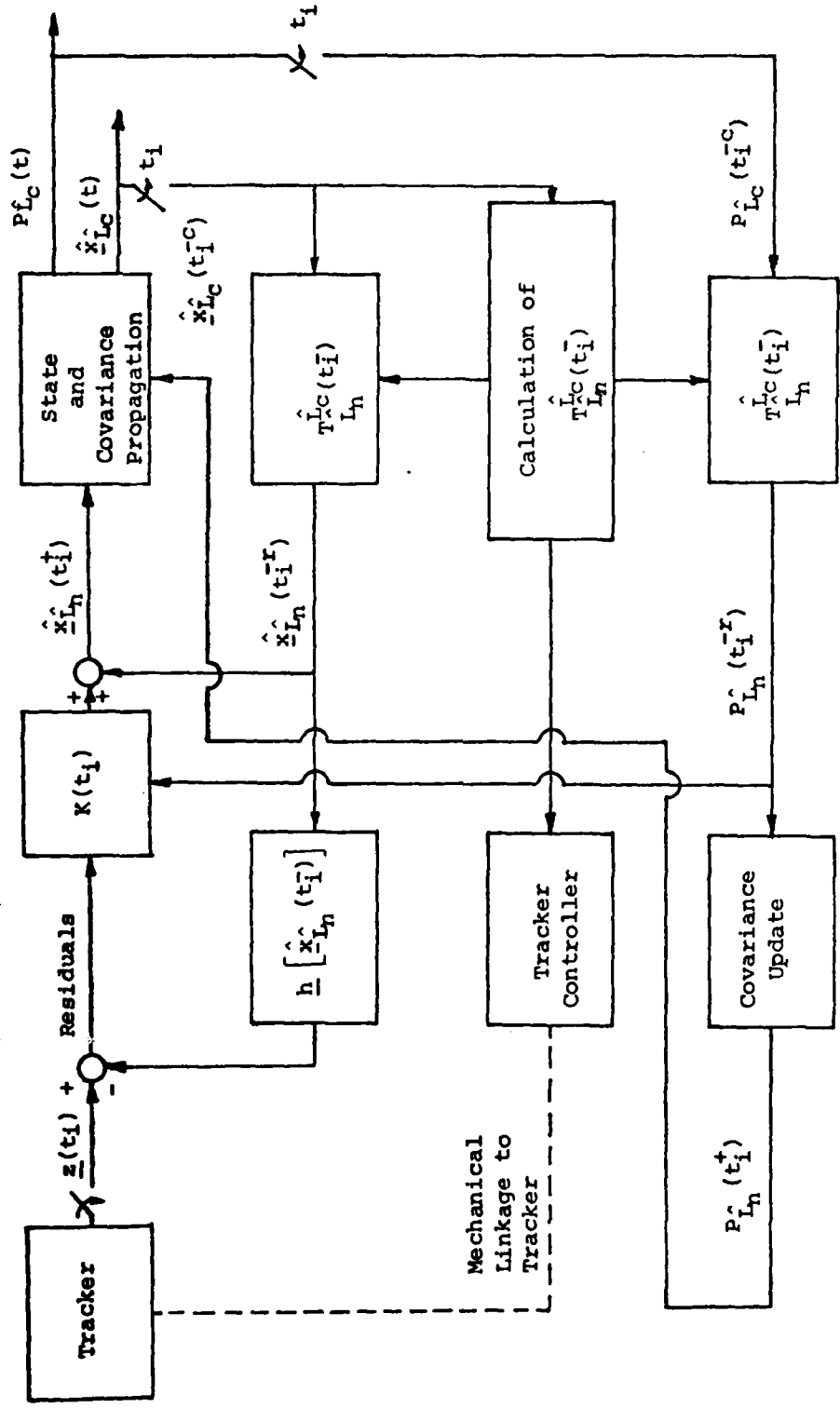


Figure IV-3. Block Diagram for GMLOS Extended Kalman Filter

angle measurements. Since the measurements of the tangent of the error angles a and e involved the transformation from the earth-fixed to the tracker coordinate system, and this transformation was a function of the position states, the fully-expanded H matrix required the partial derivative of the transformation matrix with respect to the state vector. However, the terms involving the partial derivatives of the transformation were assumed small when compared with the other terms (See Ref 6) and were ignored for the evaluation of the H matrix for the inertial filters evaluated in this thesis. Also, the denominator of Eqs III-8 and III-9 were assumed constant (Ref 6). With these assumptions, the H matrix became

$$H[\hat{\underline{x}}(t_i^-)] = \begin{bmatrix} H_1 & 0 & 0 & H_2 & 0 & 0 & H_3 & 0 & 0 \\ H_4 & 0 & 0 & H_5 & 0 & 0 & H_6 & 0 & 0 \\ H_7 & 0 & 0 & H_8 & 0 & 0 & H_9 & 0 & 0 \\ H_{10} & H_{11} & 0 & H_{12} & H_{13} & 0 & H_{14} & H_{15} & 0 \end{bmatrix} \quad (IV-25)$$

$\underline{x} = \hat{\underline{x}}(t_i^-)$

where

$$H_1 = \frac{[x_I^{T/A}(t_i)]_1}{\left([x_I^{T/A}(t_i)]_1^2 + [x_I^{T/A}(t_i)]_4^2 + [x_I^{T/A}(t_i)]_7^2 \right)^{1/2}}$$

$$H_2 = \frac{[x_I^{T/A}(t_i)]_4}{\left([x_I^{T/A}(t_i)]_1^2 + [x_I^{T/A}(t_i)]_4^2 + [x_I^{T/A}(t_i)]_7^2 \right)^{1/2}}$$

$$H_3 = \frac{[x_{\hat{I}}^{T/A}(t_i)]_7}{\left([x_{\hat{I}}^{T/A}(t_i)]_1^2 + [x_{\hat{I}}^{T/A}(t_i)]_4^2 + [x_{\hat{I}}^{T/A}(t_i)]_7^2 \right)^{1/2}}$$

$$H_4 = - \frac{[T_{\hat{L}}^I(t_i)]_{31}}{[x_{\hat{L}}^{T/A}(t_i)]_1}$$

$$H_5 = - \frac{[T_{\hat{L}}^I(t_i)]_{32}}{[x_{\hat{L}}^{T/A}(t_i)]_1}$$

$$H_6 = - \frac{[T_{\hat{L}}^I(t_i)]_{33}}{[x_{\hat{L}}^{T/A}(t_i)]_1}$$

$$H_7 = \frac{[T_{\hat{L}}^I(t_i)]_{21}}{[x_{\hat{L}}^{T/A}(t_i)]_1}$$

$$H_8 = \frac{[T_{\hat{L}}^I(t_i)]_{22}}{[x_{\hat{L}}^{T/A}(t_i)]_1}$$

$$H_9 = \frac{[T_{\hat{L}}^I(t_i)]_{23}}{[x_{\hat{L}}^{T/A}(t_i)]_1}$$

$$\begin{aligned}
H_{10} = & \left\{ \left([I_{x_I^T}(t_i)]_2 - [I_{v_I^A}(t_i)]_1 \right) \left([x_I^{T/A}(t_i)]_1^2 + [x_I^{T/A}(t_i)]_4^2 + [x_I^{T/A}(t_i)]_7^2 \right) \right. \\
& - [x_I^{T/A}(t_i)]_1 \left. \left([I_{x_I^T}(t_i)]_2 - [I_{v_I^A}(t_i)]_1 \right) [x_I^{T/A}(t_i)]_1 \right. \\
& + \left([I_{x_I^T}(t_i)]_5 - [I_{v_I^A}(t_i)]_2 \right) [x_I^{T/A}(t_i)]_4 \\
& \left. + \left([I_{x_I^T}(t_i)]_8 - [I_{v_I^A}(t_i)]_3 \right) [x_I^{T/A}(t_i)]_7 \right\} \\
& / \left([x_I^{T/A}(t_i)]_1^2 + [x_I^{T/A}(t_i)]_4^2 + [x_I^{T/A}(t_i)]_7^2 \right)^{3/2}
\end{aligned}$$

$$H_{11} = \frac{[x_I^{T/A}(t_i)]_1}{\left([x_I^{T/A}(t_i)]_1^2 + [x_I^{T/A}(t_i)]_4^2 + [x_I^{T/A}(t_i)]_7^2 \right)^{1/2}}$$

$$\begin{aligned}
H_{12} = & \left\{ \left([I_{x_I^T}(t_i)]_5 - [I_{v_I^A}(t_i)]_2 \right) \left([x_I^{T/A}(t_i)]_1^2 + [x_I^{T/A}(t_i)]_4^2 + [x_I^{T/A}(t_i)]_7^2 \right) \right. \\
& - [x_I^{T/A}(t_i)]_4 \left. \left([I_{x_I^T}(t_i)]_2 - [I_{v_I^A}(t_i)]_1 \right) [x_I^{T/A}(t_i)]_1 \right. \\
& + \left([I_{x_I^T}(t_i)]_5 - [I_{v_I^A}(t_i)]_2 \right) [x_I^{T/A}(t_i)]_4 \\
& \left. + \left([I_{x_I^T}(t_i)]_8 - [I_{v_I^A}(t_i)]_3 \right) [x_I^{T/A}(t_i)]_7 \right\} \\
& / \left([x_I^{T/A}(t_i)]_1^2 + [x_I^{T/A}(t_i)]_4^2 + [x_I^{T/A}(t_i)]_7^2 \right)^{3/2}
\end{aligned}$$

$$H_{13} = \frac{[x_I^{T/A}(t_i)]_4}{\left([x_I^{T/A}(t_i)]_1^2 + [x_I^{T/A}(t_i)]_4^2 + [x_I^{T/A}(t_i)]_7^2 \right)^{1/2}}$$

$$\begin{aligned}
H_{14} = & \left\{ \left([I_{x_I^T}(t_i)]_8 - [I_{v_I^A}(t_i)]_3 \right) \left([x_I^{T/A}(t_i)]_1^2 + [x_I^{T/A}(t_i)]_4^2 + [x_I^{T/A}(t_i)]_7^2 \right) \right. \\
& - [x_I^{T/A}(t_i)]_7 \left[\left([I_{x_I^T}(t_i)]_2 - [I_{v_I^A}(t_i)]_1 \right) [x_I^{T/A}(t_i)]_1 \right. \\
& + \left. \left([I_{x_I^T}(t_i)]_5 - [I_{v_I^A}(t_i)]_2 \right) [x_I^{T/A}(t_i)]_4 \right. \\
& \left. \left. + \left([I_{x_I^T}(t_i)]_8 - [I_{v_I^A}(t_i)]_3 \right) [x_I^{T/A}(t_i)]_7 \right] \right\} \\
& / \left([x_I^{T/A}(t_i)]_1^2 + [x_I^{T/A}(t_i)]_4^2 + [x_I^{T/A}(t_i)]_7^2 \right)^{3/2} \\
& [x_I^{T/A}(t_i)]_7
\end{aligned}$$

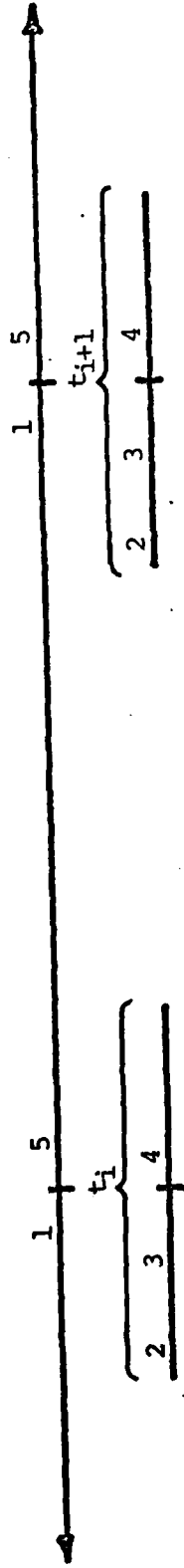
$$H_{15} = \frac{[x_I^{T/A}(t_i)]_7}{\left([x_I^{T/A}(t_i)]_1^2 + [x_I^{T/A}(t_i)]_4^2 + [x_I^{T/A}(t_i)]_7^2 \right)^{1/2}}$$

and

$$\begin{aligned}
[x_I^{T/A}(t_i)]_1 \triangleq & [T_{\hat{L}}^I(t_i)]_{11} [x_I^{T/A}(t_i)]_1 + [T_{\hat{L}}^I(t_i)]_{12} [x_I^{T/A}(t_i)]_4 \\
& + [T_{\hat{L}}^I(t_i)]_{13} [x_I^{T/A}(t_i)]_7
\end{aligned}$$

was the magnitude of the position estimate along the 1-axis of the tracker's (estimated LOS) coordinate frame.

As discussed in Section III, the tracker was pointed along the new estimated LOS calculated from the position estimates at time t_i^C . The timing sequence used for the GMI extended Kalman filter implementation is summarized in Fig IV-4, and the block diagram is presented in Fig IV-5. The state estimates $\hat{x}_I(t)$ were propagated forward in time to time t_i when the state estimates were sampled. The state estimates $\hat{x}_I(t_i^-)$ at time t_i^- were used to calculate the estimates of the measurements from the vector $h[\hat{x}_I(t_i^-)]$ and the transformation $T_{\hat{L}}^I(t_i)$ for the tracker (as discussed in Section III). The measurement residuals were



1. Propagation complete.
2. Direction cosine matrix $T_L^I(t_i)$ calculated and tracker moved to new position.
3. Ready for update.
4. Update complete.
5. Start propagation.

Figure IV-4. Timing Sequence for Extended Kalman Filter Implementation of GMI and CTRI Filters

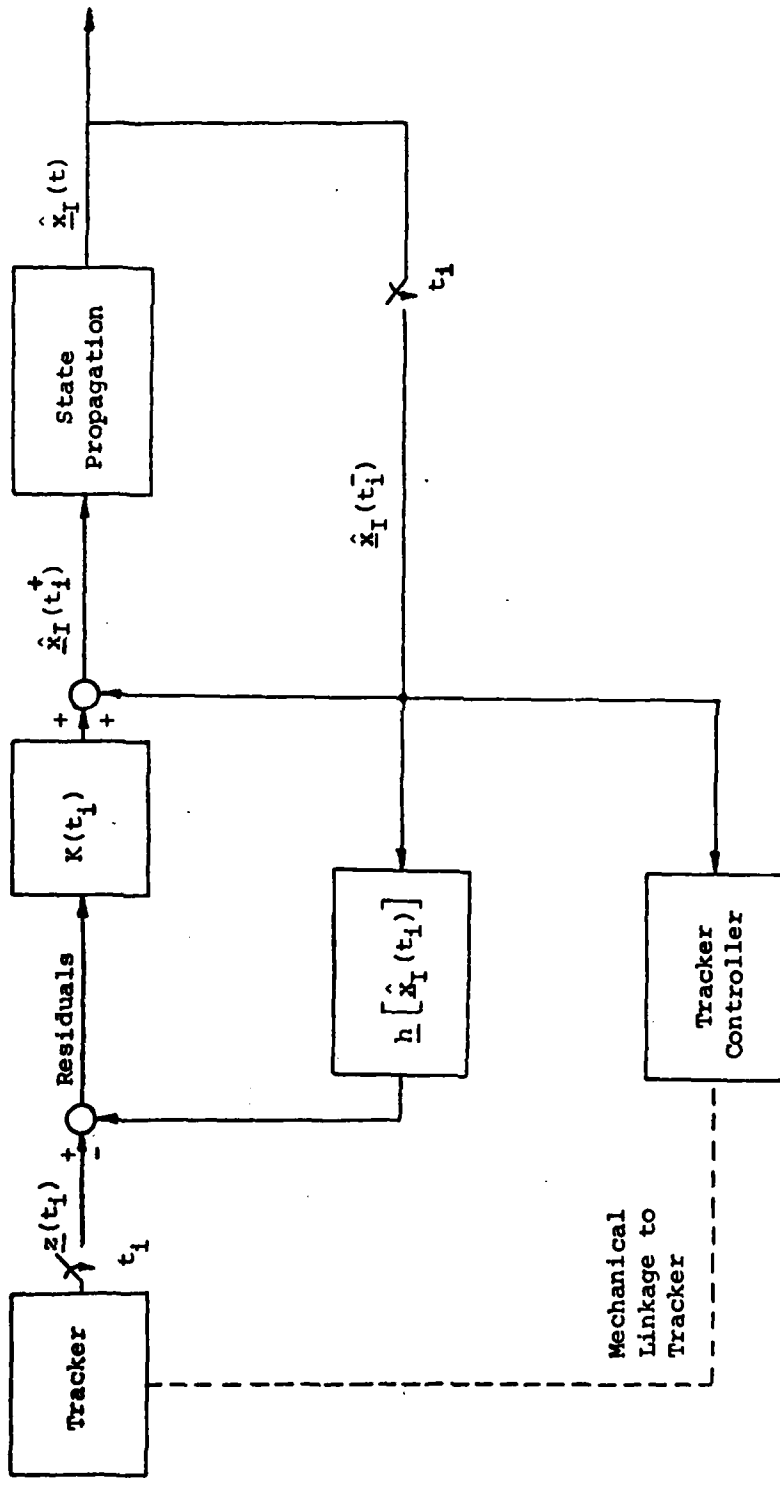


Figure IV-5. Block Diagram for GMI and CTRI Extended Filters

formed and multiplied by the Kalman filter gain $K(t_i)$ calculated from the propagation of the conditional covariance $P(t_i^-)$ at time t_i^- . This product was summed with the state estimates $\hat{x}_I(t_i^-)$ to calculate the state estimates $\hat{x}_I(t_i^+)$ used for the initial conditions of the next propagation interval.

Extended Kalman Filter for Constant Turn Rate Inertial Model

As with the GMI dynamics model, implementation of the CTRI dynamics model in the extended Kalman filter required only the evaluation of the F and H matrices since the filter's coordinate frame did not rotate. However, unlike the GMI model, the calculation of the F matrix was not trivial since the dynamics model for the CTRI filter was nonlinear. Using Eq IV-6, the F matrix for the CTRI model was

$$F[\hat{x}(t|t_i^-)] = \begin{bmatrix} 0 & F_1 & 0 & 0 & 0 & 0 & 0 & 0 & 0 \\ 0 & 0 & F_2 & 0 & 0 & 0 & 0 & 0 & 0 \\ 0 & F_3 & F_4 & 0 & F_5 & F_6 & 0 & F_7 & F_8 \\ 0 & 0 & 0 & 0 & F_9 & 0 & 0 & 0 & 0 \\ 0 & 0 & 0 & 0 & 0 & F_{10} & 0 & 0 & 0 \\ 0 & F_{11} & F_{12} & 0 & F_{13} & F_{14} & 0 & F_{15} & F_{16} \\ 0 & 0 & 0 & 0 & 0 & 0 & 0 & F_{17} & 0 \\ 0 & 0 & 0 & 0 & 0 & 0 & 0 & 0 & F_{18} \\ 0 & F_{19} & F_{20} & 0 & F_{21} & F_{22} & 0 & F_{23} & F_{24} \end{bmatrix} \quad (IV-26)$$

$x = \hat{x}(t|t_i^-)$

where

$$F_1 = F_2 = F_9 = F_{10} = F_{17} = F_{18} = 1$$

$$F_3 = - \left\{ 2 [I_{x_I^T}(t_i)]_2 \left(A_1 \left(A_2 [I_{x_I^T}(t_i)]_6 - A_3 [I_{x_I^T}(t_i)]_9 \right) \right. \right. \\ \left. \left. - 2 (A_2^2 + A_3^2 + A_4^2) [I_{x_I^T}(t_i)]_2 \right) + (A_2^2 + A_3^2 + A_4^2) A_1 \right\} / A_1^3$$

$$F_4 = -2 [I_{x_I^T}(t_i)]_2 \left(A_3 [I_{x_I^T}(t_i)]_8 - A_2 [I_{x_I^T}(t_i)]_3 \right) / A_1^2$$

$$F_5 = -2 [I_{x_I^T}(t_i)]_2 \left(A_4 [I_{x_I^T}(t_i)]_9 - A_2 [I_{x_I^T}(t_i)]_3 \right) A_1 \\ - 2 (A_2^2 + A_3^2 + A_4^2) [I_{x_I^T}(t_i)]_5 / A_1^3$$

$$F_6 = -2 [I_{x_I^T}(t_i)]_2 \left(A_2 [I_{x_I^T}(t_i)]_2 - A_4 [I_{x_I^T}(t_i)]_8 \right) / A_1^2$$

$$F_7 = -2 [I_{x_I^T}(t_i)]_2 \left(A_3 [I_{x_I^T}(t_i)]_3 - A_4 [I_{x_I^T}(t_i)]_6 \right) A_1 \\ - 2 (A_2^2 + A_3^2 + A_4^2) [I_{x_I^T}(t_i)]_8 / A_1^3$$

$$F_8 = -2 [I_{x_I^T}(t_i)]_2 \left(A_4 [I_{x_I^T}(t_i)]_5 - A_3 [I_{x_I^T}(t_i)]_2 \right) / A_1^2$$

$$F_{11} = -2 [I_{x_I^T}(t_i)]_5 \left(A_2 [I_{x_I^T}(t_i)]_6 - A_3 [I_{x_I^T}(t_i)]_9 \right) A_1 \\ - 2 (A_2^2 + A_3^2 + A_4^2) [I_{x_I^T}(t_i)]_2 / A_1^3$$

$$F_{12} = -2 [I_{x_I^T}(t_i)]_5 \left(A_3 [I_{x_I^T}(t_i)]_8 - A_2 [I_{x_I^T}(t_i)]_5 \right) / A_1^2$$

$$F_{13} = - \left\{ 2 [I_{x_I^T}(t_i)]_5 \left(A_1 \left(A_4 [I_{x_I^T}(t_i)]_9 - A_2 [I_{x_I^T}(t_i)]_3 \right) \right. \right. \\ \left. \left. - 2 (A_2^2 + A_3^2 + A_4^2) [I_{x_I^T}(t_i)]_5 \right) + (A_2^2 + A_3^2 + A_4^2) A_1 \right\} / A_1^3$$

$$F_{14} = -2 \left[I_{x_I^T}(t_i) \right]_5 \left(A_2 \left[I_{x_I^T}(t_i) \right]_2 - A_4 \left[I_{x_I^T}(t_i) \right]_8 \right) / A_1^2$$

$$F_{15} = -2 \left[I_{x_I^T}(t_i) \right]_5 \left\{ \left(A_3 \left[I_{x_I^T}(t_i) \right]_3 - A_4 \left[I_{x_I^T}(t_i) \right]_6 \right) A_1 \right. \\ \left. - 2 \left(A_2^2 + A_3^2 + A_4^2 \right) \left[I_{x_I^T}(t_i) \right]_8 \right\} / A_1^3$$

$$F_{16} = -2 \left[I_{x_I^T}(t_i) \right]_5 \left(A_4 \left[I_{x_I^T}(t_i) \right]_5 - A_3 \left[I_{x_I^T}(t_i) \right]_2 \right) / A_1^2$$

$$F_{19} = -2 \left[I_{x_I^T}(t_i) \right]_8 \left\{ A_1 \left(A_2 \left[I_{x_I^T}(t_i) \right]_6 - A_3 \left[I_{x_I^T}(t_i) \right]_9 \right) \right. \\ \left. - 2 \left(A_2^2 + A_3^2 + A_4^2 \right) \left[I_{x_I^T}(t_i) \right]_2 \right\} / A_1^3$$

$$F_{20} = -2 \left[I_{x_I^T}(t_i) \right]_8 \left(A_3 \left[I_{x_I^T}(t_i) \right]_8 - A_2 \left[I_{x_I^T}(t_i) \right]_5 \right) / A_1^2$$

$$F_{21} = -2 \left[I_{x_I^T}(t_i) \right]_8 \left\{ \left(A_4 \left[I_{x_I^T}(t_i) \right]_9 - A_2 \left[I_{x_I^T}(t_i) \right]_3 \right) A_1 \right. \\ \left. - 2 \left(A_2^2 + A_3^2 + A_4^2 \right) \left[I_{x_I^T}(t_i) \right]_5 \right\} / A_1^3$$

$$F_{22} = -2 \left[I_{x_I^T}(t_i) \right]_8 \left(A_2 \left[I_{x_I^T}(t_i) \right]_2 - A_4 \left[I_{x_I^T}(t_i) \right]_8 \right) / A_1^2$$

$$F_{23} = - \left\{ 2 \left[I_{x_I^T}(t_i) \right]_8 \left\{ A_1 \left(A_3 \left[I_{x_I^T}(t_i) \right]_1 - A_4 \left[I_{x_I^T}(t_i) \right]_6 \right) \right. \right. \\ \left. \left. - 2 \left(A_2^2 + A_3^2 + A_4^2 \right) \left[I_{x_I^T}(t_i) \right]_8 \right\} + \left(A_2^2 + A_3^2 + A_4^2 \right) A_1 \right\} / A_1^3$$

$$F_{24} = -2 \left[I_{x_I^T}(t_i) \right]_8 \left(A_4 \left[I_{x_I^T}(t_i) \right]_5 - A_3 \left[I_{x_I^T}(t_i) \right]_2 \right) / A_1^2$$

where

$$A_1 = \left[I_{x_I^T}(t_i) \right]_2^2 + \left[I_{x_I^T}(t_i) \right]_5^2 + \left[I_{x_I^T}(t_i) \right]_8^2$$

$$A_2 = \left[I_{x_I^T}(t_i) \right]_2 \left[I_{x_I^T}(t_i) \right]_6 - \left[I_{x_I^T}(t_i) \right]_3 \left[I_{x_I^T}(t_i) \right]_5$$

$$A_3 = \left[I_{x_I^T}(t_i) \right]_3 \left[I_{x_I^T}(t_i) \right]_8 - \left[I_{x_I^T}(t_i) \right]_2 \left[I_{x_I^T}(t_i) \right]_9$$

$$A_4 = \left[I_{x_I^T}(t_i) \right]_5 \left[I_{x_I^T}(t_i) \right]_9 - \left[I_{x_I^T}(t_i) \right]_6 \left[I_{x_I^T}(t_i) \right]_8$$

The H matrix for the CTRI model was the same as the one used for the GMI model since the trackers and state variables were the same for both filters. The H matrix was given by Eq IV-25. Also, the timing sequence and the block diagram for the CTRI model were identical to those of the GMI model and are presented in Fig IV-4 and Fig IV-5, respectively.

Selection of Parameters for Extended Kalman Filters

The parameters for the extended Kalman filters for the GMLOS and GMI model that had to be selected were the correlation time constants τ_1 , τ_2 , and τ_3 and the descriptor Q of the strength of the filter's dynamic driving noise. The correlation time constants were assumed to be equal for all three axes of the filter's coordinate system as discussed earlier in this section. The value for the time constants was selected to provide a reasonable frequency band for the power spectral density of the correlated acceleration. For high performance aircraft, a reasonable upper frequency for the correlated acceleration was assumed to be three radians per second (Ref 7). This value of upper frequency corresponded to a correlation time constant of two seconds.

The values for the elements of the Q matrix defined by Eq IV-8 were selected for the GMLOS and GM filter's by performing a steady state analysis for the filter's conditional covariance matrix P(t). It was assumed that the driving noises were white Gaussian zero mean noises. Further, the Q matrix was assumed to be of the form

$$Q(t) = \begin{bmatrix} 0 & 0 & 0 & & & \\ 0 & 0 & 0 & & & \\ 0 & 0 & q_1(t) & & & \\ \hline & & & 0 & 0 & 0 \\ & & & 0 & 0 & 0 \\ & & & 0 & 0 & q_2(t) \\ \hline & & & & & 0 & 0 & 0 \\ & & & & & 0 & 0 & 0 \\ & & & & & 0 & 0 & q_3(t) \end{bmatrix} \quad (IV-27)$$

where q_i = the i^{th} nonzero element of the Q matrix. This form was used since it was assumed that

$$E \{ w_i(t) w_j(t+\tau) \} = 0 \quad i \neq j \quad (IV-28)$$

for all t and τ , a standard assumption for the driving noises used for filter implementation (i.e., no correlation between the dynamic driving noises). For the steady state filter conditional covariance analysis, the Eq IV-2 for the propagation of the filter's covariance was used. In steady state, this equation was written as

$$FP + PF^T = -Q \quad (IV-29)$$

Since the dynamics model for either the GMLOS or the GM filter were decoupled along each axis, only the dynamics equations along the l-axis were evaluated to calculate the q_1 element of Q . Also, the values of the nonzero elements of the Q matrix were equal since the correlation time constants were assumed to be equal. Equation IV-29 became

$$\begin{bmatrix} 0 & 1 & 0 \\ 0 & 0 & 1 \\ 0 & 0 & -\frac{1}{\tau} \end{bmatrix} \begin{bmatrix} P_{11} & P_{12} & P_{13} \\ P_{12} & P_{22} & P_{23} \\ P_{13} & P_{23} & P_{33} \end{bmatrix} + \begin{bmatrix} P_{11} & P_{12} & P_{13} \\ P_{12} & P_{22} & P_{23} \\ P_{13} & P_{23} & P_{33} \end{bmatrix} \begin{bmatrix} 0 & 0 & 0 \\ 1 & 0 & 0 \\ 0 & 1 & -\frac{1}{\tau} \end{bmatrix} = \begin{bmatrix} 0 & 0 & 0 \\ 0 & 0 & 0 \\ 0 & 0 & -q_1 \end{bmatrix} \quad (\text{IV-30})$$

where

P_{ij} = ij^{th} element of the filter's covariance matrix in steady state operation

Evaluation of the 33th element gave

$$\frac{2}{\tau} P_{33} = q_1 \quad (\text{IV-31})$$

The value used for the filter's covariance of the target acceleration along the one axis P_{33} was calculated based on the assumption that the 3 sigma values of the error in the target acceleration estimate was 9 g's, or about 290 feet per second². Thus, the 1 sigma value was 3 g's, or approximately 97 feet per second², and the value of element P_{33} was calculated to be 9409 feet² per second⁴. This value of 9409 feet² per second⁴ was substituted into Eq IV-31, yielding a value of q_1 of 9409 feet² per second⁵ when a

correlation time constant of 2 seconds was used. For the implementation of the GMLOS and GMI filters, a value of 9000 feet² per second⁵ was selected.

For the CTRI extended Kalman filter, only the value of the nonzero elements of the Q matrix had to be selected. However, since this filter used a nonlinear dynamics model, the steady state conditional covariance analysis could not be used. The method of selecting the values of the Q matrix, which was assumed to have the form shown in Eq IV-27, was by trial and error. Initially, a value of 32 feet² per second⁵ was chosen for the q's, which represented a 1 sigma value of about 0.2 g's; but this value was too small to provide adequate performance for trajectories with high target acceleration variations. Next, a 10 fold increase in the 1 sigma value, i.e., a value of 3000 feet² per second⁵, was tried; and the performance was significantly improved. Finally, a value of 9000 feet² per second⁵, representing a 1 sigma value of about 3 g's, was evaluated. This was the value used in the CTRI filter since it provided good performance for the filter when evaluated against the trajectories used for this thesis and permitted the CTRI and GMI filter's performance to be compared with the same Q matrix. The use of the same Q matrix implied that the same order of uncertainty or variations of the filter's estimate of the trajectory was assumed for both the constant turn rate trajectory computed by the CTRI filter and the Gauss-Markov zero mean acceleration trajectory calculated by the GMI filter.

V Method of Evaluation

Monte Carlo Simulation

A modified version of the generalized digital Simulation for Optimal Filter Evaluation (SOFE) program developed at the Air Force Avionics Laboratory (Ref 5) was used to test each filter's performance. The SOFE program provided the basic functions needed to run Monte Carlo simulations of an extended Kalman filter. These functions included a numerical solution to the differential equations for both system simulation and filter propagation, a Carlson square root update of the filter's state estimates and conditional covariance, and the necessary program control for multiple simulations. Nine user written subroutines were required to define both the system simulation and the Kalman filters. For this evaluation, the system simulation was provided from external trajectory data (to be discussed later in this section). Equations II-11, III-1, III-2, III-3, III-4, IV-9, and IV-10; Eqs II-23, III-7, III-8, III-9, III-10, IV-9, and IV-25; and Eqs II-42, III-7, III-8, III-9, III-10, IV-26, and IV-25 were included in the user written subroutines to specify the filter model for the GMLOS, GMI, and CTRI filter, respectively. The outputs of the SOFE program, the true model state vector, the filter's estimate of the state vector, the measurement residual vector, the measurement residual variances, and the filter's variances for each interval were stored for post-processing by the SOFE plotting (SOFEPL) program (Ref 8), also developed by Air Force Avionics Laboratory personnel. The number of simulation passes through the simulation for each filter evaluation used for this thesis was 20. This number of passes was selected by comparing plots from the SOFEPL program for 5, 10, 15, and

20 passes (Fig B-1 to Fig B-9, Fig B-10 to Fig B-18, Fig B-19 to Fig B-27, and Fig E-10 to Fig E-18, respectively). There was little difference between the plots for 15 and 20 passes, and 20 passes were selected to provide confidence in the accuracy of the solution. Also, the choice of 20 passes kept computer execution time and storage requirements at acceptable values.

As stated above, a modified SOFE program was used for the evaluation. Two modifications, a second order Runge-Kutta integration option with fixed step size, instead of the fifth order Runge-Kutta integration provided by the SOFE program, and the use of external trajectory data for the true state vector, instead of the SOFE program calculating the true state vector during the simulation, had been previously incorporated by Air Force Avionics Laboratory personnel (Ref 9). These two modifications reduced the computational burden required to perform the integration from time t_i^+ to time t_{i+1}^- , thus reducing the time required for the 20 Monte Carlo simulations. Also, a third modification to the SOFE program was made for the GMLOS filter to allow the transformation of the filter's conditional covariance matrix $P(t_i^-)$ from the filter's current coordinate frame at time t_i^- to the realigned coordinate frame at time t_i^- as described in Section III.

The SOFEPL program calculated the ensemble average of the data from the multiple Monte Carlo simulations from the SOFE program and formatted these results into the requested plots. Sixteen different plot types were available from the SOFEPL program. For this thesis, the mean error between the truth model (target trajectory data) value and the corresponding estimate from the filter, the sum and the difference of the standard deviation of this error with the mean error itself, and the square root of the appropriate diagonal element of the filter's

conditional state covariance matrix were plotted versus time (See Fig V-1). This plot type provided the sample statistics for actual errors committed by the filter (mean error and mean error plus or minus the standard deviation of the error) and the filter's computed performance (plus or minus the square root of the filter's conditional variance) to evaluate filter tuning and performance.

Trajectory Generation and Description

The trajectories used in the evaluation of the three filters were generated by a program, TRAJ, developed by Air Force Avionics Laboratory personnel, to provide data for both the target and attacker during a gunnery pass (Ref 9). The program allowed the user to fly the target through a maneuver by varying the thrust, roll rate, and normal acceleration while the attacker tracked the target using a gunnery lead collision scheme. The outputs of the program which were calculated every 0.02 seconds (50 times per second) included the time, position, inertial velocity, and inertial acceleration of both the target and the attacker in an earth-fixed reference frame and the transformation from the earth-fixed reference frame to the attacker body coordinates. The origin of the earth-fixed reference frame was located on the surface of the earth with the attacker's center of gravity cg on the negative down axis at the initial time (Fig V-2).

Three trajectories, picked to represent typical target maneuvers during an aerial gunnery engagement, were developed using the TRAJ program. Each engagement lasted 12 seconds, providing adequate time for the performance evaluation of the filters.

Trajectory 1 was selected to demonstrate the performance of each filter against a target flying a constant normal acceleration maneuver. Initially, the target and attacker were flying on the same heading parallel to the north axis of the earth-fixed reference frame at the same altitude

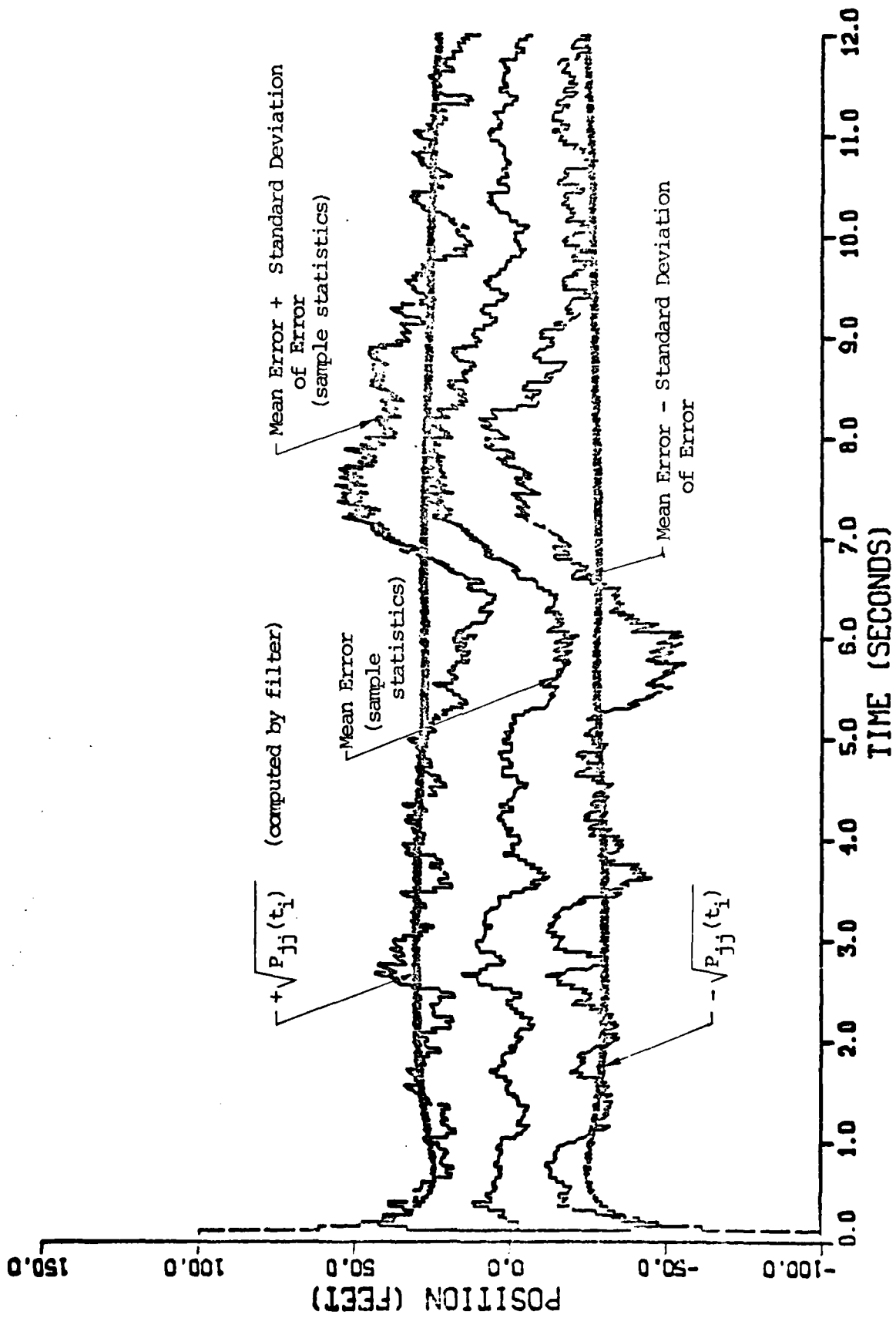


Figure V-1. Representative Output From the SOFEPL Program

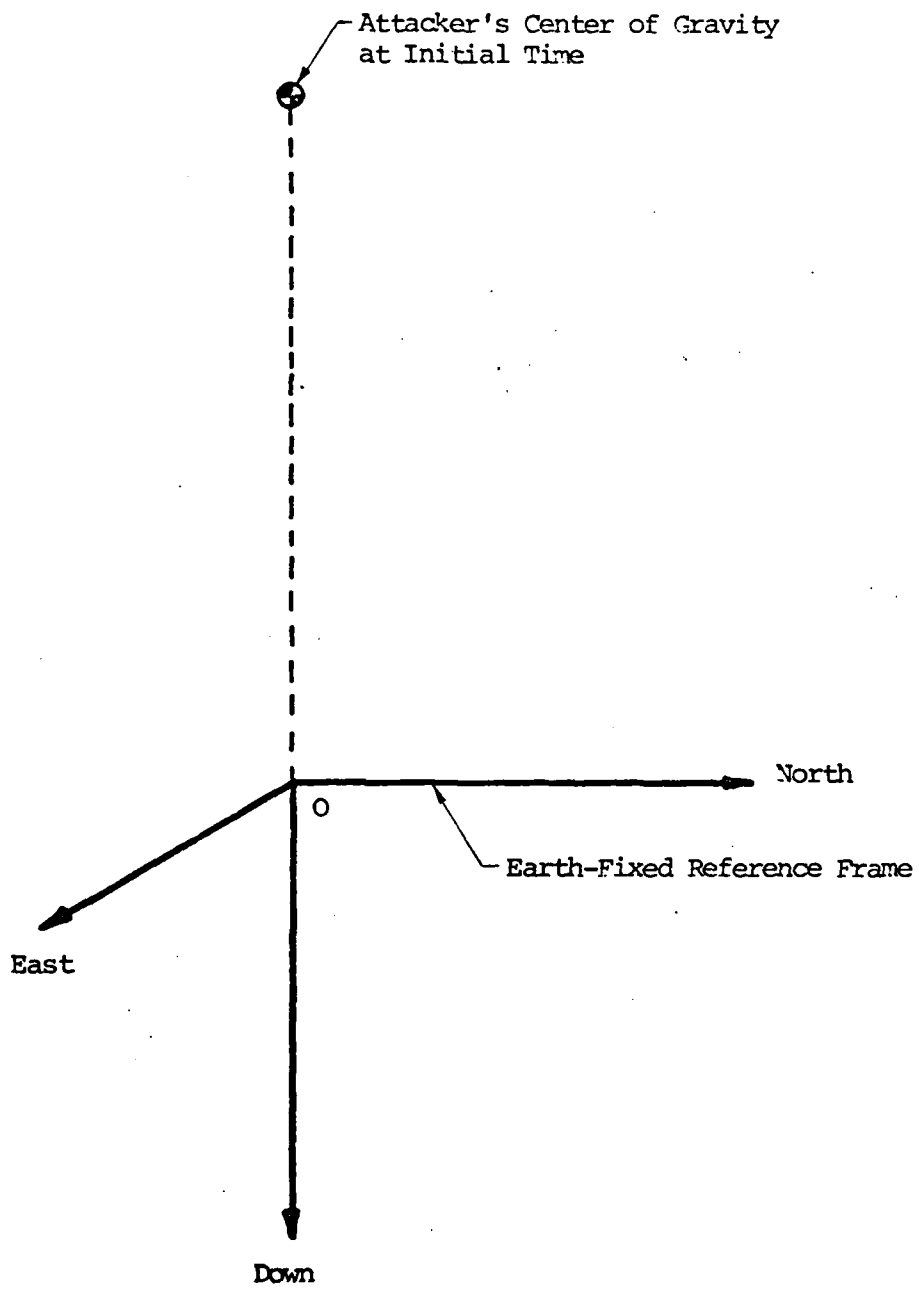


Figure V-2. Relation Between the Earth-Fixed Coordinate Frame Used by the Trajectory Generation Program and the Attacker's Center of Gravity at the Initial Time

of 5000 feet. The target was 7500 feet in front of the attacker and offset 2000 feet to the attacker's right (See Fig V-3). The initial speed of the target was 800 feet per second (approximately 500 knots), and the initial speed of the attacker was 750 feet per second (approximately 440 knots). Furthermore, the target was established in a 5g normal acceleration level left turn (approximately 78 degrees left bank). For the duration of the trajectory, 12 seconds, the target maintained the 5g constant normal acceleration left turn.

Trajectory 2 provided a highly dynamic maneuvering target with out-of-plane maneuvers to evaluate the filters' performance, and it was designed to represent a typical target reversal and dive out of the engagement. The target and attacker had the same initial conditions as in Trajectory 1 except the initial altitude of both was 10000 feet (See Fig V-4). For the initial five seconds, the target performed the same five g normal acceleration level left turn. Then the target initiated a one radian per second roll to the right while maintaining five g's normal acceleration. The roll continued until the target was inverted with wings parallel to the north-east plane of the earth-fixed reference frame (wings level). The roll rate was then set to zero, the normal acceleration was increased to seven g's, and the target completed a "split s" maneuver to upright level flight.

Trajectory 3 was chosen to demonstrate the filters' performance for a nose-to-nose (front) engagement. The engagement was designed to represent a typical front engagement where the target attempts to gain a firing position behind the attacker. Initially, the target and attacker were flying with wings level on opposite headings parallel to the north axis of the earth-fixed reference frame. The target was 15000 feet in front of the attacker and 2000 feet to the attacker's right (See Fig V-5). Both the target and the attacker were at the same altitude, 5000 feet,

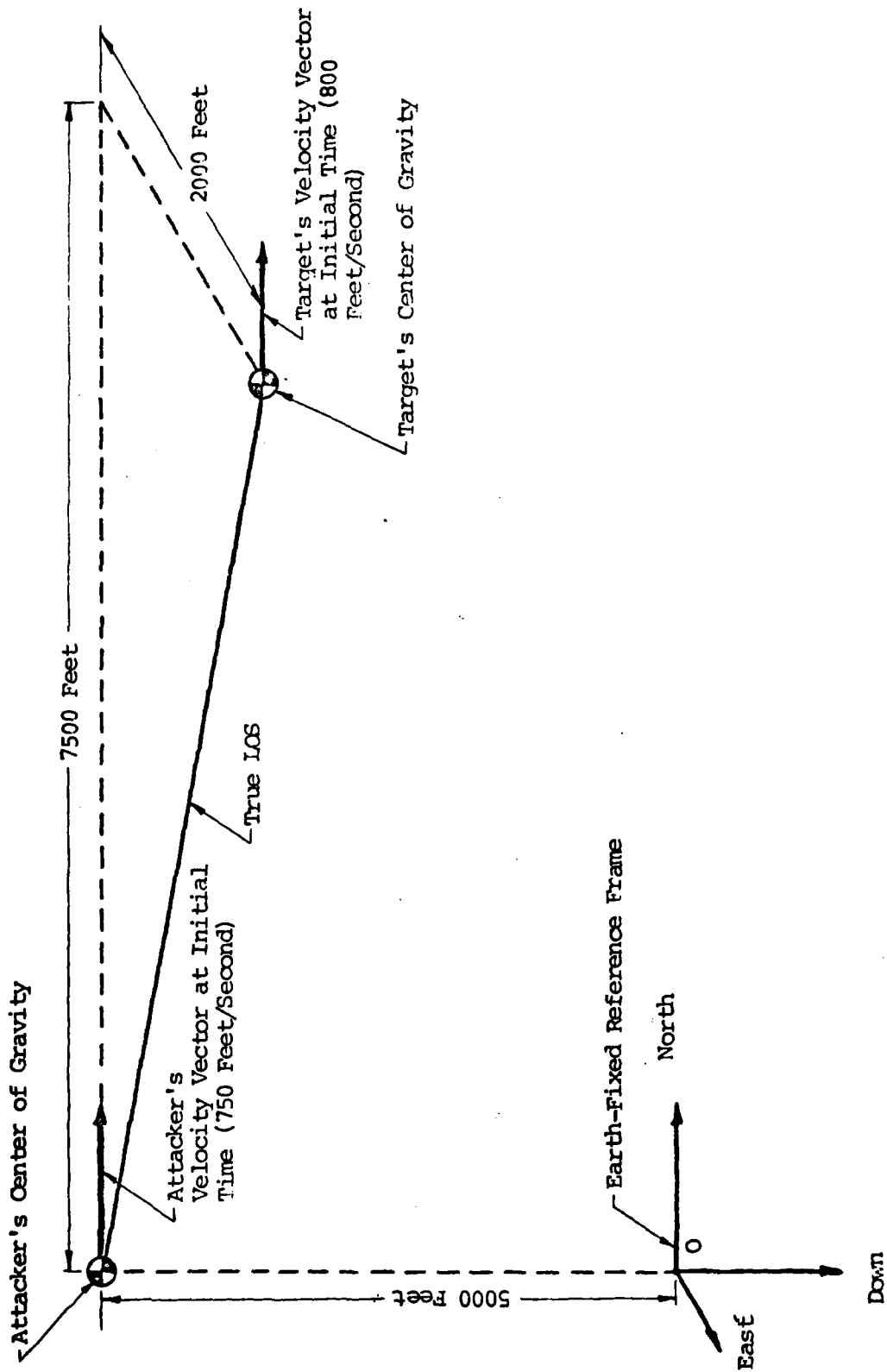


Figure V-3. Initial Positions and Velocities For Trajectory 1 Relative to the Earth-Fixed Reference Frame

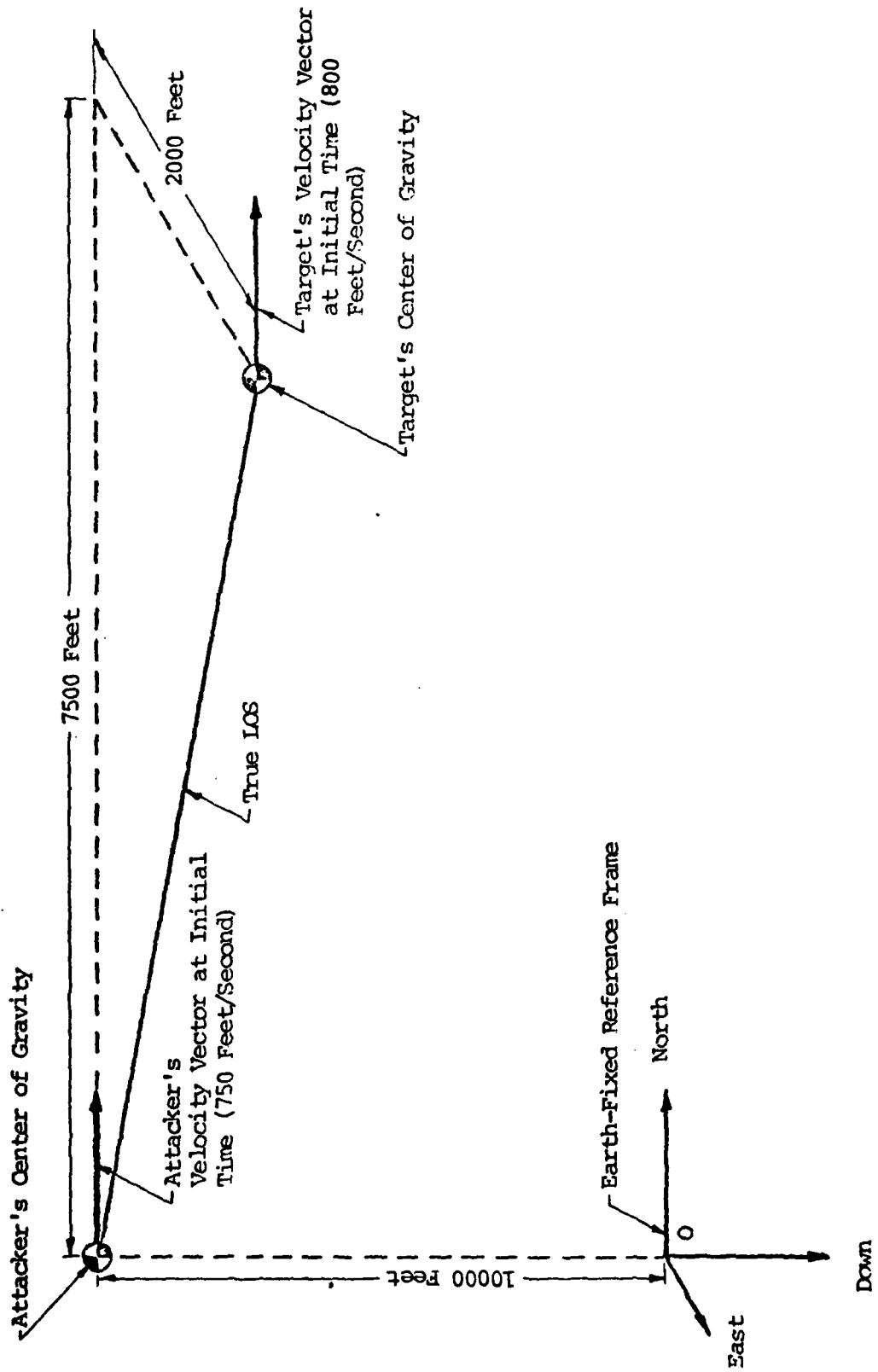


Figure V-4. Initial Positions and Velocities For Trajectory 2 Relative to the Earth-Fixed Reference Frame

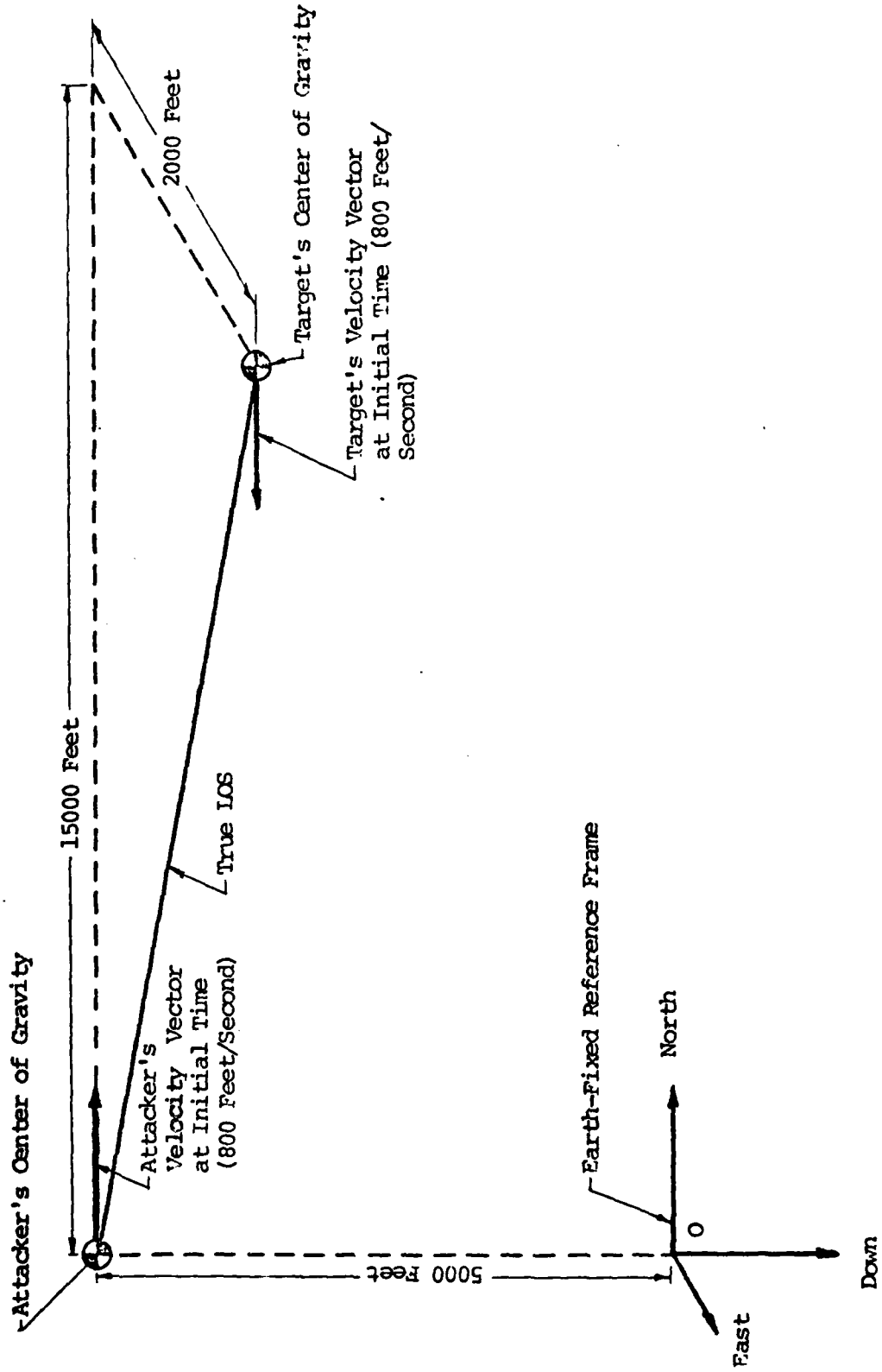


Figure V-5. Initial Positions and Velocities For Trajectory 3 Relative to the Earth-Fixed Reference Frame

and same speed, 800 feet per second (approximately 475 knots). Four seconds after the start of the engagement, the target established a 4g normal acceleration climbing left turn which was held for 4.5 seconds. Then the target rolled right at one half radian per second while maintaining four g's normal acceleration. Once the target obtained 75 degrees of right bank angle, the roll rate was set to zero, and the target continued in a 4g normal acceleration level right turn until the end of the engagement.

Measurement Update Rates

The baseline update rate selected for the comparison of the three filters was 25 times per second (0.04 seconds between updates). This rate was selected since it was compatible with the time increment of the trajectory generating program and was consistent with measurement rates available from current sensors (Ref 4). To evaluate the sensitivity of the CTPI filter to variations in update rate, update rates of $12\frac{1}{2}$ times per second (0.08 seconds between updates), $6\frac{1}{2}$ times per second (0.16 seconds between updates), and $3\frac{1}{8}$ times per second (0.24 seconds between updates) were selected. Faster update rates were considered but computer storage requirements prohibited the evaluation of these rates. The descriptor of the strength of the dynamic driving noise Q was held constant during this evaluation. Table V-1 summarizes the update rates used with each filter.

Variations in Measurement Noises

The baseline values used for the elements of the noise covariance matrix R (as discussed in Section III) for the filter only were varied systematically to evaluate the effect on the CTPI filter's performance when flown against Trajectory 2. The value of each variance was independently

TABLE V-1

Sample Periods Investigated For Each Filter

Filter	Sample Period (Seconds)			
	0.04	0.08	0.16	0.24
Gauss-Markov Line of Sight	Yes	No	No	No
Gauss-Markov Inertial	Yes	No	No	No
Constant Turn Rate Inertial	Yes	Yes	Yes	Yes

increased and decreased by an order of magnitude for both the range and range rate measurements. For the error angle measurements, the variances of both error angle measurements were increased and decreased by an order of magnitude concurrently. Finally, the CTPI filter was evaluated with each measurement not available and the variances for the other measurements set at the baseline values. Again, both error angle measurements were removed at the same time. A summary of the variances used to investigate the sensitivity of the CTPI filter to variations in the measurement noises is presented in Table V-2.

Figures of Merit

Various figures of merit were employed for the comparison of the three filter models and the evaluation of the effect of different update rates on the performance of the CTPI filter. Nine figures of merit were calculated for the comparison of the GMLOS, GM, and CTPI filters. These figures were:

- 1) the scalar magnitude of the three dimensional vector of the approximate time average of the mean errors of position, and similarly calculated scalar magnitudes for velocity and acceleration (all rounded to the nearest whole number),

- 2) the peak scalar magnitude of the three dimensional vector of the mean error of position, and similarly calculated scalar magnitudes for velocity and acceleration (all rounded to the nearest whole number), and

- 3) the scalar magnitude of the approximate time average of the three dimensional standard deviation vector of the errors committed by the filter for position, and similarly calculated scalar magnitudes for velocity and acceleration (rounded to the largest whole number).

TABLE V-2

Combinations of the Measurement Noise Variances
Used to Evaluate Filter Sensitivity

Variation in Measurement Noise	$\sigma_{R,2}^2$ (feet ²)	σ_e^2	σ_a^2	σ_R^2 (feet ² /second ²)
Baseline	10000.0	0.0001	0.001	625.0
Range	1000.0	0.0001	0.001	625.0
	100000.0	0.0001	0.001	625.0
	no measurement	0.0001	0.001	625.0
Error Angle	10000.0	0.00001	0.00001	625.0
	10000.0	0.001	0.001	625.0
	10000.0	no measurement	no measurement	625.0
Range Rate	10000.0	0.0001	0.0001	62.5
	10000.0	0.0001	0.0001	6250.0
	10000.0	0.0001	0.0001	no measurement

The scalar magnitudes of the average of the mean errors were calculated by first estimating the time average of the mean error for each component of the position, velocity, and acceleration vectors. Then, using these components of the average mean errors, the rss magnitudes for the average mean errors of position, velocity, and acceleration were computed. The peak scalar magnitudes of the mean errors were calculated by using the mean error for each component of the desired vectory (position, velocity, and acceleration) at time t that produced the largest magnitude of the mean error. Finally, the scalar magnitudes of the time average of the standard deviation were computed by estimating the time average of the standard deviation of the errors committed by the filter from the SOFEPL-generated plots for each component of position, velocity, and acceleration. Then, the rss magnitude of the standard deviation for the position, velocity, and acceleration vectors were calculated using these estimates. For Trajectory 1, the nine figures of merit were computed over the total 12 seconds of the simulation, while the figures of merit for Trajectory 2 and Trajectory 3 were calculated over the intervals of 5 to 12 seconds and 4 to 12 seconds, respectively. These shorter intervals for Trajectory 2 and Trajectory 3 were used to eliminate the influence of the initial 5 g normal acceleration turn on the figures of merit for these trajectories since the inclusion of the initial 5 g normal acceleration turn would bias the results. (Note that the SOFEPL plots provide results from 0 to 12 seconds.)

For the evaluation of the effect of update rates on the performance of the CTRI filter, the time average of the standard deviation of the errors committed by the filter for each state variable was plotted versus the update interval for which the average was calculated. Only simulations against Trajectory 2 were used to evaluate the effect of update rates since this trajectory was the most difficult of the three simulated tra-

jectories for the CTPI filter to track (See Section VI).

To evaluate the effect of different variances of the measurement noises, the plots for each of the state variables from the SOFEPL program for the CTPI filter with the different variance(s) were compared directly with the corresponding plot of the same state variable using the baseline measurement noise variances (as described in Section III); the percent difference (rounded to the nearest percent) was then calculated. This approach was used since not all the state variables were affected by changes in the measurement noise variances. Also, only simulations using Trajectory 2 were evaluated for the same reason discussed above.

VI Results

General Performance of the Three Filters

Before the direct comparison between filters is made, the general performance of each filter will be discussed to provide physical insight into the results. Figures C-1 to C-27 are the plots of the results from the Monte Carlo simulations of the GMLOS filter for the three trajectories used. The GMLOS filter was characterized by a nearly unbiased estimate of the position along the estimated LOS and oscillatory biased estimates of the two cross range (2- and 3-axes of the filter's coordinate frame) positions, the three velocity components, and the three acceleration components. Furthermore, when a high rate of change of acceleration was present as in Trajectory 2 and Trajectory 3, these eight estimates exhibited large mean errors. The biases in the estimates and the large mean errors were a result of the inadequacy of the assumed target relative acceleration model. This model, a first order zero mean Gauss-Markov process, did not accurately model the target acceleration when the target acceleration was not highly correlated with attacker acceleration (See Section II) as was the case in Trajectory 2 and Trajectory 3. Thus, the GMLOS filter had an inherent lag in the estimates of the states when unmodeled maneuvers with persistent turning accelerations were encountered. Furthermore, the measurement updates kept the filter from diverging while the unmodeled maneuver was occurring. The oscillations apparent in the estimates had both high frequency and low frequency characteristics. The high frequency oscillation readily seen in the plot of the position estimate along the 2-axis of the filter's coordinate frame for all three trajectories (Fig C-4, Fig C-13, and Fig C-22) was caused by the impulsive realignment of the filter's coordinate frame just before an update. The low frequency

oscillation appeared to be strongly trajectory-dependent. For Trajectory 1, this oscillation persisted for the duration of the simulation; while for Trajectory 2 and Trajectory 3, the intervals where the target maneuver was fairly dynamic appeared to aid in reducing the amplitude of low frequency oscillation. One feasible explanation was that the increased maneuvering overcame an observability problem that occurred during Trajectory 1 (constant target maneuver). Also, the zero-mean Gauss-Markov model was more representative of target accelerations levels that were more dynamic and less persistent.

For Trajectory 1, the mean errors of all the estimates of the states were within the envelope of plus or minus the square root of the corresponding filter-computed conditional variance. This was expected since the target and attacker accelerations were correlated (the target's acceleration was closely approximated by the attacker's acceleration). However for Trajectory 2 and Trajectory 3, the mean errors for most of the estimates of the states exceeded this envelope. Furthermore, in the case of Trajectory 3, this envelope necked down during the interval when the target acceleration was rapidly changing and was uncorrelated with the attacker's acceleration. (That is, the attacker's acceleration provided no information about the target's acceleration.) The large mean errors and the failure of the filter's conditional variance to reflect the growth of the mean errors indicated that the filter was putting too much weight on the results from the dynamics model and not enough weight on the information contained in the measurements. Therefore, the tuning issue for the GMLOS filter should be further explored or the use of adaptive Kalman filter techniques should be investigated to alleviate this problem.

The plots of the results from the Monte Carlo simulations for the GM filter for the three trajectories are presented in Fig D-1 to D-27. The characteristics of the GM filter were a nearly unbiased estimate of

the position along the north-axis of the filter's coordinate system and low frequency oscillatory biased estimates of the positions along the east- and down-axis, the three components of velocity, and the three components of acceleration. (Note that if the trajectories had been flown along the east-axis, the results would be rotated +90 degrees about the filter's down-axis). Moreover, when the filter was required to track a target with a high rate of change of acceleration as for Trajectory 2 and Trajectory 3, large mean errors resulted for these eight estimates. The biases in these estimates observed for all three trajectories and the large mean errors for Trajectory 2 and Trajectory 3 were caused by the inability of the assumed target acceleration model to represent the actual target acceleration accurately. The target acceleration model used for the GMI filter assumed that the total inertial target acceleration was adequately modeled by a first order Gauss-Markov process with a zero mean, while the actual target acceleration was not zero-mean nor a first order Gauss-Markov process. Thus, when unmodeled maneuvers were encountered, the GMI filter did not accurately predict the states and had an inherent lag in the estimates of the states. Furthermore, the information provided by the measurement updates maintained the stability of the filter until the unmodeled maneuver was completed. Like the GMLOS filter, the low frequency oscillations appeared to be trajectory-dependent (as discussed above).

The mean errors of the estimates of the GMI filter for Trajectory 1 were all within the envelope of plus or minus the square root of the filter's corresponding conditional variance, as expected, since the actual target acceleration was not drastically different from the assumed model. However, for Trajectory 2 and Trajectory 3, the mean errors of the estimates exhibited large excursions outside the envelope of the filter's corresponding

AD-A094 767

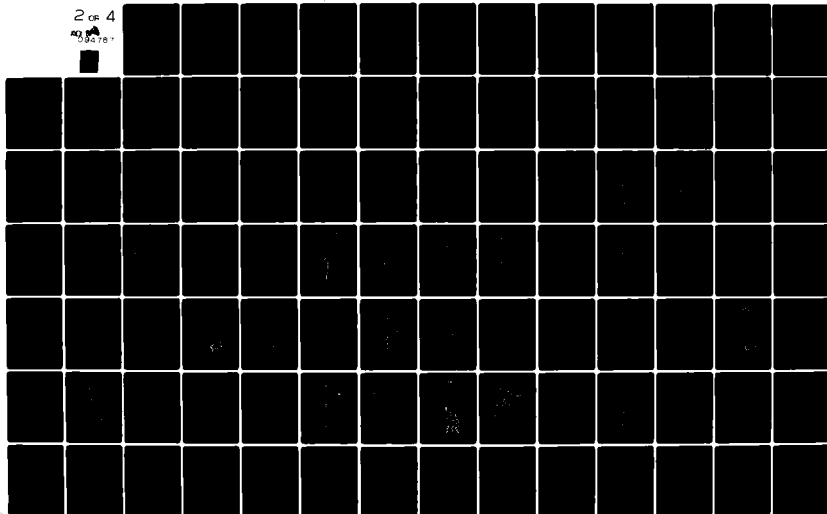
AIR FORCE INST OF TECH WRIGHT-PATTERSON AFB OH SCHOO--ETC F/8 19/5
COMPARISON OF THREE EXTENDED KALMAN FILTERS FOR AIR-TO-AIR TRAC--ETC(U)
DEC 80 W H WORSLEY
AFIT/GAE/AA/80S-2

UNCLASSIFIED

NL

2 of 4

AD
50478



conditional standard deviation. Furthermore, the filter's variances for Trajectory 2 or Trajectory 3 did not reflect the growth of the mean errors during the intervals where the assumed target acceleration model was providing incorrect predictions of the states. As with the GMLOS filter the CMI filter appeared to be weighting the results from the dynamics model too much and not weighting the information provided by the measurement updates enough. Two alternatives, retuning the filter or using adaptive Kalman filter techniques should be explored to eliminate these problems.

The plots of the results from the Monte Carlo simulations of the CTRI filter for the three trajectories are presented in Fig E-1 to E-27. The results were characterized by nearly unbiased estimates of the states, except during initial transients for estimates of the position and velocity states along the east-axis. The small bias values observed were expected since the trajectories were well described as constant turn rate trajectories except during the intervals of rapid acceleration changes. Large mean errors occurred during these intervals and were a result of the inadequacy of the assumed constant turn rate model to represent the rapidly varying actual target acceleration. The inadequacy of the model caused incorrect estimates of the states, and the filter lagged the actual target parameters; however the CTRI model was more representative of actual typical maneuvers than either first order Gauss-Markov target acceleration models (except possibly during transient changes).

The mean errors of the estimates for the CTRI evaluated against Trajectory 1 were within the envelope of plus or minus the square root of the filter's corresponding conditional variance. However, as with the GMLOS filter and CMI filter, the mean errors of most of the estimates for the CTRI when evaluated against Trajectory 2 and Trajectory 3 exceeded

this envelope. The filter's attempt to increase the conditional variances significantly lagged the onset of the maneuver. The large increase in mean errors and the failure of the filter to increase the conditional variances indicated that too much weight was given to the predictions of the dynamics model and too little weight was given to the information provided by the measurements. Retuning the filter or use of adaptive Kalman filter techniques should be explored to alleviate these problems.

Comparison of the Three Filters

The figures of merit for each filter for the three trajectories are presented in Table VI-1 and Table VI-2. As seen from these tables, the GMI filter provided estimates of the states where both the scalar magnitudes of the time average of the three components of mean error and the peak scalar magnitudes of the three components of mean error were equal to or less than the corresponding values for the GMLOS filter for all three trajectories evaluated. (A difference between corresponding values of ten percent or less was considered insignificant because of the errors that possibly could occur in determining both the time average and peak values from the plots.) Furthermore, the scalar magnitudes of the standard deviations of the errors committed by the GMI filter were also equal to or smaller than the corresponding values for the GMLOS filter. (Again, a difference between corresponding values of ten percent or less was considered insignificant because of the errors that possibly could occur in determining the values of the standard deviation from the plots.) True superiority of the GMI filter over the GMLOS filter was demonstrated when both filters were flown against Trajectory 3. The scalar magnitudes of the average mean errors, the peak scalar magnitudes of the mean errors, and the scalar magnitudes of the standard deviations of the errors for

TABLE VI-1. Comparison of the Scalar Magnitudes of the Three Components of Mean Error for Position, Velocity, and Acceleration

Filter	Trajectory	Magnitudes of the Mean Error (Time Averaged/Peak)		
		Position (feet)	Velocity (feet/second)	Acceleration (feet/second ²)
GMLOS	1	15/37	22/82	25/115
	2	15/37	46/150	52/208
	3	24/29	23/120	31/325
GMI	1	15/27	19/76	27/120
	2	15/26	47/118	55/202
	3	16/23	14/53	22/139
CTRI	1	10/28	13/67	11/101
	2	13/36	22/113	29/118
	3	11/24	15/60	20/148

TABLE VI-2. Comparison of the Scalar Magnitudes of the Approximate Time Average of the Three Components of the Standard Deviation of the Errors Committed by the Filter

Filter	Trajectory	Magnitudes of the Standard Deviation of the Errors		
		Position (feet)	Velocity (feet/second)	Acceleration (feet/second ²)
GMLOS	1	37	50	40
	2	42	72	50
	3	42	58	59
GMI	1	38	40	37
	2	38	54	48
	3	27	41	41
CTRI	1	42	44	47
	2	30	58	44
	3	30	44	45

the GM filter were 20 to 57 percent less than the corresponding values for the GMLOS filter. This trend was expected. The target acceleration model for the GM filter assumed no correlation between the accelerations of the target and attacker while the GMLOS filter's target acceleration model assumed correlated accelerations between the target and attacker (as discussed in Section II). Since the actual target and attacker accelerations were nearly uncorrelated during the maneuver for Trajectory 3, the GM filter's acceleration model was a better approximation of the actual target acceleration than the acceleration model for the GMLOS filter.

When the performance of the CTRI filter was compared to the performance of the GM filter using the scalar magnitudes of the average mean errors and the peak scalar magnitudes of the mean errors, the CTRI filter performed as well as or better than the GM filter except for the peak scalar magnitude of the mean error for position. (A difference of corresponding values of ten percent or less was considered insignificant as discussed above.) However, when the scalar magnitudes of the standard deviations of the errors were compared, the superiority of the CTRI filter was not apparent. For example, for Trajectory 1, the GM filter had lower scalar magnitudes of the standard deviations than did the CTRI filter. However, this comparison was dependent on how well the GM filter was tuned compared to how well the CTRI filter was tuned, and the issue was not explored further because of the complexity of the CTRI acceleration model and time constraints. The true superiority of the CTRI filter over the GM filter was demonstrated by the decrease in the scalar magnitude of the average mean errors and peak scalar magnitudes of the mean errors for the acceleration states by 47 and 41 percent, respectively, and the decrease in the magnitudes of the average mean error for the

velocity states by 53 percent. The trend exhibited by these decreases was anticipated since the CTRI filter's acceleration model more nearly represented the actual target acceleration for Trajectory 2 than did the GMI filter's acceleration model. Furthermore, the rms error (defined as the square root of the square of the mean error plus the variance of the error) should be evaluated.

Finally, when comparing the filter's performances, the opportunity for an actual gunnery solution had to be considered before finally selecting between the GMI and CTRI target acceleration model. For example, during the high roll rate maneuver of Trajectory 2, the attacker, using gunnery lead collision tracking, could not obtain a gunnery solution until the completion of the maneuver assuming the roll rates of the two aircraft were equal. The direction of the velocity vector of the attacker would lag the direction of the velocity vector of the target by some fixed angle (a function of the pilot's reaction time) until the target aircraft completed the roll. Therefore, the attacker would not be able to obtain the relative position needed to provide the gunnery solution, and the errors in the estimates provided by the filter would not be critical as long as the filter recovered from these errors rapidly. However, for Trajectory 3, the situation was entirely different since the gunnery solution must be achieved during the period when the angular rate of the target with respect to the attacker is large. This was the only time when the attacker had an opportunity to obtain a gunnery solution during the attack, assuming both aircraft could obtain the same normal acceleration value. As the target continued the turn into the attacker, the attacker could eventually not be able to pull enough lead on the target. At that moment, the attacker's firing opportunity would be lost. Thus the filter's estimates during the interval were extremely important, and any errors in these estimates would be critical to the accuracy of the gunsight. Another consideration in actual implementation would be the

computer resources required. The CTRI filter required 176 multiplications, 223 additions, and 20 divisions for each propagation step while the GMI filter required 18 multiplications, 162 additions, and no divisions. The computer resources required for an update were the same since both filters used the same measurement equations. Thus, the requirement for increased accuracy as provided by the CTRI filter would have to be weighed against the substantially increased computer requirements. Finally, the relative robustness of both the GMI and CTRI filters to variations in parameters, measurement noise, tuning, and imperfect initial conditions should be investigated to provide additional insight into which filter is the better choice for implementation.

Effect of Update Rate on CTRI Filter Performance

The plots of the three components of the time average of the standard deviations of the errors committed by the CTRI filter are presented in Fig VI-1, Fig VI-2, and Fig VI-3 for the position, velocity, and acceleration, respectively. The points for these plots were obtained from Fig F-1 to Fig F-27 and from Fig E-10 to Fig E-18. The results presented in Fig VI-1, Fig VI-2, and Fig VI-3 indicate that when the sample period was increased from 0.04 seconds to 0.24 seconds, the performance of the CTRI filter against Trajectory 2 was not significantly degraded. However, the actual plots of the results from the Monte Carlo simulation Fig F-1 to Fig F-27 and Fig E-10 to Fig E-18 indicate that as the sample period was increased, the mean error plots exhibited larger excursions from the mean error of the corresponding state for a sample period of 0.04 seconds. Further, the condition variance of the filter for each state grew as the update interval was increased. These trends were expected; however, the deviation of the mean error with an increase in sample period was more

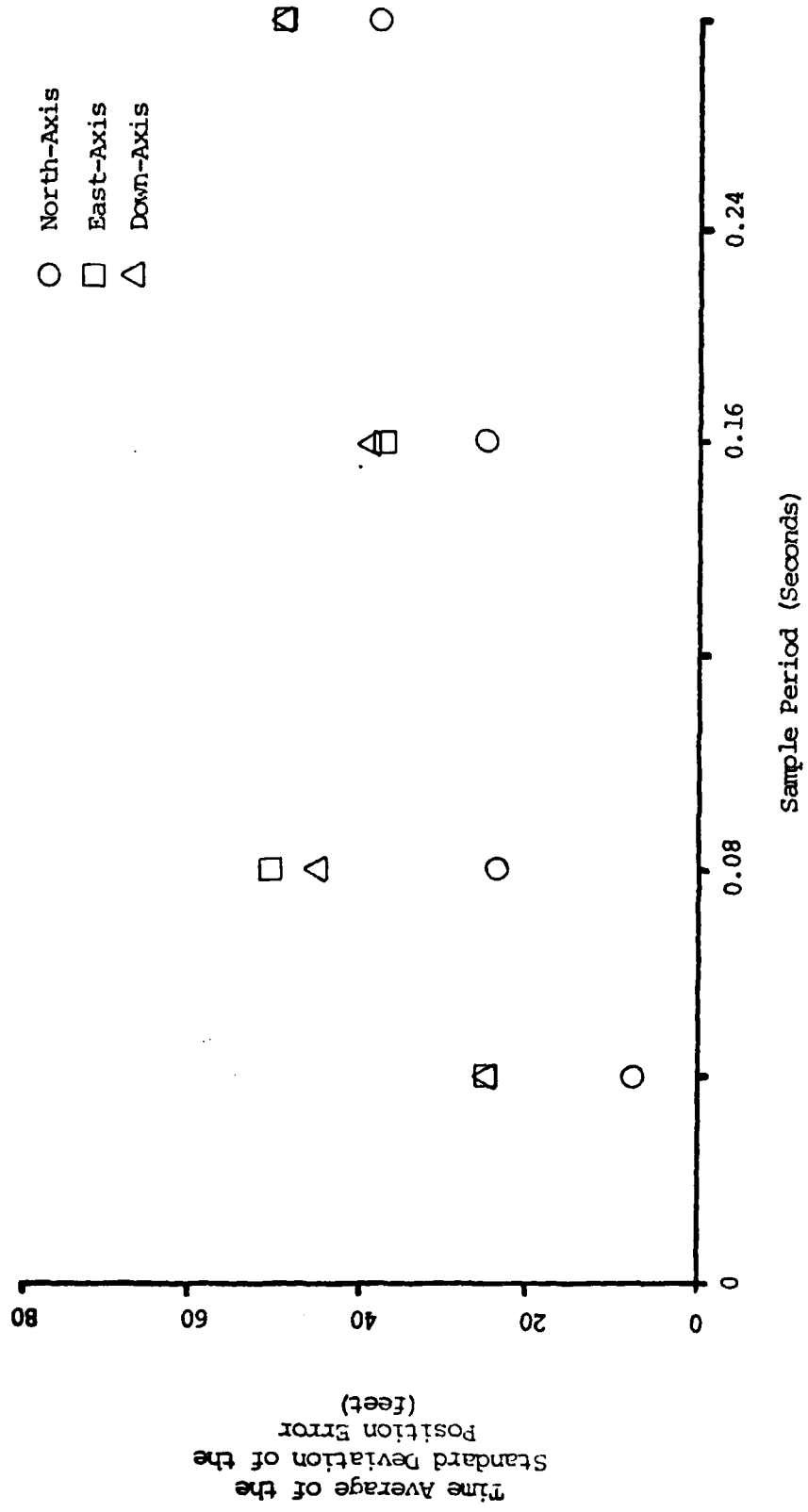


Figure VI-1. Performance of the Position Estimates for the CIRI Filter When Flown Against Trajectory 2 for Various Sample Periods

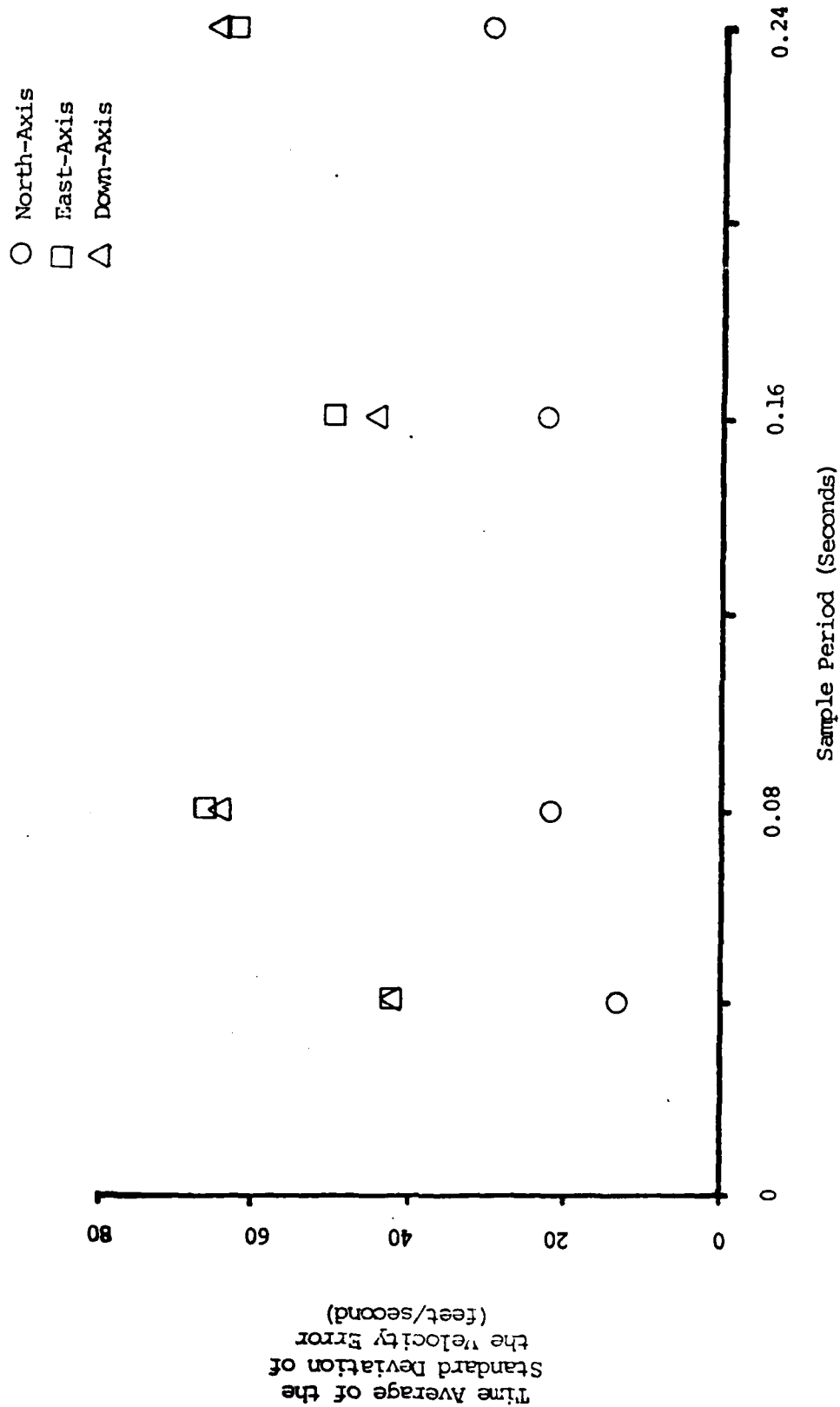


Figure VI-2. Performance of the Velocity Estimates for the CPRI Filter When Flown Against Trajectory 2 for Various Sample Periods

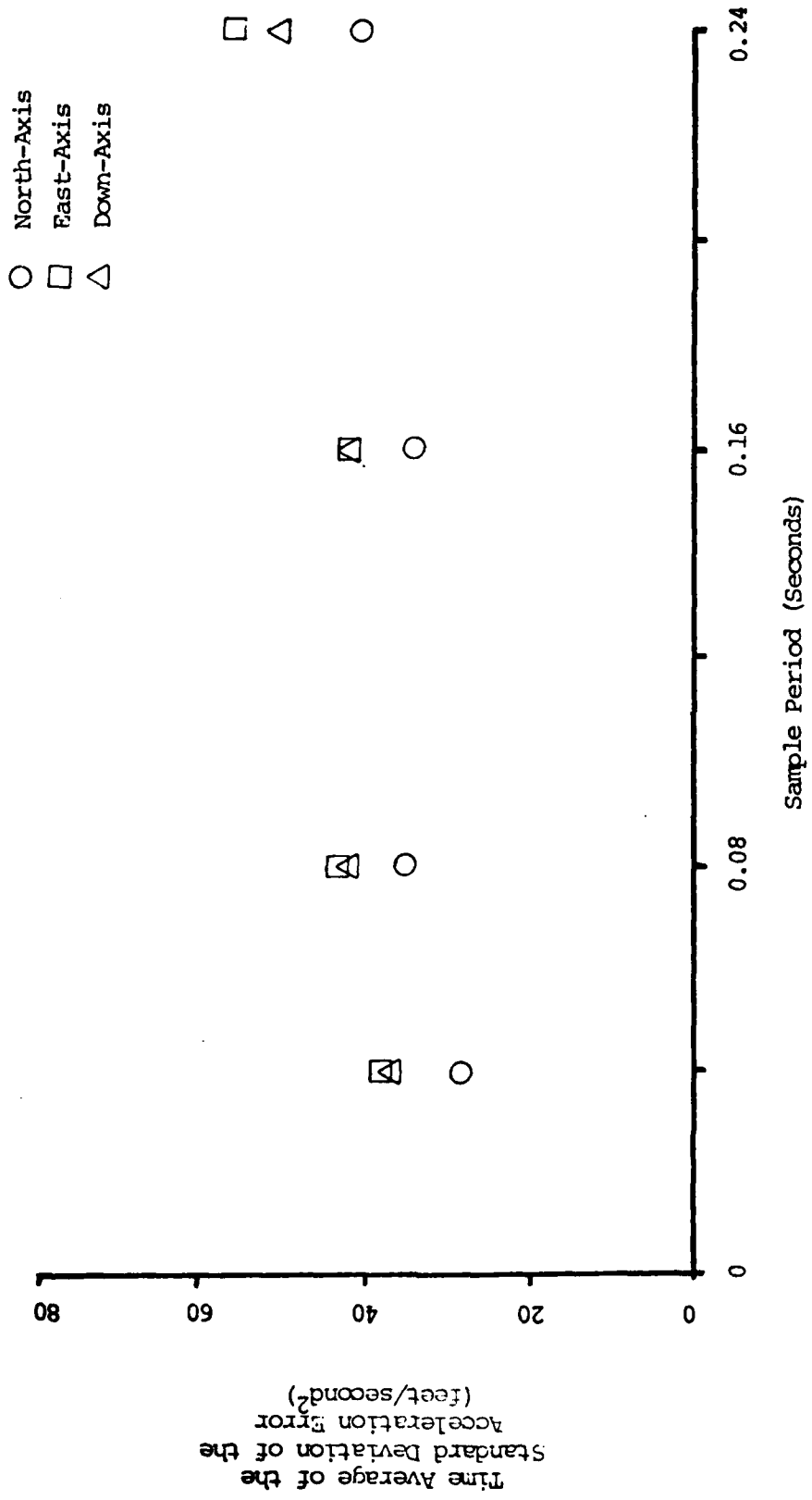


Figure VI-3. Performance of the Acceleration Estimates for the CIRI Filter When Flown Against Trajectory 2 for Various Sample Periods

irregular than expected especially for sample periods of 0.16 seconds and 0.24 seconds. (The rms error should be evaluated for confirm the results.) Apparently, the use of a constant descriptor Q of the dynamic driving noise to evaluate the performance of the CTRI filter for the longer sample period was inappropriate even though the dynamics were considered to be continuous functions of time. The filter was dependent on a necessarily erroneous dynamics model for the longer intervals so additional pseudonoise would be required as the sample period was increased. Additional evaluations of the filter's performance with increased pseudonoise should be accomplished if longer sample periods are required. However, sample periods of less than 0.08 seconds could be used with confidence.

Effects of Variations in Measurement Noise for the CTRI Filter

The results for the variations in the elements of the descriptor R of the measurement noises for the CTRI filter only (as discussed in Section V) are presented in Table VI-3, Table VI-4, and Table VI-5. The plots of the results of the Monte Carlo simulations which were used to calculate the approximate percent change between the time average of the values for the baseline case and the case being evaluated over the interval from 5 to 12 seconds are presented in Fig E-10 to Fig E-18 (baseline case), Fig G-1 to Fig G-27 (variations of the variance of the range measurement noise), Fig H-1 to Fig H-2 (variations of the variances of the error angle measurement noises), and Fig I-1 to Fig I-27 (variations of the variance of the range rate measurement noise). As the variance of the range noise σ_R^2 was increased, the performance of the CTRI filter against Trajectory 2 varied significantly only in the position estimate along the north-axis. The time average of the standard deviation of the errors and the time average of the square root of the filter's conditional variance increased 200 percent as the variance of the range measurement noise

TABLE VI-3. Effect of Variations of the Variance of the Range Measurement σ_R^2 on the Performance of the CTRI Filter When Flown Against Trajectory 2

σ_R^2 (feet ²)	Approximate Percent Change With Respect to Baseline Case ($\sigma_R^2 = 10000 \text{ feet}^2$)											
	$\left(\frac{\text{Mean Error}}{\text{Standard Deviation of Error}} \right)$ $\left(\frac{\text{Square Root of Filter Variance}}{\text{Square Root of Filter Variance}} \right)$											
	Position			Velocity			Acceleration					
	North	East	Down	North	East	Down	North	East	Down	North	East	Down
1000	0	0	0	0	0	0	0	0	0	0	0	0
	-50	0	0	0	0	0	0	0	0	0	0	0
	-50	0	0	0	0	0	0	0	0	0	0	0
100000	0	0	0	0	0	0	0	0	0	0	0	0
	+50	0	0	0	0	0	0	0	0	0	0	0
	+50	0	0	0	0	0	0	0	0	0	0	0
No Measurement	+100	0	0	0	0	0	0	0	0	0	0	0
	+150	0	0	0	0	0	0	0	0	0	0	0
	+150	0	0	0	0	0	0	0	0	0	0	0

TABLE VI-4. Effect of Variations of the Variance of the Error Angle Measurements σ_a^2 and σ_e^2 on the Performance of the CTRI Filter When Flown Against Trajectory 2

σ_a^2 and σ_e^2 (radians ²)	Approximate Percent Change With Respect to Baseline Case ($\sigma_a^2 = \sigma_e^2 = .0001$ radians ²)														
	Position						Velocity						Acceleration		
	North	East	Down	North	East	Down	North	East	Down	North	East	Down	North	East	Down
0.00001	0	-25	-10	-5	-30	-10	-10	-30	-10	-30	-10	0	-30	0	0
	0	-50	-50	-10	-30	-50	-10	-30	-40	-30	-40	0	-20	-10	-10
	0	-30	-50	-10	-30	-50	-10	-30	-40	-30	-40	0	-20	-10	-10
0.001	+30	+60	+100	+40	+10	+100	+40	+10	+10	+100	+40	+50	+10	+10	+10
	+20	+100	+60	+50	+100	+60	+50	+100	+100	+100	+50	+20	+10	+50	+50
	+20	+100	+80	+50	+100	+80	+50	+100	+120	+100	+50	0	+10	+20	+20
No Measurement	Divergent	Divergent	Divergent	Divergent	Divergent	Divergent	Divergent	Divergent	Divergent	Divergent	Divergent	Divergent	Divergent	Divergent	Divergent

TABLE VI-5. Effect of Variations of the Variance of the Range Rate Measurement σ_R^2 on the Performance of the CTRL Filter When Against Trajectory 2

σ_R^2 (feet ² / seconds ²)	Approximate Percent Change With Respect to Baseline Case ($\sigma_R^2 = 625 \text{ feet}^2/\text{second}^2$)											
	Position						Velocity			Acceleration		
	North	East	Down	North	East	Down	North	East	Down	North	East	Down
62.5	0	0	0	0	0	0	0	0	-25	0	0	0
	-5	0	0	-5	0	0	0	0	-30	0	0	0
	-5	0	0	-5	0	0	0	0	-25	0	0	0
6250.0	0	0	0	+25	0	0	0	0	+10	0	0	0
	+30	0	0	+30	0	0	0	0	+30	0	0	0
	+30	0	0	+60	0	0	0	0	+25	0	0	0
No Measurement	+10	+10	+5	+10	+10	+5	+5	+5	+10	+10	+5	+5
	+125	+15	+5	+200	+10	+5	+5	+5	+80	+20	+5	+5
	+125	+15	+5	+270	+10	+5	+5	+5	+100	+10	+5	+5

Mean Error
(Standard Deviation of Error)
Square Root of Filter Variance

increased by two orders of magnitude. Since the range measurement was along the north-axis for most of Trajectory 2, the effect of a variation in the variance of the range measurement noise was expected along that axis. Furthermore, since the velocity estimates were one integration removed from the range measurement and the acceleration estimates were two integrations removed, the effects of the variation of the variance of the range measurement noise had little effect on these estimates. Moreover, when no range measurements were available, the CTRE filter still was able to estimate the states, when provided the exact initial conditions, without diverging. (Note that the range rate measurement was still available and would provide range information.)

For variations of the variances of the error angle measurement noises σ_a^2 and σ_e^2 , the major effect was apparent in the position and velocity estimates along the east- and down-axis. As these variances were increased by two orders of magnitude, the time average of the mean error, the standard deviation of the error, and the square root of the filter's conditional variance of these estimates increased approximately 110 percent. The information available from the error angle measurements for Trajectory 2 was mostly along the east- and down-axis. Thus, the effects of the variation of the variances of the error angle measurement noises visible in these estimates were as expected. Furthermore, when the error angle measurements were not available, the filter was not able to estimate the states even though the filter started from perfect initial conditions. The lack of these measurements apparently created an observability problem.

When the variance of the range rate measurement noise σ_R^2 was varied, the position, velocity and acceleration estimates along the north-axis showed the major effects. As the variance was increased by two orders

of magnitude the time average of the standard deviation of the error and the square root of the filter's conditional variance increased approximately 40 percent while the mean error did not vary significantly. As with the range measurement, the range rate measurement for Trajectory 2 provided information along the north-axis, and the variation of the three estimates along the north-axis with changes in the variance of the range-rate measurement noise was as expected. Furthermore, the CTRI filter was able to estimate the states without a range rate measurement from perfect initial conditions without diverging. (Note that the range measurement was still available and would provide range rate information.)

Based on these results, the CTRI filter demonstrated the ability to perform adequately even for large changes in the variances of the range and range rate measurement noises used for the filter. However, the filter was sensitive to variations in the variances of the error angle measurement noises. Furthermore, the filter was evaluated with perfect initial conditions provided to the filter, and additional evaluations of the filter for uncertain initial conditions should be performed to establish the sensitivity of the filter to the changes of the variances of the measurement noises.

VII Conclusions and Recommendations

Conclusions

The CTRI filter and the GMI filter provide performance equal to or superior to the performance of the GMLOS filter for the three trajectories evaluated for this thesis. When the target acceleration profiles are not demanding (as in Trajectory 1), the performance is nearly the same for the three filters. However, as the target acceleration profiles become more demanding (Trajectory 2 and Trajectory 3) the performance of the GMLOS filter is worse than the performance of either of the other two filters. The figures of merit for the GMI filter are at least 20 percent less than the corresponding figures for the GMLOS filter for Trajectory 3, while the figures of merit (except for the scalar magnitude of the time average of the standard deviation of the error) for the CTRI filter are in general at least 20 percent less than the corresponding figure for the GMLOS filter. Furthermore, for Trajectory 2, the CTRI filter provides the best estimates of the states, as expected, since the actual target acceleration is better modeled by a CTRI acceleration model than by either the GMLOS or GMI acceleration models. Moreover, for the more demanding target acceleration trajectories, there is a tuning issue that requires further study to explore the reduction of the large excursions of the mean error experienced during the periods of poorly modeled actual target accelerations. Finally, the CTRI filter requires substantially more arithmetic operations (176 multiplications for the CTRI filter versus 18 for the GMI filter, 223 additions for the CTRI filter versus 162 for the GMI filter, and 20 divisions for the CTRI filter versus none for the GMI filter) than the GMI filter for each propagation step.

Sample periods for the CTRI filter of 0.04 seconds and 0.08 seconds provide estimates of the states that are not significantly different. However, as the sample period is increased to 0.16 seconds and 0.24 seconds, the estimates of the states become very irregular, and the use of the same descriptor Q of the dynamic driving noise apparently is inappropriate. The CTRI filter depends on an erroneous dynamics model for longer intervals requiring the addition of pseudonoise as the sample period is increased. In any case, sample periods of less than 0.08 seconds provide adequate filter performance, and should be used for implementation.

The effects of the variations of the variances of the measurement noises are as expected for the CTRI filter. When the variance of the range measurement noise is increased by two orders of magnitude, only the time average of the standard deviation of the error and the time average of the square root of the filter's conditional variance of the position estimate along the estimated LOS are increasing approximately 200 percent. When there is no range measurement, but perfect initial conditions are available, the CTRI filter is able to estimate the states without diverging. For an increase of two orders of magnitude of the variances of the error angle measurement noises, only the time average of the mean error, the time average of the standard deviation of the error, and the time average of the square root of the filter's conditional variance for the position and velocity along the east- and down-axis (over the same interval) increase with the increase approximately 110 percent. Furthermore, when the error angle measurements are not available, the filter can not estimate the states even though perfect initial conditions were provided since the filter diverges, indicating that there is an observability problem. Increasing the variance of the range rate measurement noise by two orders of magnitude increases

only the time average of the standard deviations of the error and the time average of the square root of the filter's conditional variance for the same interval along the estimated LOS for position, velocity, and acceleration with the increase approximately 40 percent. If the range rate measurement is not available, the CTRI filter still is able to estimate the states from perfect initial conditions without diverging. The CTRI filter is most sensitive to variations in the accuracy of the measurements of the error angles while the accuracy of the range and range rate measurements are not as critical.

Recommendations

The GMI and CTRI filters should be developed with noise added to the measurements provided by the IMU and with a dynamics model for the tracker. The use of an imperfect IMU would affect the propagation (by noisy attacker velocity measurements) and the update (by the noisy transformations from the earth-fixed reference frame to the attacker's body axis) for both filters. Also, the GMLOS filter should be modified to include the tracker dynamics. These new models would allow evaluation of filters that more nearly represent the actual system that would be implemented. Then these filters should be evaluated versus several different trajectories to insure that the trends identified in this thesis are also true for the more realistic models.

Additional evaluations of the effects of different update rates should be accomplished with the CTRI filter retuned for each different update rate with pseudonoise added to compensate for the dependence of the filter on an erroneous dynamics for longer periods as the sample period is increased. Further, the GMI filter should also be included in this evaluation since it is certainly a good candidate for implementation.

The robustness of the GMLOS, GM, and CTRE filters using the new models discussed above should be evaluated to determine the effect of variations in dynamics and measurement model parameters, dynamic driving noise statistics, and measurement noise statistics.

All three filters should be investigated to explore the effect of a retuning effort on the mean errors, standard deviations of the errors, and the peak mean errors. The filters should be tuned to match the filter's computed conditional variances with the root mean square of the true errors committed by the filter to guard against severe biases.

The recovery from bad initial conditions of the three filters should be investigated since this issue was not addressed in the results presented in this thesis. If additional robustness is required, a constant gain extended Kalman filter implementation should be explored.

Finally, if the retuning of the filters does not provide substantially better performance, the addition of a bias correction term or the use of adaptive Kalman filter techniques should be explored to provide the desired reductions of the mean errors, standard deviation of the error, and peak mean errors.

Bibliography

1. Fosha, Charles E., Anthony L. Leatham, and Roger P. Neeland, "A Digital Line of Sight Estimator Employing the Ascot Electro-Optical Sensor For Air-to-Air Gunnery Engagements", Technical Report USAFA-TR-77-11, prepared for the Avionics Laboratory, Wright Patterson AFB, OH, Jun 1977.
2. Reid, J. Gary, "Modern Principles of Avionics Fire Control and Armament", Lecture Notes, Air Force Institute of Technology, 1980.
3. Maybeck, Peter S., "Stochastic Estimation and Control", Lecture Notes, 1980.
4. Silverthorn, James T., Discussions concerning performance of current trackers, Mar 1980.
5. Musick, Stanton H., "SOFE: A Generalized Digital Simulation for Optimal Filter Evaluation User's Manual", Technical Memorandum AFAL-TM-78-19, Revision A, Nov 1978.
6. Farrell, James L., Elmen C. Quesinberry, Charles D. Morgan, and Michael Tom, "Dynamic Scaling for Air-to-Air Tracking", IEEE Proceedings of the National Aerospace Electronics Conference, NAECON 1975, Dayton, OH, May 1975.
7. Individual flight test reports (unpublished) of tests conducted at the USAF Test Pilot School, Sep 1975 to Jun 1976.
8. Musick, Stanton H., Briefings on the use of the SOFEPL program, Apr 1980.
9. Bryant, Ralph S., "Cooperative Estimation of Targets By Multiple Aircraft", M.S. Thesis, Air Force Institute of Technology, Jun 1980.

APPENDIX A

Coordinate Transformation

General

Two coordinate transformations were calculated by the filter used for this thesis. One was the transformation of a vector coordinatized in the earth-fixed reference frame coordinates to the estimated LOS coordinated frame (and its inverse) and the other was the transformation of a vector coordinatized in the attacker's body frame reference system to the estimated LOS coordinate frame coordinates (and its inverse). (These axes systems are defined in Section II and Section III.) Both transformations involved only rotations about two axes; the corresponding axis for each transformation had no rotation. Furthermore, the Euler angles η and ν with rotations in that order were similarly defined for each transformation, and both transformations used the right hand rule to determine positive rotations. Therefore, only one transformation form was required.

Transformation Development

The transformation from coordinate frame A to coordinate frame B with the constraint that the y_B -axis remained in the plane of the x_A - y_A axis required only two Euler rotation angles η and ν to completely determine the transformation. By convention, the first rotation occurred about the z_A -axis as shown in Fig A-1 to an intermediate coordinate frame C. The transformation T_I^A of the unit vectors x_A , y_A , and z_A of coordinate frame A to the unit vectors x_C , y_C , and z_C of coordinate frame C is given by

$$\begin{bmatrix} x_C \\ y_C \\ z_C \end{bmatrix} = \begin{bmatrix} \cos \eta & \sin \eta & 0 \\ -\sin \eta & \cos \eta & 0 \\ 0 & 0 & 1 \end{bmatrix} \begin{bmatrix} x_A \\ y_A \\ z_A \end{bmatrix} = T_C^A \begin{bmatrix} x_A \\ y_A \\ z_A \end{bmatrix} \quad (A-1)$$

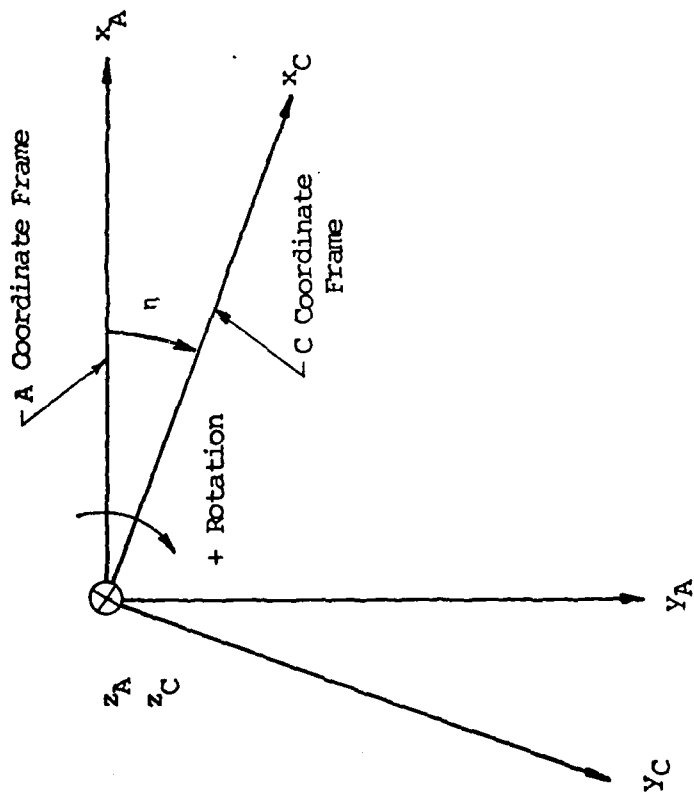


Figure A-1. Rotation About z_A -Axis

The second rotation about the y_C -axis (shown in Fig A-2) in which the unit vectors x_C , y_C , and z_C of the C coordinate frame were transformed to the unit vectors x_B , y_B , and z_C of the B coordinate frame is given by

$$\begin{bmatrix} x_B \\ y_B \\ z_B \end{bmatrix} = \begin{bmatrix} \cos v & 0 & -\sin v \\ 0 & 1 & 0 \\ \sin v & 0 & \cos v \end{bmatrix} \begin{bmatrix} x_C \\ y_C \\ z_C \end{bmatrix} = T_B^C \begin{bmatrix} x_C \\ y_C \\ z_C \end{bmatrix} \quad (A-2)$$

Combining the transformations in the proper order, the transformation T_B^A from the A coordinate frame to the B coordinate frame is given by

$$T_B^A = T_B^C T_C^A = \begin{bmatrix} c\eta cv & s\eta cv & -sv \\ -s\eta & c\eta & 0 \\ c\eta sv & s\eta sv & cv \end{bmatrix} \quad (A-3)$$

where c and s denote cosine and sine, respectively.

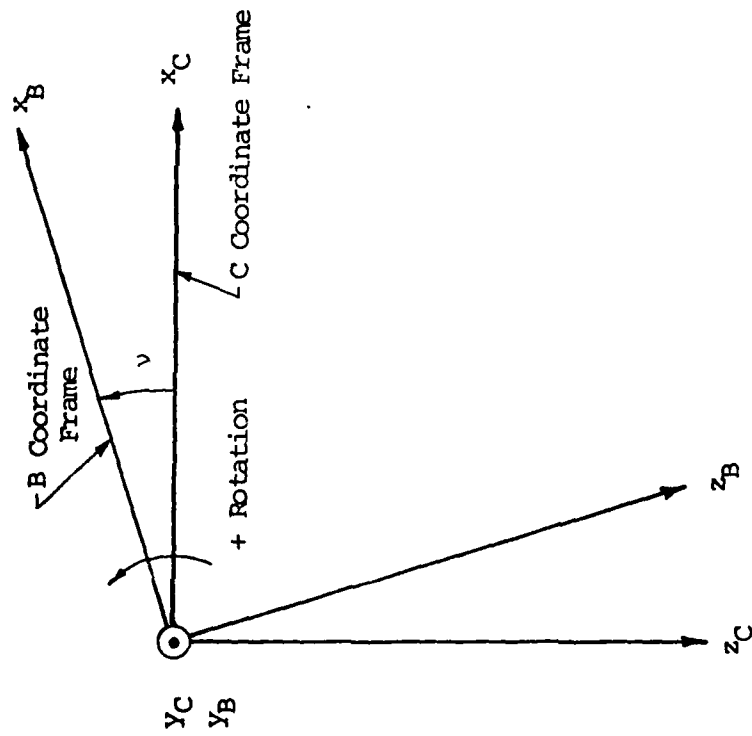


Figure A-2. Rotation About Y_C -Axis

APPENDIX B

Graphical Results of the Effect of Increasing Number
of Monte Carlo Simulations on Solution Accuracy

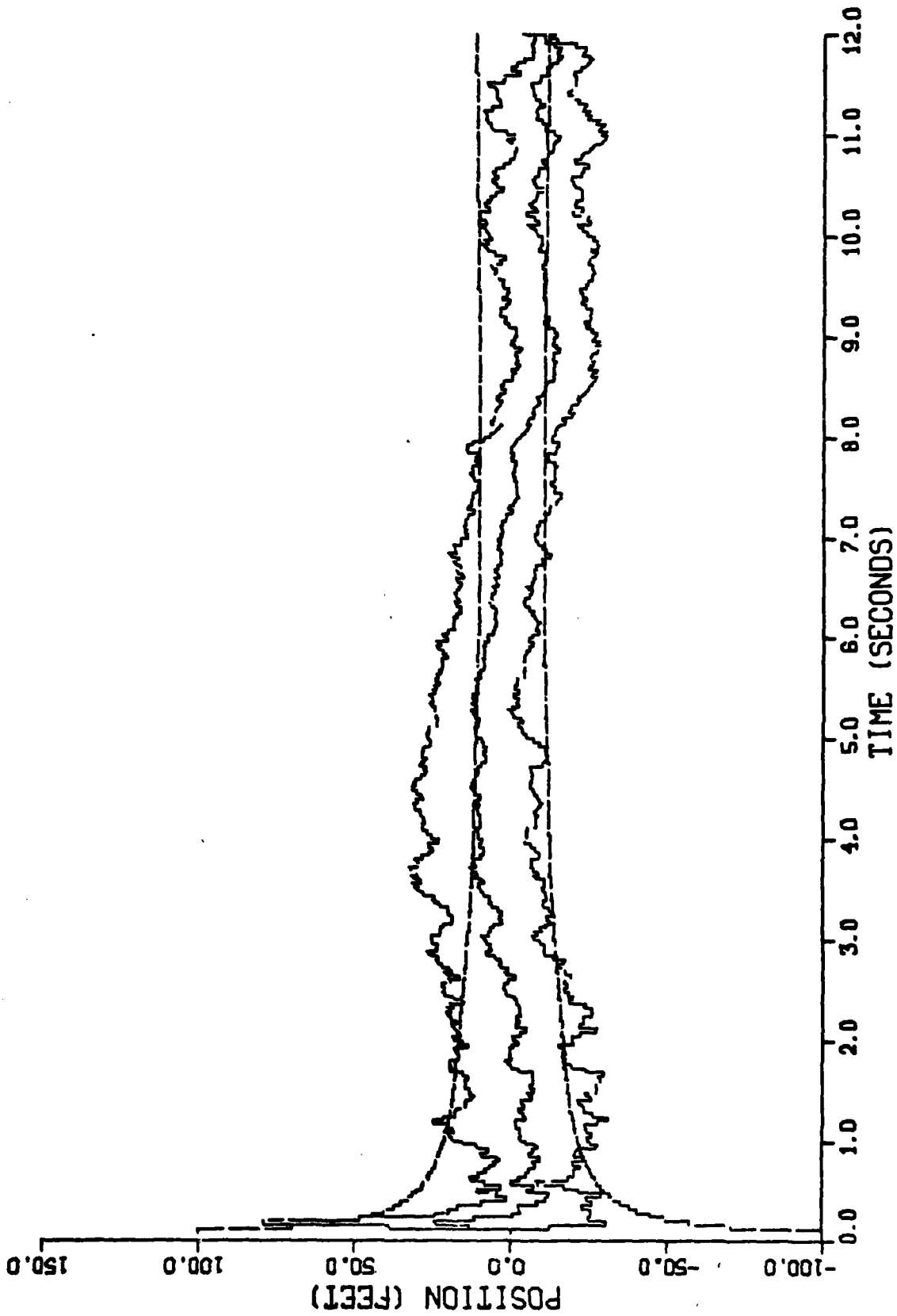


Figure B-1. Performance of the Constant Turn Rate Inertial Coordinate Filter Along the North-Axis for Trajectory 2 for 5 Monte Carlo Simulations

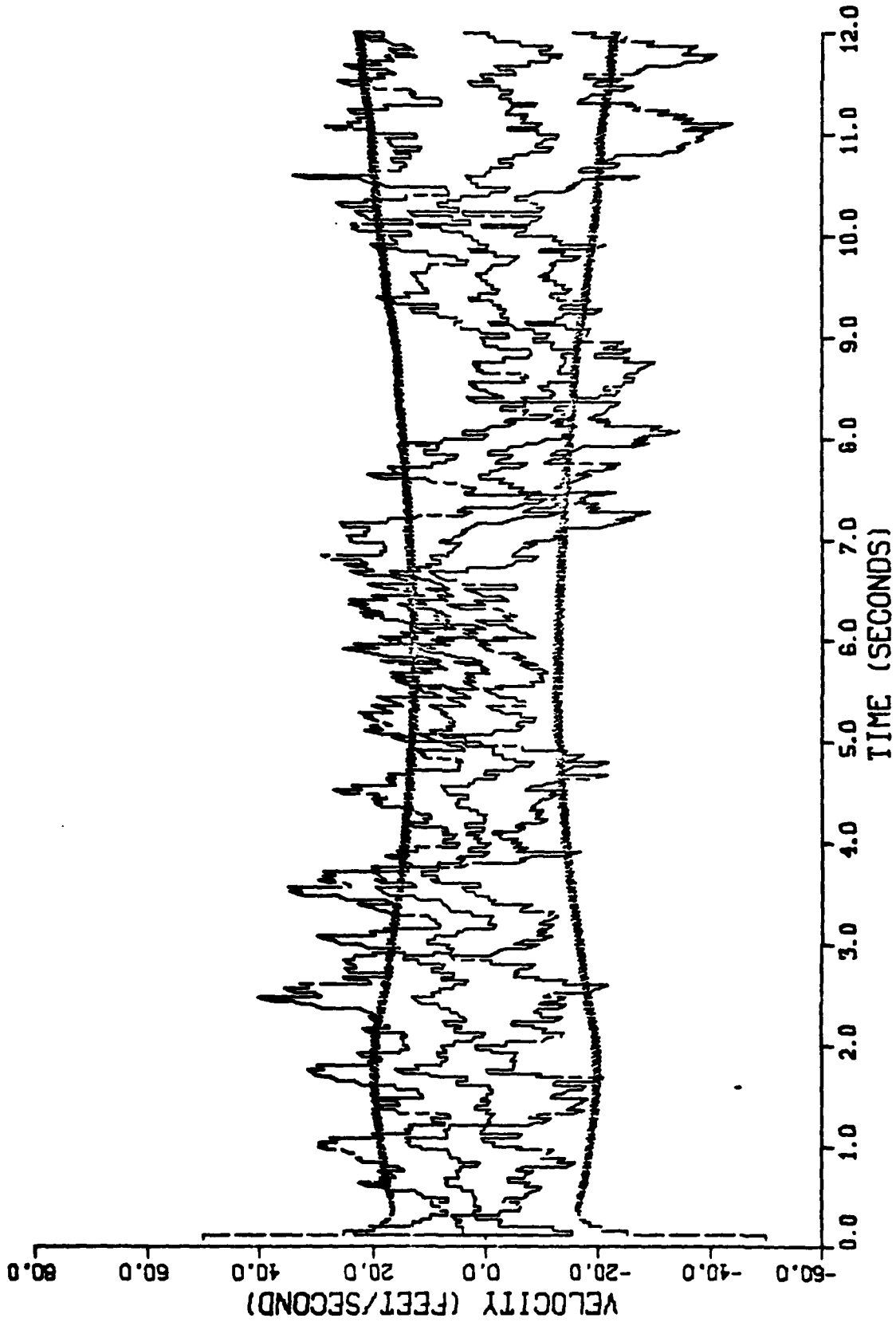


Figure B-2. Performance of the Constant Turn Rate Inertial Coordinate Filter Along the North-Axis for Trajectory 2 for 5 Monte Carlo Simulations

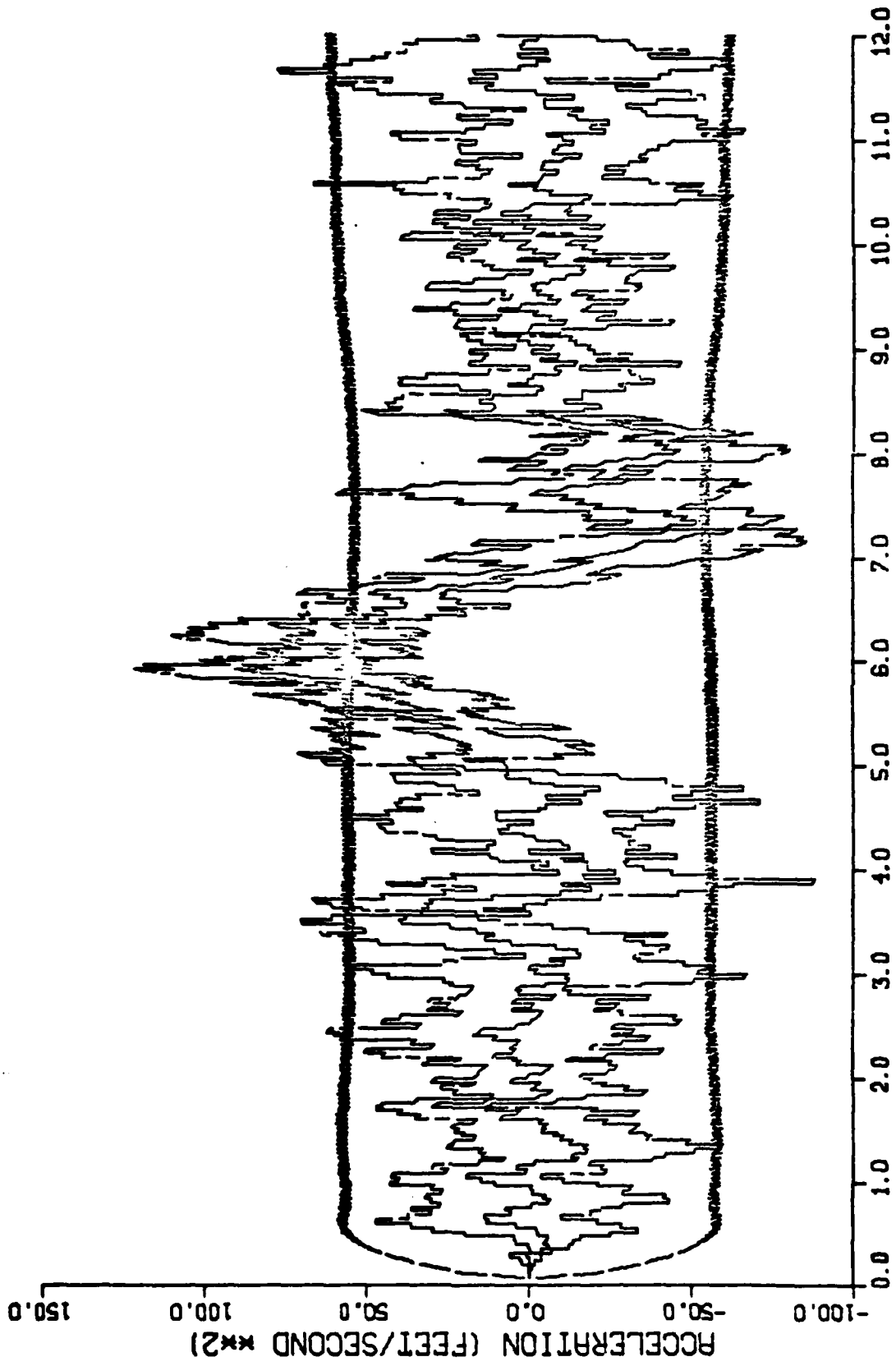


Figure B-3. Performance of the Constant Turn Rate Inertial Coordinate Filter Along the North-Axis for Trajectory 2 for 5 Monte Carlo Simulations

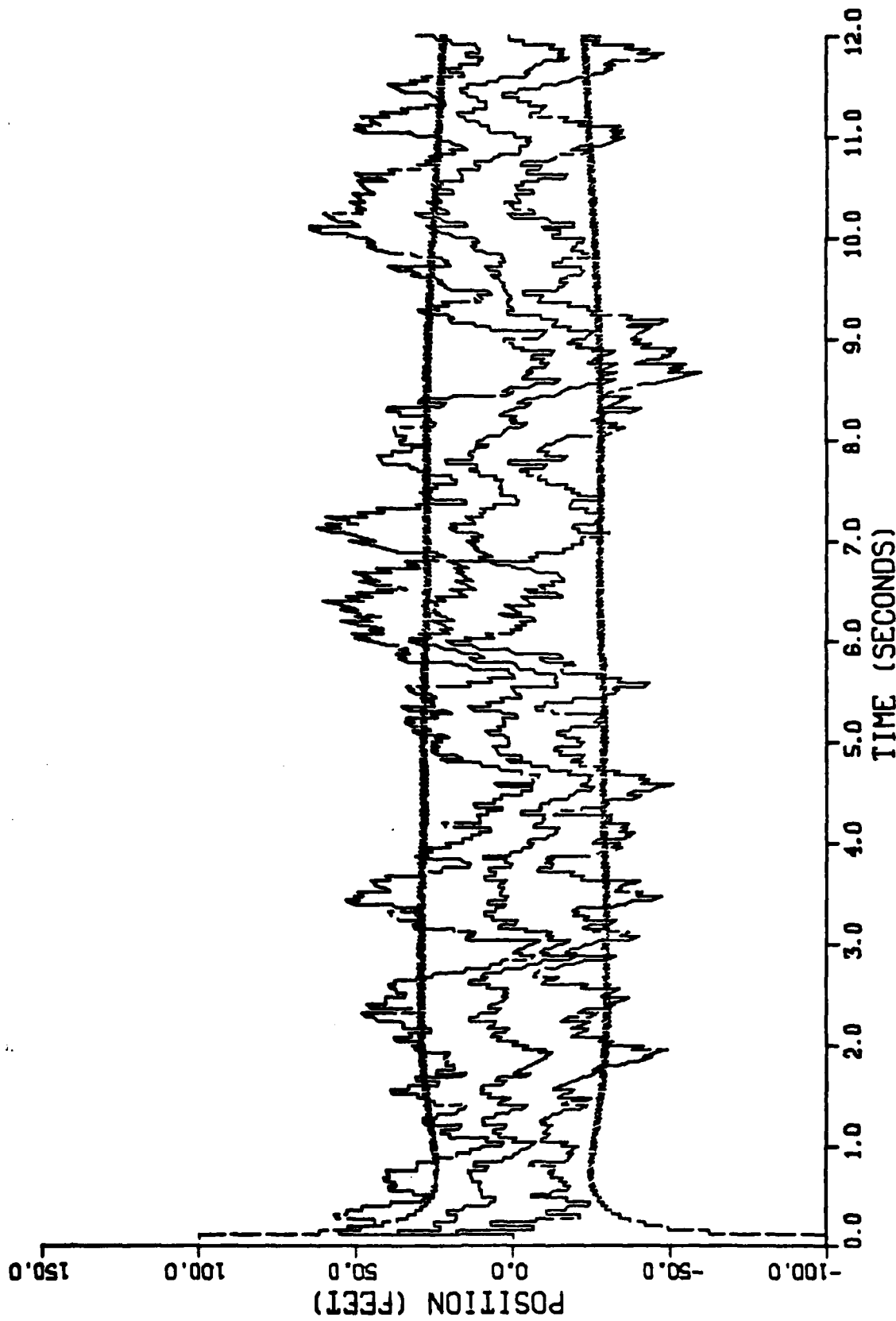


Figure B-4. Performance of the Constant Turn Rate Inertial Coordinate Filter Along the East-Axis for Trajectory 2 for 5 Monte Carlo Simulations

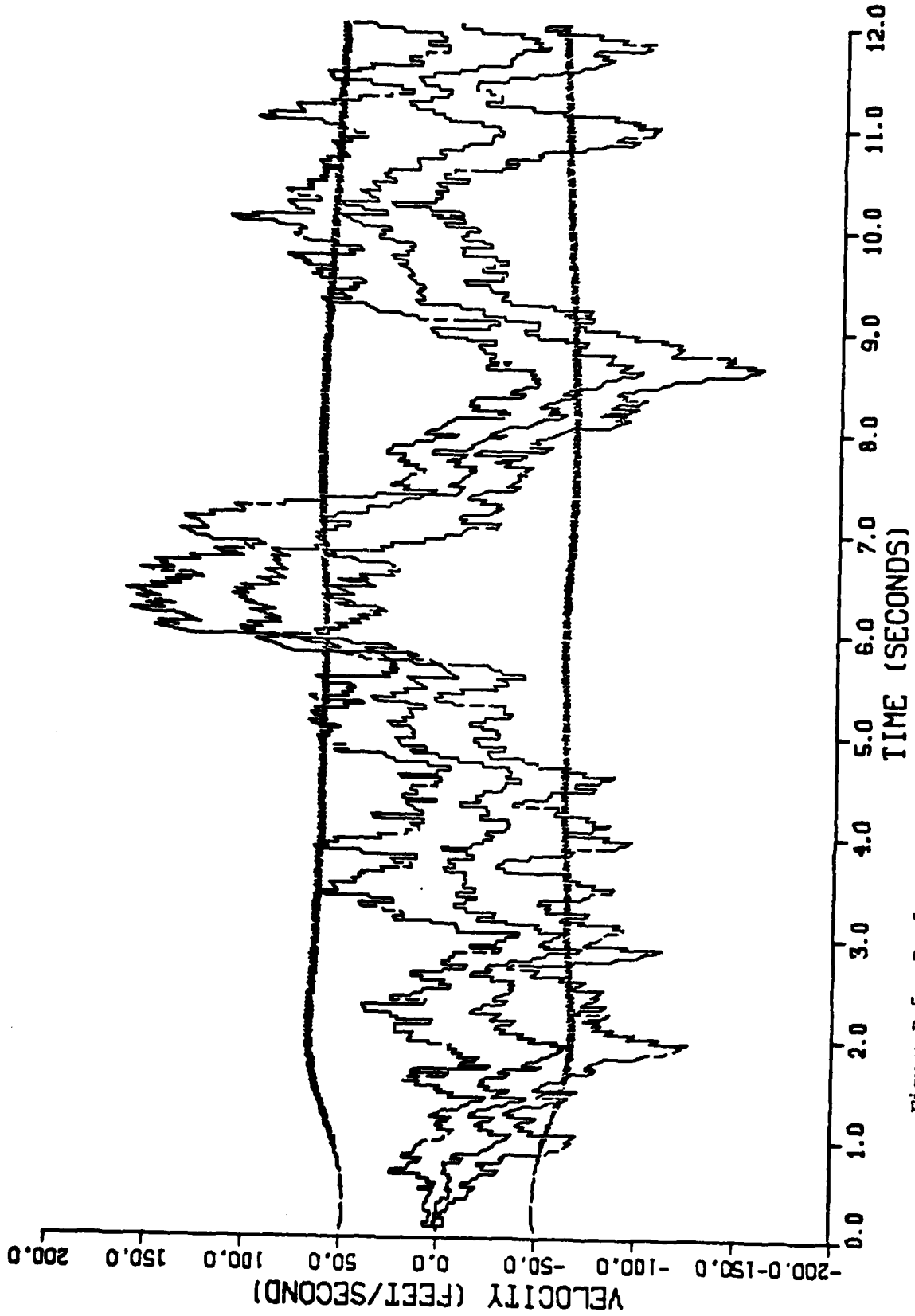


Figure B-5. Performance of the Constant Turn Rate Inertial Coordinate Filter Along the East-Axis for Trajectory 2 for 5 Monte Carlo Simulations

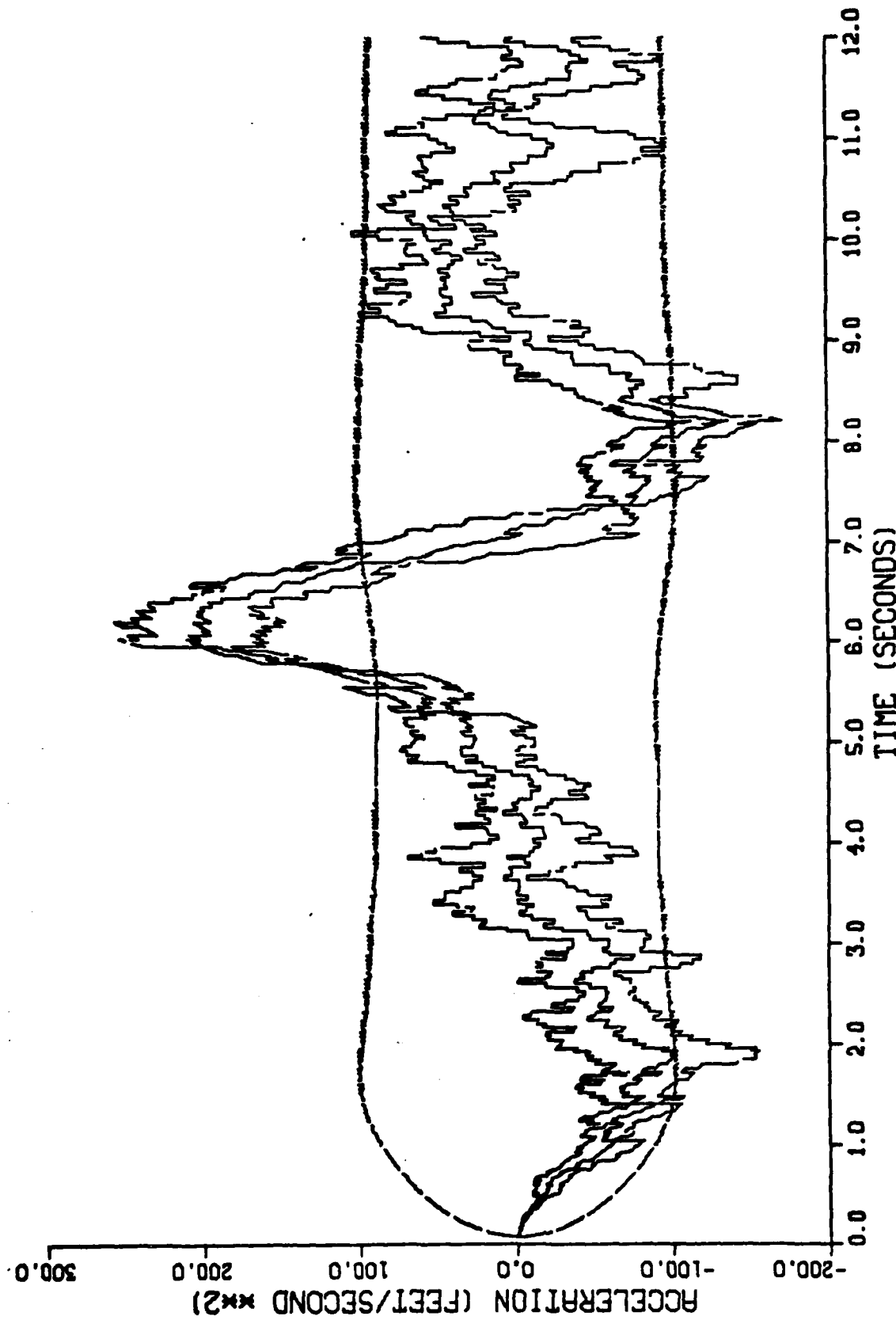


Figure B-6. Performance of the Constant Turn Rate Inertial Coordinate Filter Along the East-Axis for Trajectory 2 for 5 Monte Carlo Simulations

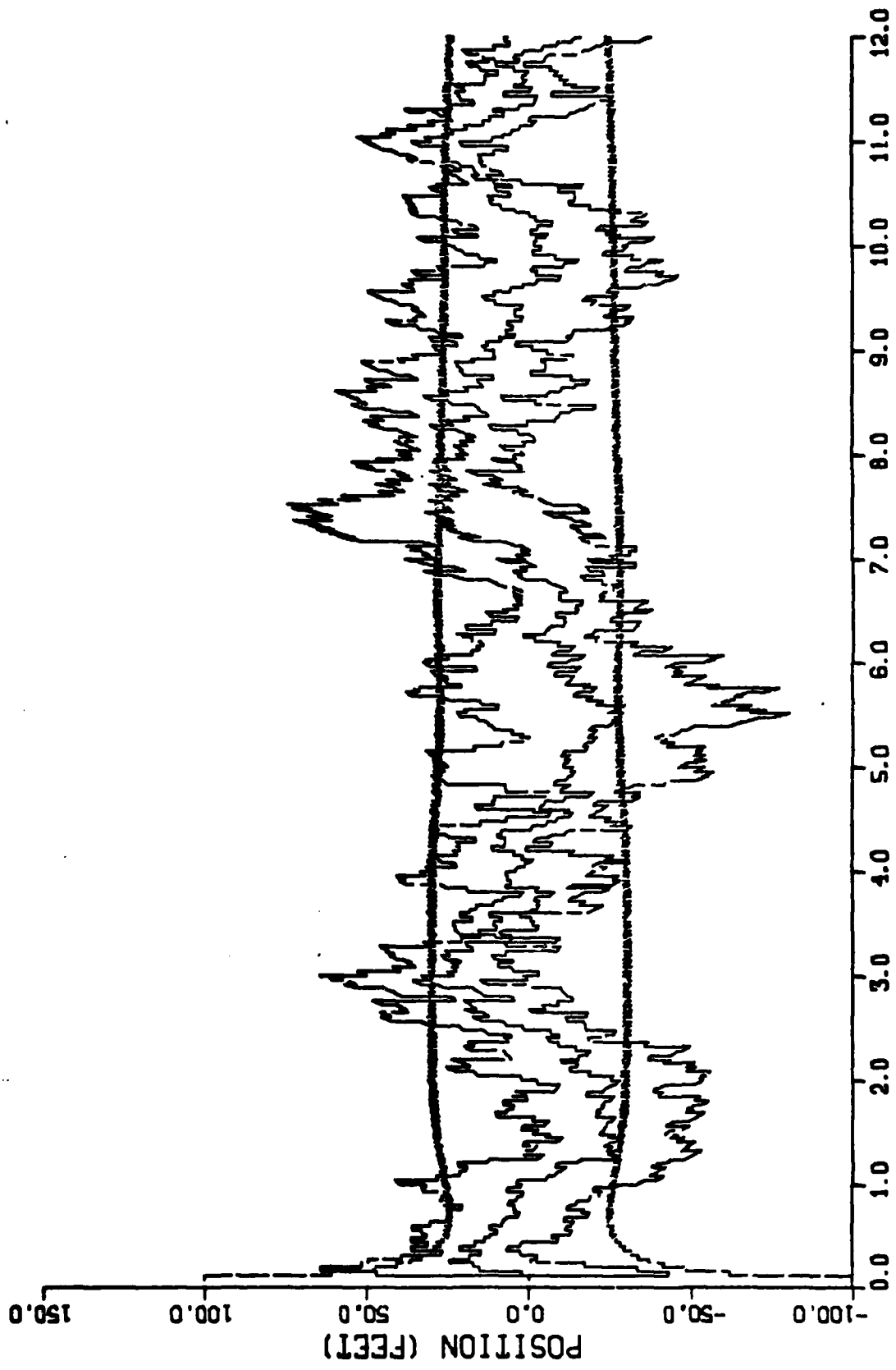


Figure B-7. Performance of the Constant Turn Rate Inertial Coordinate Filter Along the Down-Axis for Trajectory 2 for 5 Monte Carlo Simulations

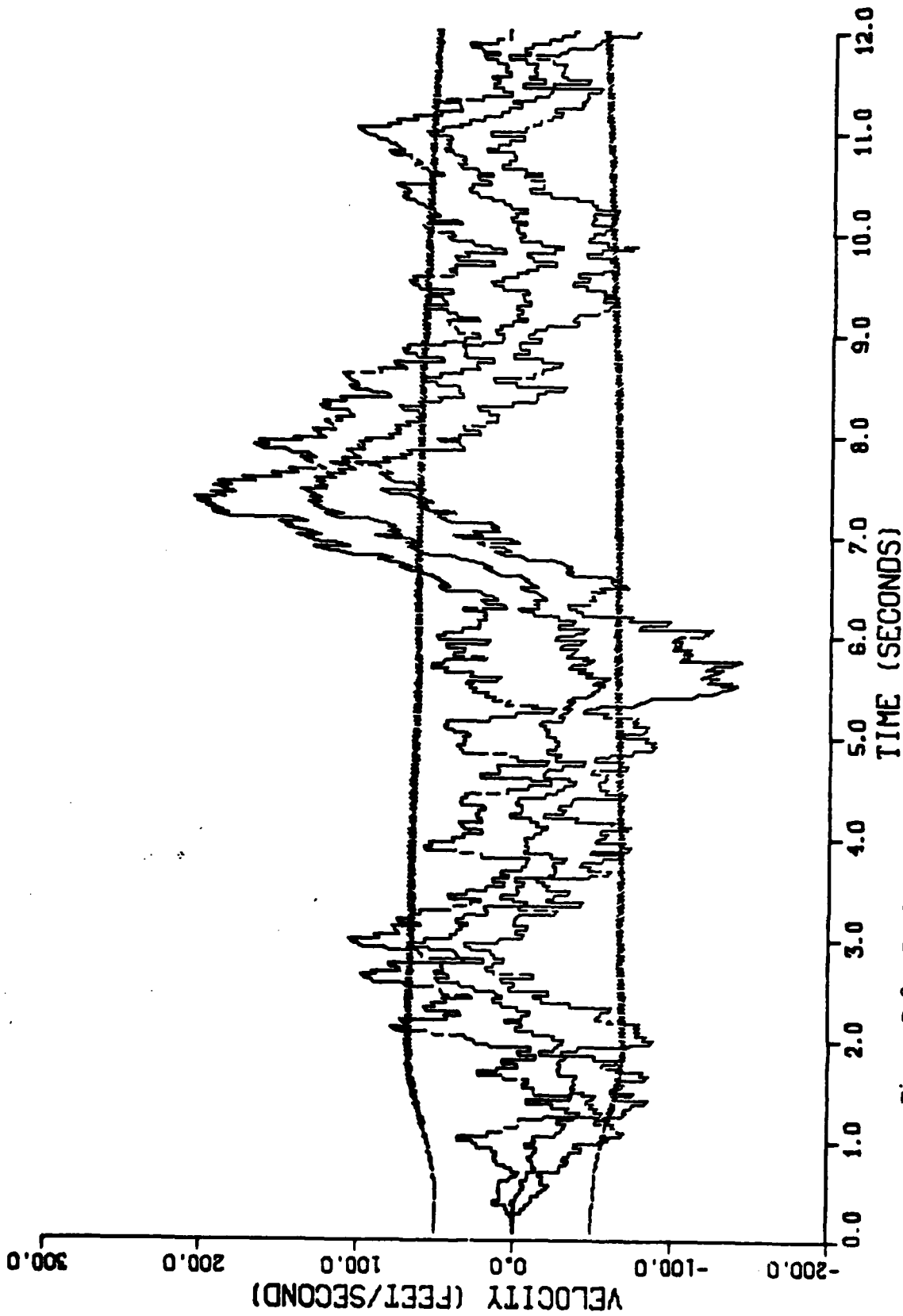


Figure B-8. Performance of the Constant Turn Rate Inertial Coordinate Filter Along the Down-Axis for Trajectory 2 for 5 Monte Carlo Simulations

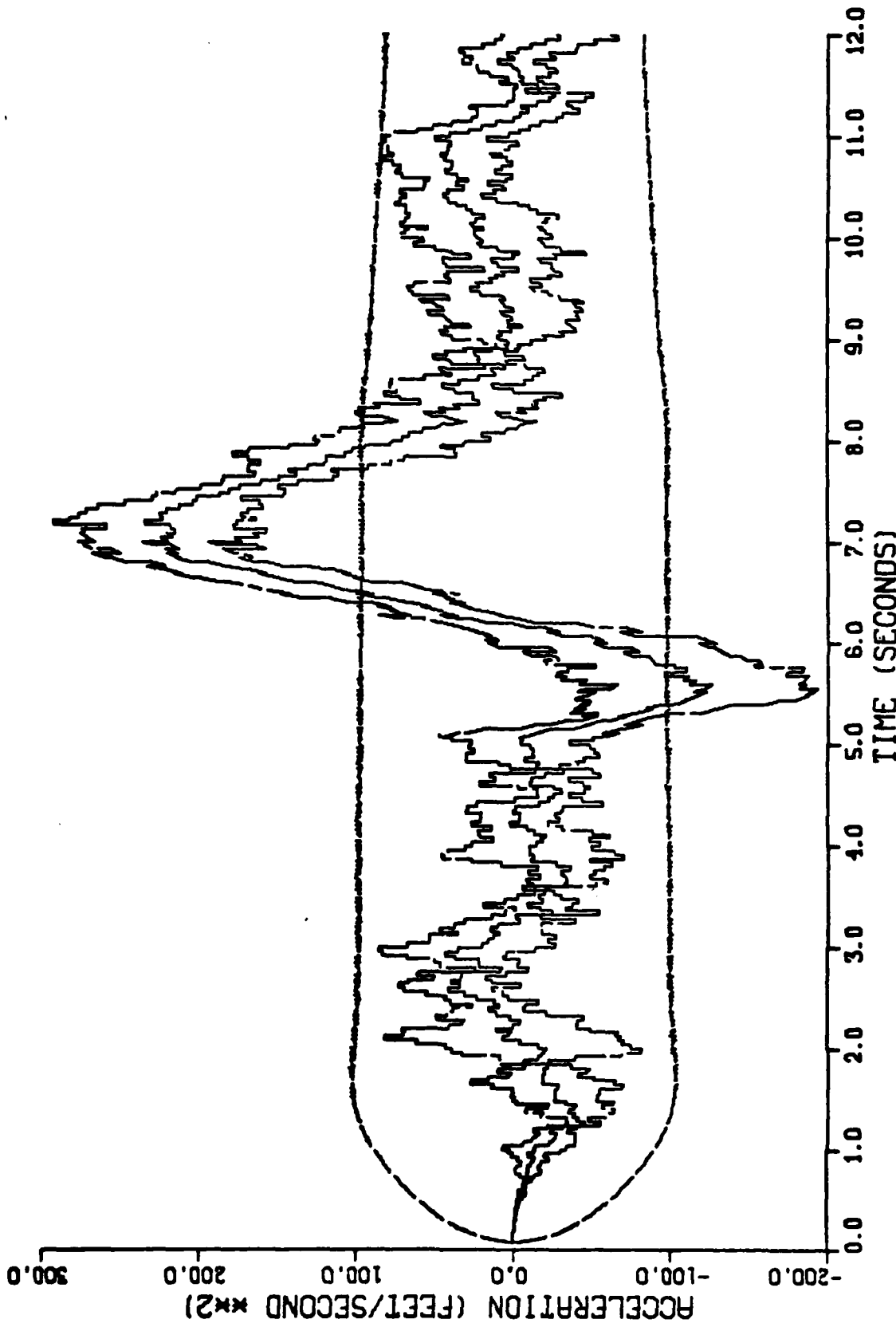


Figure B-9. Performance of the Constant Turn Rate Inertial Coordinate Filter Along the Down-Axis for Trajectory 2 for 5 Monte Carlo Simulations

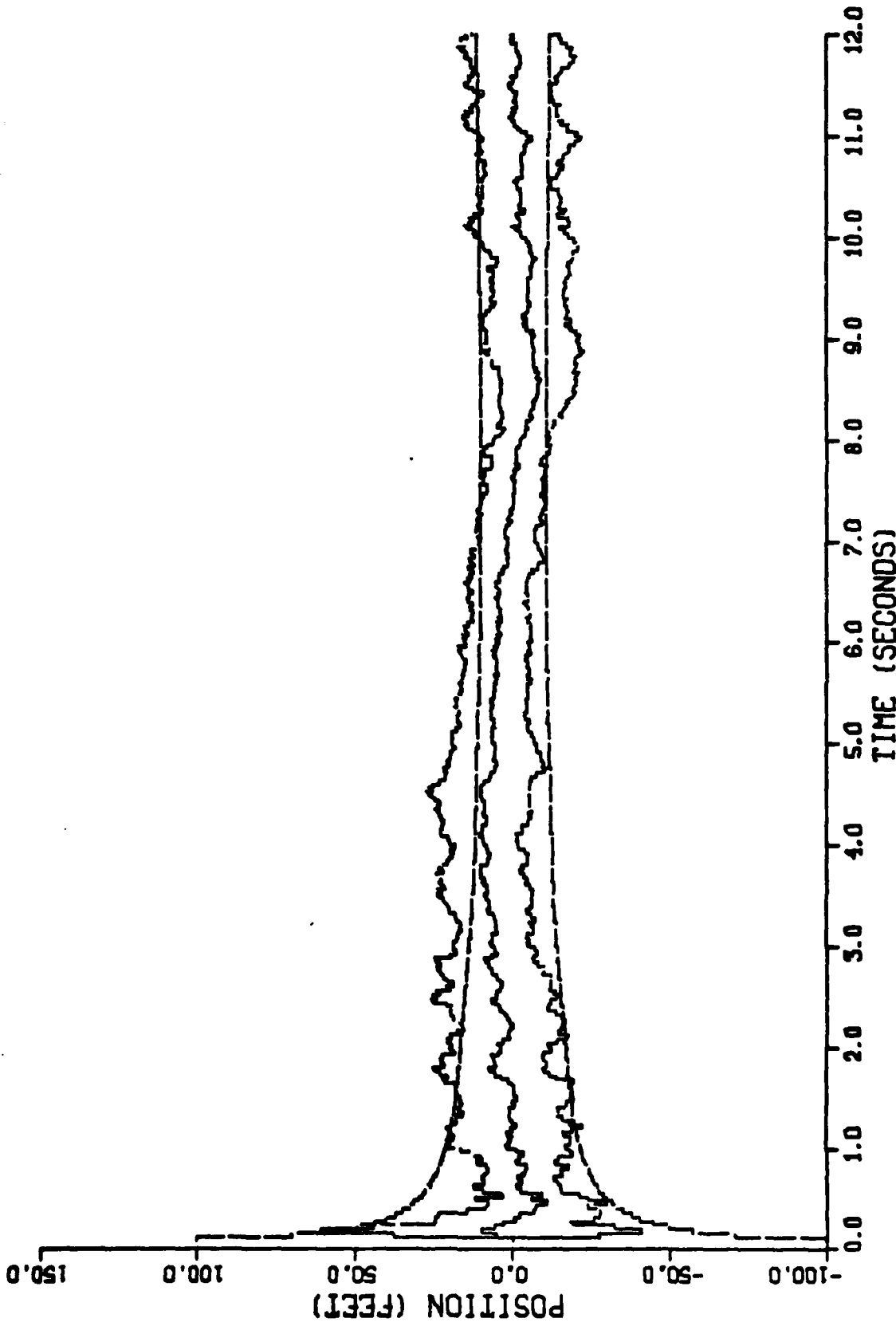


Figure B-10. Performance of the Constant Turn Rate Inertial Coordinate Filter Along the North-Axis for Trajectory 2 for 10 Monte Carlo Simulations

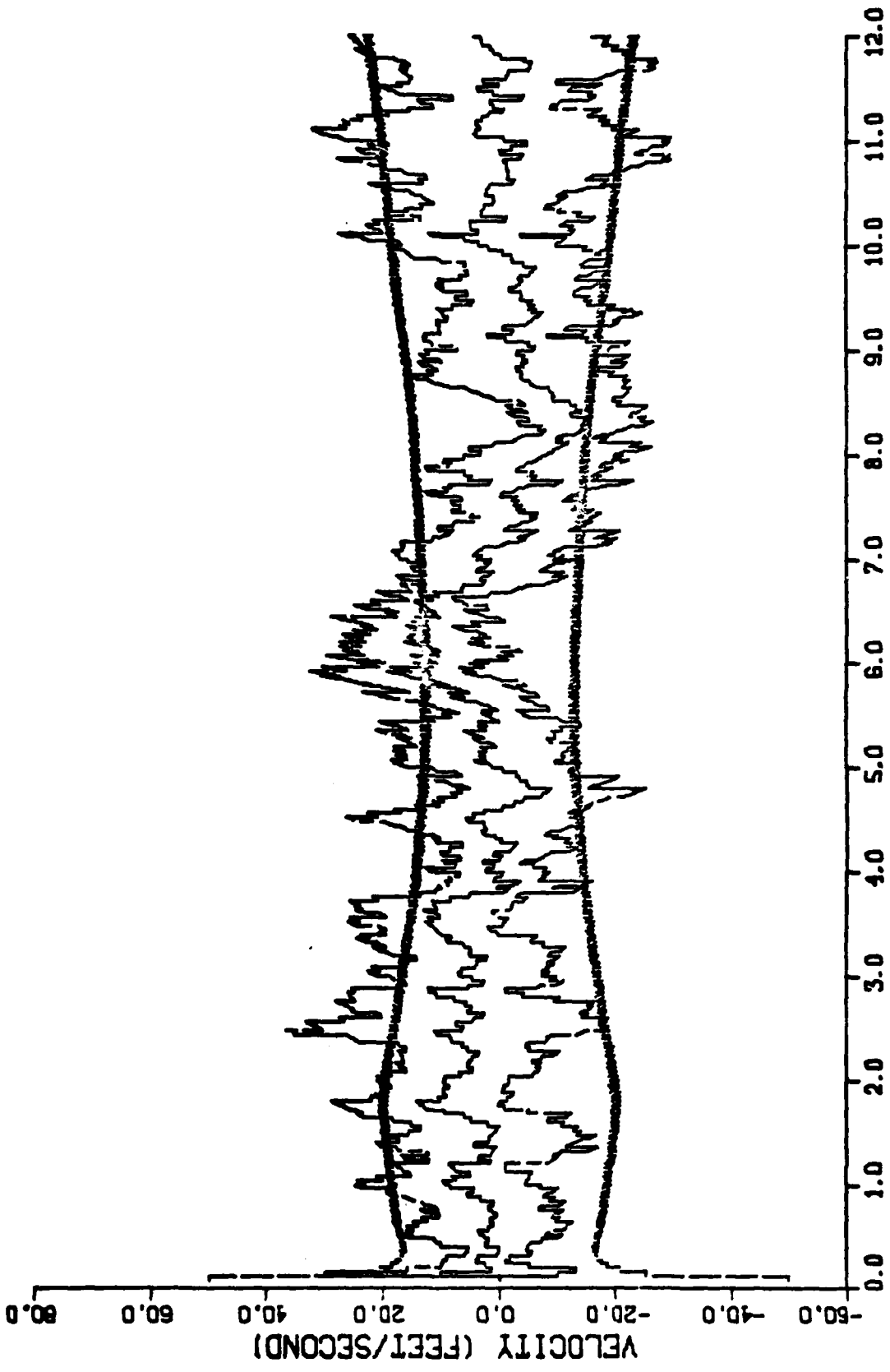


Figure B-11. Performance of the Constant Turn Rate Inertial Coordinate Filter Along the North-Axis for Trajectory 2 for 10 Monte Carlo Simulations

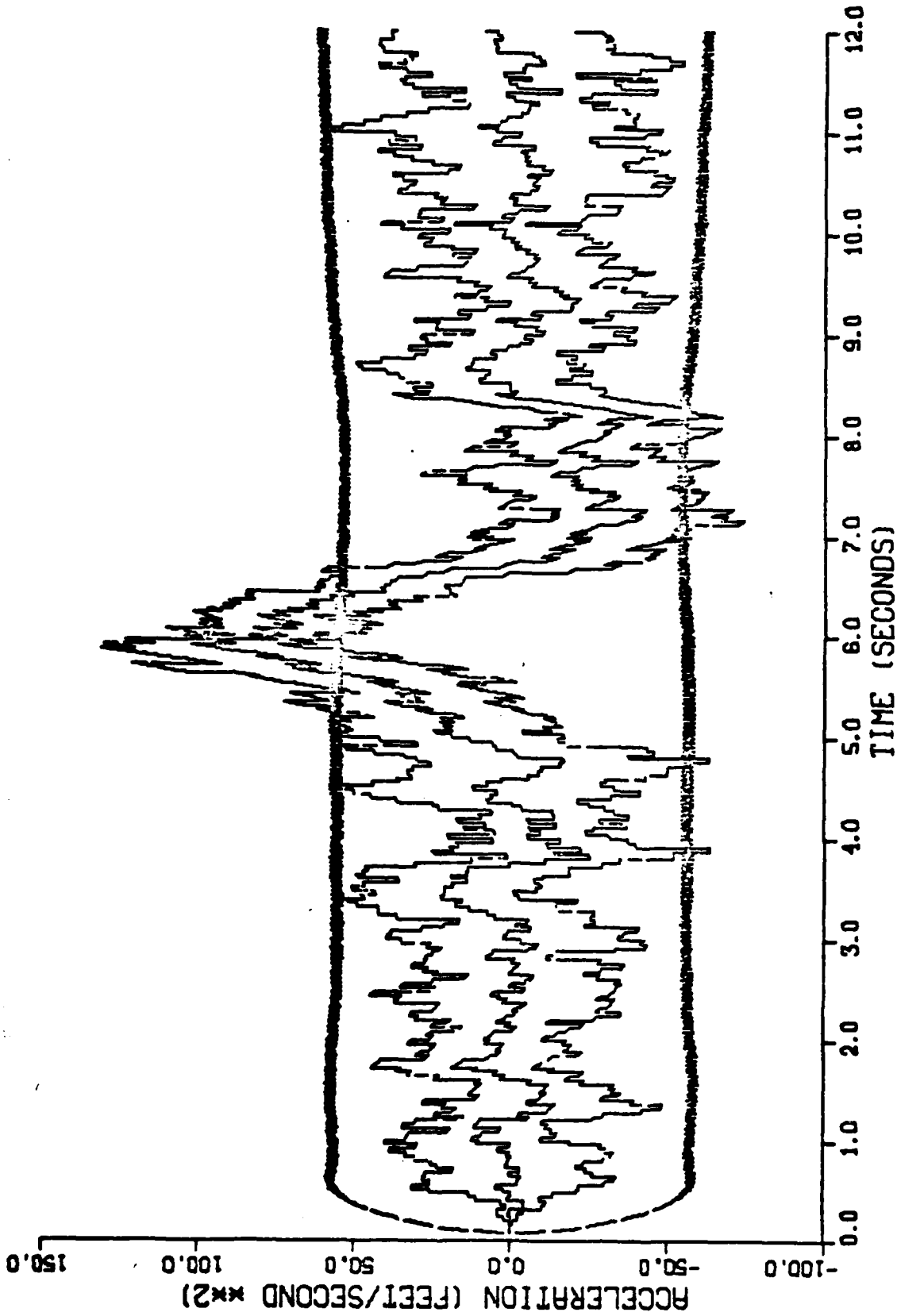


Figure B-12. Performance of the Constant Turn Rate Inertial Coordinate Filter Along the North-Axis for Trajectory 2 for 10 Monte Carlo Simulations

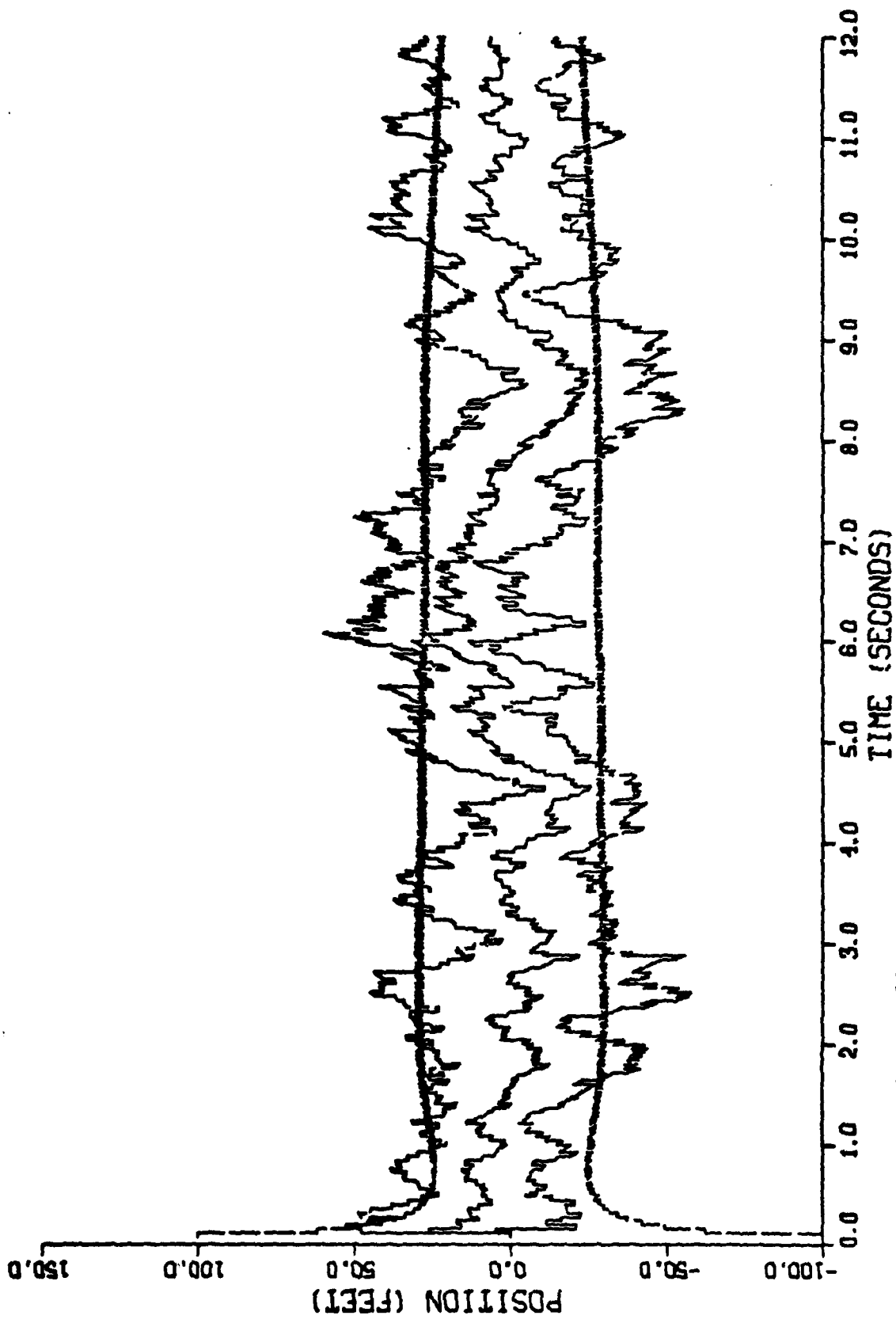


Figure B-13. Performance of the Constant Turn Rate Inertial Coordinate Filter Along the East-Axis for Trajectory 2 for 10 Monte Carlo Simulations

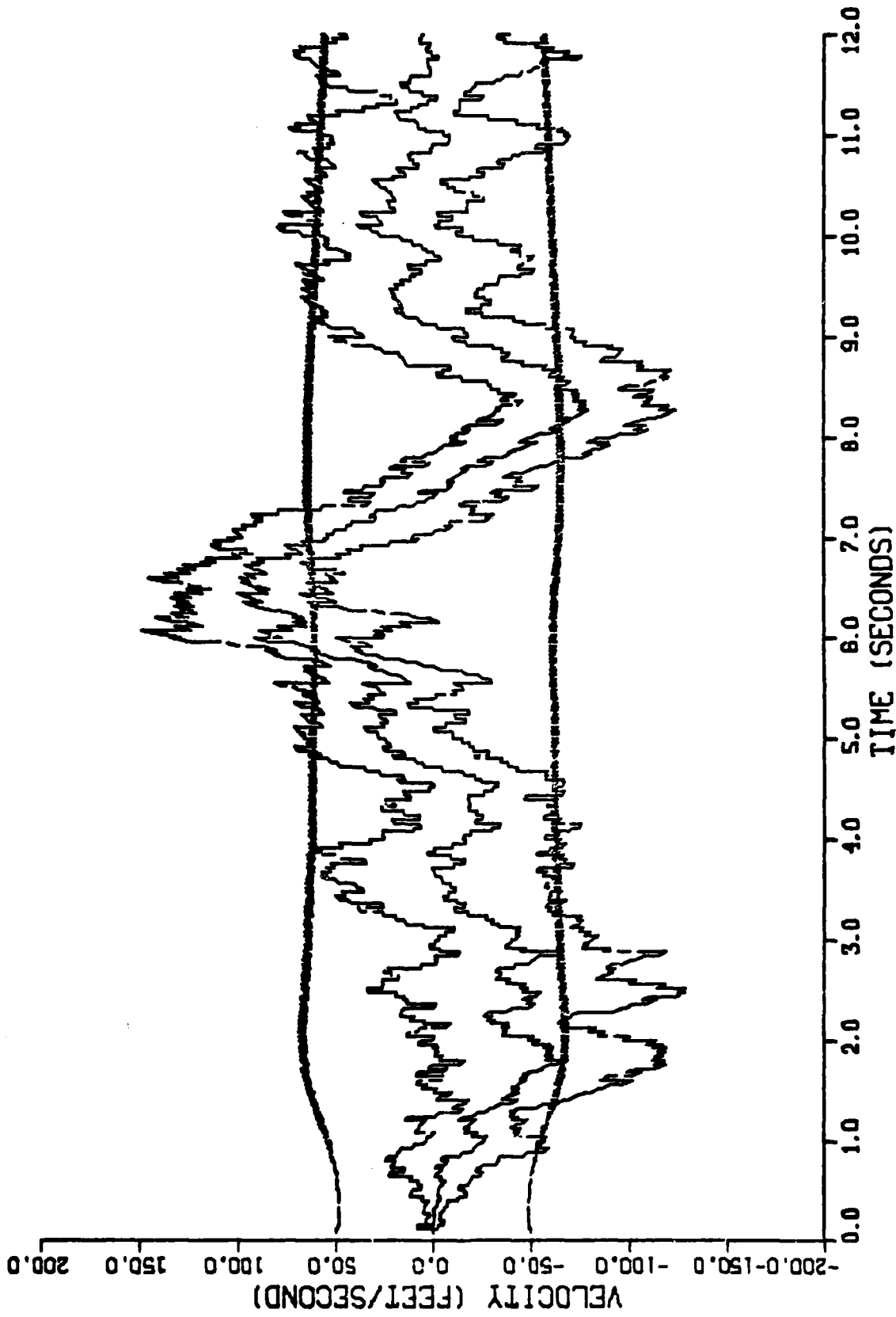


Figure B-14. Performance of the Constant Turn Rate Inertial Coordinate Filter Along the East-Axis for Trajectory 2 for 10 Monte Carlo Simulations

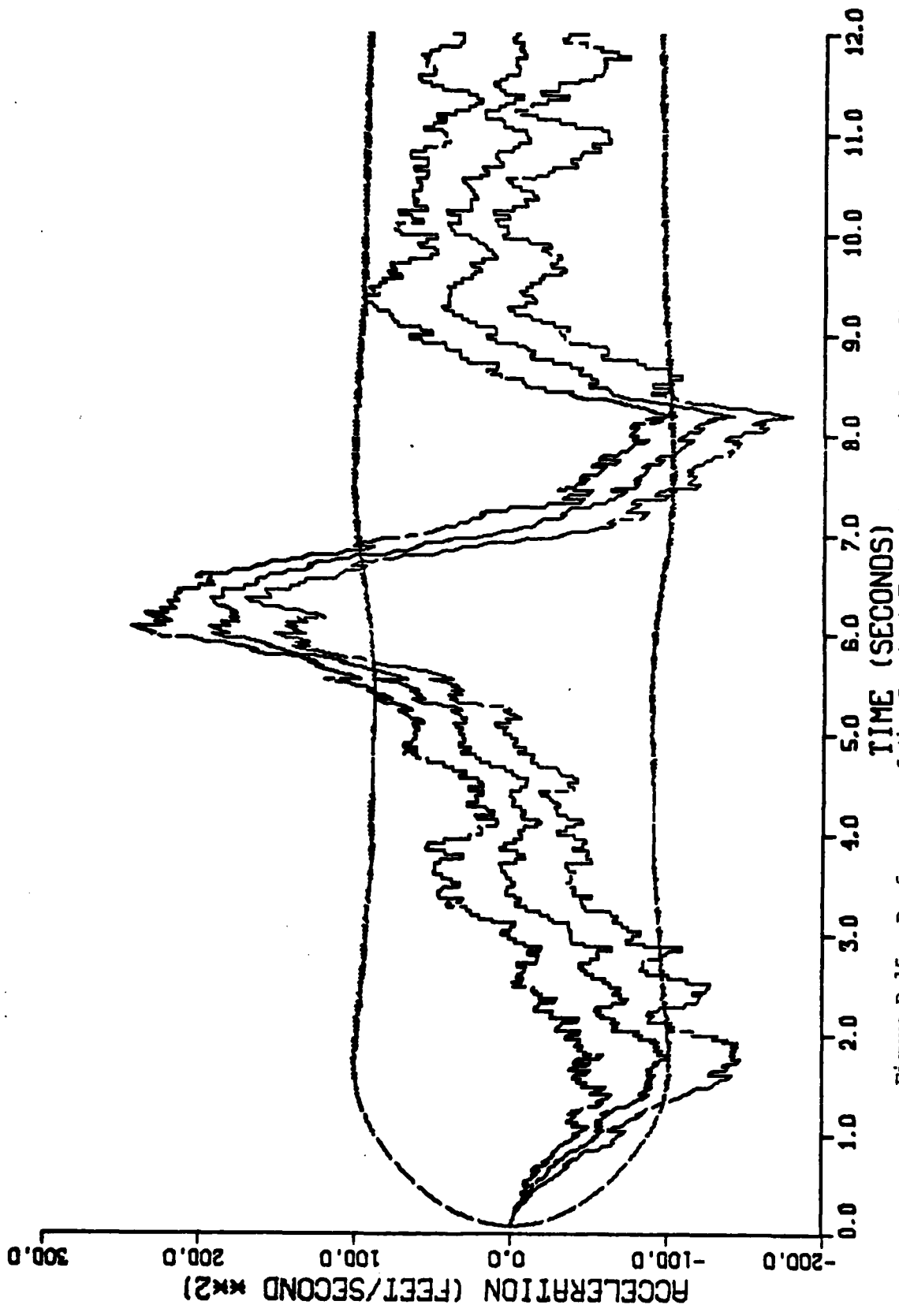


Figure B-15. Performance of the Constant Turn Rate Inertial Coordinate Filter Along the East-Axis for Trajectory 2 for 10 Monte Carlo Simulations

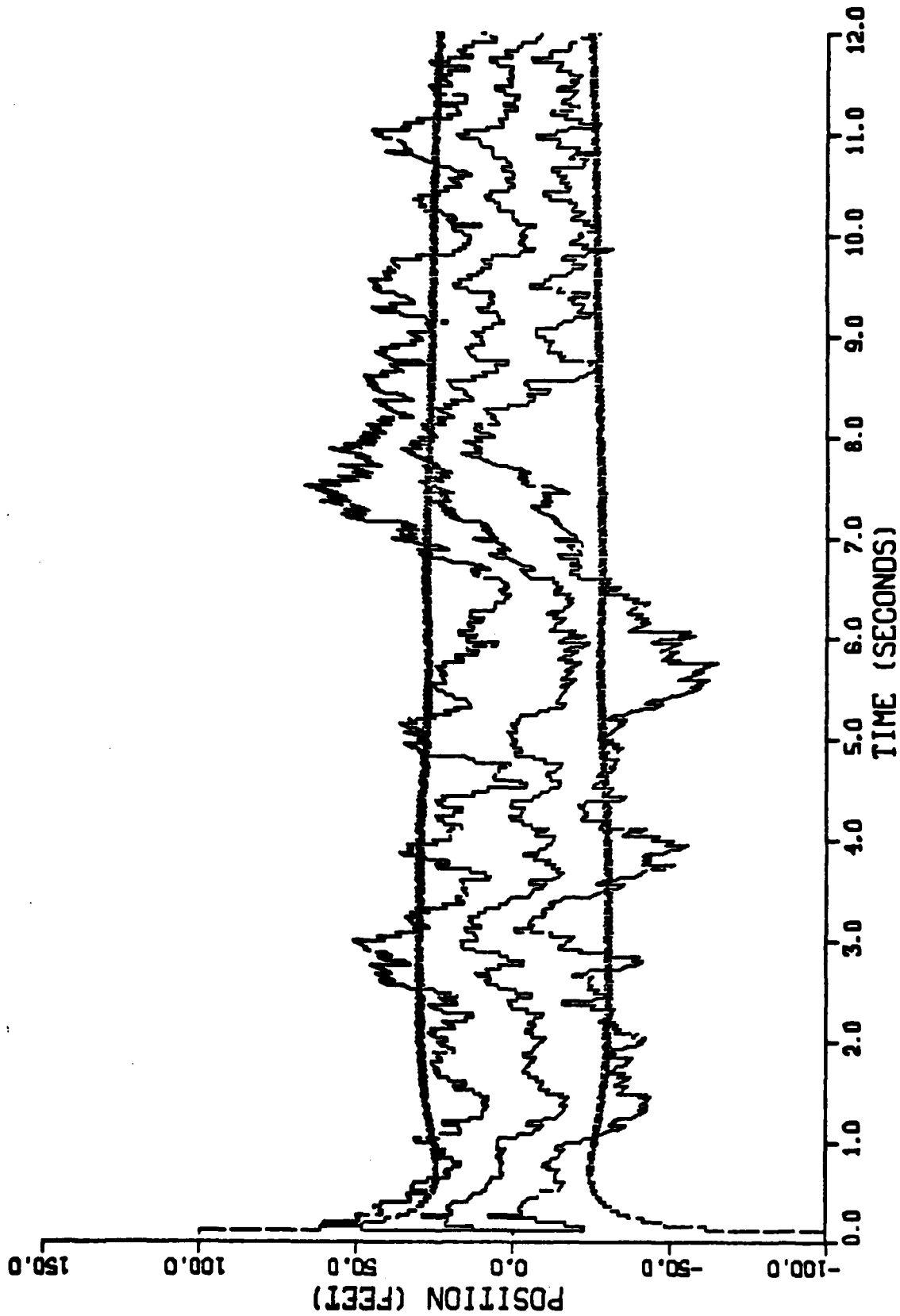


Figure B-16. Performance of the Constant Turn Rate Inertial Coordinate Filter
 Along the Down-Axis for Trajectory 2 for 10 Monte Carlo Simulations

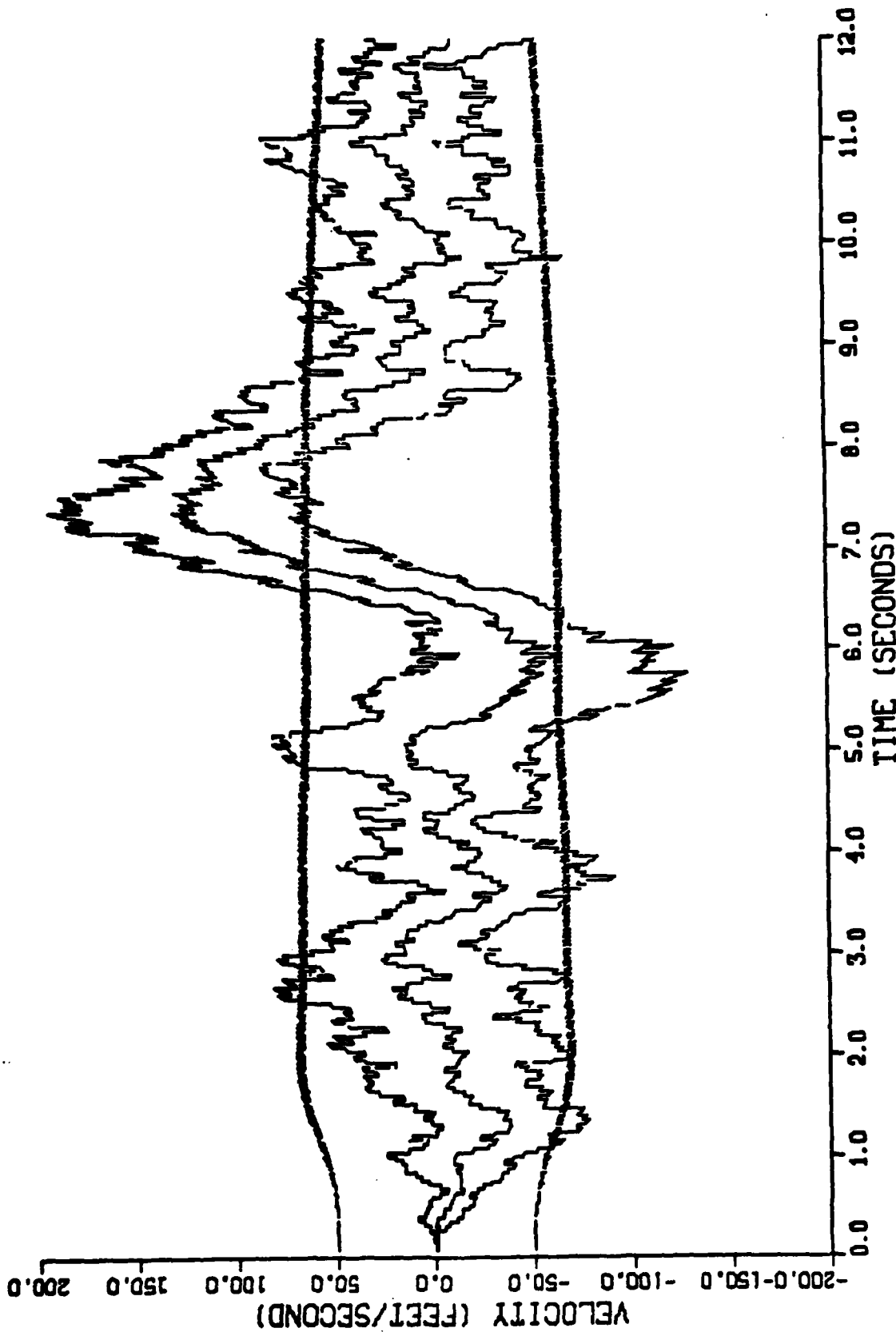


Figure B-17. Performance of the Constant Turn Rate Inertial Coordinate Filter Along the Down-Axis for Trajectory 2 for 10 Monte Carlo Simulations

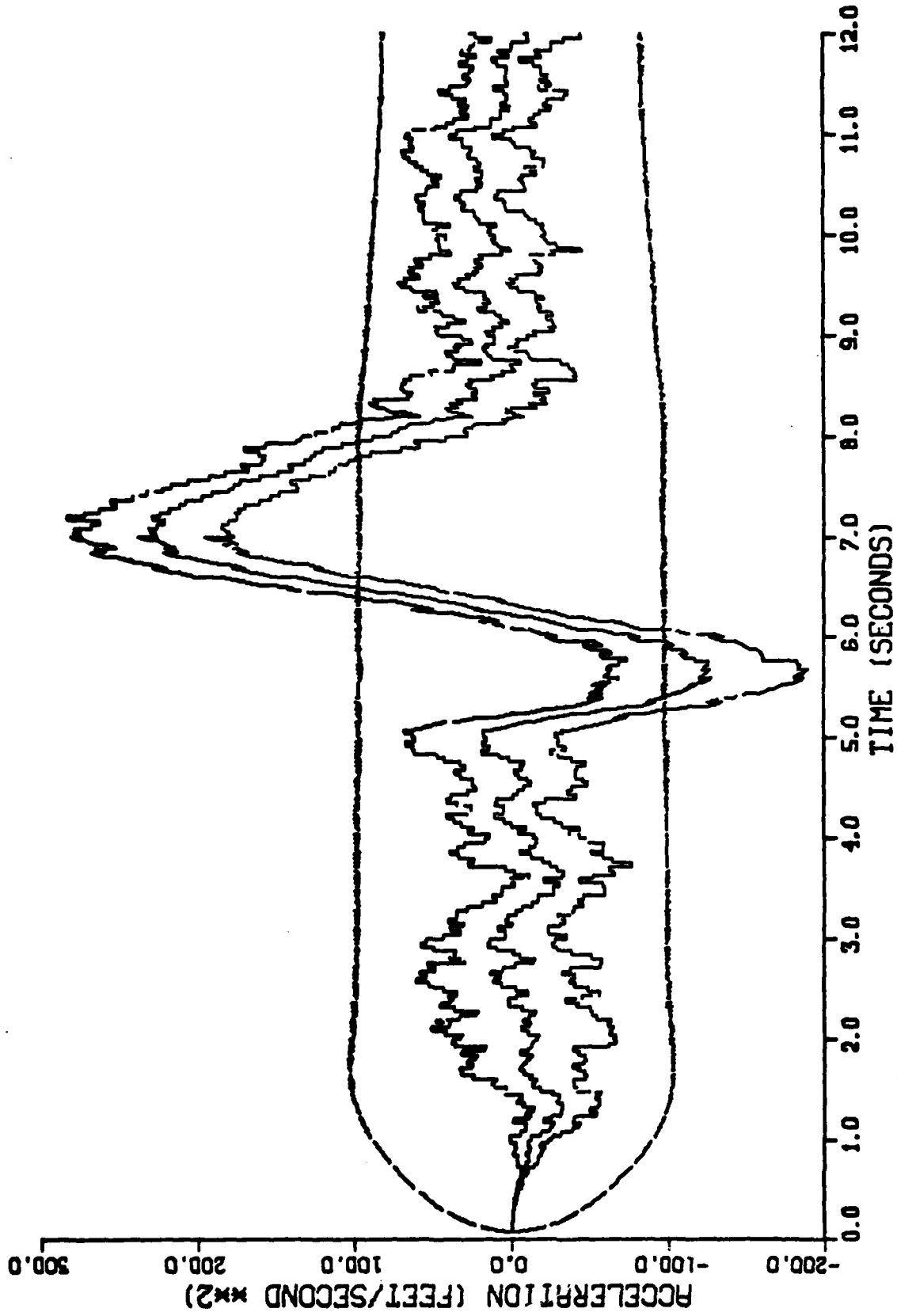


Figure B-18. Performance of the Constant Turn Rate Inertial Coordinate Filter Along the Down-Axis for Trajectory 2 for 10 Monte Carlo Simulations

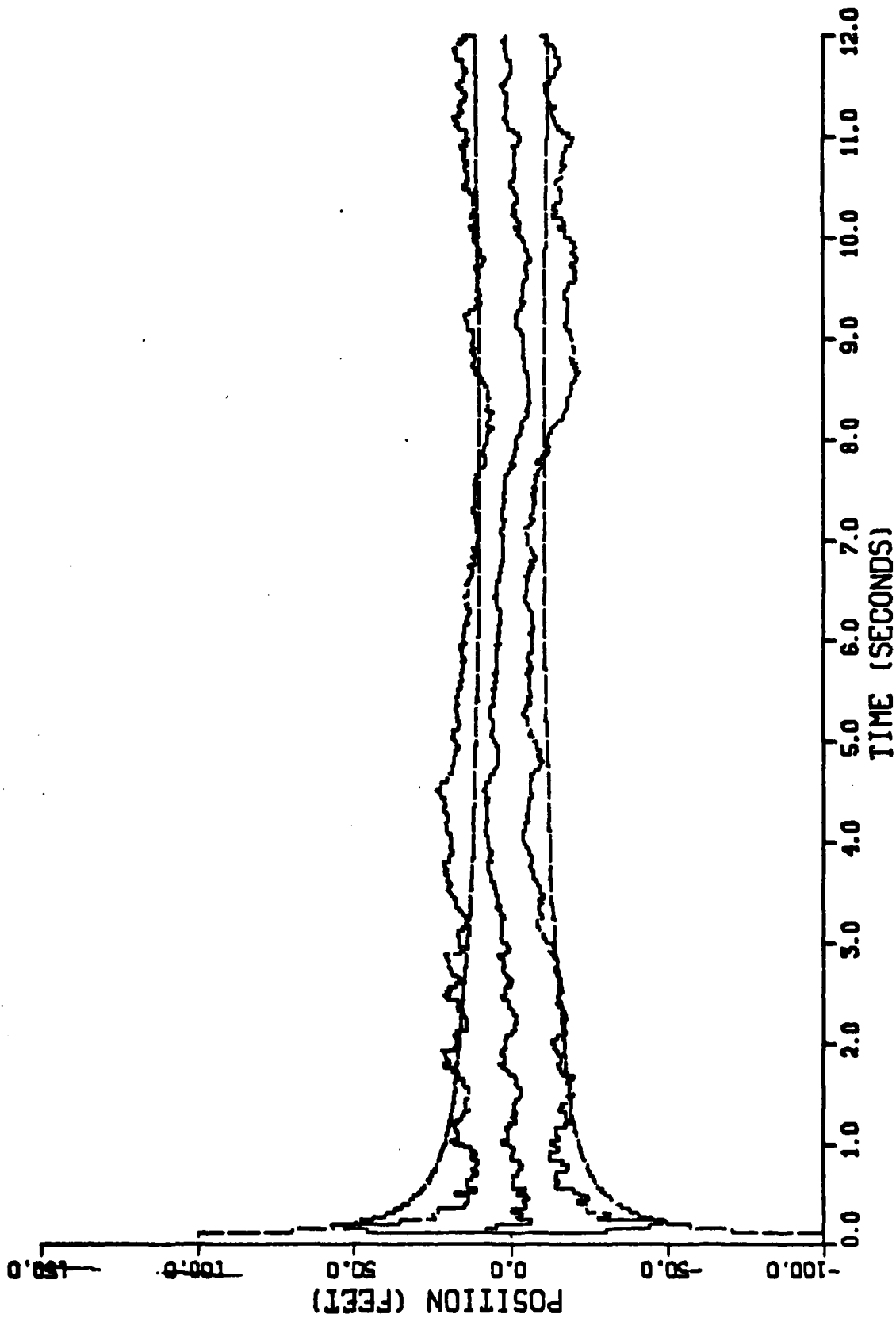


Figure B-19. Performance of the Constant Turn Rate Inertial Coordinate Filter
 Along the North-Axis for Trajectory 2 for 15 Monte Carlo Simulations

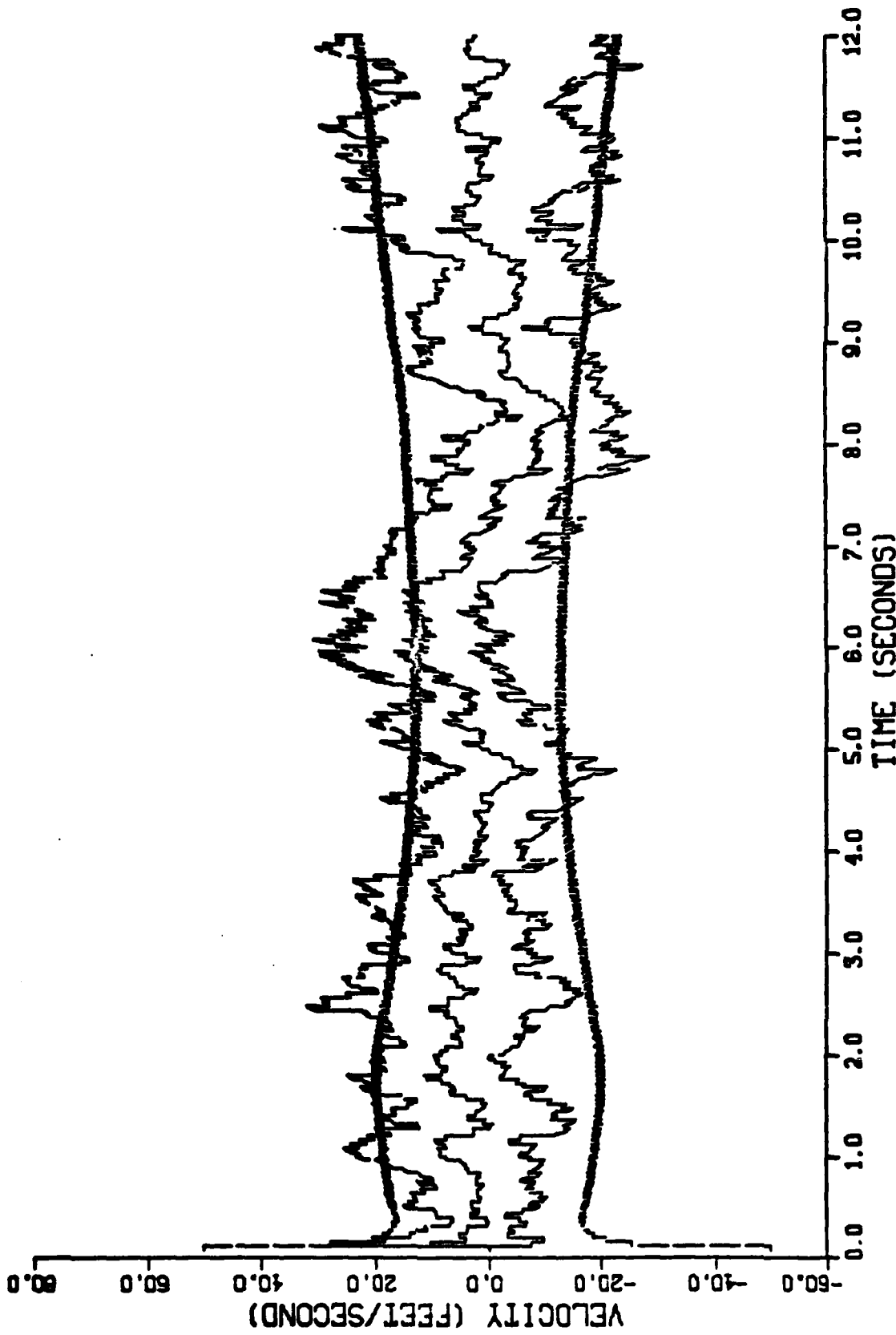


Figure B-20. Performance of the Constant Turn Rate Inertial Coordinate Filter Along the North-Axis for Trajectory 2 for 15 Monte Carlo Simulations

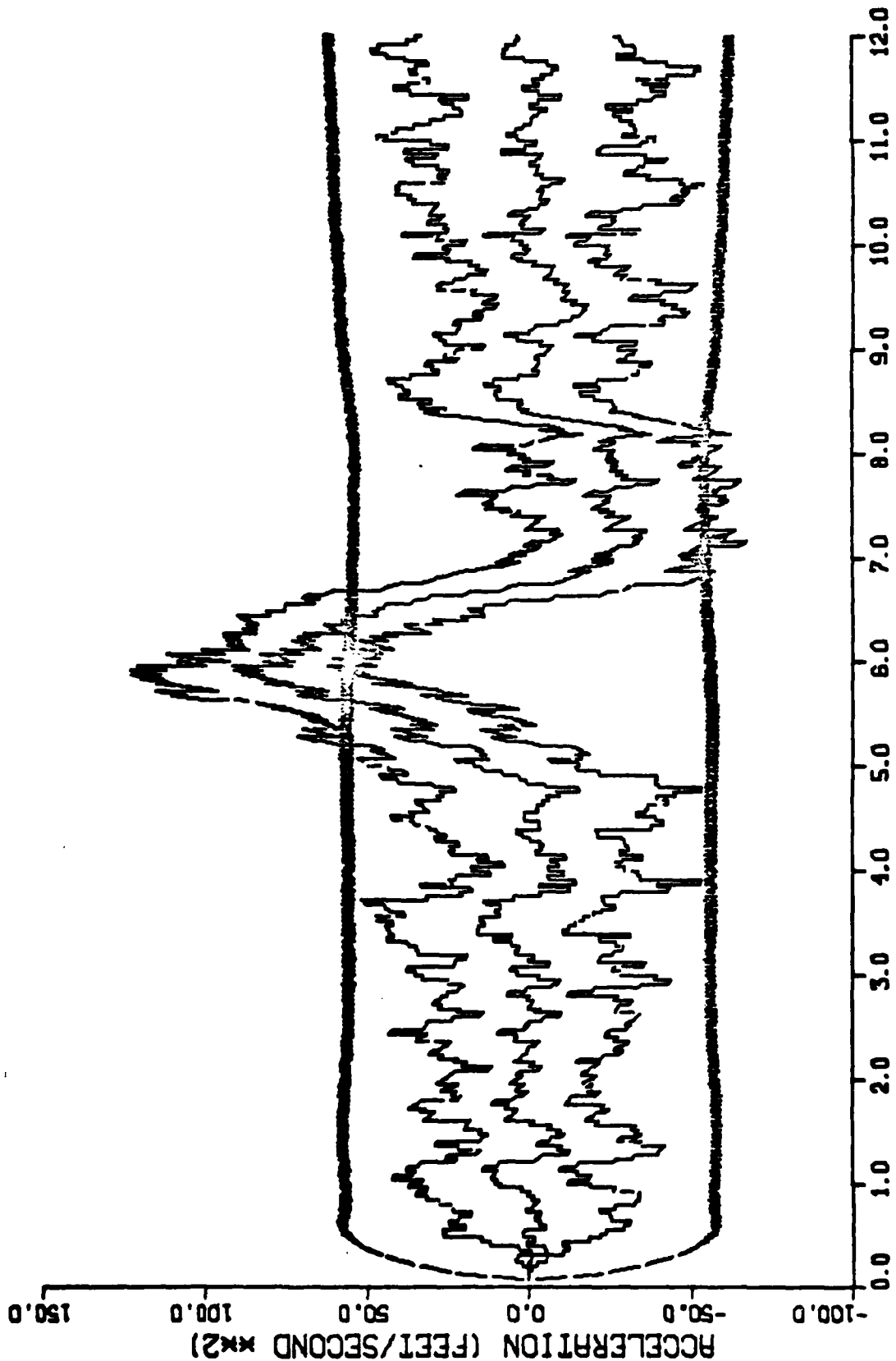


Figure B-21. Performance of the Constant Turn Rate Inertial Coordinate Filter Along the North-Axis for Trajectory 2 for 15 Monte Carlo Simulations

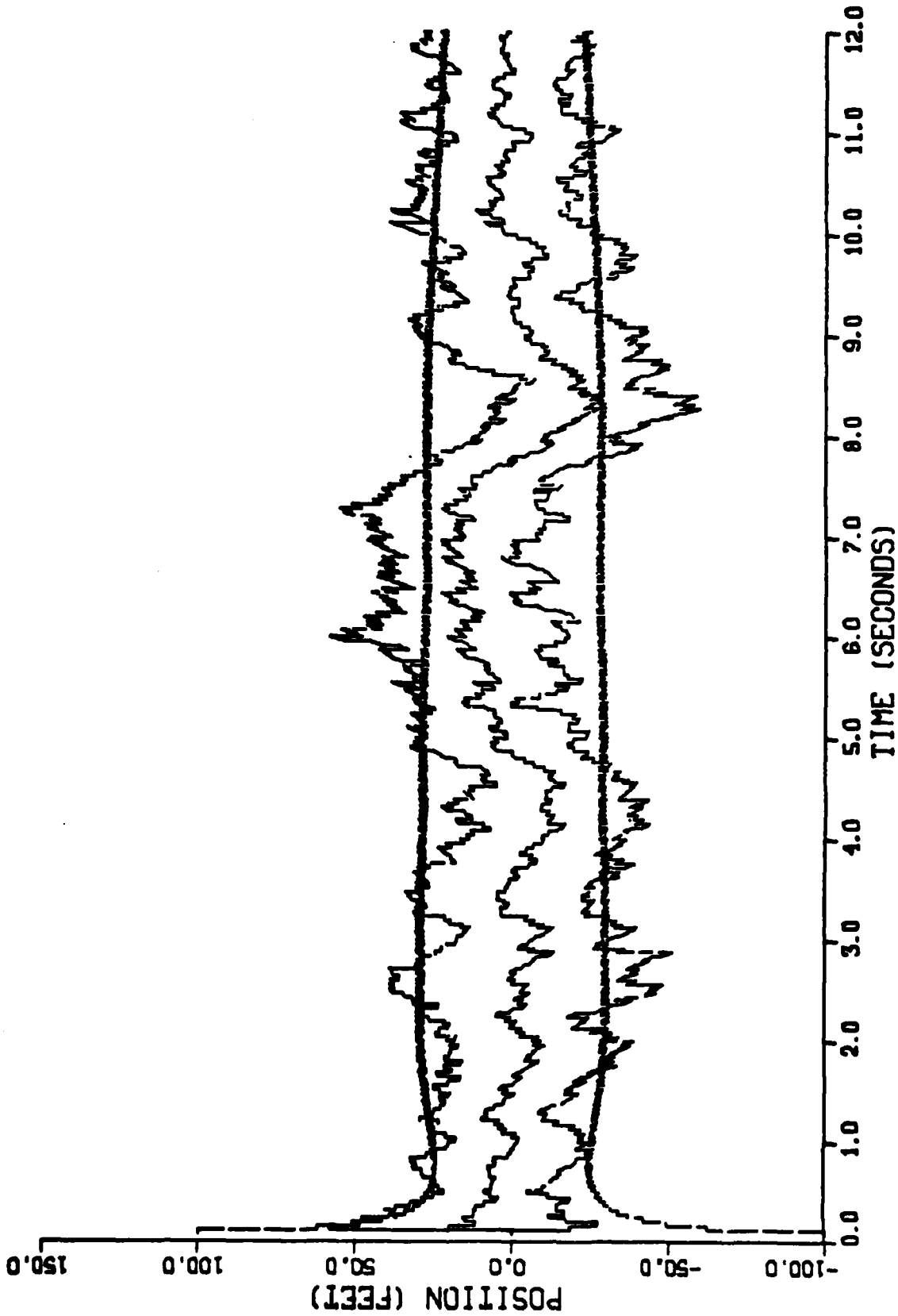


Figure B-22. Performance of the Constant Turn Rate Inertial Coordinate Filter
Along the East-Axis for Trajectory 2 for 15 Monte Carlo Simulations

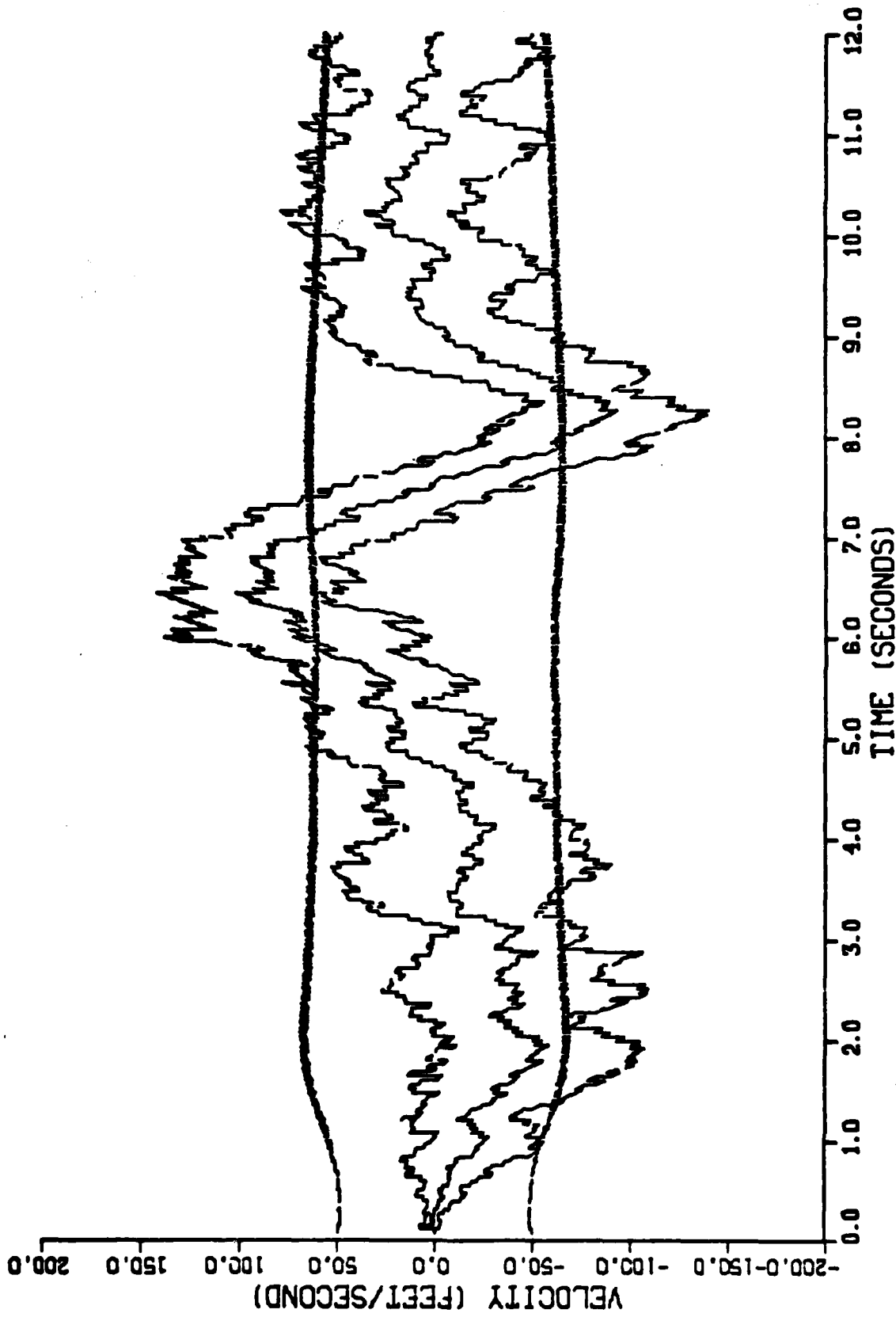


Figure B-23. Performance of the Constant Turn Rate Inertial Coordinate Filter Along the East-Axis for Trajectory 2 for 15 Monte Carlo Simulations

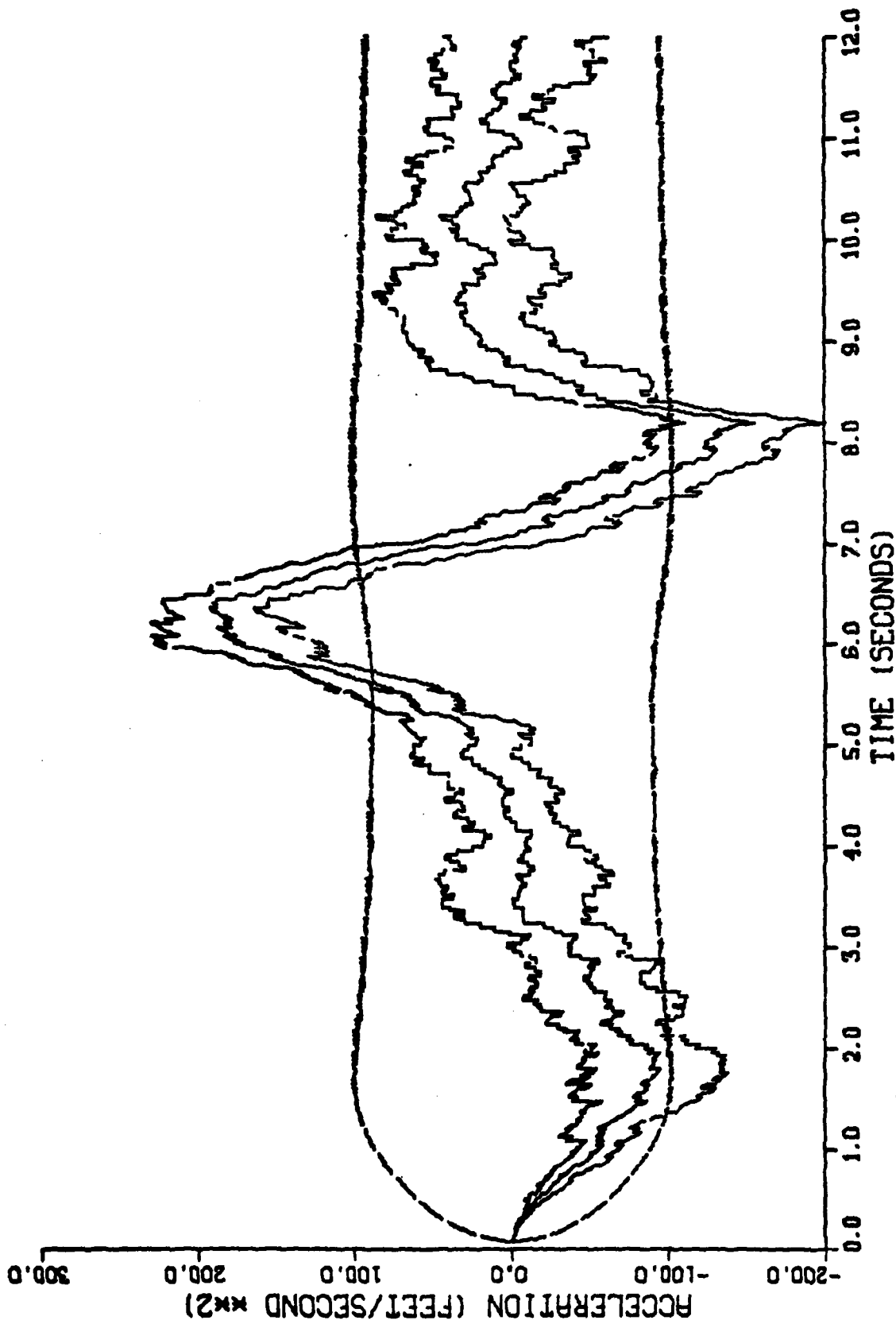


Figure B-24. Performance of the Constant Turn Rate Inertial Coordinate Filter Along the East-Axis for Trajectory 2 for 15 Monte Carlo Simulations

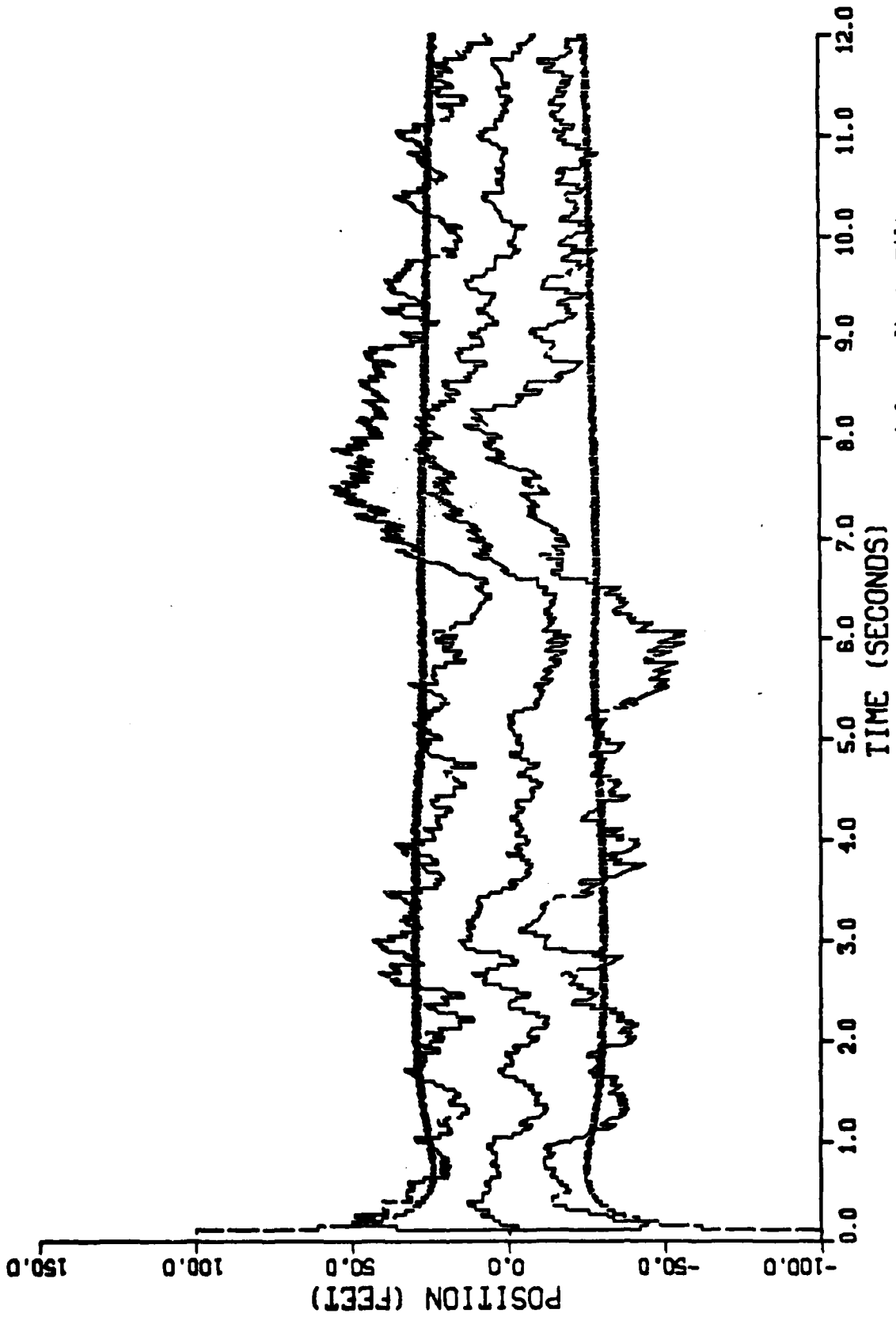


Figure B-25. Performance of the Constant Turn Rate Inertial Coordinate Filter Along the Down-Axis for Trajectory 2 for 15 Monte Carlo Simulations

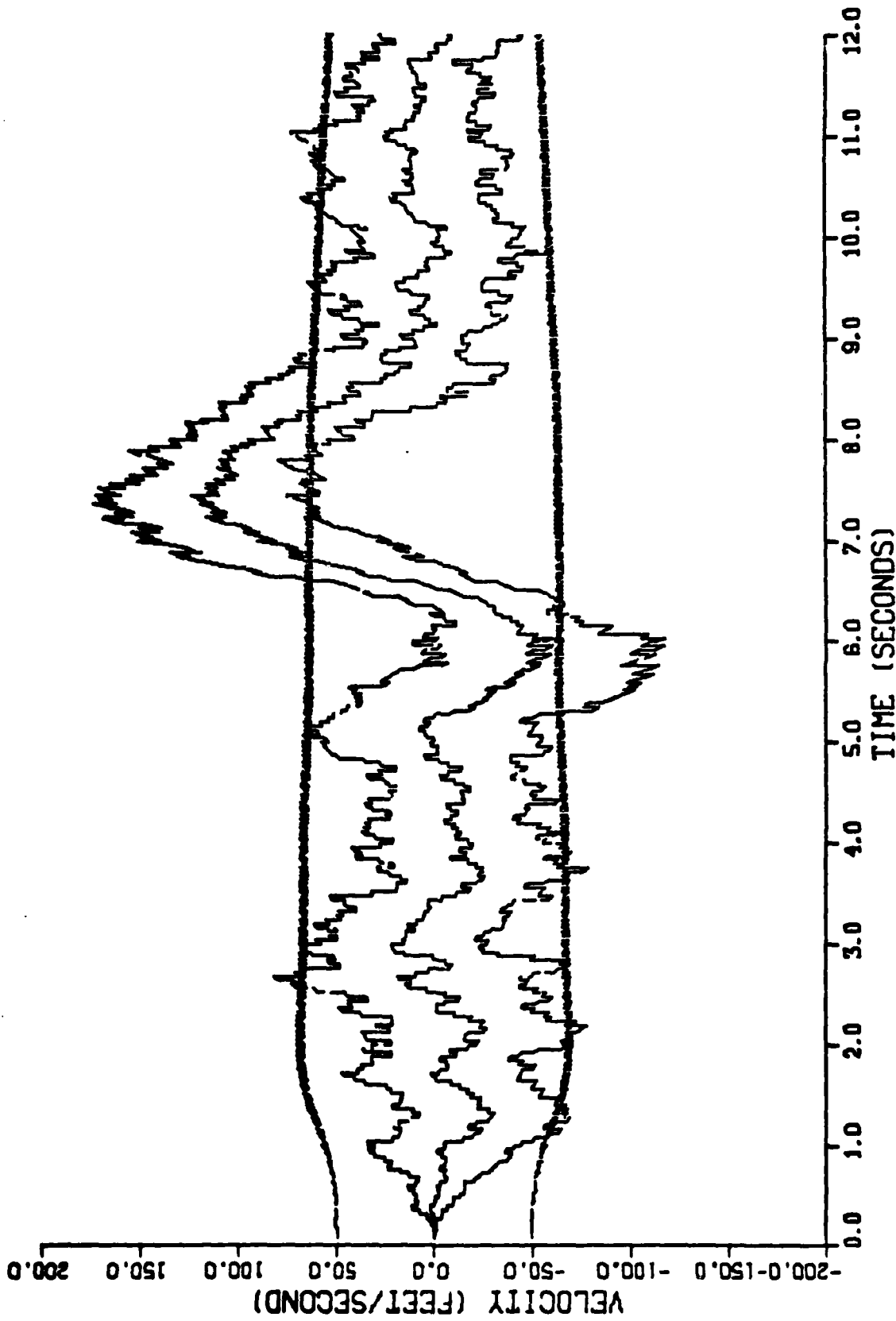


Figure B-26. Performance of the Constant Turn Rate Inertial Coordinate Filter Along the Down-Axis for Trajectory 2 for 15 Monte Carlo Simulations

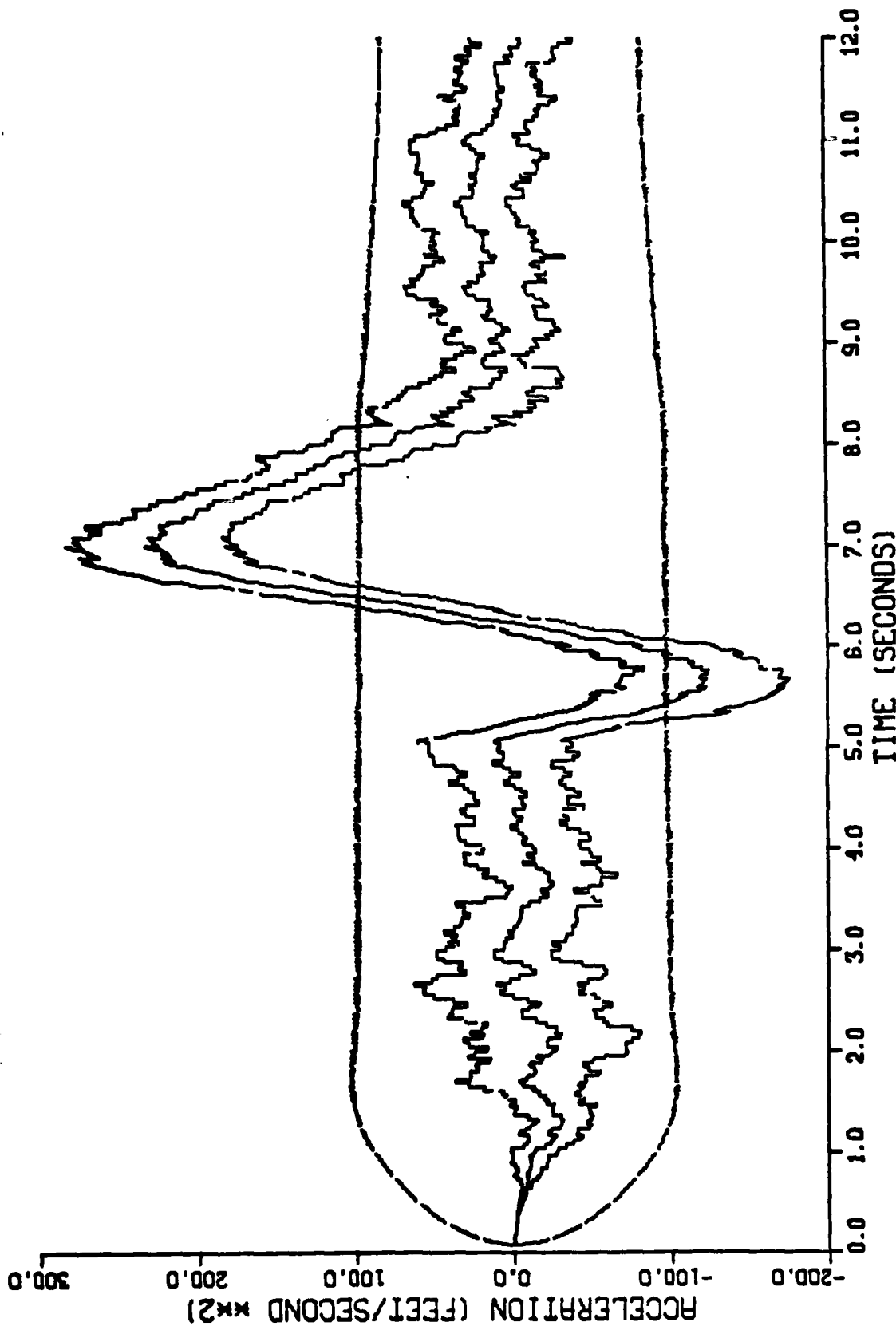


Figure B-27. Performance of the Constant Turn Rate Inertial Coordinate Filter Along the Down-Axis for Trajectory 2 for 15 Monte Carlo Simulations

APPENDIX C

Graphical Results for the Gauss-Markov
Line of Sight Filter

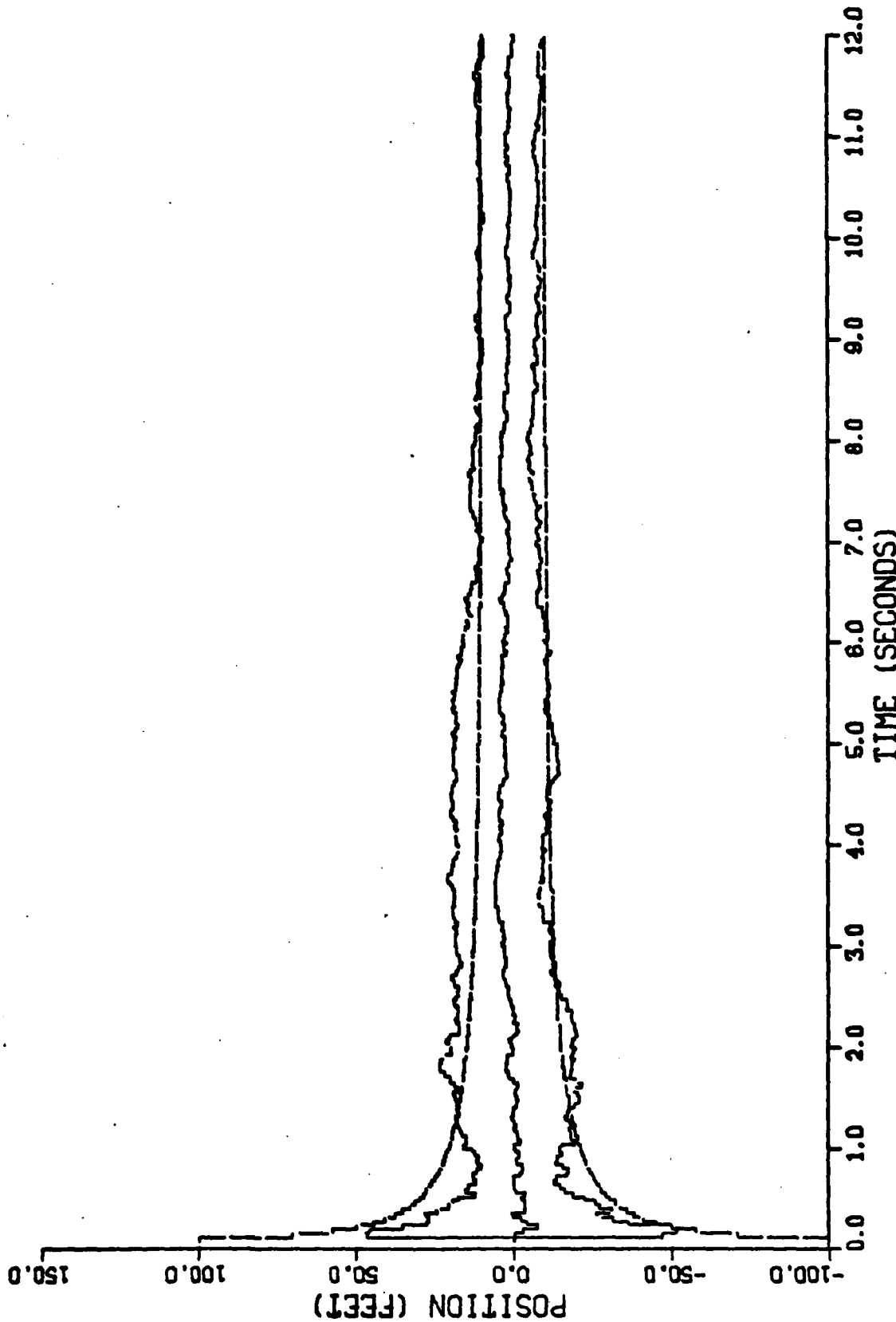


Figure C-1. Performance of the Gauss-Markov Line of Sight Filter Along the 1-Axis for Trajectory 1

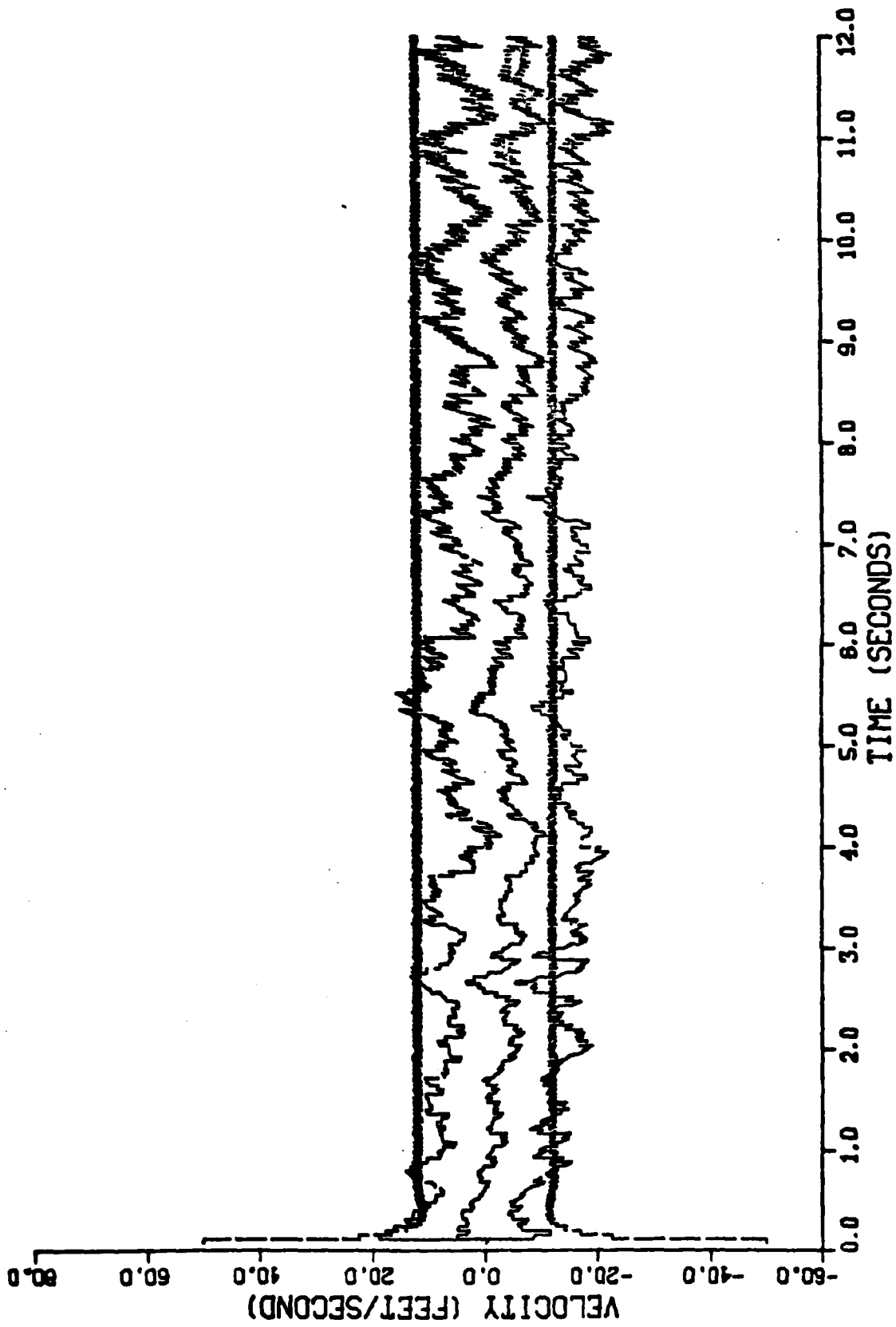


Figure C-2. Performance of the Gauss-Markov Line of Sight Filter
Along the 1-Axis for Trajectory 1

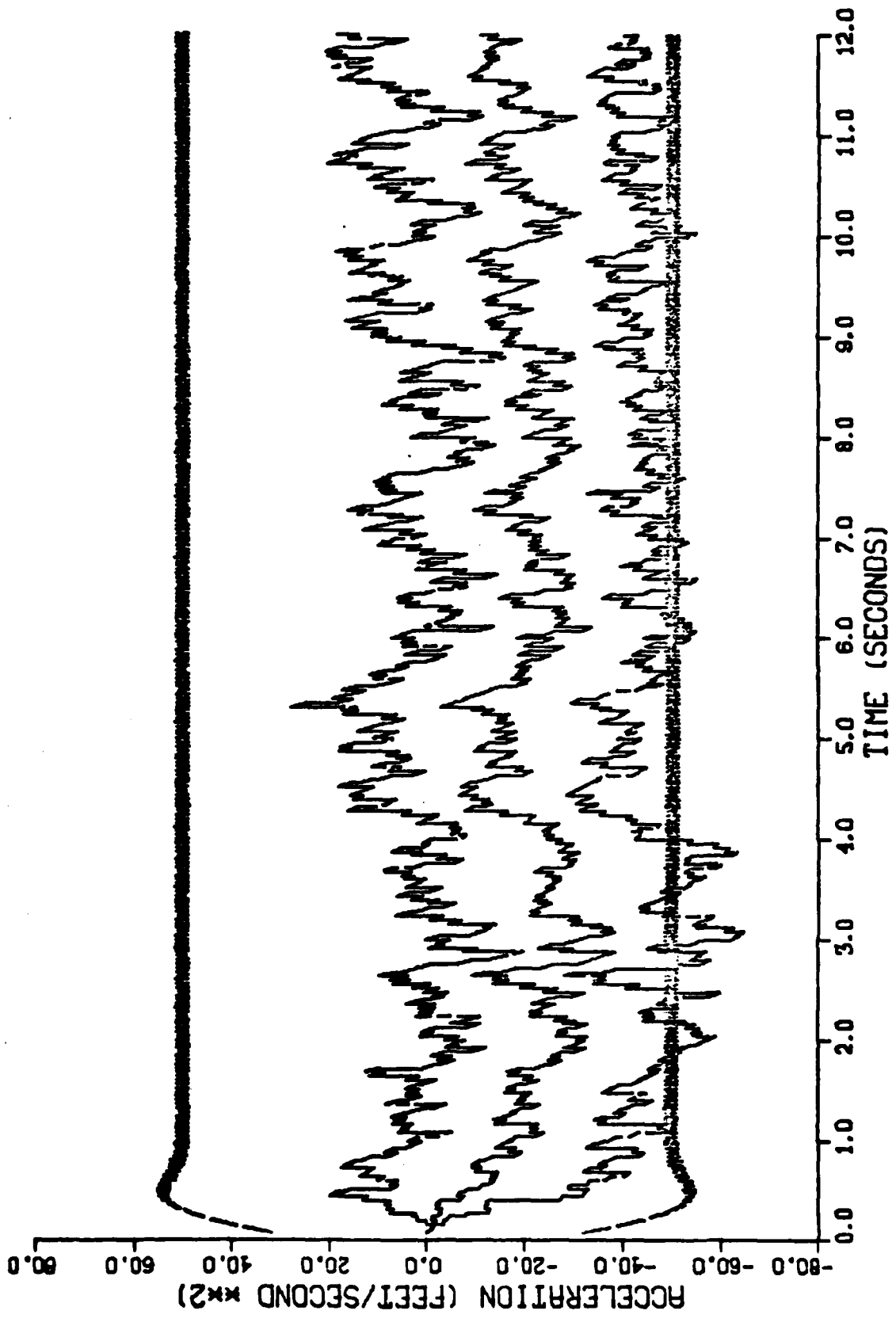


Figure C-3. Performance of the Gauss-Markov Line of Sight Filter Along the 1-Axis for Trajectory 1

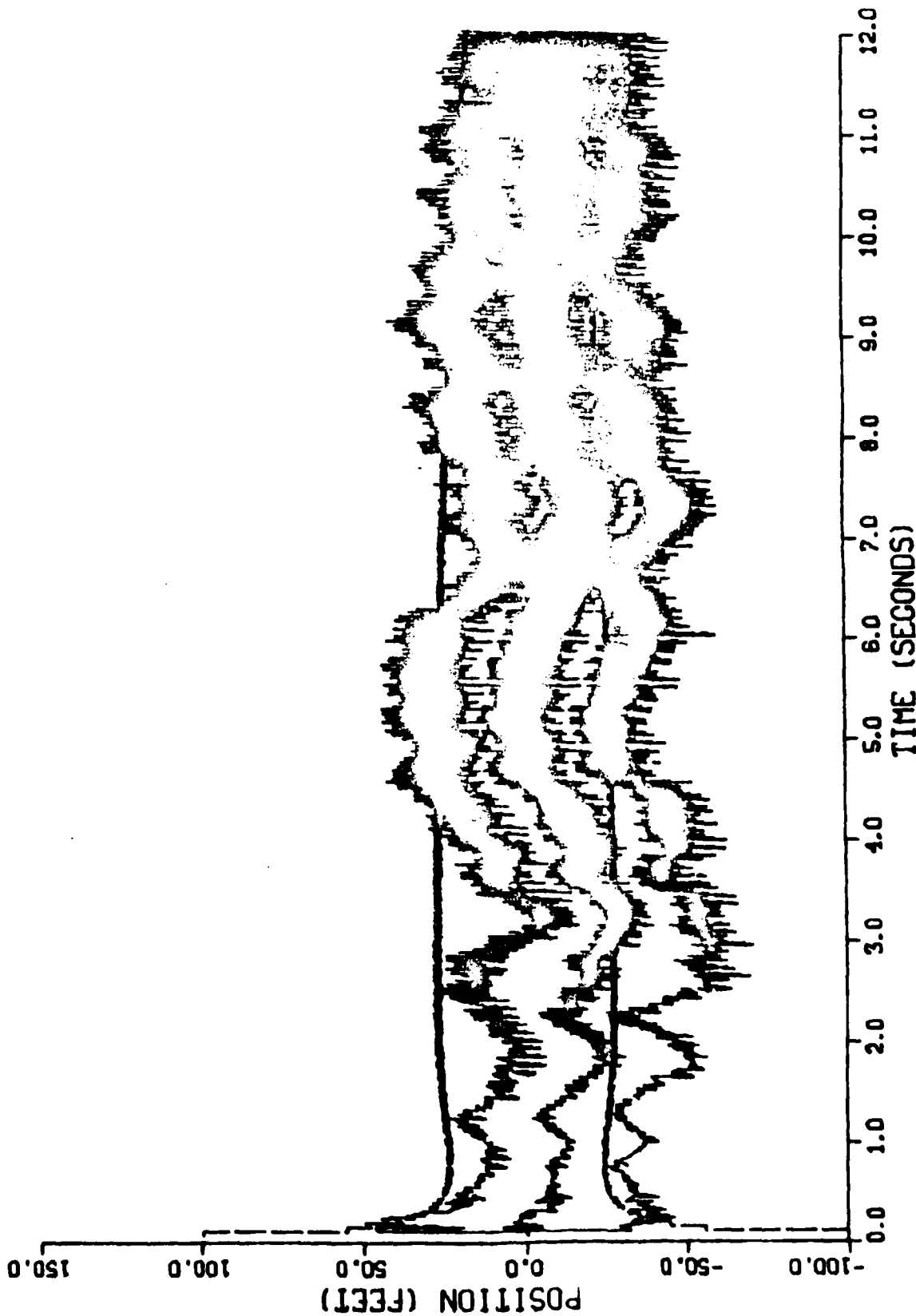


Figure C-4. Performance of the Gauss-Markov Line of Sight Filter Along the 2-Axis for Trajectory 1

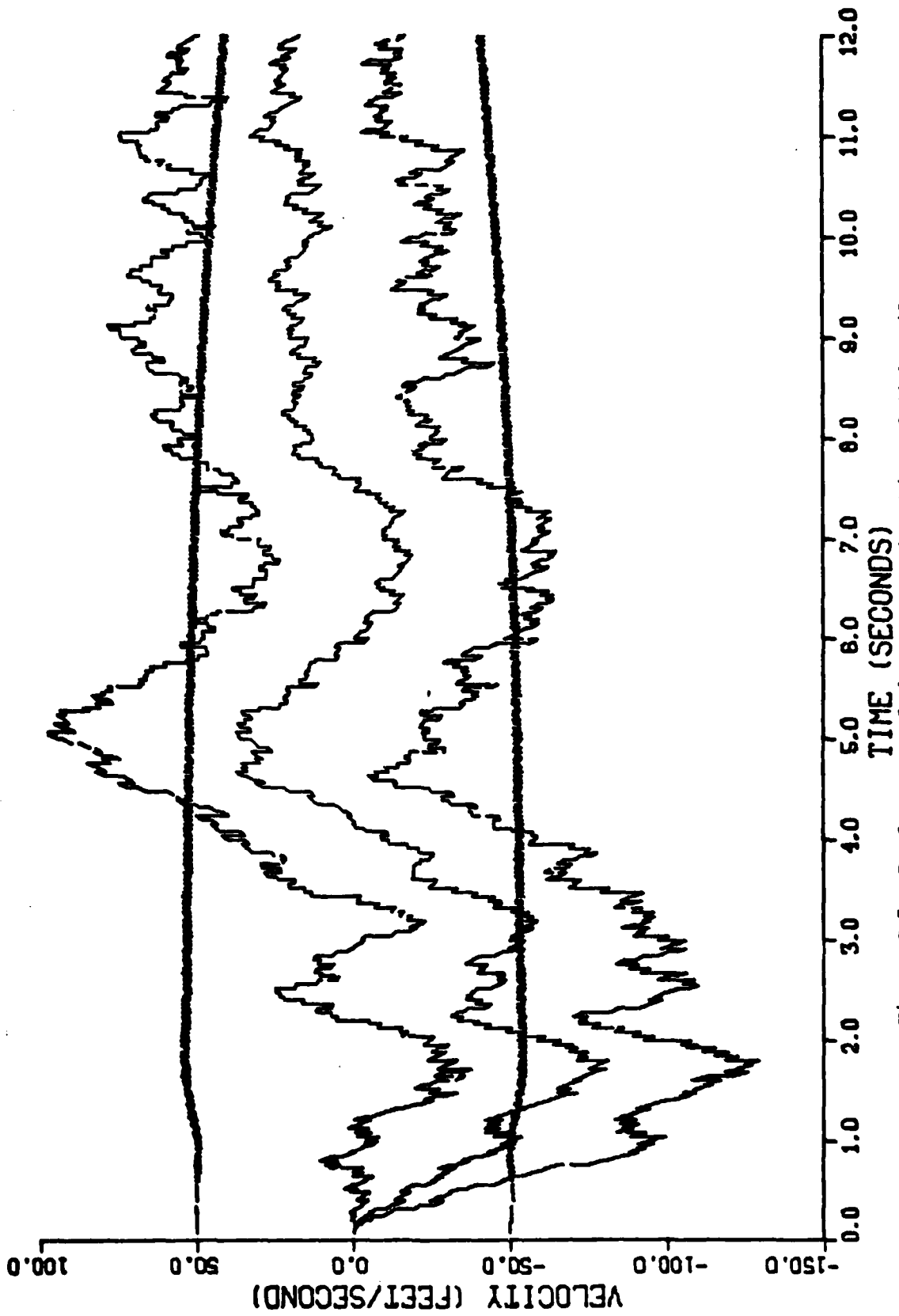


Figure C-5. Performance of the Gauss-Markov Line of Sight Filter Along the 2-Axis for Trajectory 1

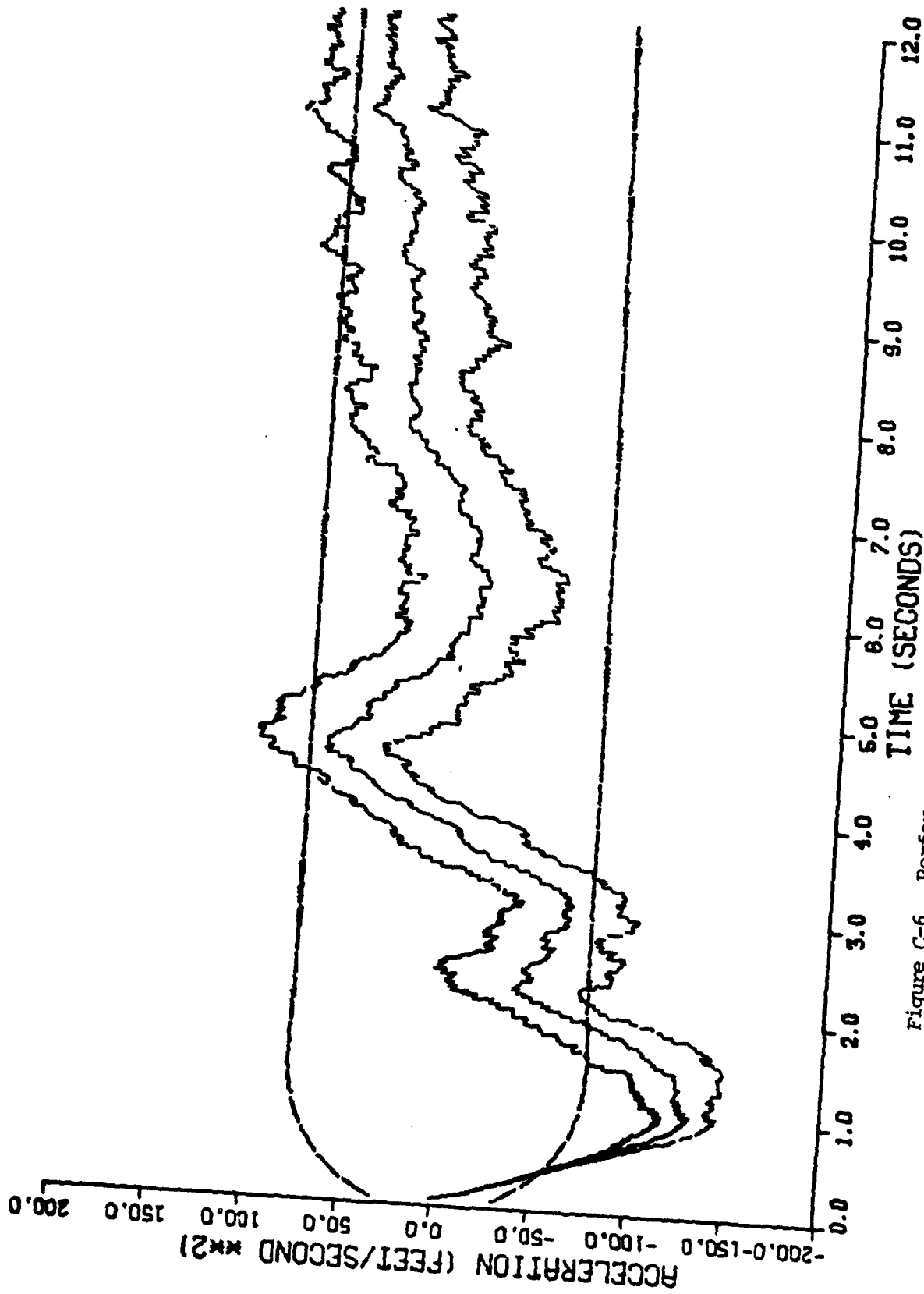


Figure C-6. Performance of the Gauss-Markov Line of Sight Filter Along the 2-Axis for Trajectory 1

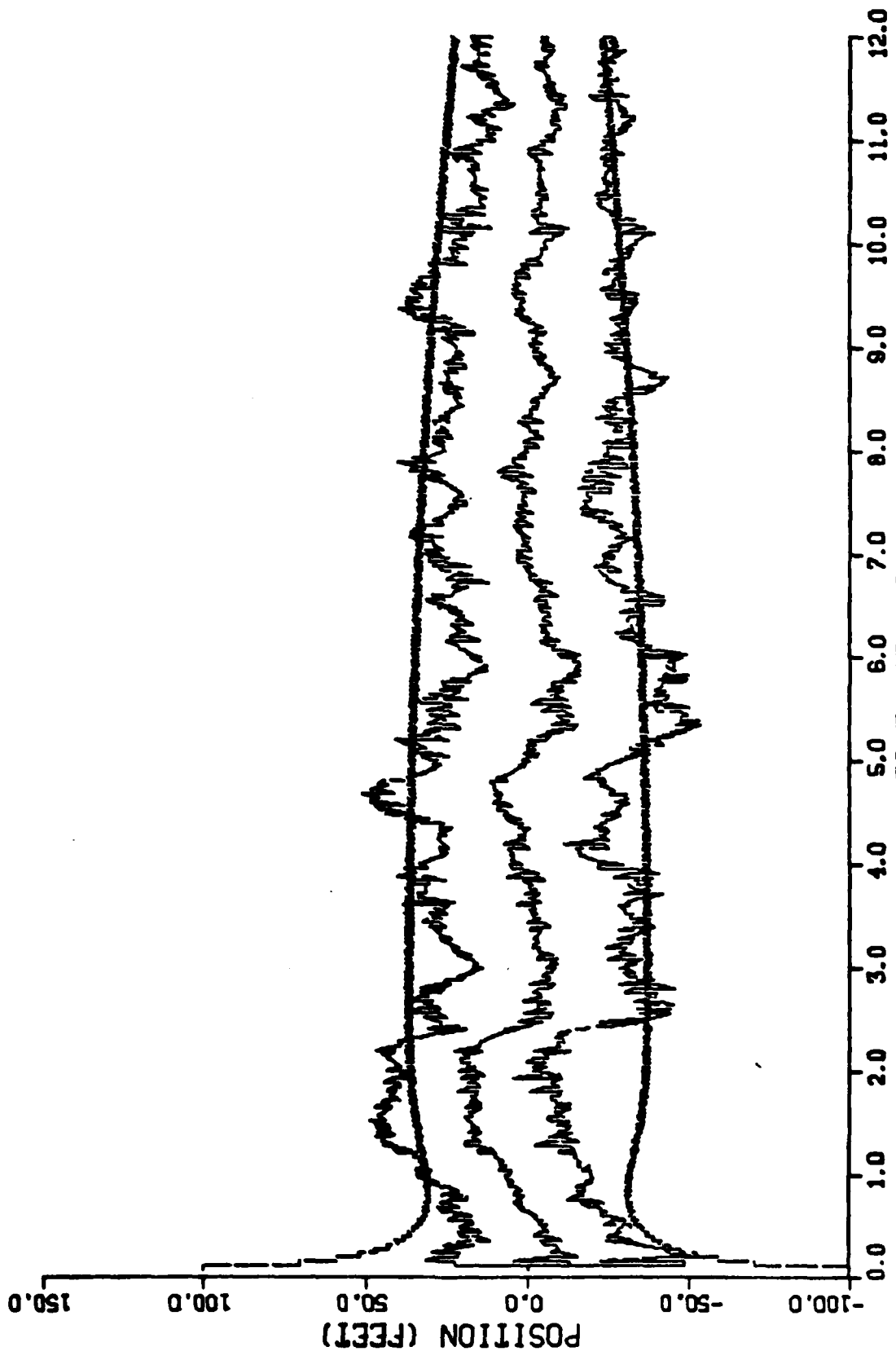


Figure C-7. Performance of the Gauss-Harkov Line of Sight Filter
Along the 3-Axis for Trajectory 1

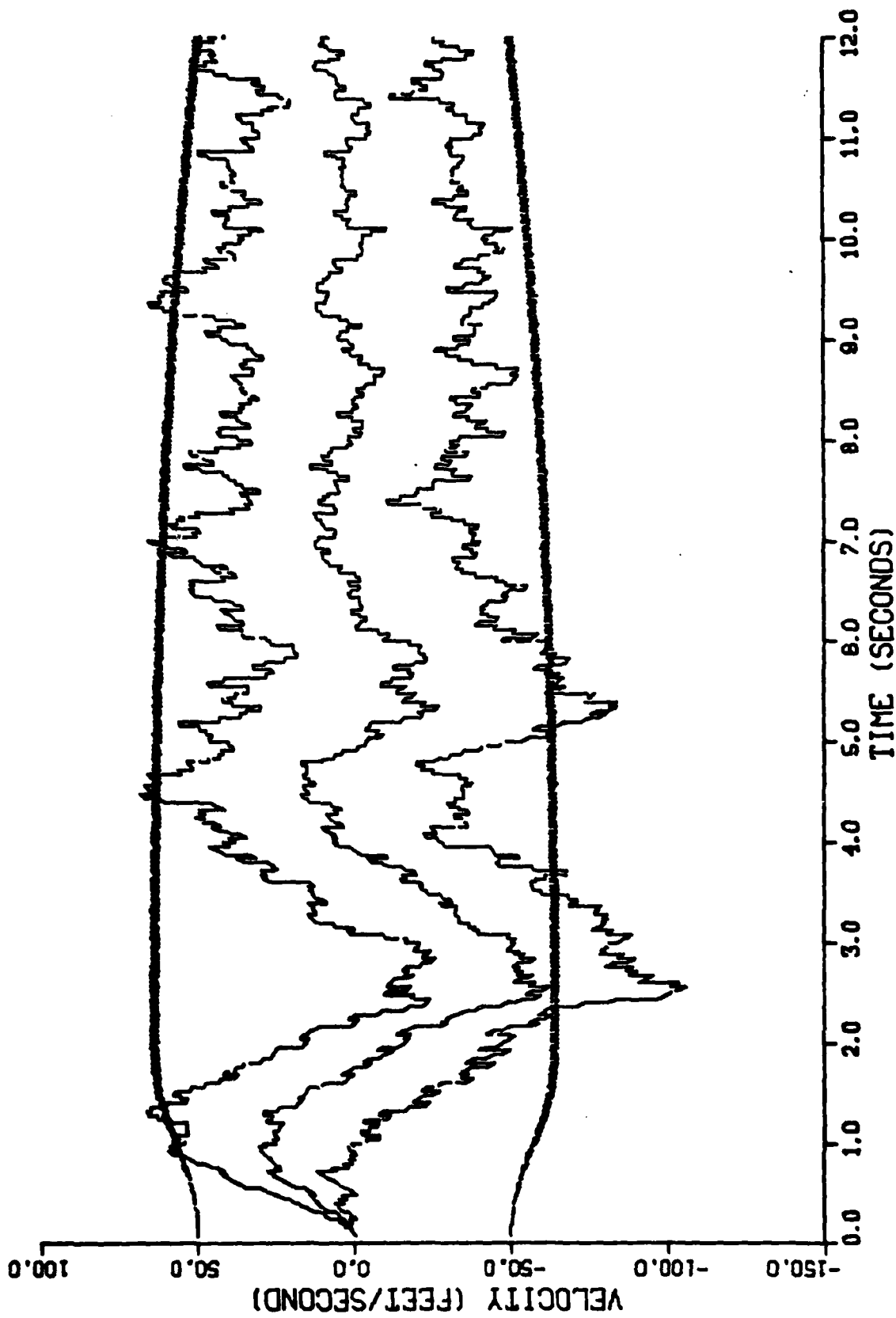


Figure C-8. Performance of the Gauss-Markov Line of Sight Filter Along the 3-Axis for Trajectory 1

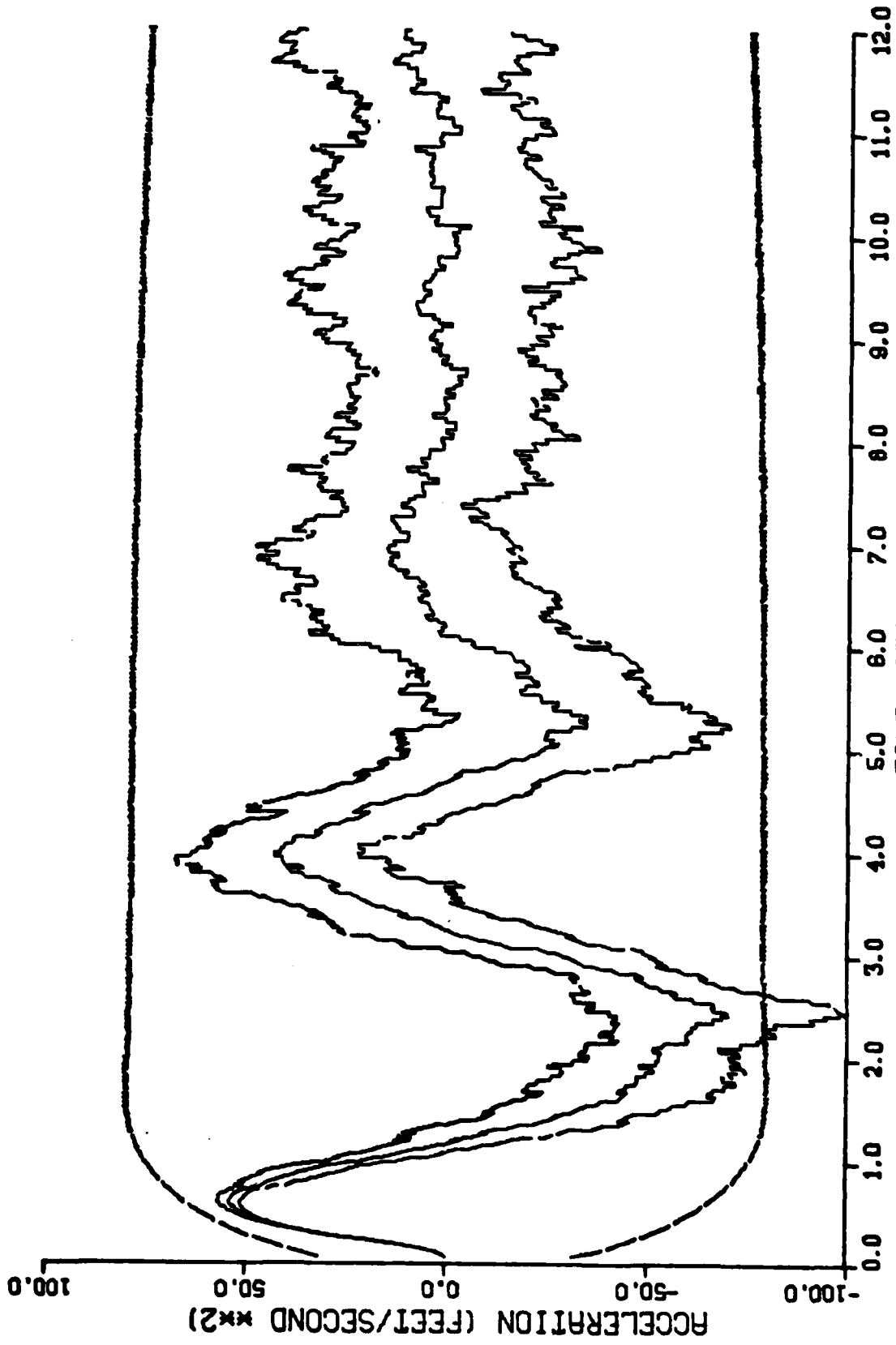


Figure C-9. Performance of the Gauss-Markov Line of Sight Filter Along the 3-Axis for Trajectory 1

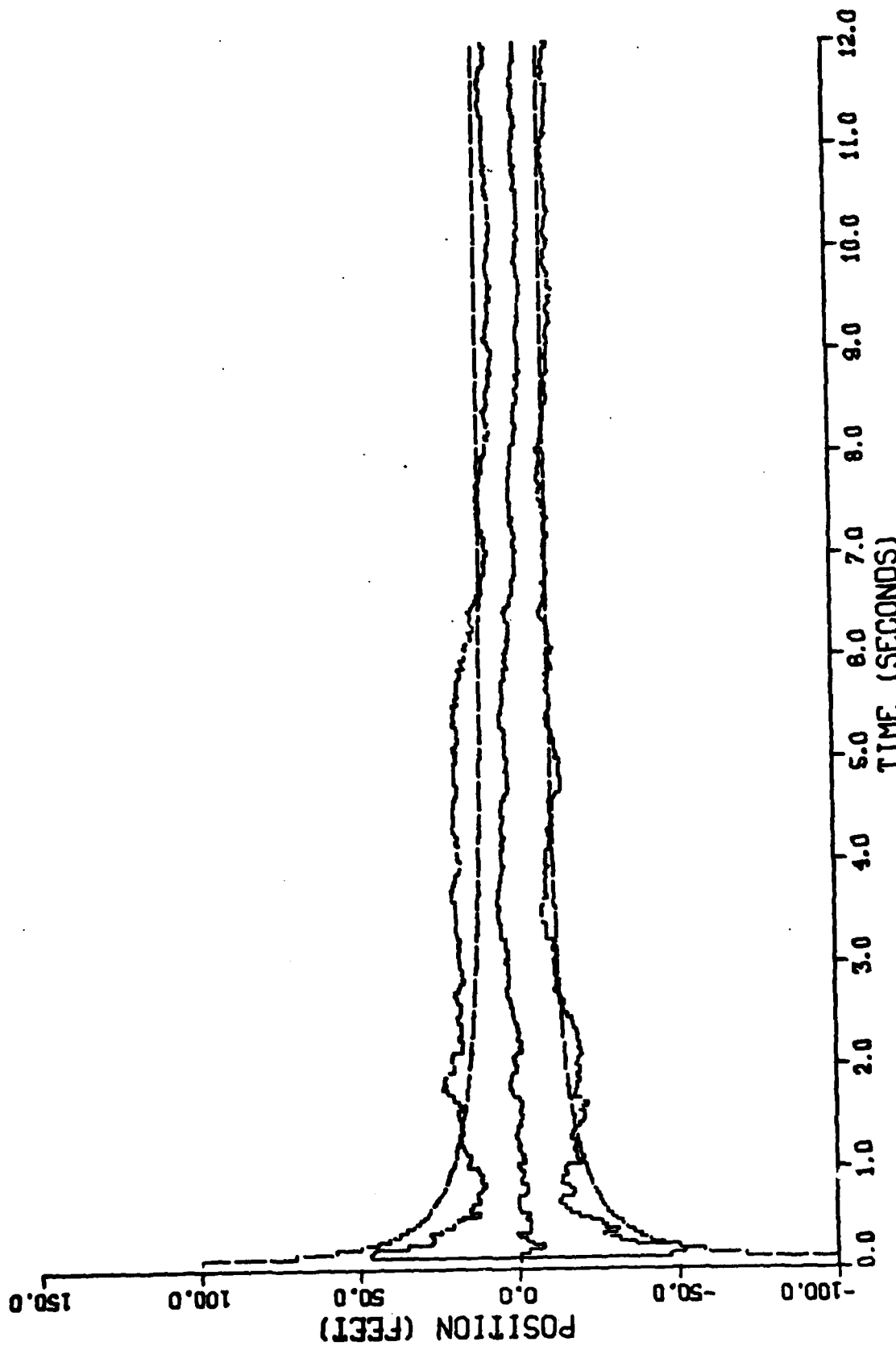


Figure C-10. Performance of the Gauss-Markov Line of Sight Filter Along the 1-Axis for Trajectory 2

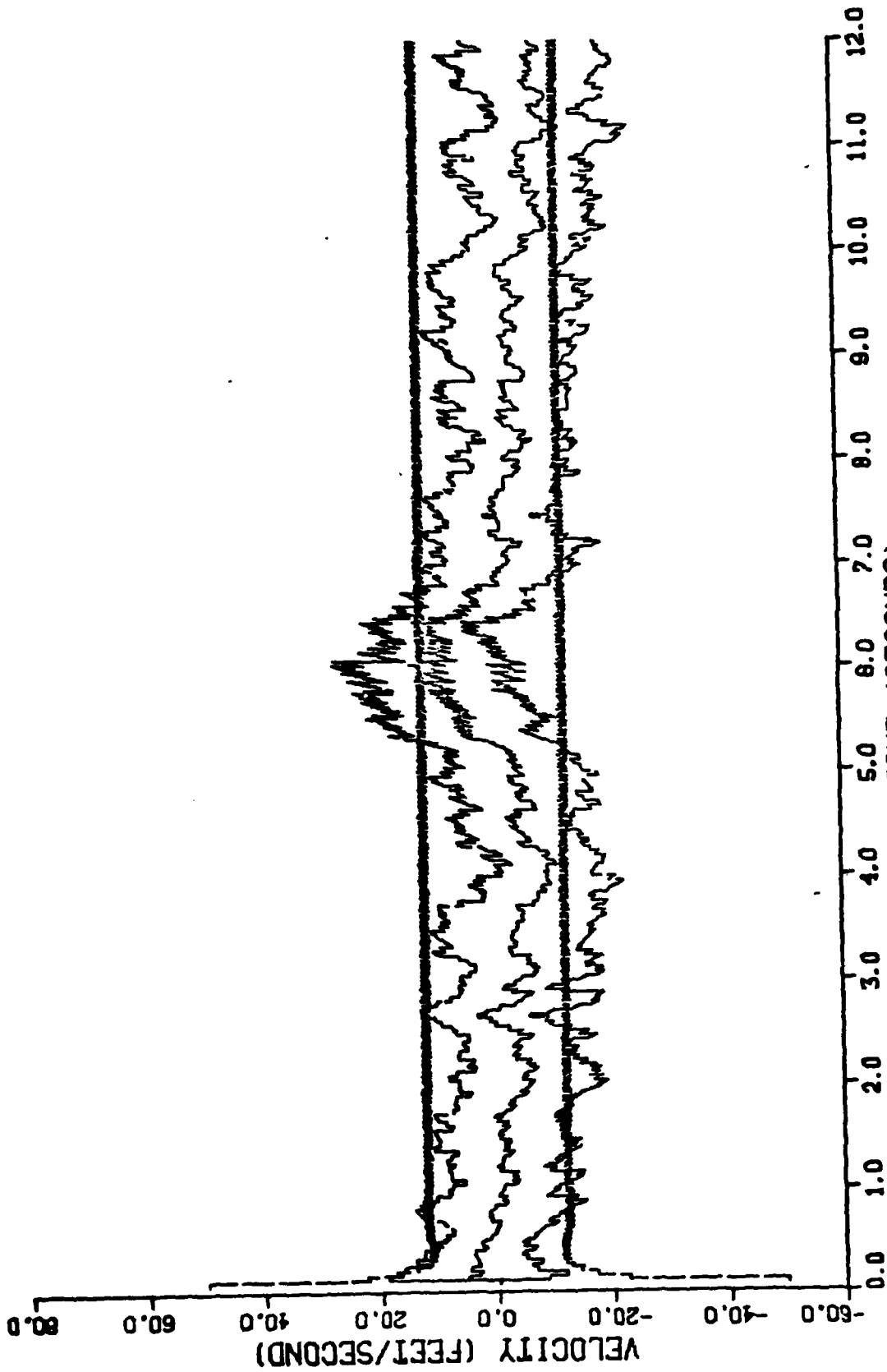


Figure C-11. Performance of the Gauss-Markov Line of Sight Filter Along the 1-Axis for Trajectory 2

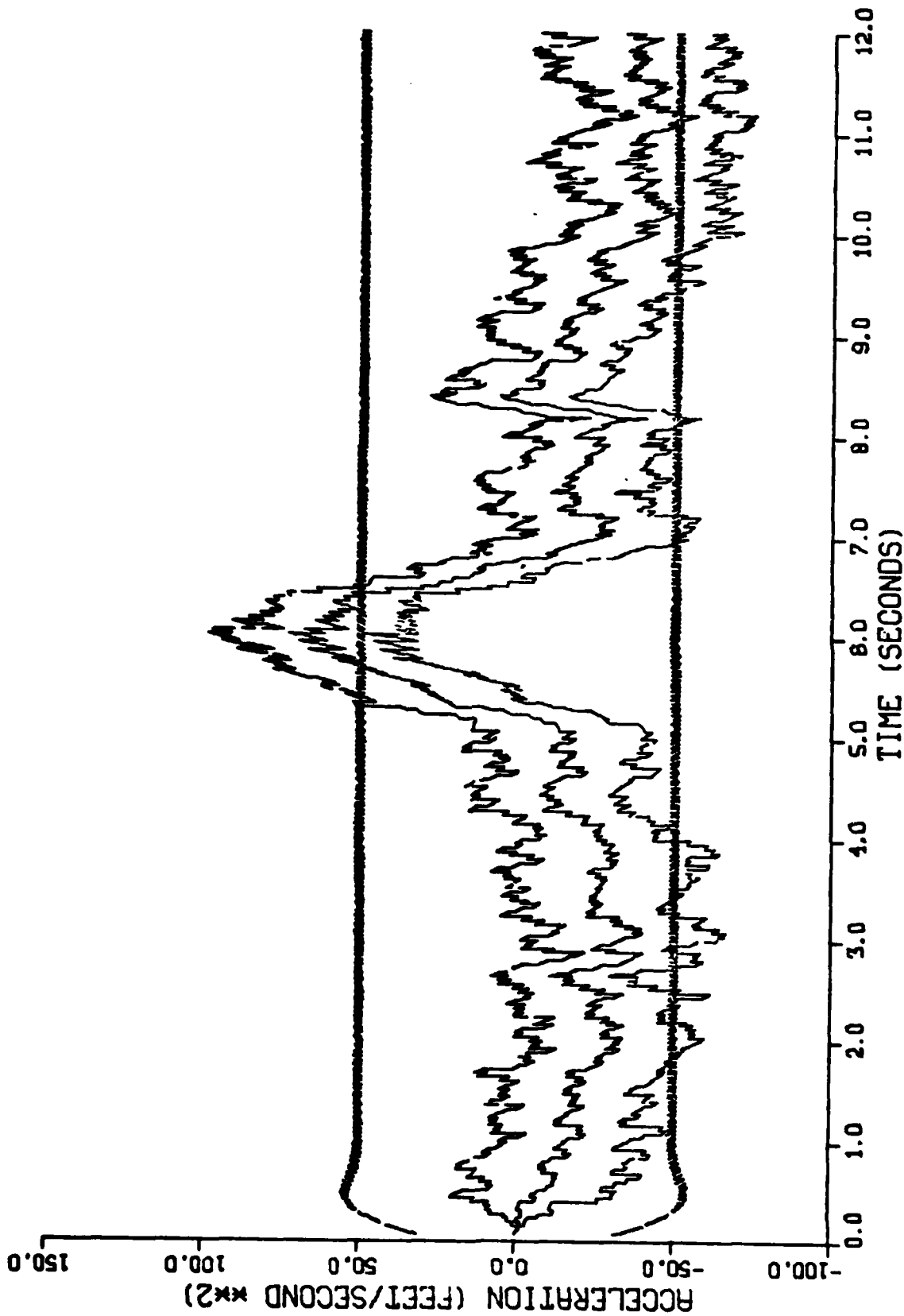


Figure C-12. Performance of the Gauss-Markov Line of Sight Filter Along the 1-Axis for Trajectory 2

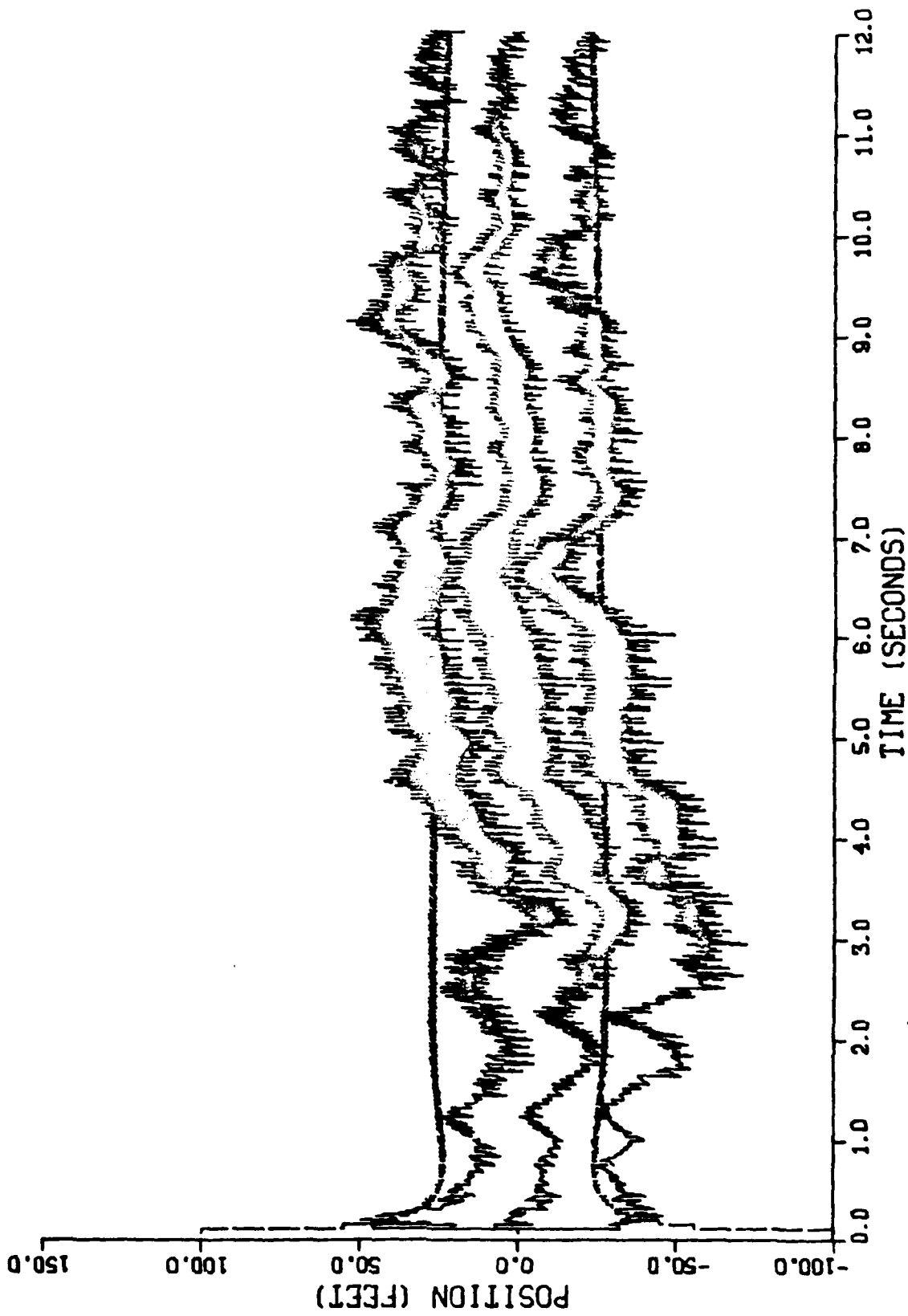


Figure C-13. Performance of the Gauss-Markov Line of Sight Filter Along the 2-Axis for Trajectory 2

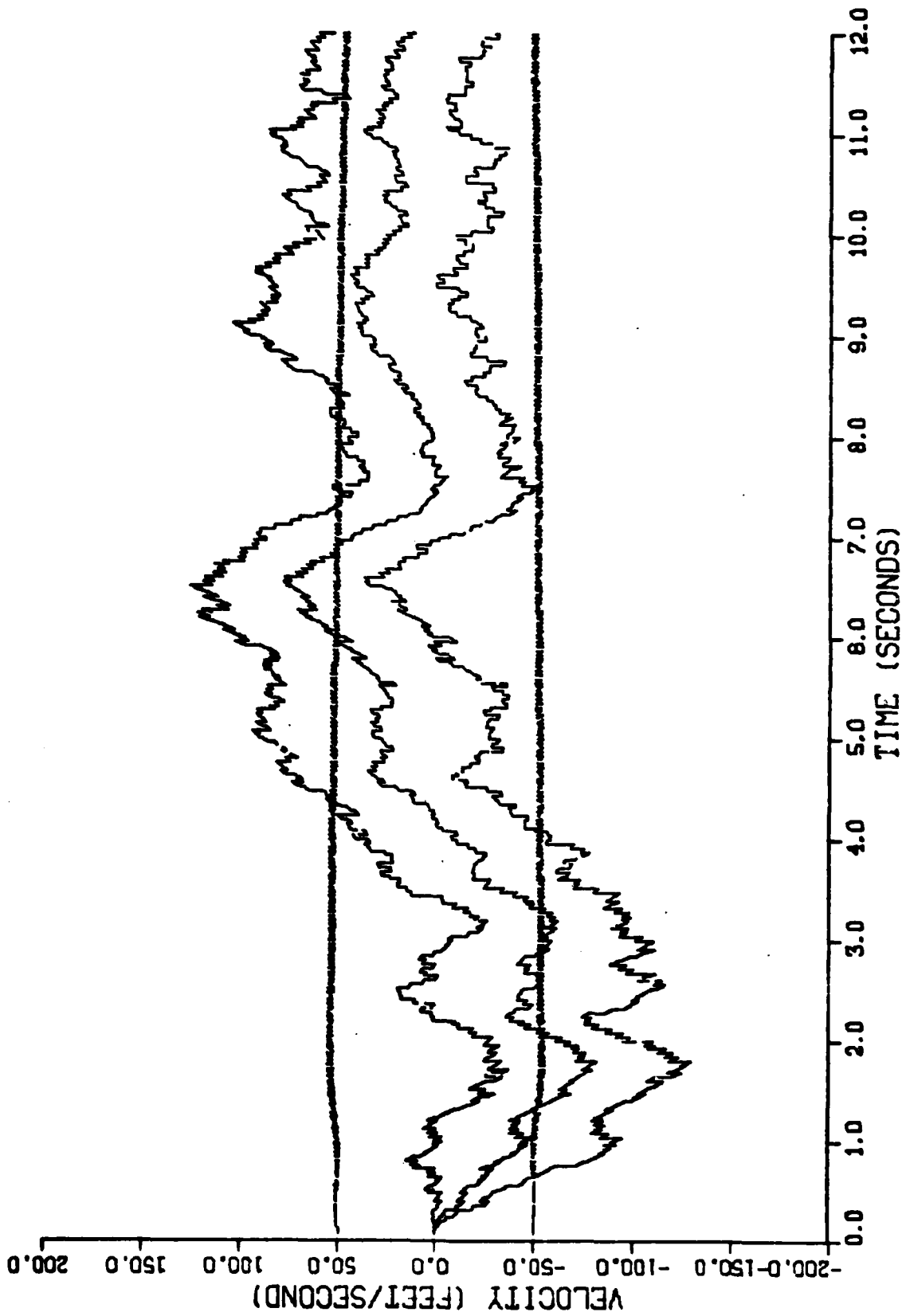


Figure C-14. Performance of the Gauss-Markov Line of Sight Filter Along the 2-Axis for Trajectory 2

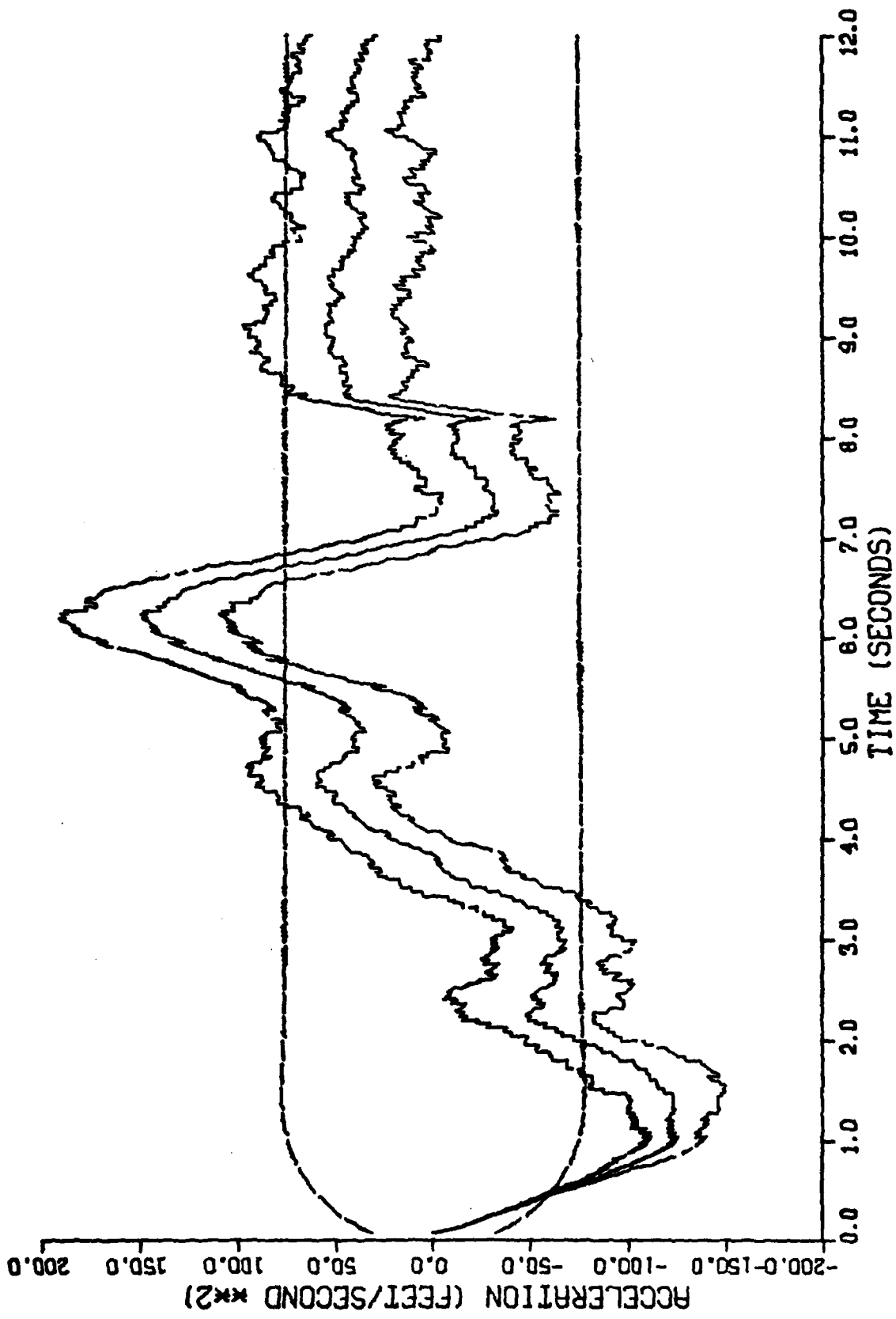


Figure C-15. Performance of the Gauss-Markov Line of Sight Filter Along the 2-Axis for Trajectory 2

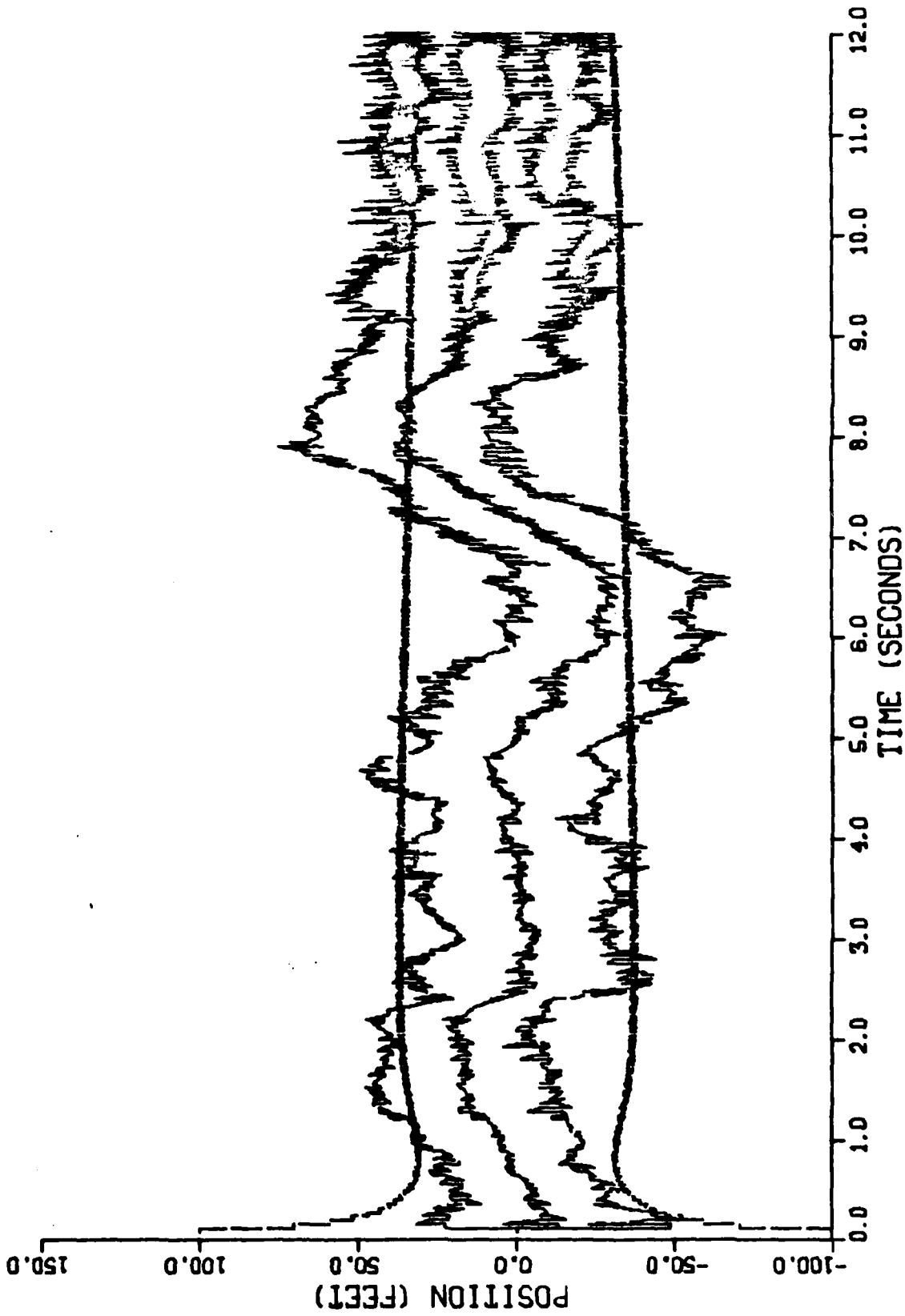


Figure C-16. Performance of the Gauss-Markov Line of Sight Filter Along the 3-Axis for Trajectory 2

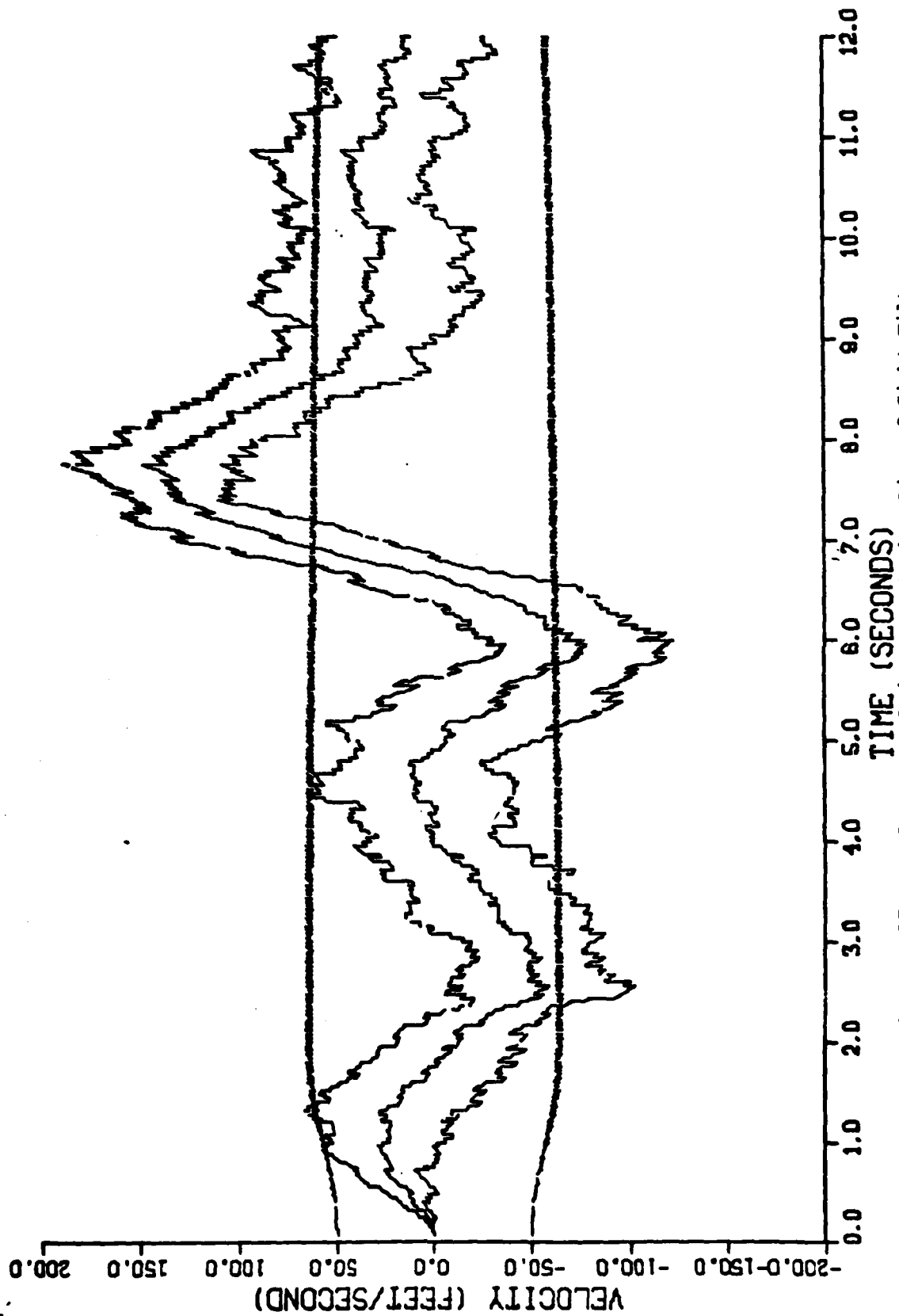


Figure C-17. Performance of the Gauss-Markov Line of Sight Filter
Along the 3-Axis for Trajectory 2

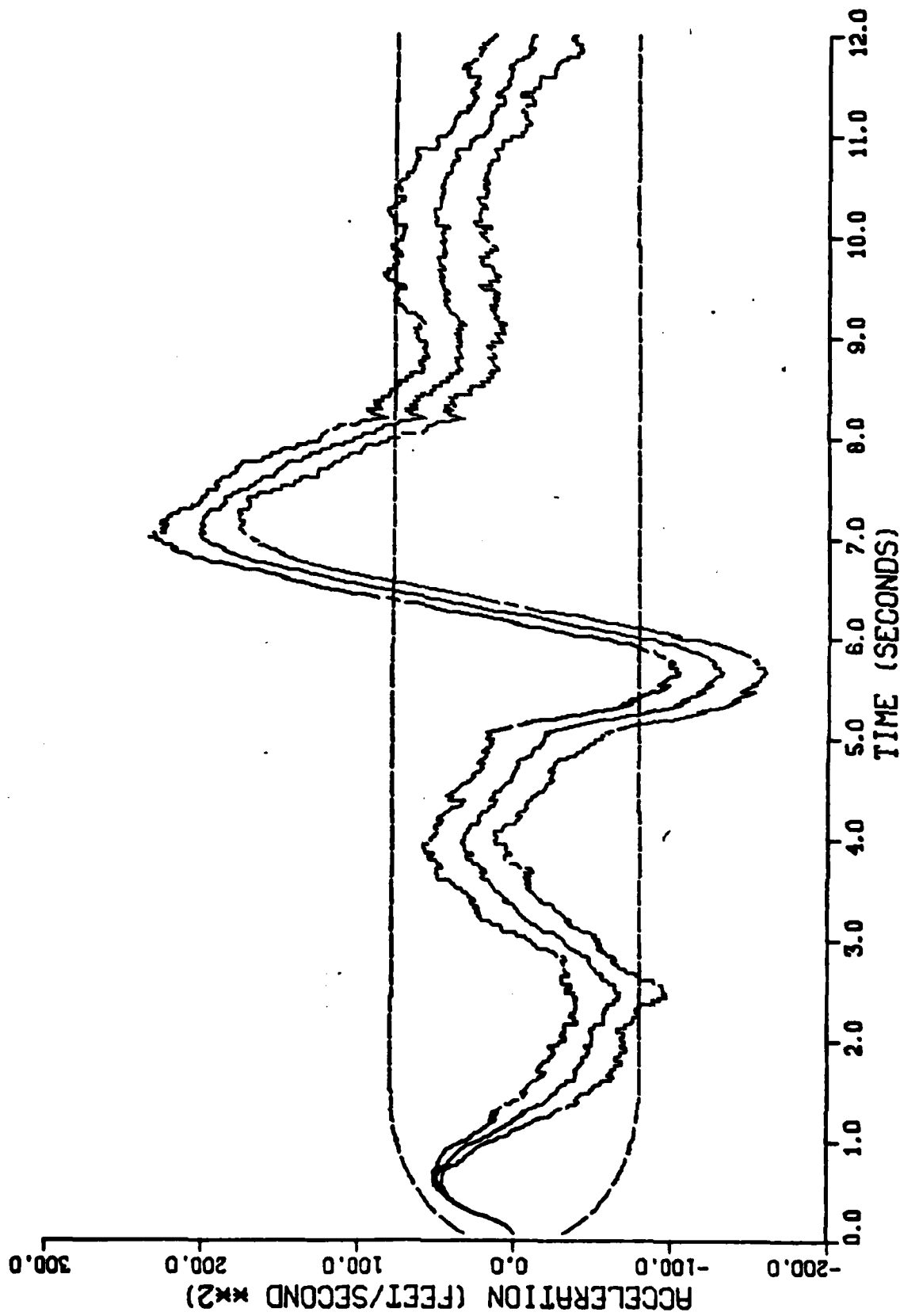


Figure C-18. Performance of the Gauss-Markov Line of Sight Filter Along the 3-Axis for Trajectory 2

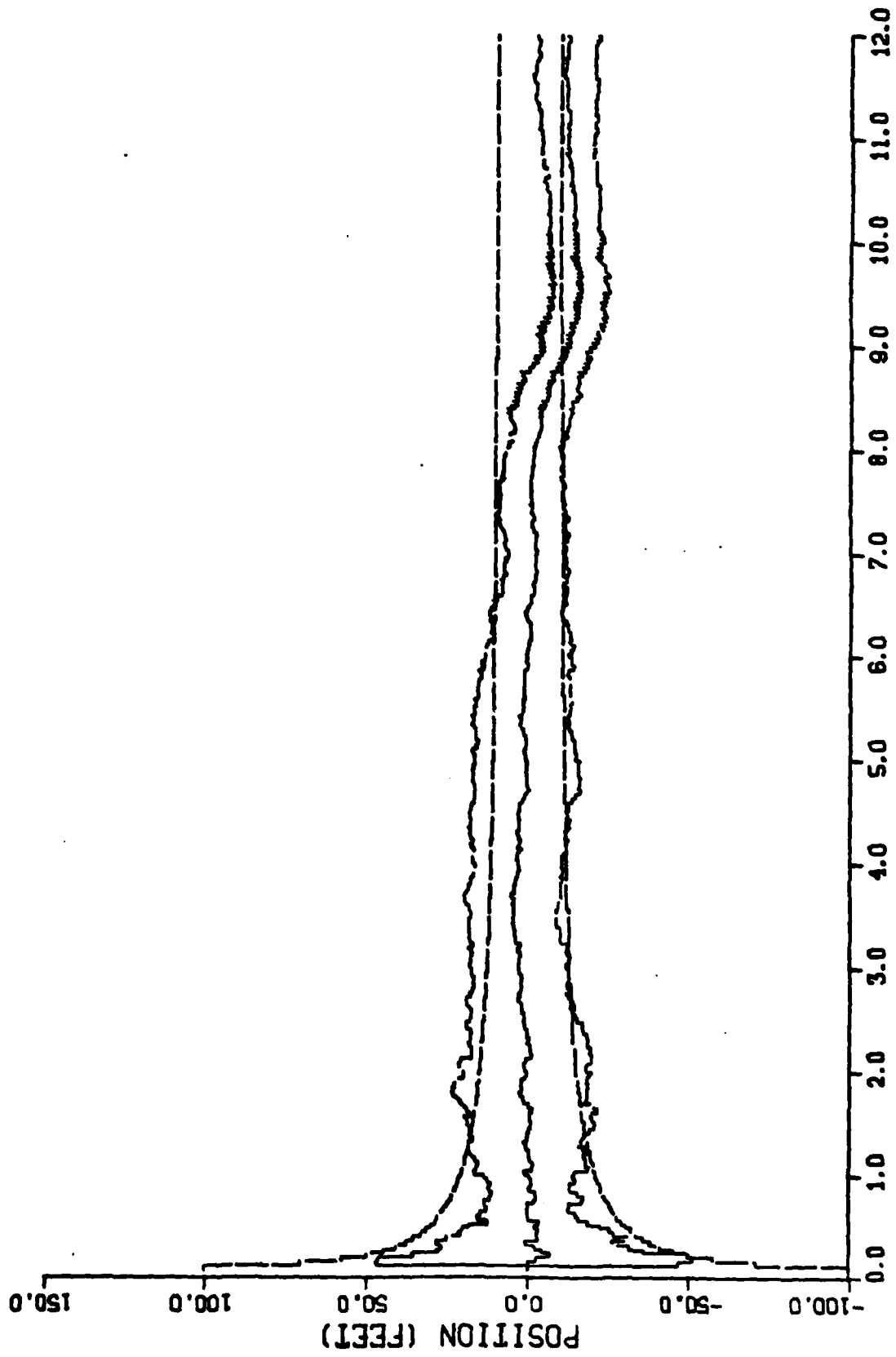


Figure C-19. Performance of the Gauss-Markov Line of Sight Filter Along the 1-Axis for Trajectory 3

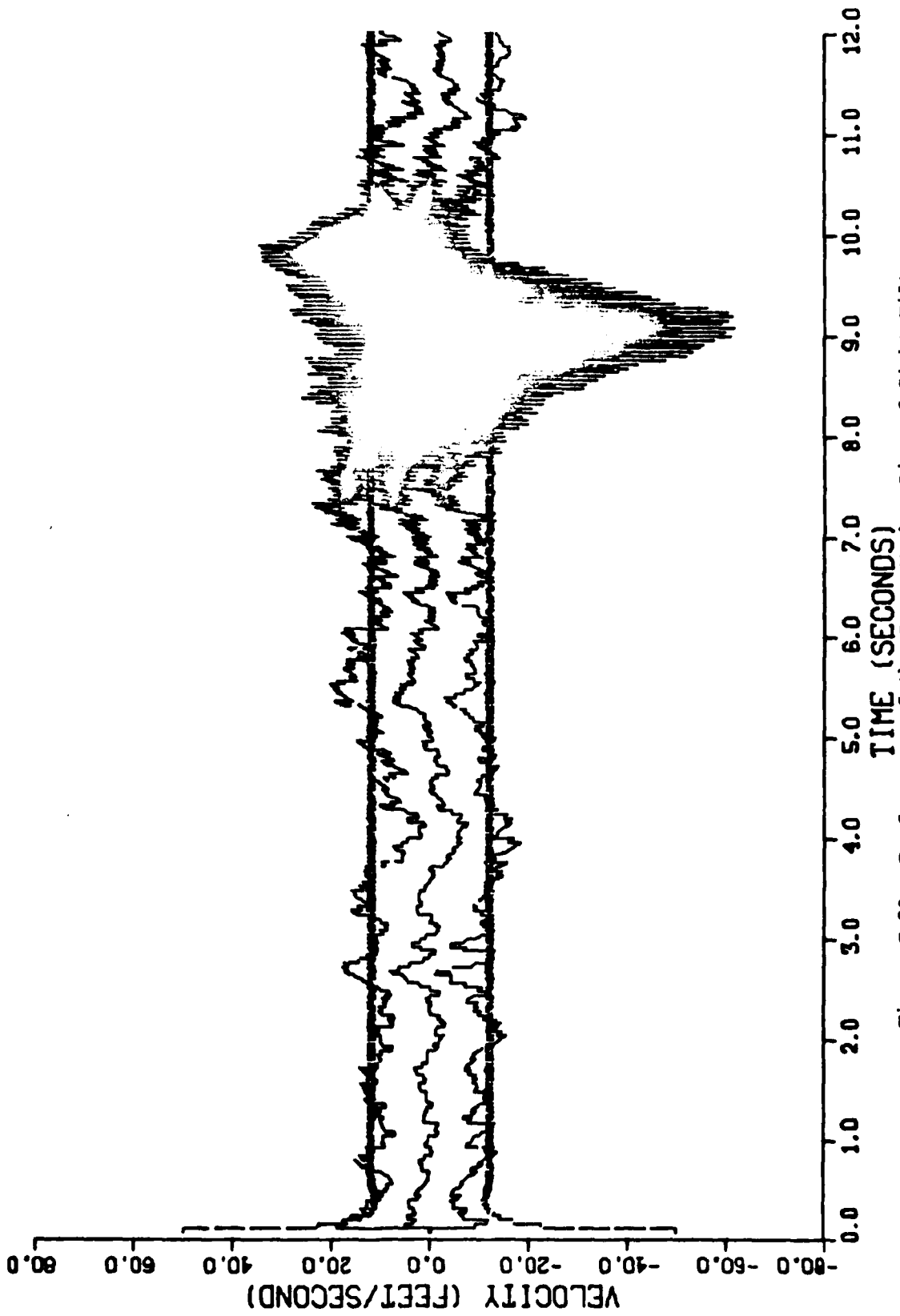


Figure C-20. Performance of the Gauss-Markov Line of Sight Filter Along the 1-Axis for Trajectory 3

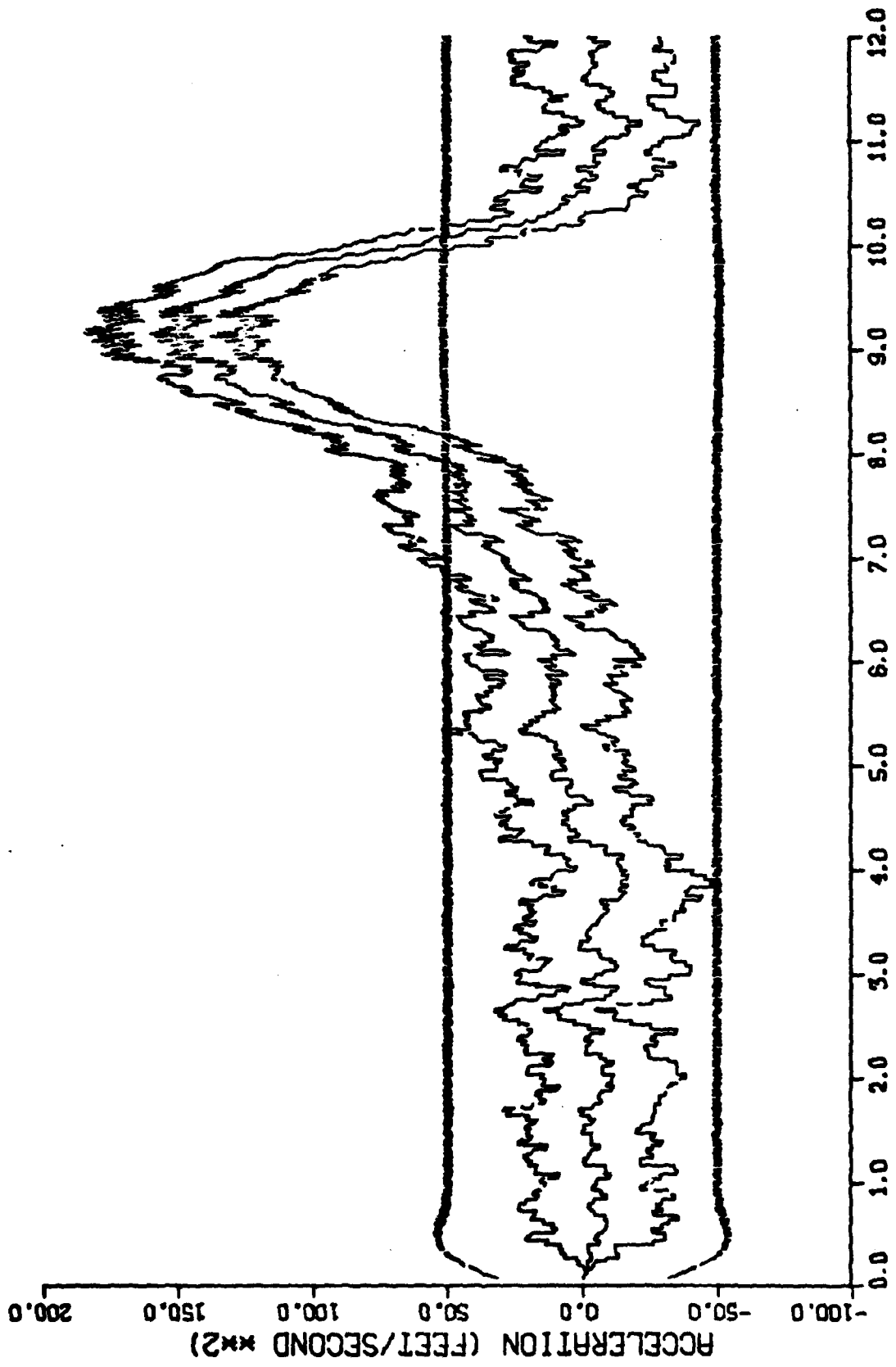


Figure C-21. Performance of the Gauss-Markov Line of Sight Filter Along the I-Axis for Trajectory 3

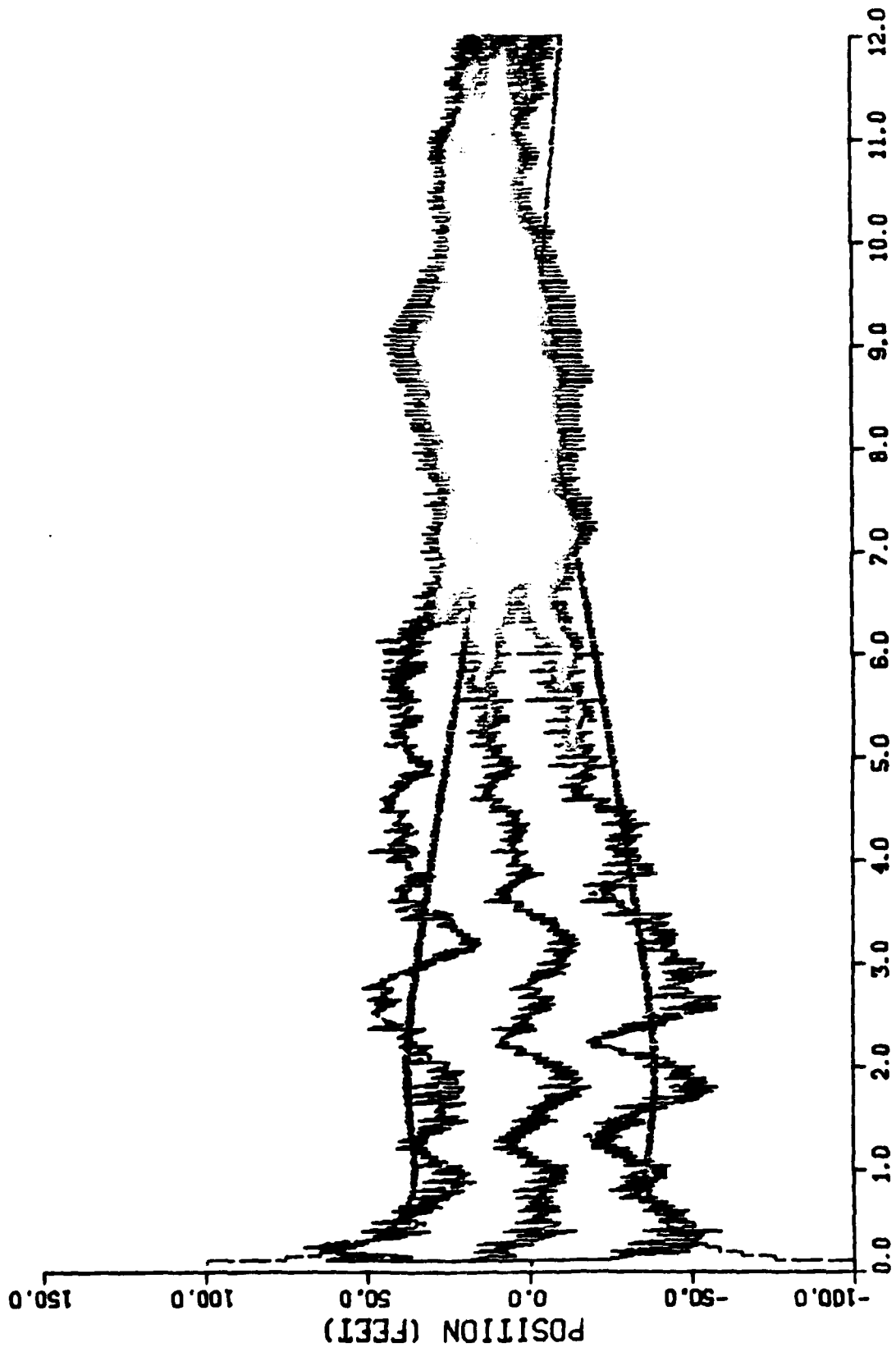


Figure C-22. Performance of the Gauss-Markov Line of Sight Filter Along the 2-Axis for Trajectory 3

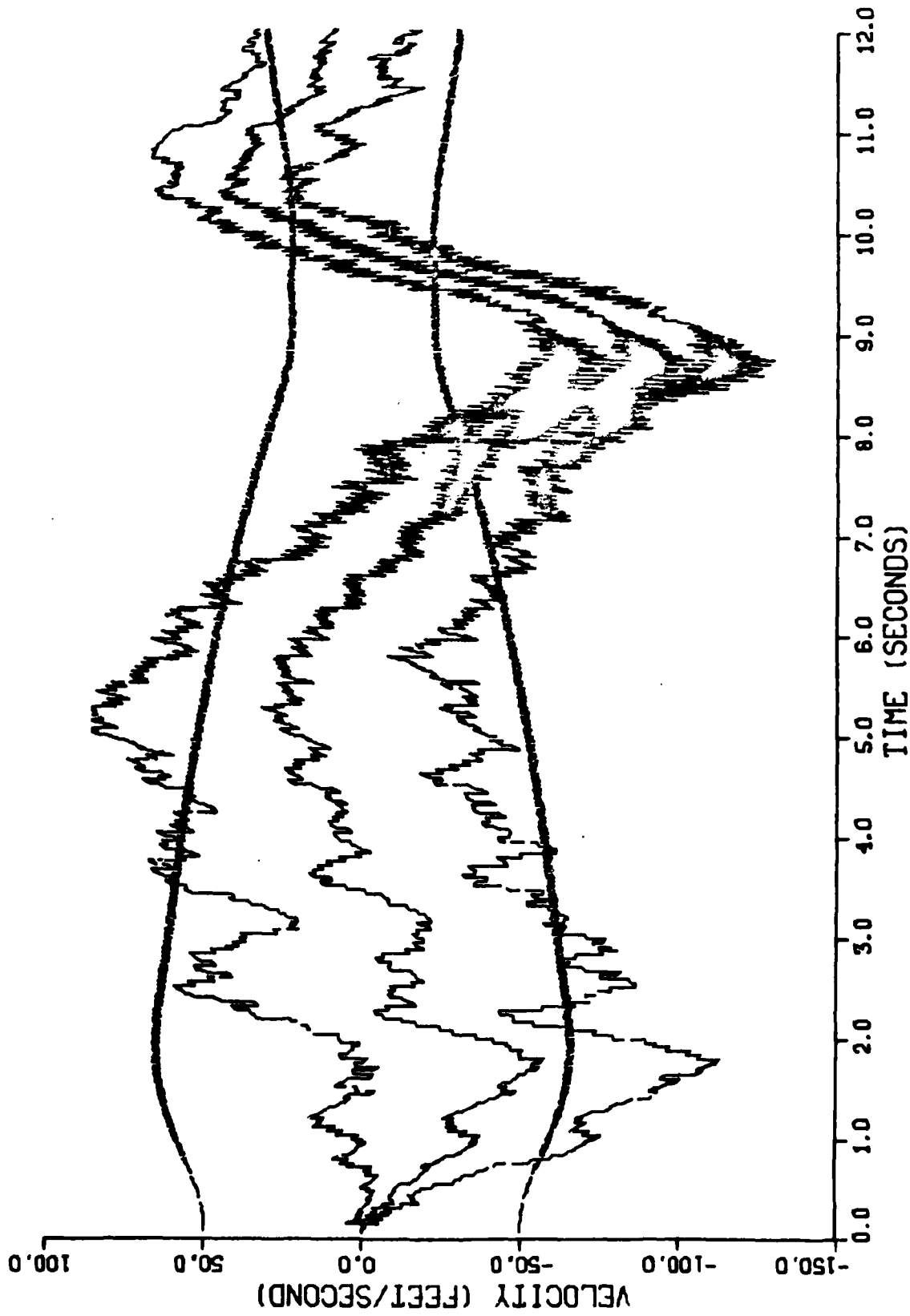


Figure C-23. Performance of the Gauss-Markov Line of Sight Filter Along the 2-Axis for Trajectory 3

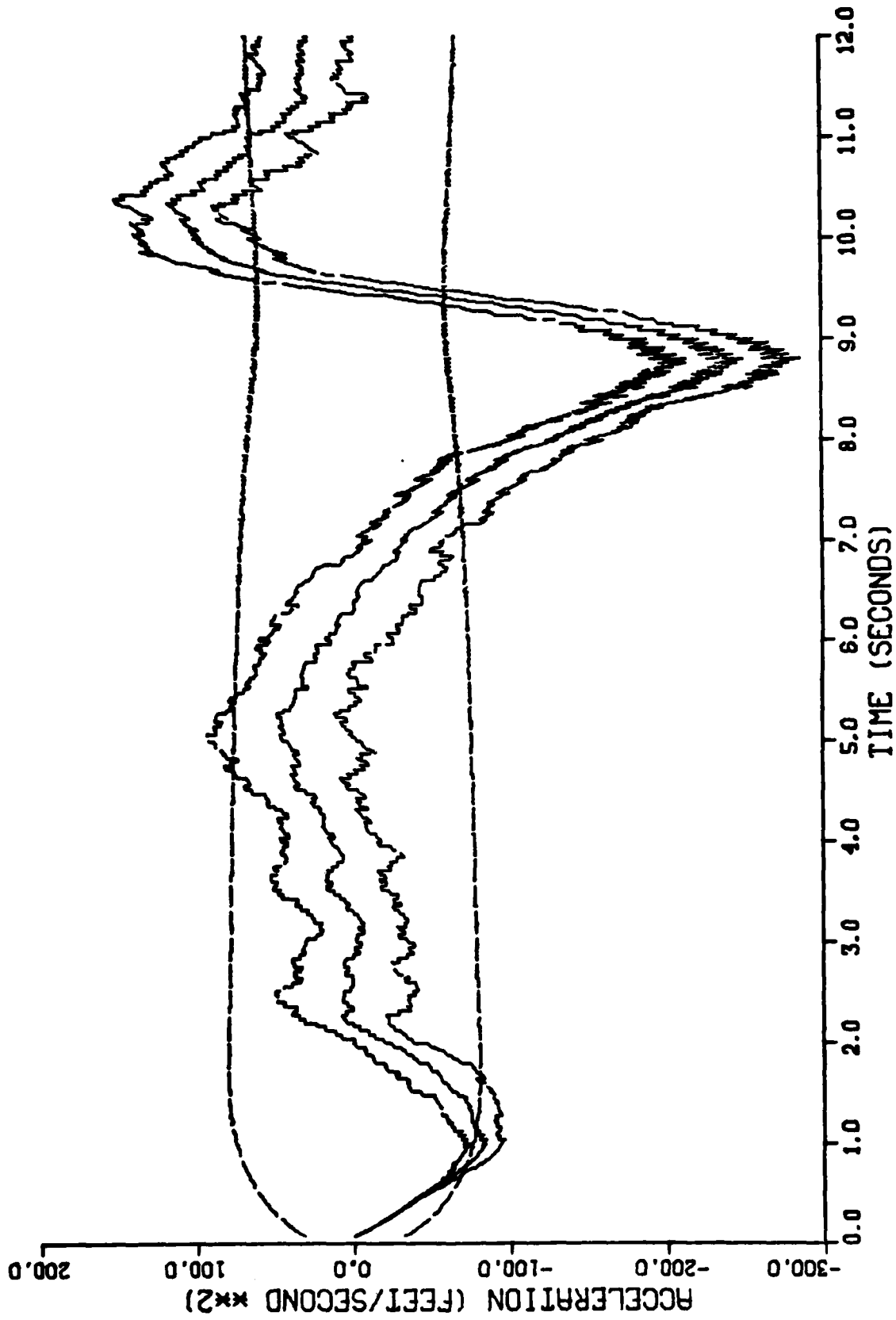


Figure C-24. Performance of the Gauss-Markov Line of Sight Filter Along the 2-Axis for Trajectory 3

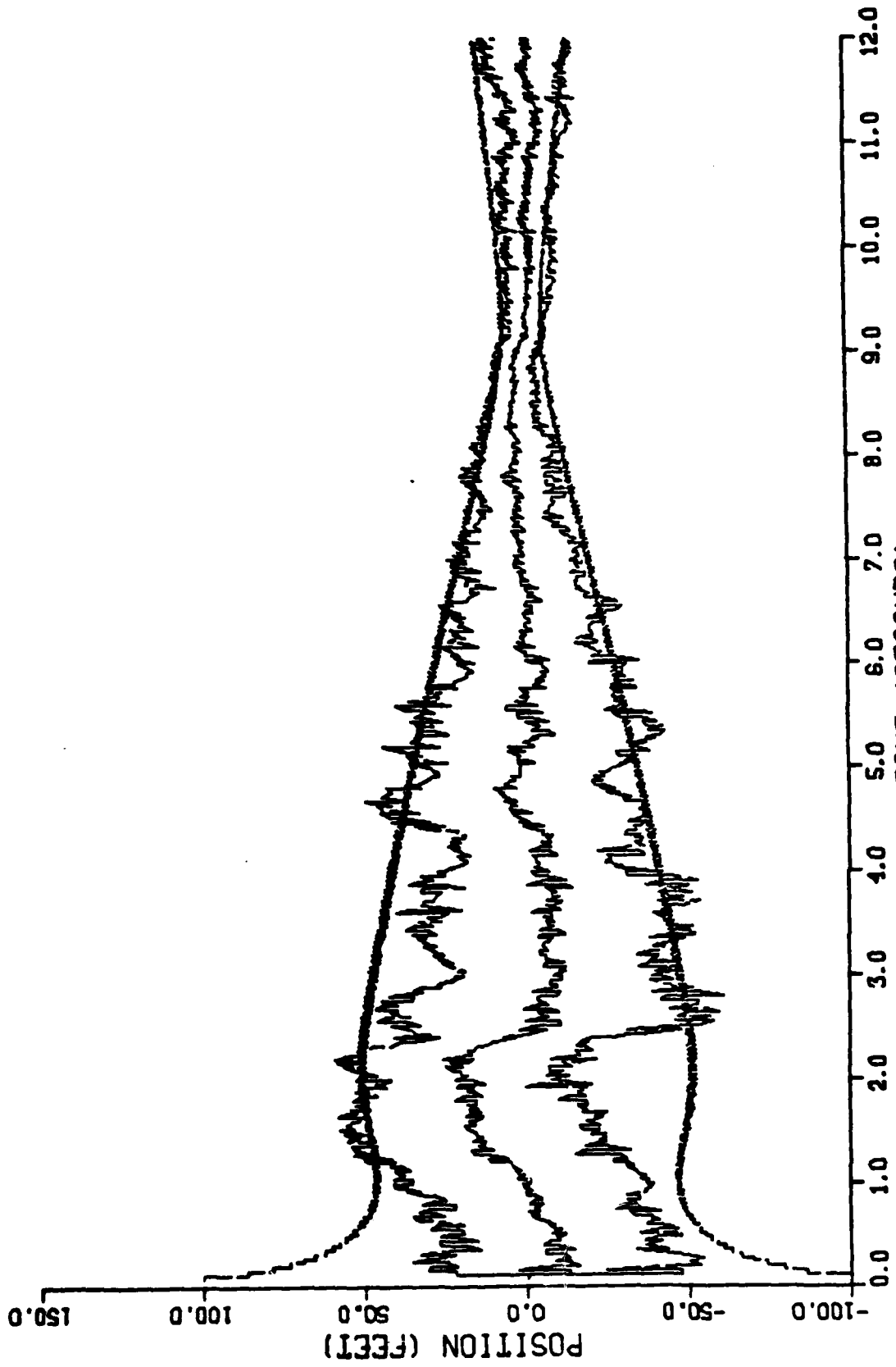


Figure C-25. Performance of the Gauss-Markov Line of Sight Filter Along the 3-Axis for Trajectory 3

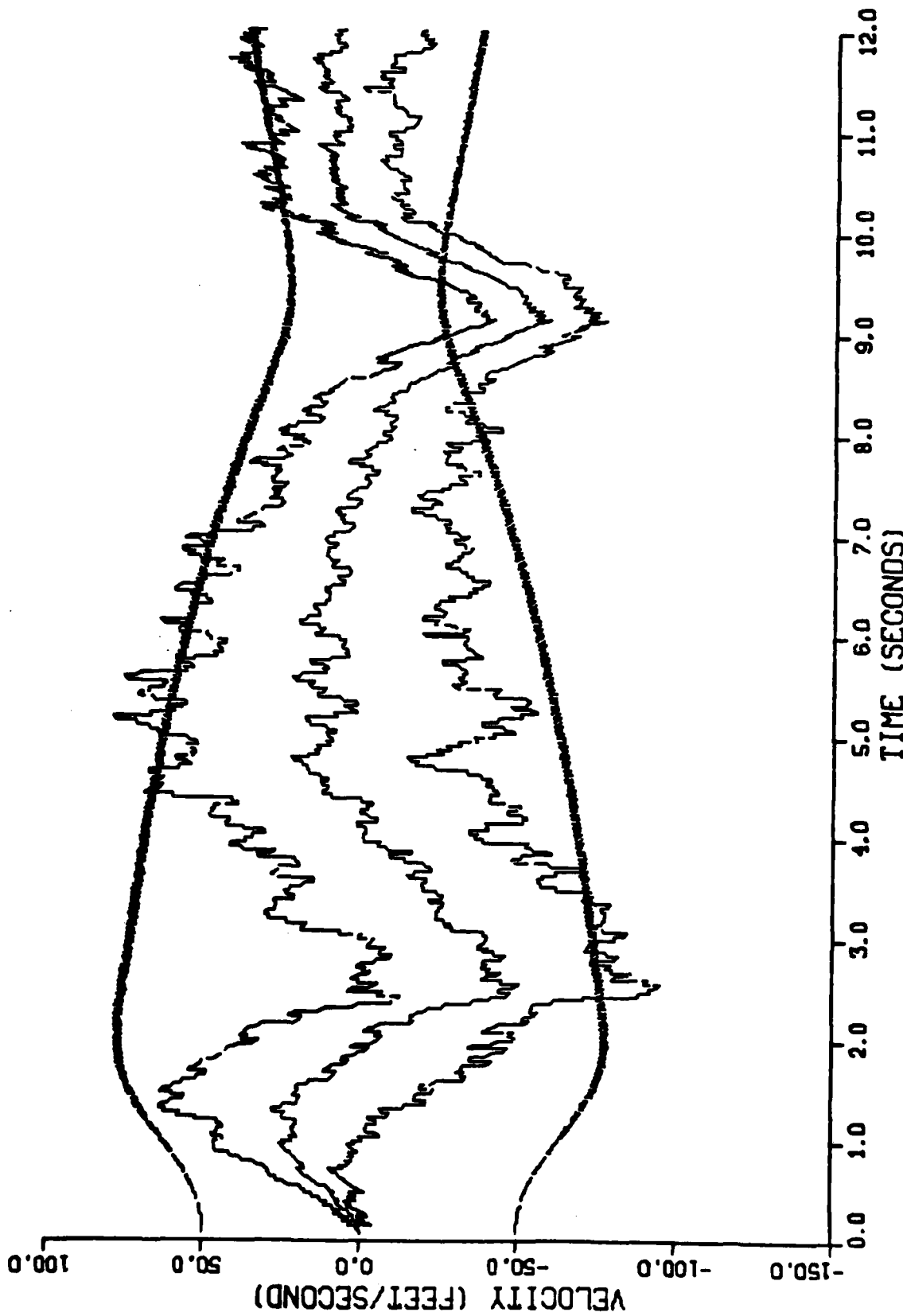


Figure C-26. Performance of the Gauss-Markov Line of Sight Filter Along the 3-Axis for Trajectory 3

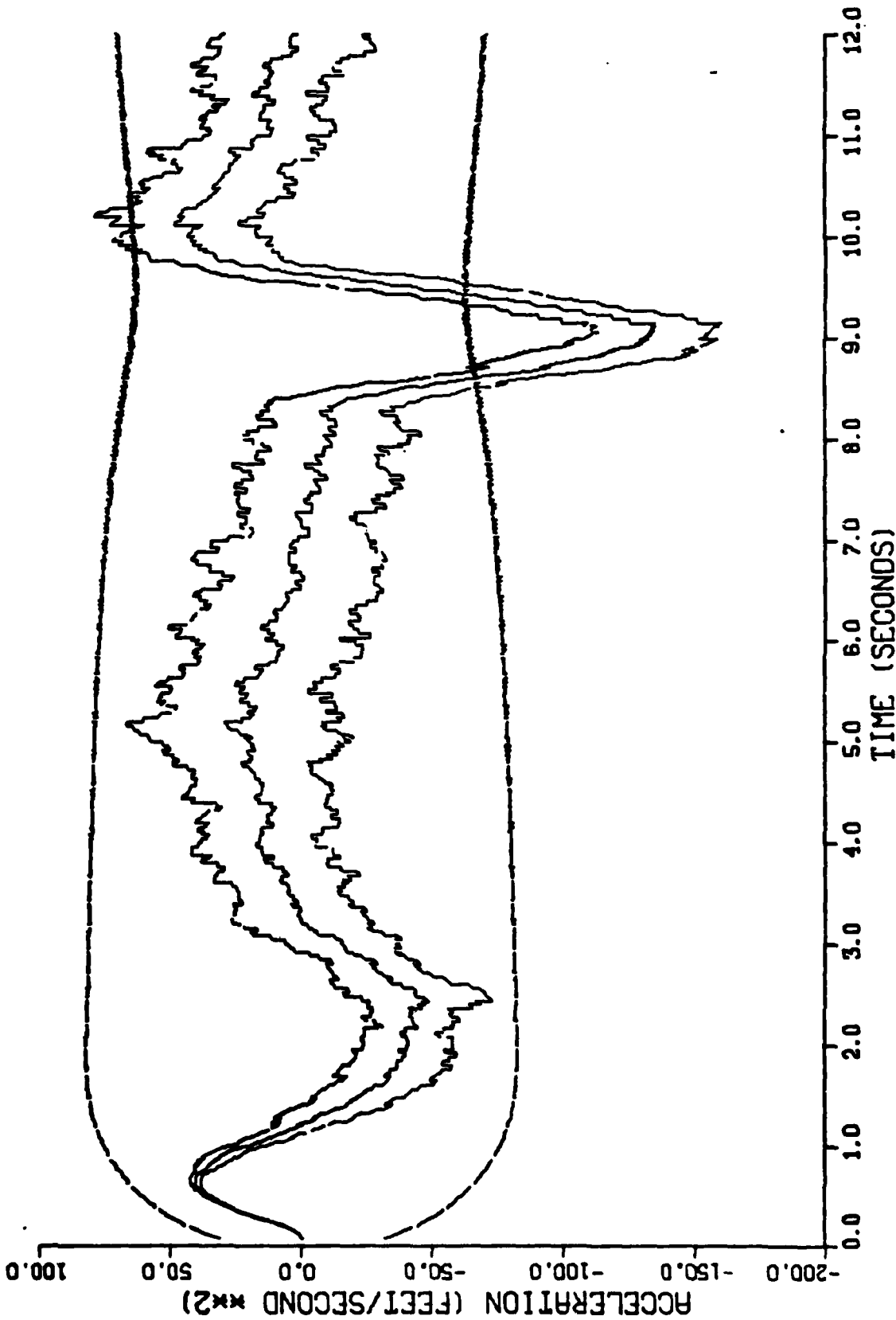


Figure C-27. Performance of the Gauss-Markov Line of Sight Filter Along the 3-Axis for Trajectory 3

APPENDIX D

Graphical Results for the Gauss-Markov
Inertial Coordinate Filter

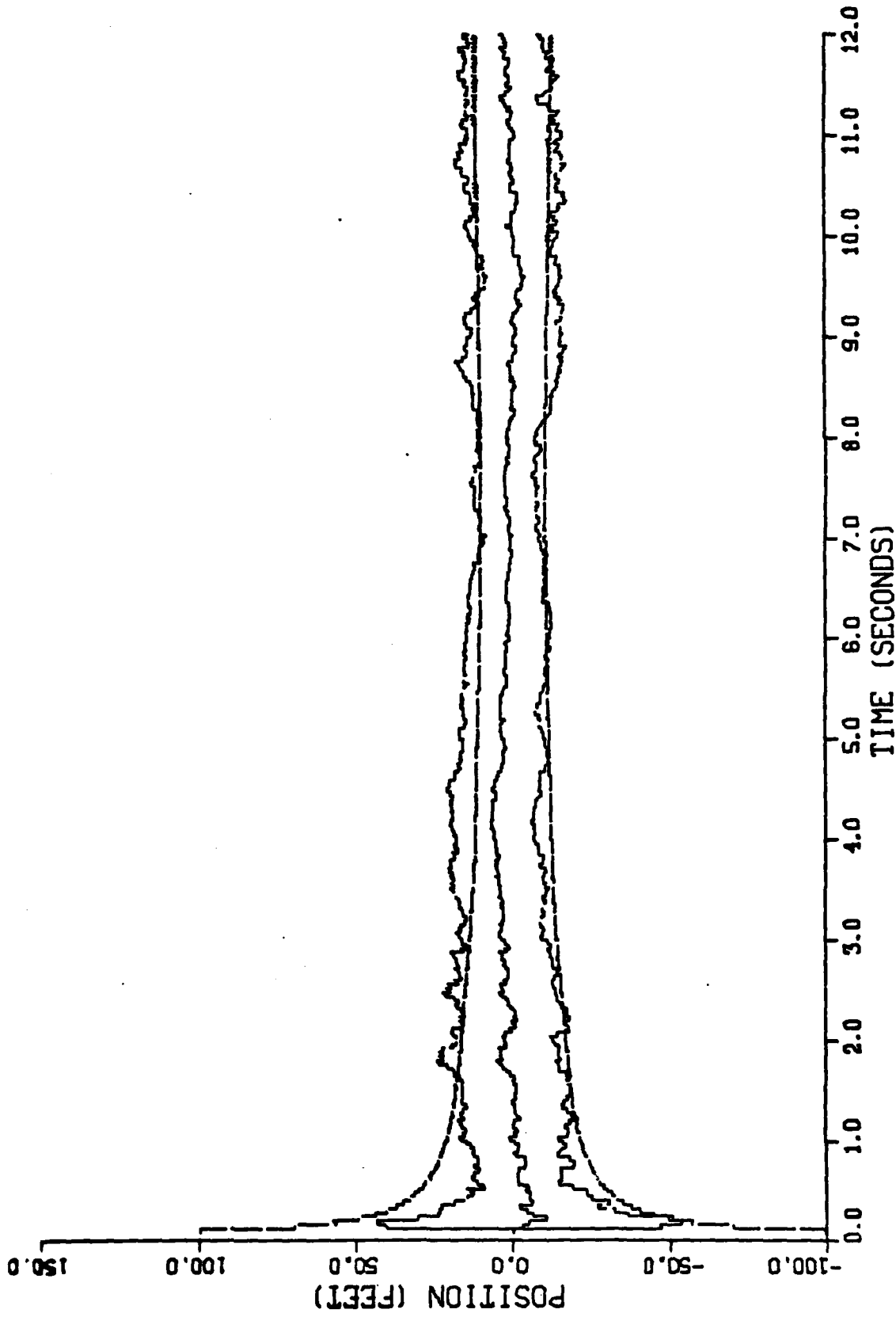


Figure D-1. Performance of the Gauss-Markov Inertial Coordinate Filter Along the North-Axis for Trajectory 1

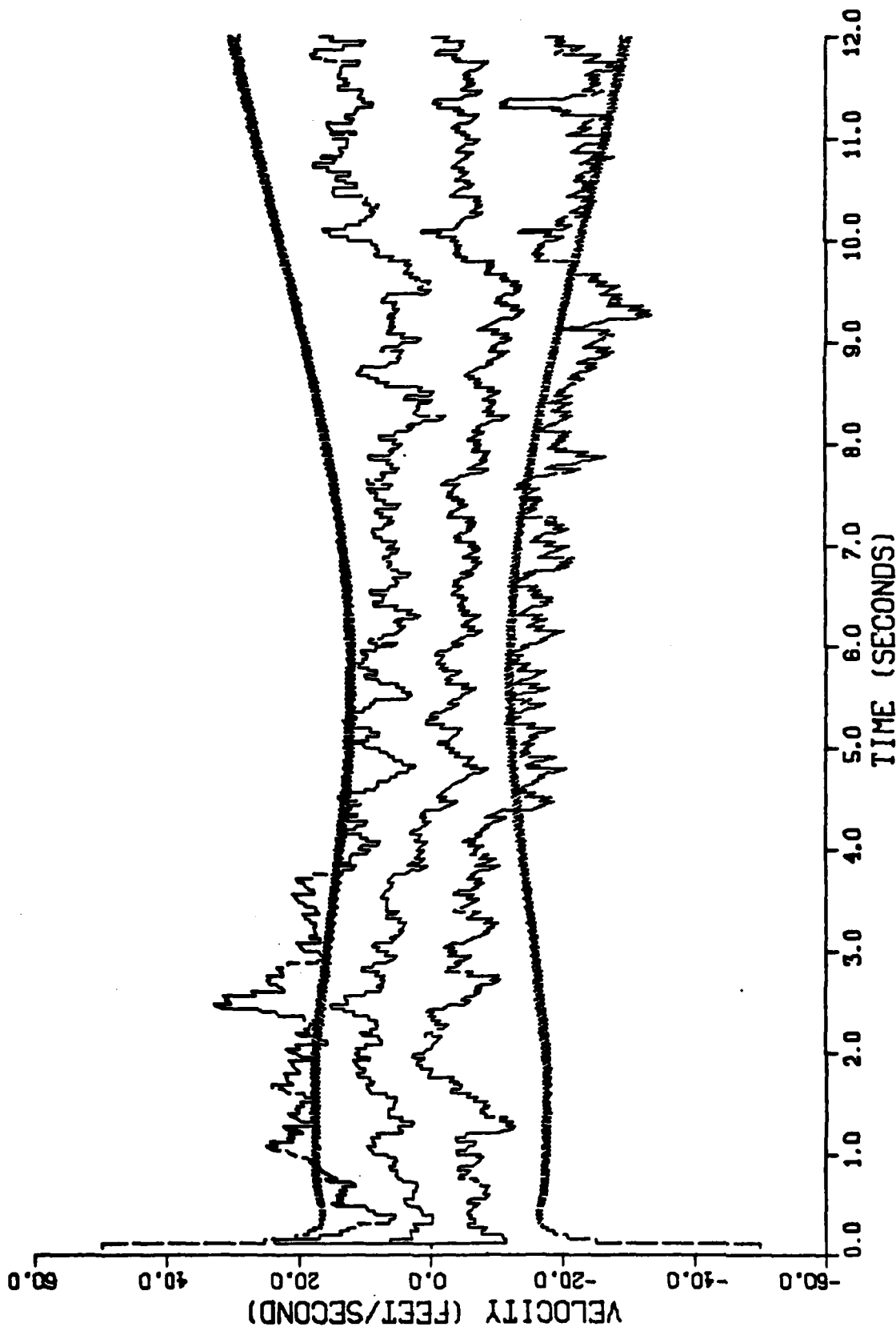


Figure D-2. Performance of the Gauss-Markov Inertial Coordinate Filter Along the North-Axis for Trajectory 1

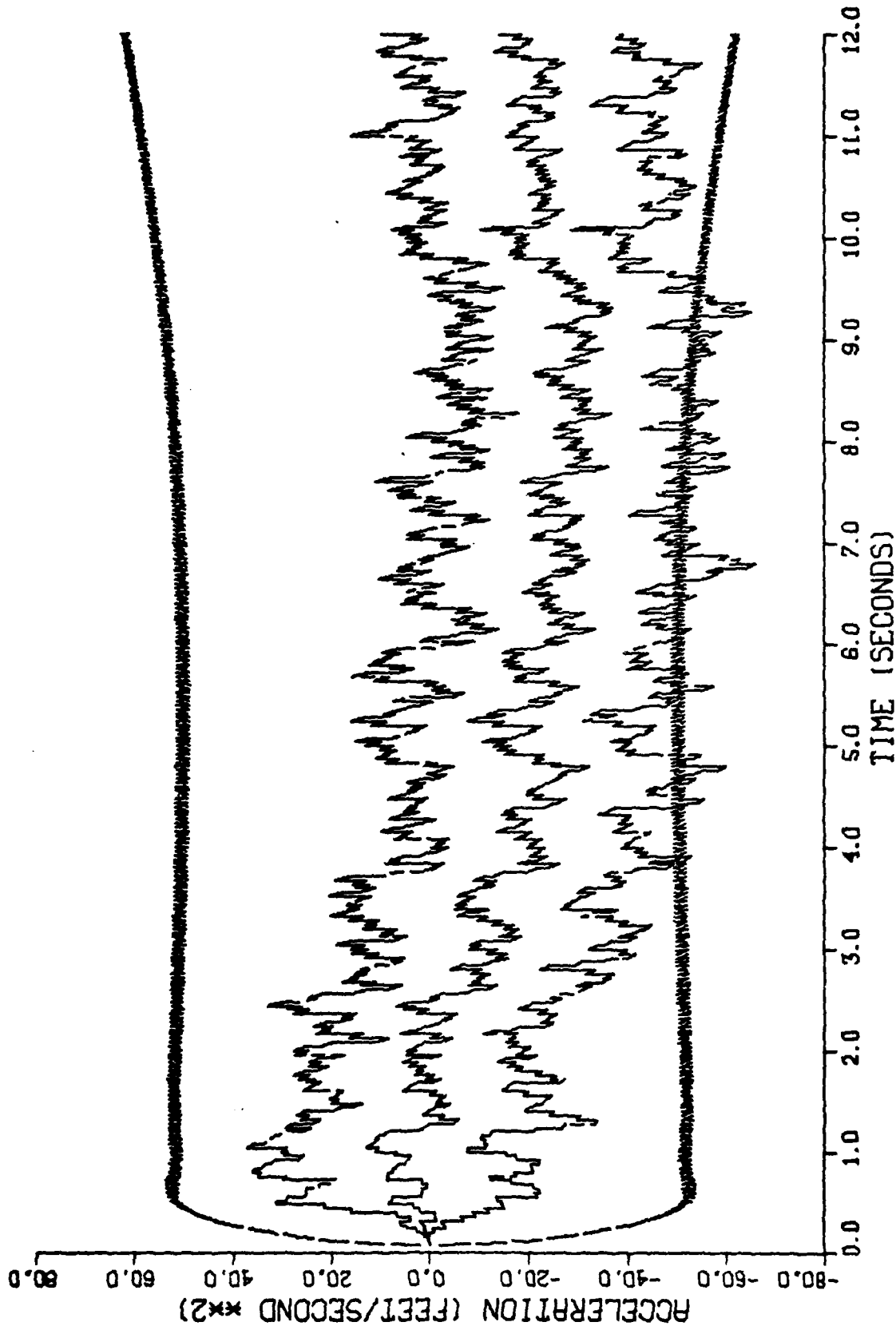


Figure D-3. Performance of the Gauss-Markov Inertial Coordinate Filter Along the North-Axis for Trajectory 1

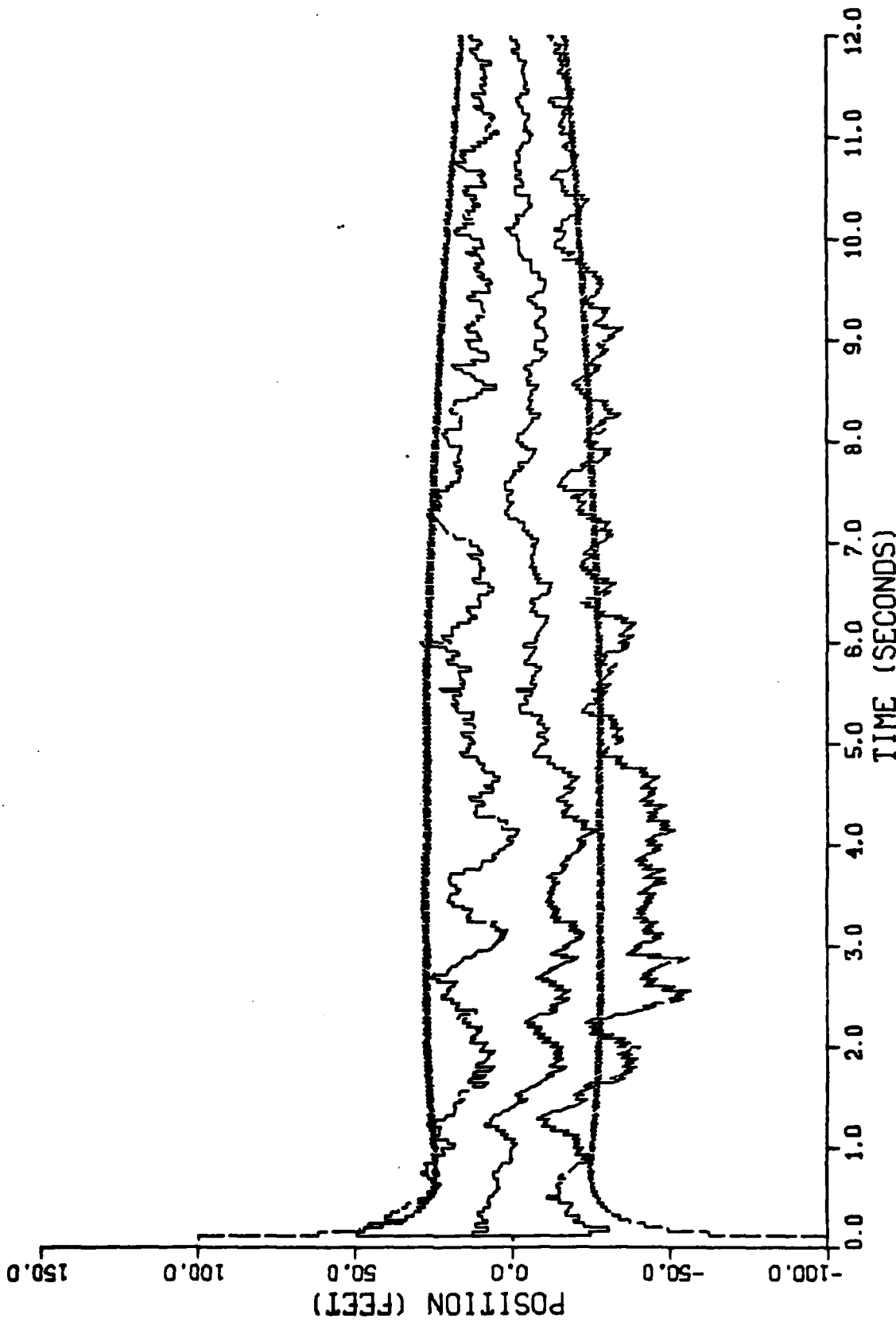


Figure D-4. Performance of the Gauss-Markov Inertial Coordinate Filter Along the East-Axis for Trajectory 1

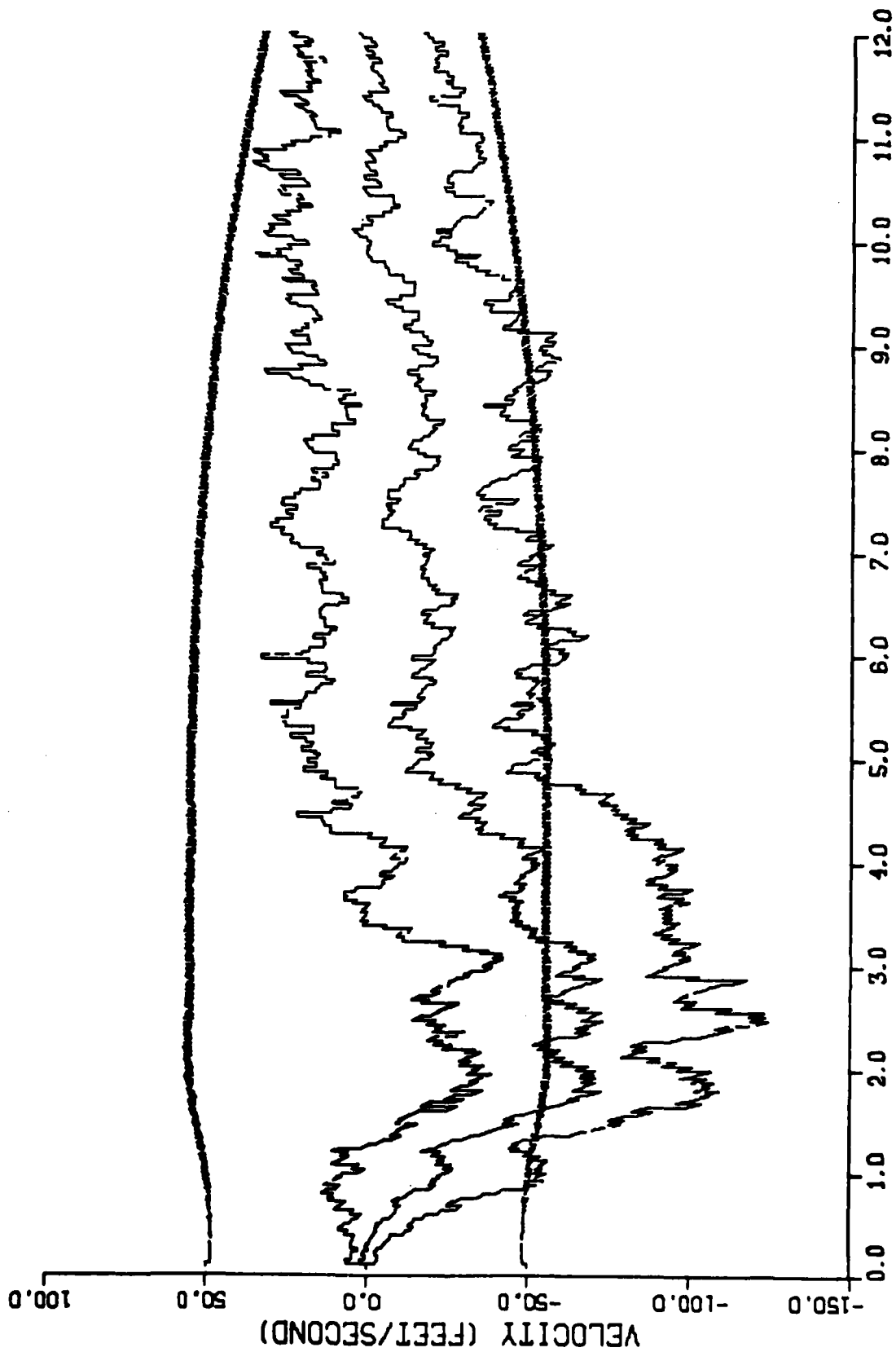


Figure D-5. Performance of the Gauss-Markov Inertial Coordinate Filter
Along the East-Axis for Trajectory 1

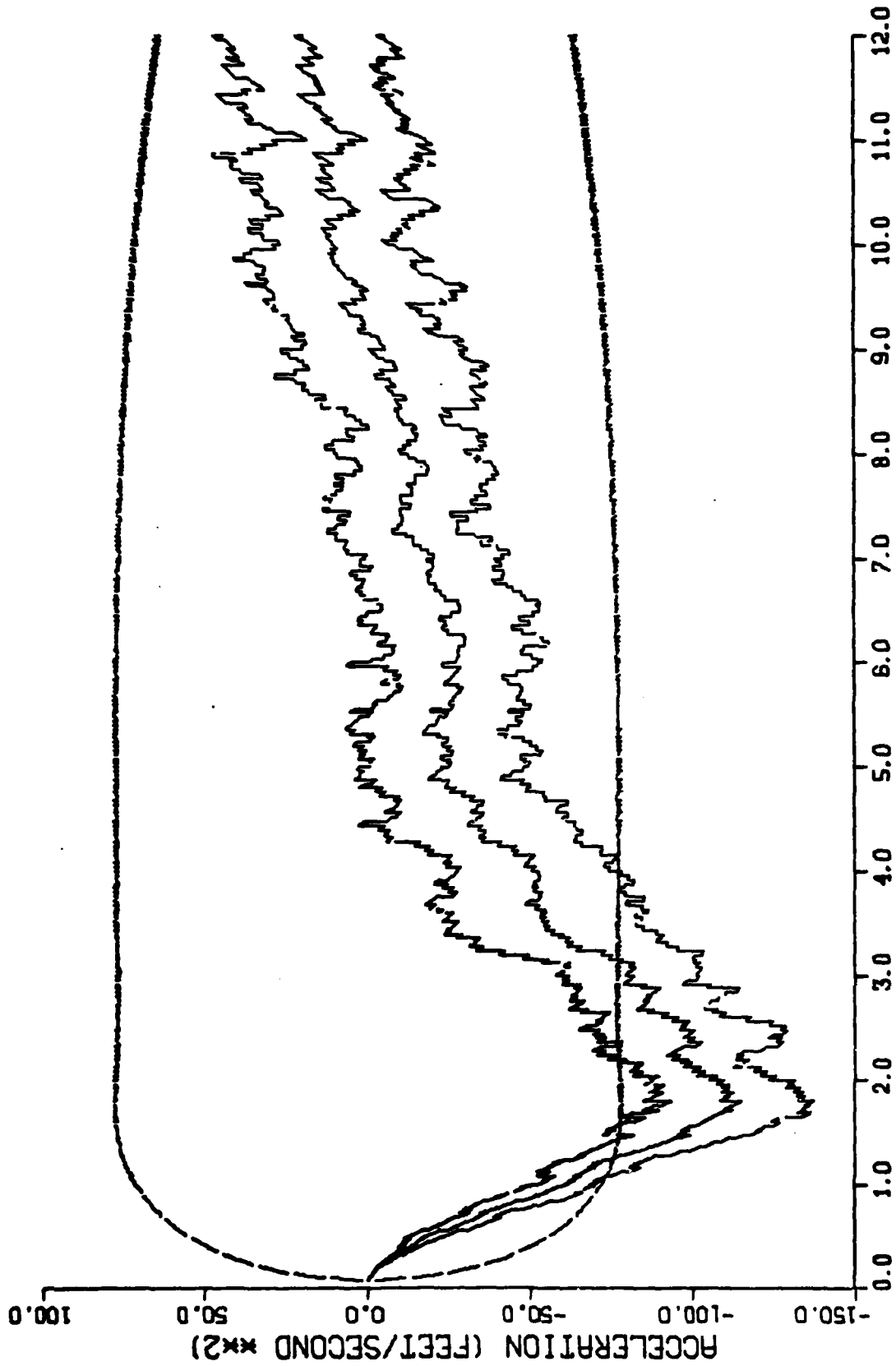


Figure D-6. Performance of the Gauss-Markov Inertial Coordinate Filter
Along the East-Axis for Trajectory 1

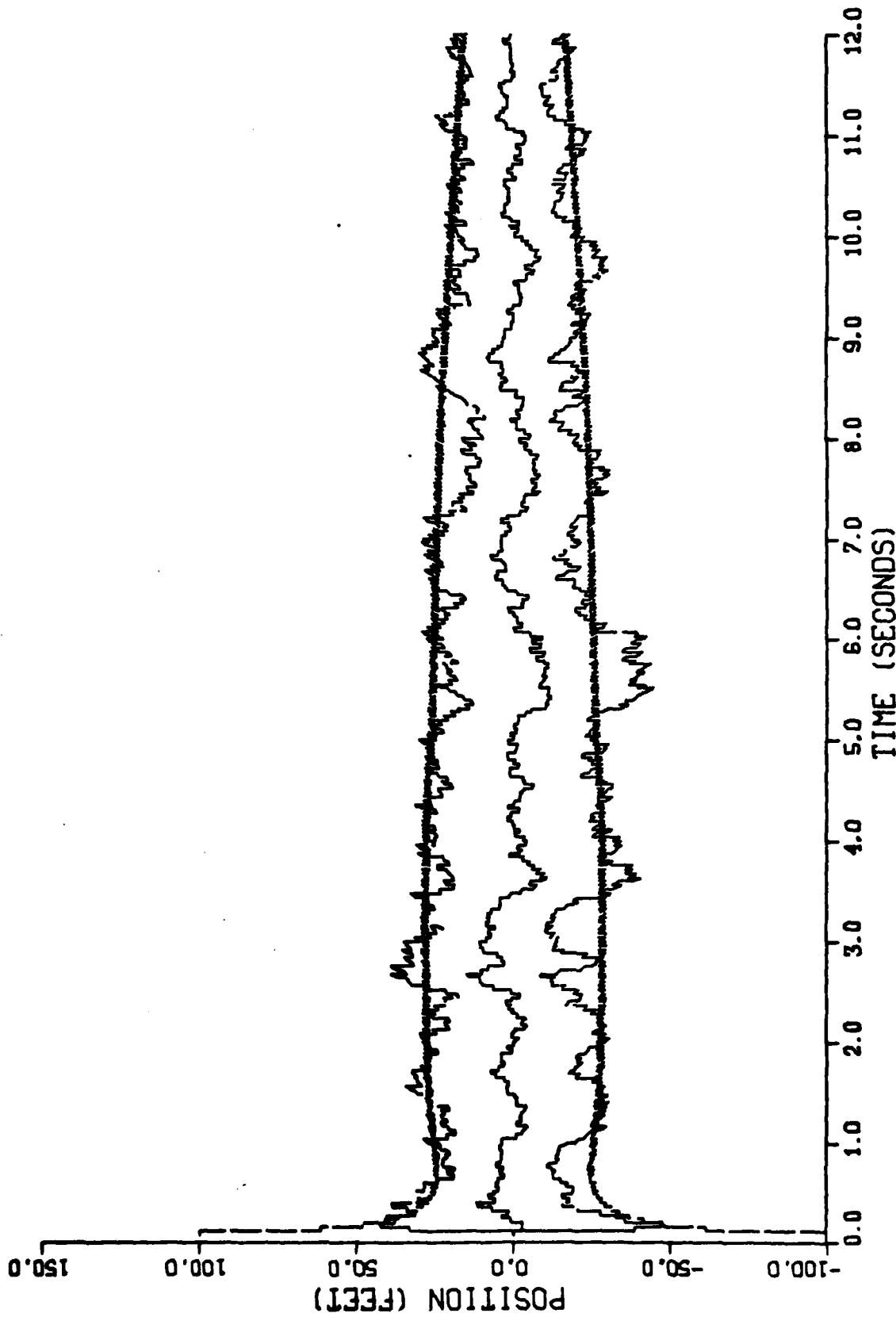


Figure D-7. Performance of the Gauss-Markov Inertial Coordinate Filter Along the Down-Axis for Trajectory 1

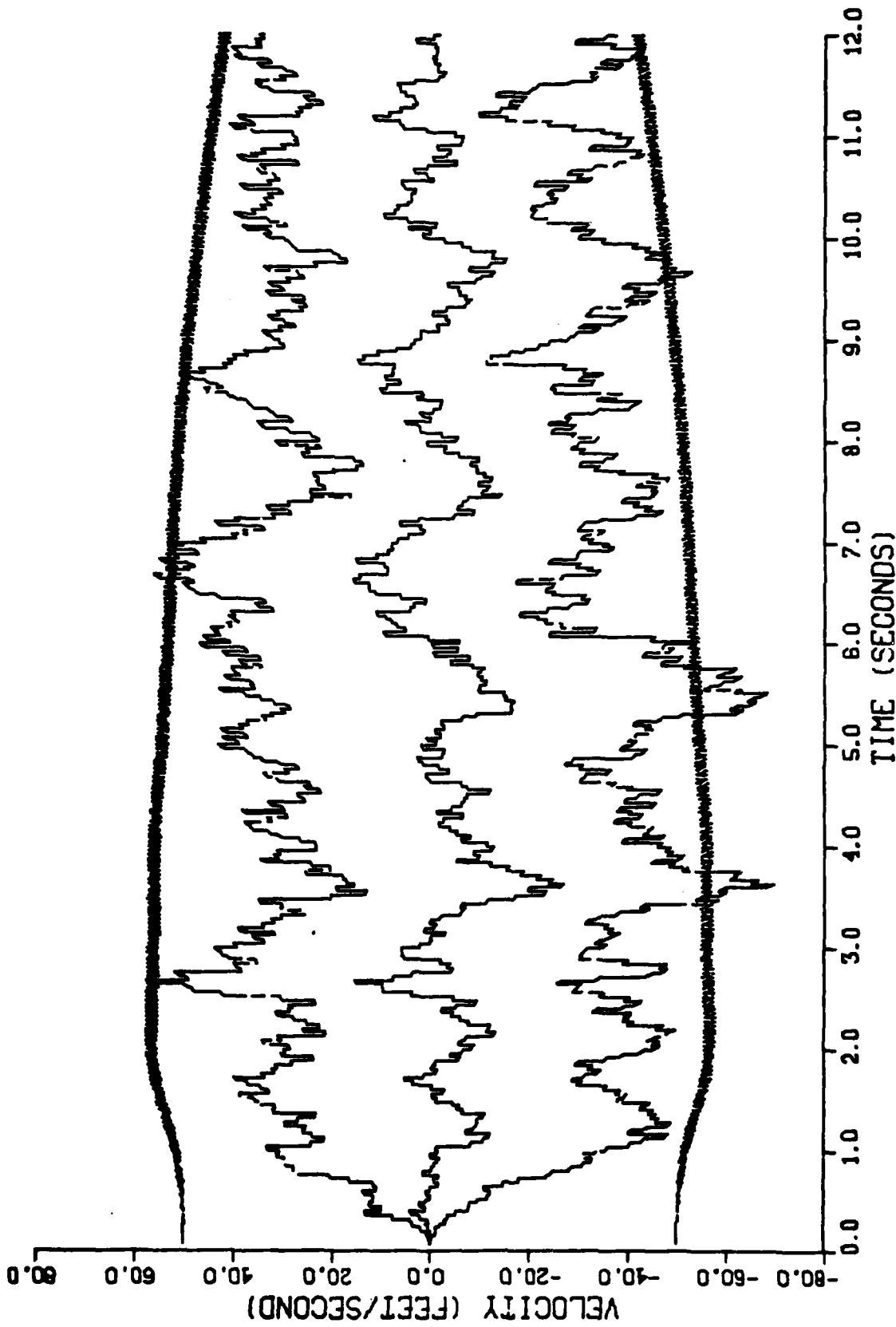


Figure D-8. Performance of the Gauss-Markov Inertial Coordinate Filter Along the Down-Axis for Trajectory 1

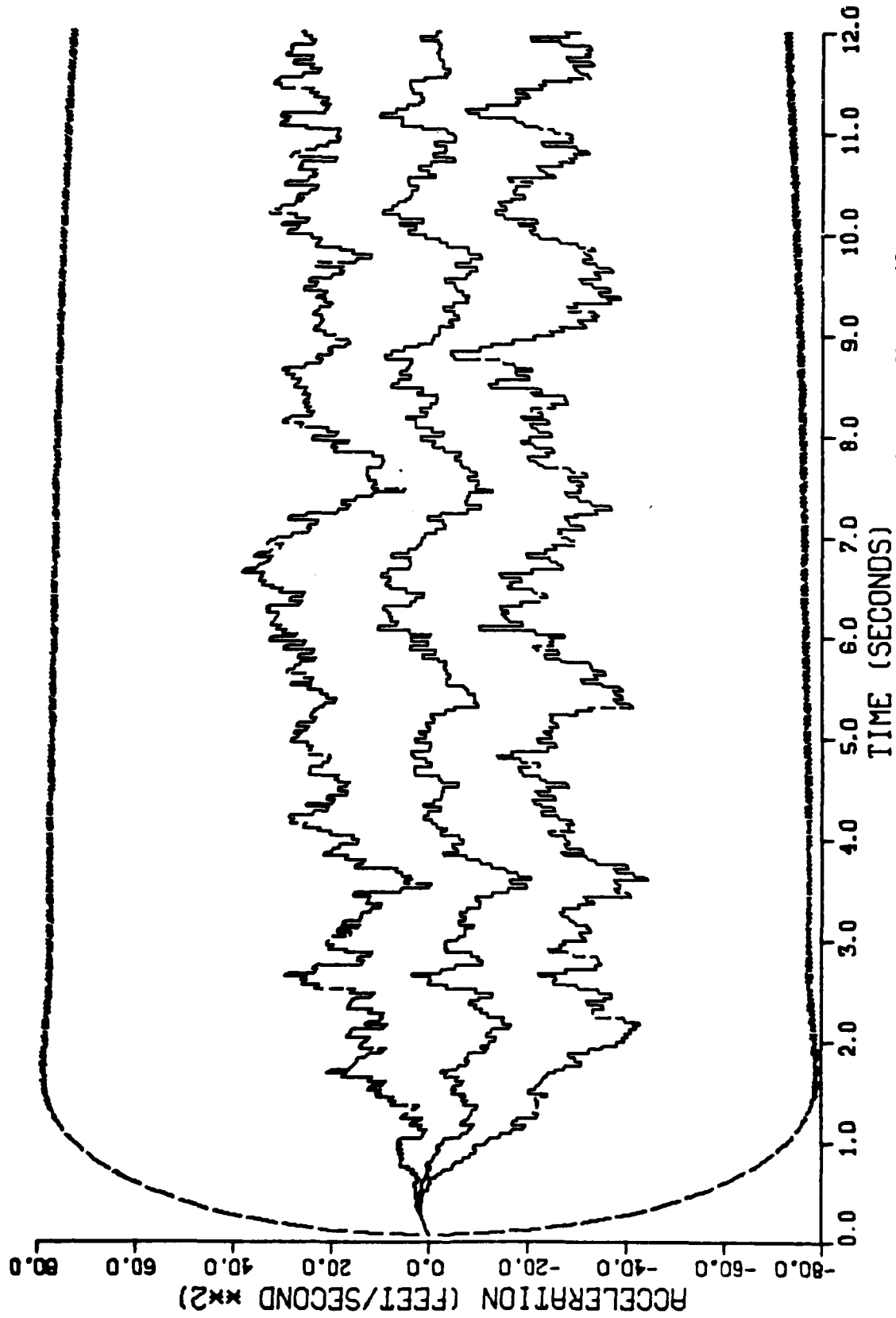


Figure D-9. Performance of the Gauss-Markov Inertial Coordinate Filter Along the Down-Axis for Trajectory 1

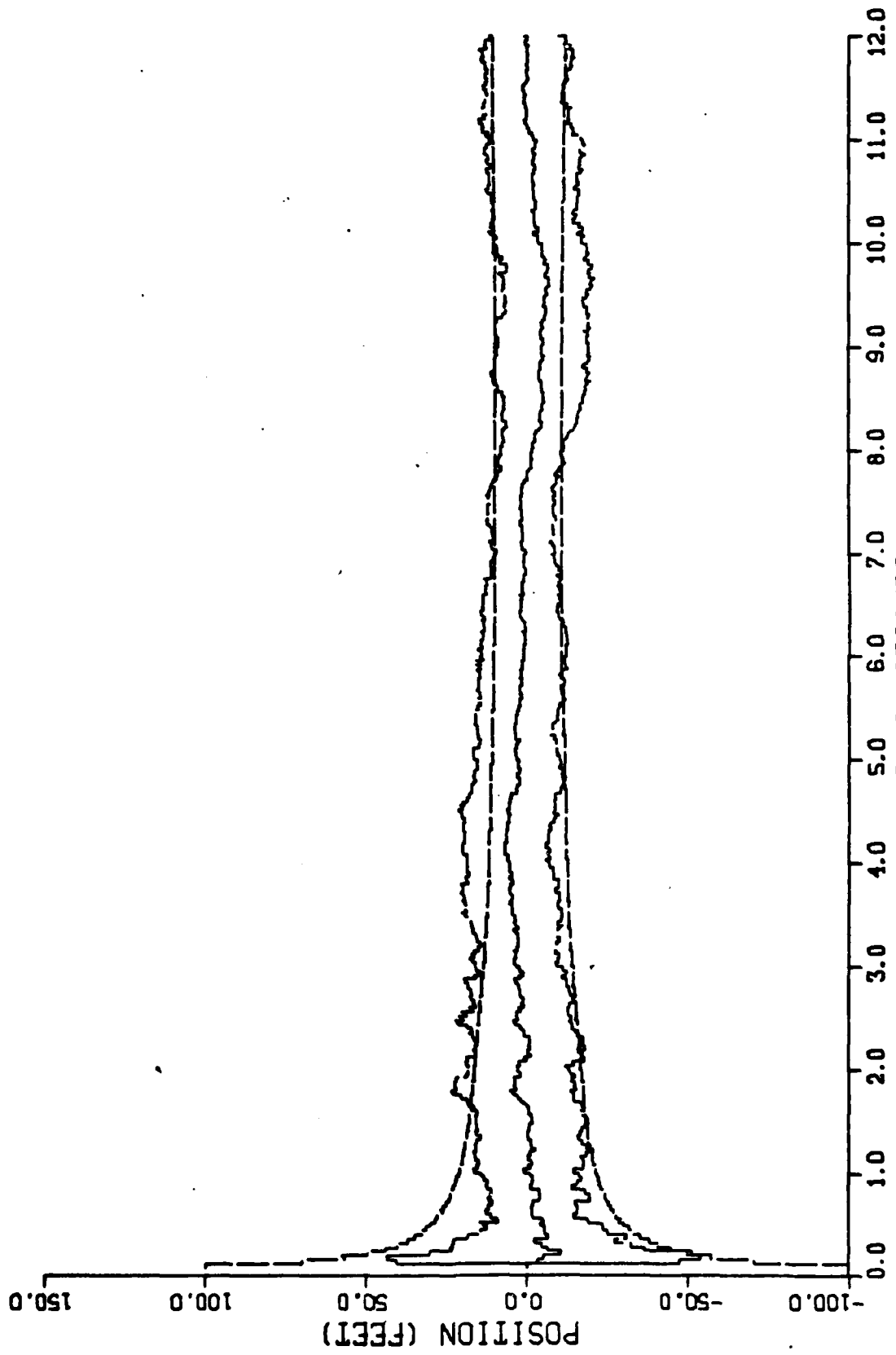


Figure D-10. Performance of the Gauss-Markov Inertial Coordinate Filter Along the North-Axis for Trajectory 2

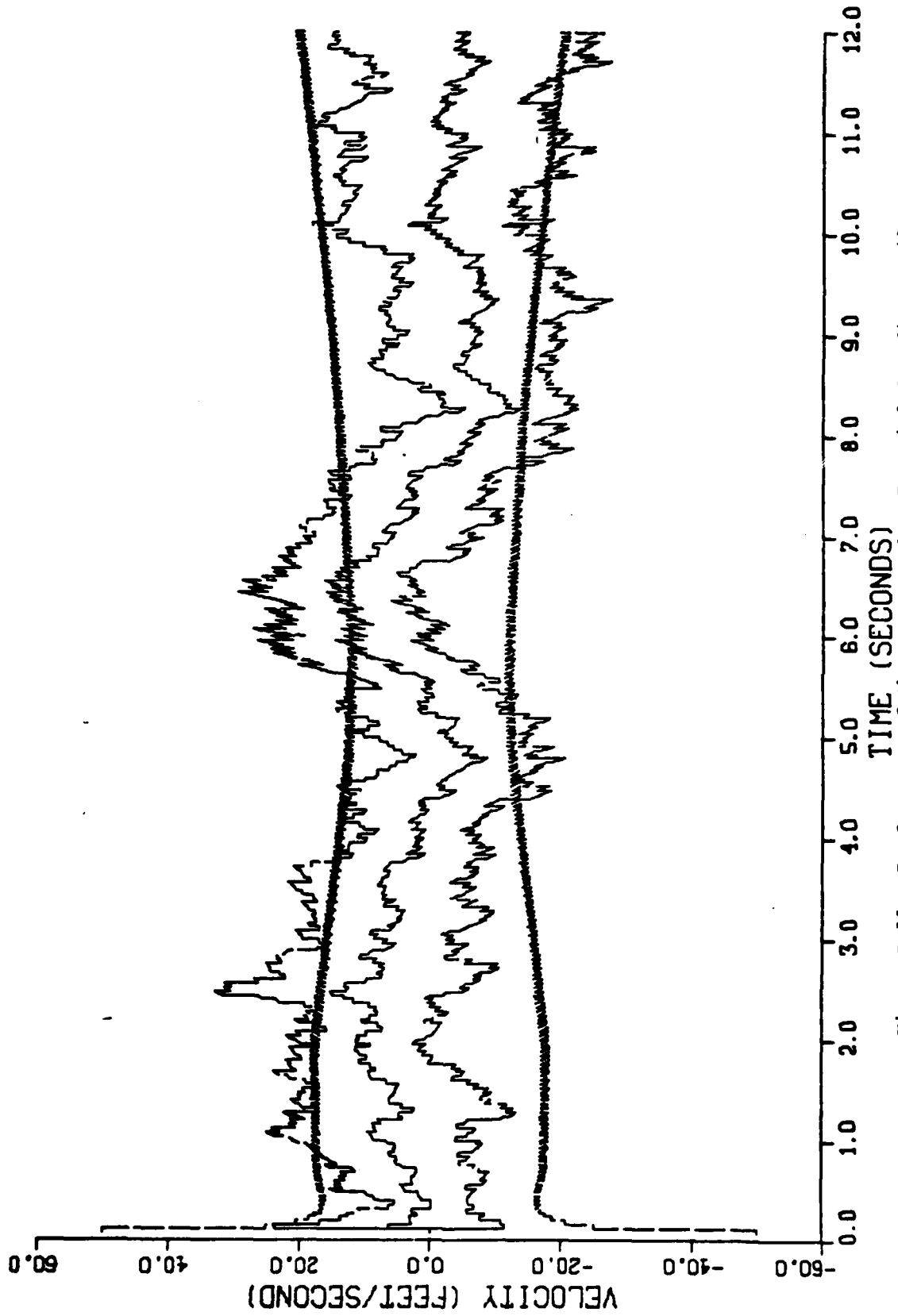


Figure D-11. Performance of the Gauss-Markov Inertial Coordinate Filter Along the North-Axis for Trajectory 2

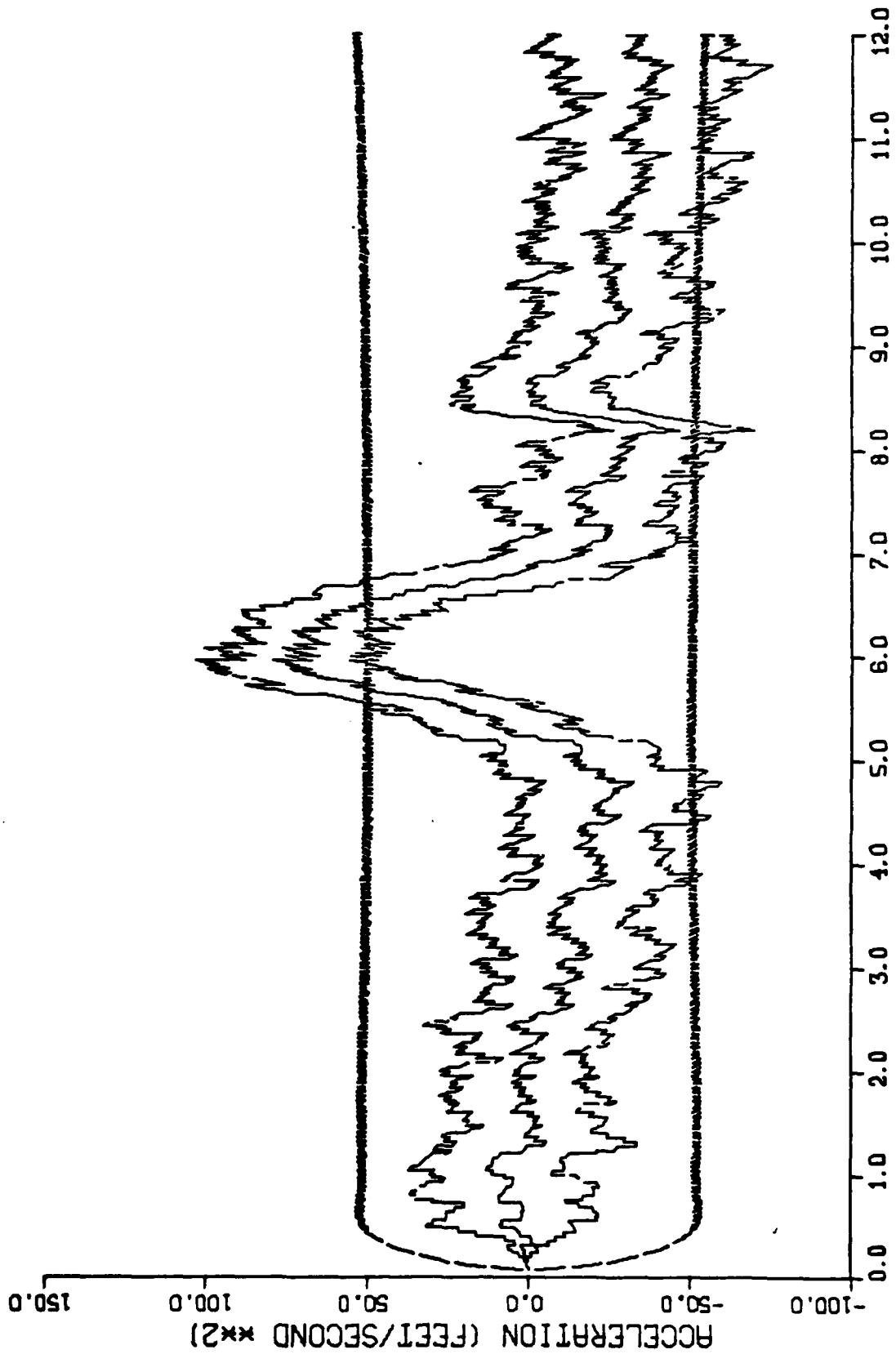


Figure D-12. Performance of the Gauss-Markov Inertial Coordinate Filter Along the North-Axis for Trajectory 2

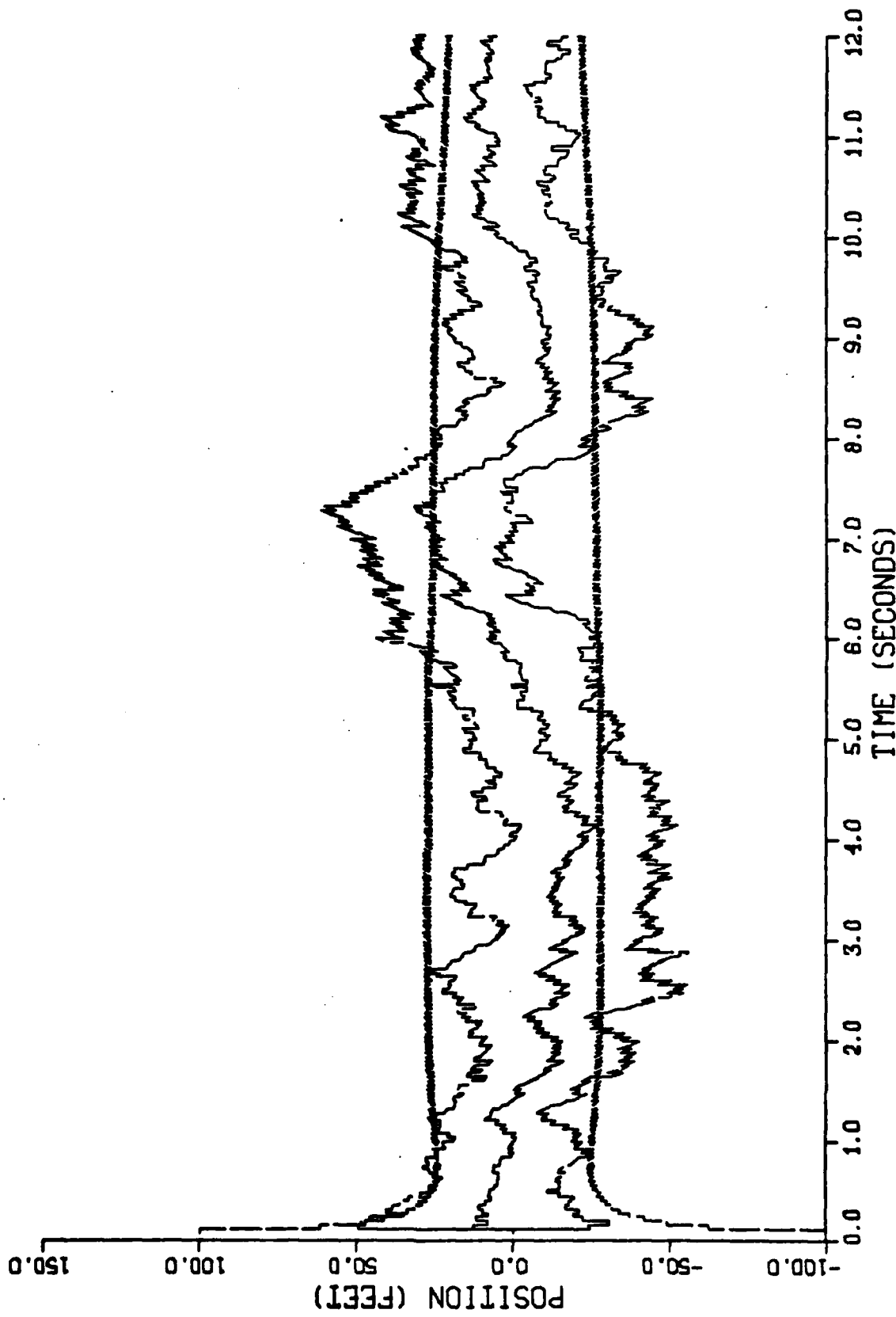


Figure D-13. Performance of the Gauss-Markov Inertial Coordinate Filter Along the East-Axis for Trajectory 2

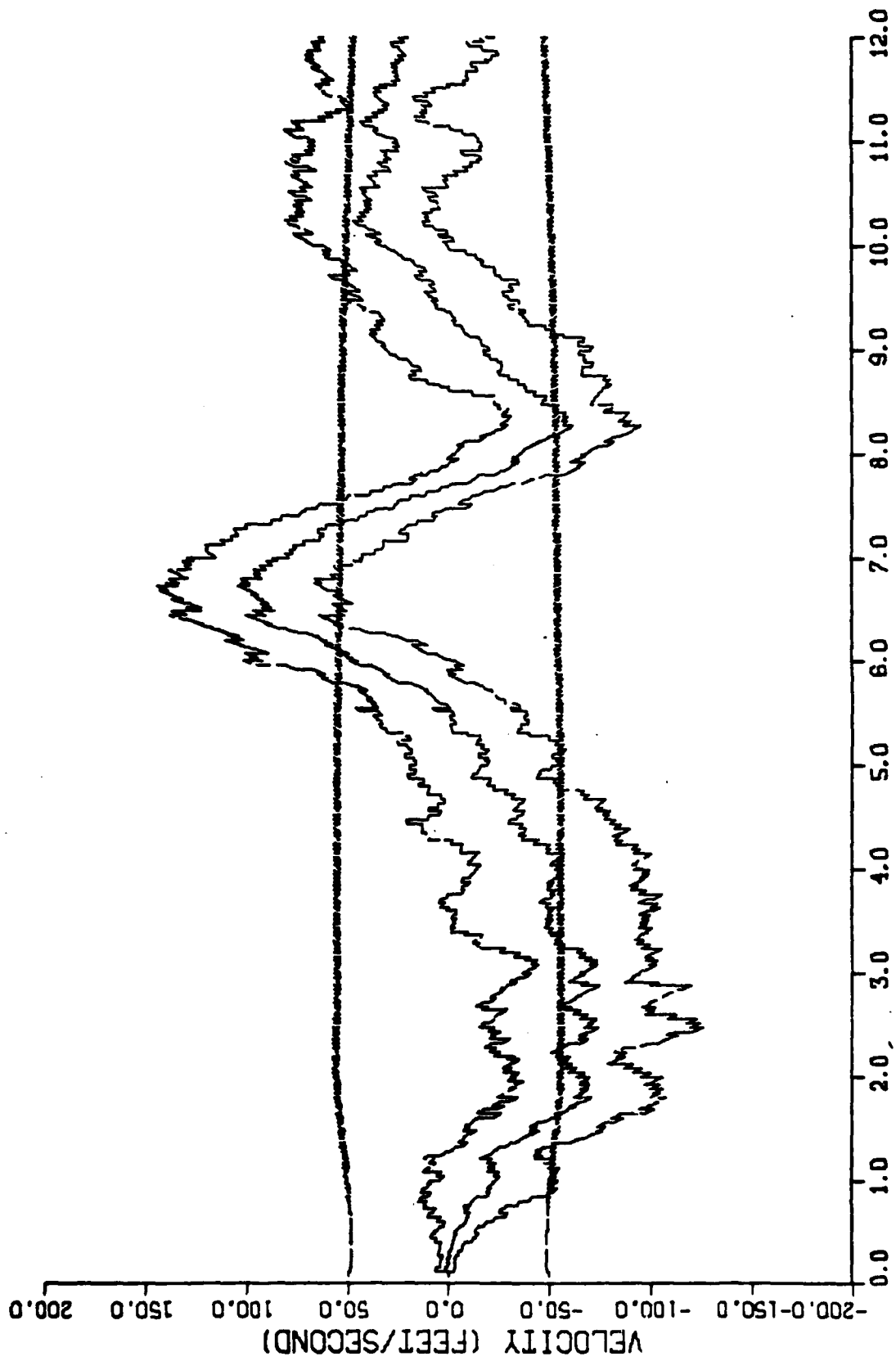


Figure D-14. Performance of the Gauss-Markov Inertial Coordinate Filter Along the East-Axis for Trajectory 2

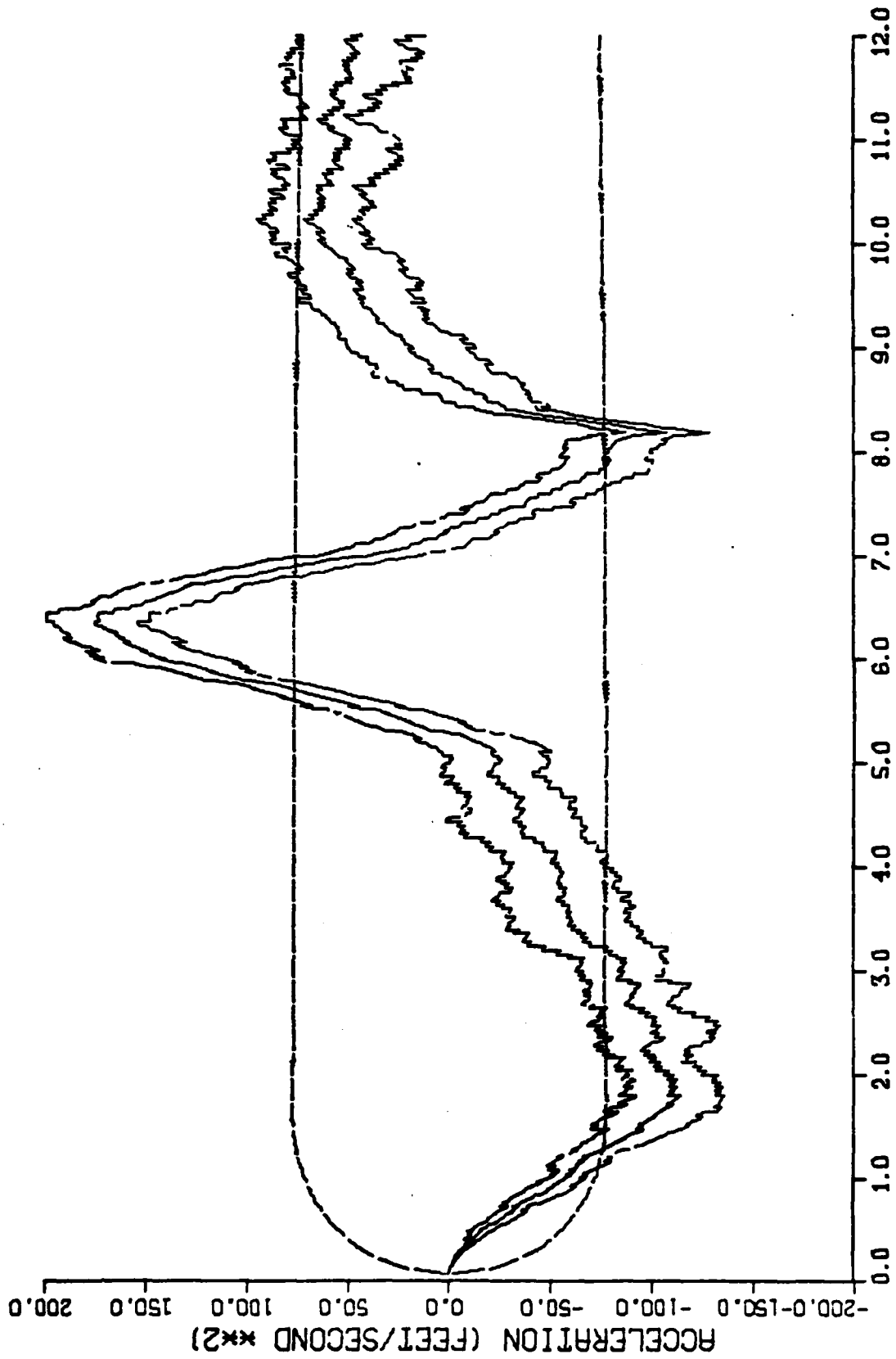


Figure D-15. Performance of the Gauss-Markov Inertial Coordinate Filter Along the East-Axis for Trajectory 2

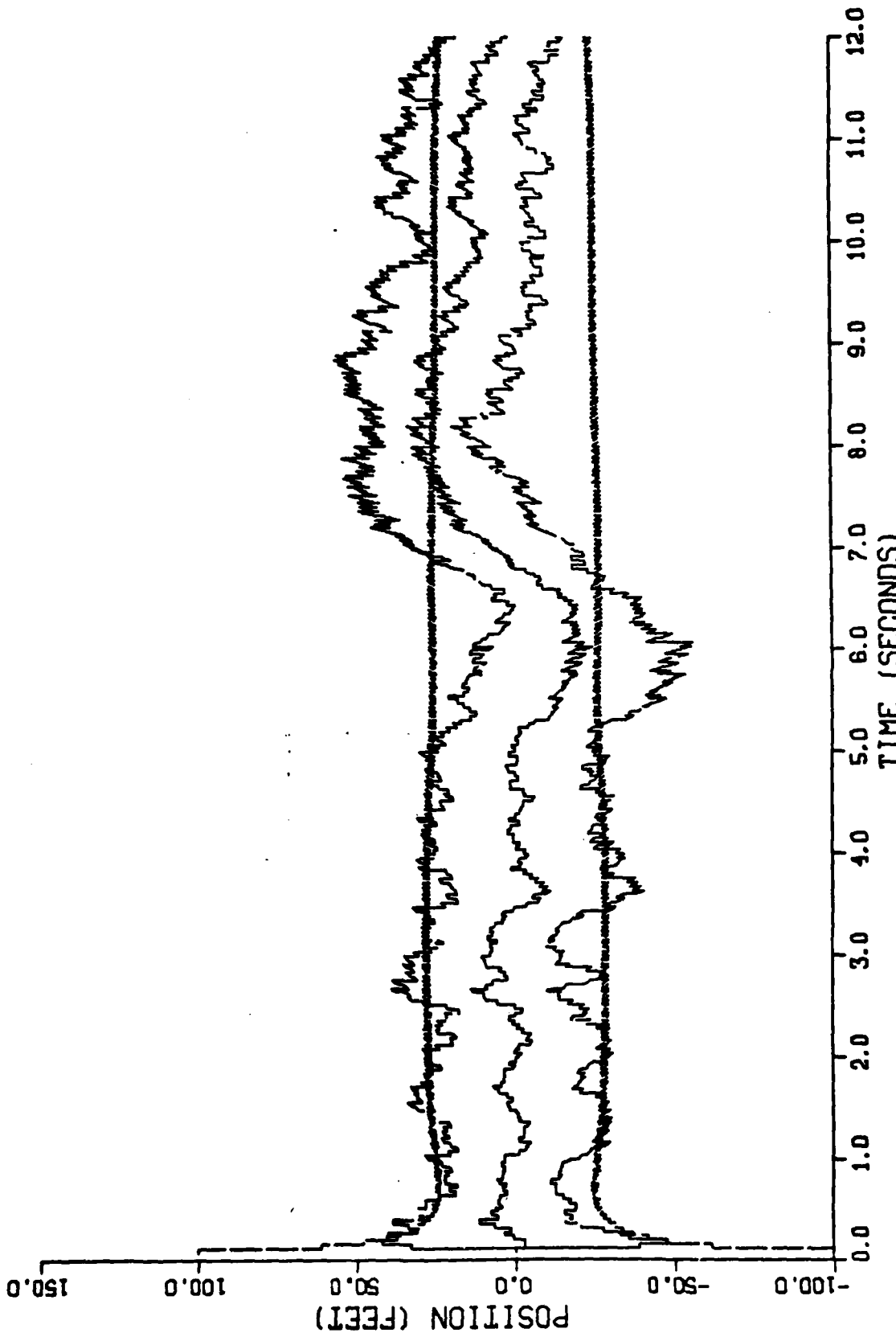


Figure D-16. Performance of the Gauss-Markov Inertial Coordinate Filter Along the Down-Axis for Trajectory 2

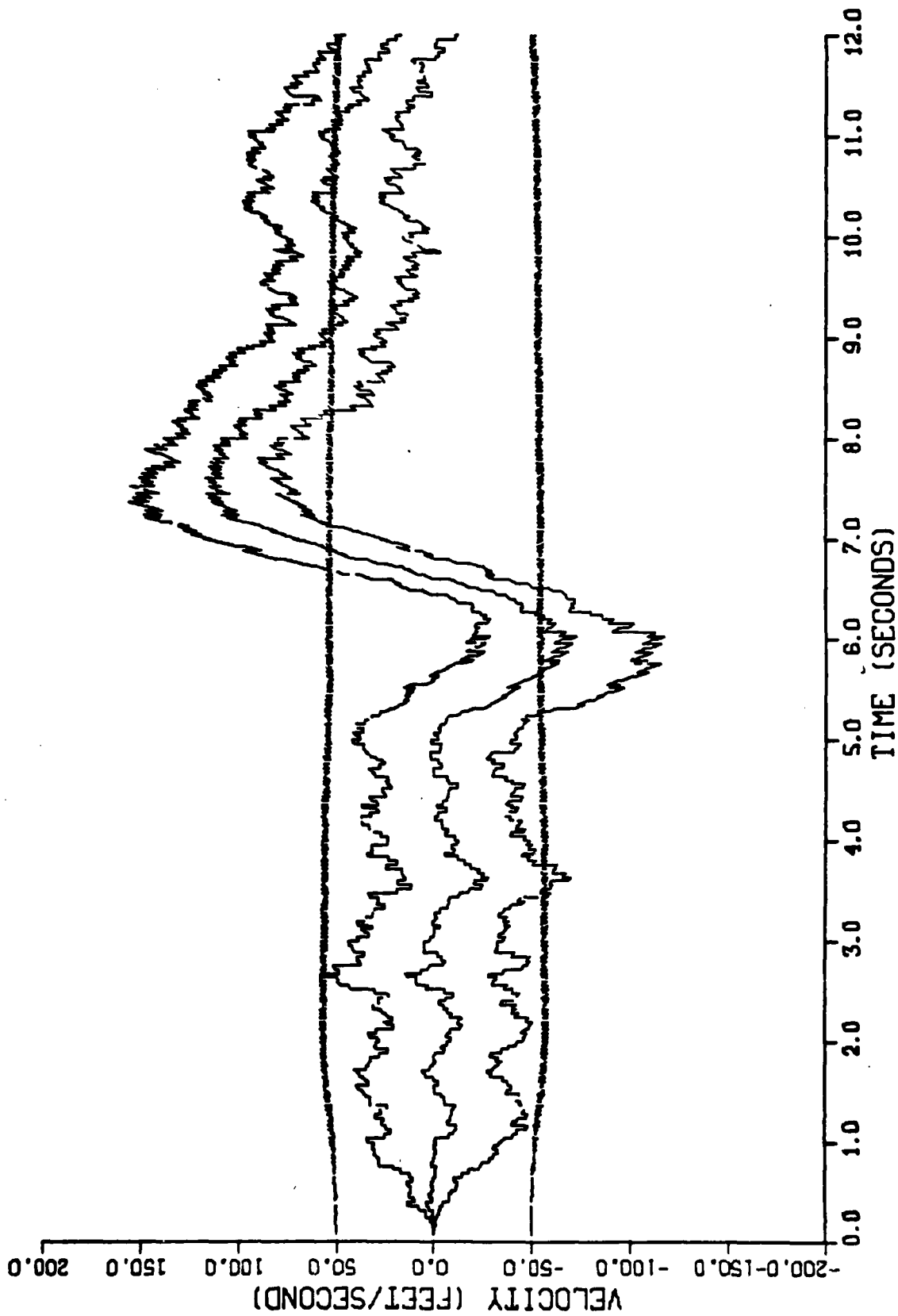


Figure D-17. Performance of the Gauss-Markov Inertial Coordinate Filter
Along the Down-Axis for Trajectory 2

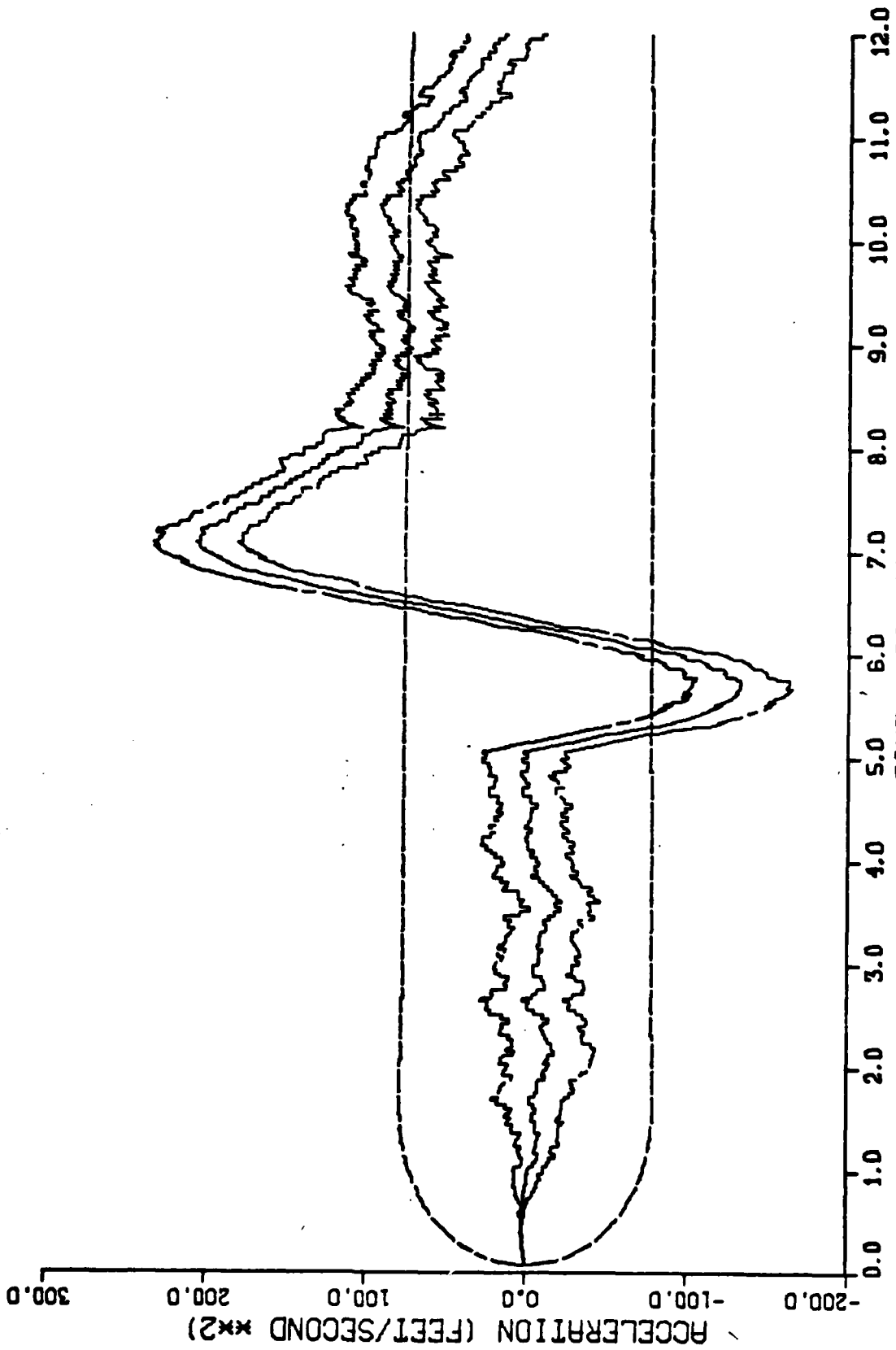


Figure D-18. Performance of the Gauss-Markov Inertial Coordinate Filter Along the Down-Axis for Trajectory 2

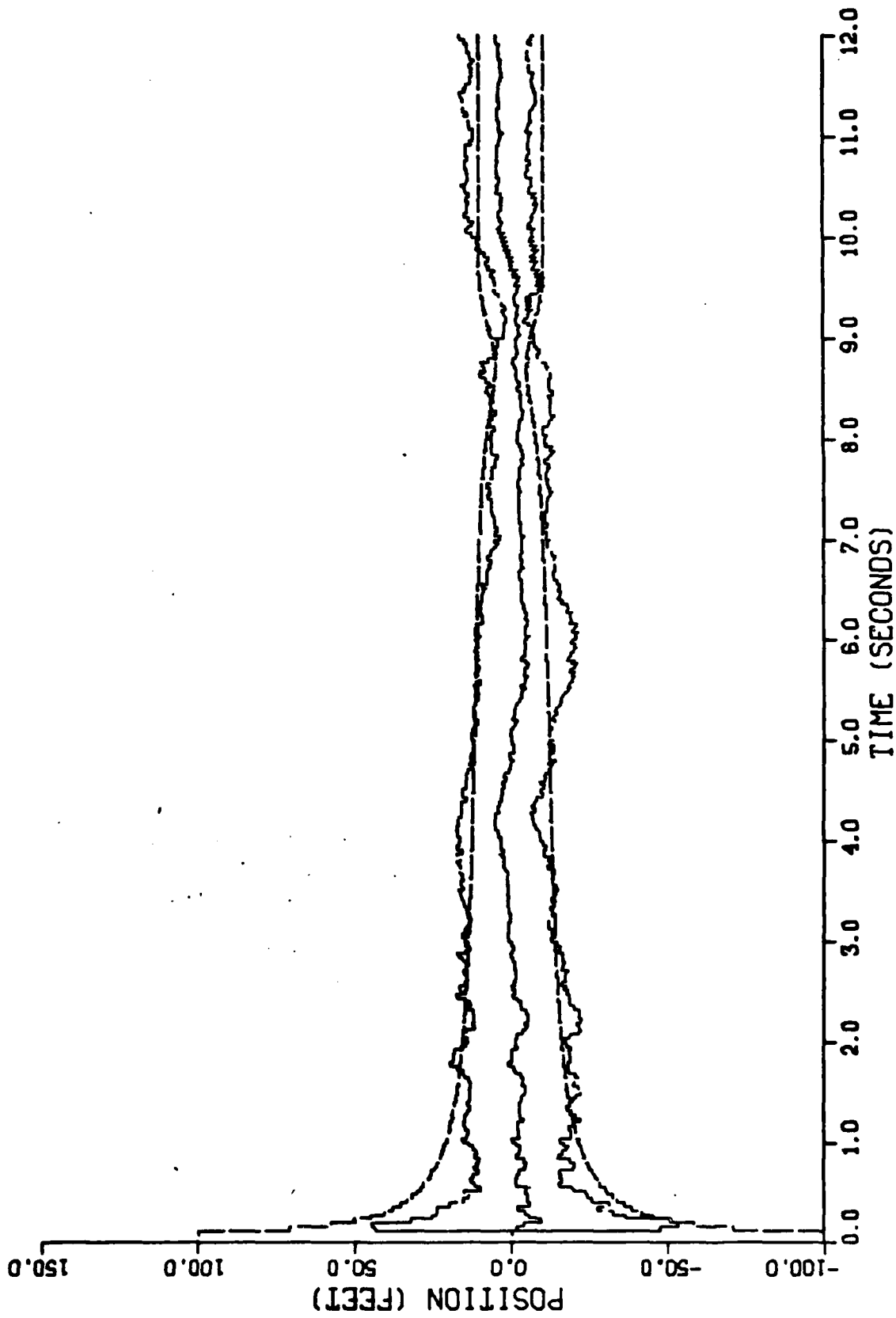


Figure D-19. Performance of the Gauss-Markov Inertial Coordinate Filter Along the North-Axis for Trajectory 3

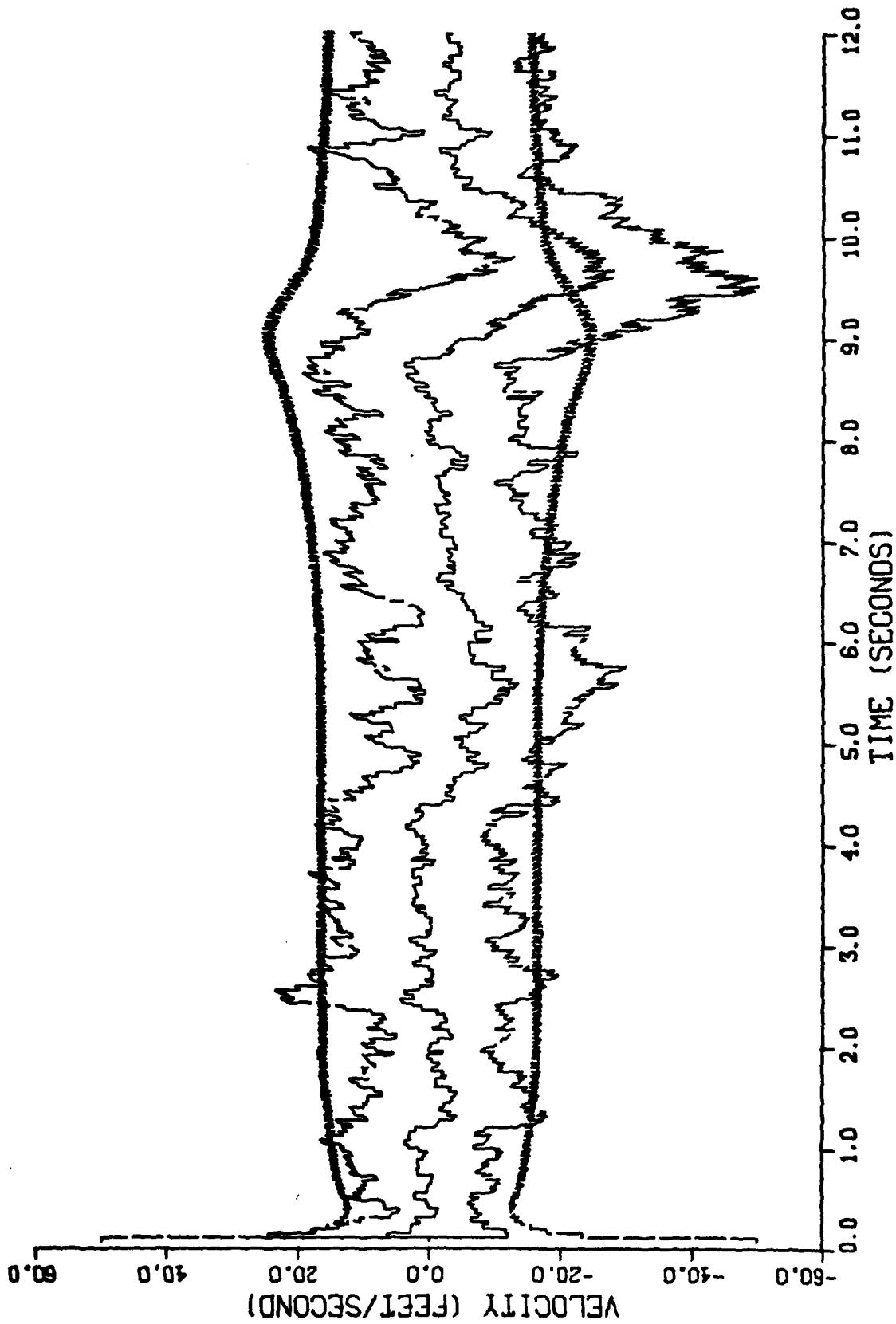


Figure D-20. Performance of the Gauss-Markov Inertial Coordinate Filter
Along the North-Axis for Trajectory 3

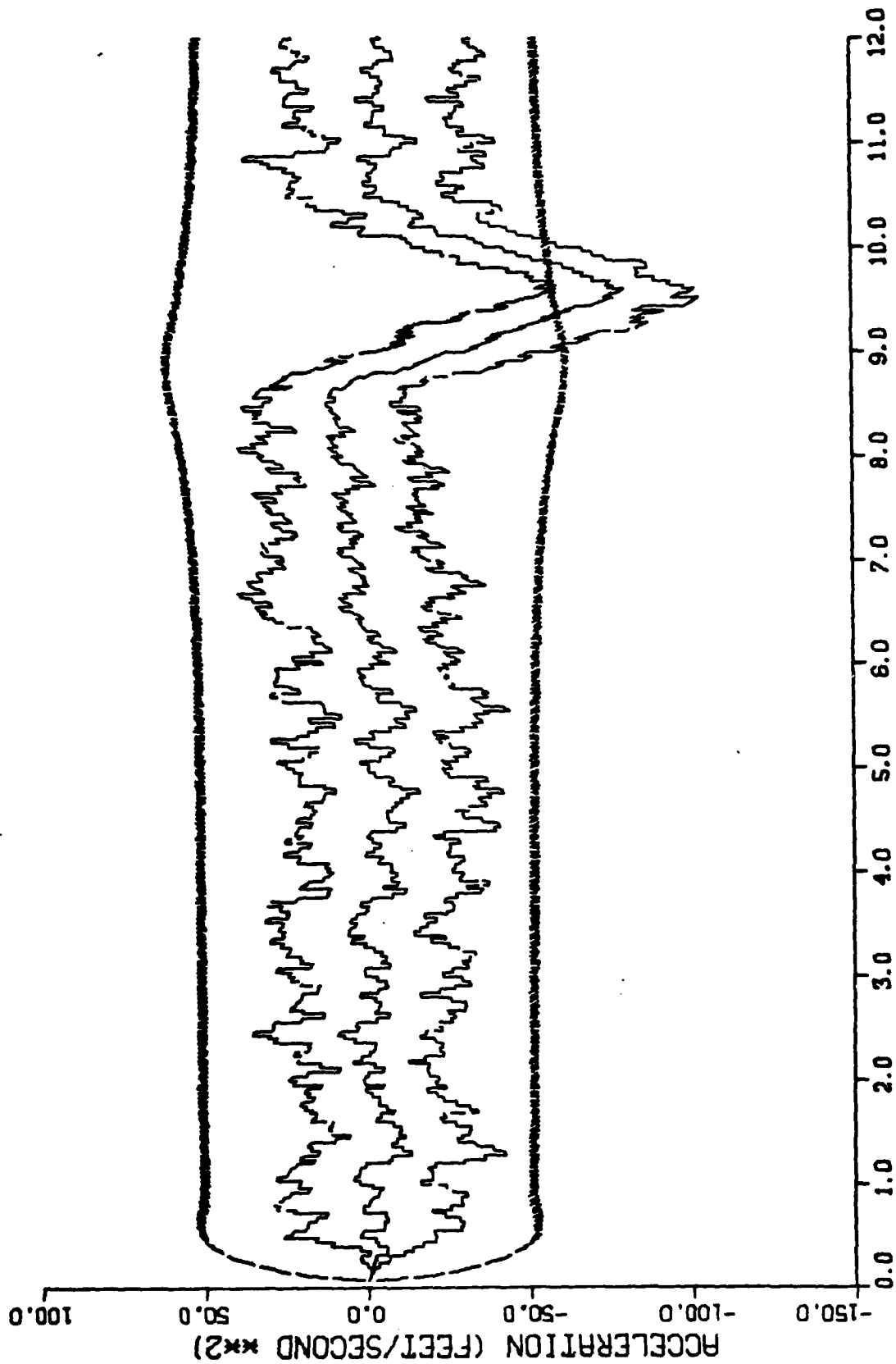


Figure D-21. Performance of the Gauss-Markov Inertial Coordinate Filter Along the North-Axis for Trajectory 3

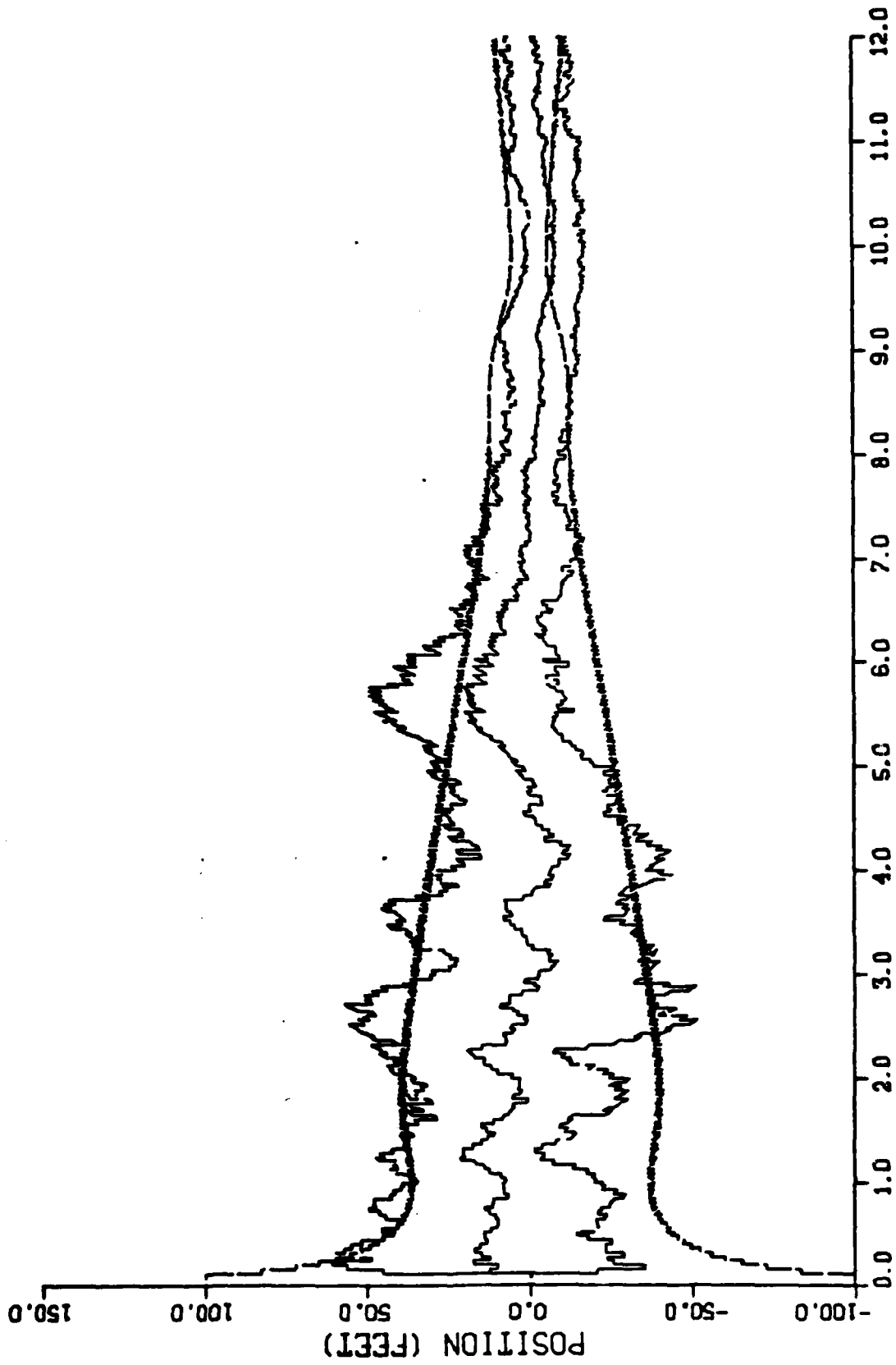


Figure D-22. Performance of the Gauss-Markov Inertial Coordinate Filter
Along the East-Axis for Trajectory 3

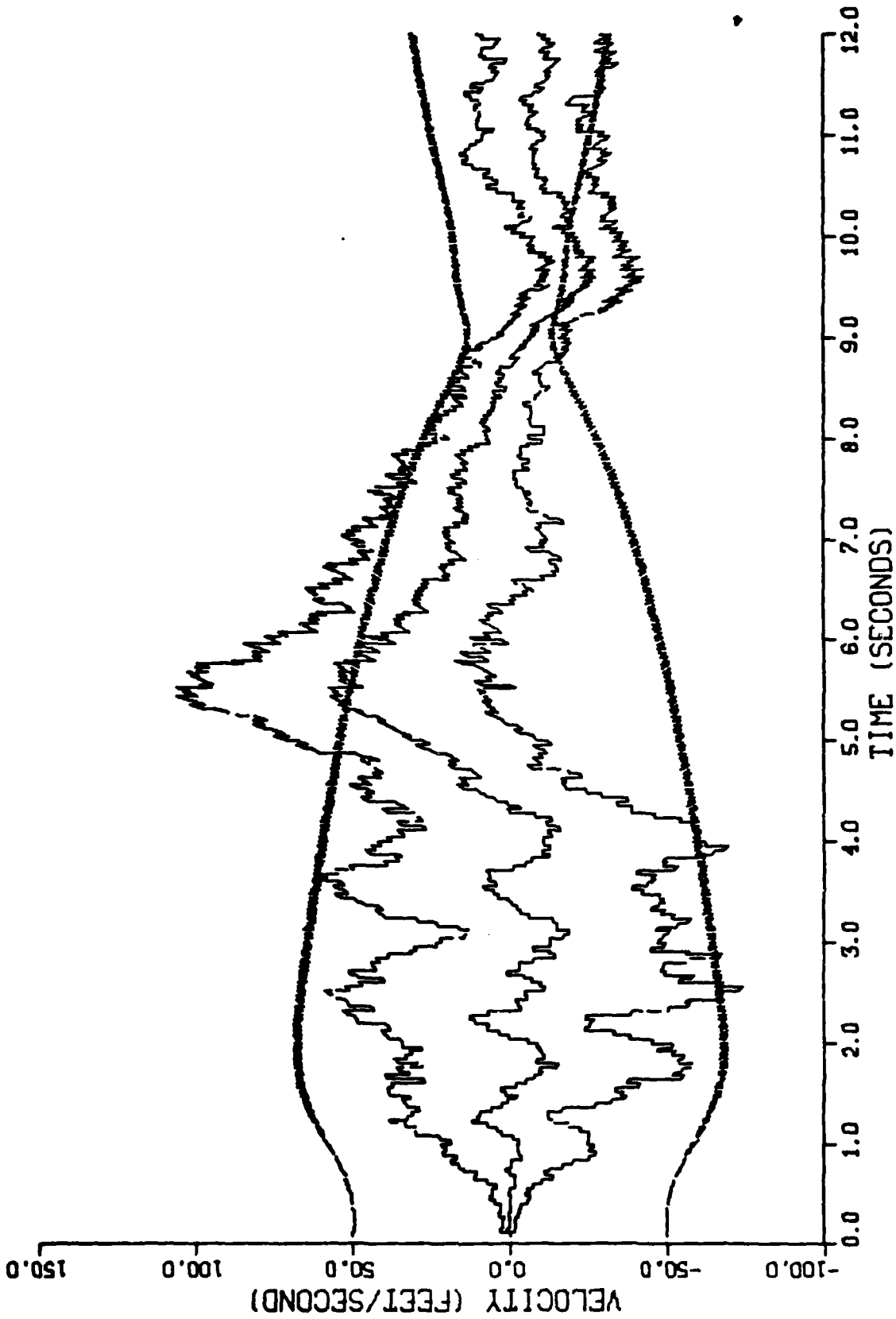


Figure D-23. Performance of the Gauss-Markov Inertial Coordinate Filter Along the East-Axis for Trajectory 3

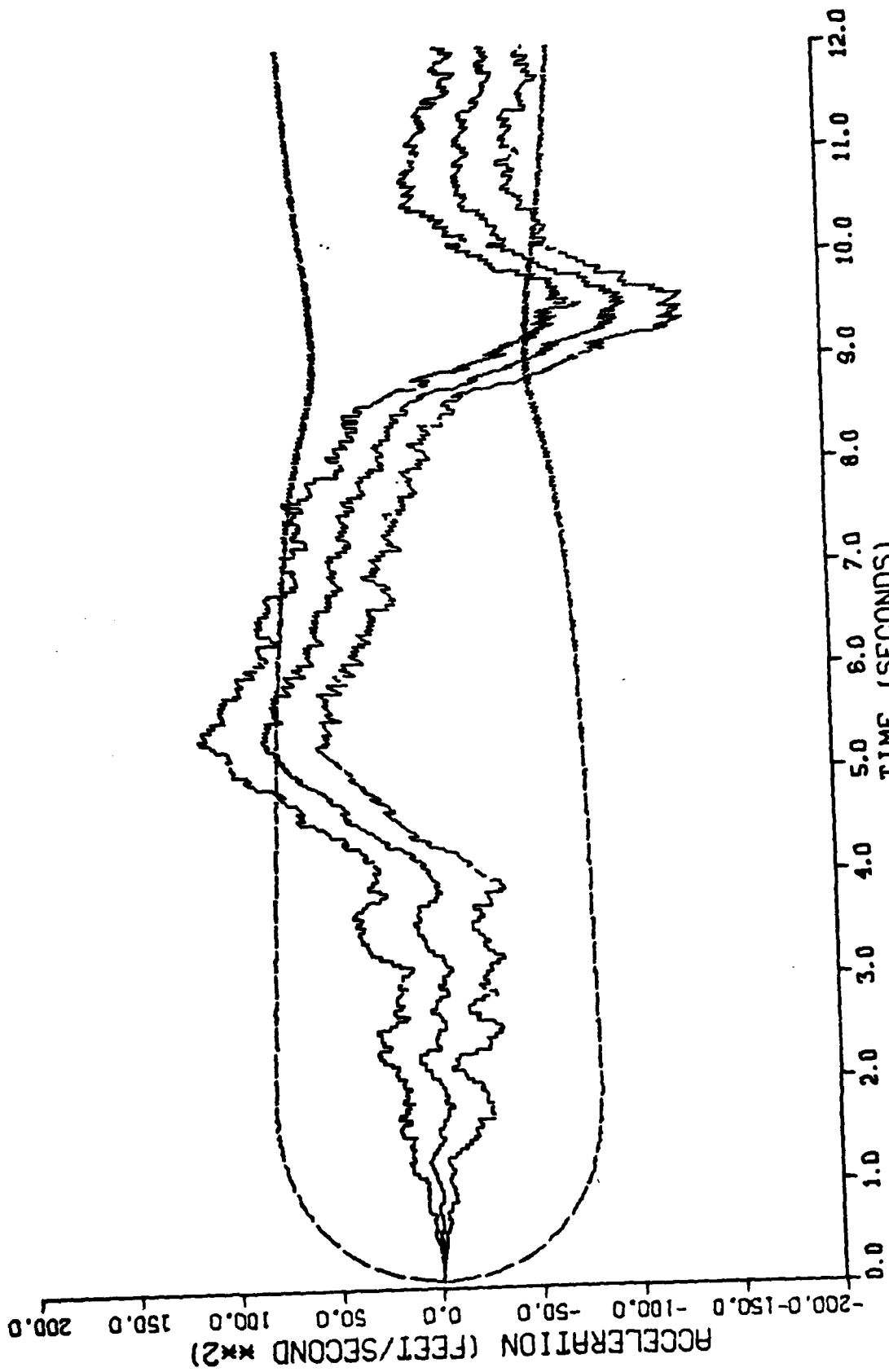


Figure D-24. Performance of the Gauss-Markov Inertial Coordinate Filter Along the East-Axis for Trajectory 3

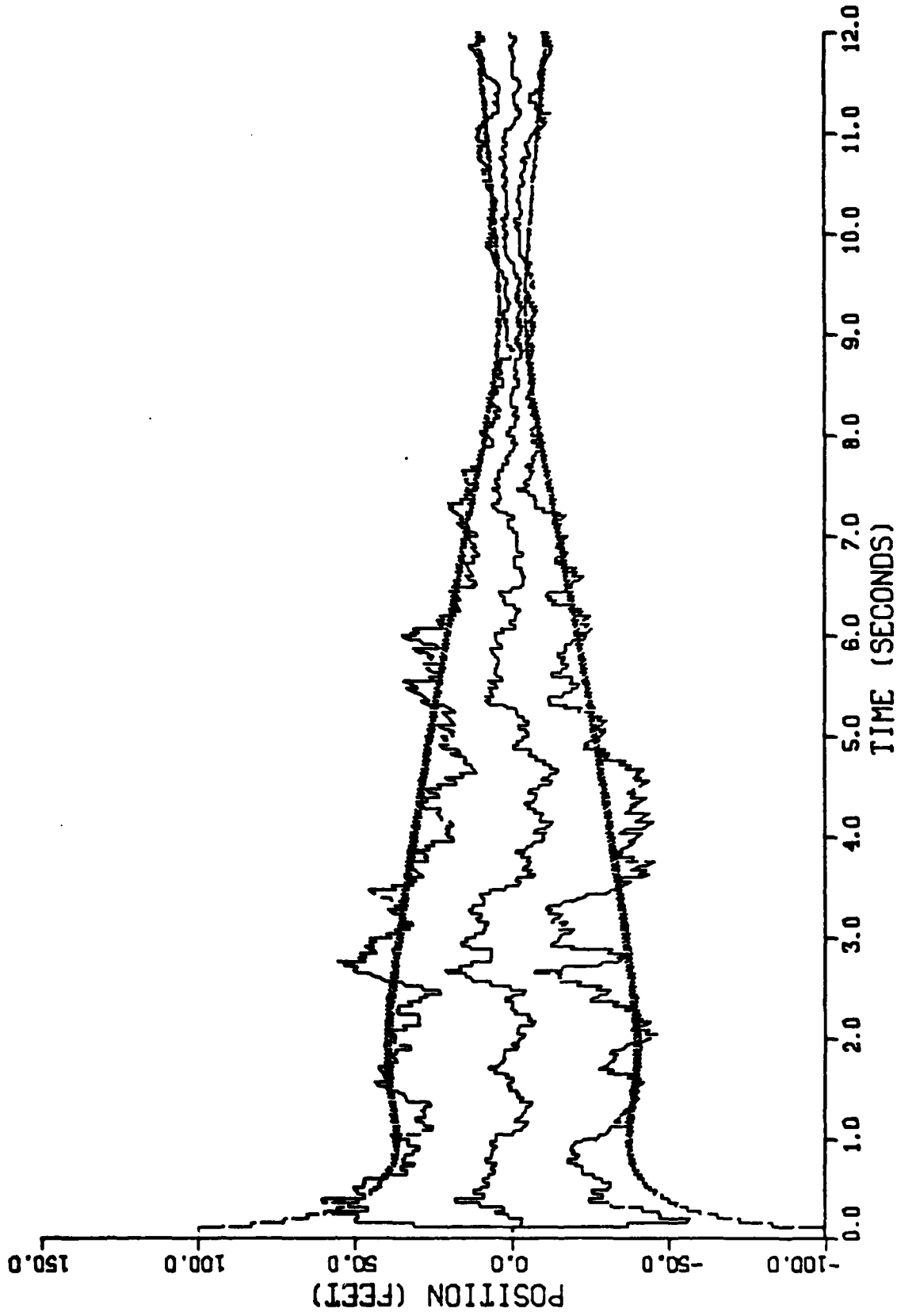


Figure D-25. Performance of the Gauss-Markov Inertial Coordinate Filter Along the Down-Axis for Trajectory 3

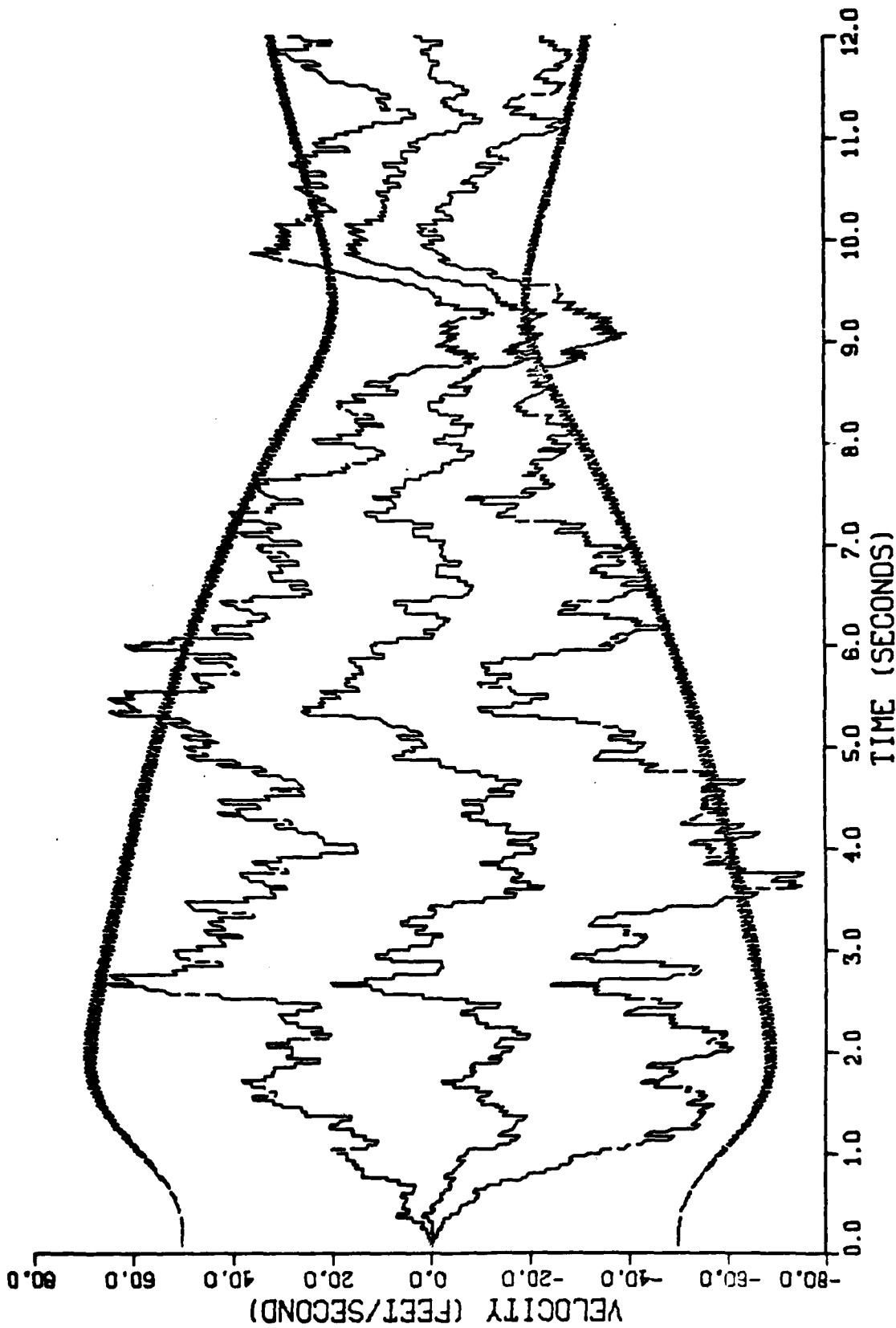


Figure D-26. Performance of the Gauss-Markov Inertial Coordinate Filter Along the Down-Axis for Trajectory 3

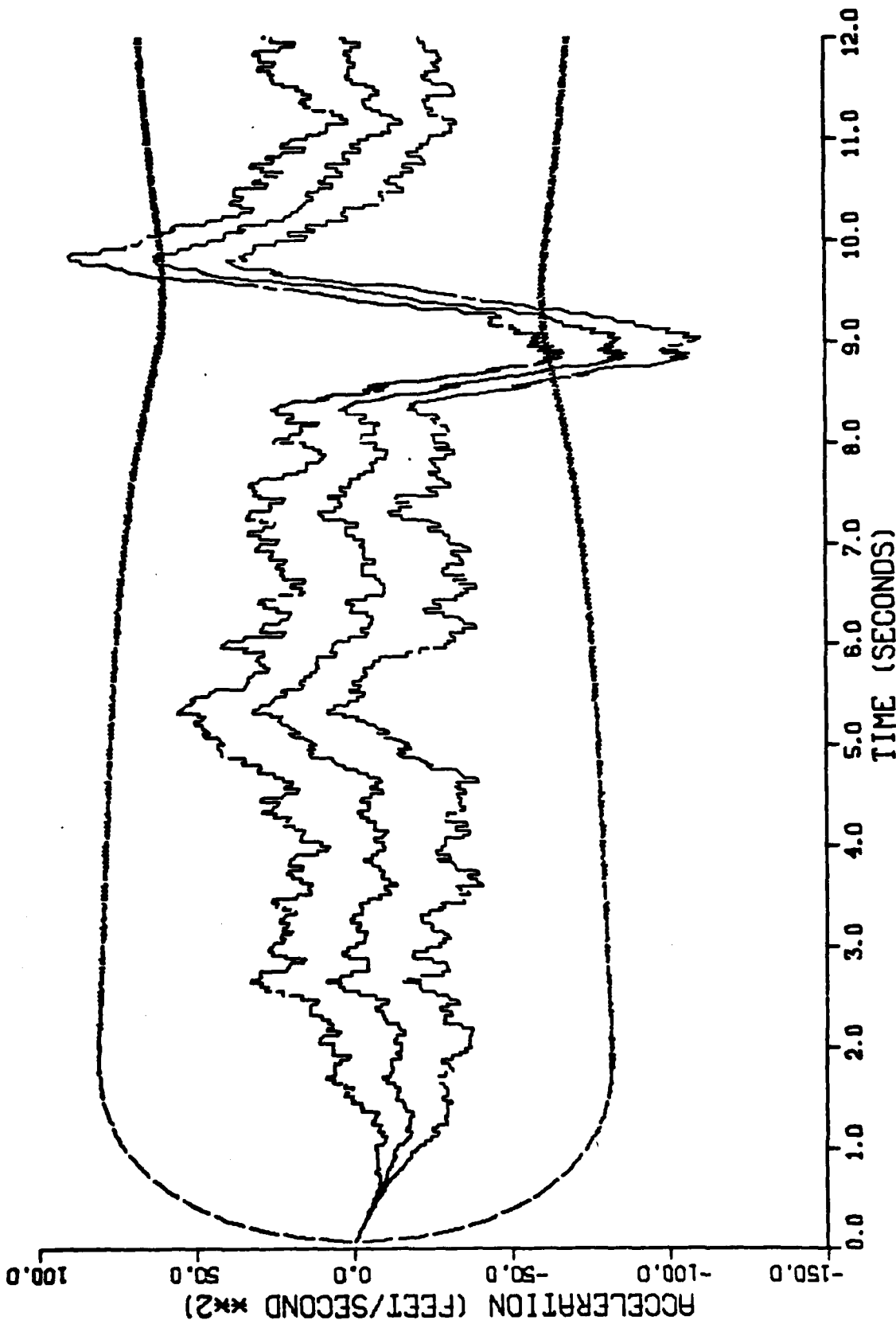


Figure D-27. Performance of the Gauss-Markov Inertial Coordinate Filter Along the Down-Axis for Trajectory 3

APPENDIX E

Graphical Results for the Constant Turn Rate
Inertial Coordinate Filter

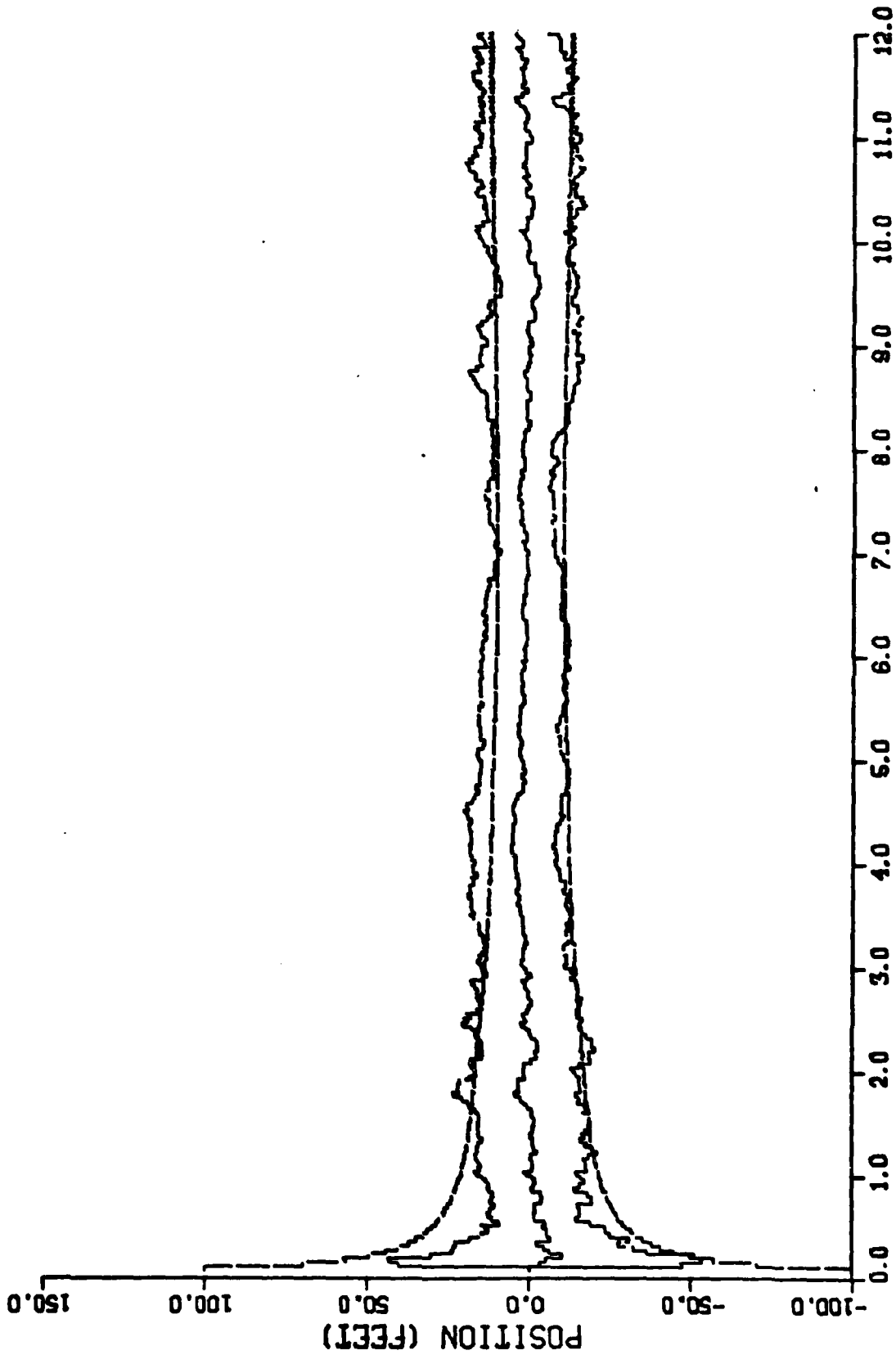


Figure E-1. Performance of the Constant Turn Rate Inertial Coordinate Filter Along the North-Axis for Trajectory 1

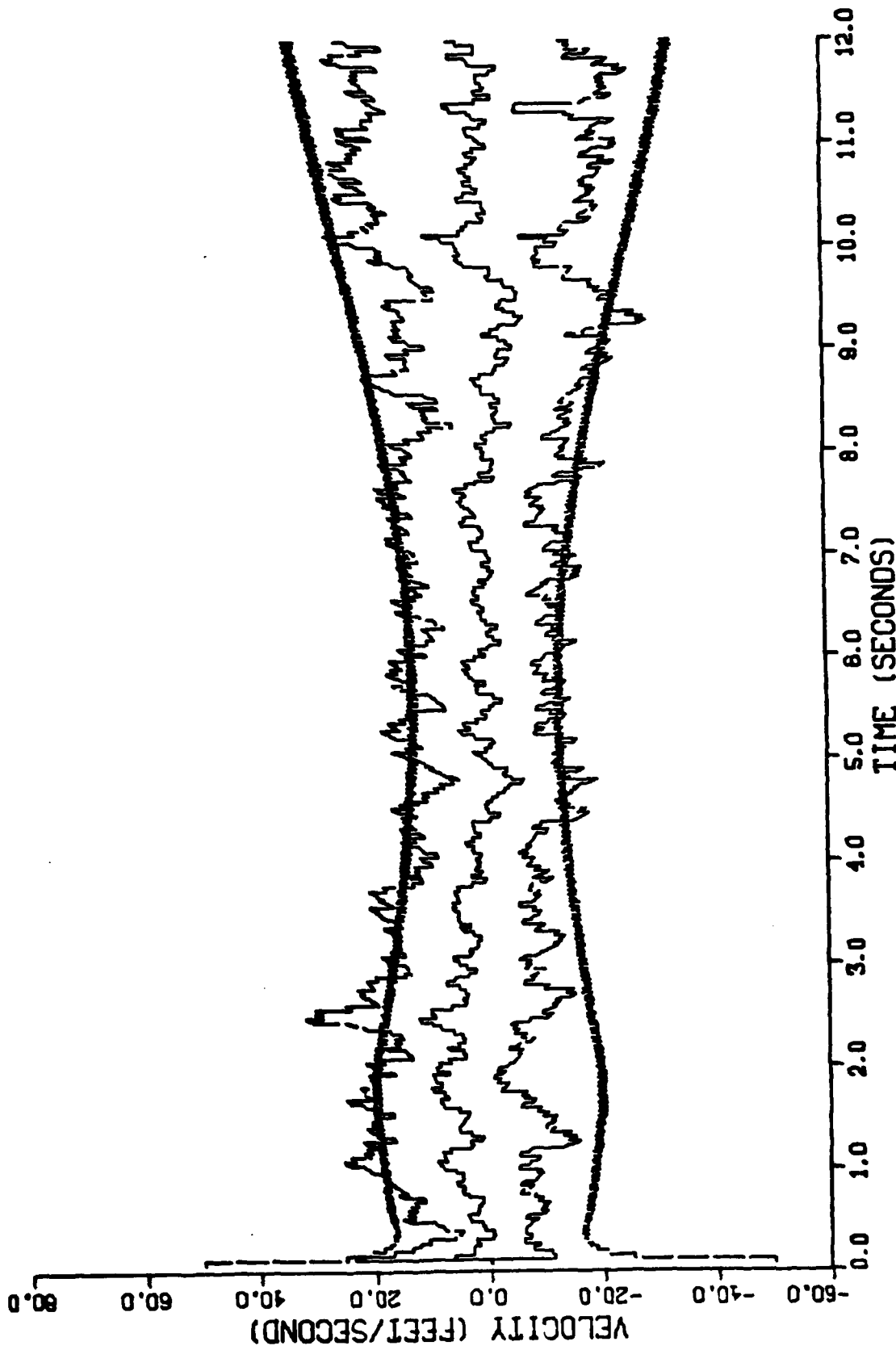


Figure E-2. Performance of the Constant Turn Rate Inertial Coordinate Filter Along the North-Axis for Trajectory 1

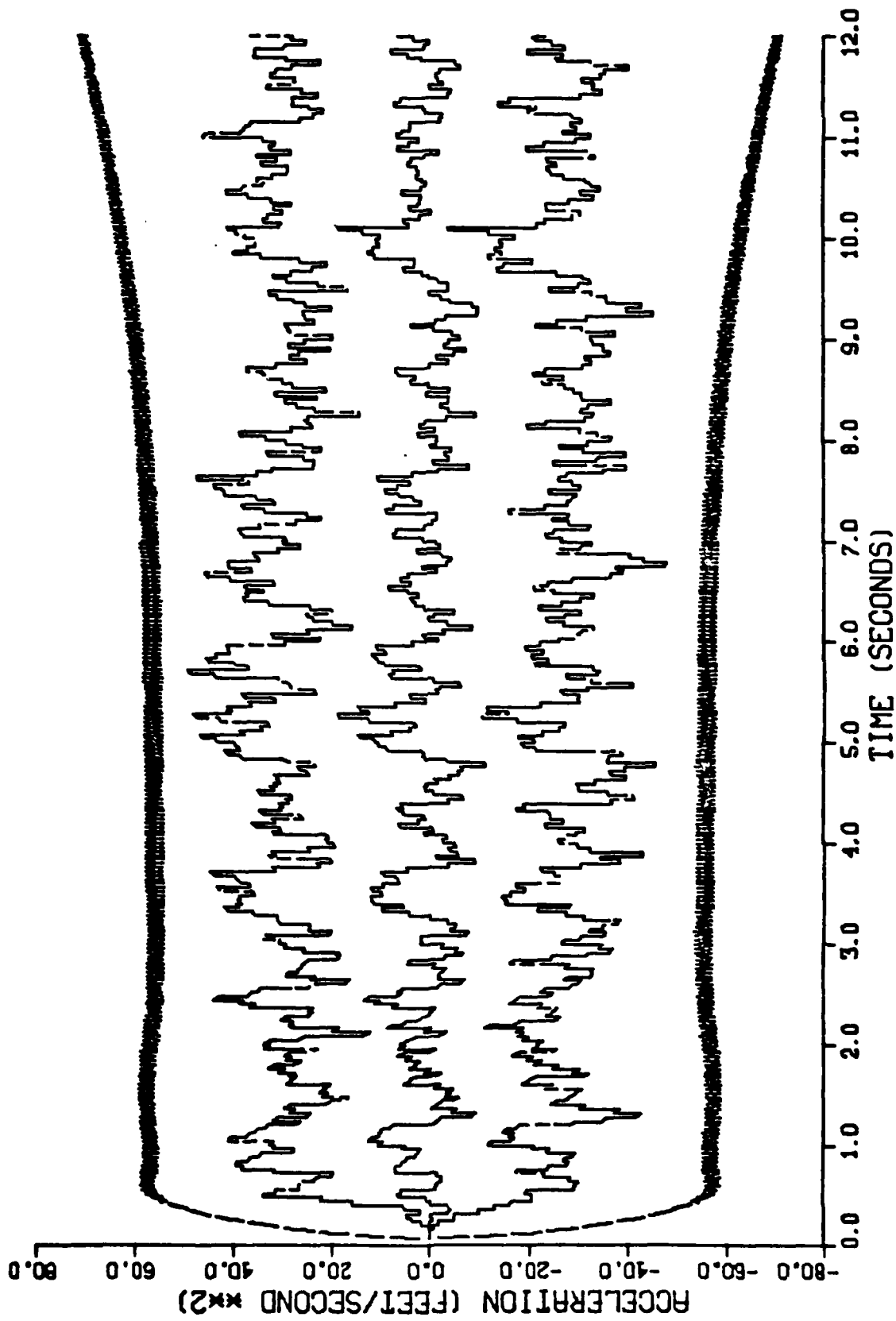


Figure E-3. Performance of the Constant Turn Rate Inertial Coordinate Filter Along the North-Axis for Trajectory 1

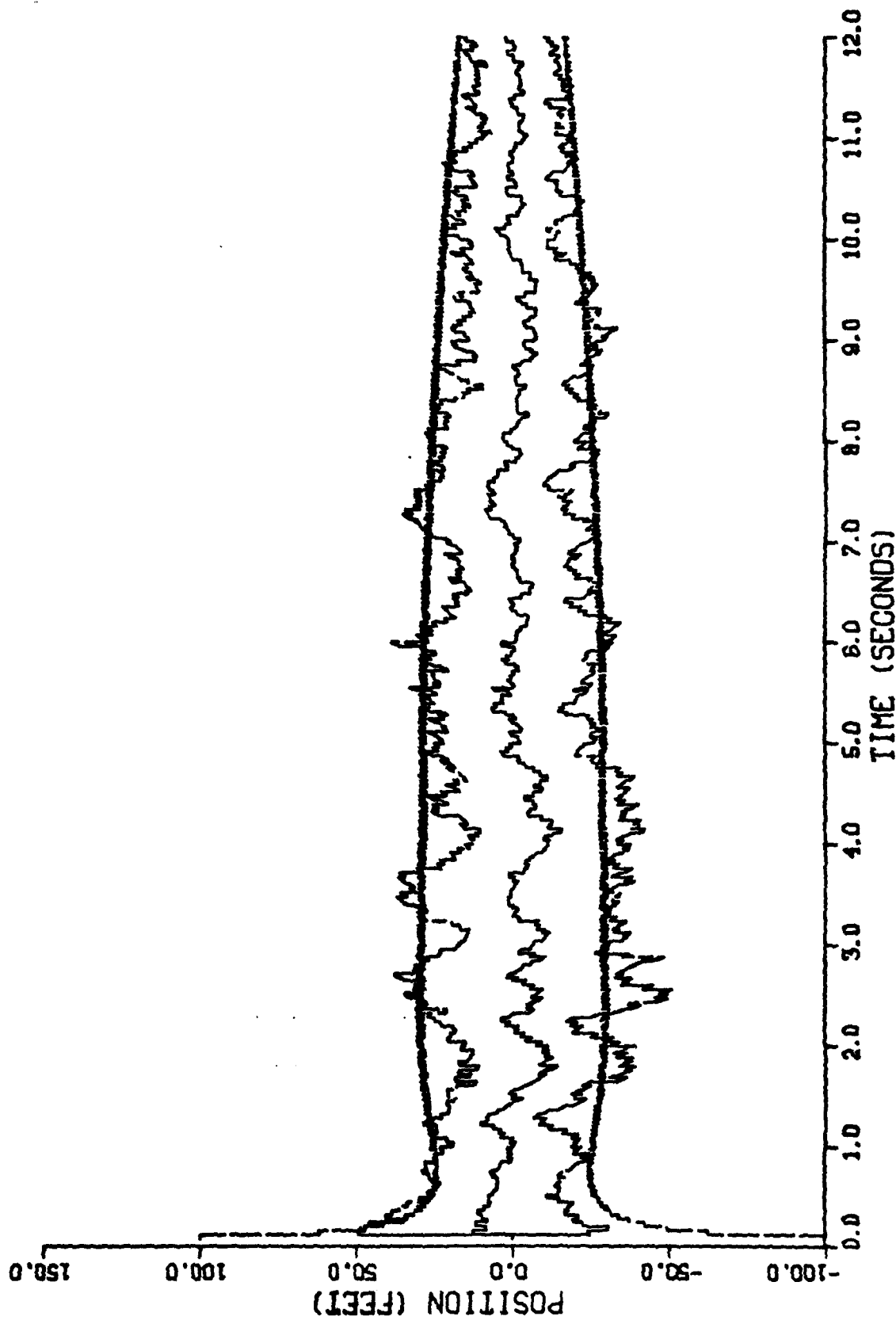


Figure E-4. Performance of the Constant Turn Rate Inertial Coordinate Filter Along the East-Axis for Trajectory 1

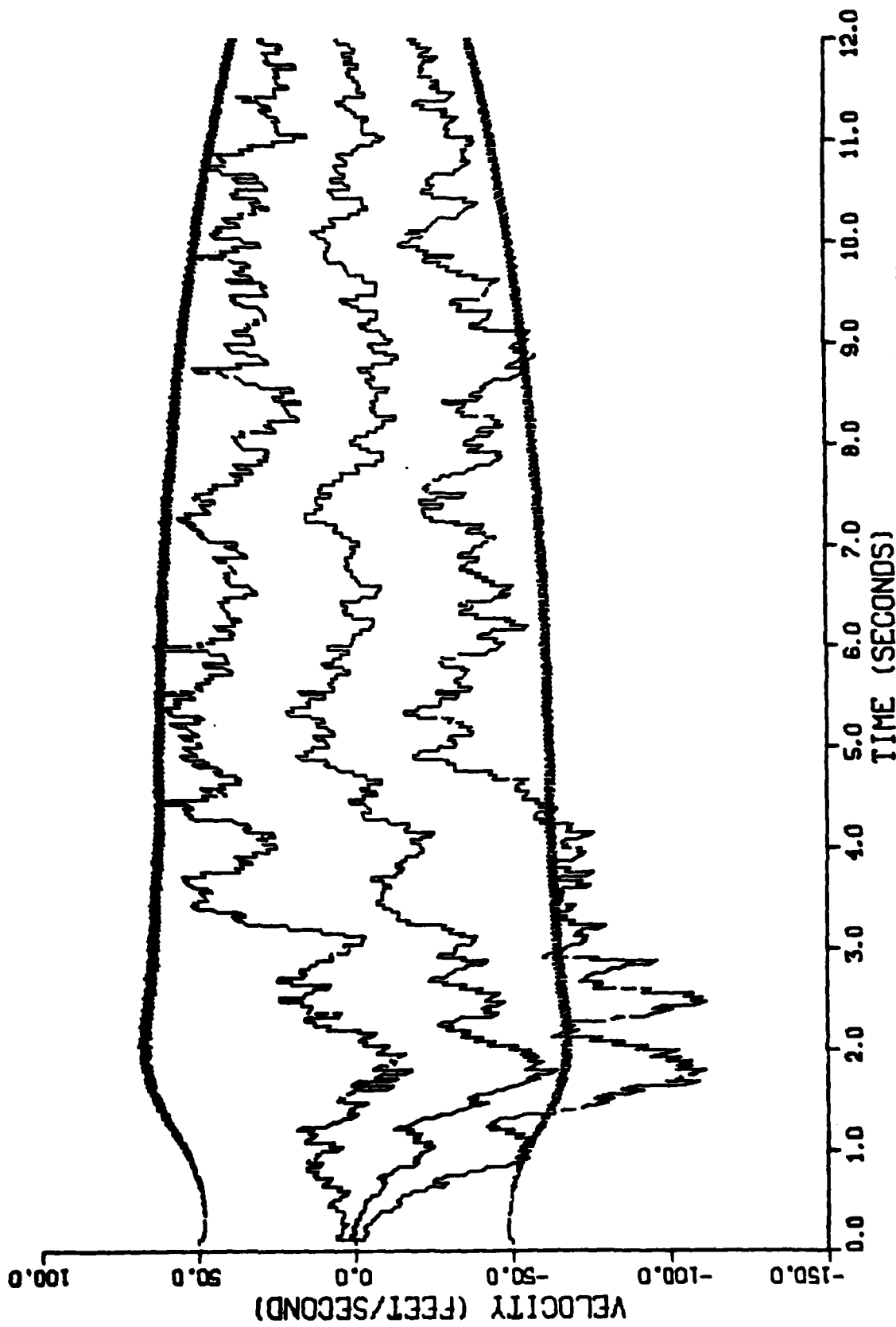


Figure E-5. Performance of the Constant Turn Rate Inertial Coordinate Filter Along the East-Axis for Trajectory 1

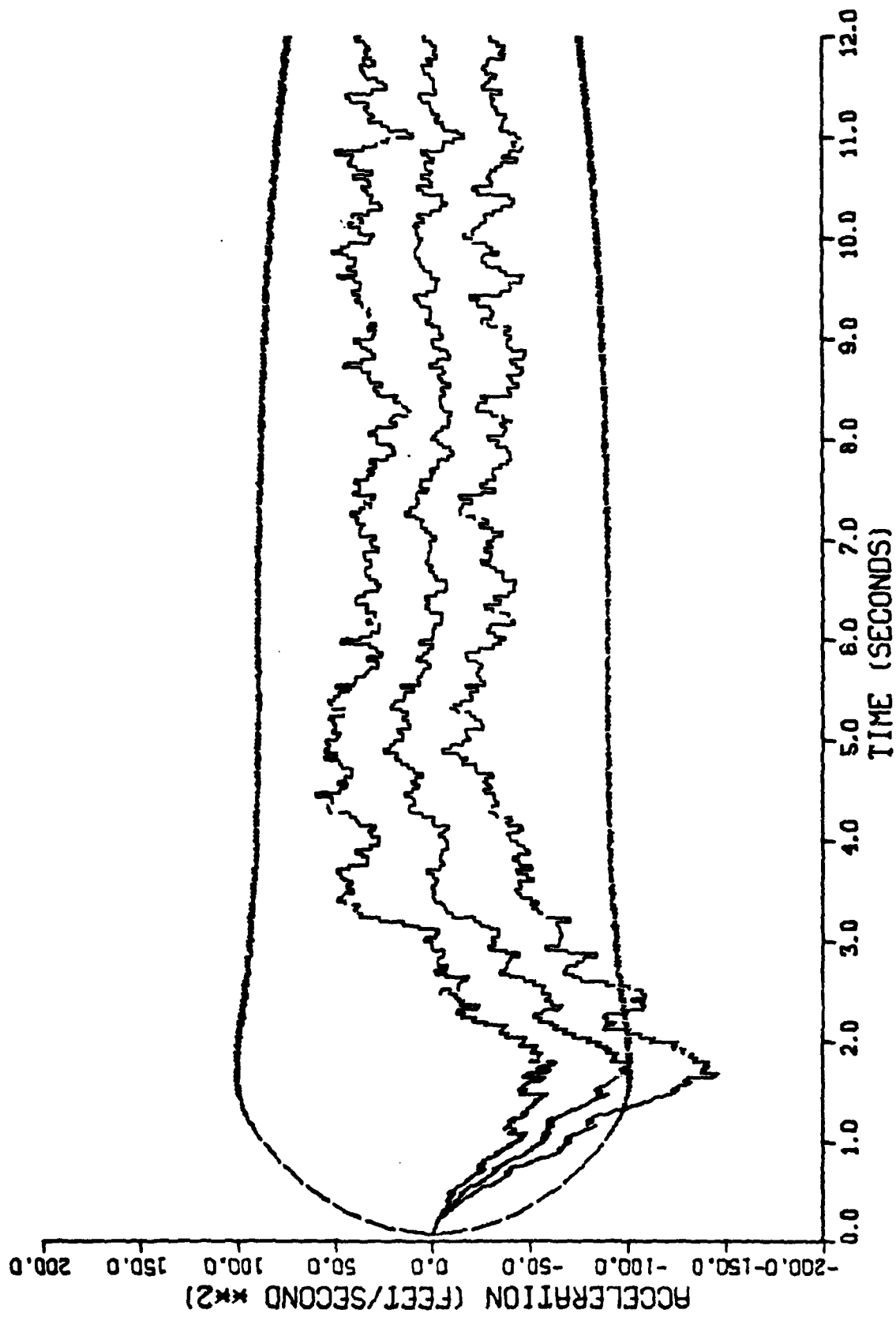


Figure E-6. Performance of the Constant Turn Rate Inertial Coordinate Filter Along the East-Axis for Trajectory 1

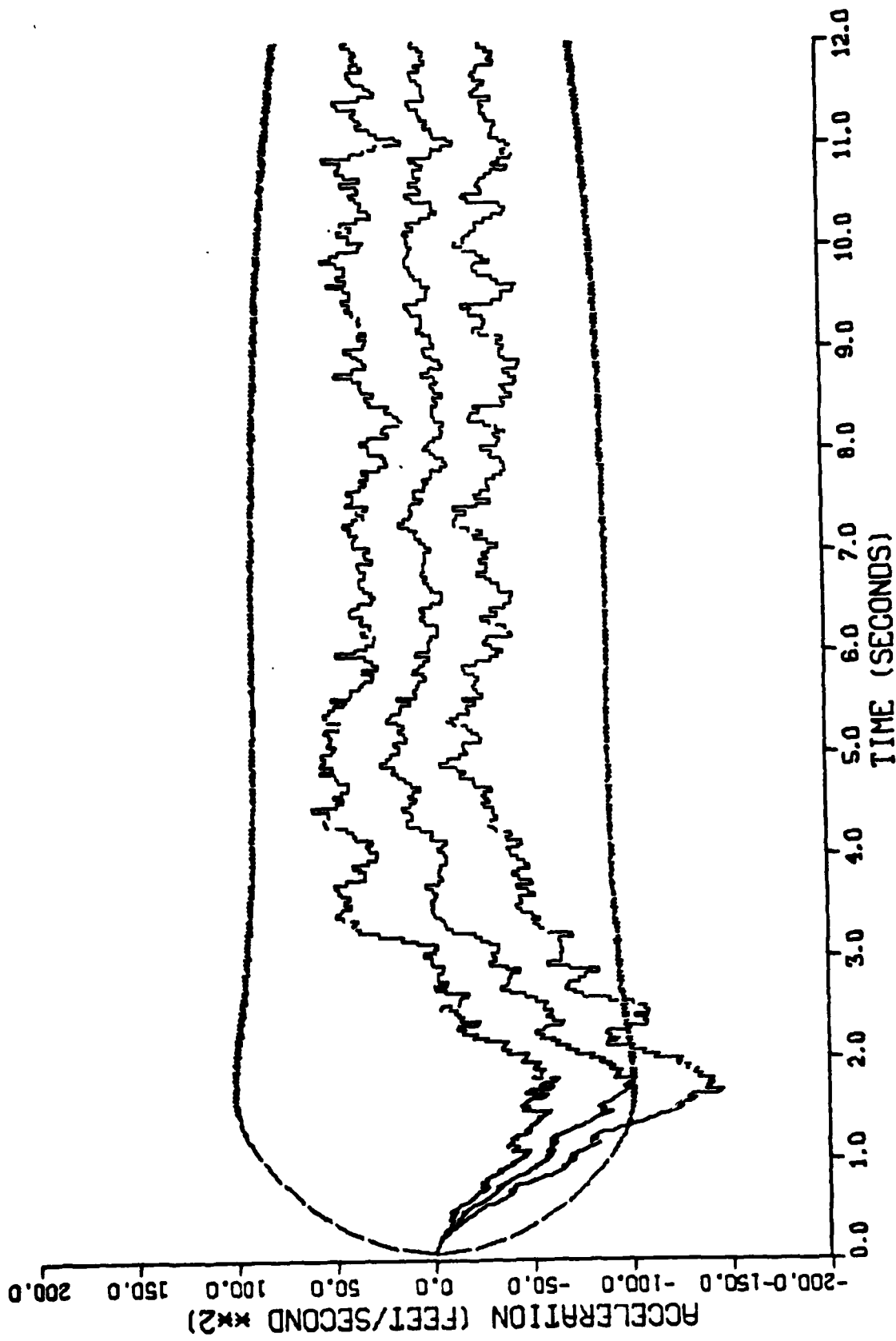


Figure E-6. Performance of the Constant Turn Rate Inertial Coordinate Filter Along the East-Axis for Trajectory 1

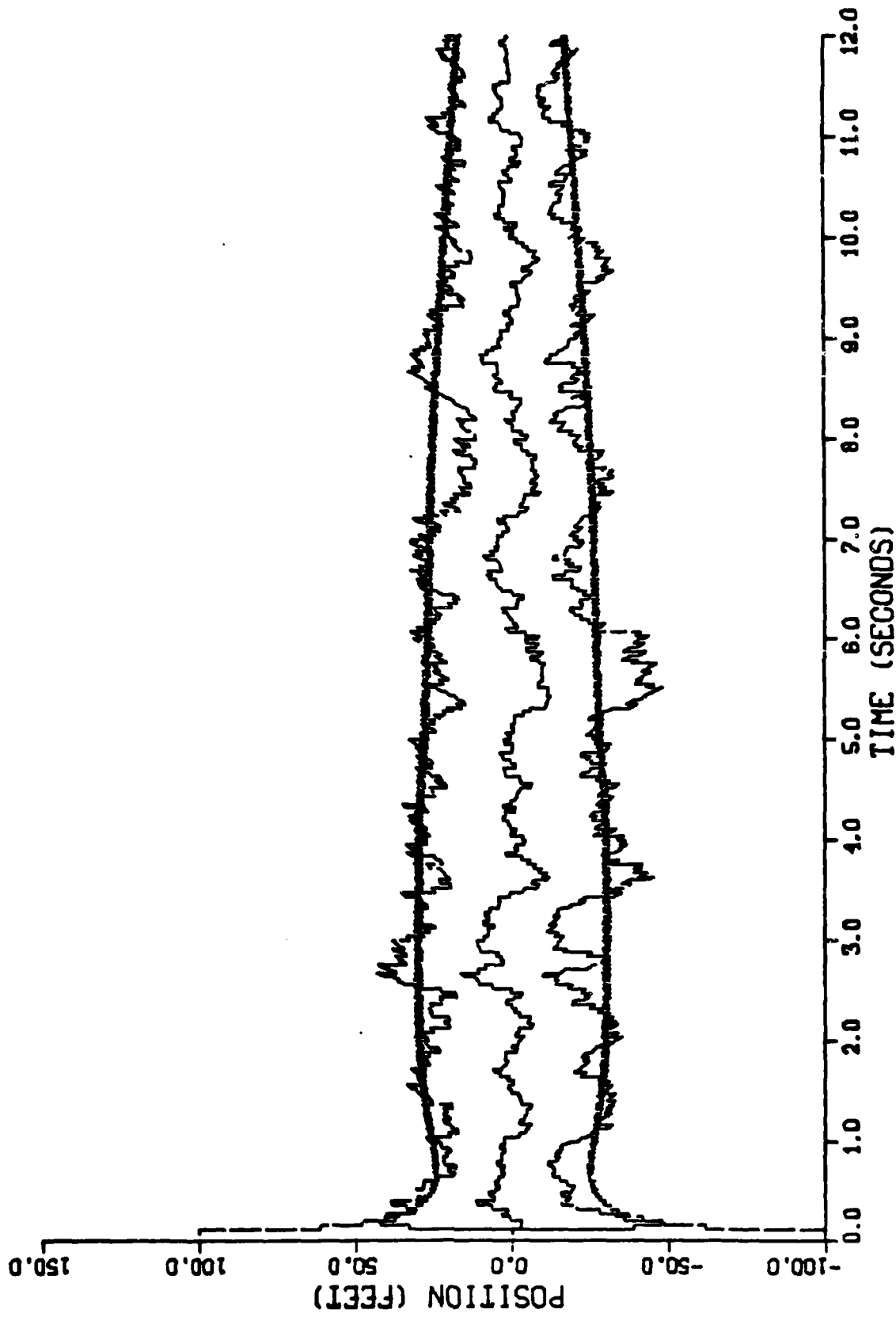


Figure F-7. Performance of the Constant Turn Rate Inertial Coordinate Filter Along the Down-Axis for Trajectory 1

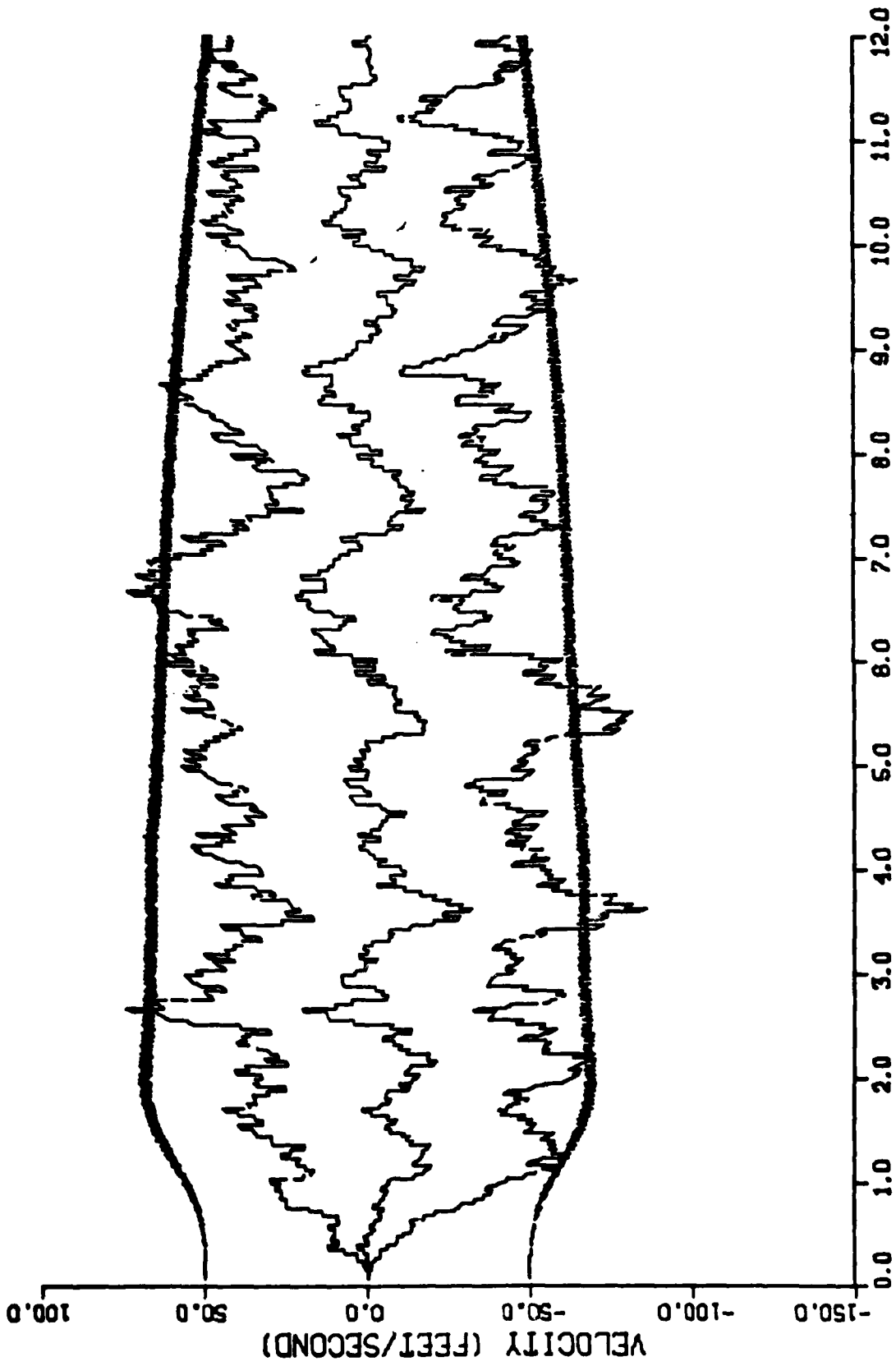


Figure E-8. Performance of the Constant Turn Rate Inertial Coordinate Filter Along the Down-Axis for Trajectory 1

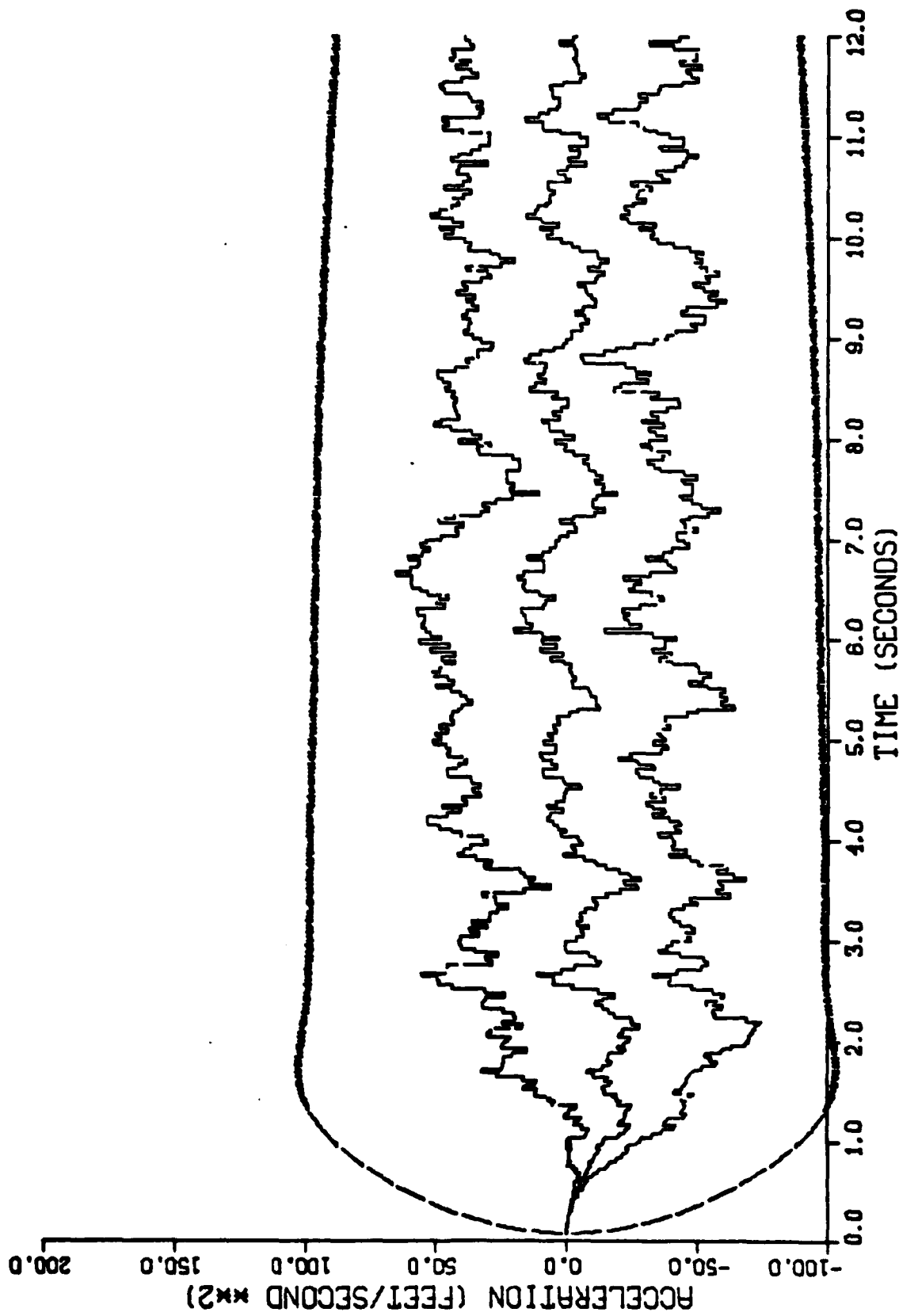


Figure E-9. Performance of the Constant Turn Rate Inertial Coordinate Filter Along the Down-Axis for Trajectory 1

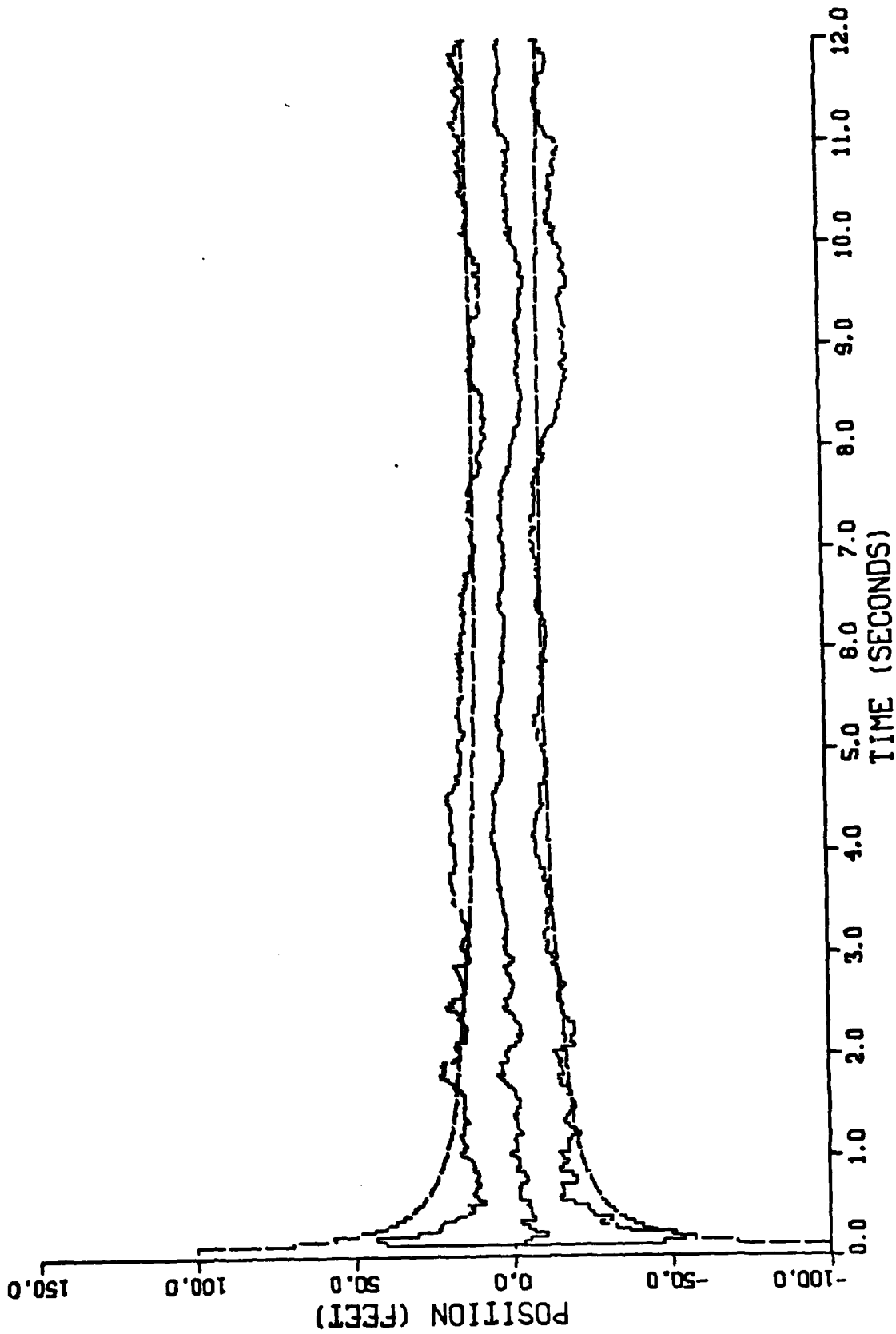


Figure E-10. Performance of the Constant Turn Rate Inertial Coordinate Filter Along the North-Axis for Trajectory 2

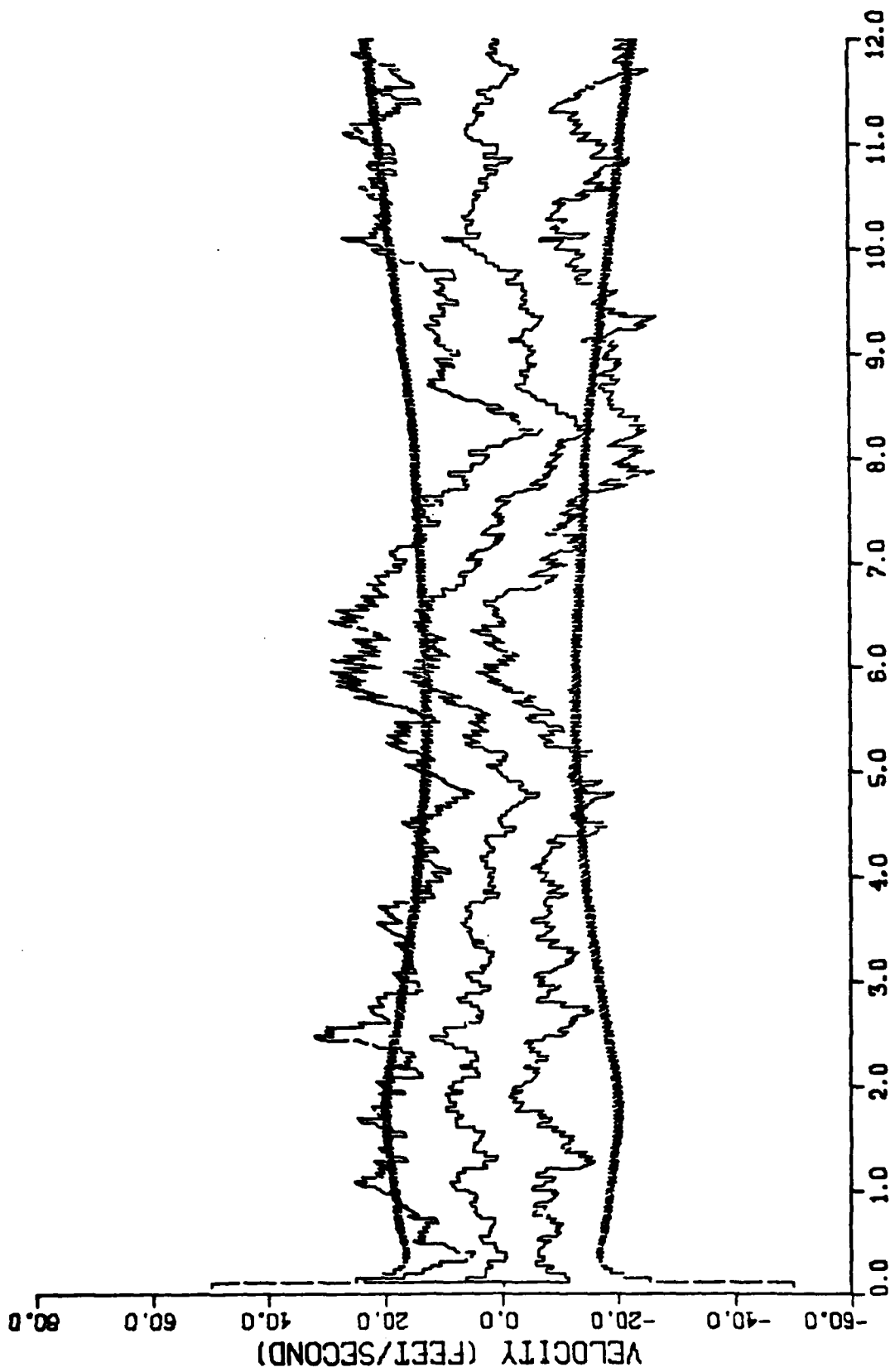


Figure E-11. Performance of the Constant Turn Rate Inertial Coordinate Filter Along the North-Axis for Trajectory 2

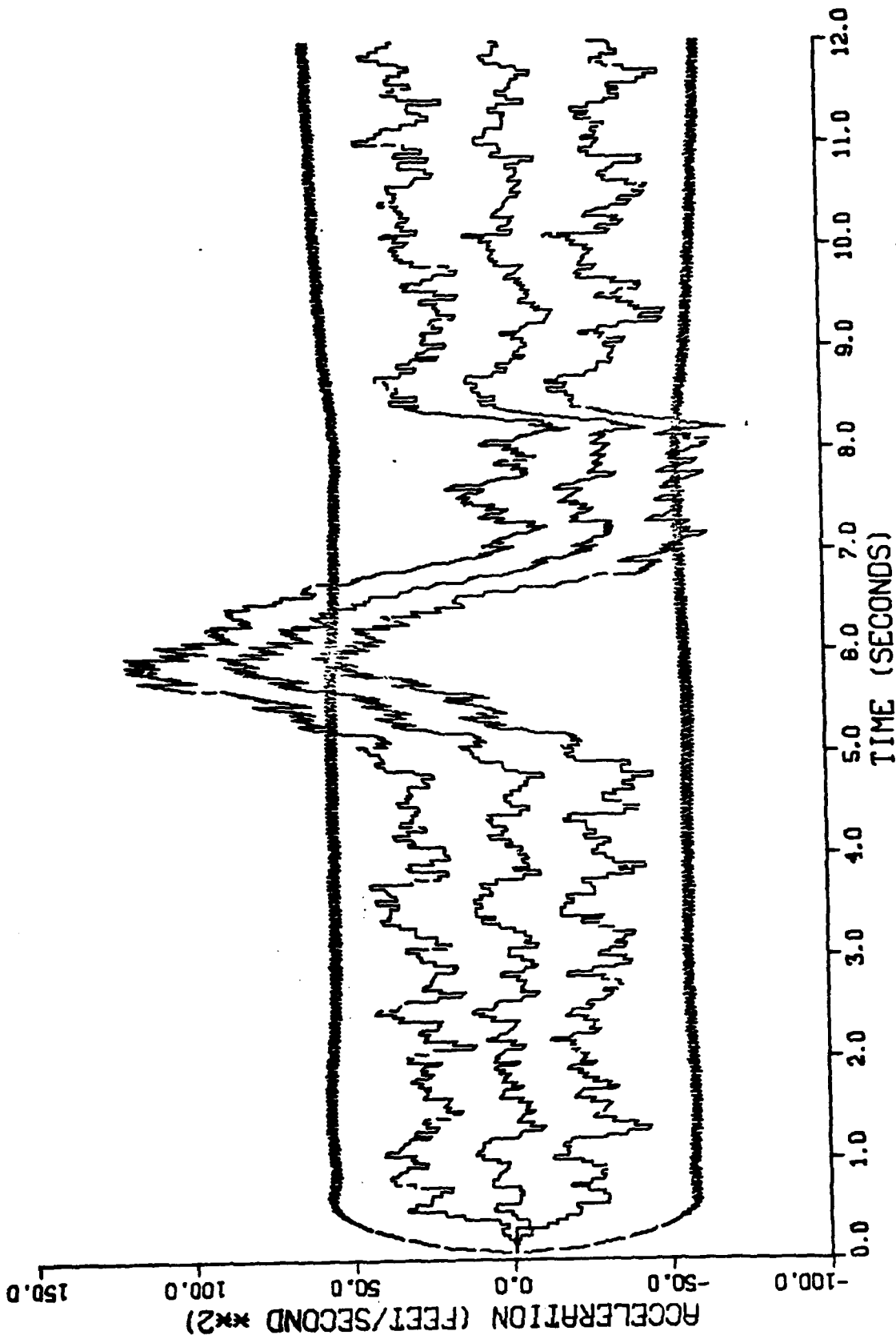


Figure E-12. Performance of the Constant Turn Rate Inertial Coordinate Filter Along the North-Axis for Trajectory 2

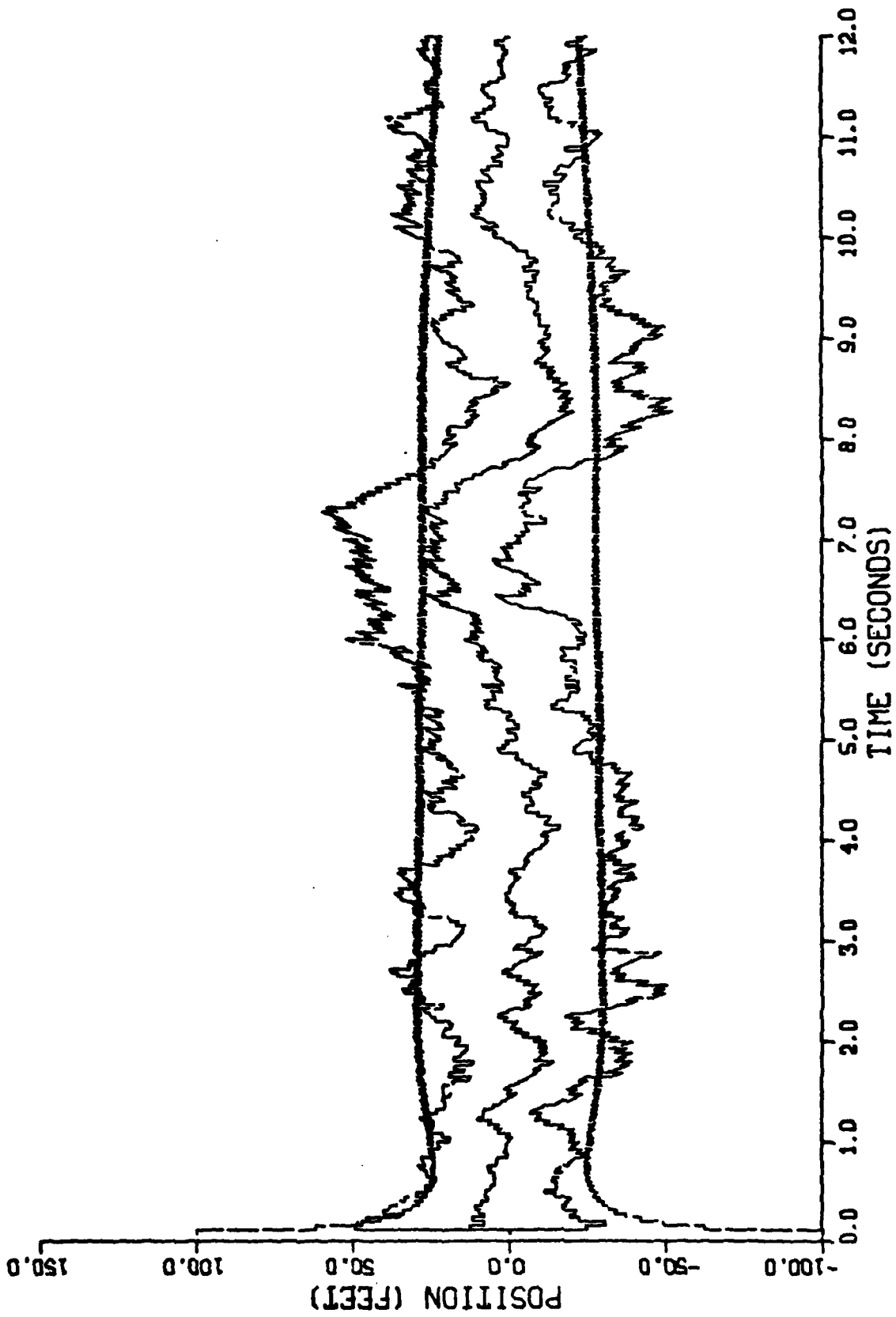


Figure E-13. Performance of the Constant Turn Rate Inertial Coordinate Filter Along the East-Axis for Trajectory 2

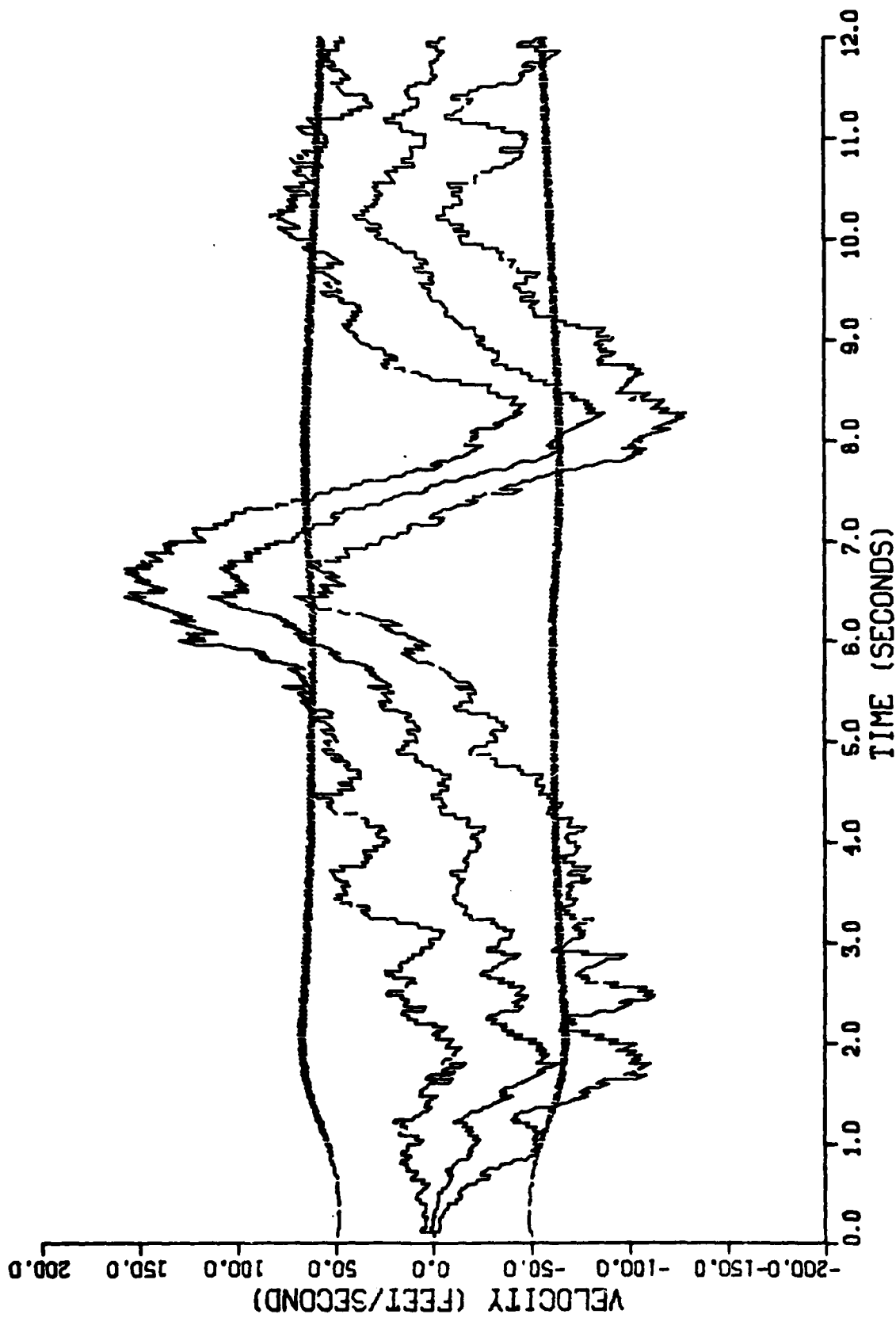


Figure E-14. Performance of the Constant Turn Rate Inertial Coordinate Filter Along the East-Axis for Trajectory 2

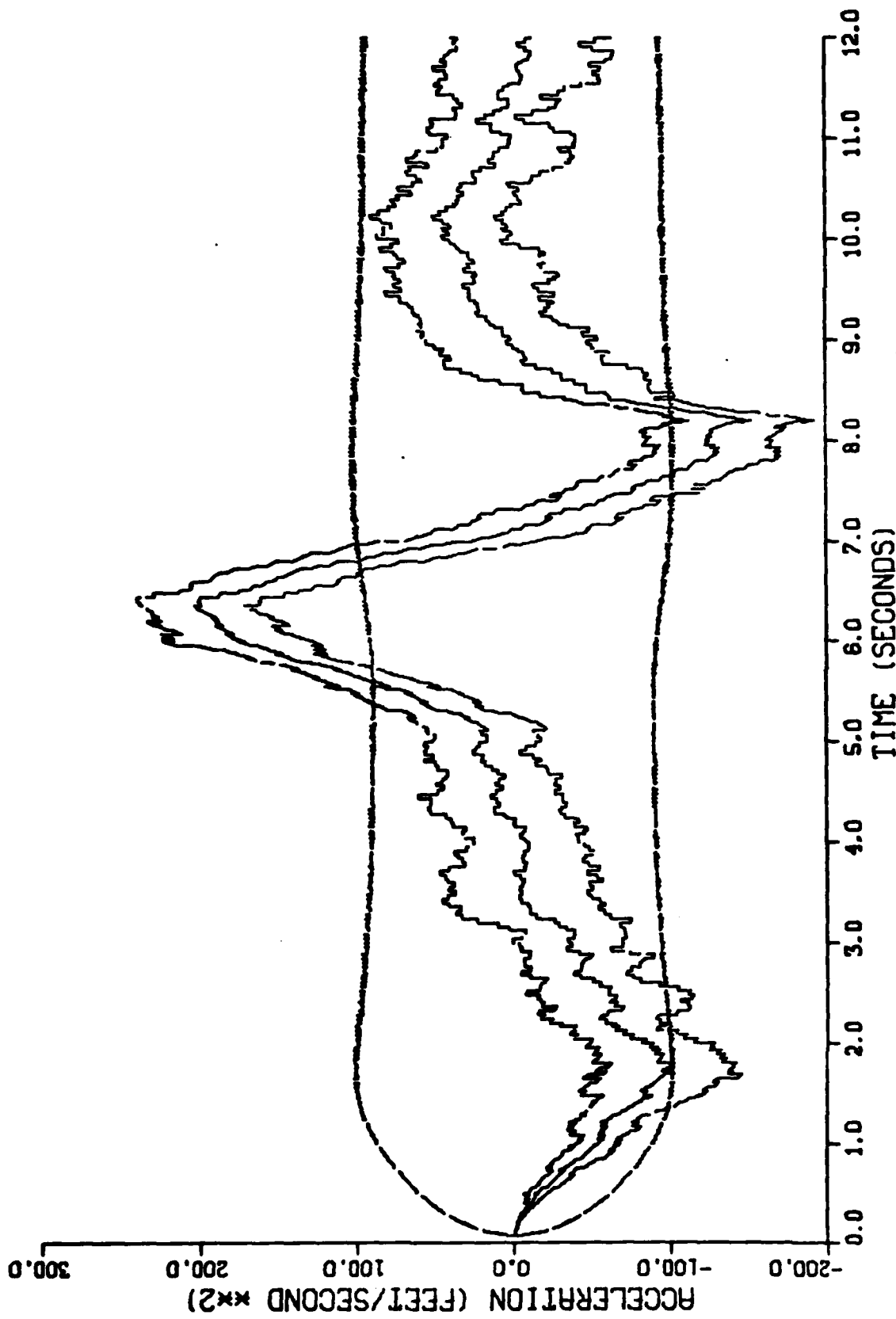


Figure E-15. Performance of the Constant Turn Rate Inertial Coordinate Filter Along the East-Axis for Trajectory 2

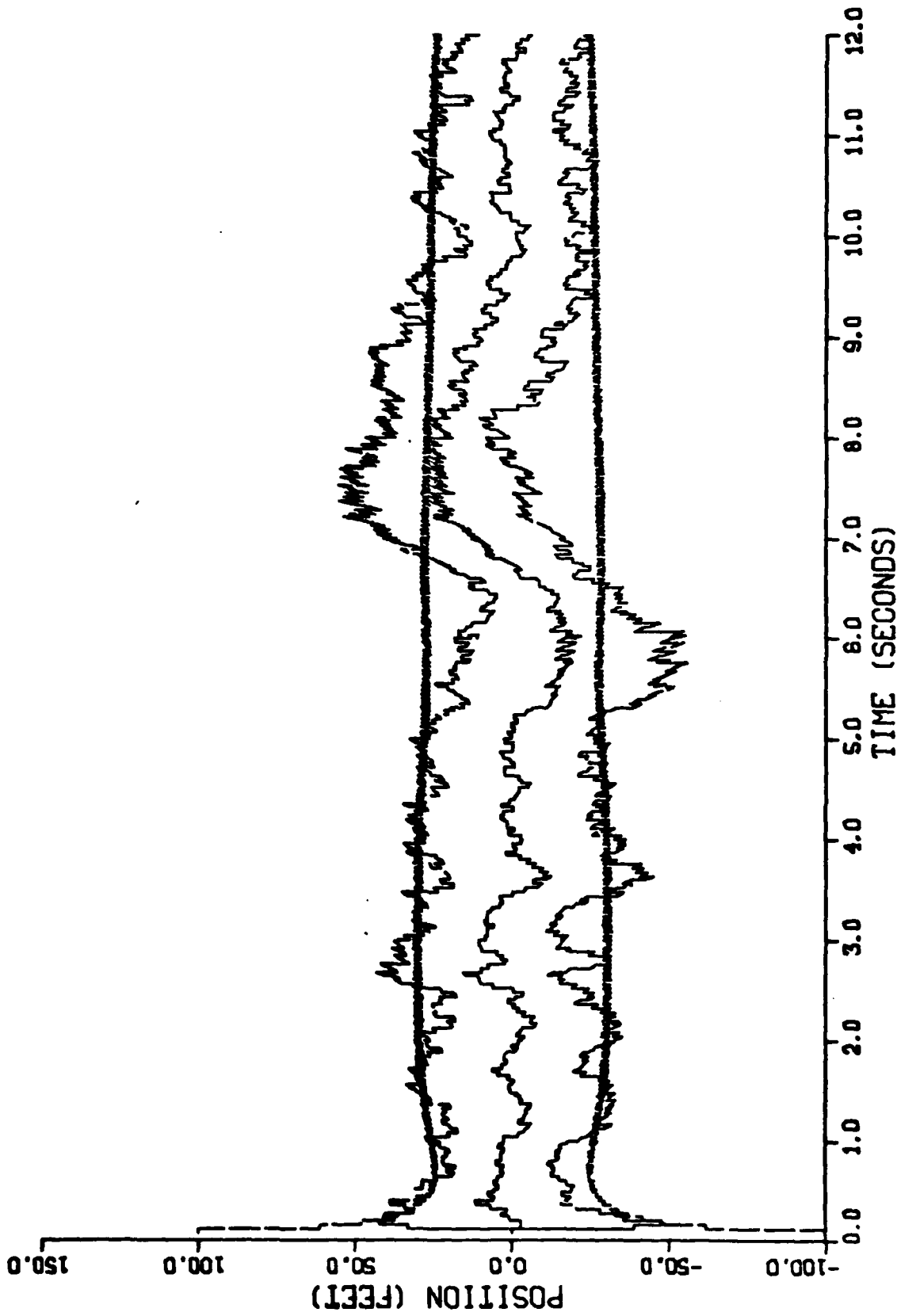


Figure E-16. Performance of the Constant Turn Rate Inertial Coordinate Filter Along the Down-Axis for Trajectory 2

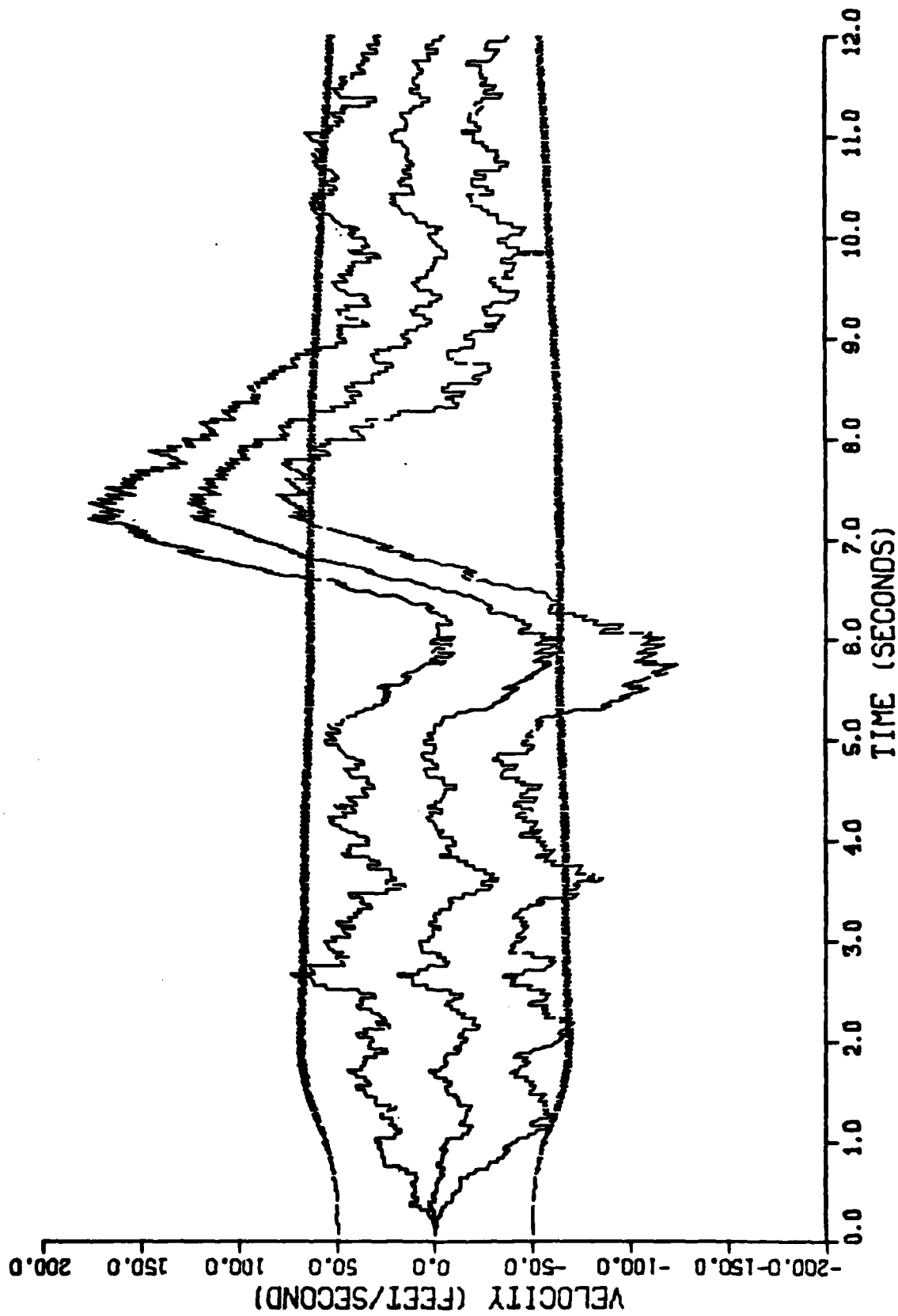


Figure F-17. Performance of the Constant Turn Rate Inertial Coordinate Filter Along the Down-Axis for Trajectory 2

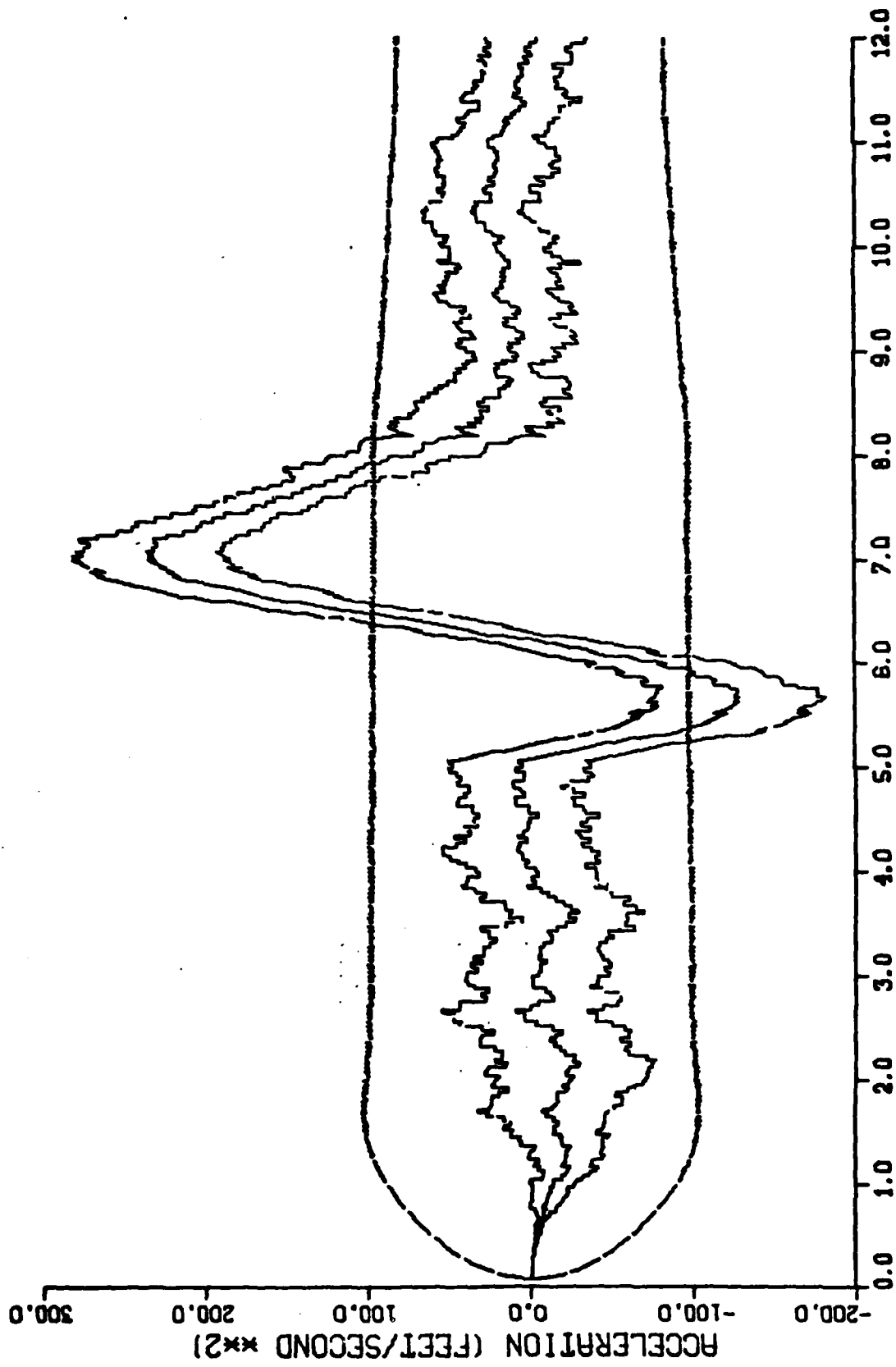


Figure E-18. Performance of the Constant Turn Rate Inertial Coordinate Filter Along the Down-Axis for Trajectory 2

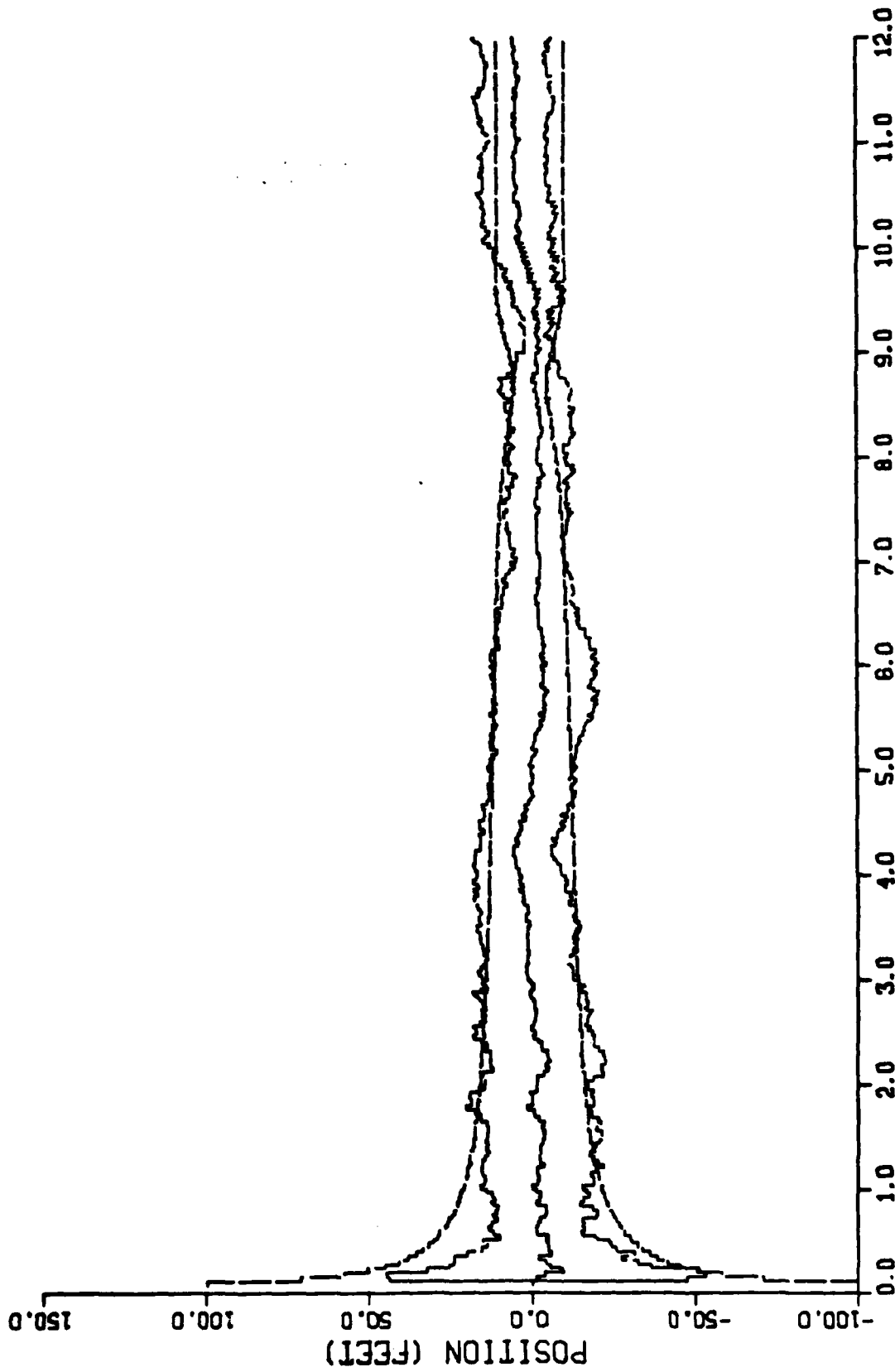


Figure F-19. Performance of the Constant Turn Rate Inertial Coordinate Filter Along the North-Axis for Trajectory 3

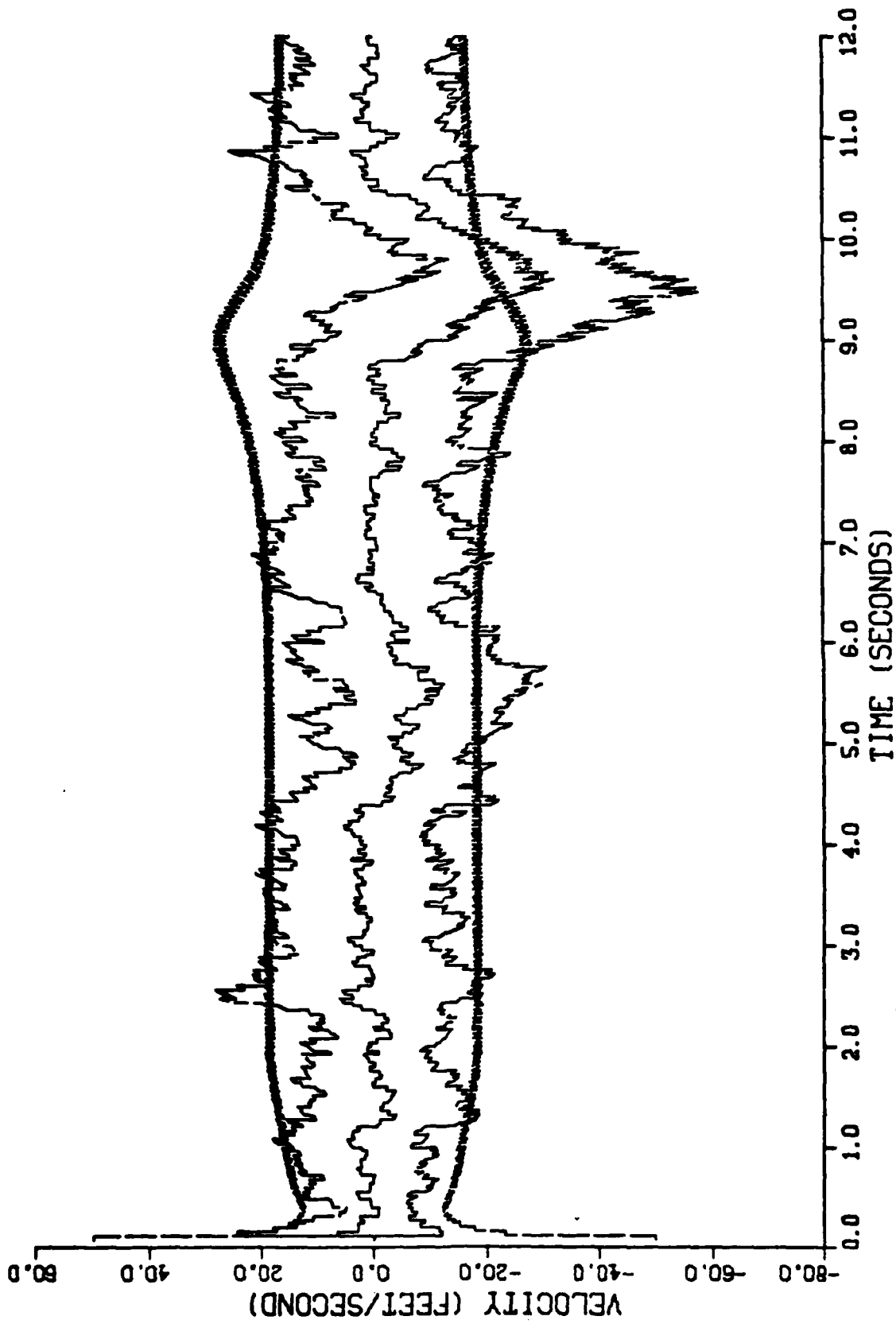


Figure E-20. Performance of the Constant Turn Rate Inertial Coordinate Filter Along the North-Axis for Trajectory 3

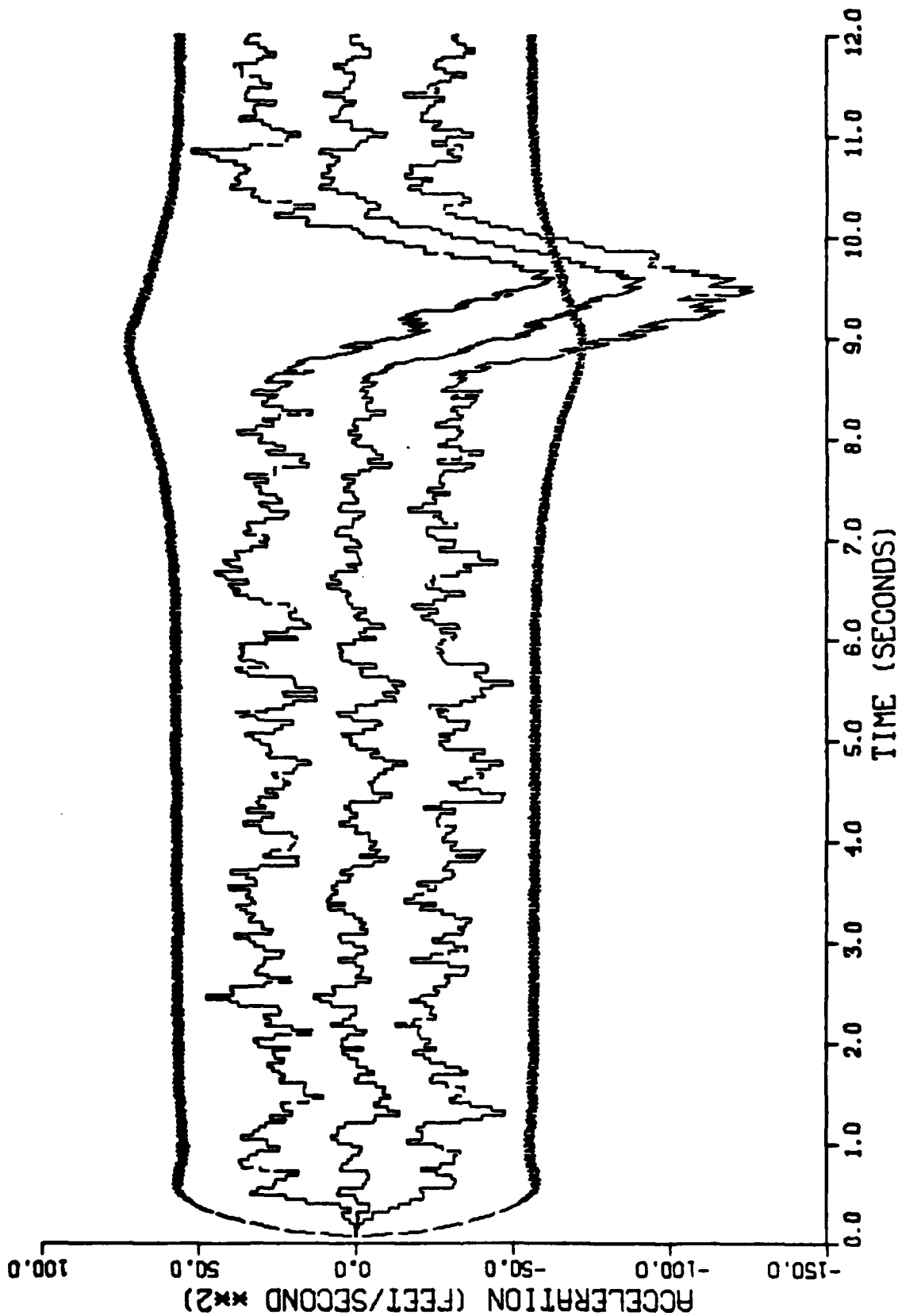


Figure E-21. Performance of the Constant Turn Rate Inertial Coordinate Filter Along the North-Axis for Trajectory 3

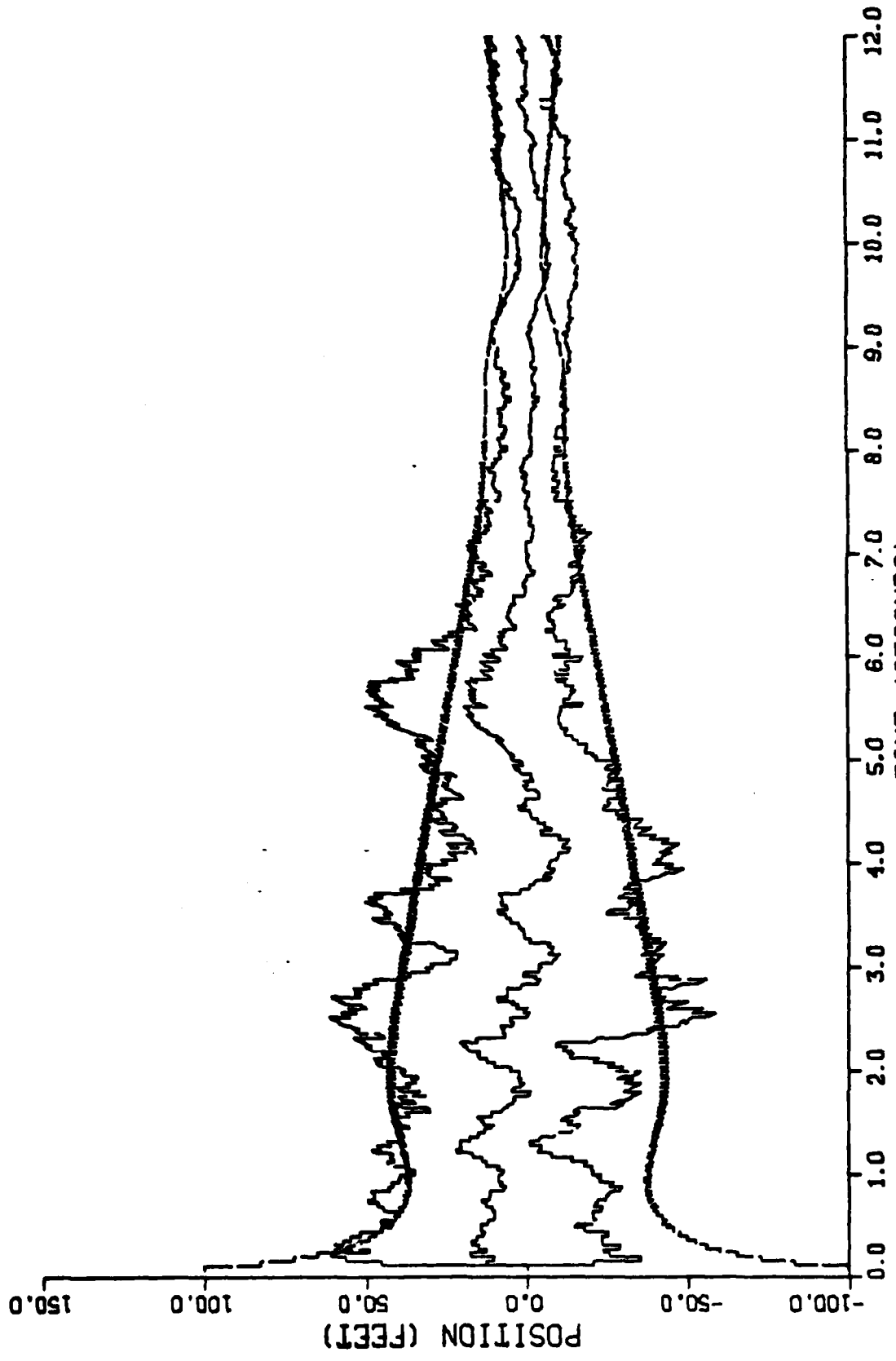


Figure E-22. Performance of the Constant Turn Rate Inertial Coordinate Filter Along the East-Axis for Trajectory 3

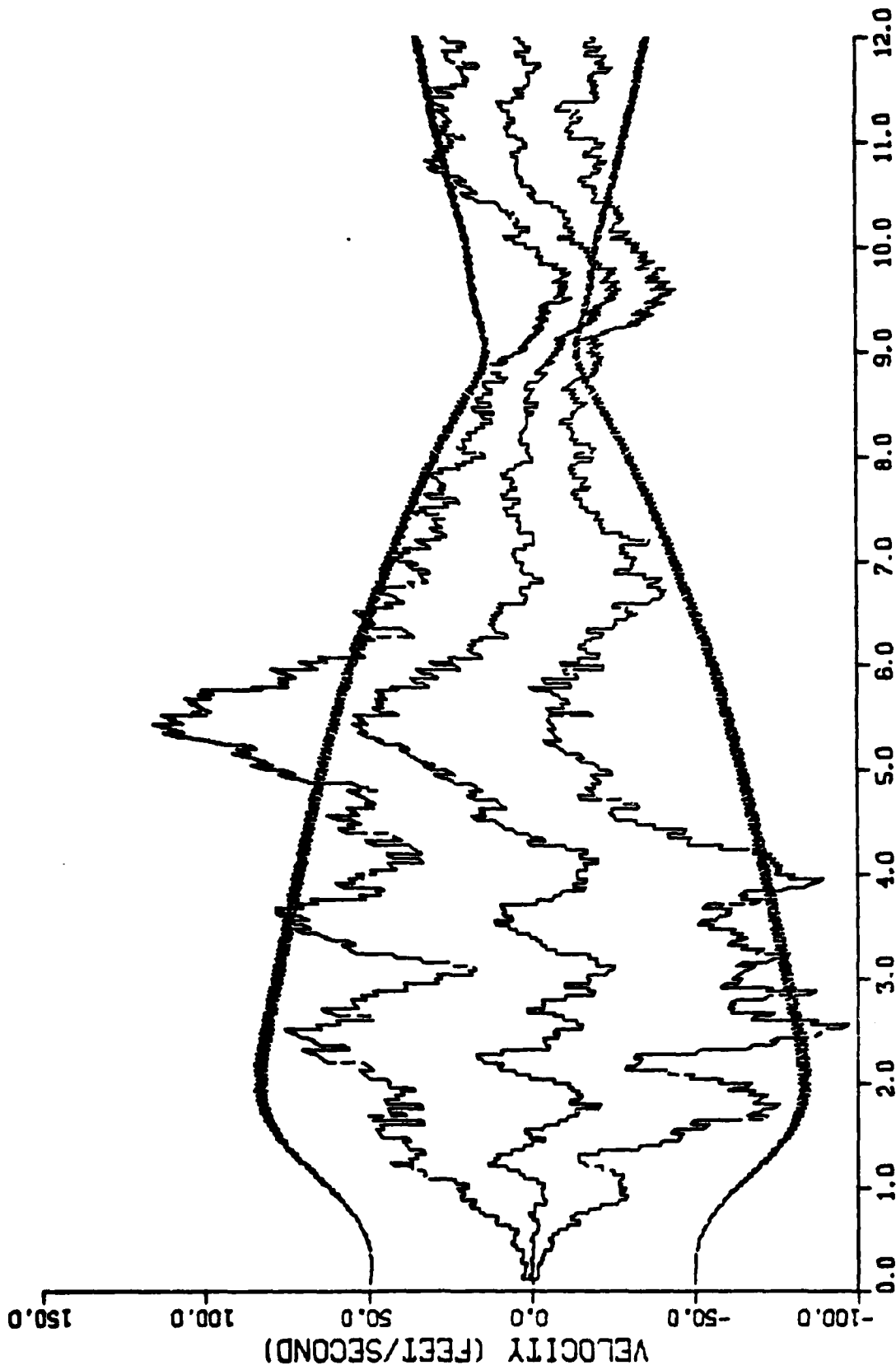


Figure E-23. Performance of the Constant Turn Rate Inertial Coordinate Filter Along the East-Axis for Trajectory 3

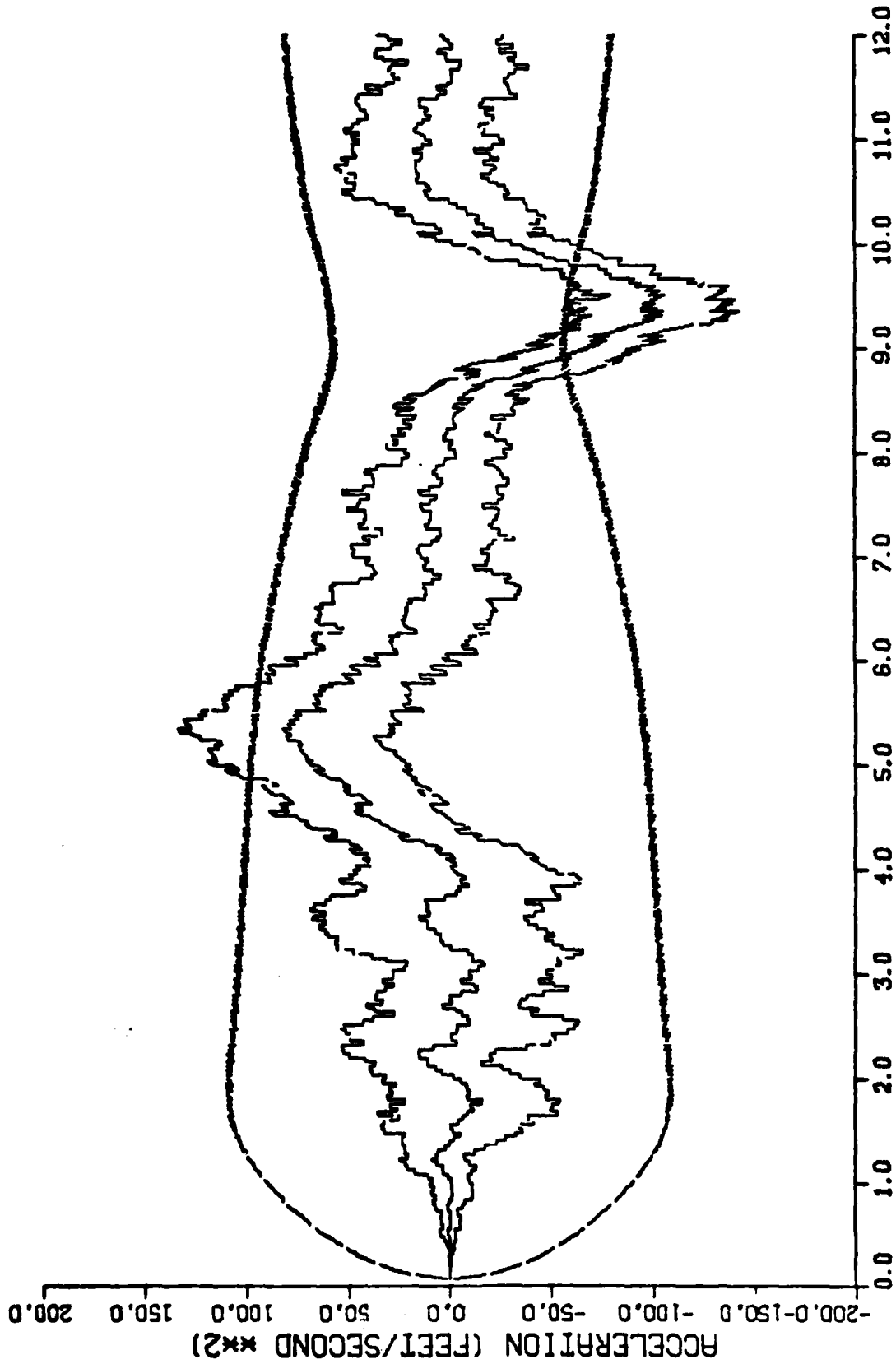


Figure E-24. Performance of the Constant Turn Rate Inertial Coordinate Filter Along the Fast-Axis for Trajectory 3

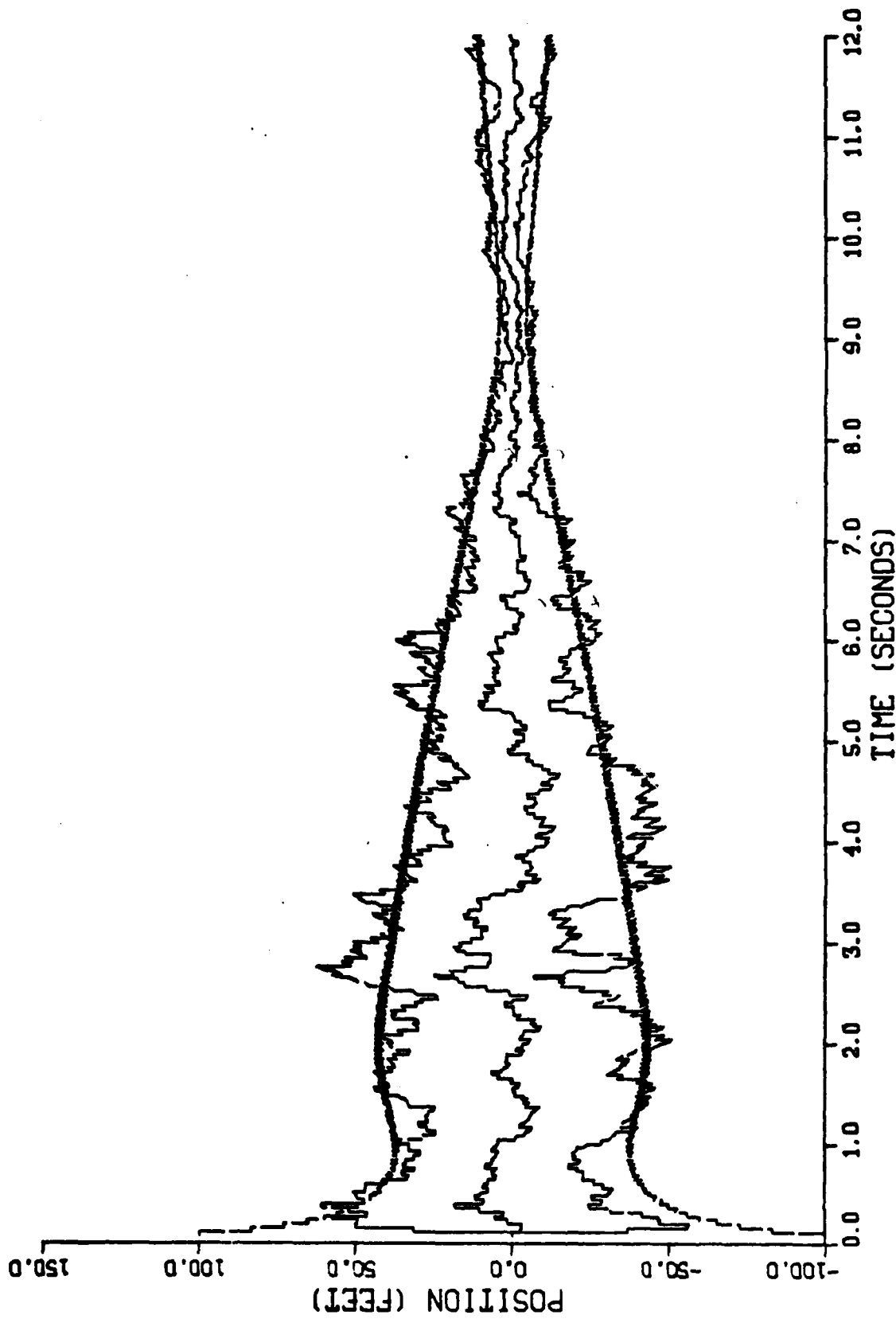


Figure E-25. Performance of the Constant Turn Rate Inertial Coordinate Filter Along the Down-Axis for Trajectory 3

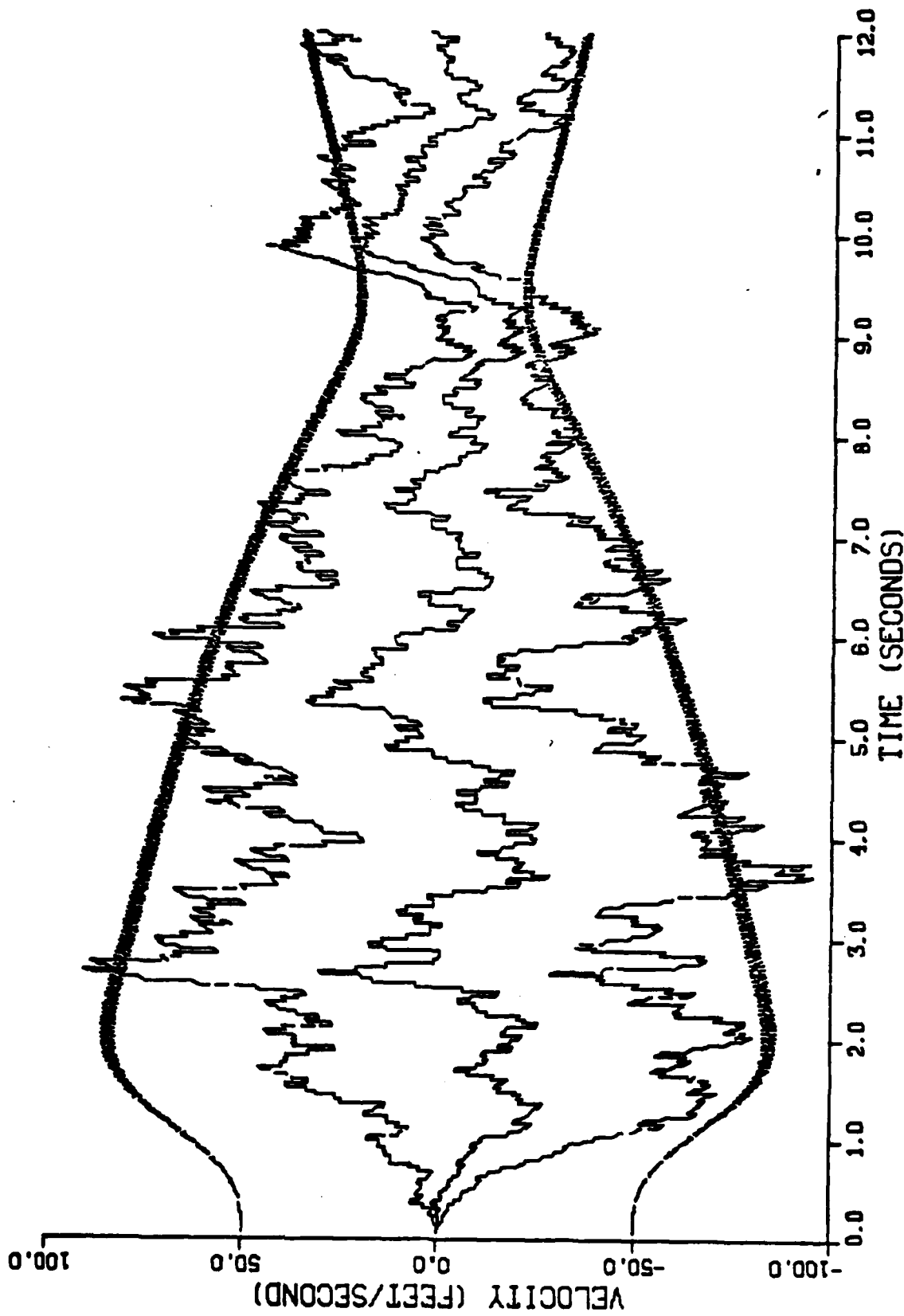


Figure E-26. Performance of the Constant Turn Rate Inertial Coordinate Filter Along the Down-Axis for Trajectory 3

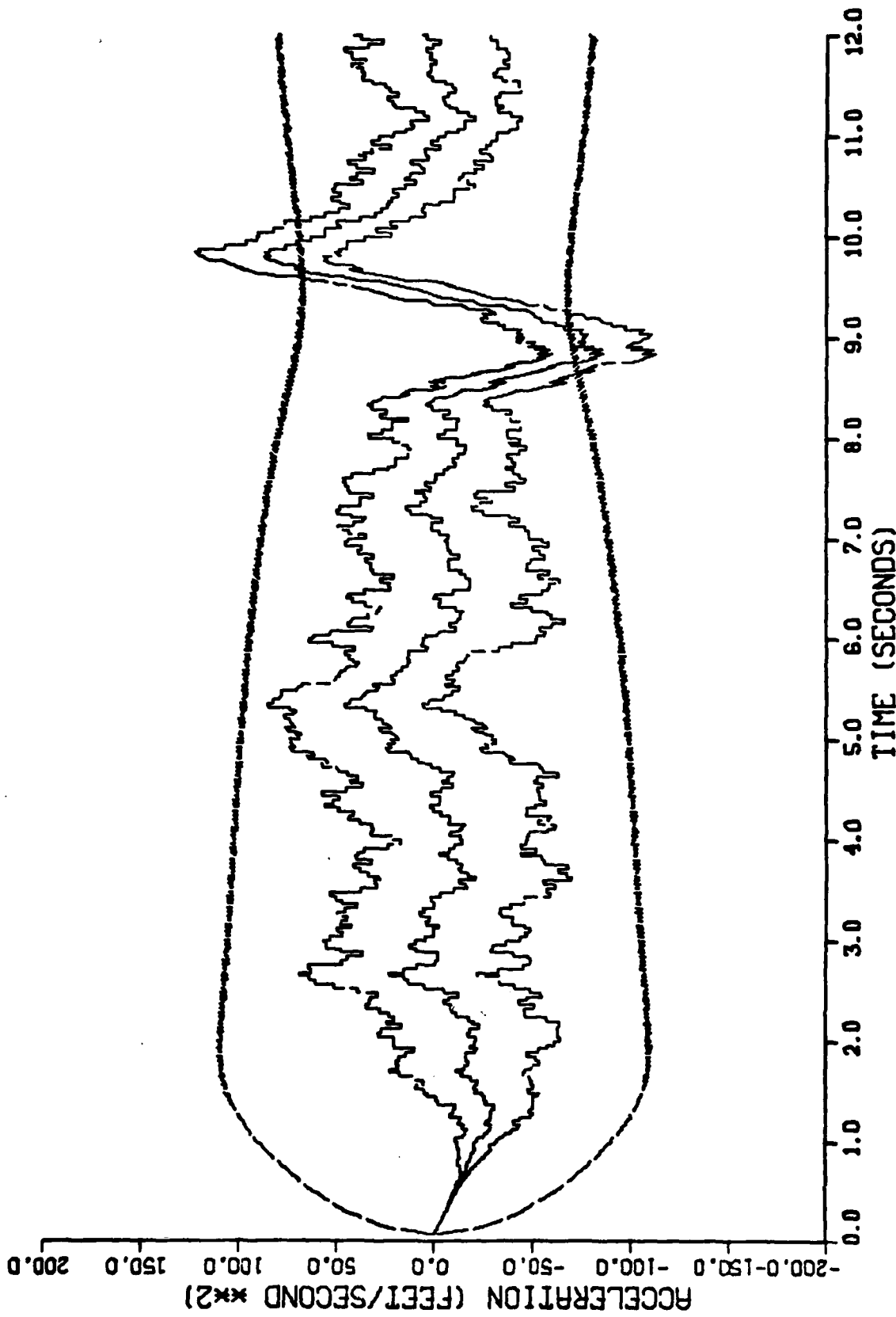


Figure E-27. Performance of the Constant Turn Rate Inertial Coordinate Filter Along the Down-Axis for Trajectory 3

APPENDIX F

Graphical Results of the Effect of Variations in
Update Rates on the Performance of the Constant
Turn Rate Inertial Coordinate Filter

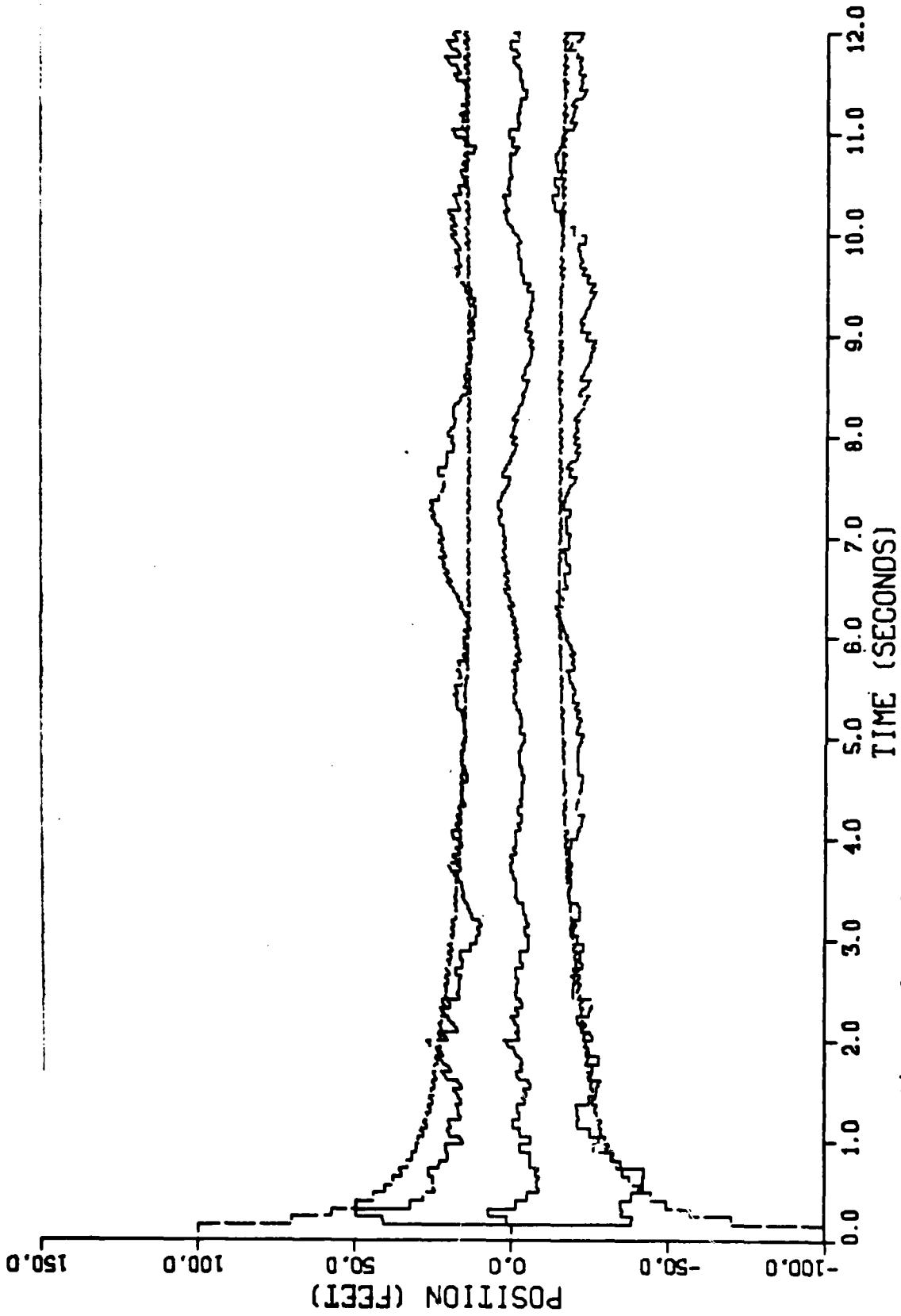


Figure F-1. Performance of the Constant Turn Rate Inertial Coordinate Filter
 Along the North-Axis for Trajectory 2 with a 0.08 Second Sample Period

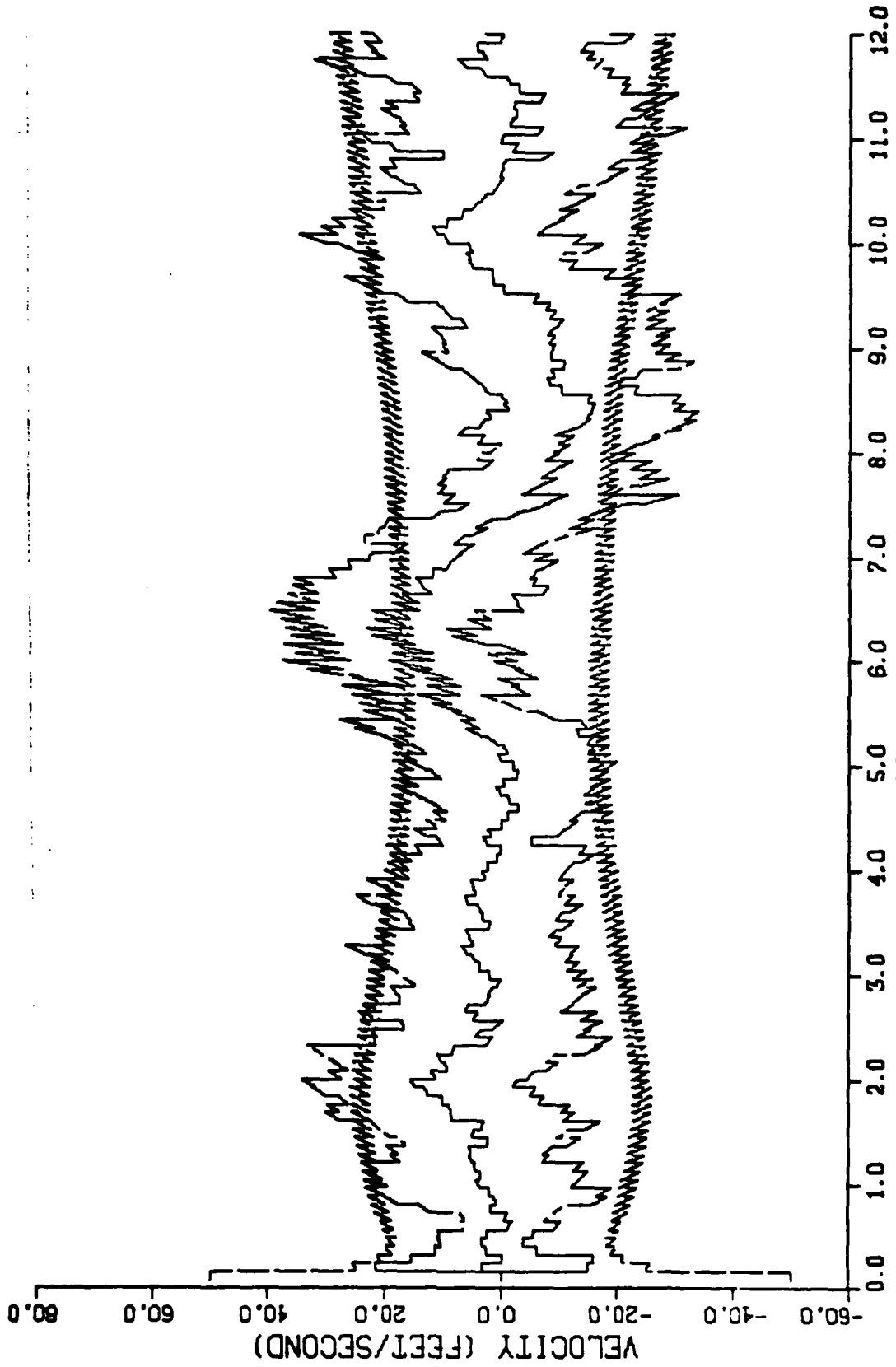


Figure F-2. Performance of the Constant Turn Rate Inertial Coordinate Filter Along the North-Axis for Trajectory 2 with a 0.08 Second Sample Period

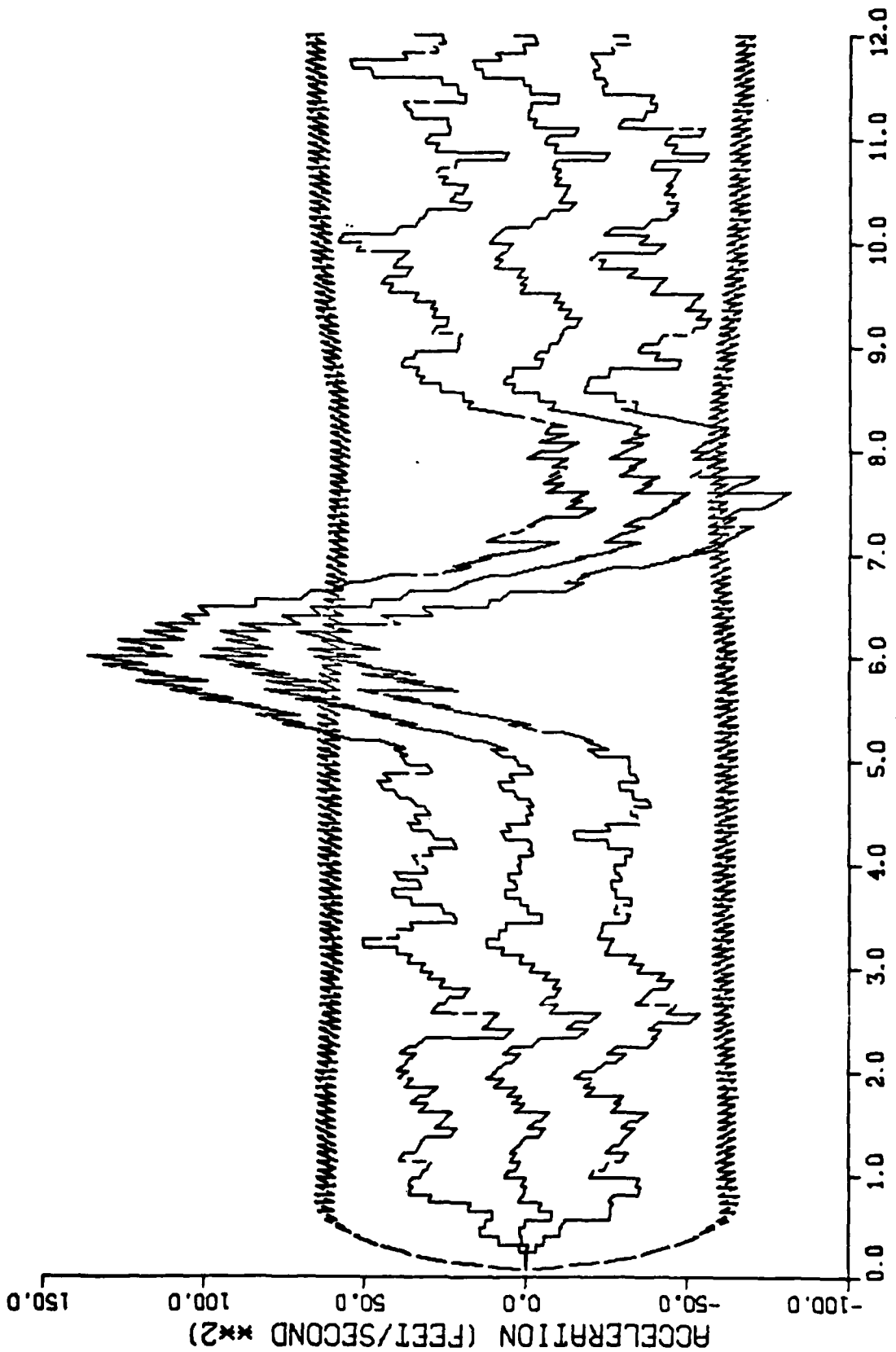


Figure F-3. Performance of the Constant Turn Rate Inertial Coordinate Filter Along the North-Axis for Trajectory 2 with a 0.08 Second Sample Period

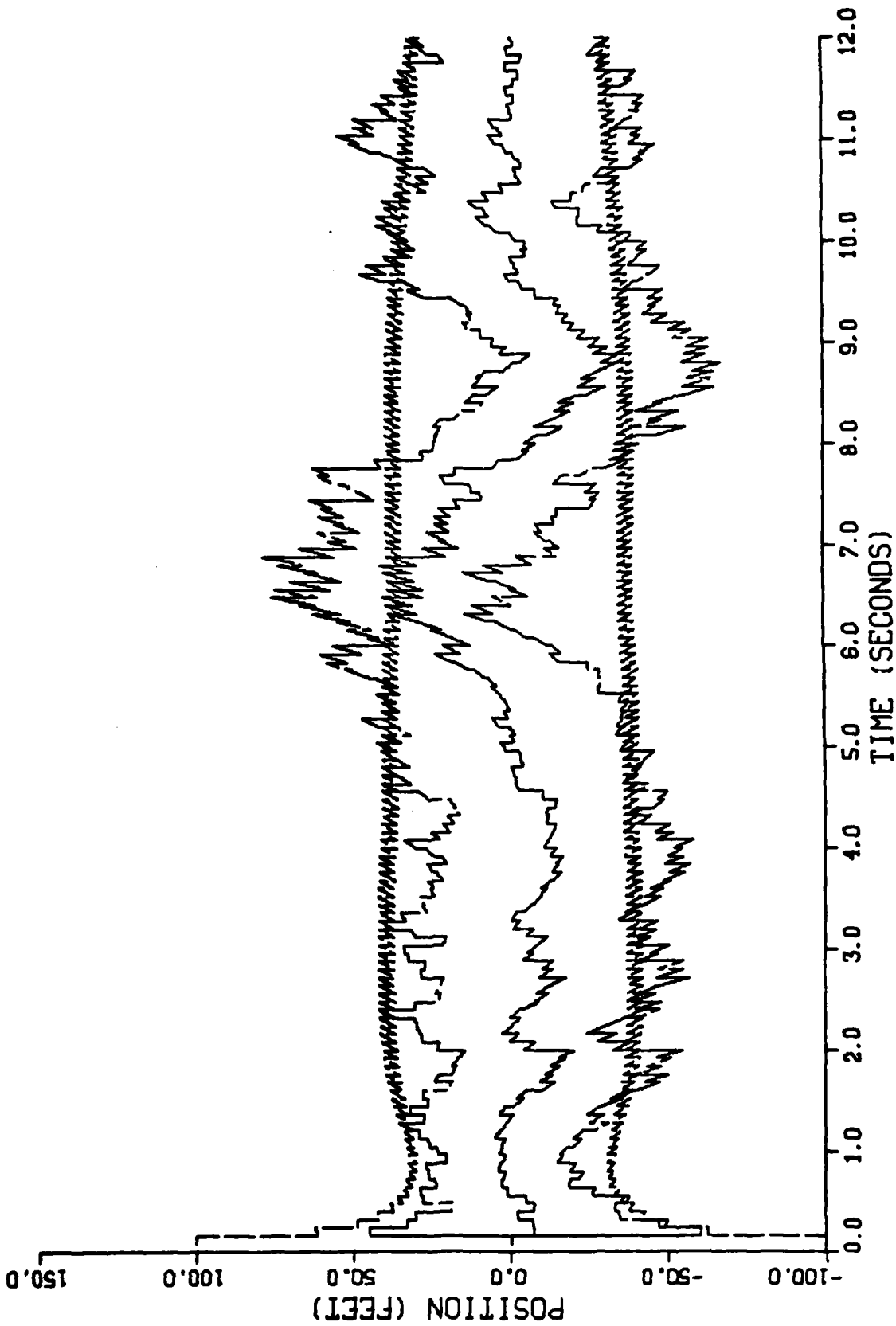


Figure F-4. Performance of the Constant Turn Rate Inertial Coordinate Filter Along the East-Axis for Trajectory 2 with a 0.08 Second Sample Period

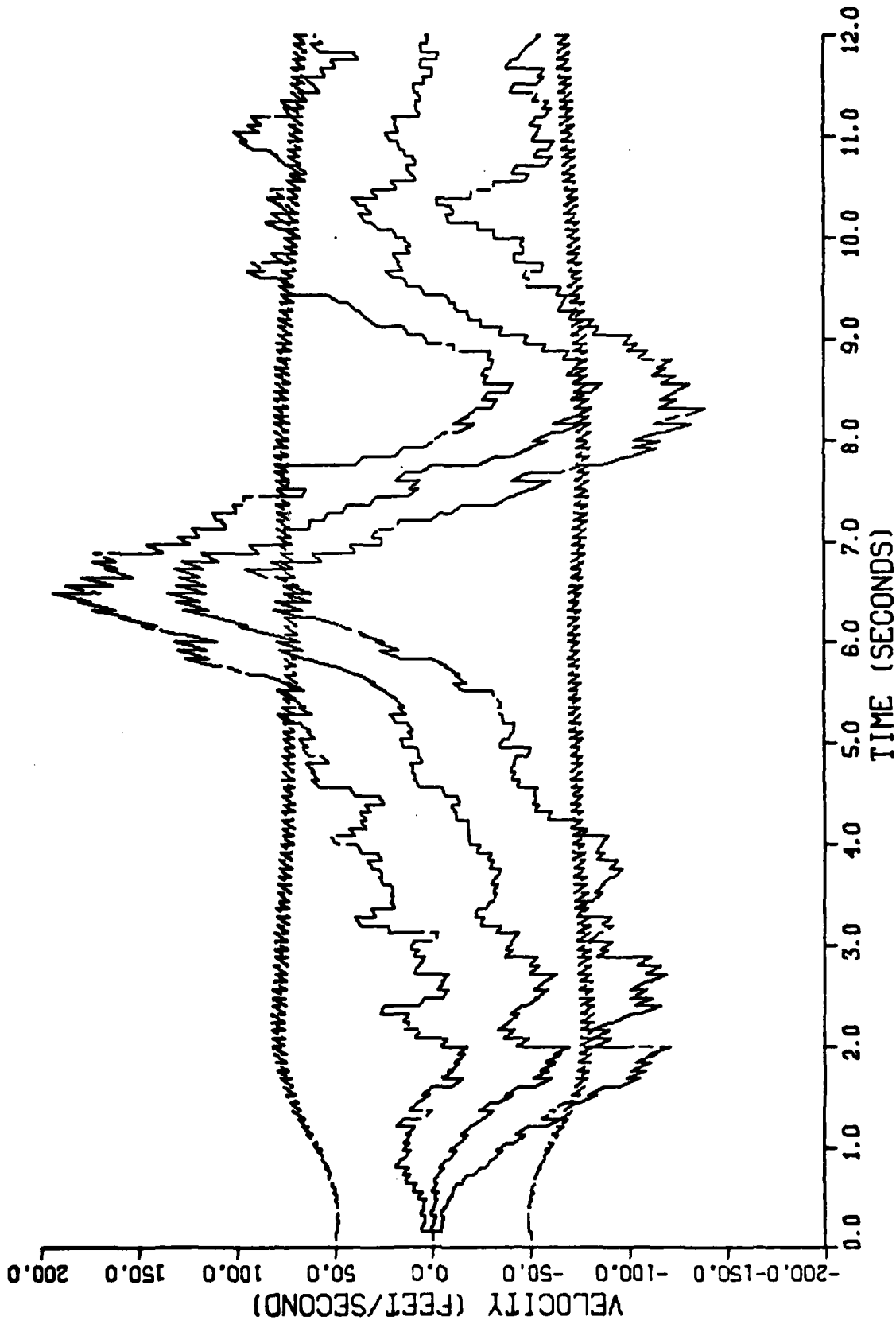


Figure F-5. Performance of the Constant Turn Rate Inertial Coordinate Filter Along the East-Axis for Trajectory 2 with a 0.08 Second Sample Period

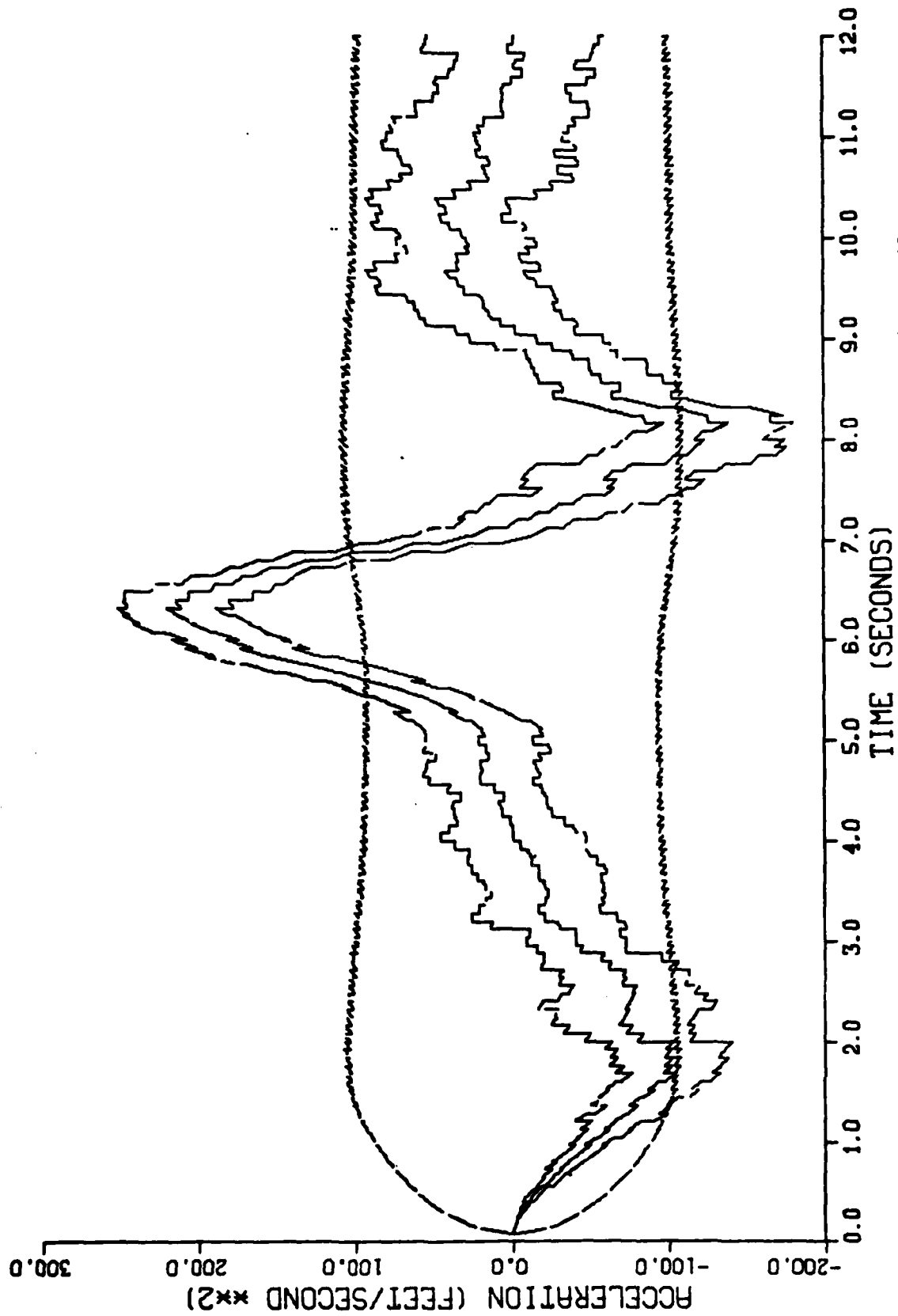


Figure F-6. Performance of the Constant Turn Rate Inertial Coordinate Filter Along the East-Axis for Trajectory 2 with a 0.08 Second Sample Period

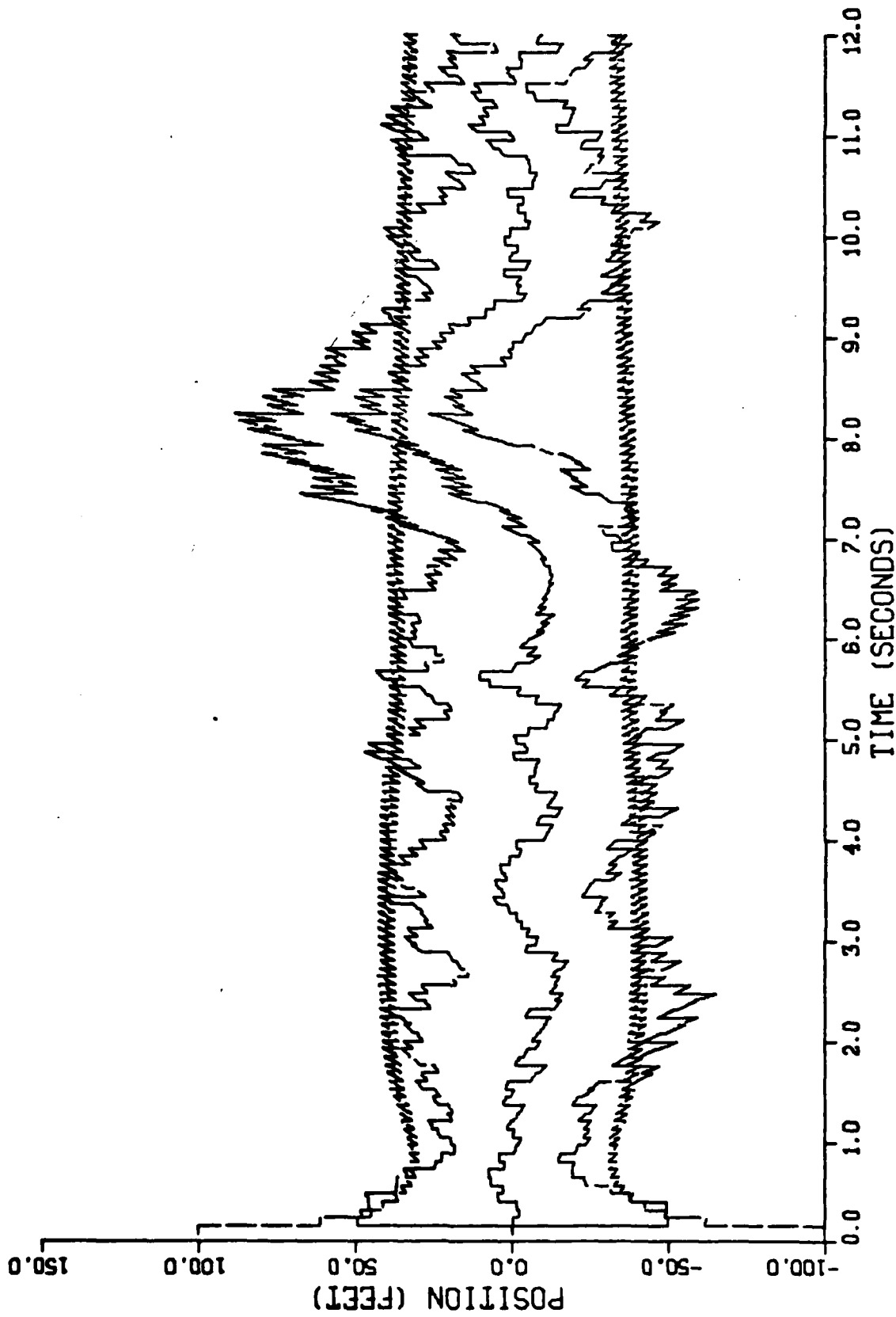


Figure F-7. Performance of the Constant Turn Rate Inertial Coordinate Filter Along the Down-Axis for Trajectory 2 with a 0.08 Second Sample Period

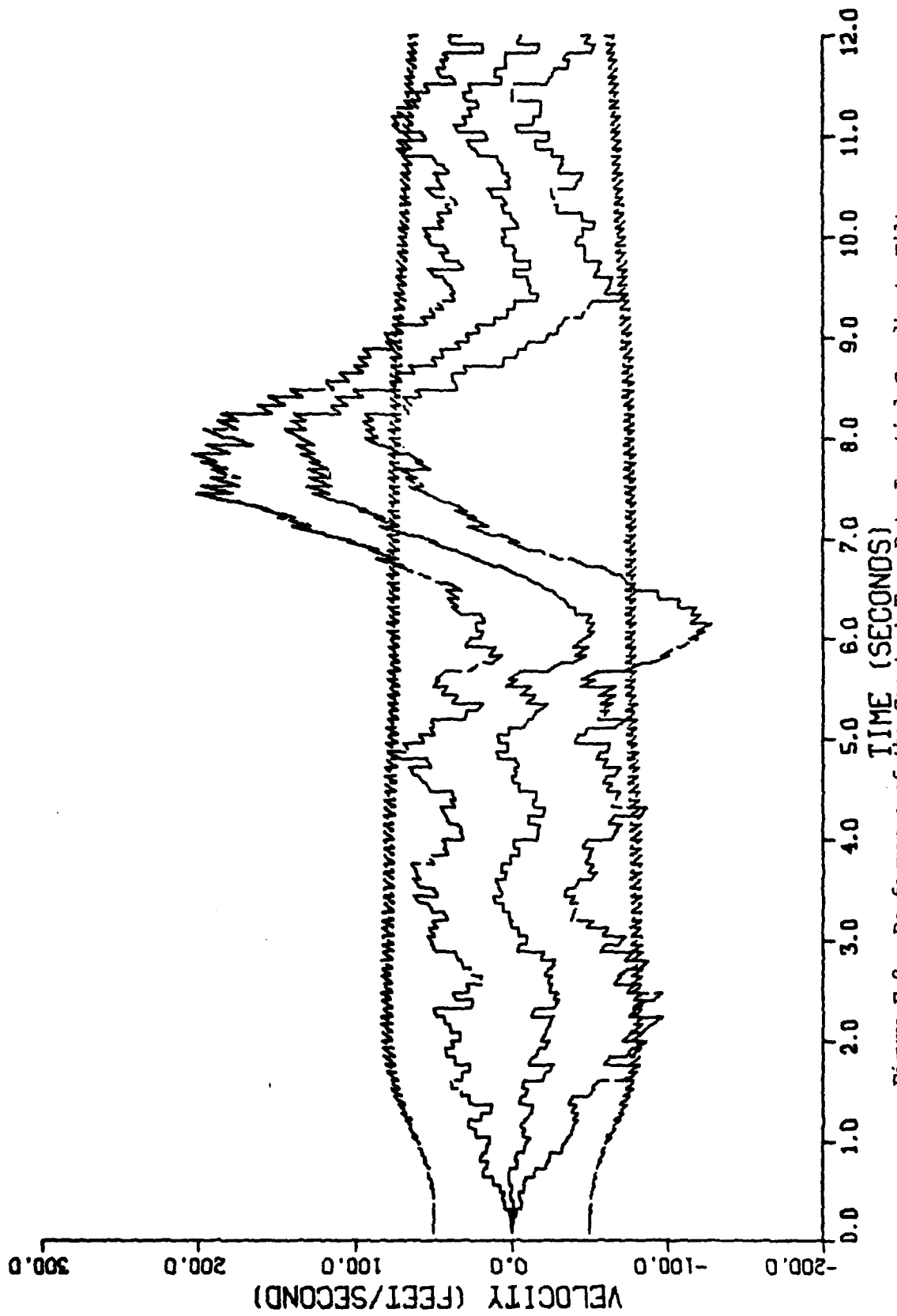


Figure F-8. Performance of the Constant Turn Rate Inertial Coordinate Filter Along the Down-Axis for Trajectory 2 with a 0.08 Second Sample Period

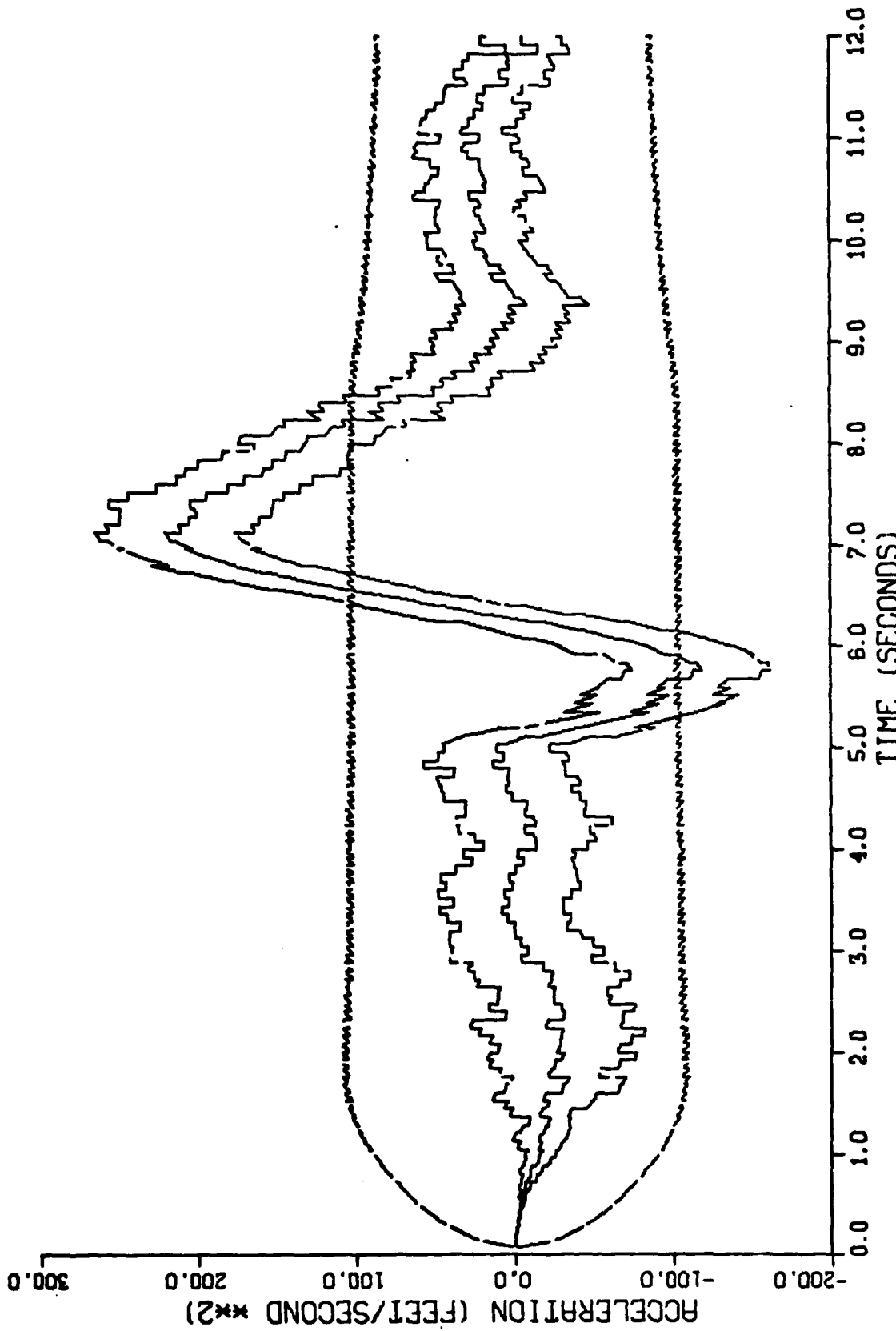


Figure F-9. Performance of the Constant Turn Rate Inertial Coordinate Filter Along the Down-Axis for Trajectory 2 with a 0.08 Second Sample Period

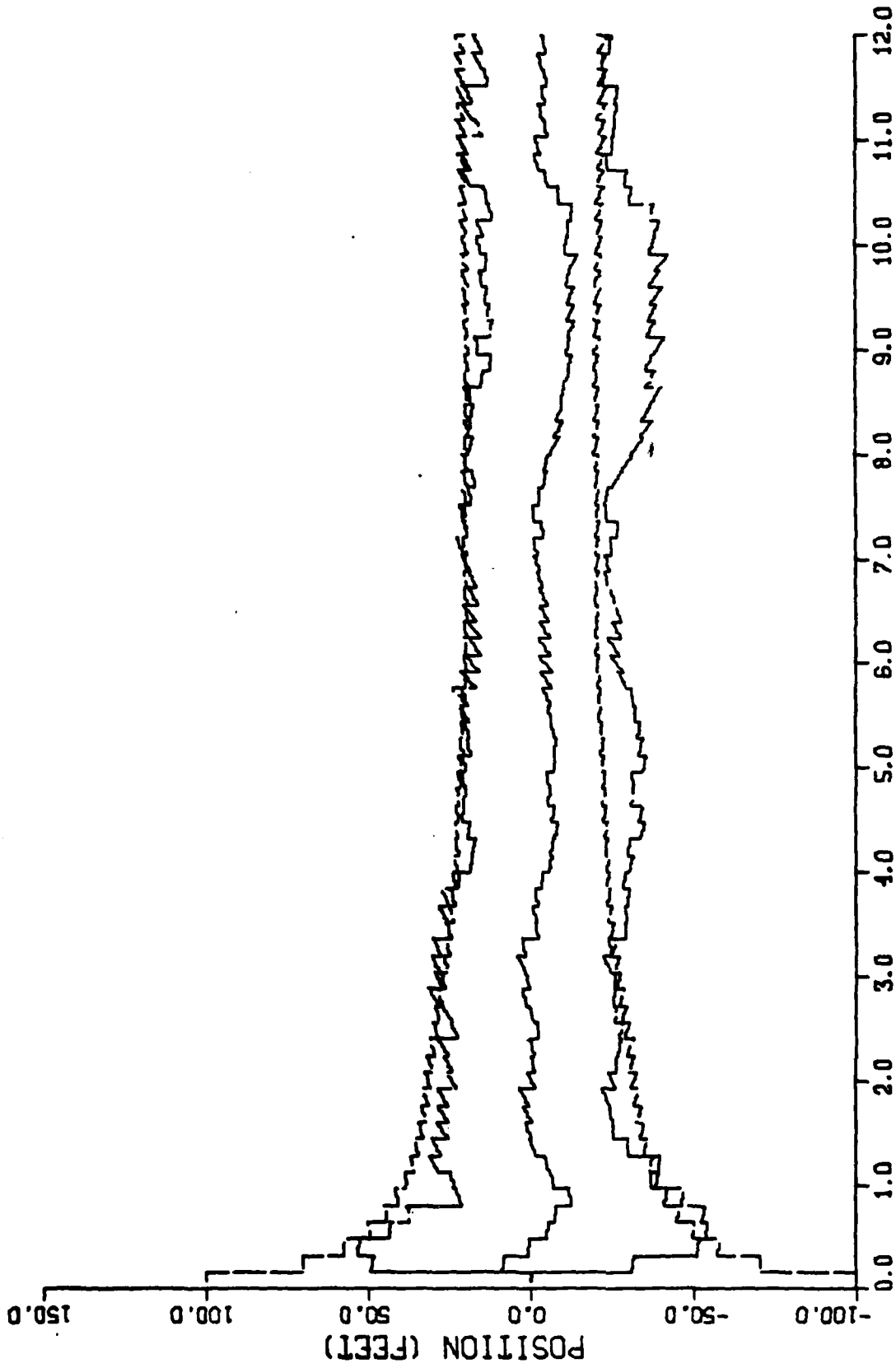


Figure F-10. Performance of the Constant Turn Rate Inertial Coordinate Filter Along the North-Axis for Trajectory 2 with a 0.16 Second Sample Period

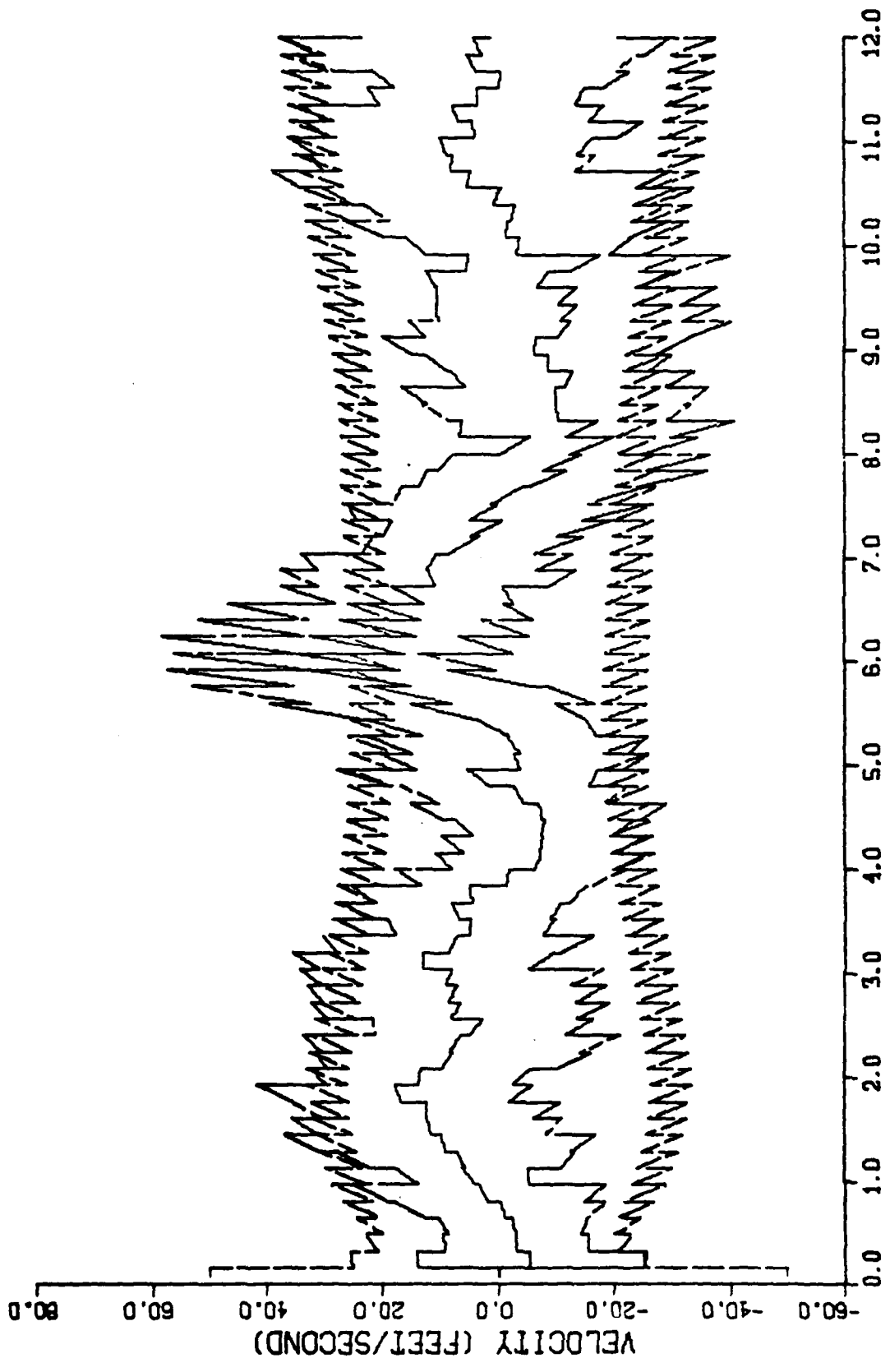


Figure F-11. Performance of the Constant Turn Rate Inertial Coordinate Filter Along the North-Axis for Trajectory 2 with a 0.16 Second Sample Period

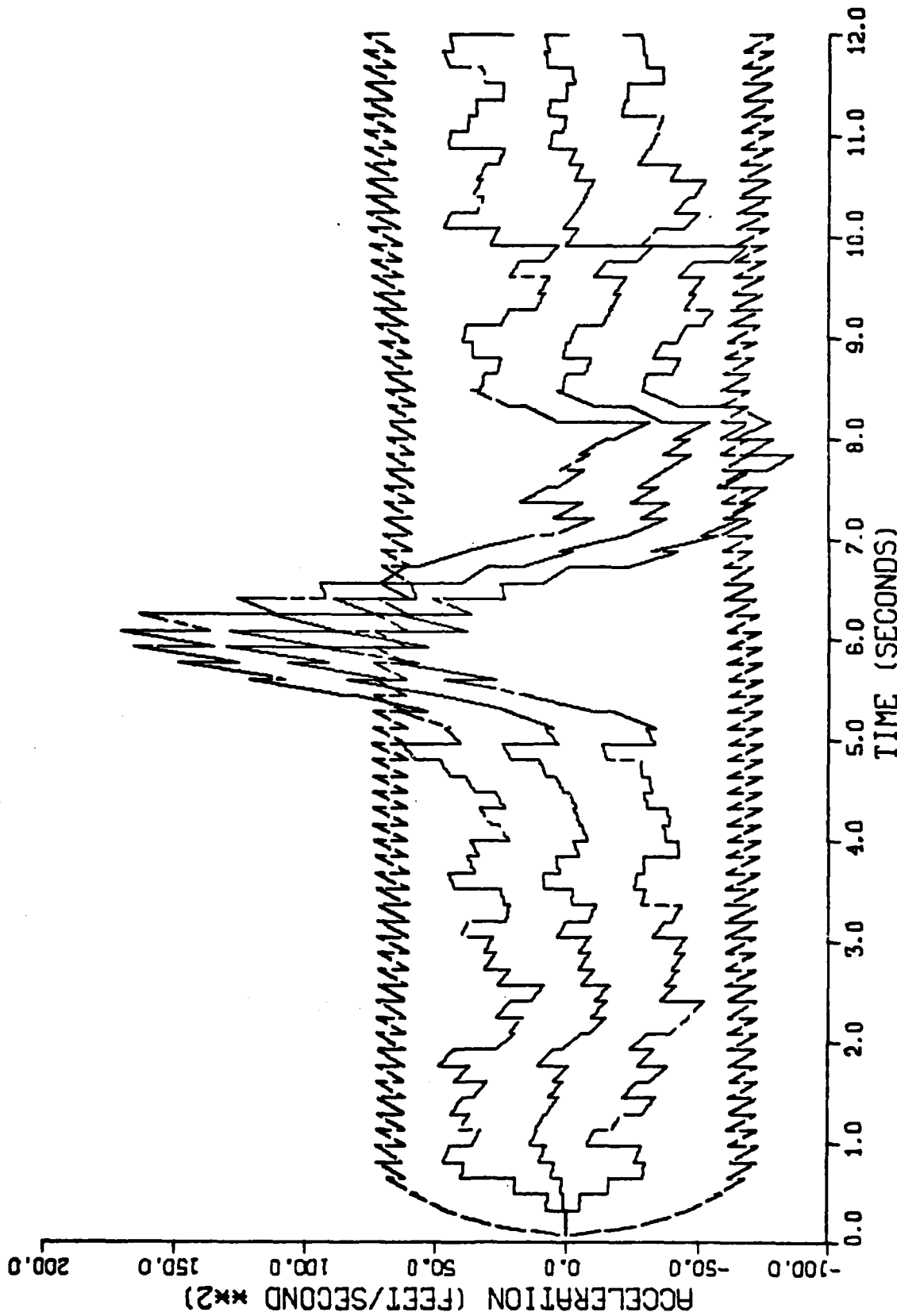


Figure F-12. Performance of the Constant Turn Rate Inertial Coordinate Filter Along the North-Axis for Trajectory 2 with a 0.16 Second Sample Period

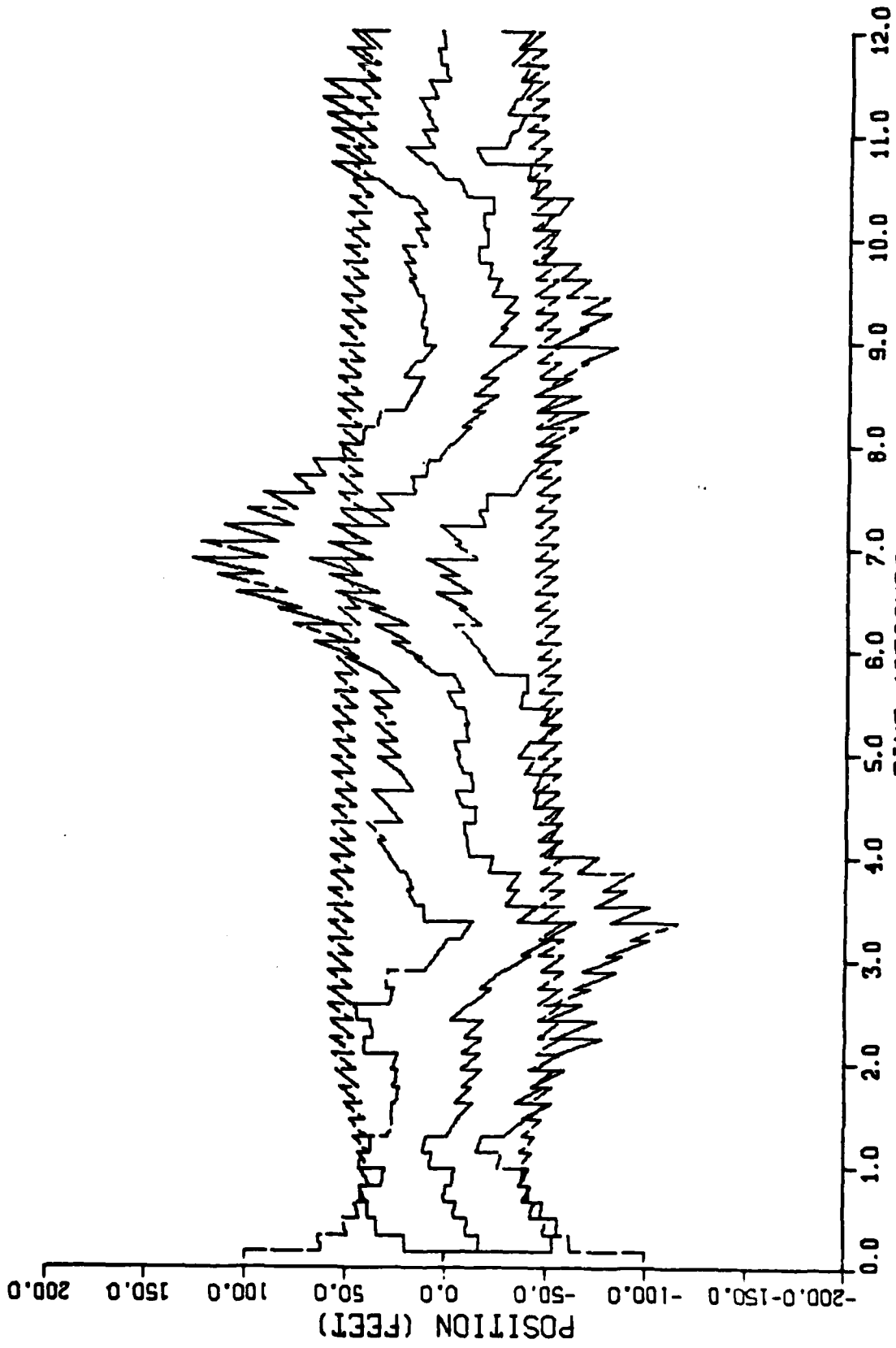


Figure F-13. Performance of the Constant Turn Rate Inertial Coordinate Filter Along the East-Axis for Trajectory 2 with a 0.16 Second Sample Period

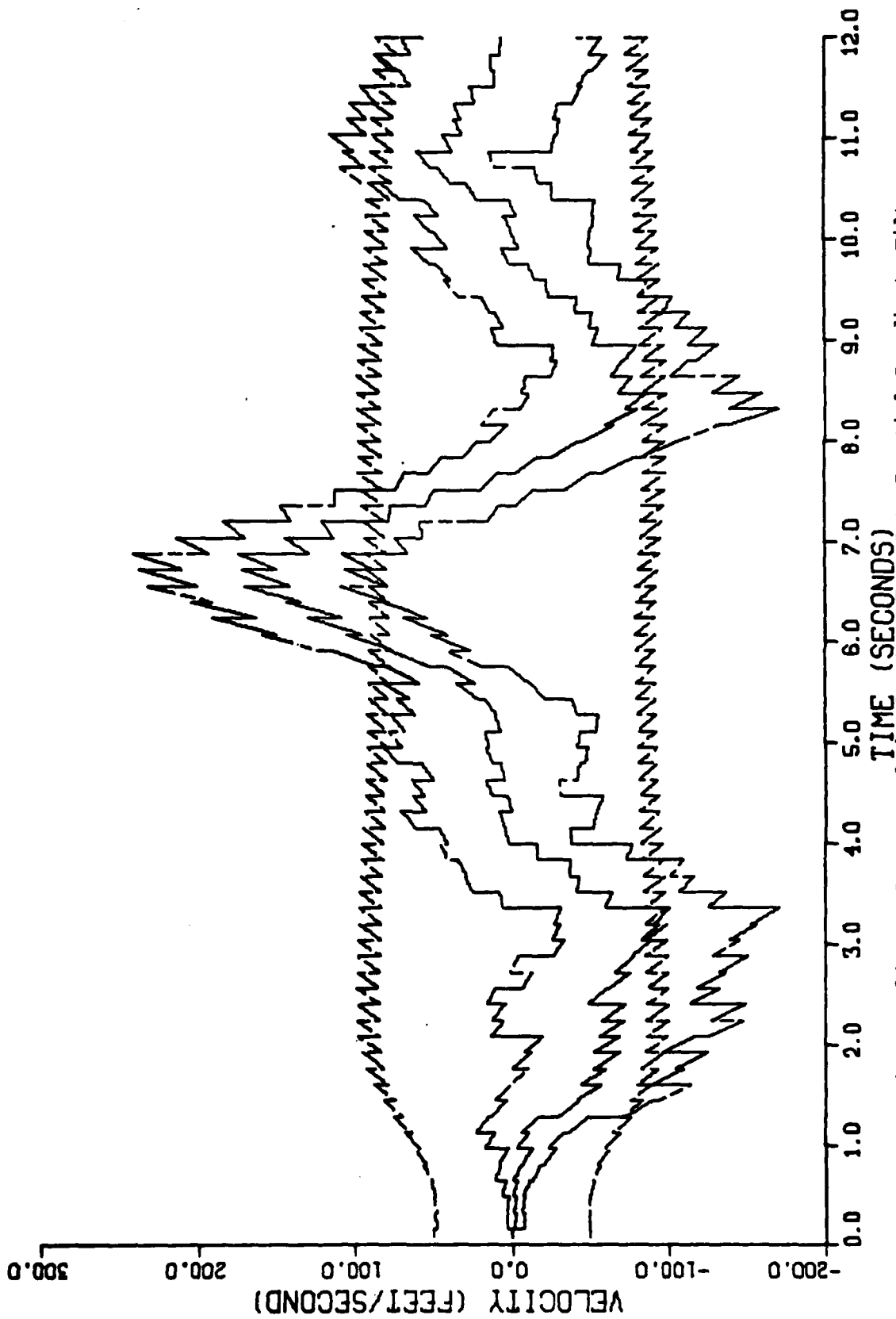


Figure F-14. Performance of the Constant Turn Rate Inertial Coordinate Filter Along the East-Axis for Trajectory 2 with a 0.16 Second Sample Period

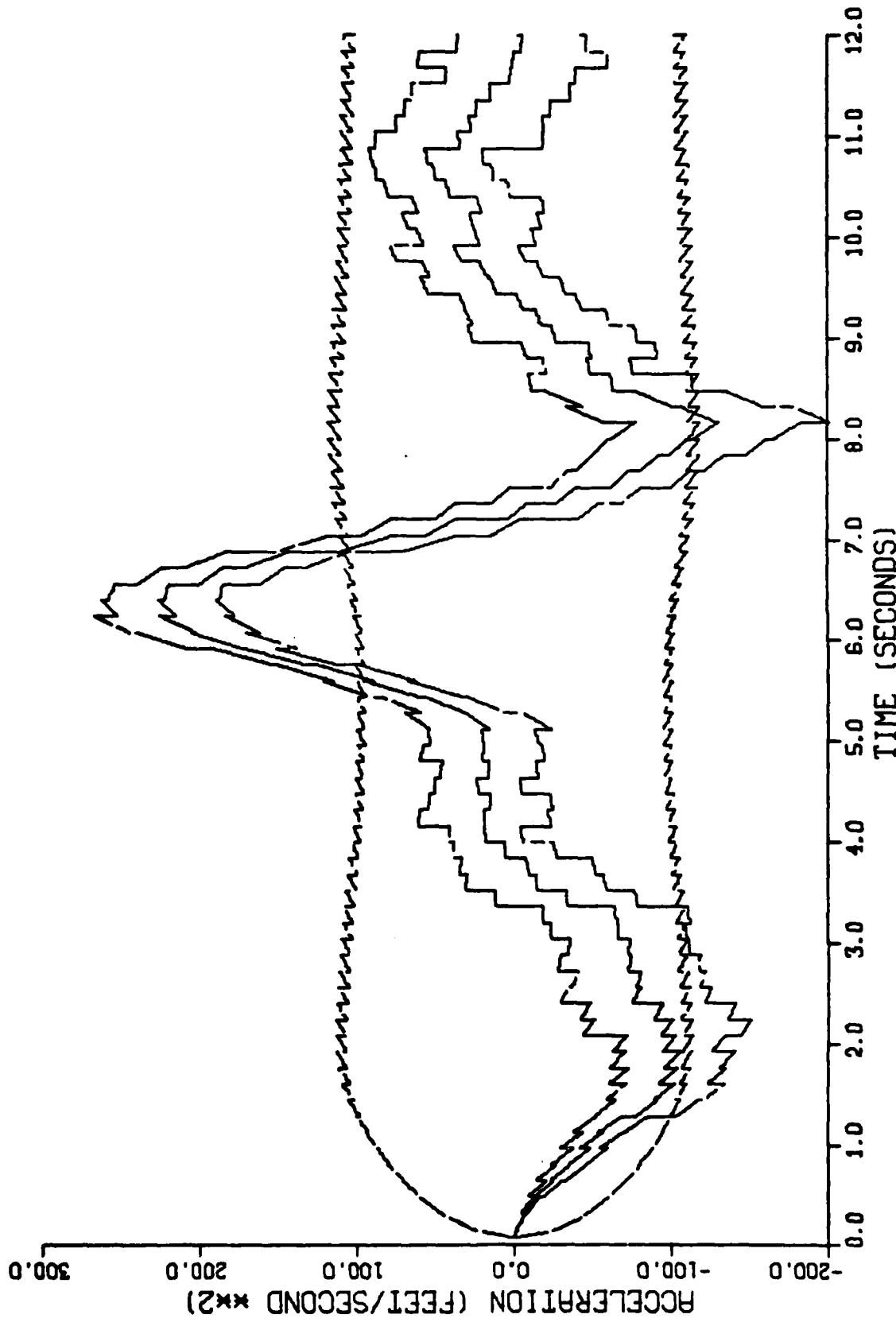


Figure F-15. Performance of the Constant Turn Rate Inertial Coordinate Filter Along the East-Axis for Trajectory 2 with a 0.16 Second Sample Period

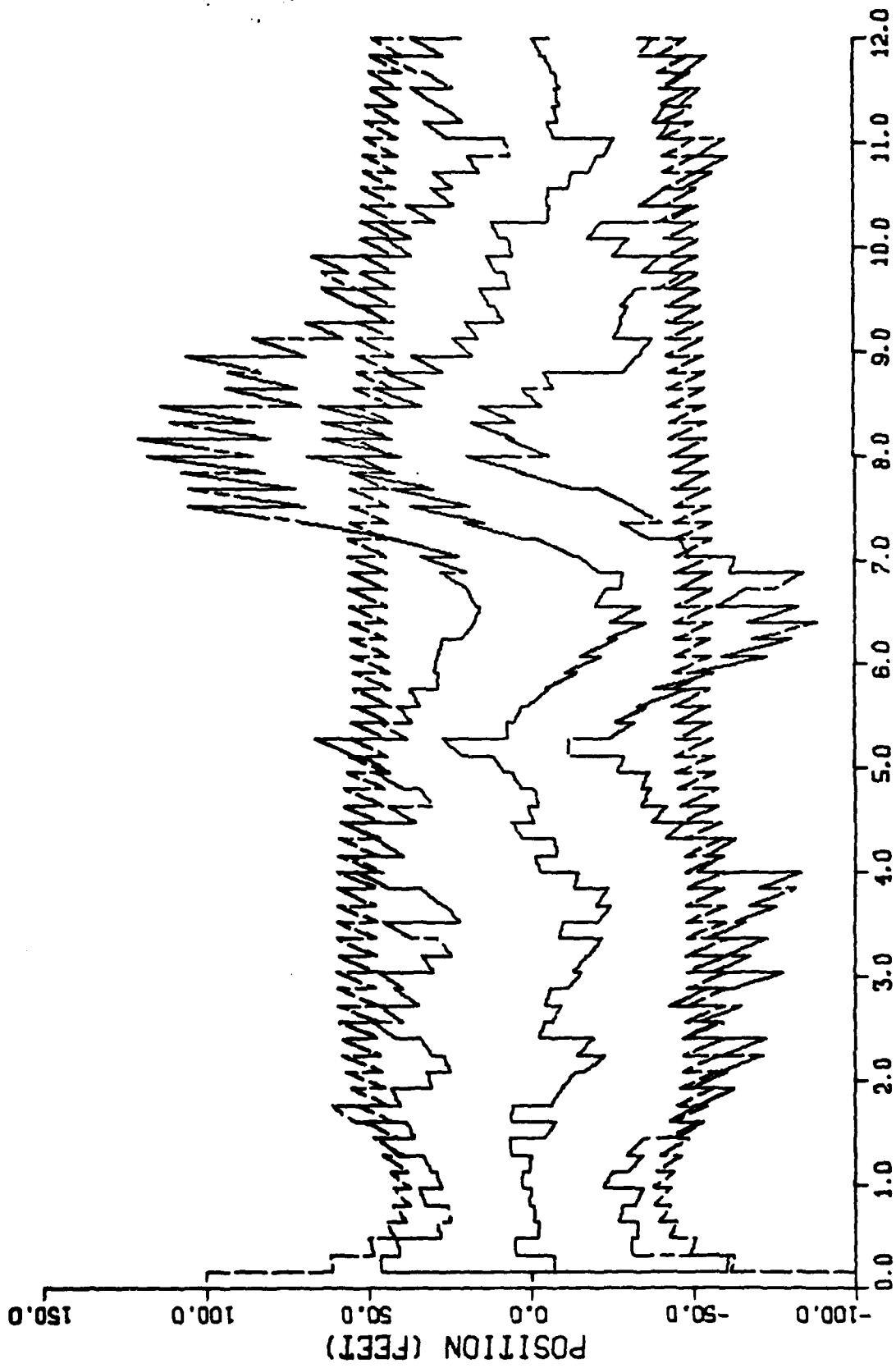


Figure F-16. Performance of the Constant Turn Rate Inertial Coordinate Filter Along the Down-Axis for Trajectory 2 with a 0.16 Second Sample Period

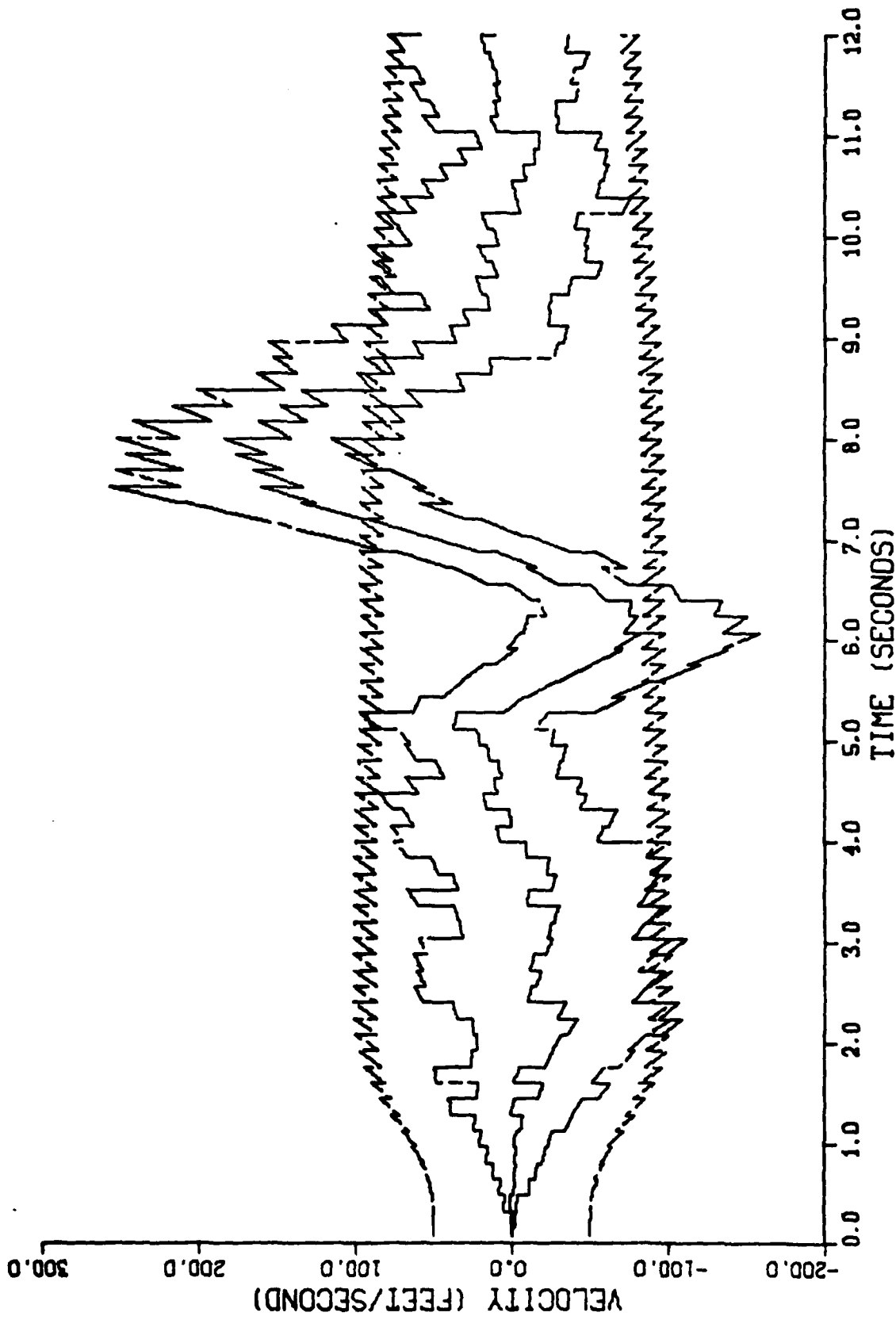


Figure F-17. Performance of the Constant Turn Rate Inertial Coordinate Filter Along the Down-Axis for Trajectory 2 with a 0.16 Second Sample Period

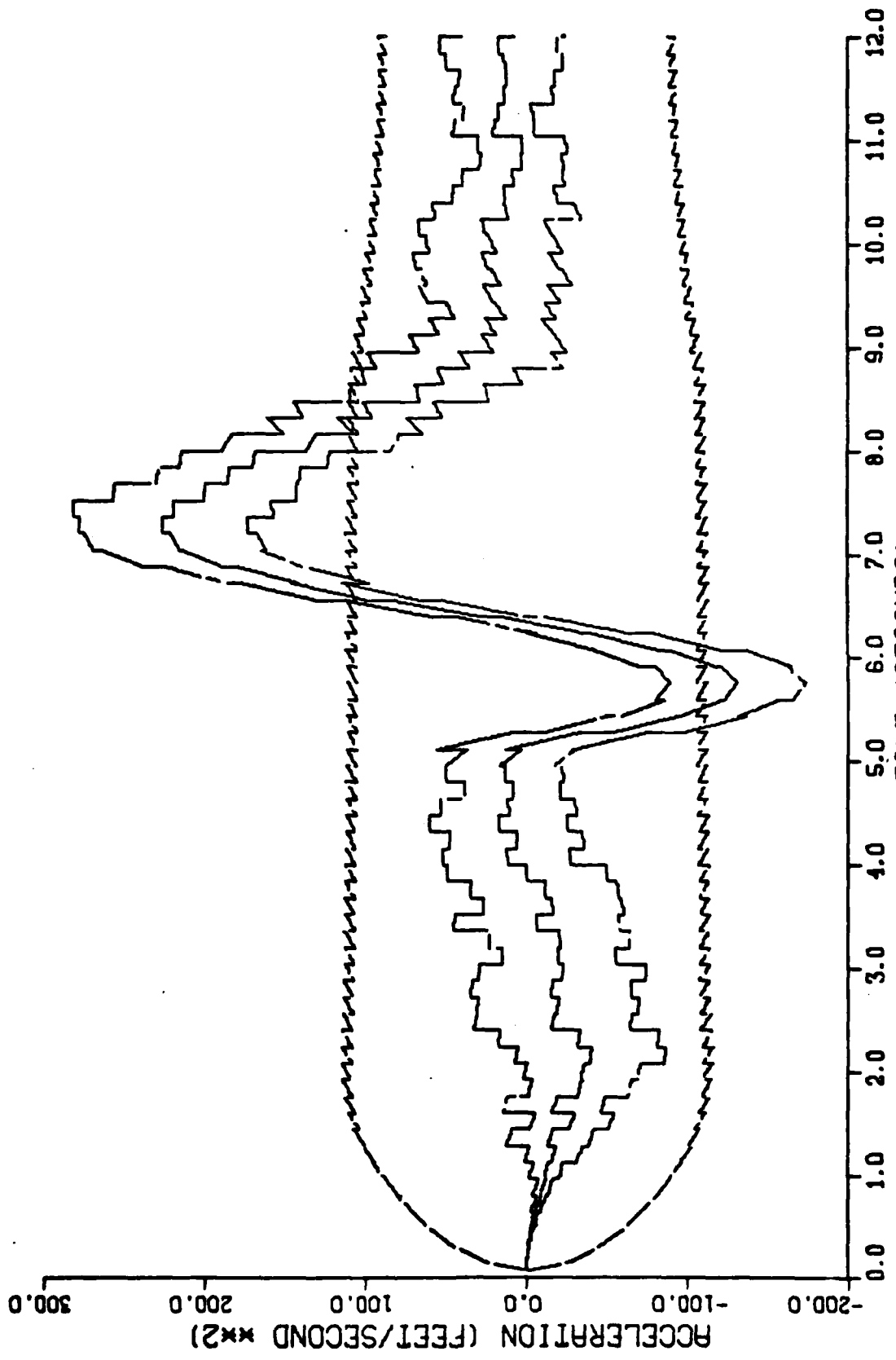


Figure F-18. Performance of the Constant Turn Rate Inertial Coordinate Filter
 Along the Down-Axis for Trajectory 2 with a 0.16 Second Sample Period

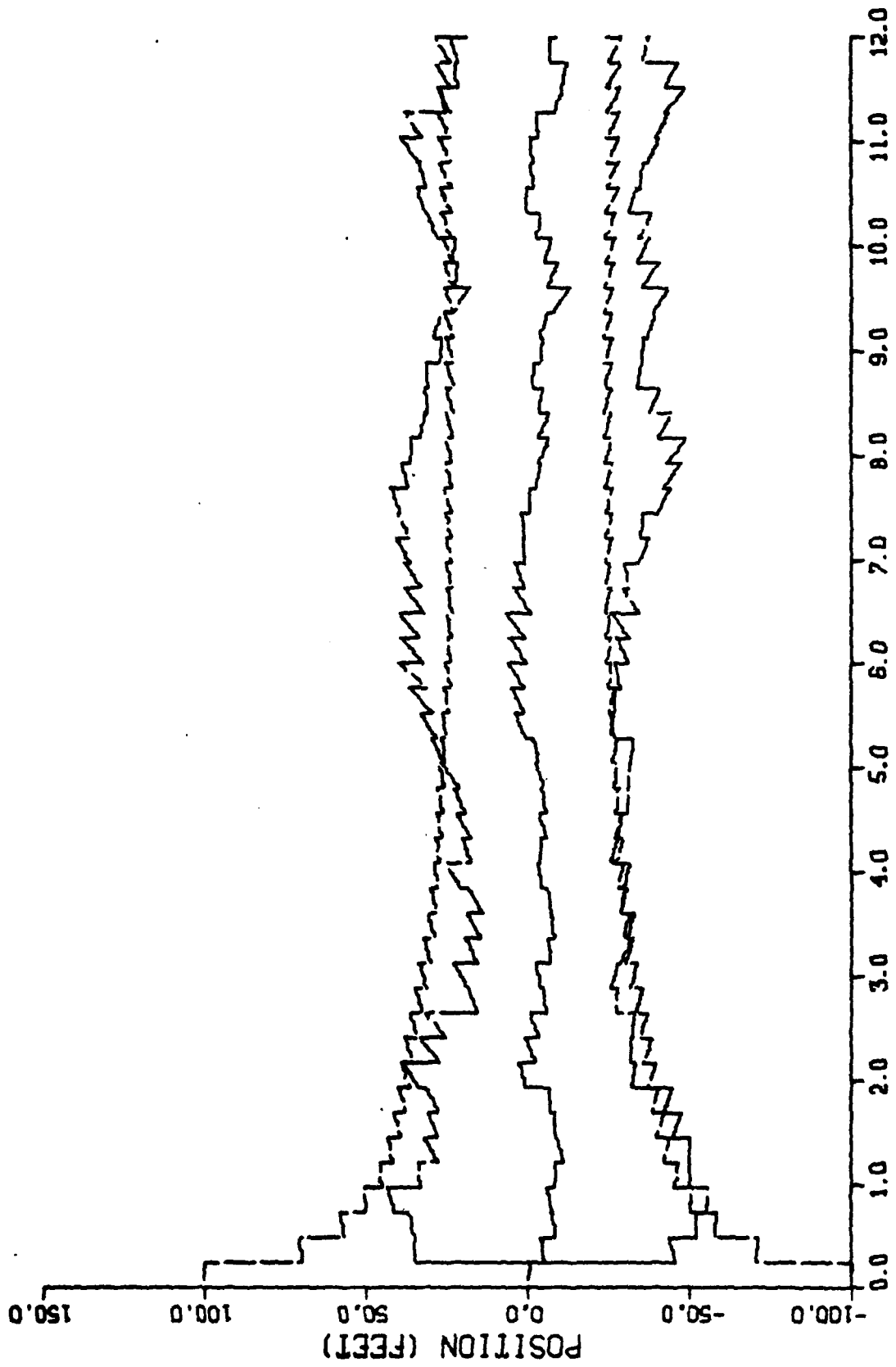


Figure F-19. Performance of the Constant Turn Rate Inertial Coordinate Filter Along the North-Axis for Trajectory 2 with a 0.24 Second Sample Period

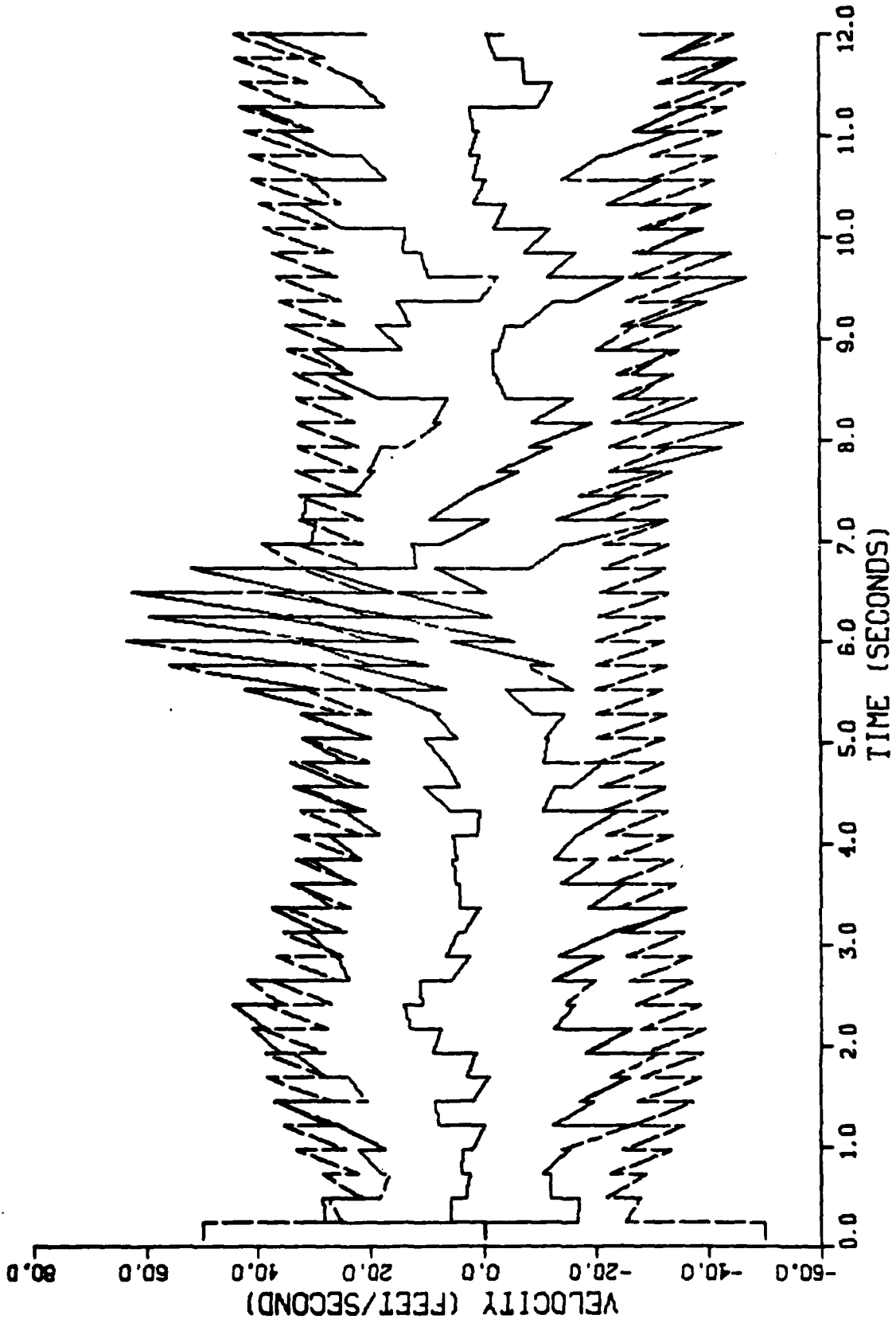


Figure F-20. Performance of the Constant Turn Rate Inertial Coordinate Filter Along the North-Axis for Trajectory 2 with a 0.24 Second Sample Period

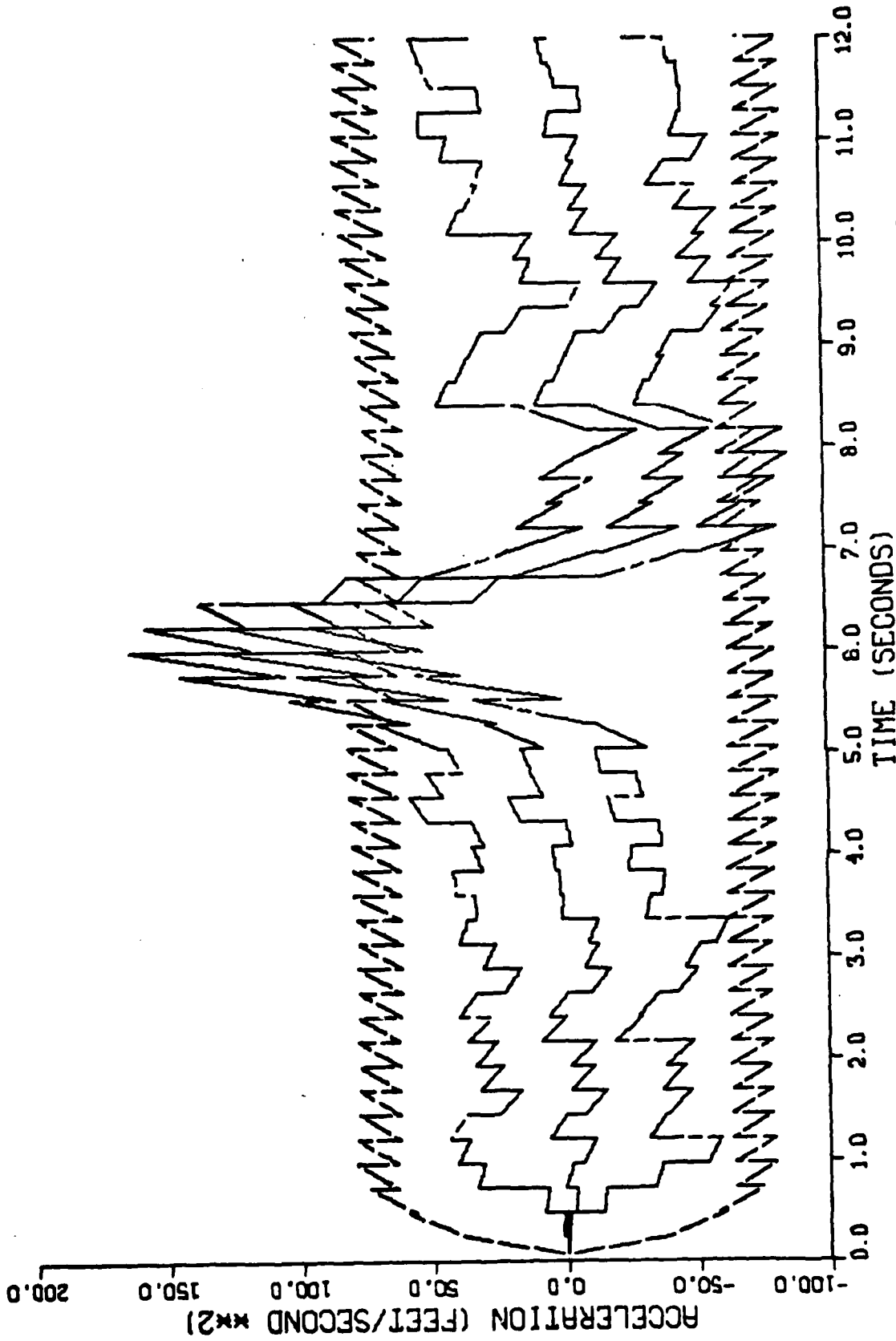


Figure F-21. Performance of the Constant Turn Rate Inertial Coordinate Filter Along the North-Axis for Trajectory 2 with a 0.24 Second Sample Period

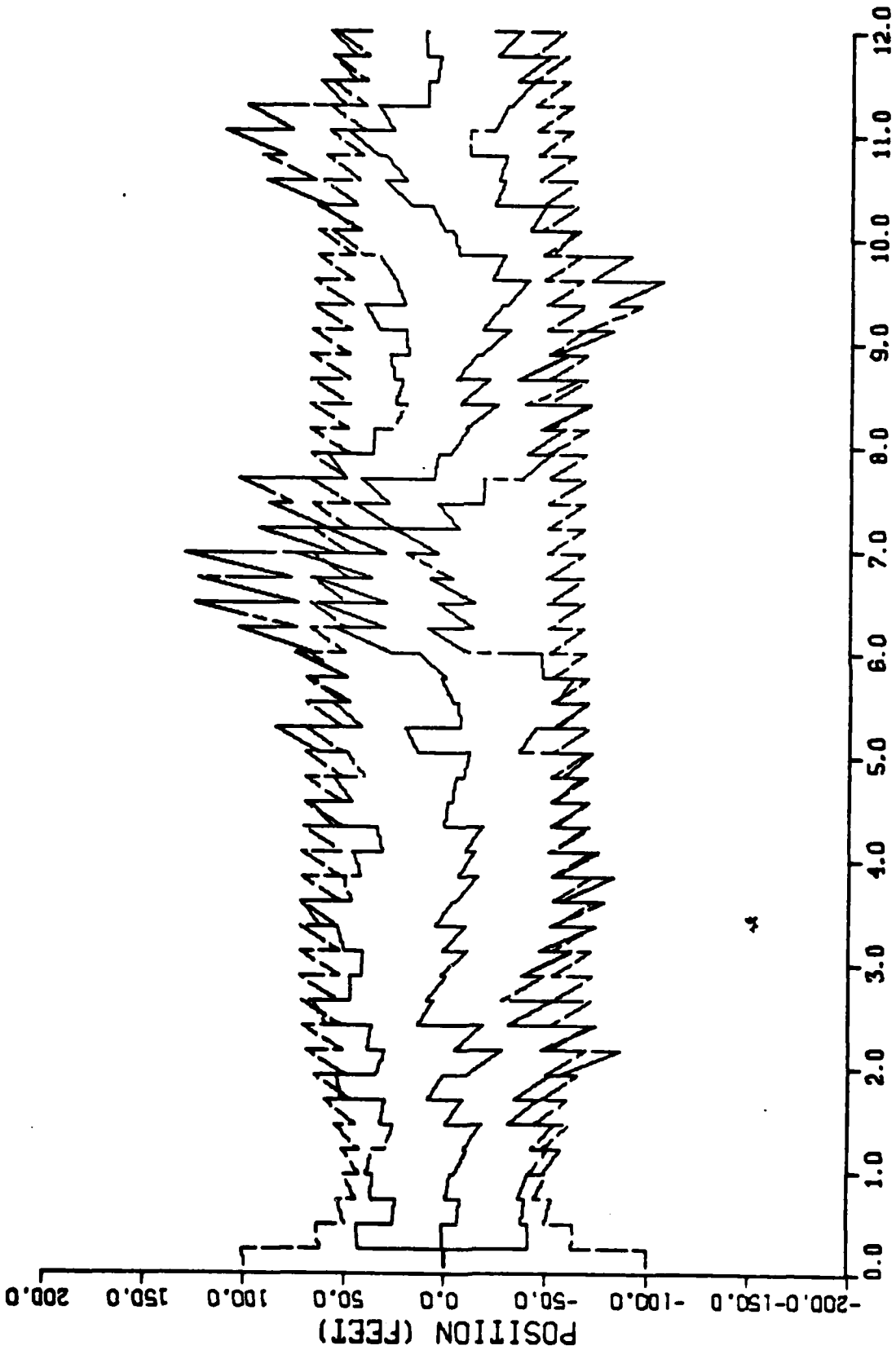


Figure F-22. Performance of the Constant Turn Rate Inertial Coordinate Filter Along the East-Axis for Trajectory 2 with a 0.24 Second Sample Period

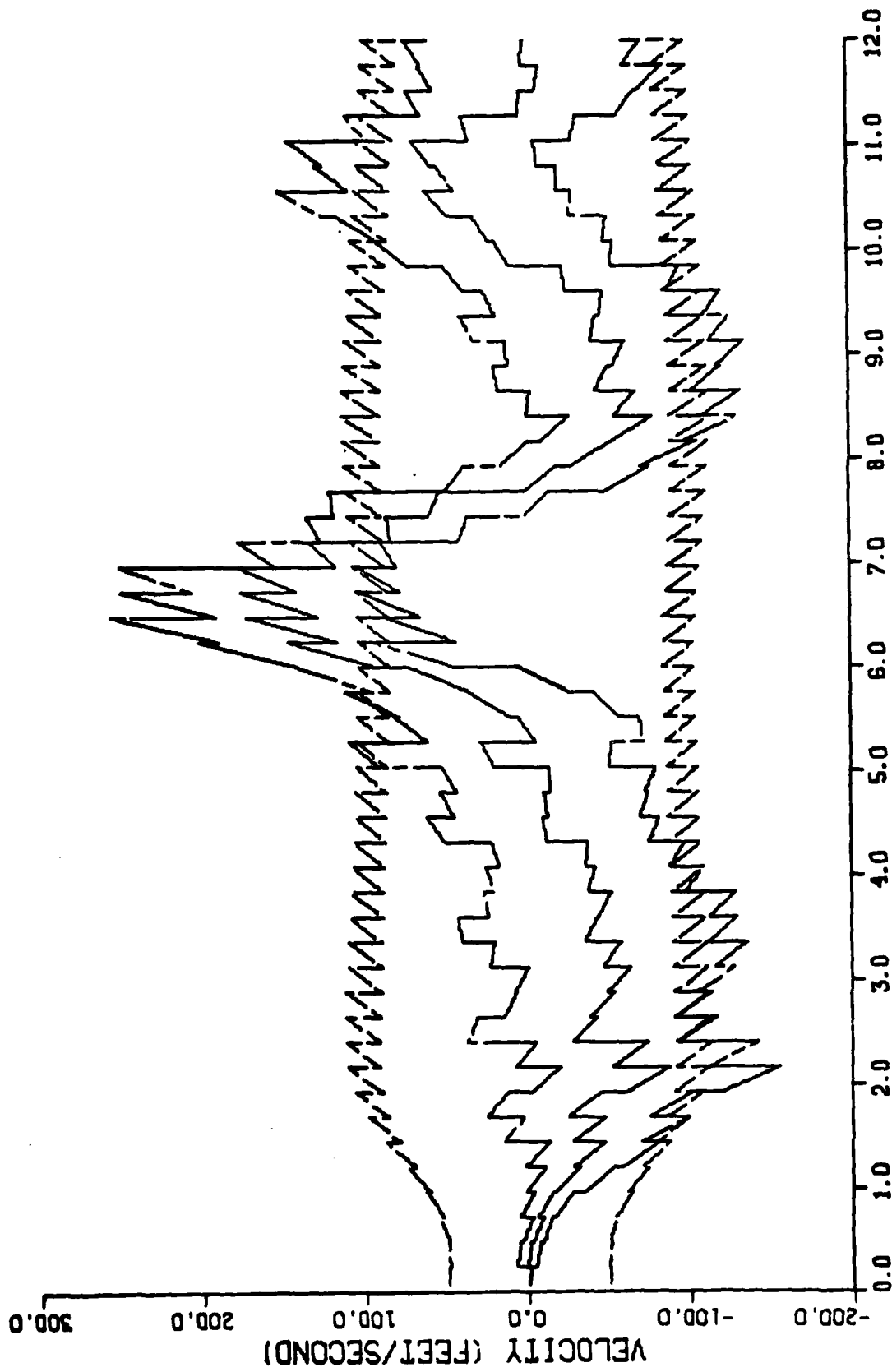


Figure F-23. Performance of the Constant Turn Rate Inertial Coordinate Filter Along the East-Axis for Trajectory 2 with a 0.24 Second Sample Period

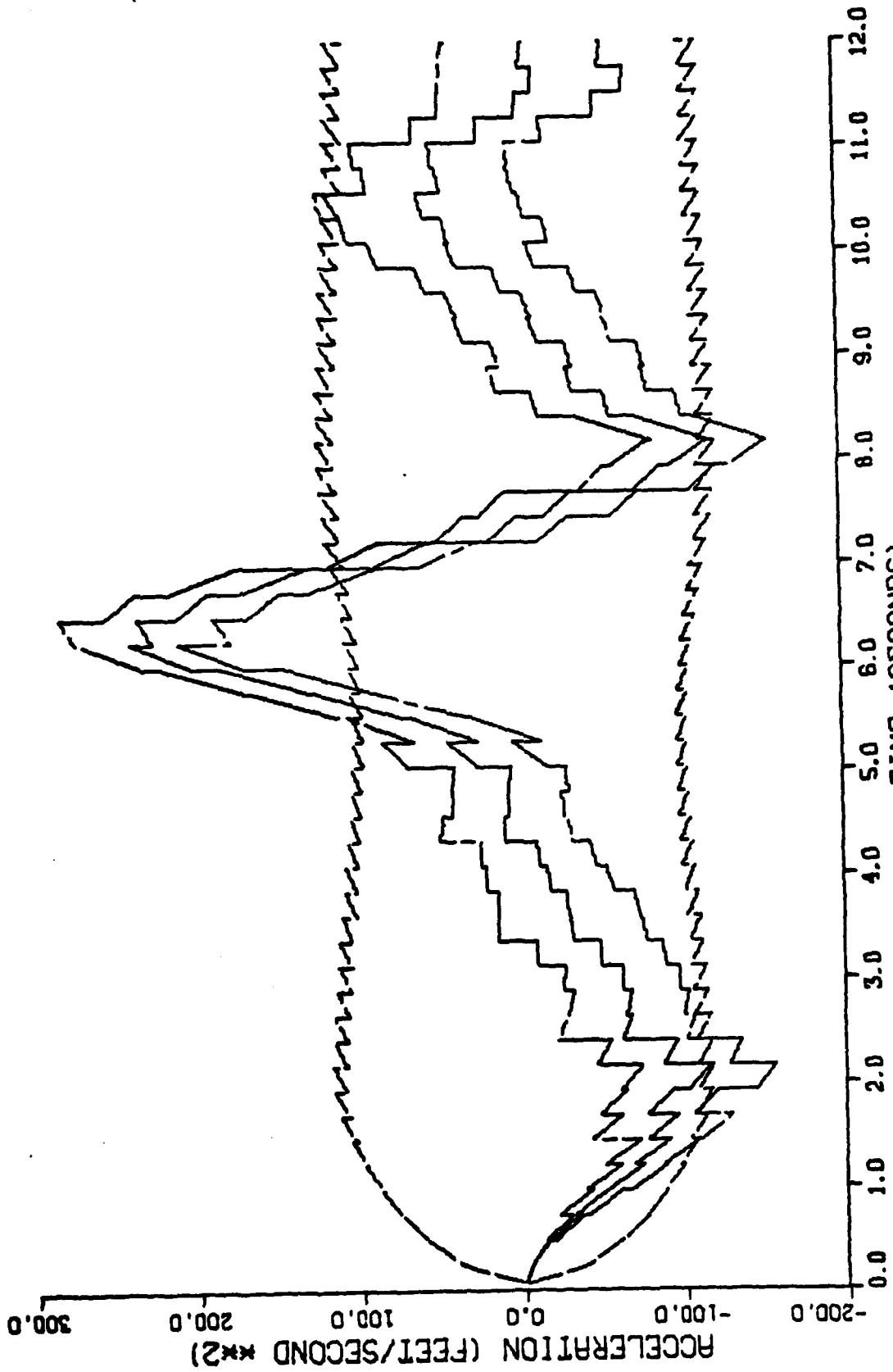


Figure F-24. Performance of the Constant Turn Rate Inertial Coordinate Filter Along the East-Axis for Trajectory 2 with a 0.24 Second Sample Period

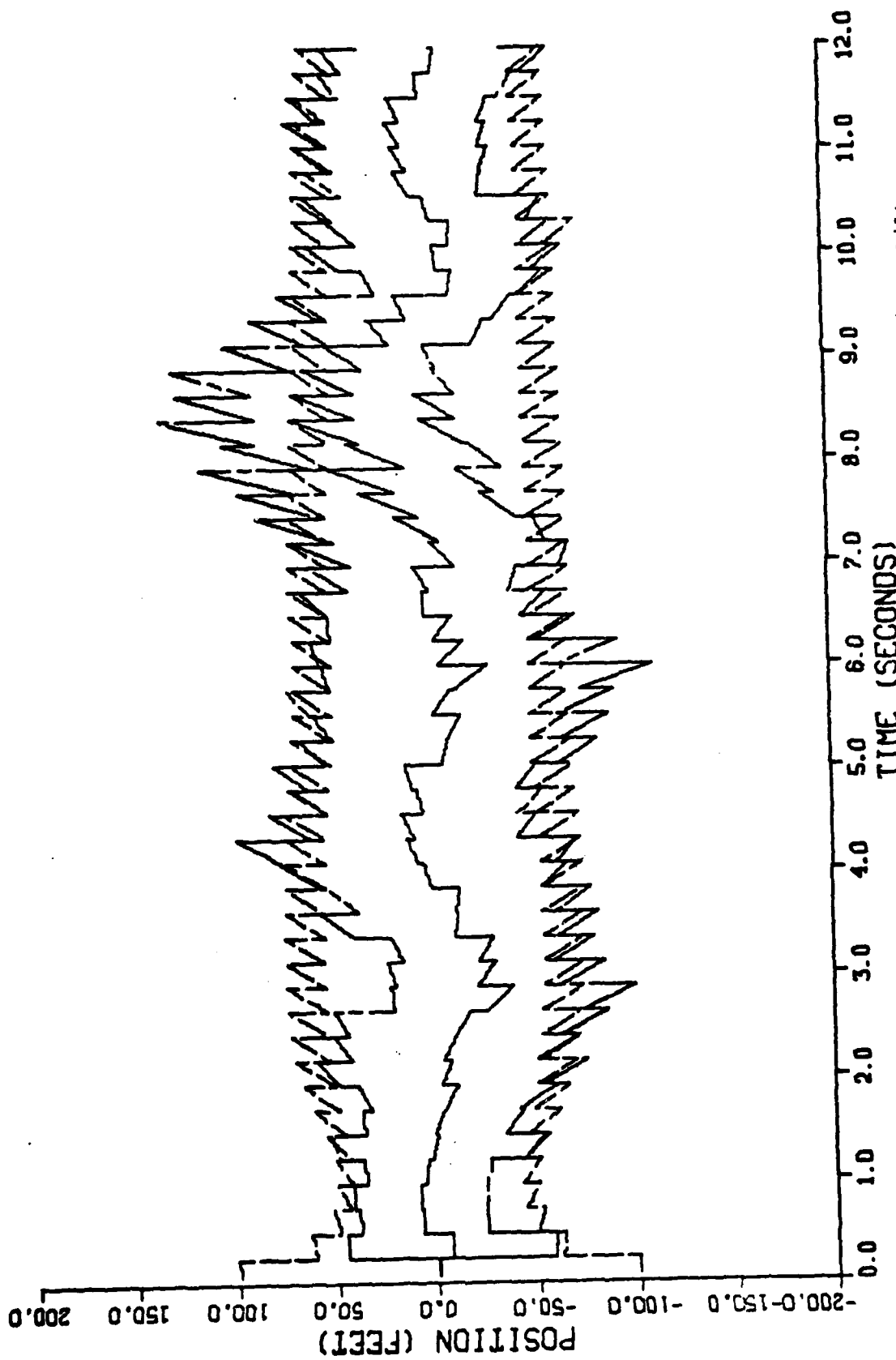


Figure F-25. Performance of the Constant Turn Rate Inertial Coordinate Filter Along the Down-Axis for Trajectory 2 with a 0.24 Second Sample Period

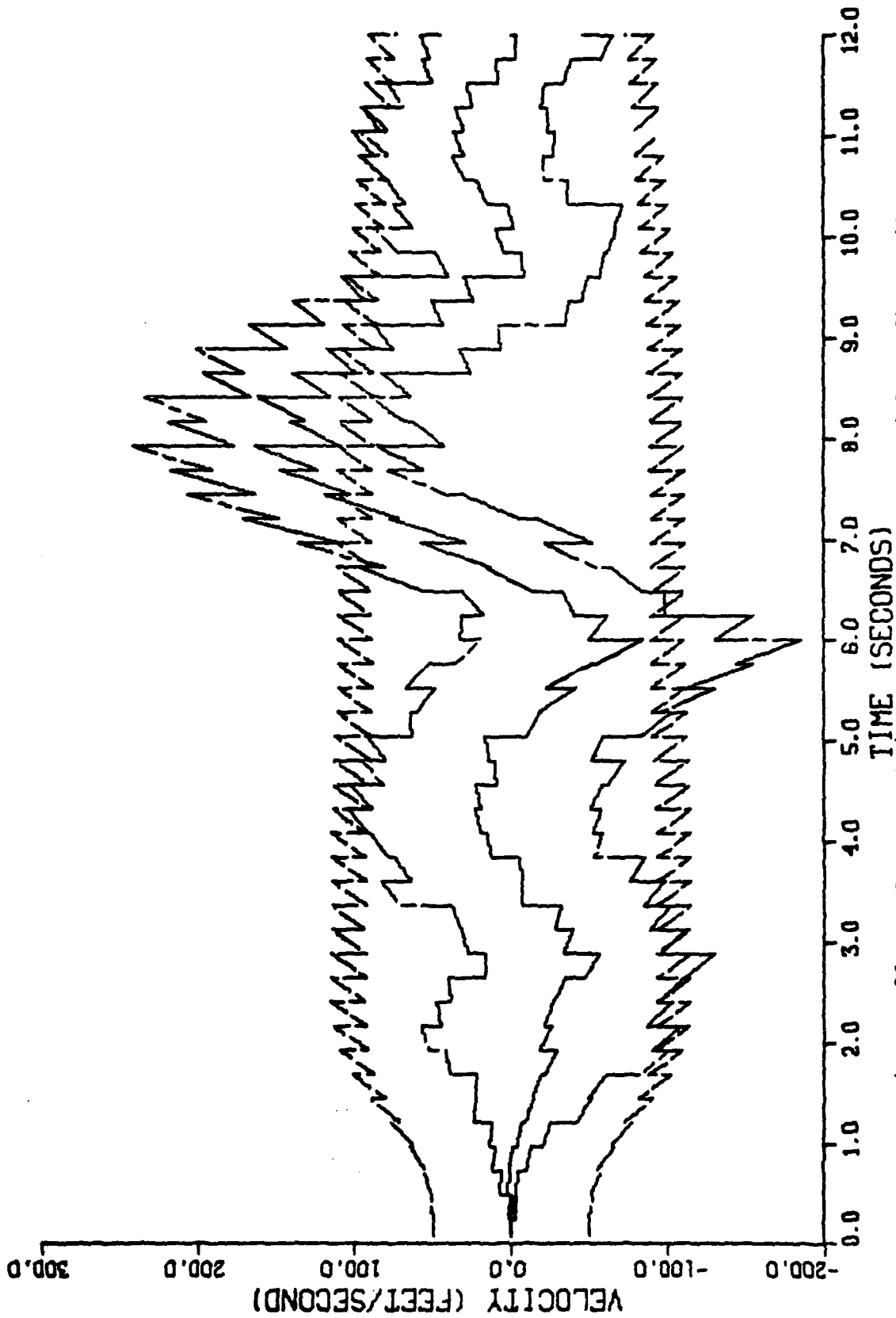


Figure F-26. Performance of the Constant Turn Rate Inertial Coordinate Filter Along the Down-Axis for Trajectory 2 with a 0.24 Second Sample Period

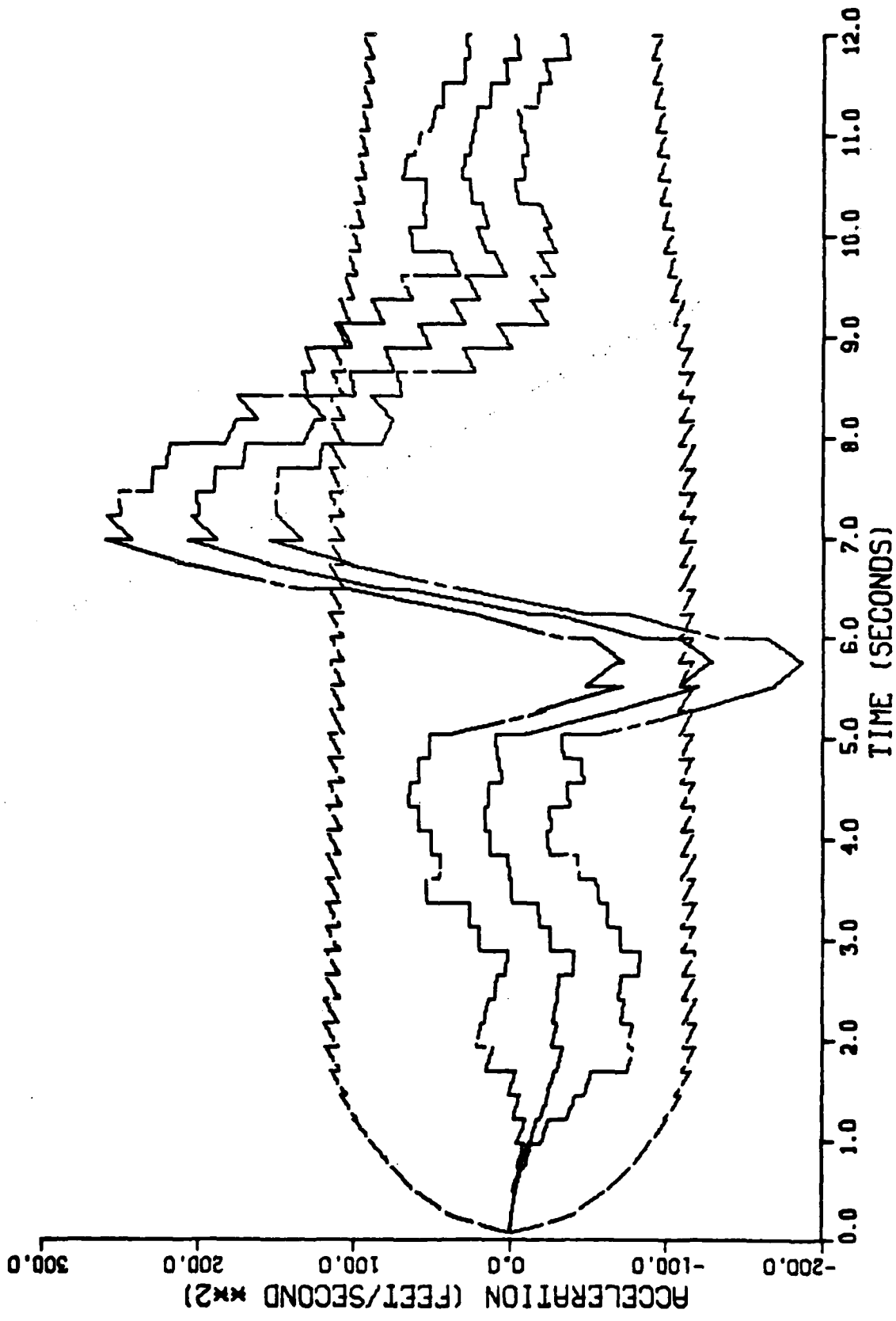


Figure F-27. Performance of the Constant Turn Rate Inertial Coordinate Filter Along the Down-Axis for Trajectory 2 with a 0.24 Second Sample Period

APPENDIX G

Graphical Results of the Effect of Variations in
the Range Measurement Noise on the Performance of
the Constant Turn Rate Inertial Coordinate Filter

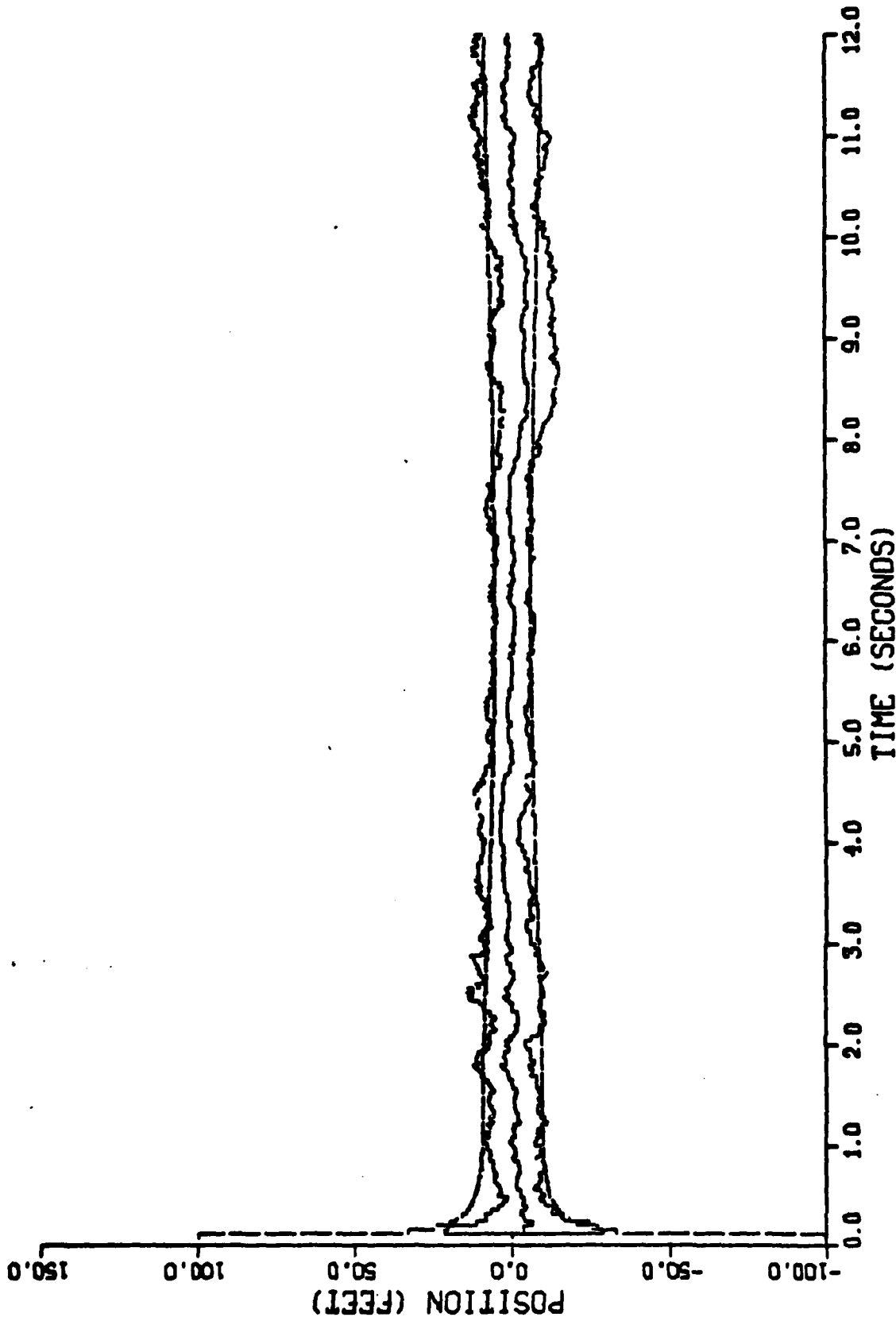


Figure G-1. Performance of the Constant Turn Rate Inertial Coordinate Filter Along the North-Axis for Trajectory 2 with a Range Measurement Noise Variance of 1000 feet²

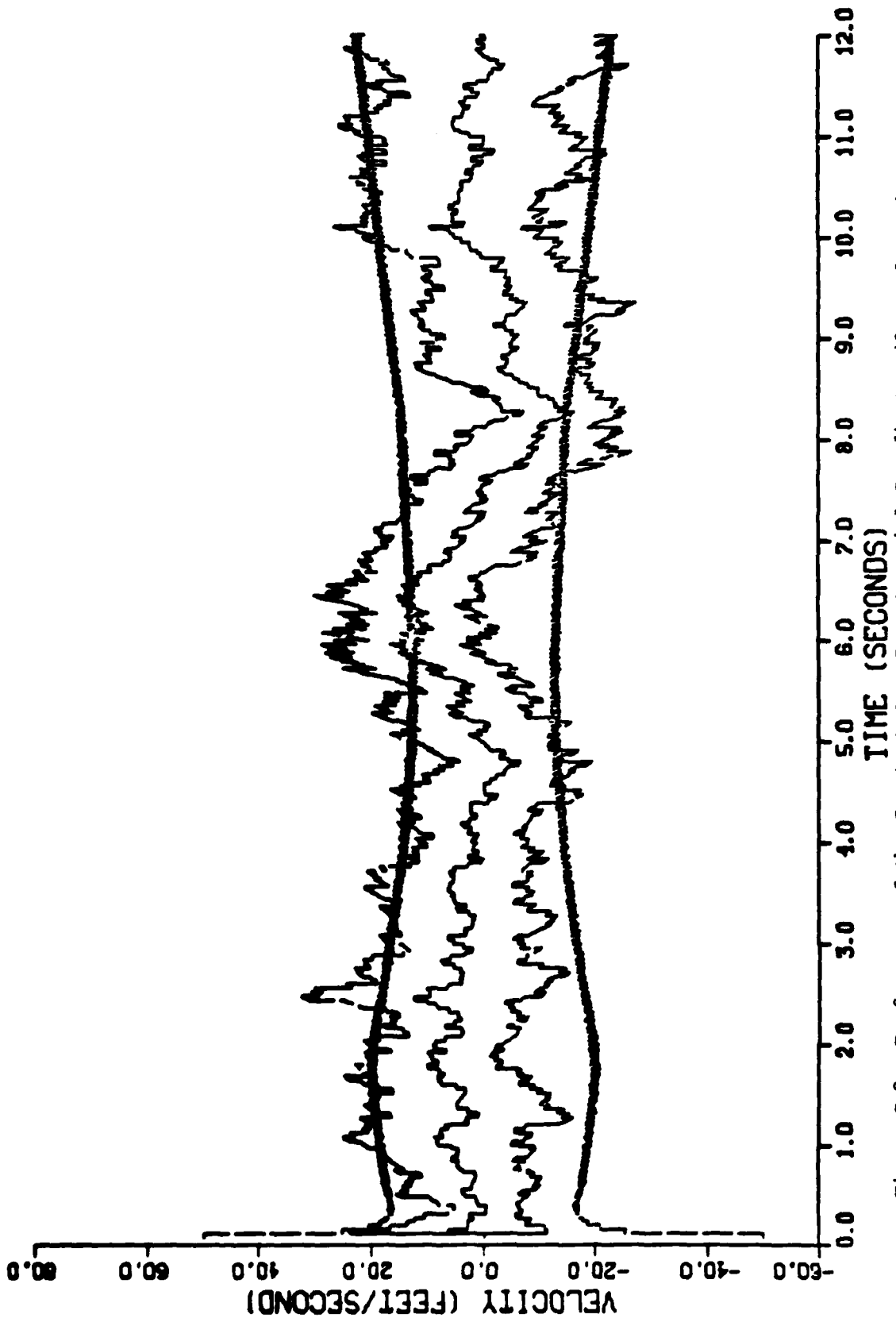


Figure G-2. Performance of the Constant Turn Rate Inertial Coordinate Filter Along the North-Axis for Trajectory 2 with a Range Measurement Noise Variance of 1000 Feet²

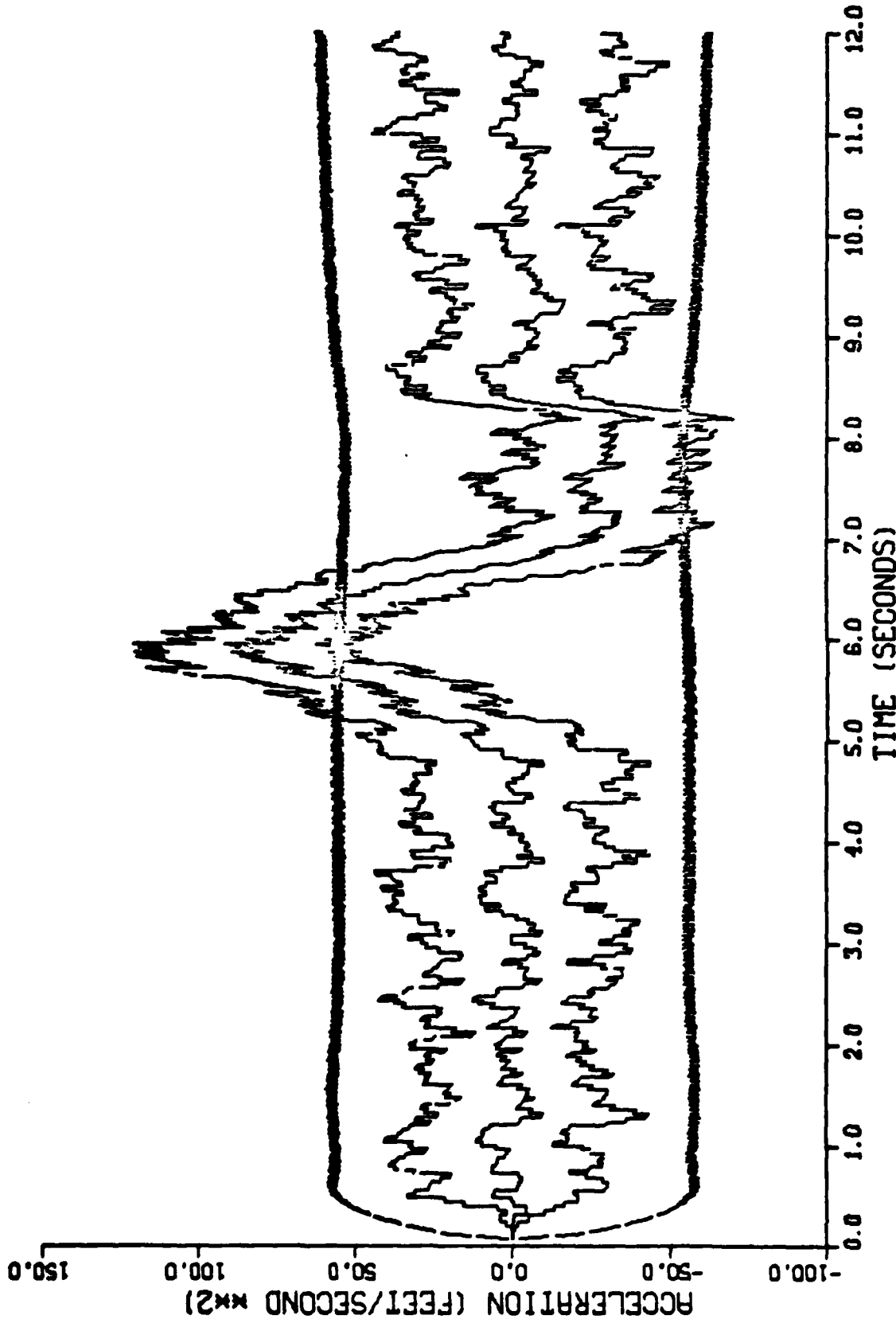


Figure G-3. Performance of the Constant Turn Rate Inertial Coordinate Filter Along the North-Axis for Trajectory 2 with a Range Measurement Noise Variance of 1000 Feet²

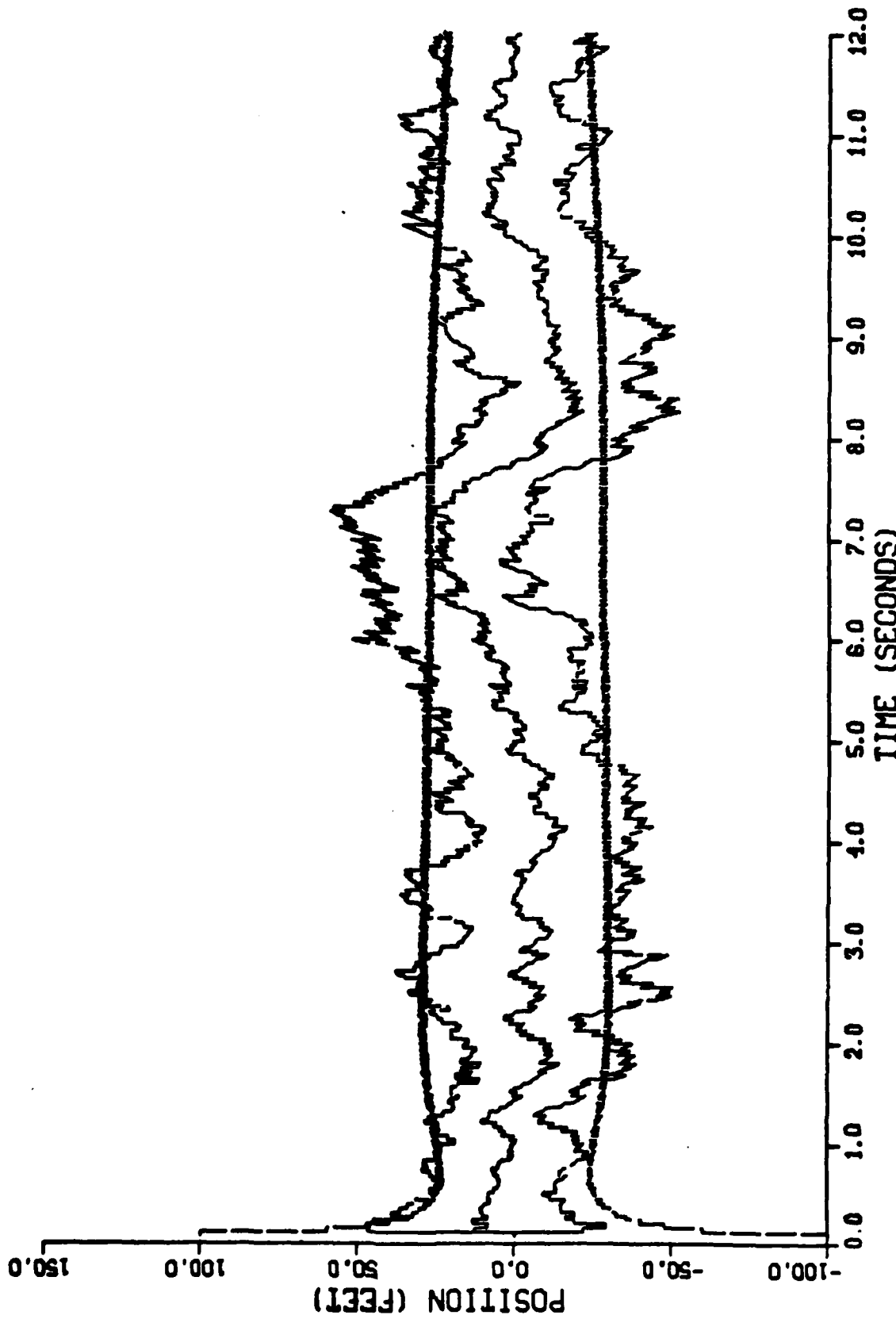


Figure G-4. Performance of the Constant Turn Rate Inertial Coordinate Filter Along the East-Axis for Trajectory 2 with a Range Measurement Noise Variance of 1000 Feet²

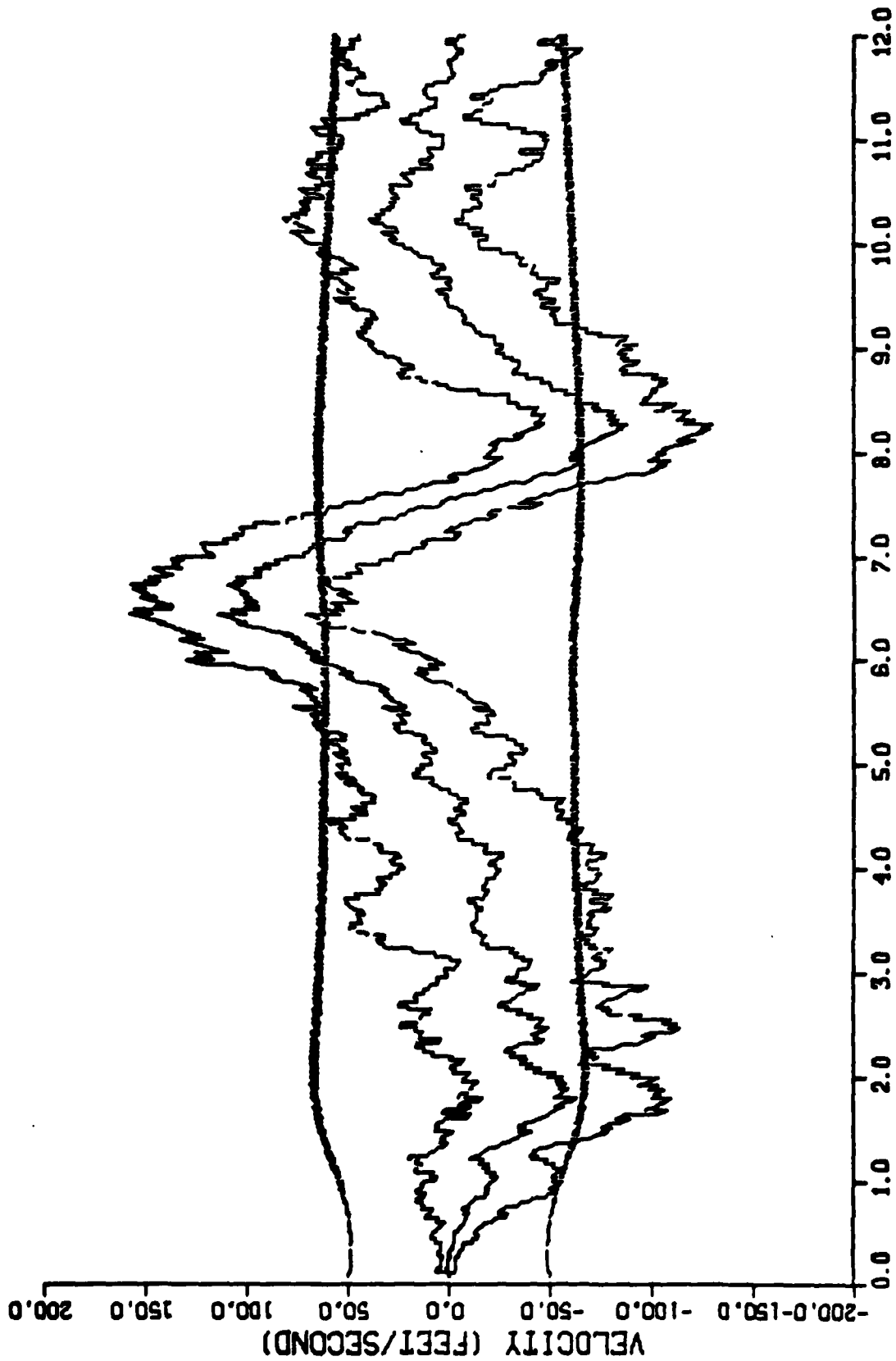


Figure G-5. Performance of the Constant Turn Rate Inertial Coordinate Filter Along the East-Axis for Trajectory 2 with a Range Measurement Noise Variance of 1000 Feet²

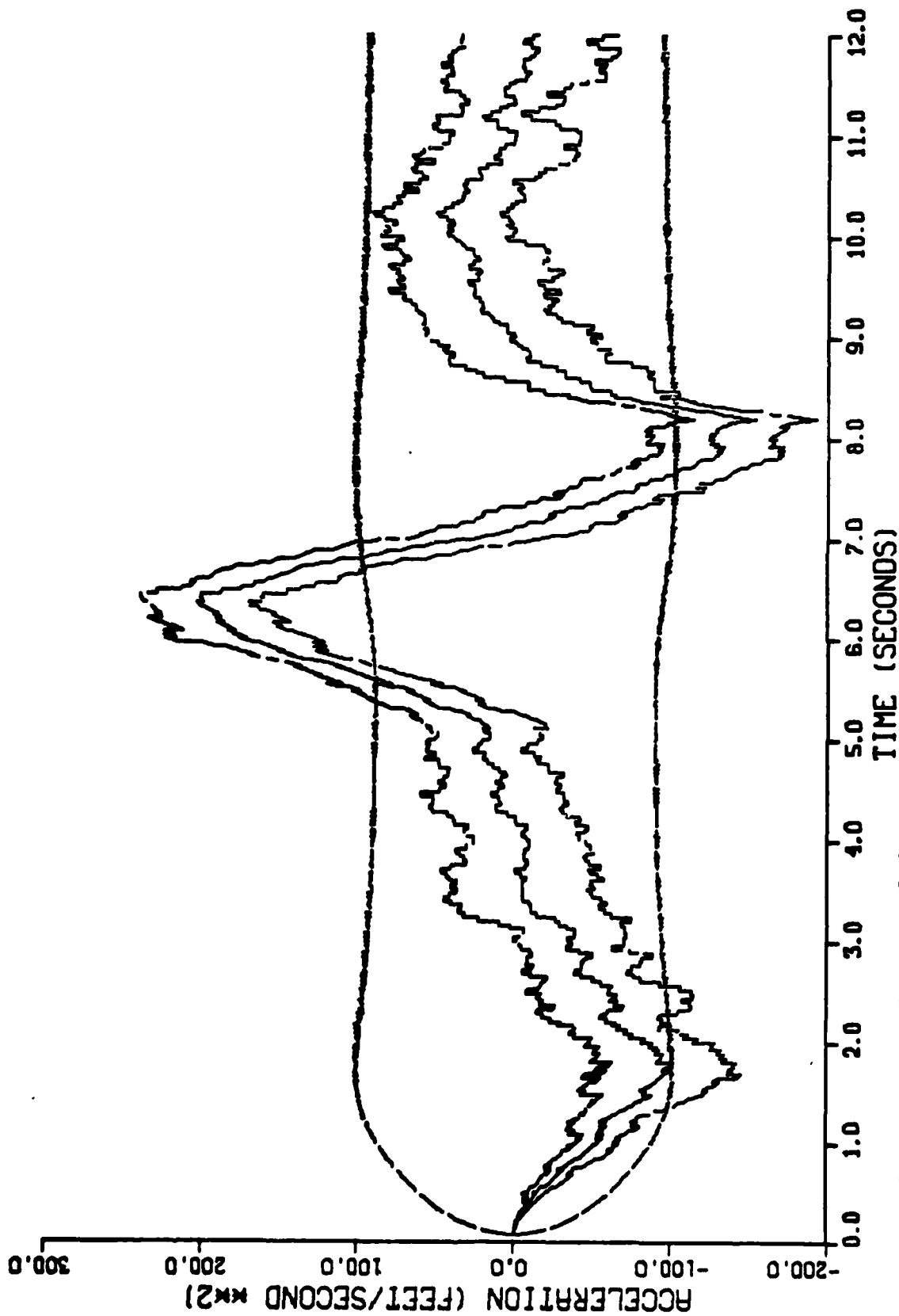


Figure G-6. Performance of the Constant Turn Rate Inertial Coordinate Filter Along the East-Axis for Trajectory 2 with a Range Measurement Noise Variance of 1000 Feet²

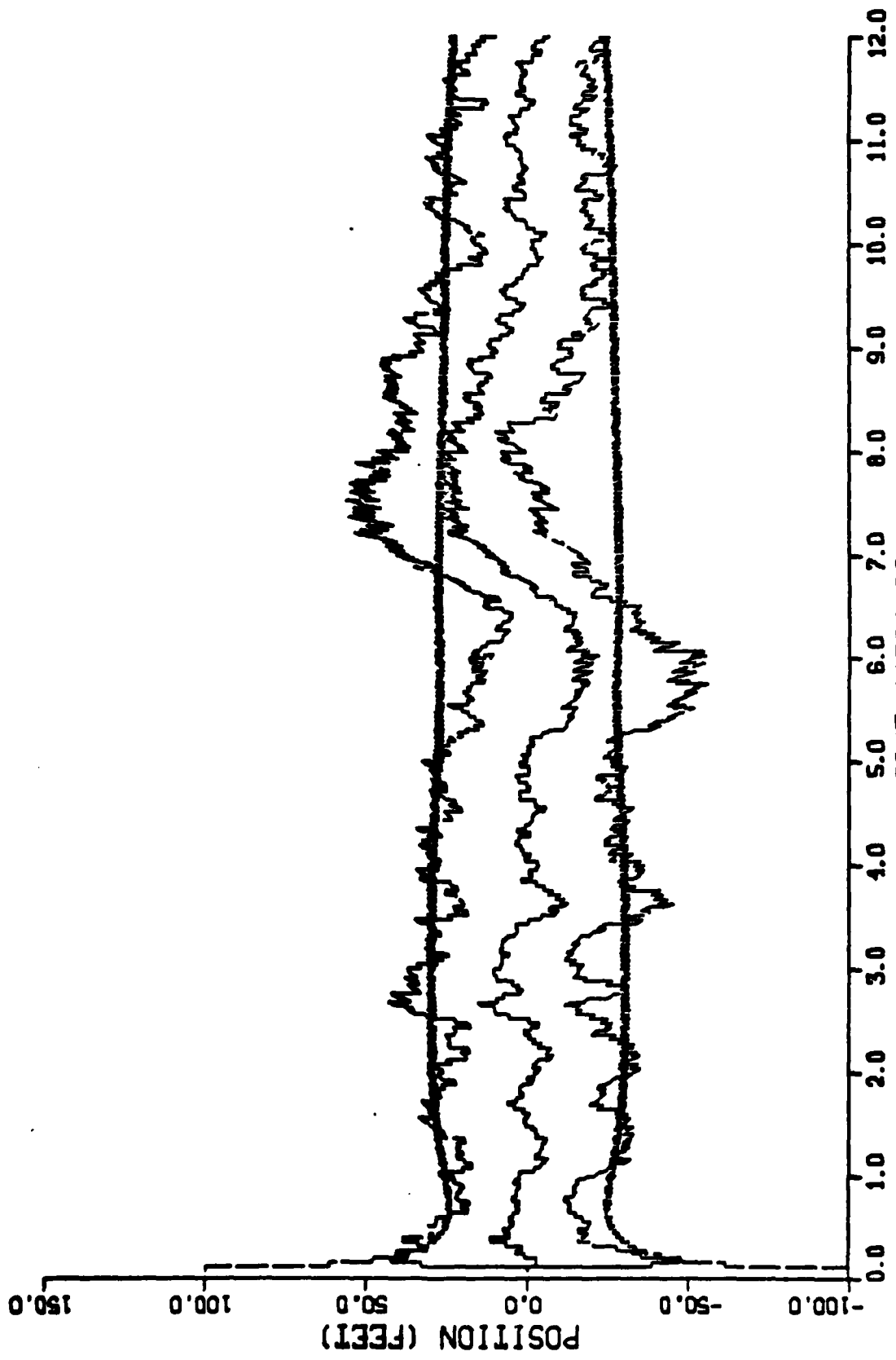


Figure G-7. Performance of the Constant Turn Rate Inertial Coordinate Filter Along the Down-Axis for Trajectory 2 with a Range Measurement Noise Variance of 1000 Feet²

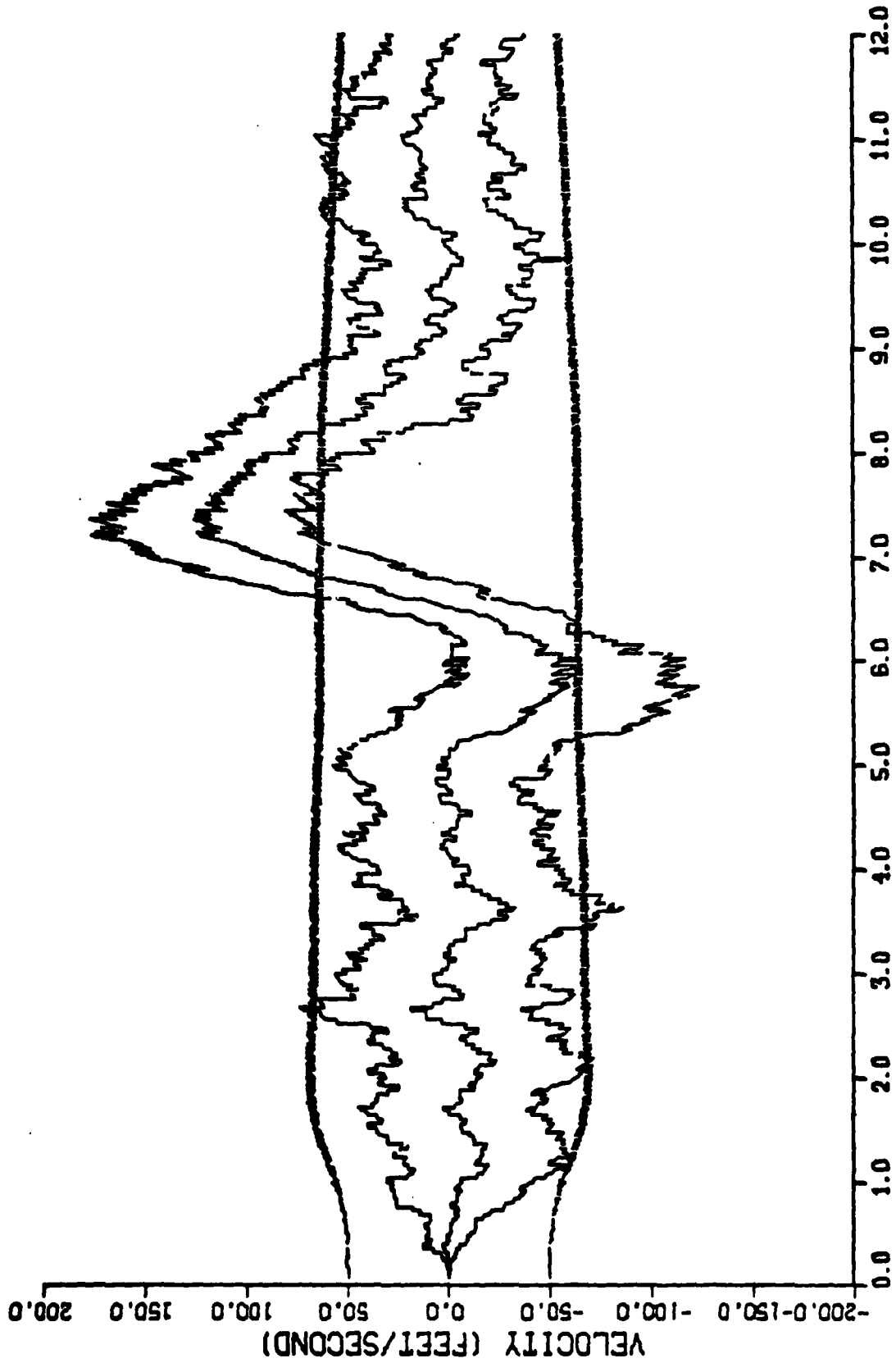


Figure G-8. Performance of the Constant Turn Rate Inertial Coordinate Filter Along the Down-Axis for Trajectory 2 with a Range Measurement Noise Variance of 1000 Feet²

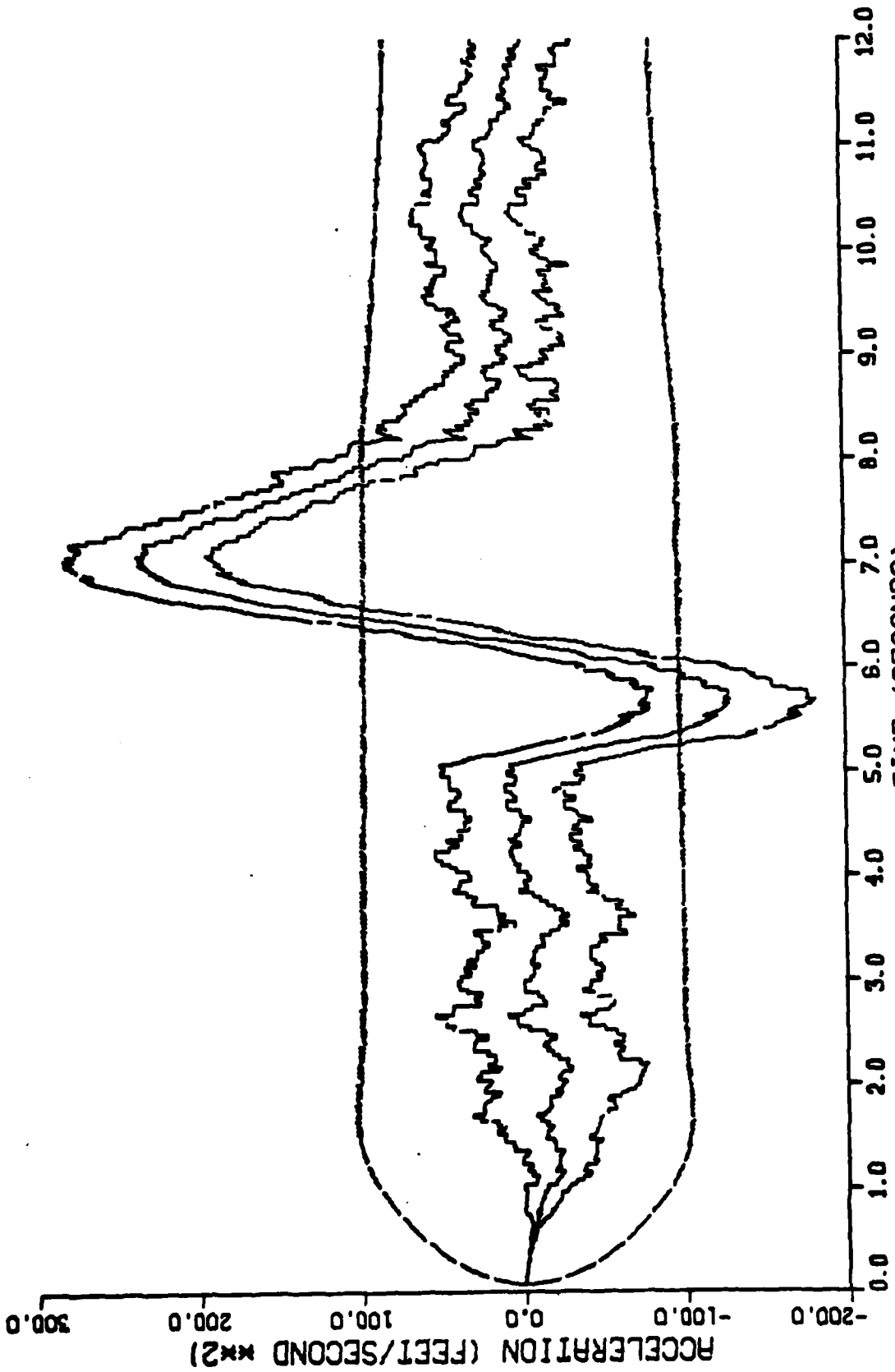


Figure G-9. Performance of the Constant Turn Rate Inertial Coordinate Filter Along the Down-Axis for Trajectory 2 with a Range Measurement Noise Variance of 1000 Feet²

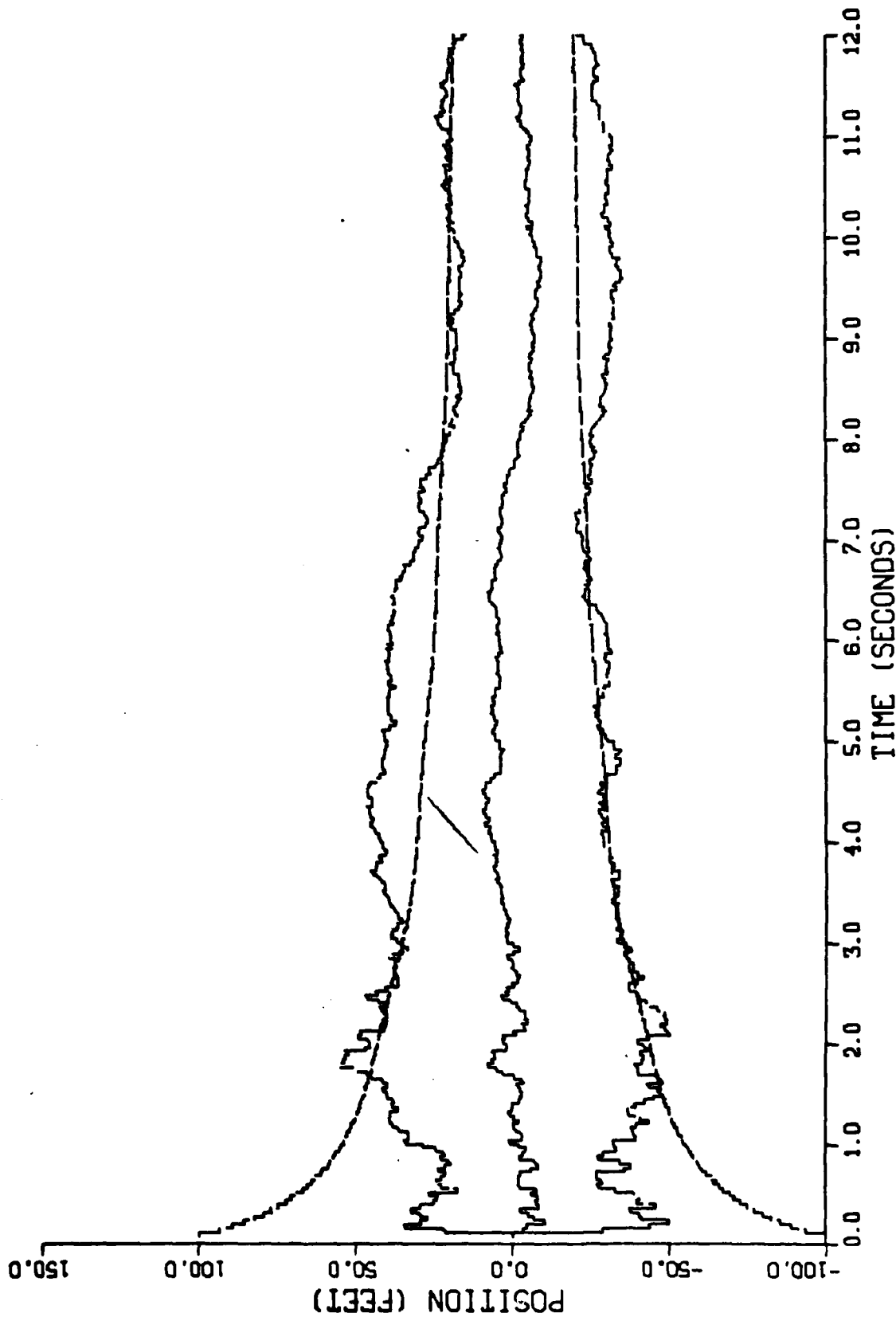


Figure G-10. Performance of the Constant Turn Rate Inertial Coordinate Filter Along the North-Axis for Trajectory 2 with a Range Measurement Noise Variance of 100000 Feet²

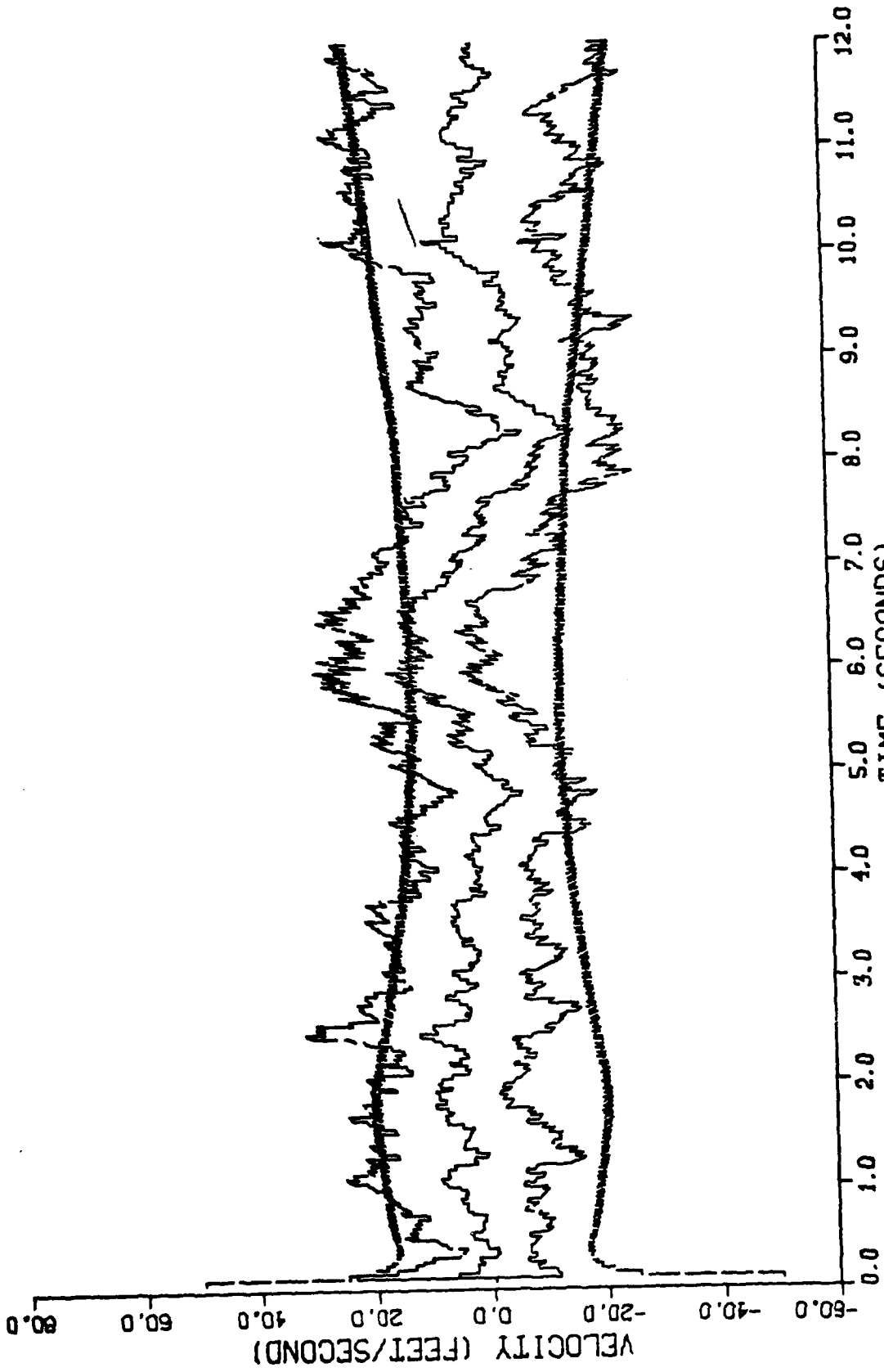


Figure G-11. Performance of the Constant Turn Rate Inertial Coordinate Filter Along the North-Axis for Trajectory 2 with a Range Measurement Noise Variance of 100000 Feet²

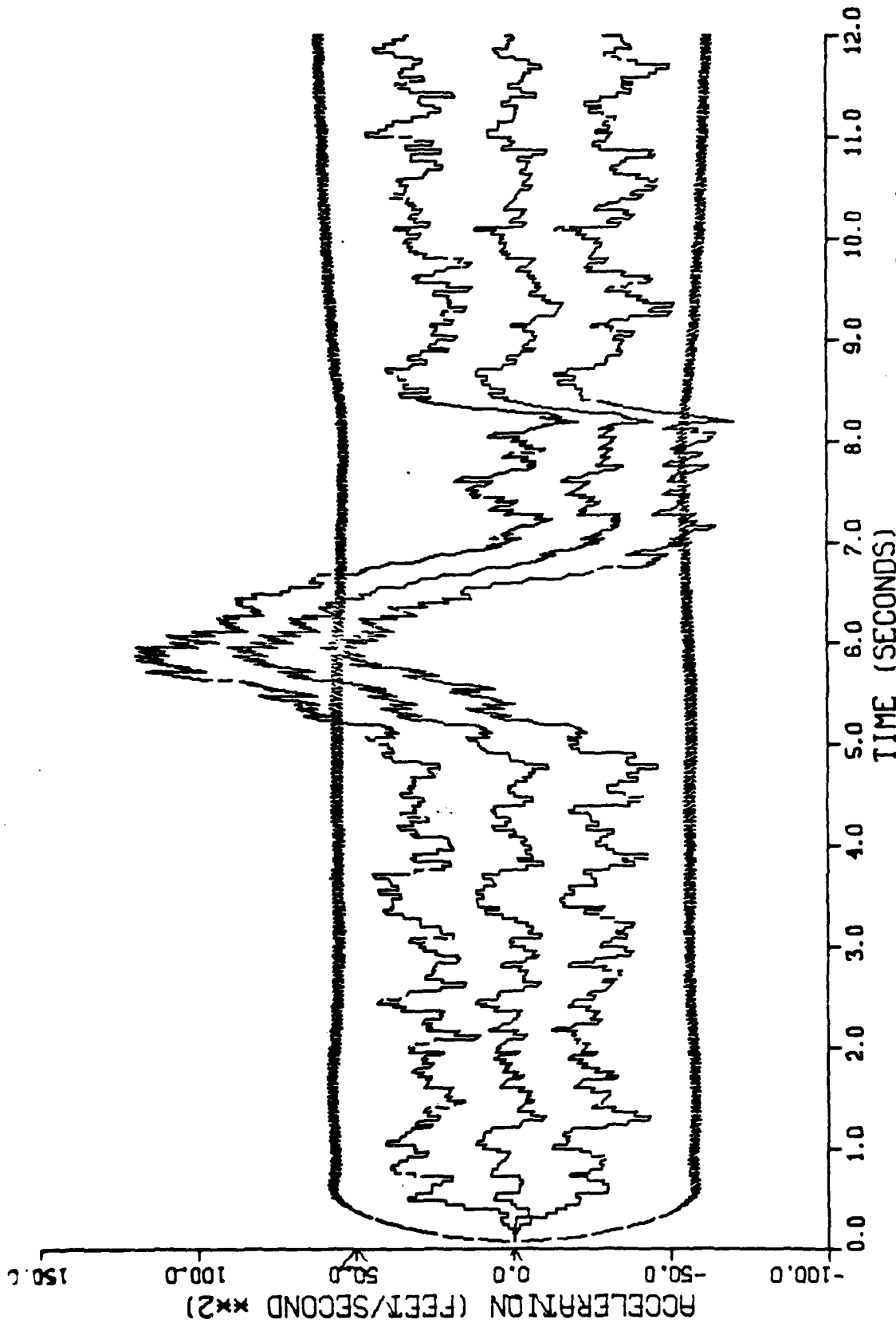


Figure G-12. Performance of the Constant Turn Rate Inertial Coordinate Filter Along the North-Axis for Trajectory 2 with a Range Measurement Noise Variance of 100000 feet²

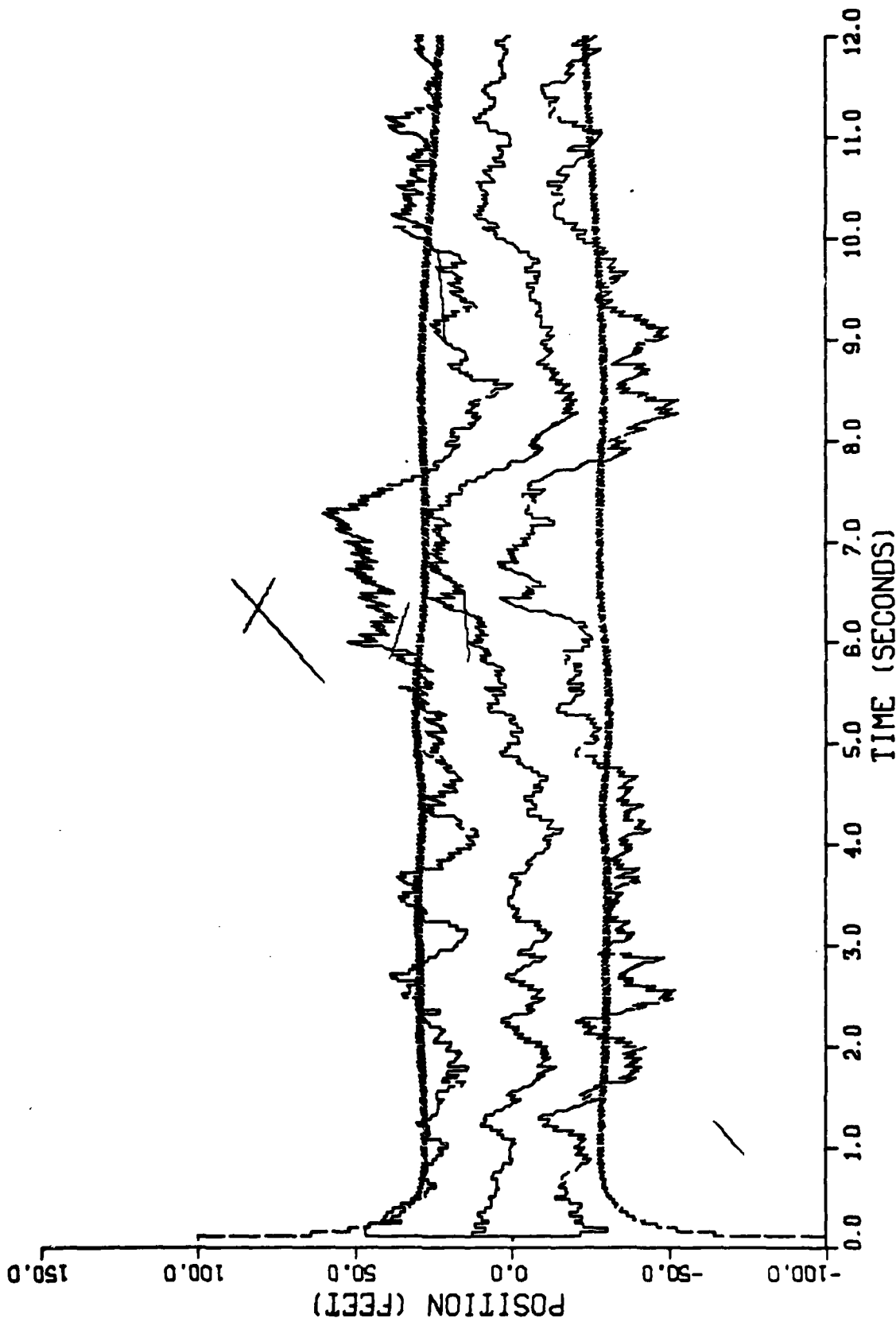


Figure G-13. Performance of the Constant Turn Rate Inertial Coordinate Filter Along the East-Axis for Trajectory 2 with a Range Measurement Noise Variance of 100000 Feet²

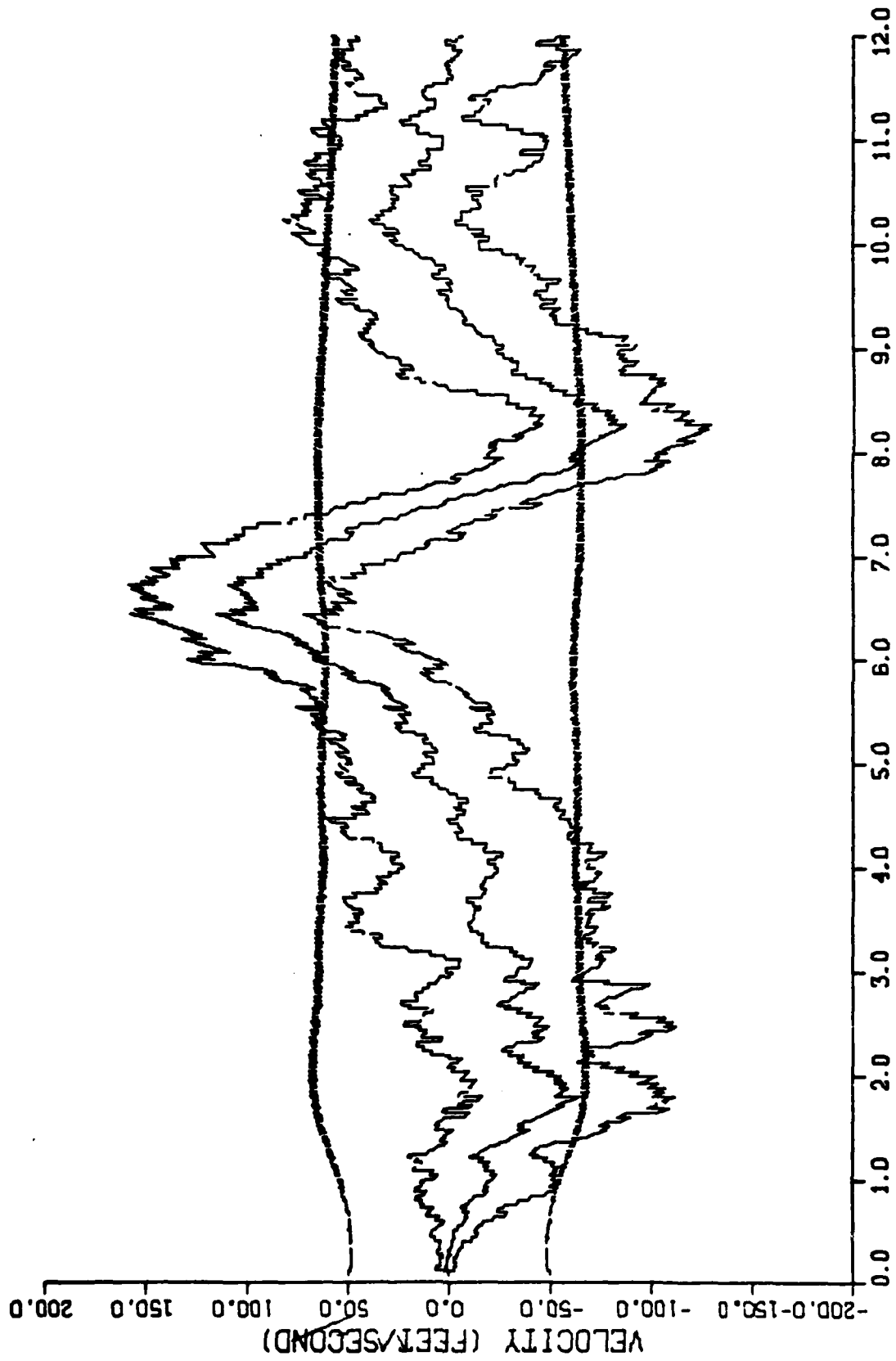


Figure G-14. Performance of the Constant Turn Rate Inertial Coordinate Filter Along the Fast-Axis for Trajectory 2 with a Range Measurement Noise Variance of 10000 Feet²

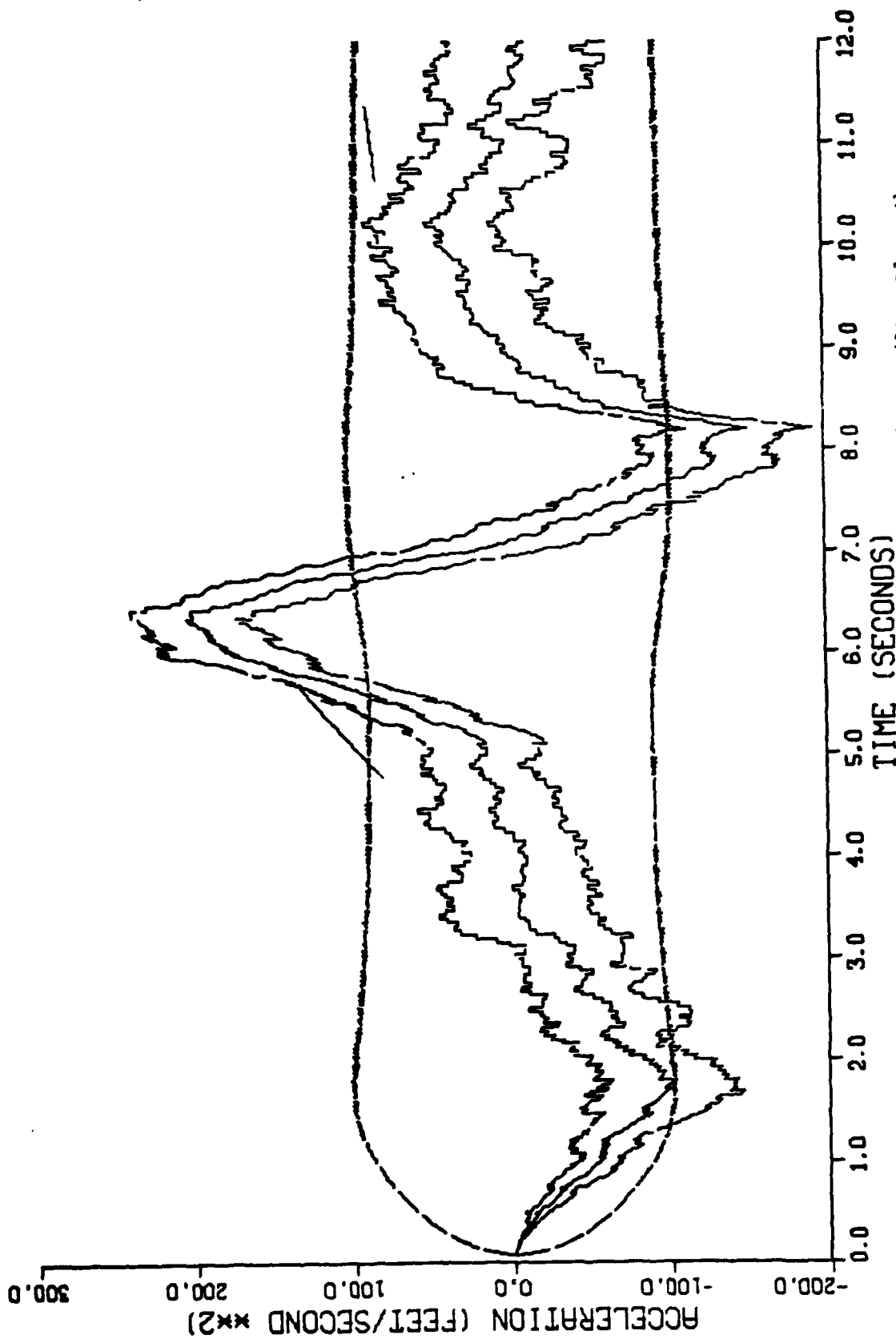


Figure G-15. Performance of the Constant Turn Rate Inertial Coordinate Filter Along the East-Axis for Trajectory 2 with a Range Measurement Noise Variance of 100000 Feet²

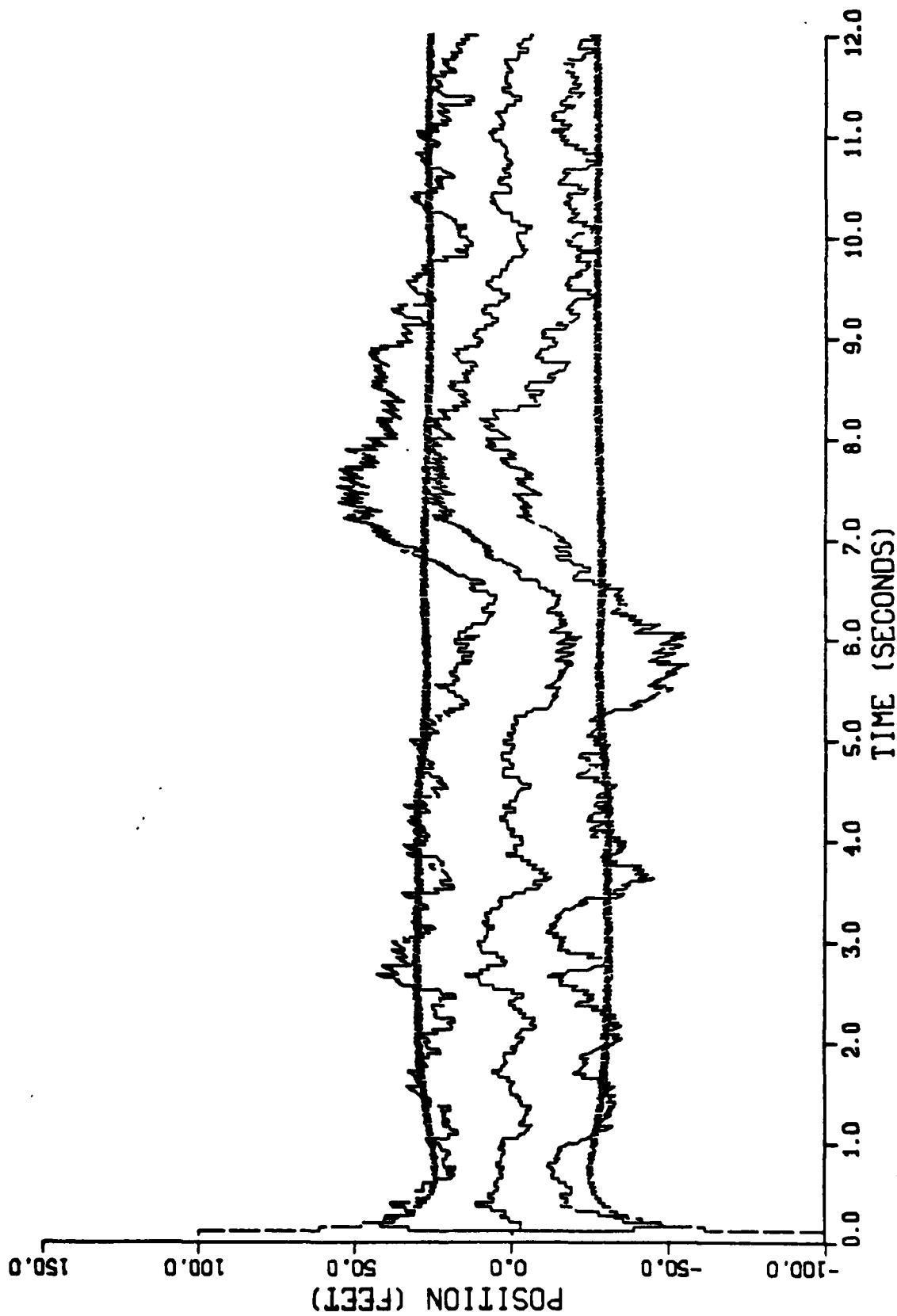


Figure G-16. Performance of the Constant Turn Rate Inertial Coordinate Filter Along the Down-Axis for Trajectory 2 with a Range Measurement Noise Variance of 100000 Feet²

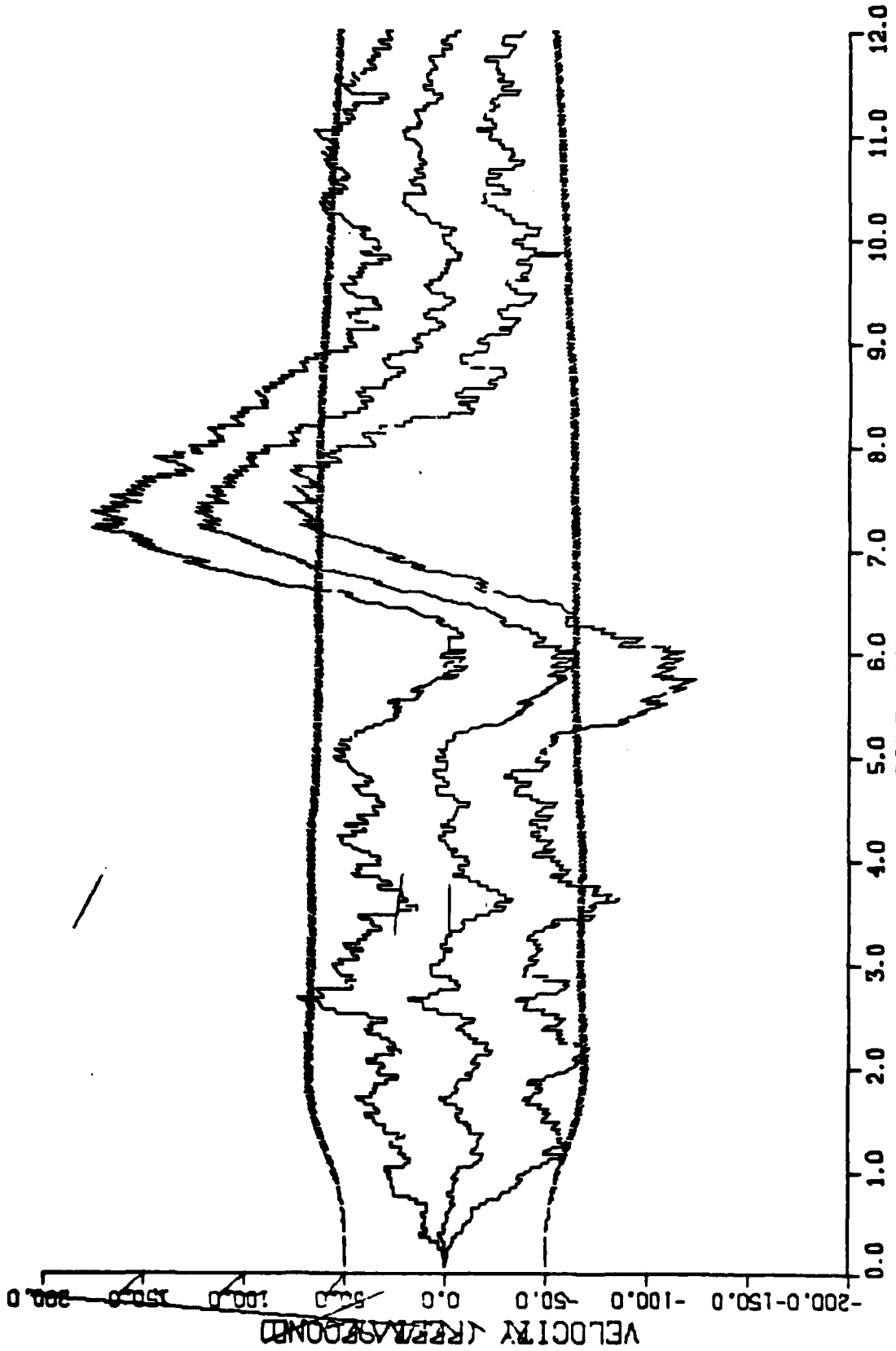


Figure G-17. Performance of the Constant Turn Rate Inertial Coordinate Filter Along the Down-Axis for Trajectory 2 with a Range Measurement Noise Variance of 100000 Feet²

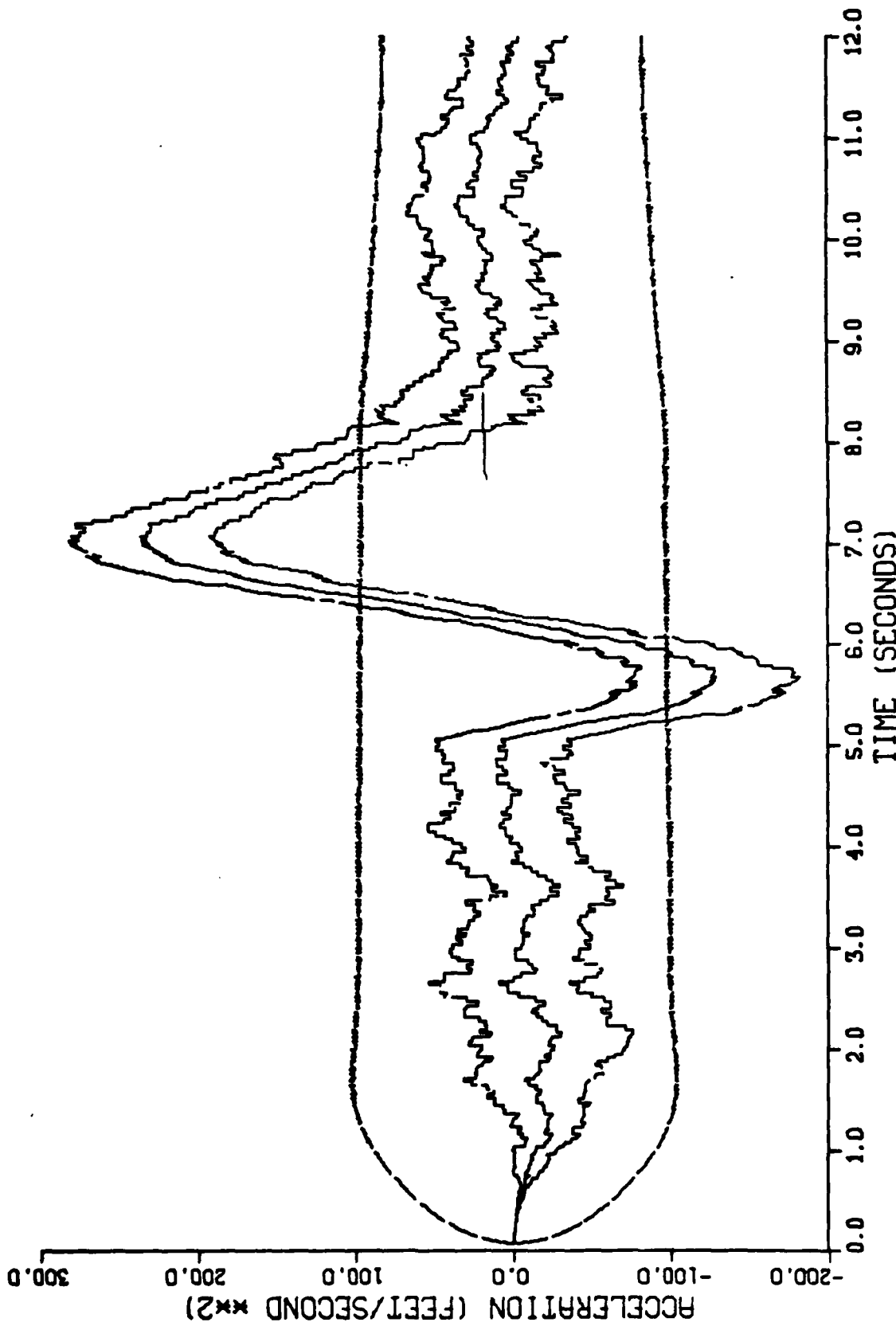


Figure G-18. Performance of the Constant Turn Rate Inertial Coordinate Filter Along the Down-Axis for Trajectory 2 with a Range Measurement Noise Variance of 10000 Feet²

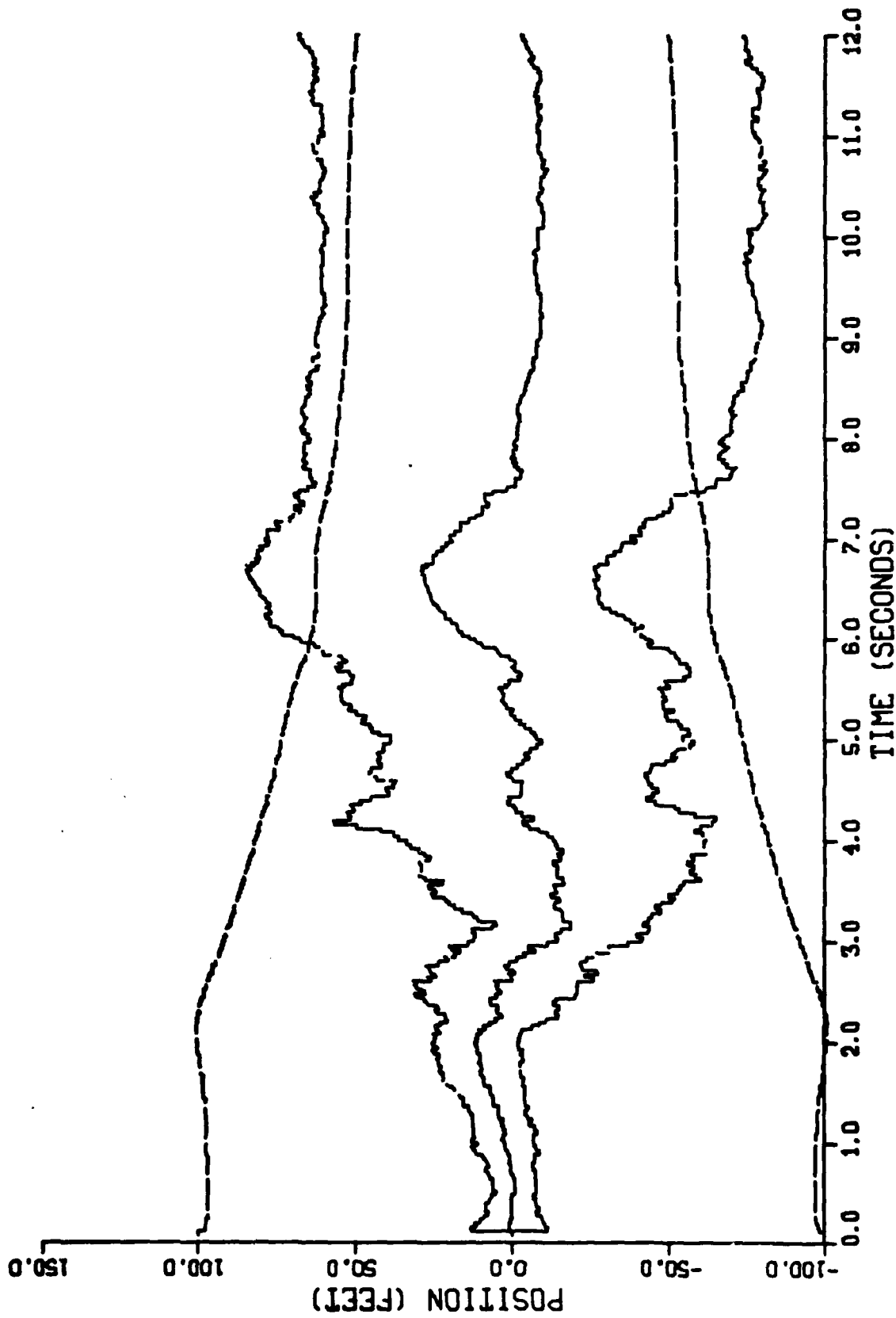


Figure G-19. Performance of the Constant Turn Rate Inertial Coordinate Filter Along the North-Axis for Trajectory 2 with No Range Measurement

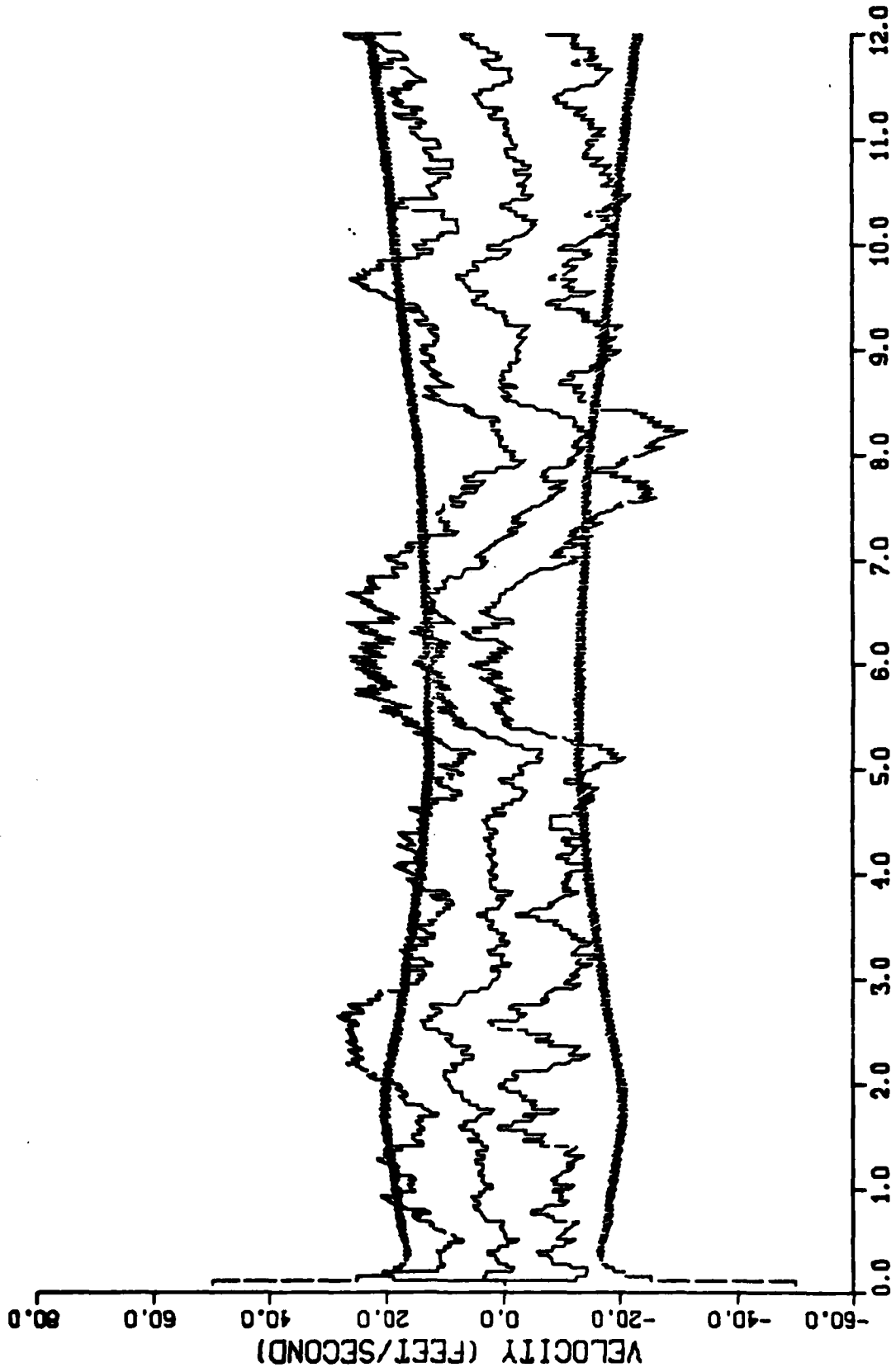


Figure G-20. Performance of the Constant Turn Rate Inertial Coordinate Filter Along the North-Axis for Trajectory 2 with No Range Measurement

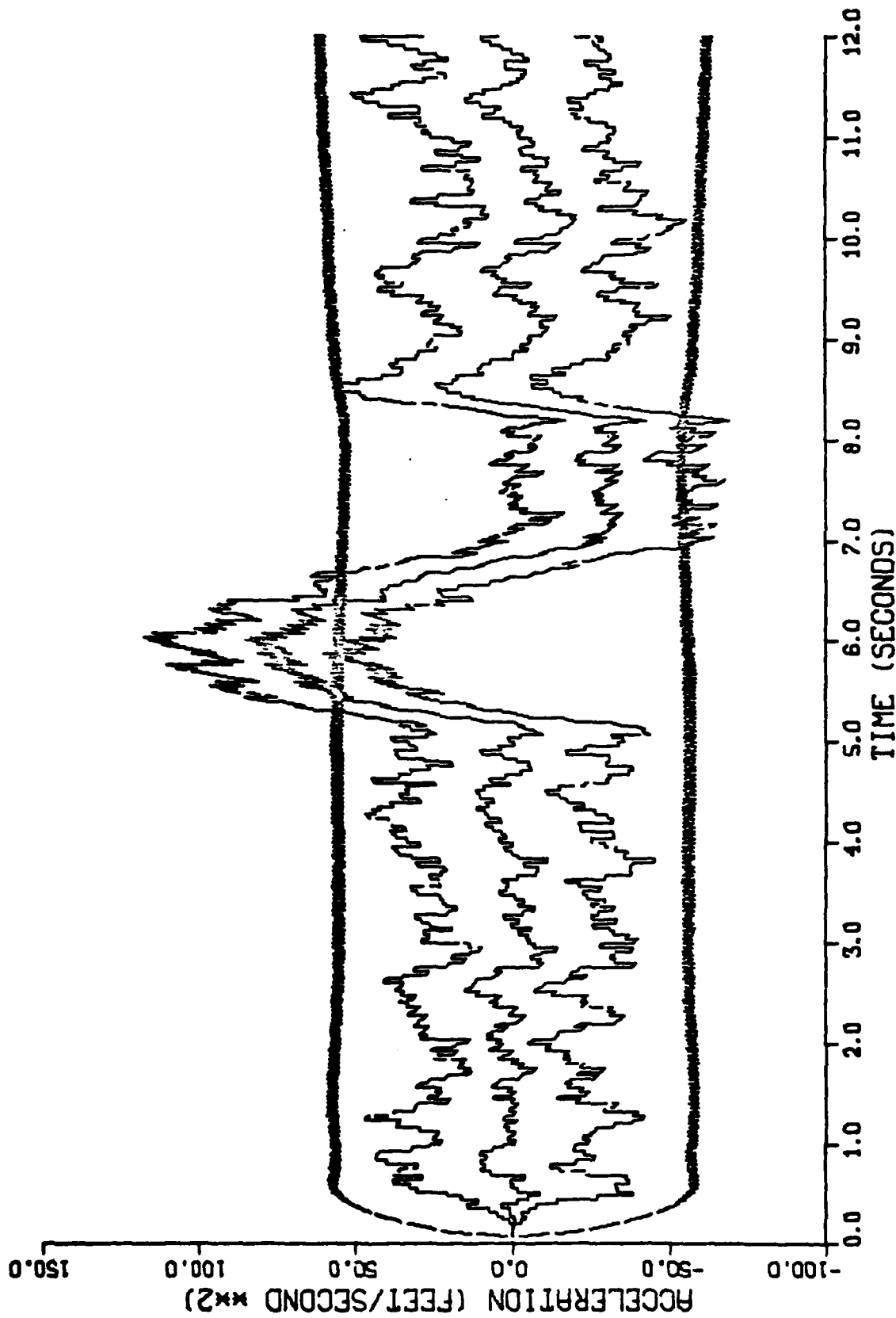


Figure G-21. Performance of the Constant Turn Rate Inertial Coordinate Filter Along the North-Axis for Trajectory 2 with No Range Measurement

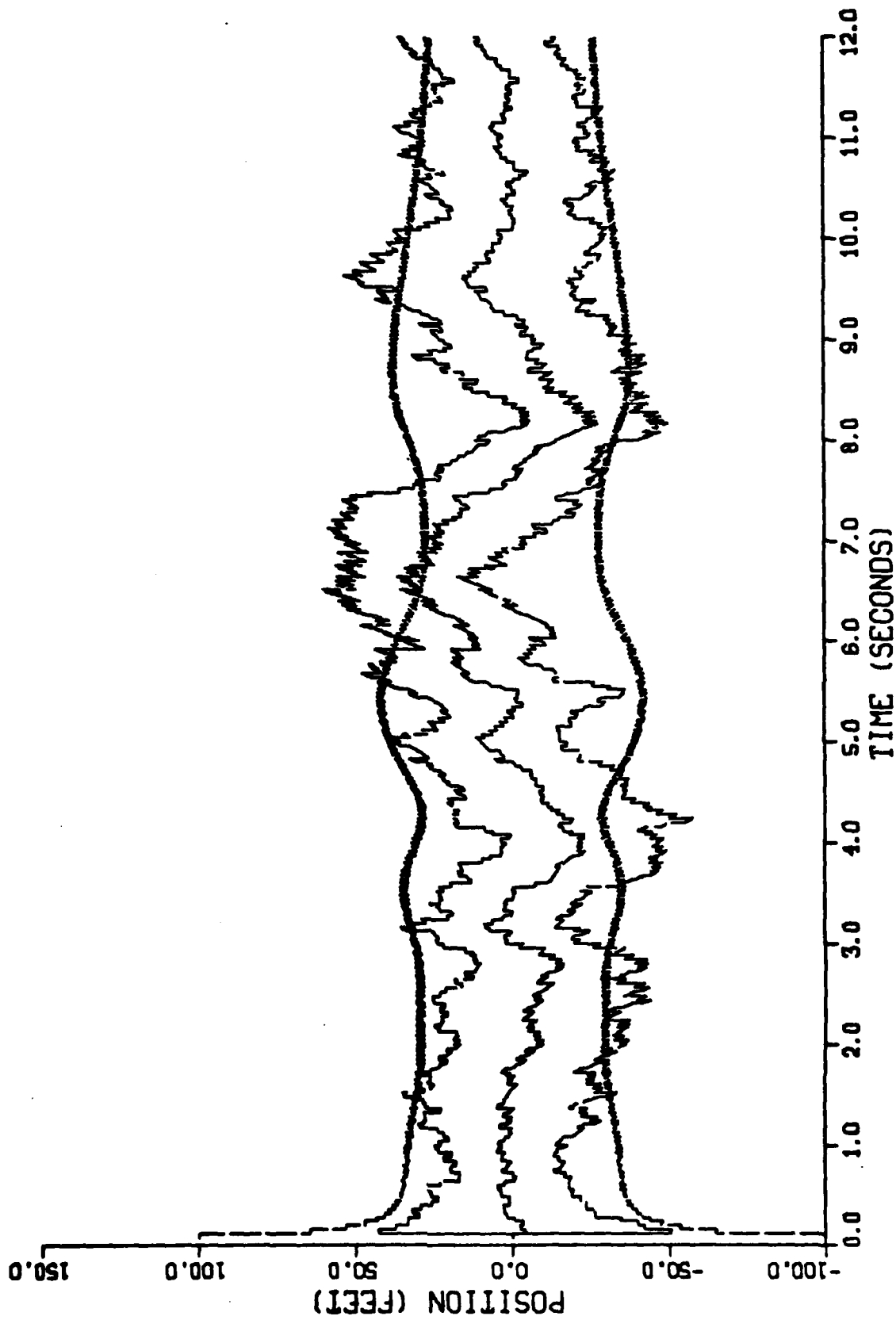


Figure G-22. Performance of the Constant Turn Rate Inertial Coordinate Filter Along the East-Axis for Trajectory 2 with No Range Measurement

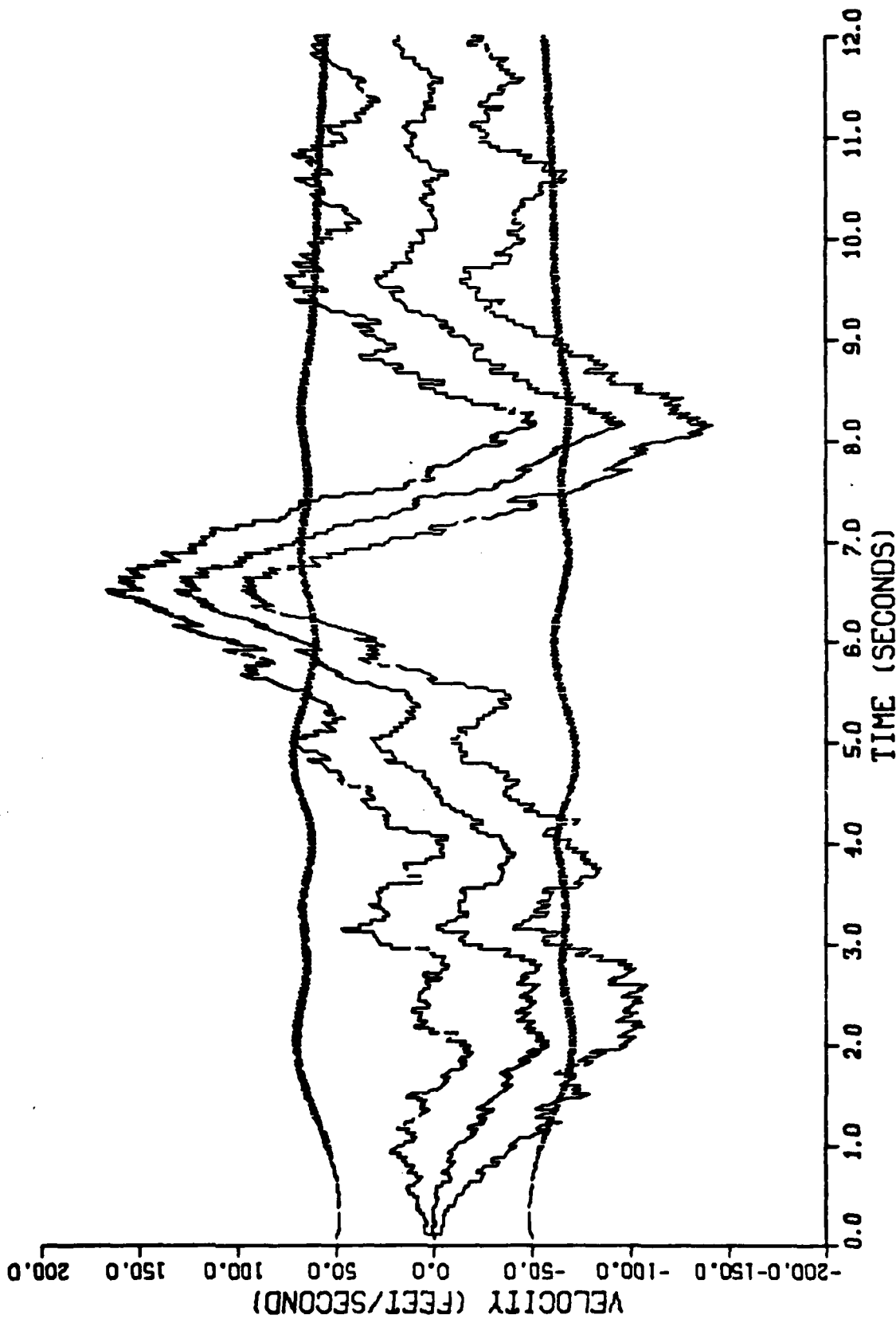


Figure G-23. Performance of the Constant Turn Rate Inertial Coordinate Filter Along the East-Axis for Trajectory 2 with No Range Measurement

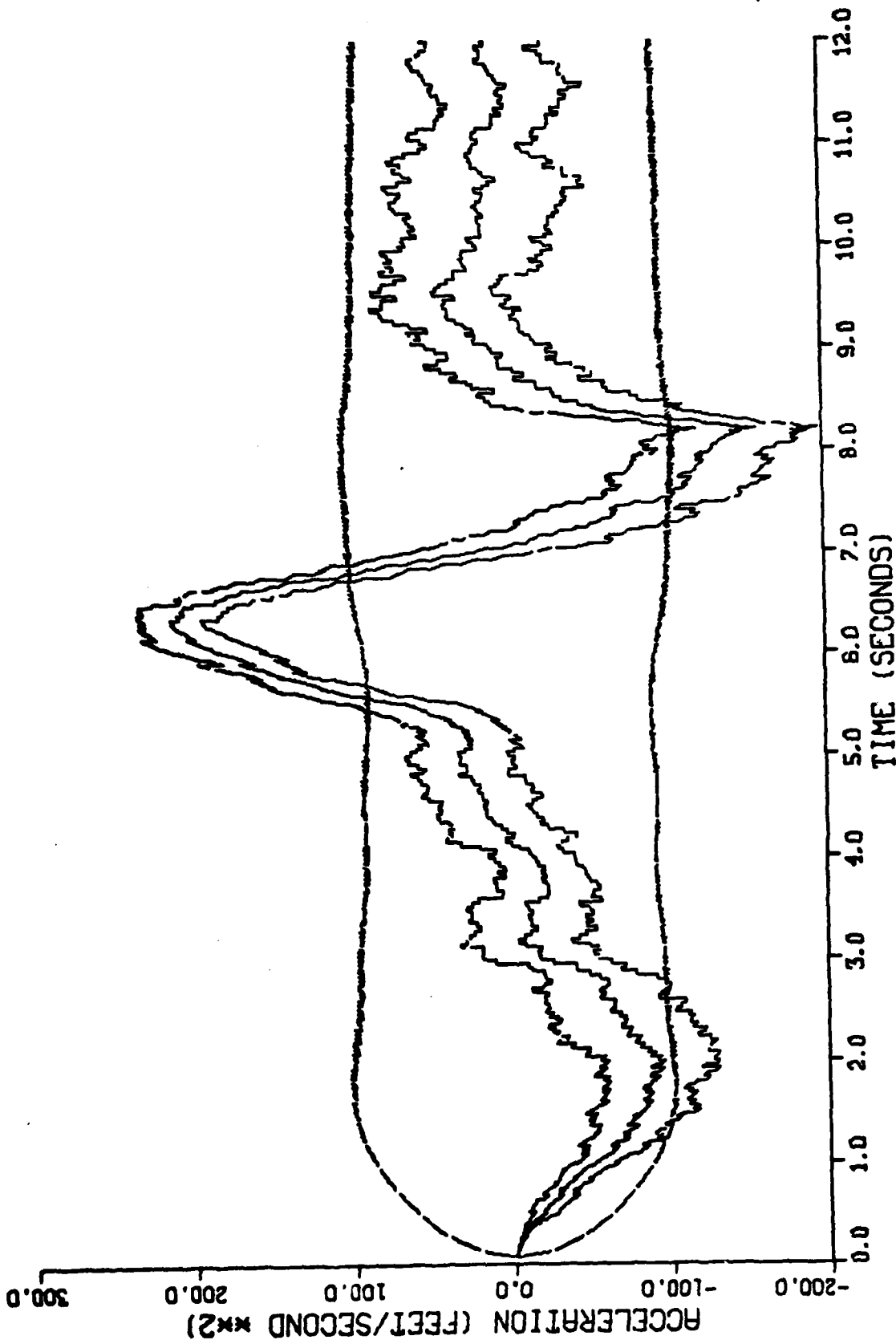


Figure G-24. Performance of the Constant Turn Rate Inertial Coordinate Filter Along the East-Axis for Trajectory 2 with No Range Measurement

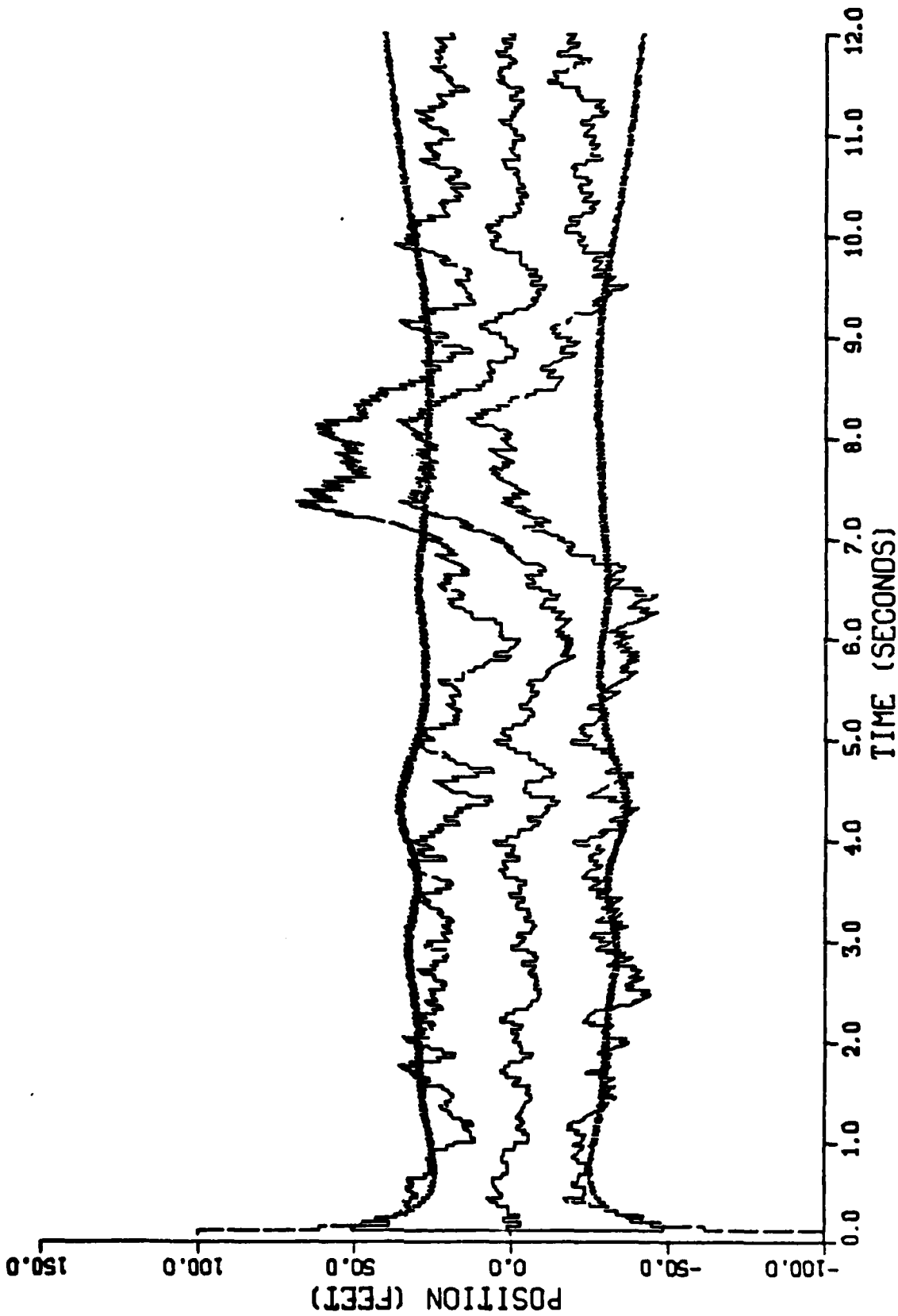


Figure G-25. Performance of the Constant Turn Rate Inertial Coordinate Filter Along the Down-Axis for Trajectory 2 with No Range Measurement

AD-A094 767

AIR FORCE INST OF TECH WRIGHT-PATTERSON AFB OH SCHOO--ETC F/8 19/5
COMPARISON OF THREE EXTENDED KALMAN FILTERS FOR AIR-TO-AIR TRAC--ETC(U)
DEC 80 W H WORSLEY
AFIT/6AE/AA/805-2

UNCLASSIFIED

NL

4 of 4

NO 094767

END

DATE

FORMED

3-81

DTIC

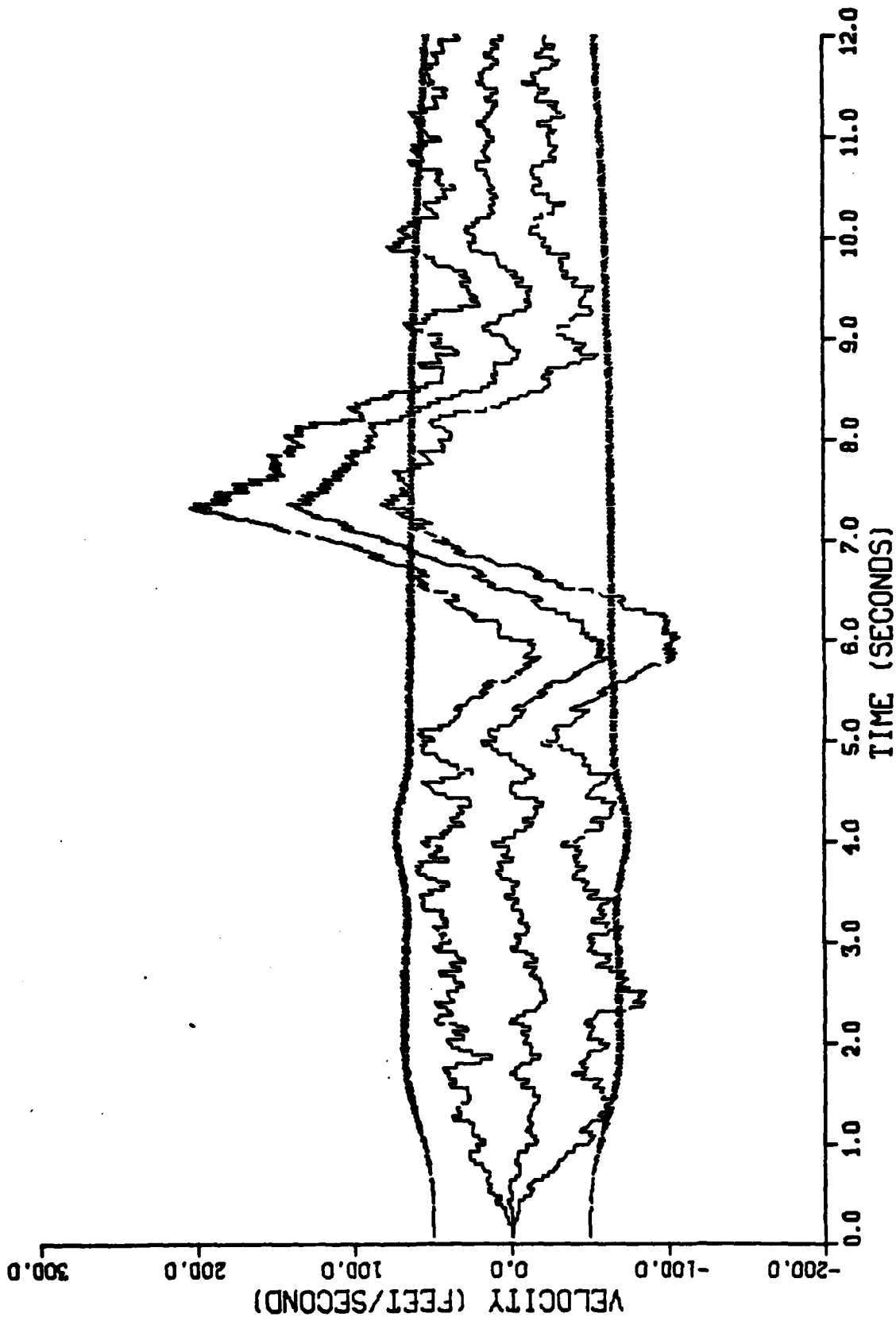


Figure G-26. Performance of the Constant Turn Rate Inertial Coordinate Filter Along the Down-Axis for Trajectory 2 with No Range Measurement

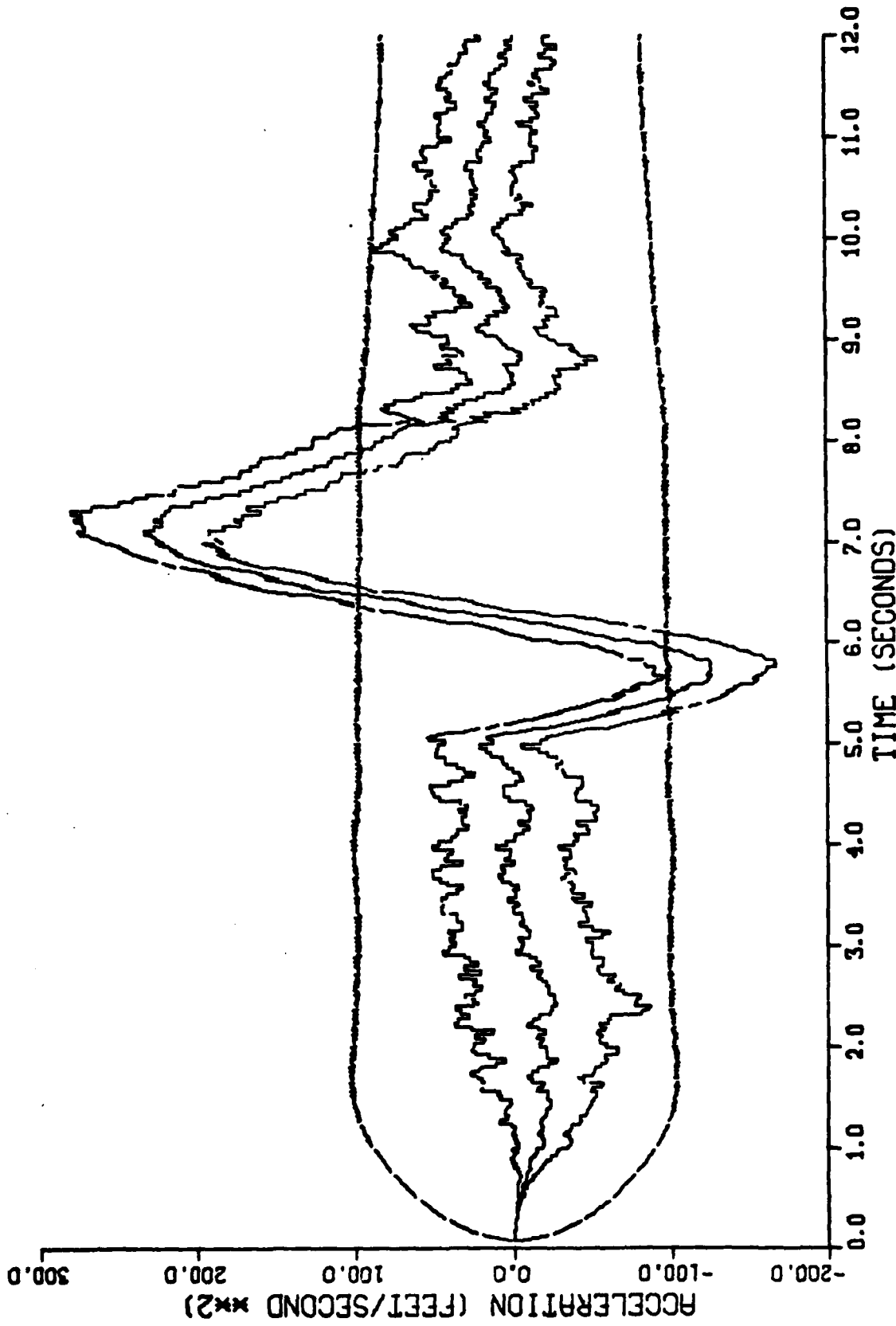


Figure G-27. Performance of the Constant Turn Rate Inertial Coordinate Filter Along the Down-Axis for Trajectory 2 with No Range Measurement

APPENDIX H

Graphical Results of the Effect of Variations of
the Error Angle Measurement Noises of the Performance
of the Constant Turn Rate Inertial Coordinate Filter

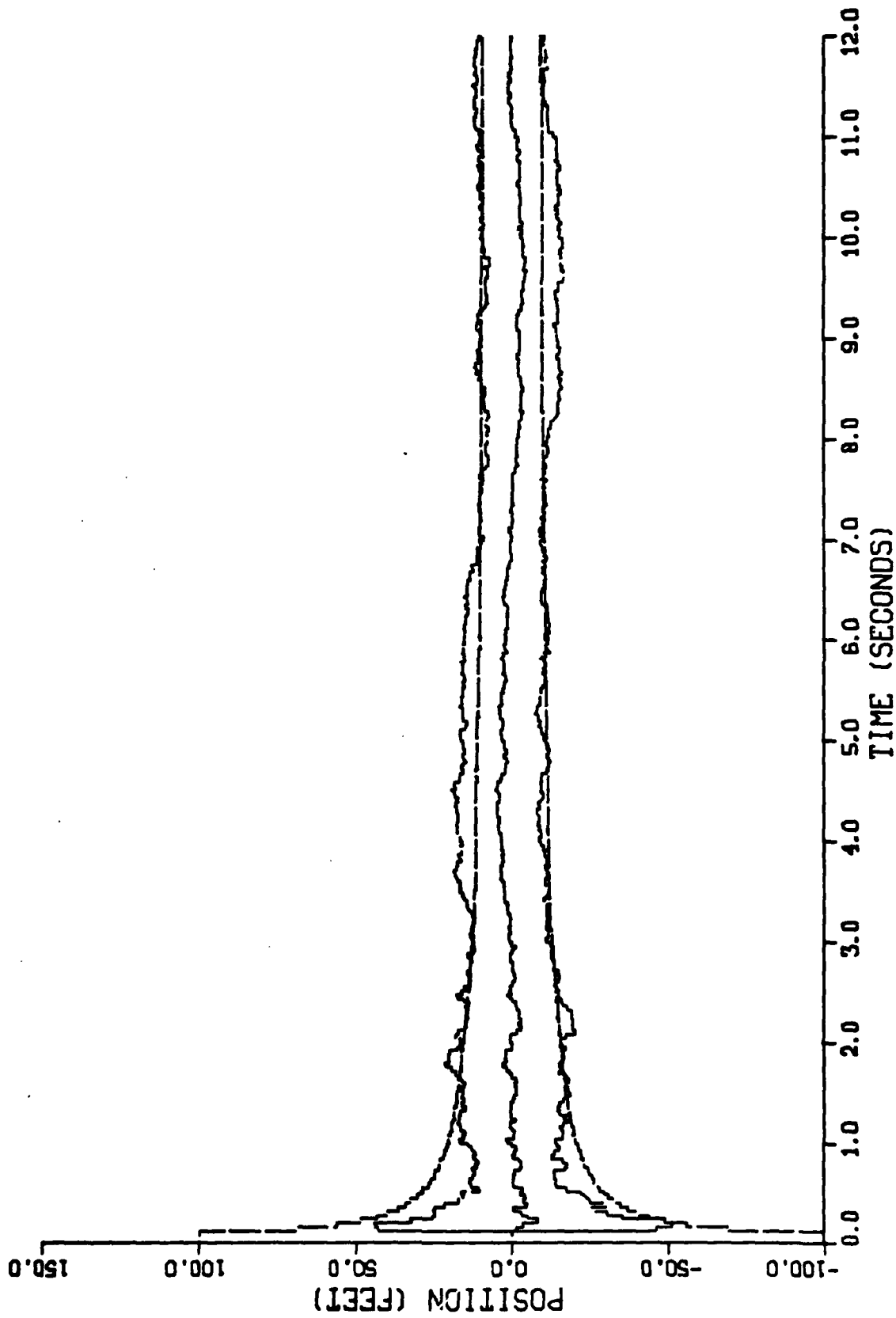


Figure H-1. Performance of the Constant Turn Rate Inertial Coordinate Filter Along the North-Axis for Trajectory 2 with Error Angle Measurement Noise Variances of 0.00001 Radians²

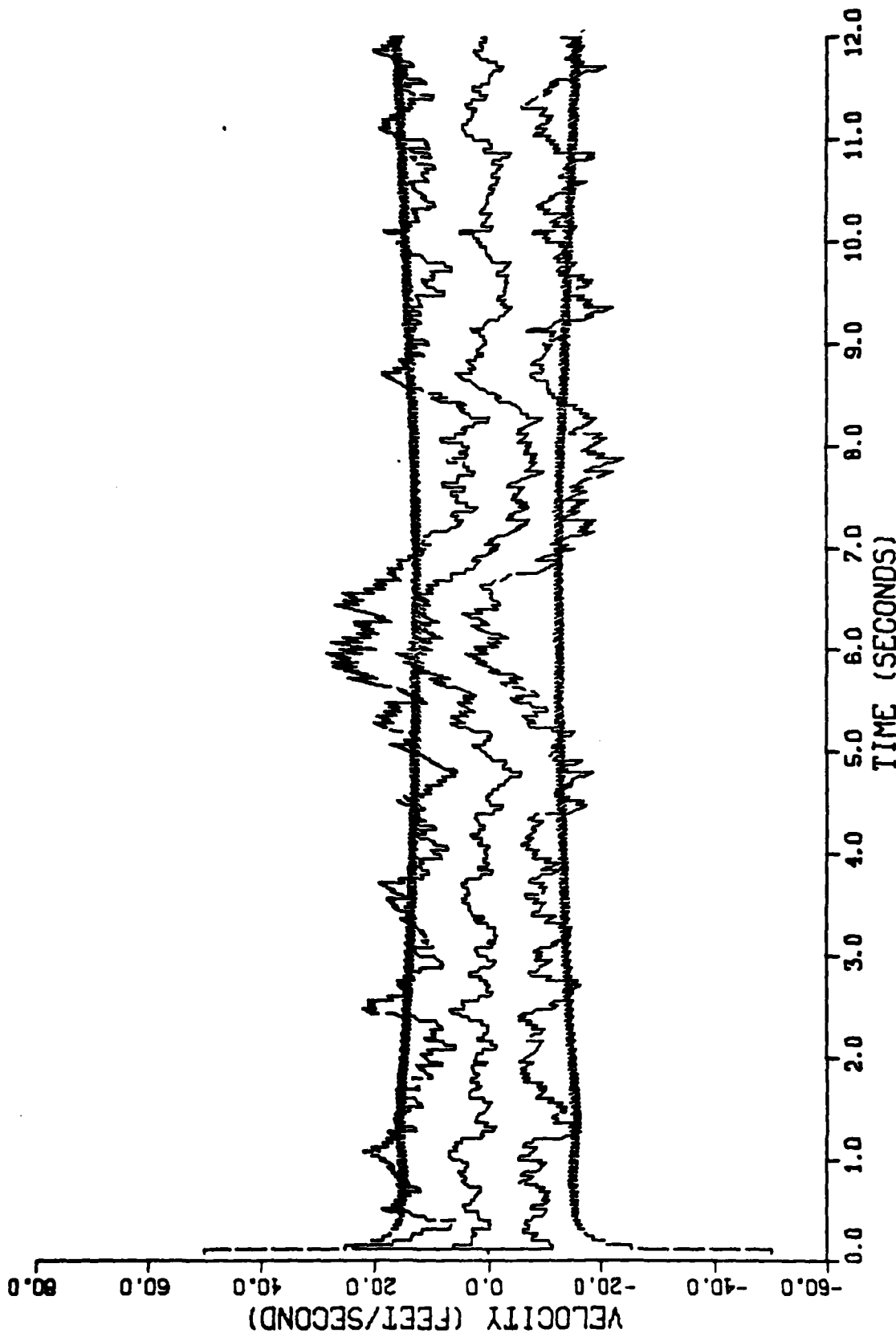


Figure H-2. Performance of the Constant Turn Rate Inertial Coordinate Filter Along the North-Axis for Trajectory 2 with Error Angle Measurement Noise Variances of 0.00001 Radians²

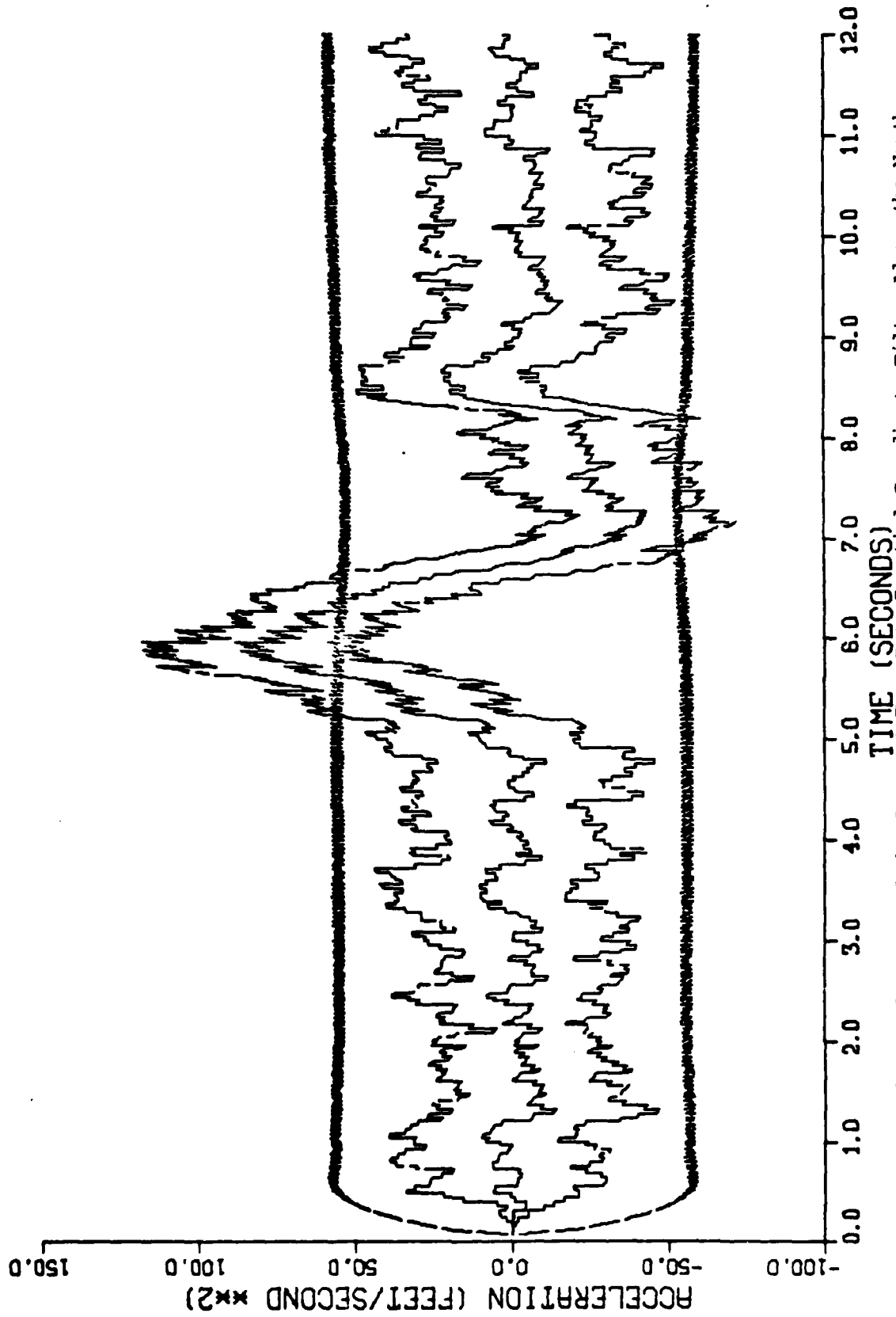


Figure H-3. Performance of the Constant Turn Rate Inertial Coordinate Filter Along the North-Axis for Trajectory 2 with Error Angle Measurement Noise Variances of 0.00001 Radians²

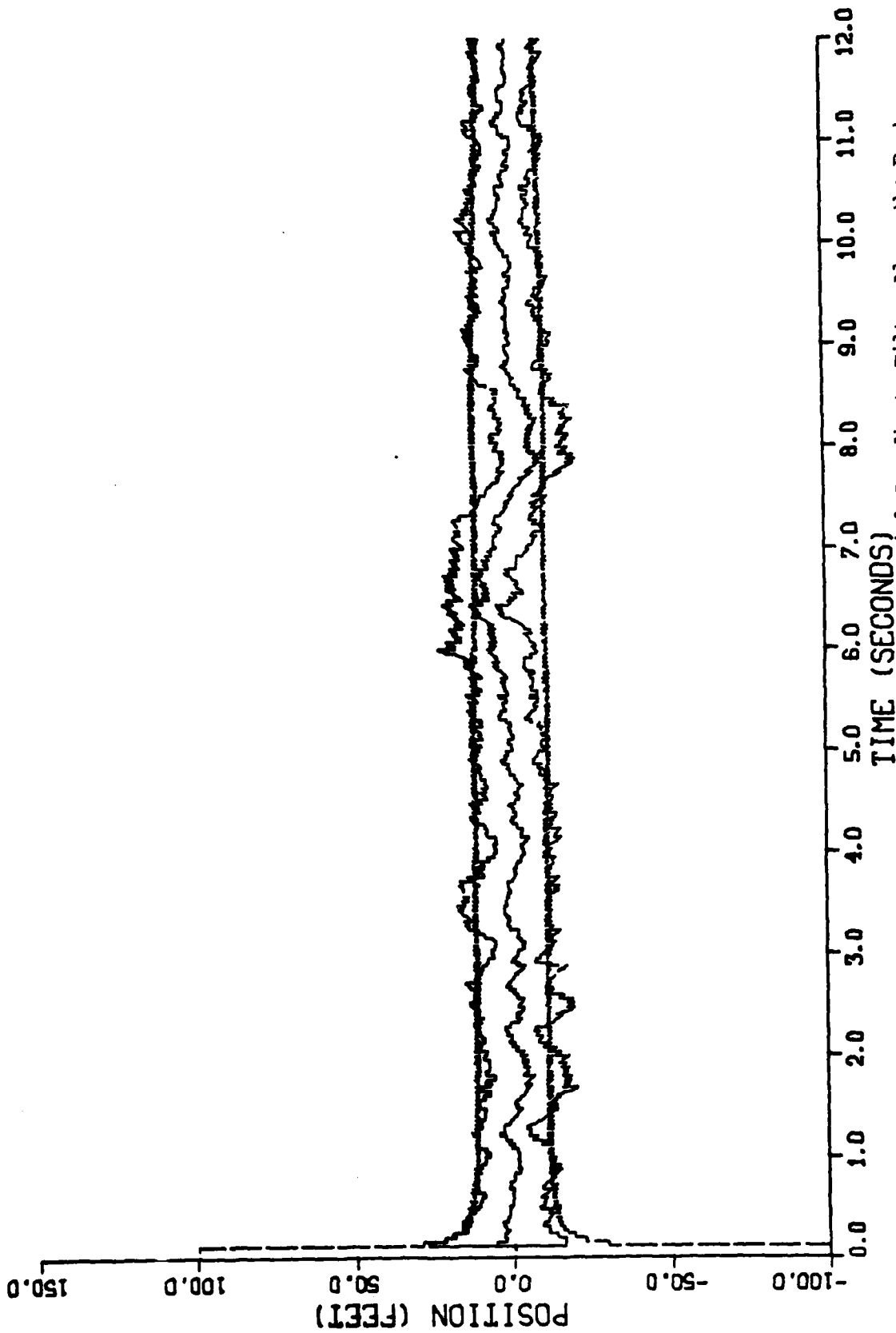


Figure H-4. Performance of the Constant Turn Rate Inertial Coordinate Filter Along the East-Axis for Trajectory 2 with Error Angle Measurement Noise Variances of $0.00001 \text{ Radians}^2$

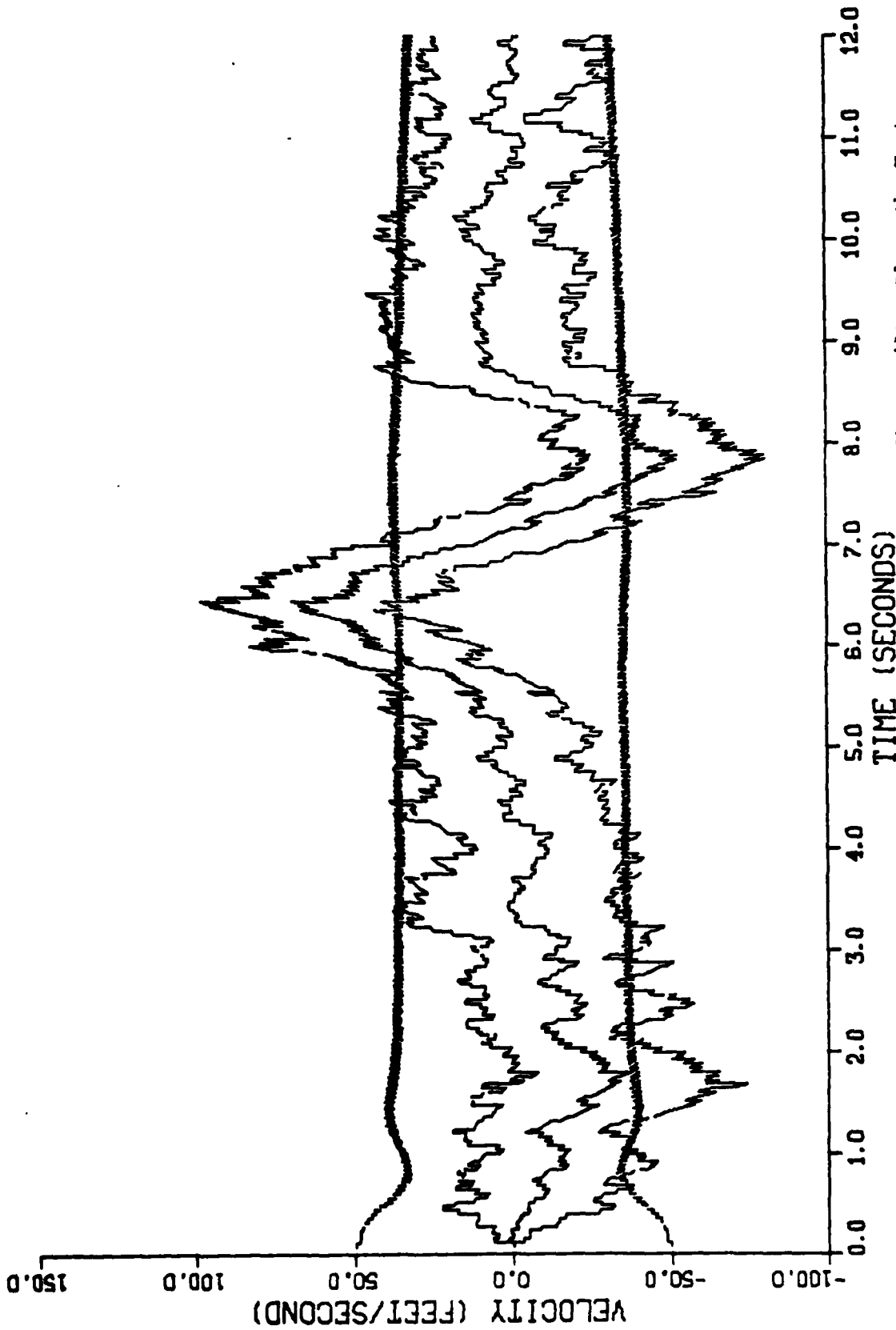


Figure H-5. Performance of the Constant Turn Rate Inertial Coordinate Filter Along the East-Axis for Trajectory 2 with Error Angle Measurement Noise Variances of 0.00001 Radians²

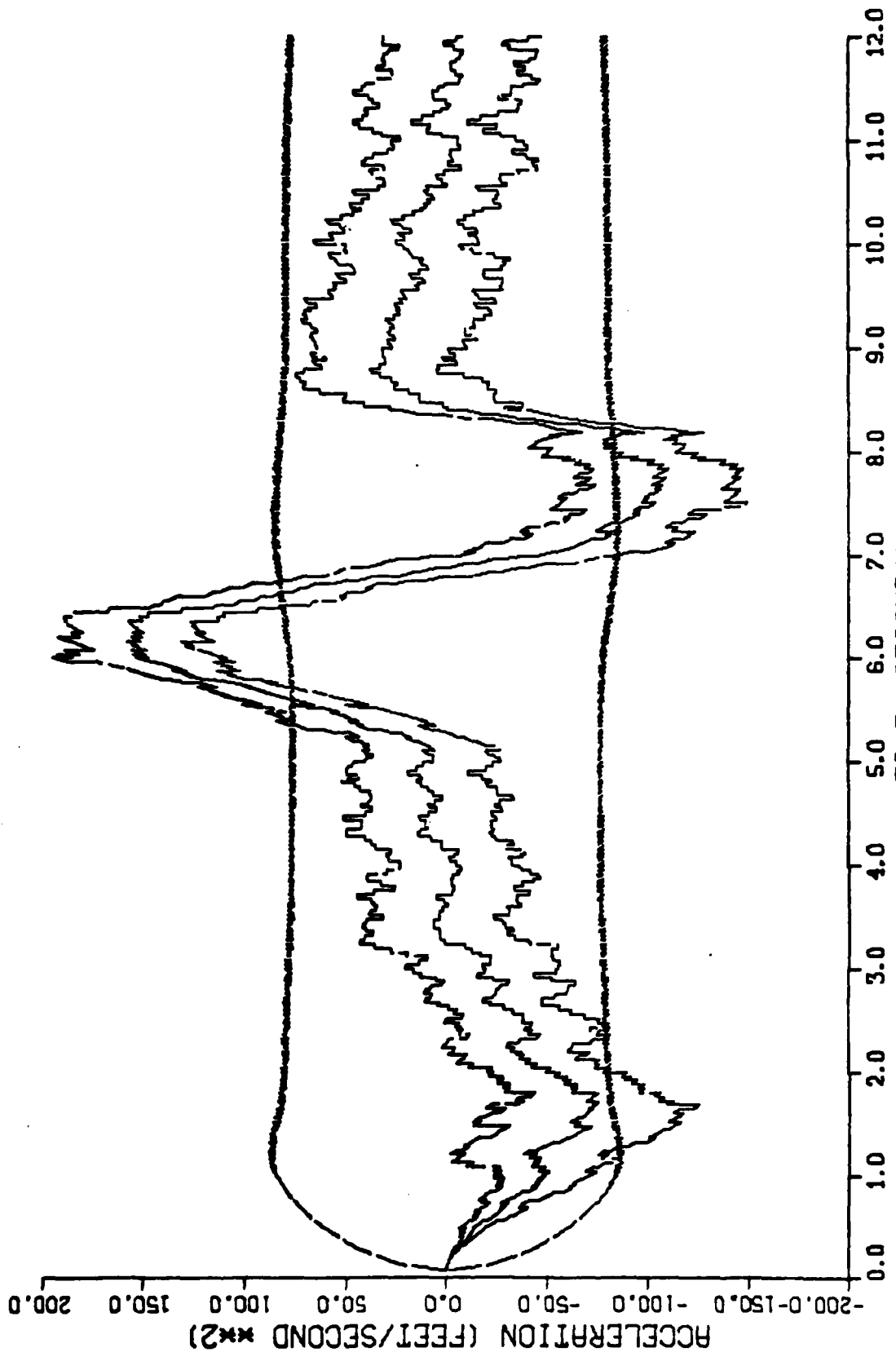


Figure H-6. Performance of the Constant Turn Rate Inertial Coordinate Filter Along the East-Axis for Trajectory 2 with Error Angle Measurement Noise Variances of 0.00001 Radians²

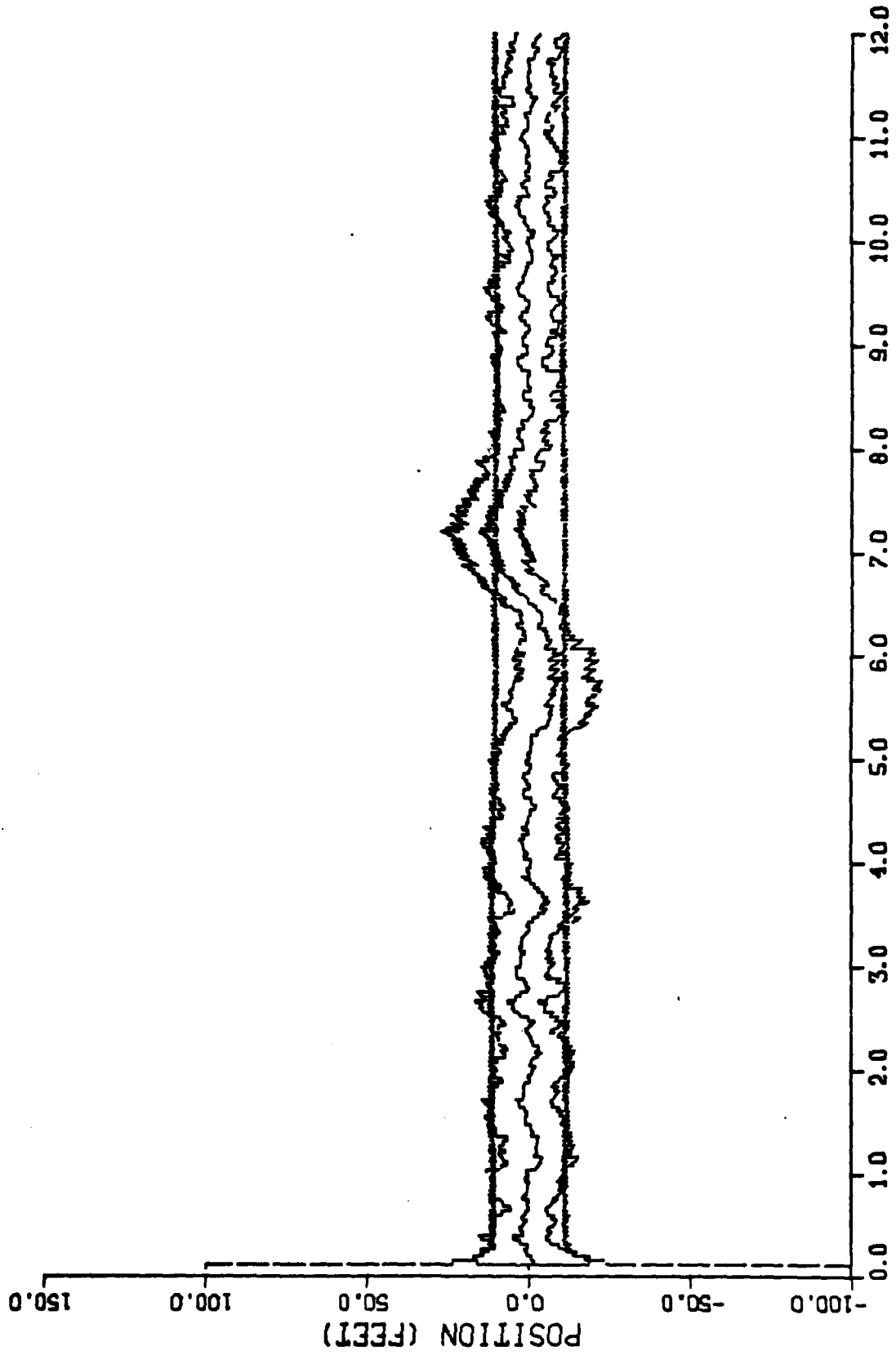


Figure H-7. Performance of the Constant Turn Rate Inertial Coordinate Filter Along the Down-Axis for Trajectory 2 with Error Angle Measurement Noise Variances of 0.00001 Radians²

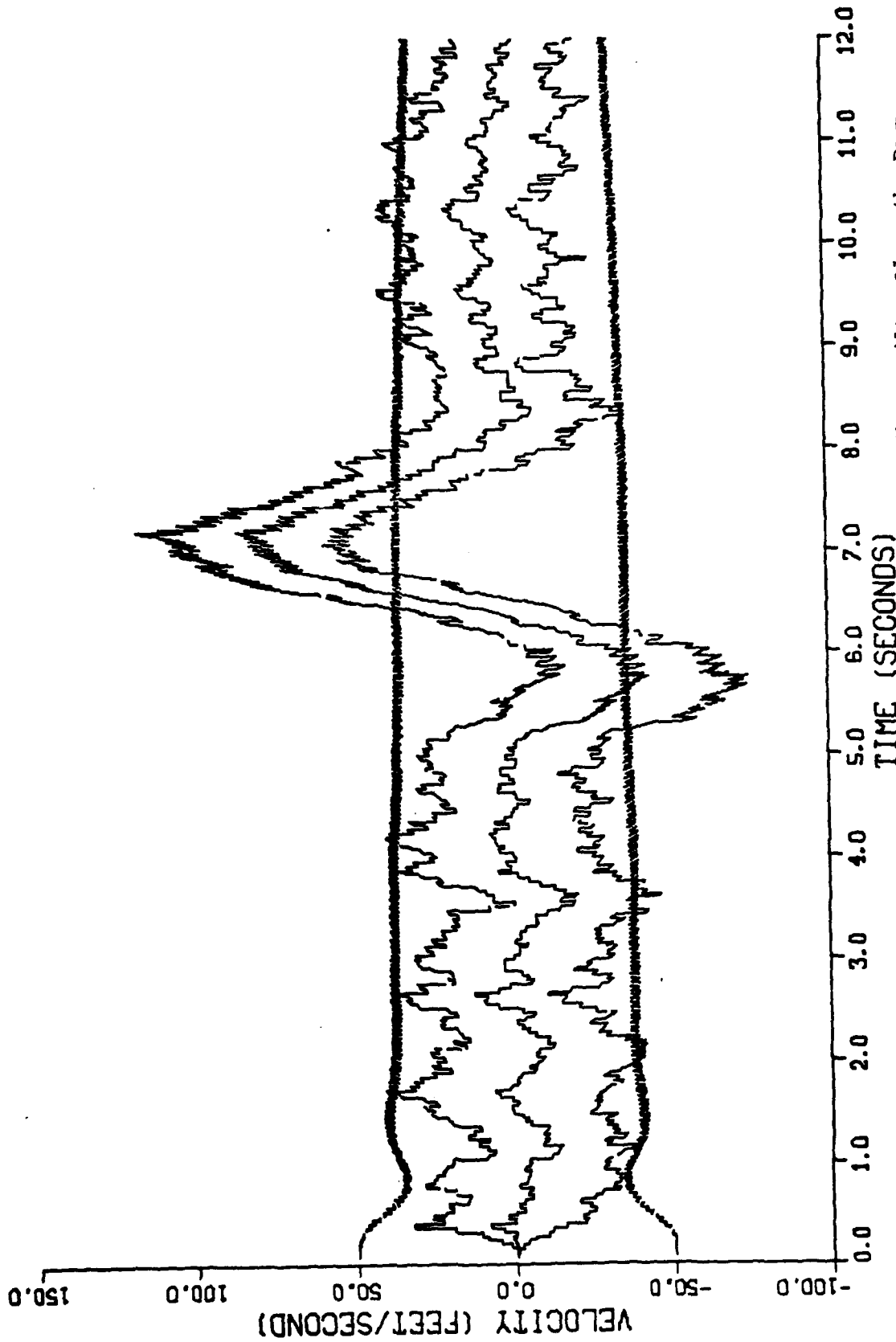


Figure H-8. Performance of the Constant Turn Rate Inertial Coordinate Filter Along the Down-Axis for Trajectory 2 with Error Angle Measurement Noise Variances of 0.00001 Radians²

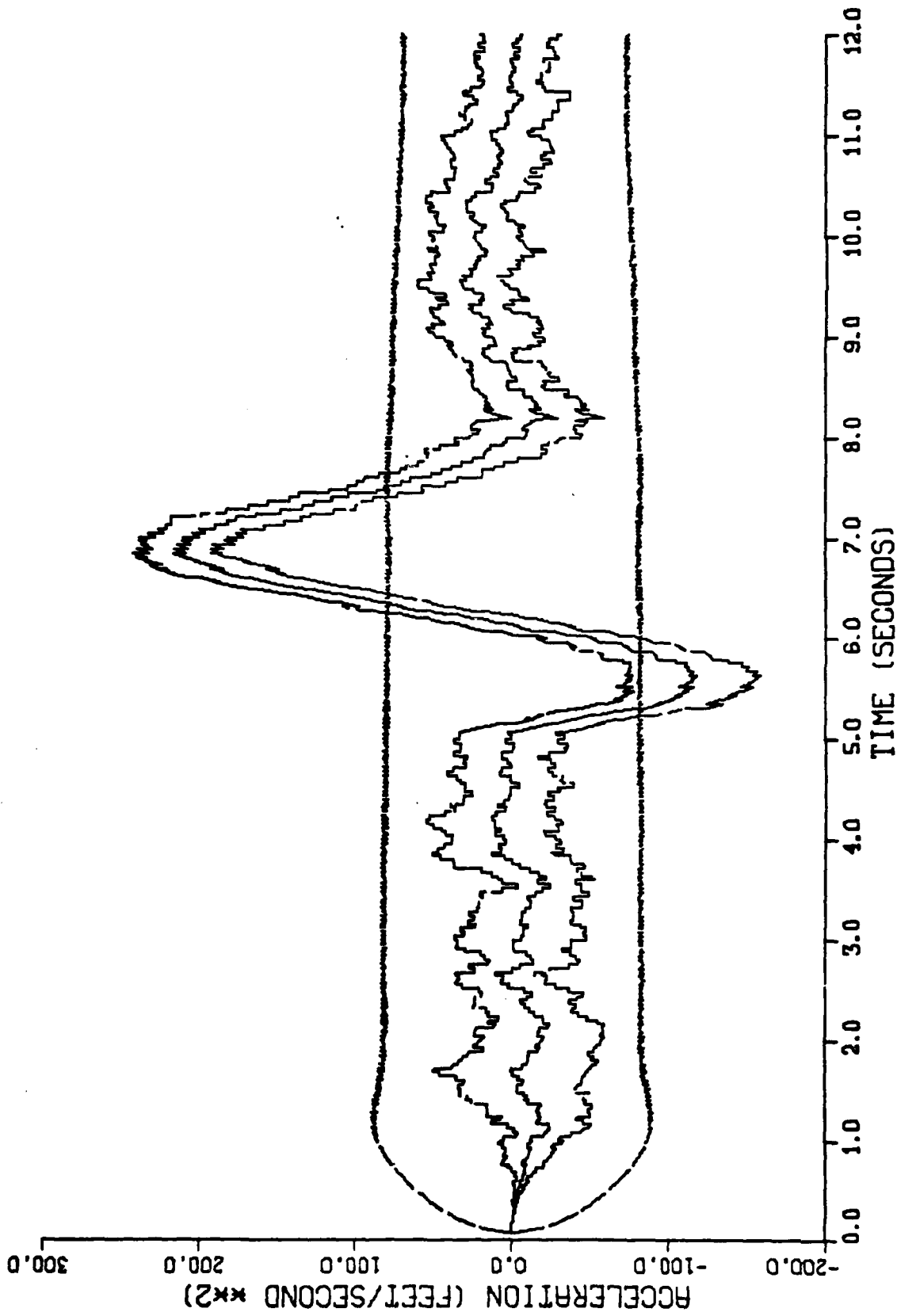


Figure H-9. Performance of the Constant Turn Rate Inertial Coordinate Filter Along the Down-Axis for Trajectory 2 with Error Angle Measurement Noise Variances of 0.00001 Radians²

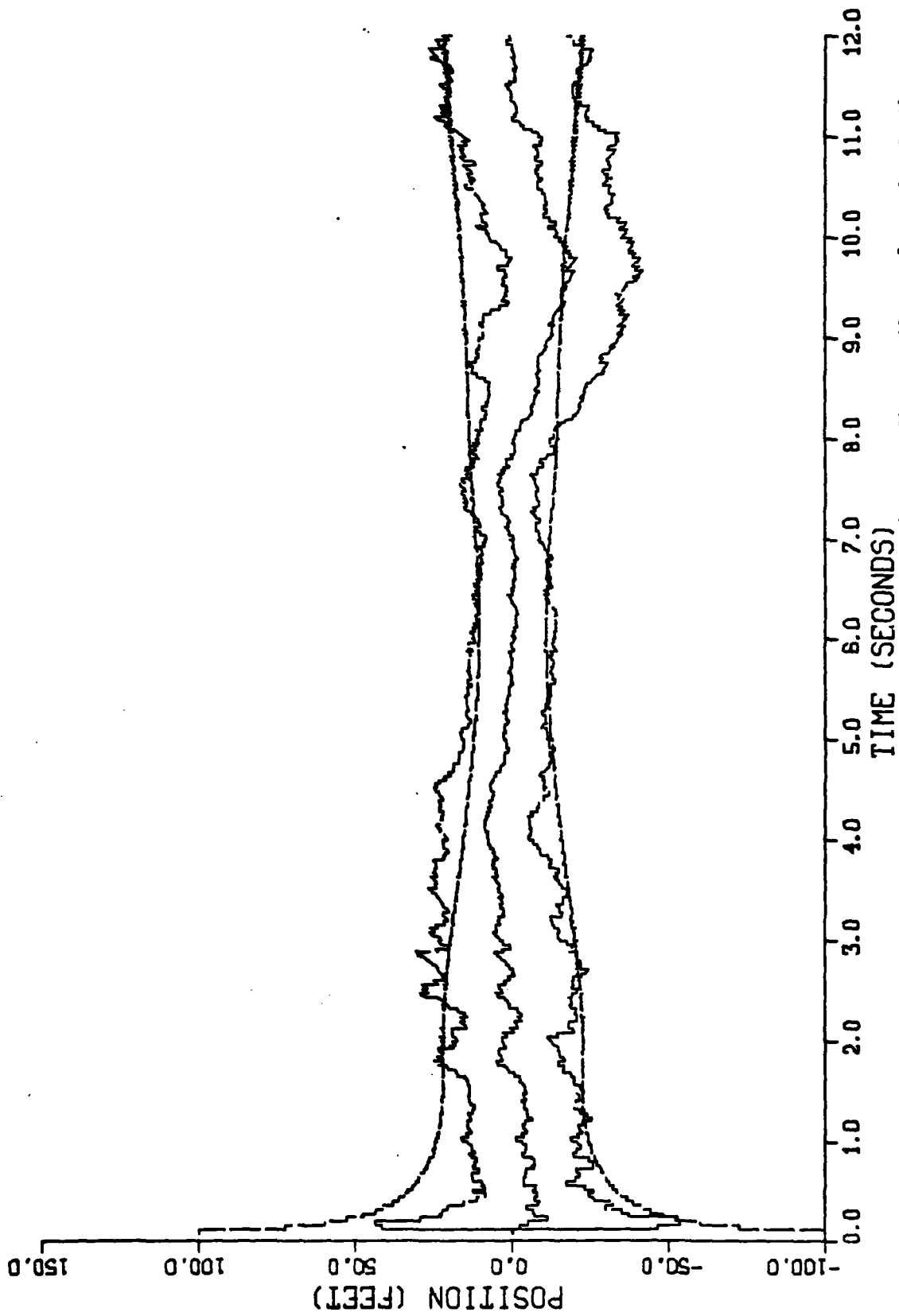


Figure H-10. Performance of the Constant Turn Rate Inertial Coordinate Filter Along the North-Axis for Trajectory 2 with Error Angle Measurement Noise Variances of 0.001 Radians²

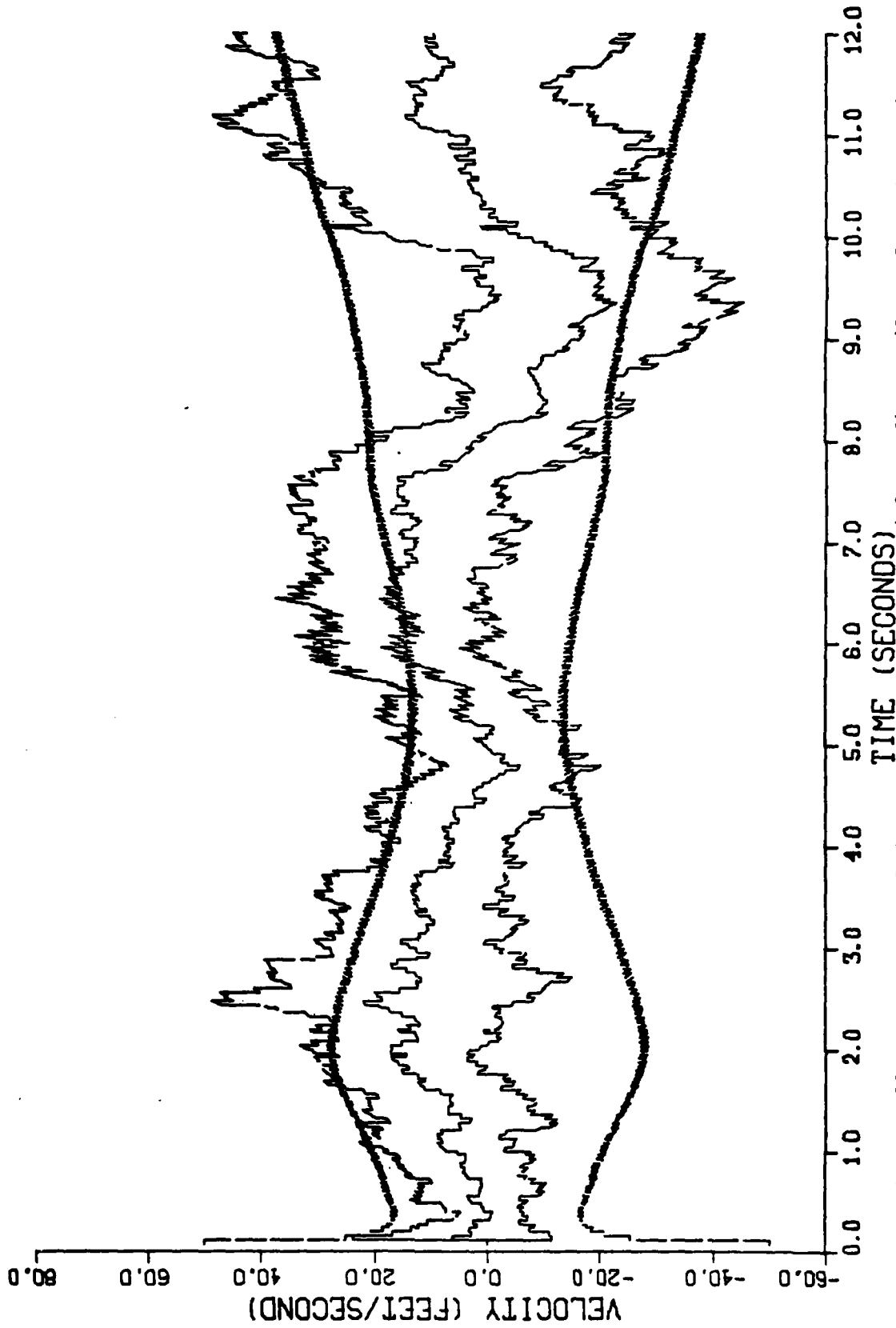


Figure H-11. Performance of the Constant Turn Rate Inertial Coordinate Filter Along the North-Axis for Trajectory 2 with Error Angle Measurement Noise Variances of 0.001 Radians²

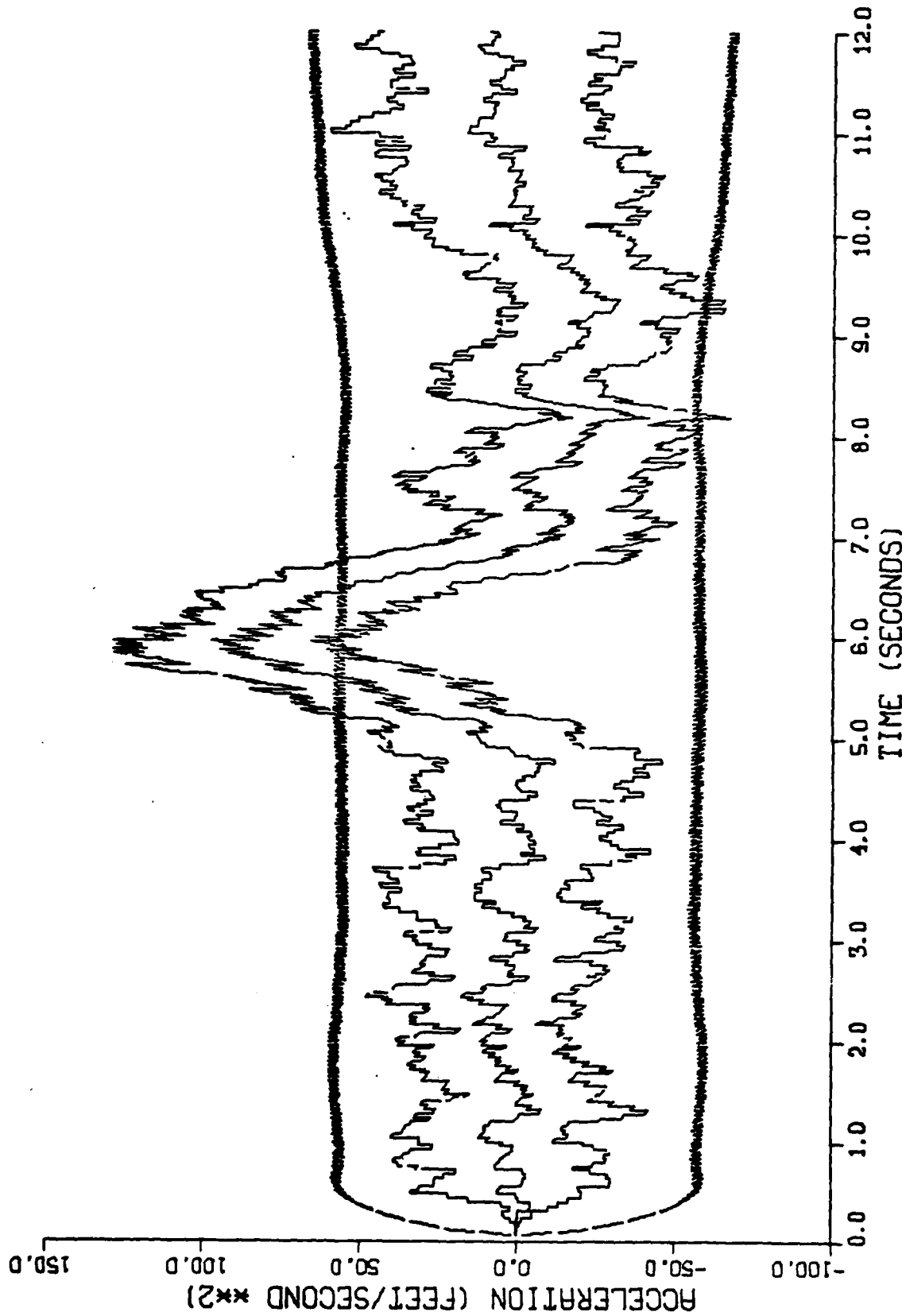


Figure H-12. Performance of the Constant Turn Rate Inertial Coordinate Filter Along the North-Axis for Trajectory 2 with Error Angle Measurement Noise Variances of 0.001 Radians²

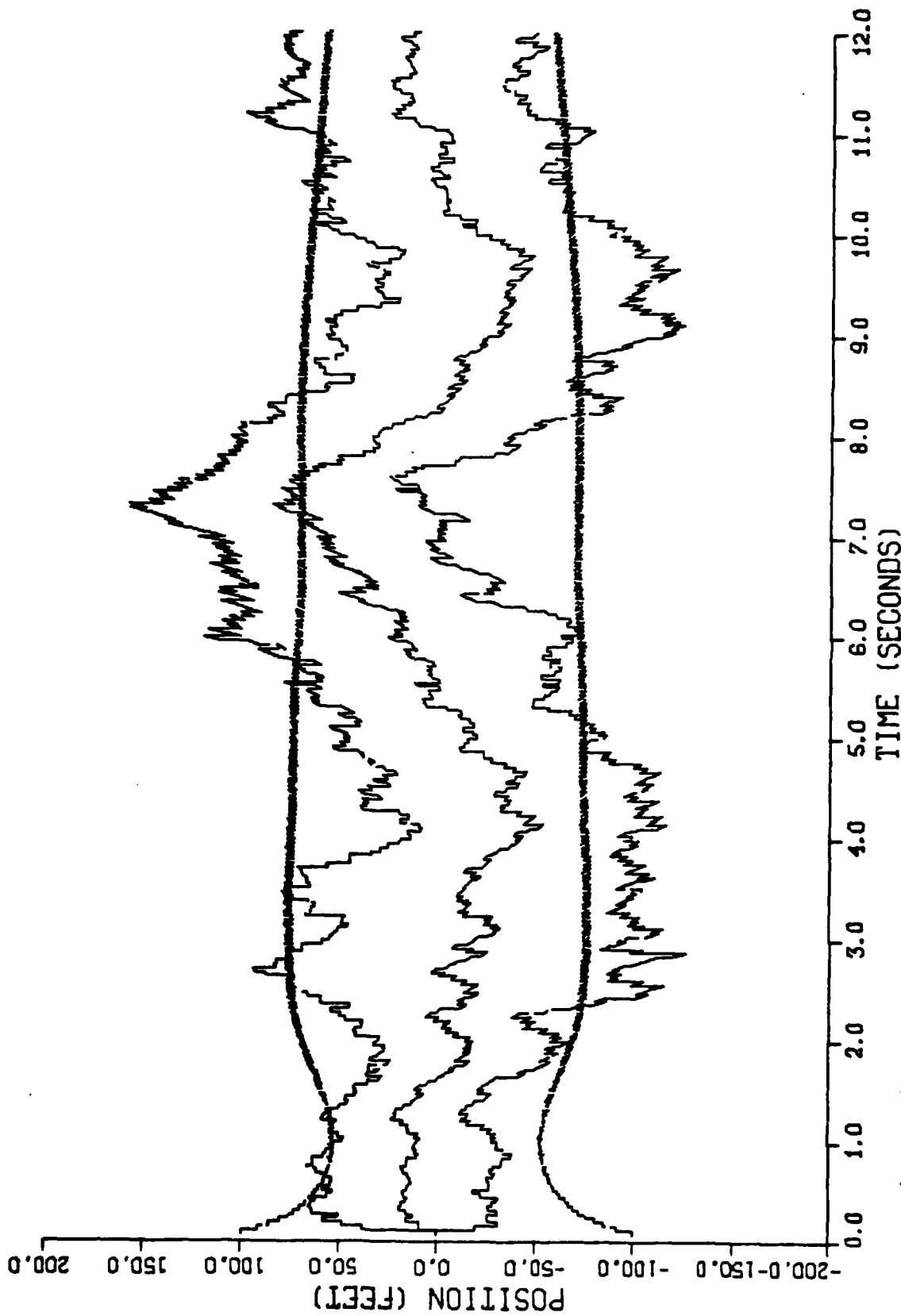


Figure H-13. Performance of the Constant Turn Rate Inertial Coordinate Filter Along the East-Axis for Trajectory 2 with Error Angle Measurement Noise Variances of 0.001 Radians²

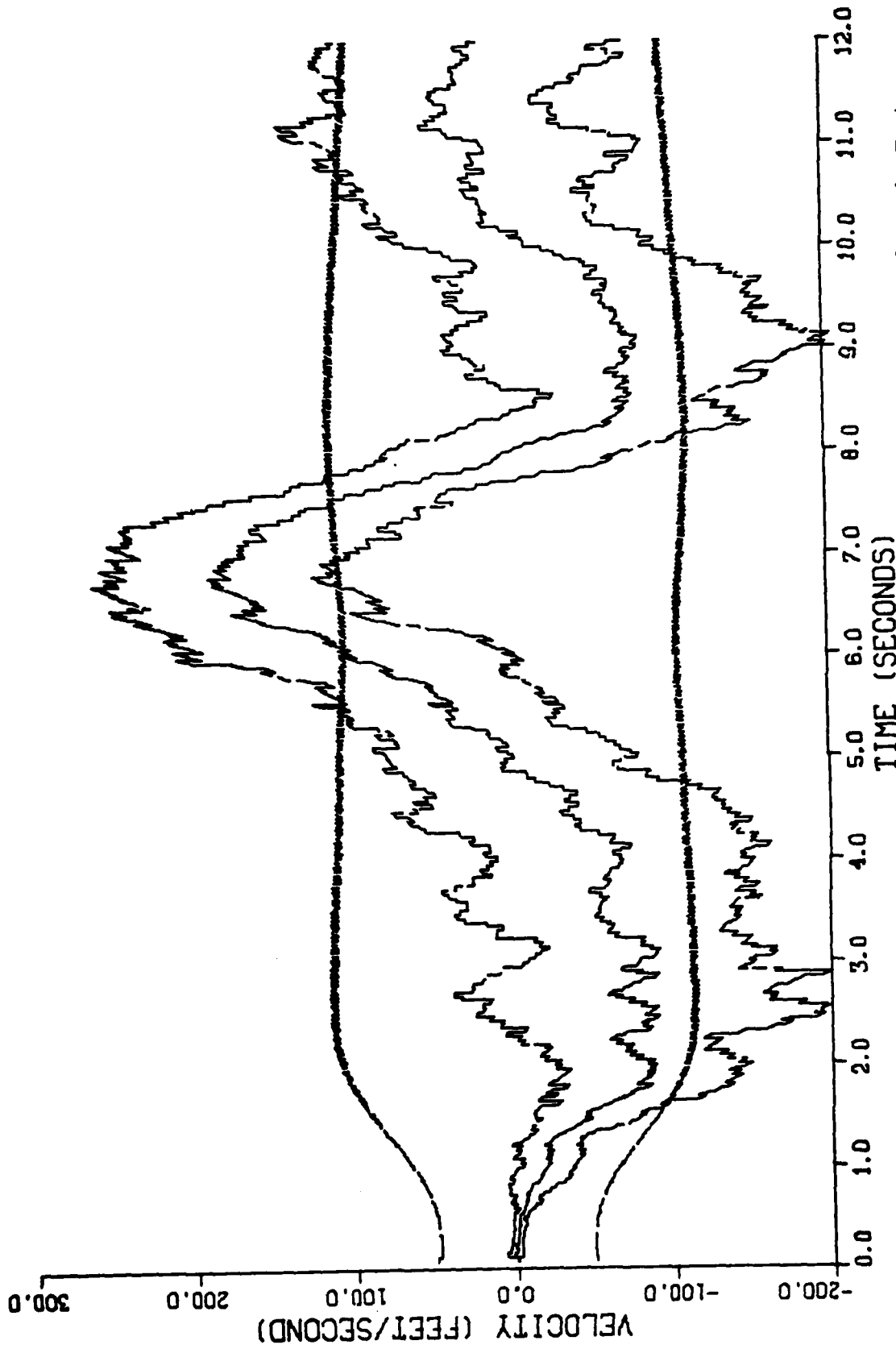


Figure H-14. Performance of the Constant Turn Rate Inertial Coordinate Filter Along the East-Axis for Trajectory 2 with Error Angle Measurement Noise Variances of 0.001 Radians²

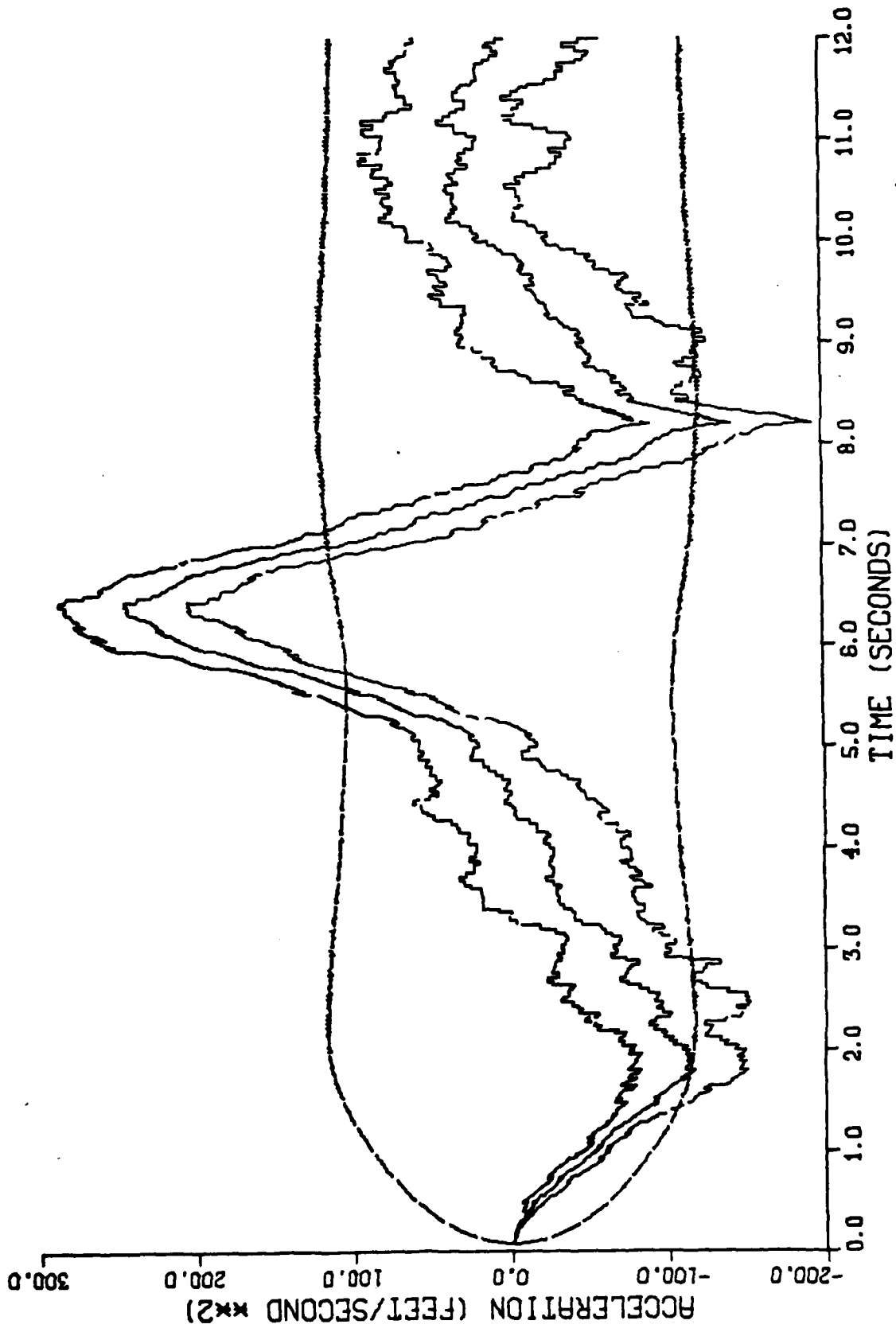


Figure H-15. Performance of the Constant Turn Rate Inertial Coordinate Filter Along the East-Axis for Trajectory 2 with Error Angle Measurement Noise Variances of 0.001 Radians²

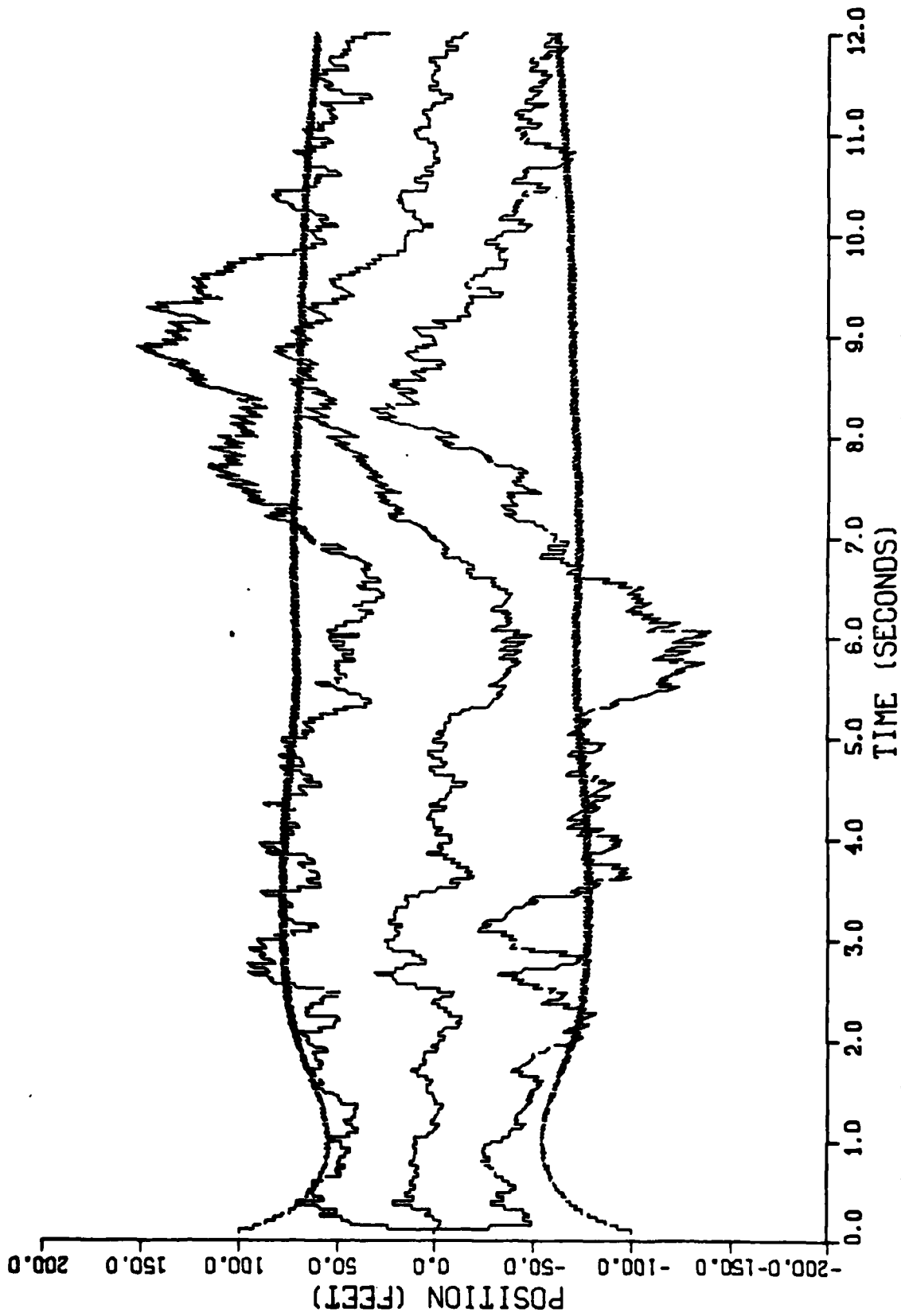


Figure H-16. Performance of the Constant Turn Rate Inertial Coordinate Filter Along the Down-Axis for Trajectory 2 with Error Angle Measurement Noise Variances of 0.001 Radians²

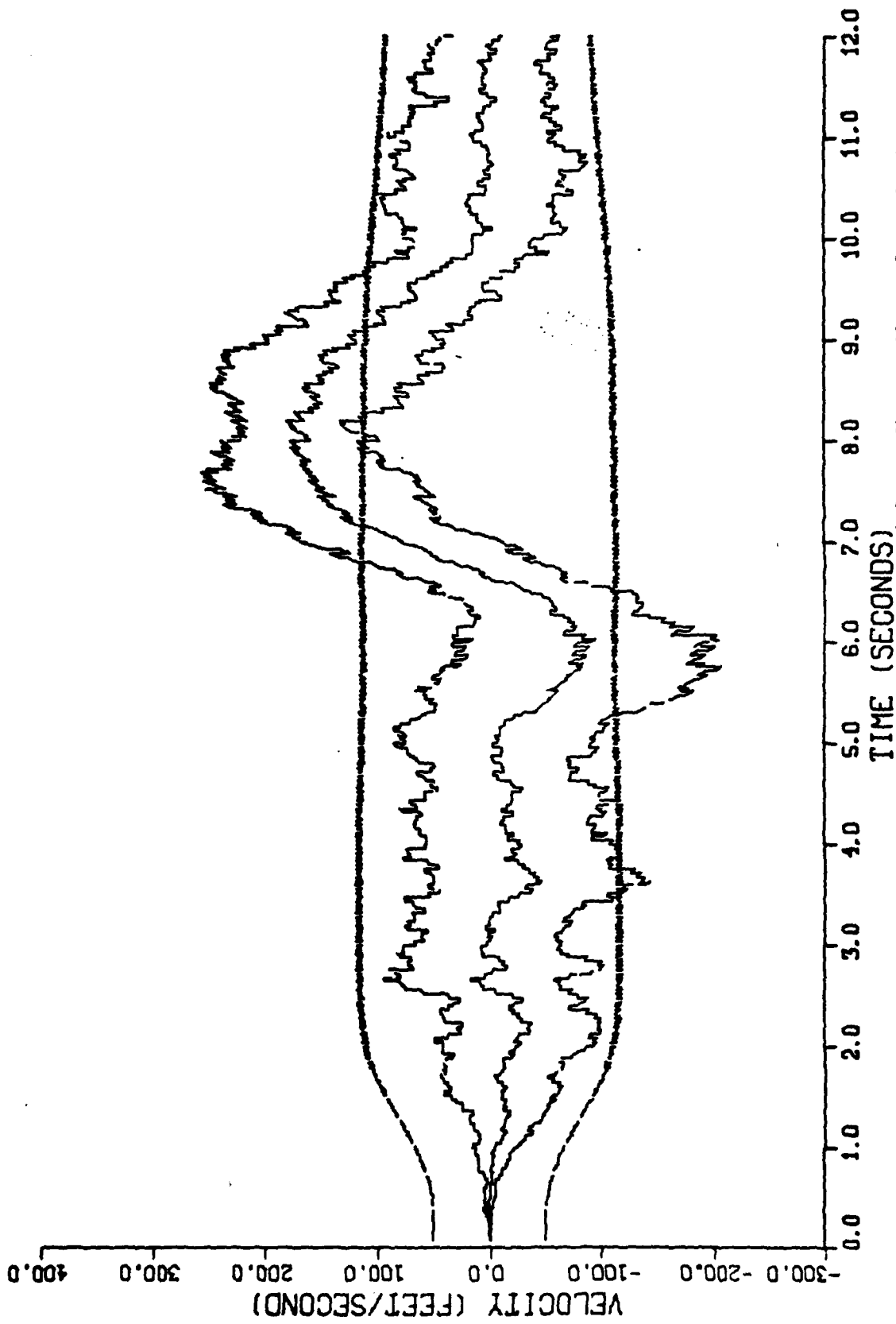


Figure H-17. Performance of the Constant Turn Rate Inertial Coordinate Filter Along the Down-Axis for Trajectory 2 with Error Angle Measurement Noise Variances of 0.001 Radians²

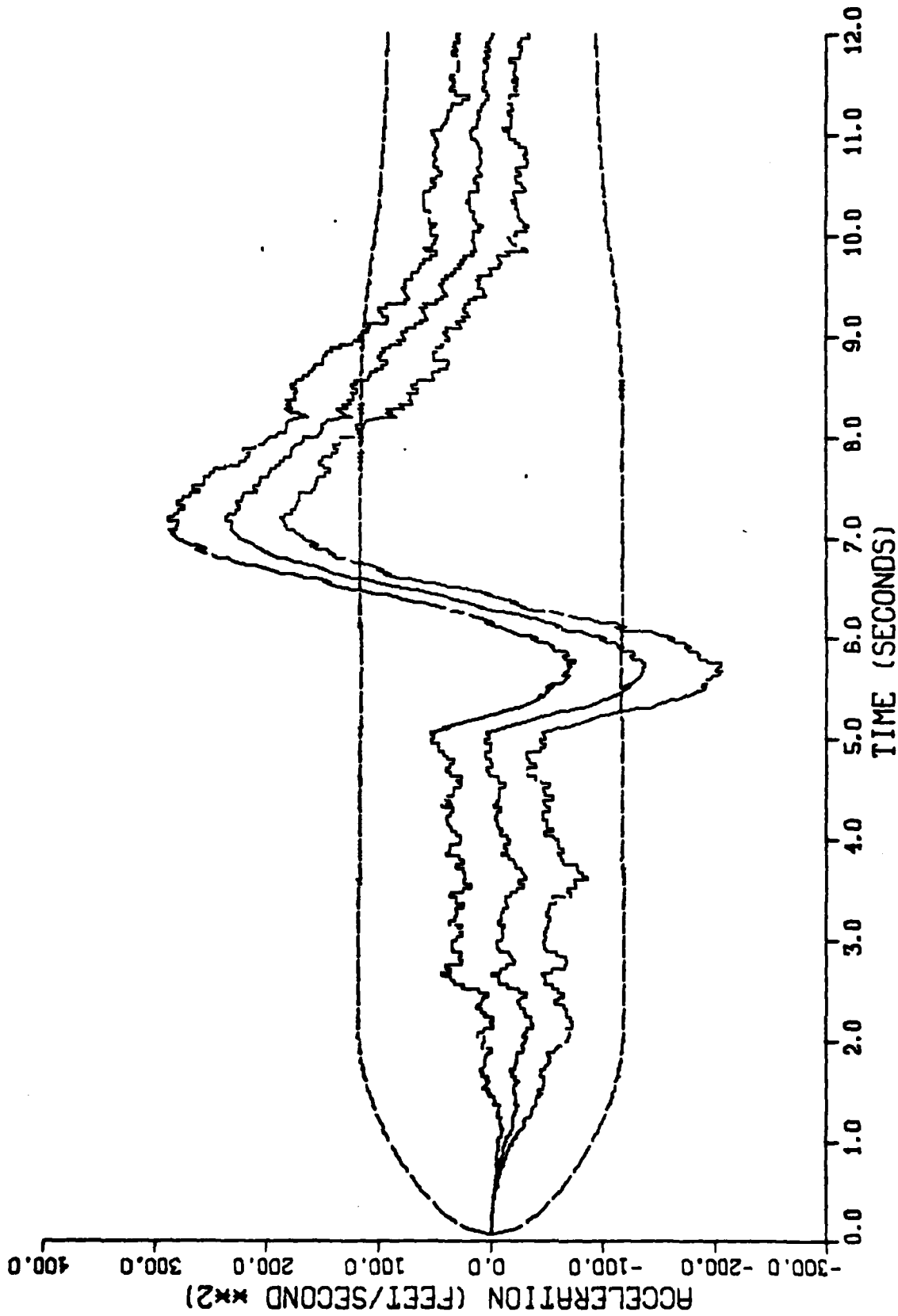


Figure H-18. Performance of the Constant Turn Rate Inertial Coordinate Filter Along the Down-Axis for Trajectory 2 with Error Angle Measurement Noise Variances of 0.001 Radians²

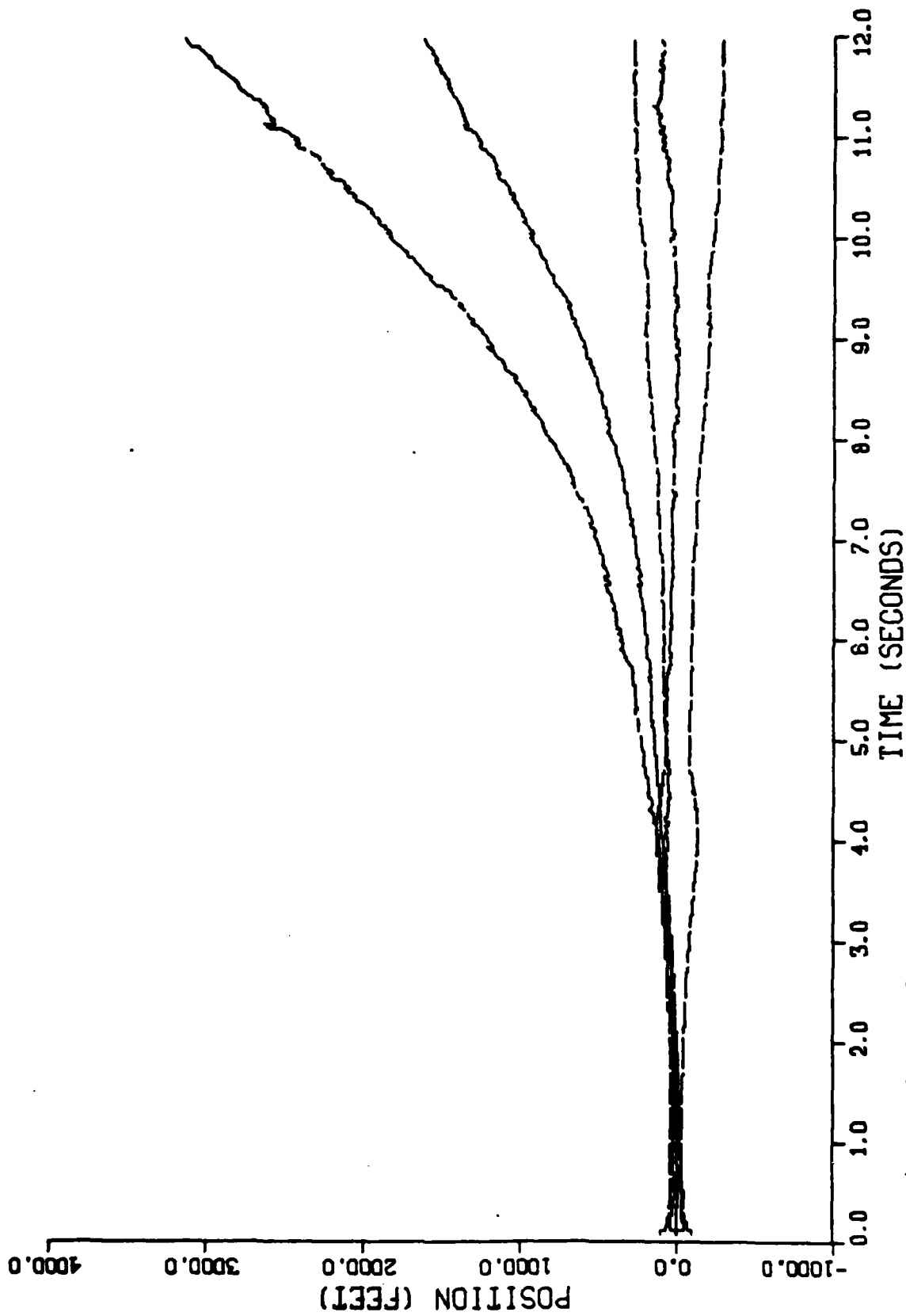


Figure H-19. Performance of the Constant Turn Rate Inertial Coordinate Filter Along the North-Axis for Trajectory 2 with No Error Angle Measurements

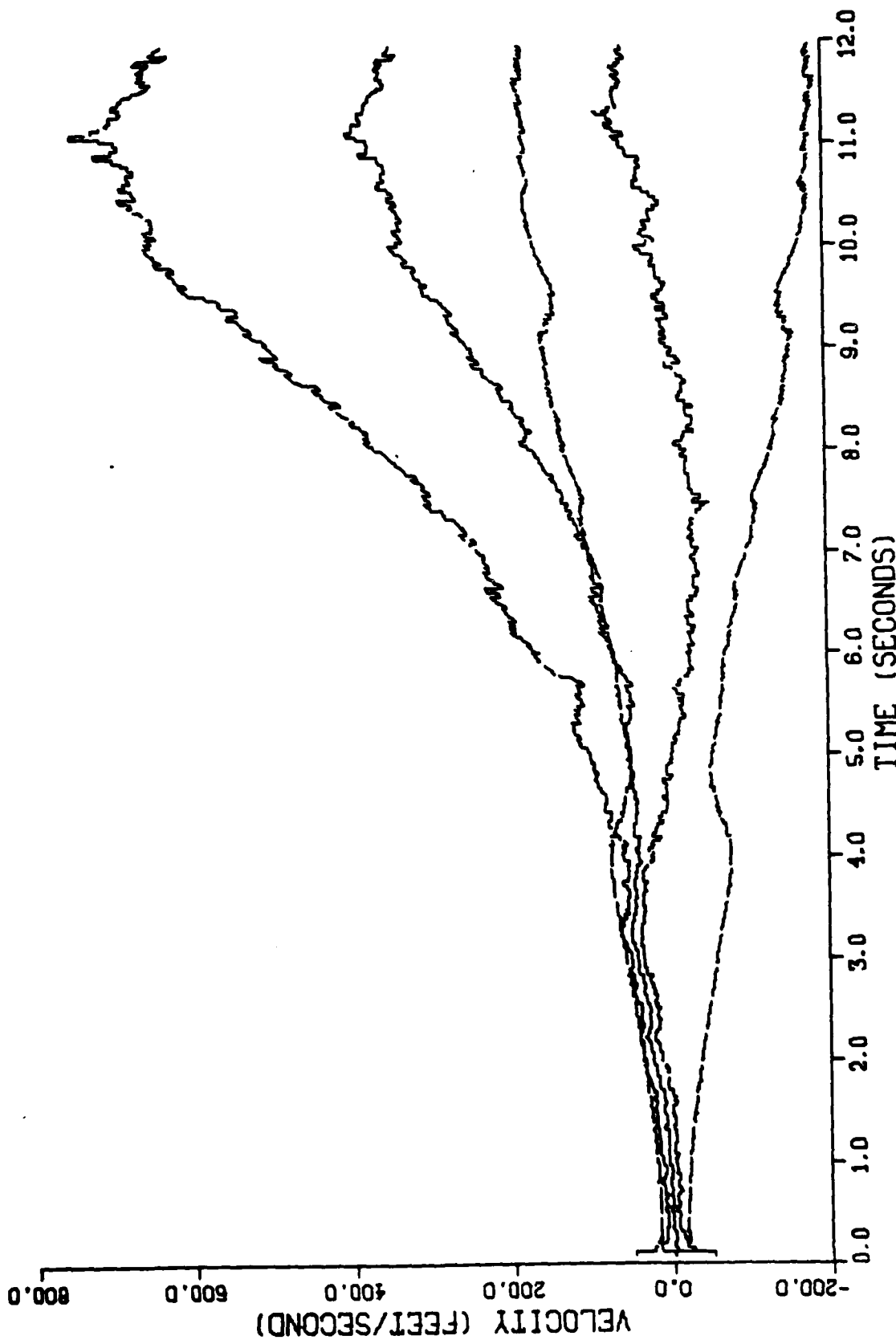


Figure H-20. Performance of the Constant Turn Rate Inertial Coordinate Filter Along the North-Axis for Trajectory 2 with No Error Angle Measurements

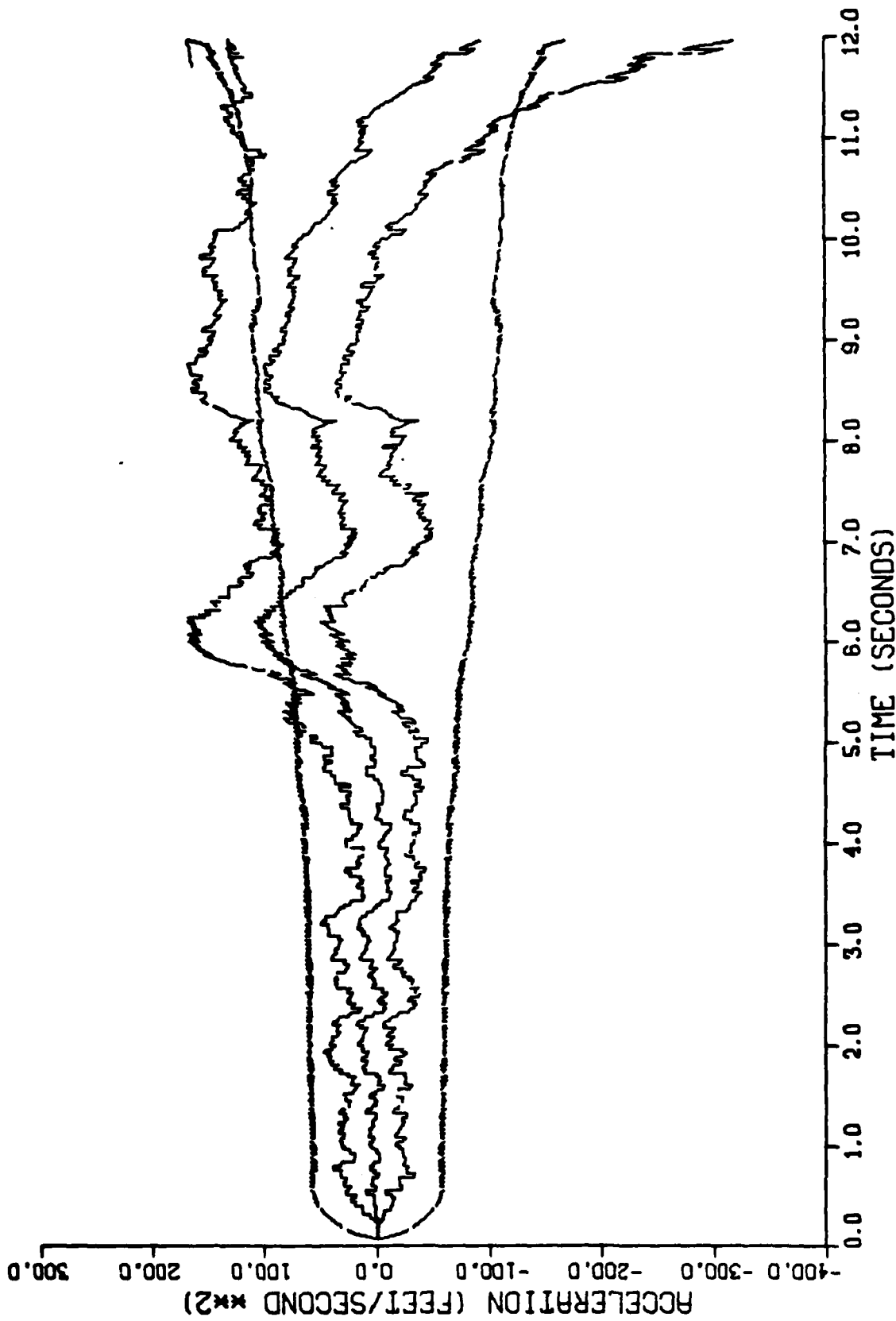


Figure H-21. Performance of the Constant Turn Rate Inertial Coordinate Filter Along the North-Axis for Trajectory 2 with No Error Angle Measurements

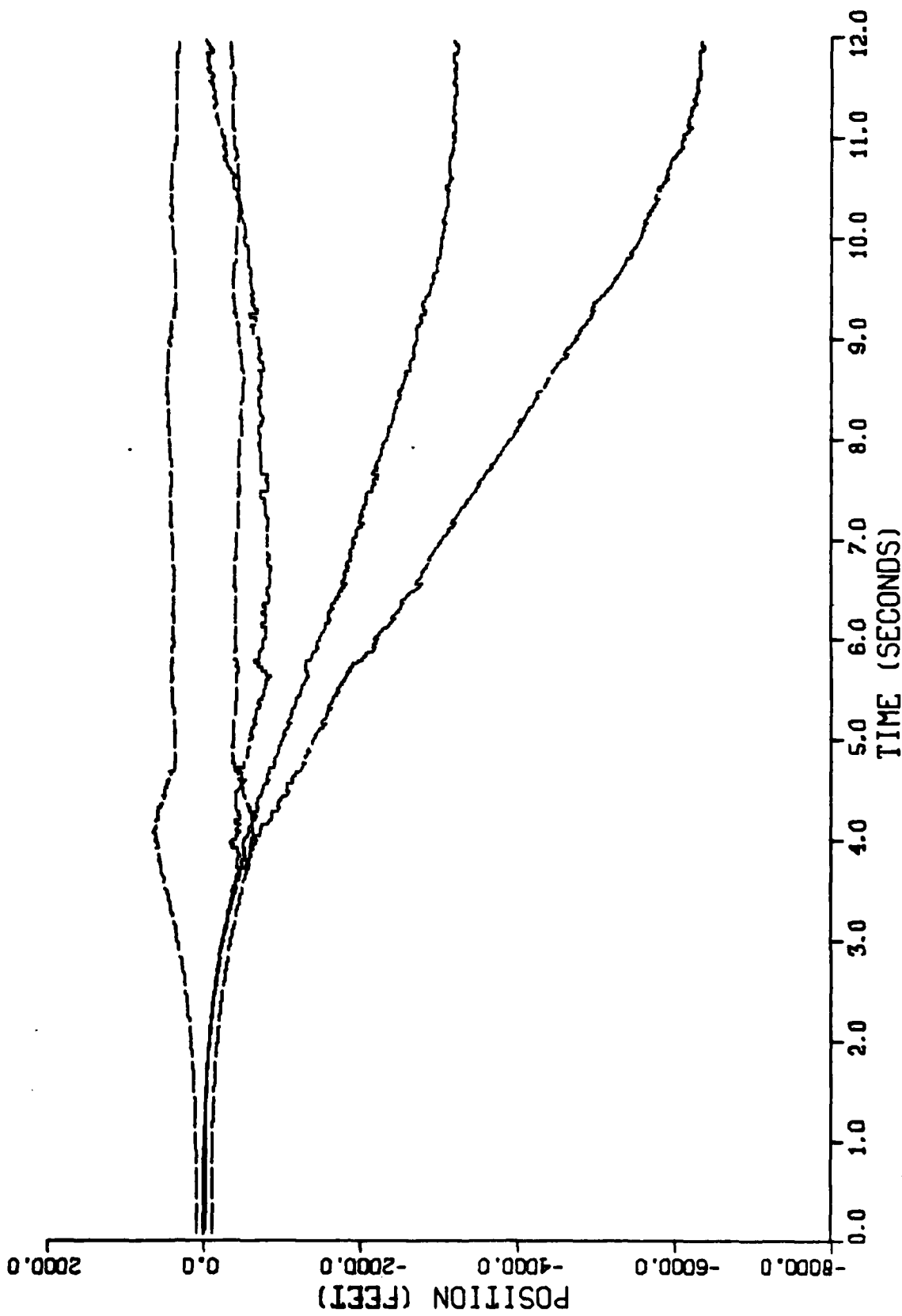


Figure H-22. Performance of the Constant Turn Rate Inertial Coordinate Filter Along the East-Axis for Trajectory 2 with No Error Angle Measurements

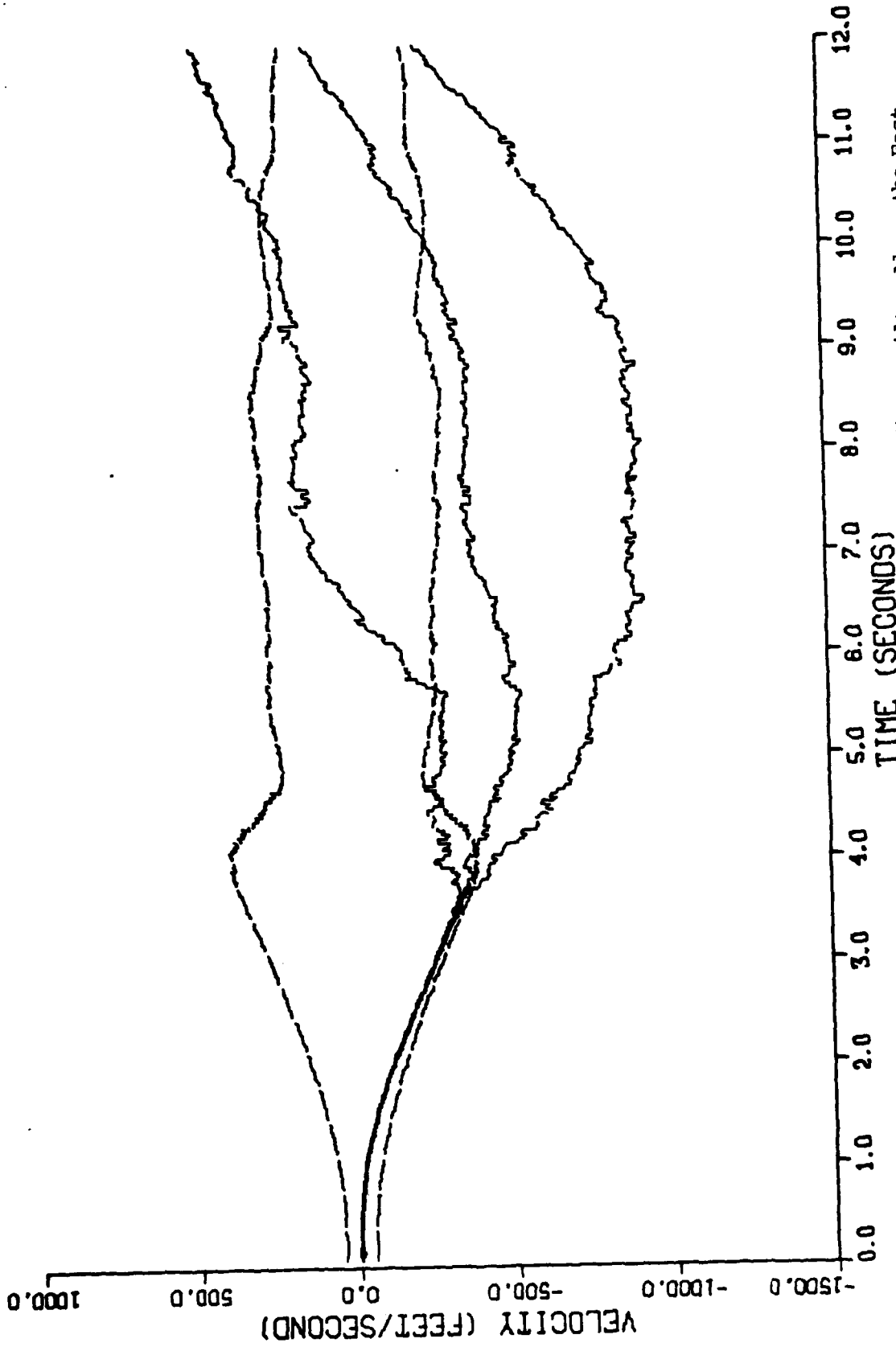


Figure H-23. Performance of the Constant Turn Rate Inertial Coordinate Filter Along the East-Axis for Trajectory 2 with No Error Angle Measurements

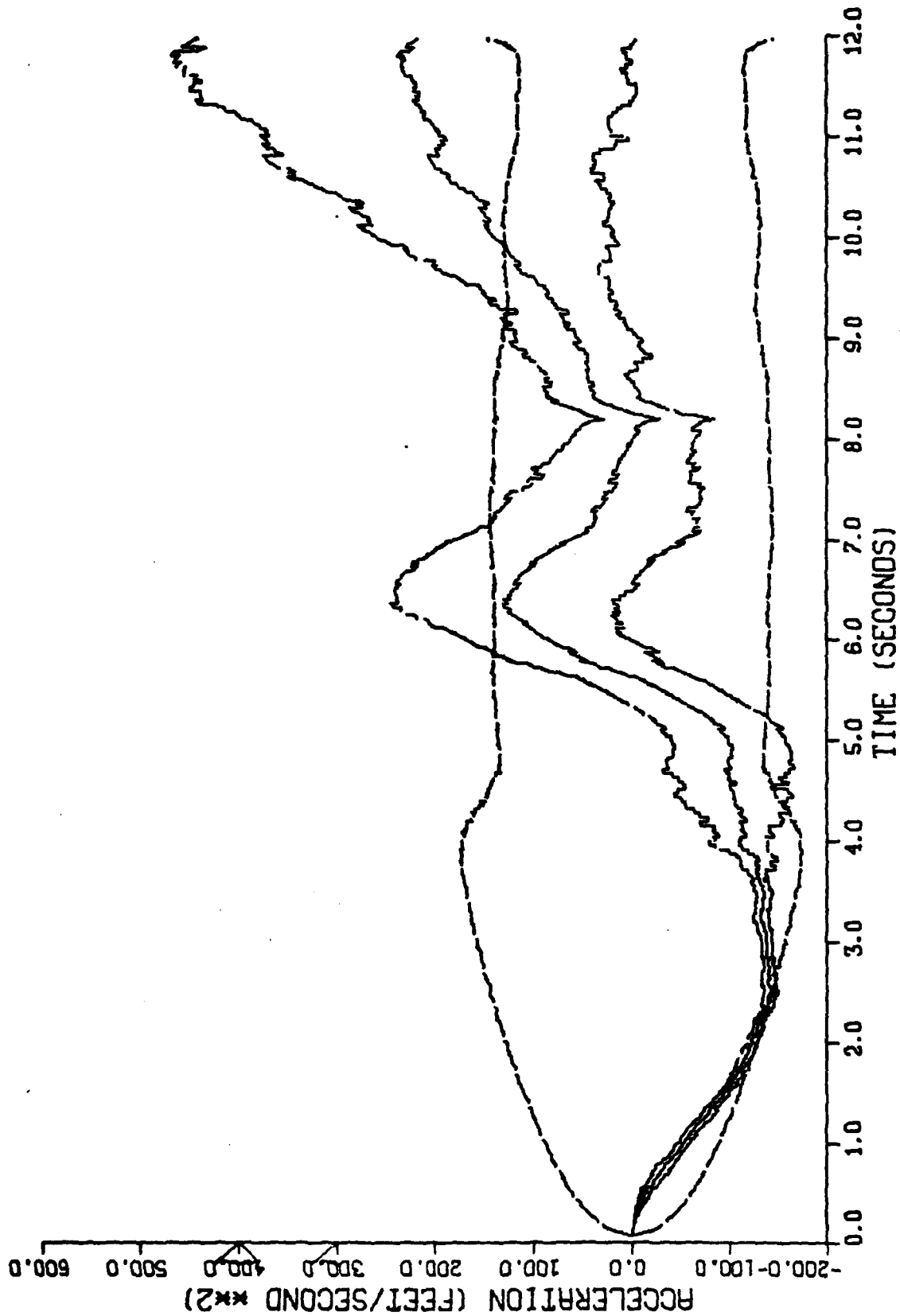


Figure H-24. Performance of the Constant Turn Rate Inertial Coordinate Filter Along the East-Axis for Trajectory 2 with No Error Angle Measurements

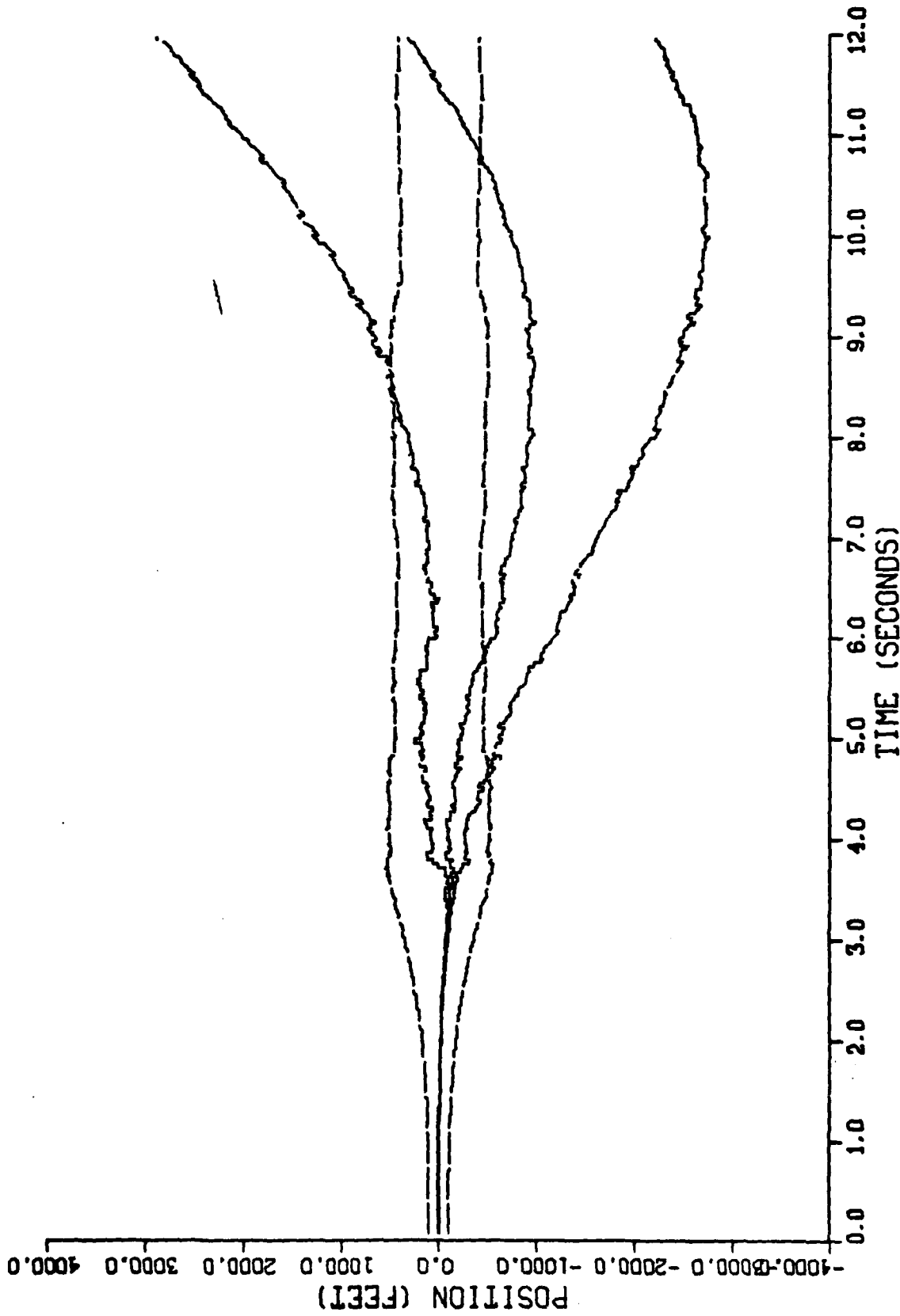


Figure H-25. Performance of the Constant Turn Rate Inertial Coordinate Filter Along the Down-Axis for Trajectory 2 with No Error Angle Measurements

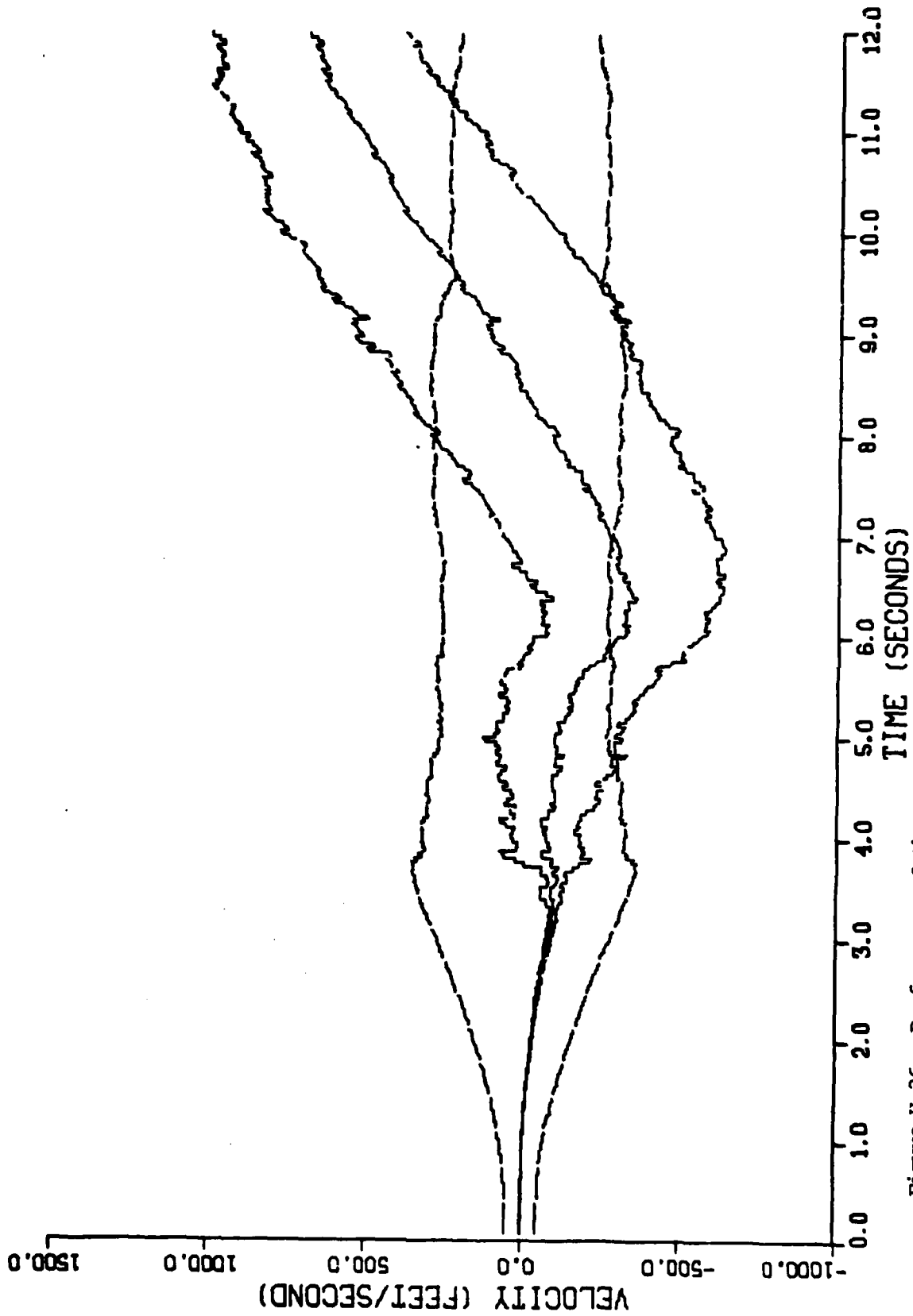


Figure H-26. Performance of the Constant Turn Rate Inertial Coordinate Filter Along the Down-Axis for Trajectory 2 with No Error Angle Measurements

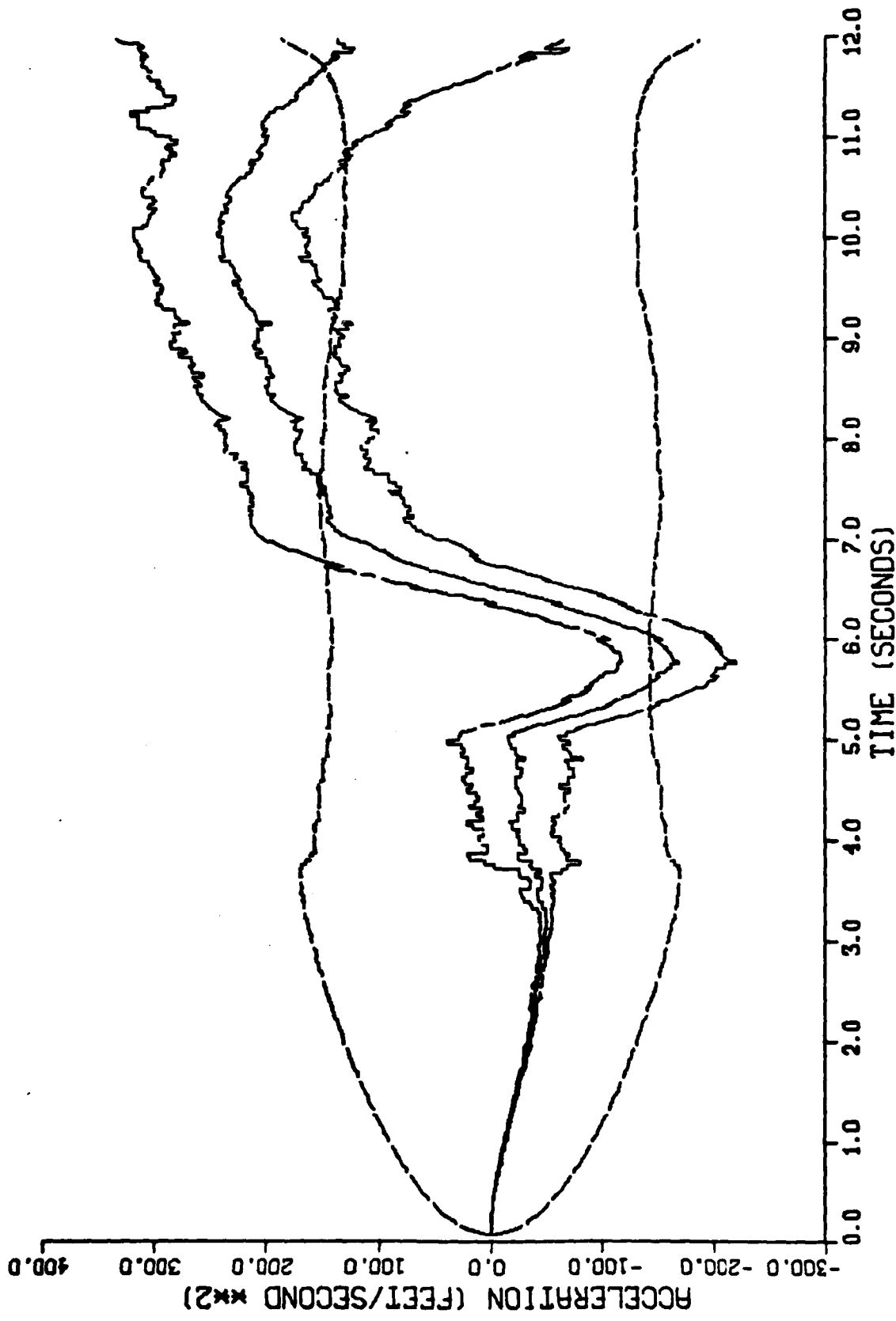


Figure H-27. Performance of the Constant Turn Rate Inertial Coordinate Filter Along the Down-Axis for Trajectory 2 with No Error Angle Measurements

APPENDIX I

Graphical Results of the Effect of Variations of
The Range Rate Measurement Noise on the Performance
of the Constant Turn Rate Inertial Coordinate Filter

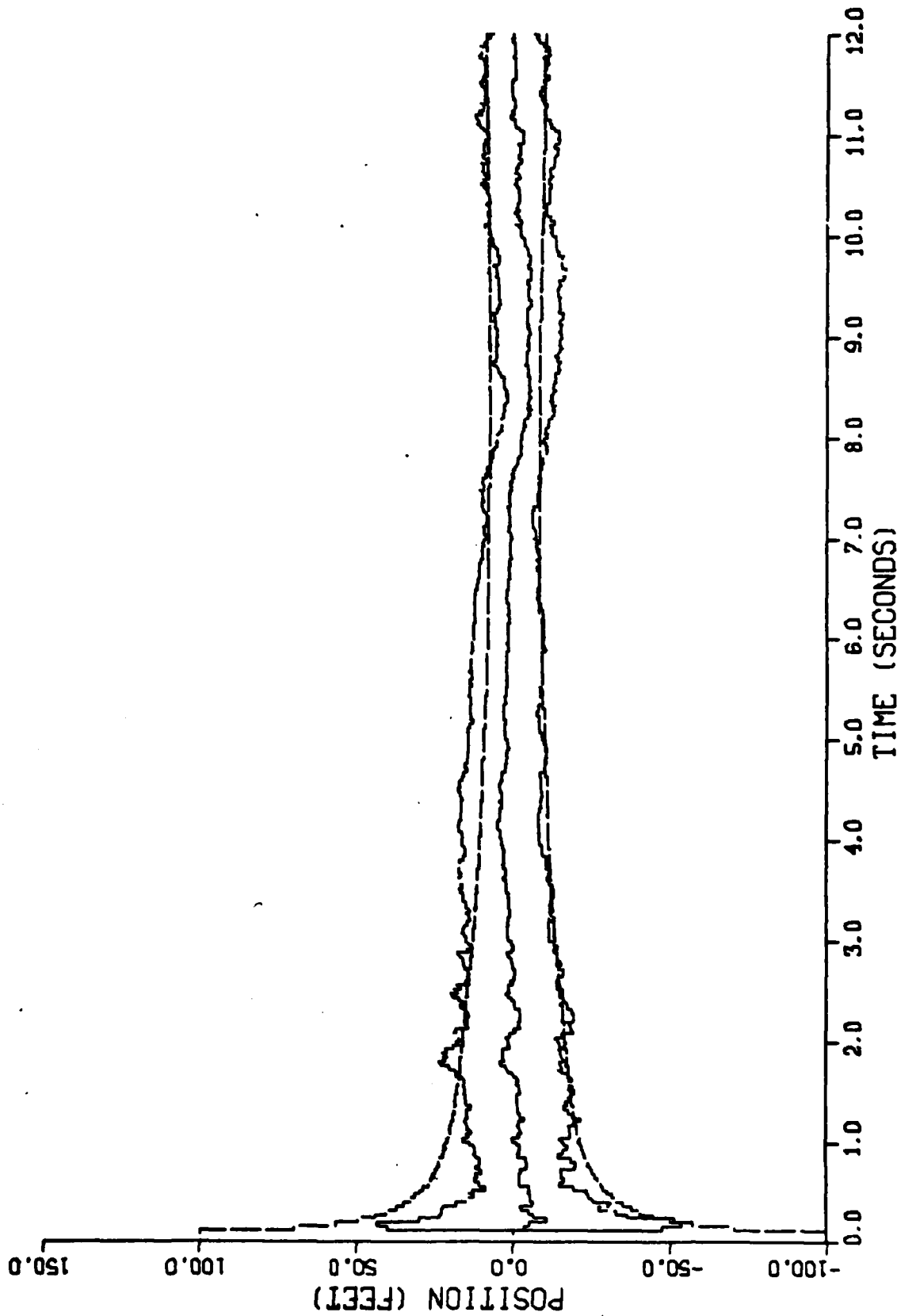


Figure I-1. Performance of the Constant Turn Rate Inertial Coordinate Filter Along the North-Axis for Trajectory 2 with a Range Rate Measurement Noise Variance of $62.5 \text{ Feet}^2/\text{Second}^2$

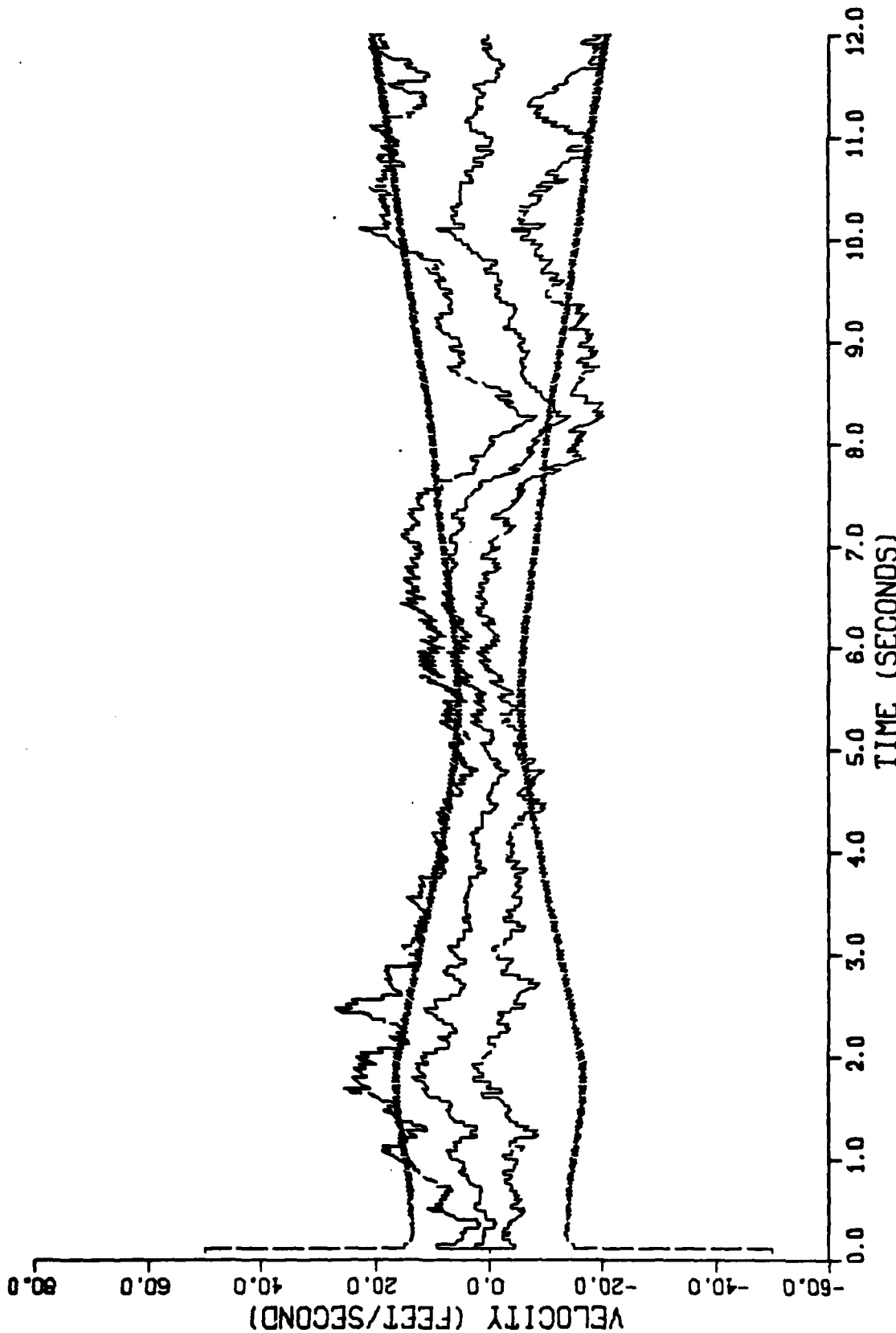


Figure I-2. Performance of the Constant Turn Rate Inertial Coordinate Filter Along the North-Axis for Trajectory 2 with a Range Rate Measurement Noise Variance of 62.5 Feet²/Second²

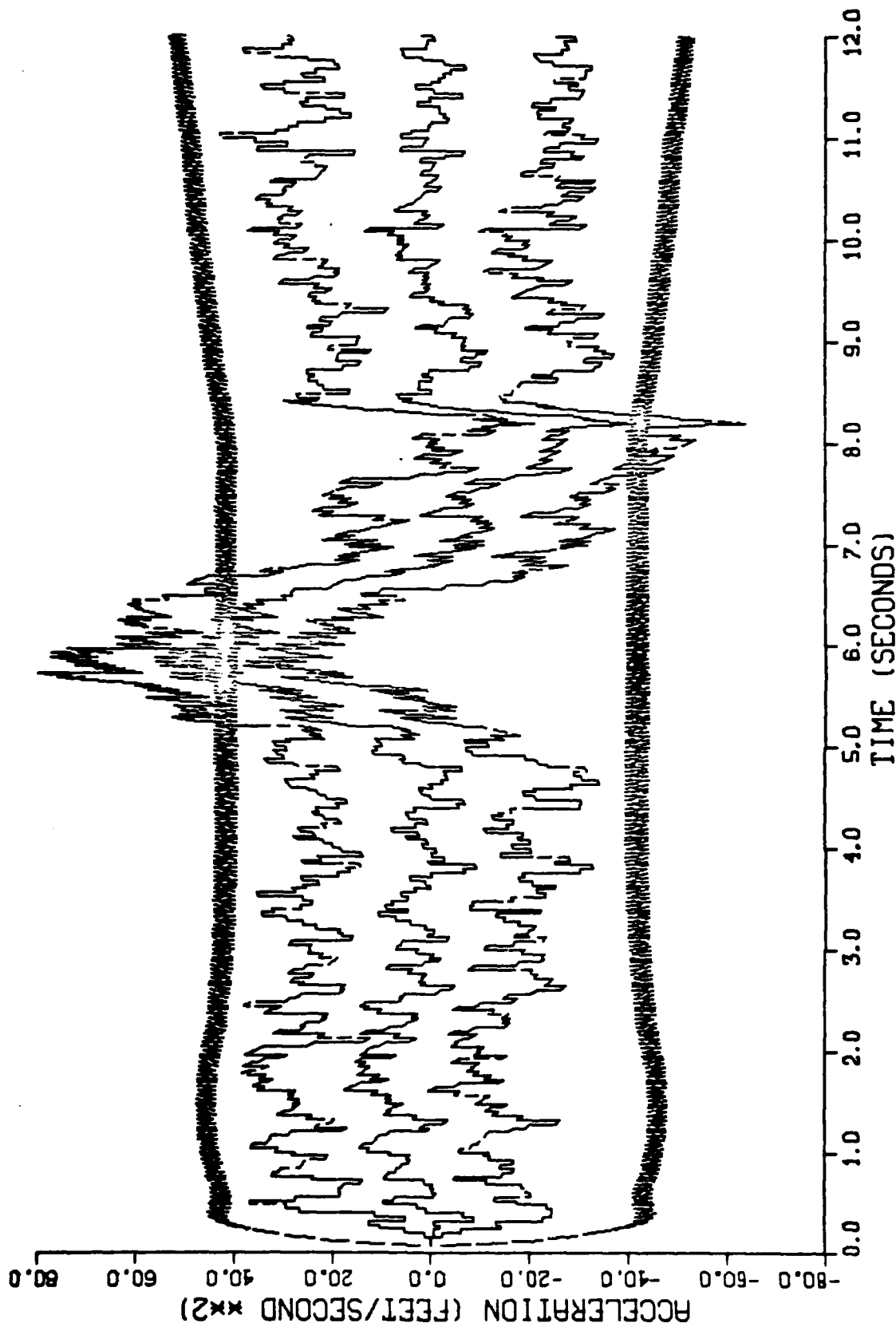


Figure I-3. Performance of the Constant Turn Rate Inertial Coordinate Filter Along the North-Axis for Trajectory 2 with a Range Rate Measurement Noise Variance of $62.5 \text{ Feet}^2/\text{Second}^2$

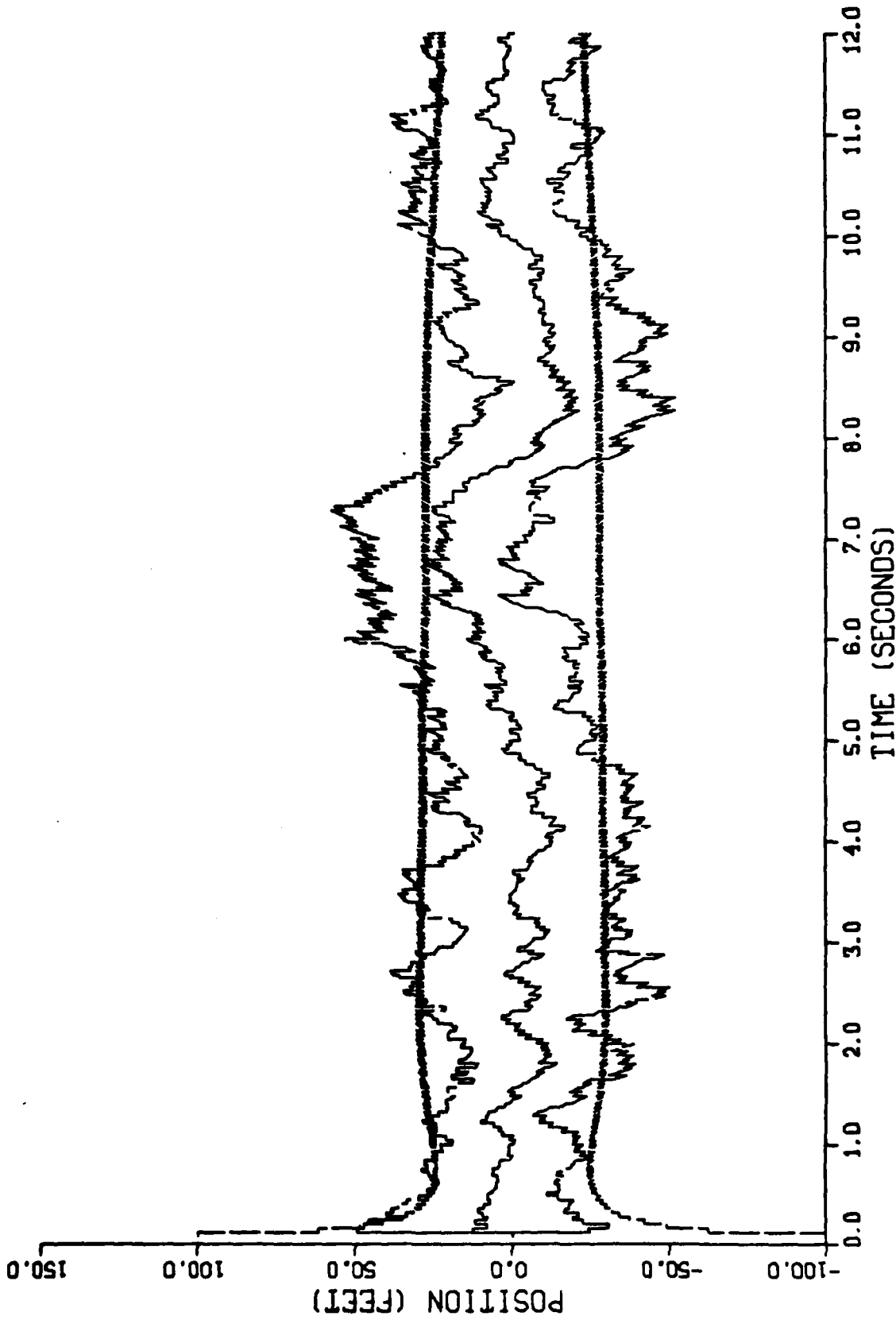


Figure I-4. Performance of the Constant Turn Rate Inertial Coordinate Filter Along the East-Axis for Trajectory 2 with a Range Rate Measurement Noise Variance of $62.5 \text{ Feet}^2/\text{Second}^2$

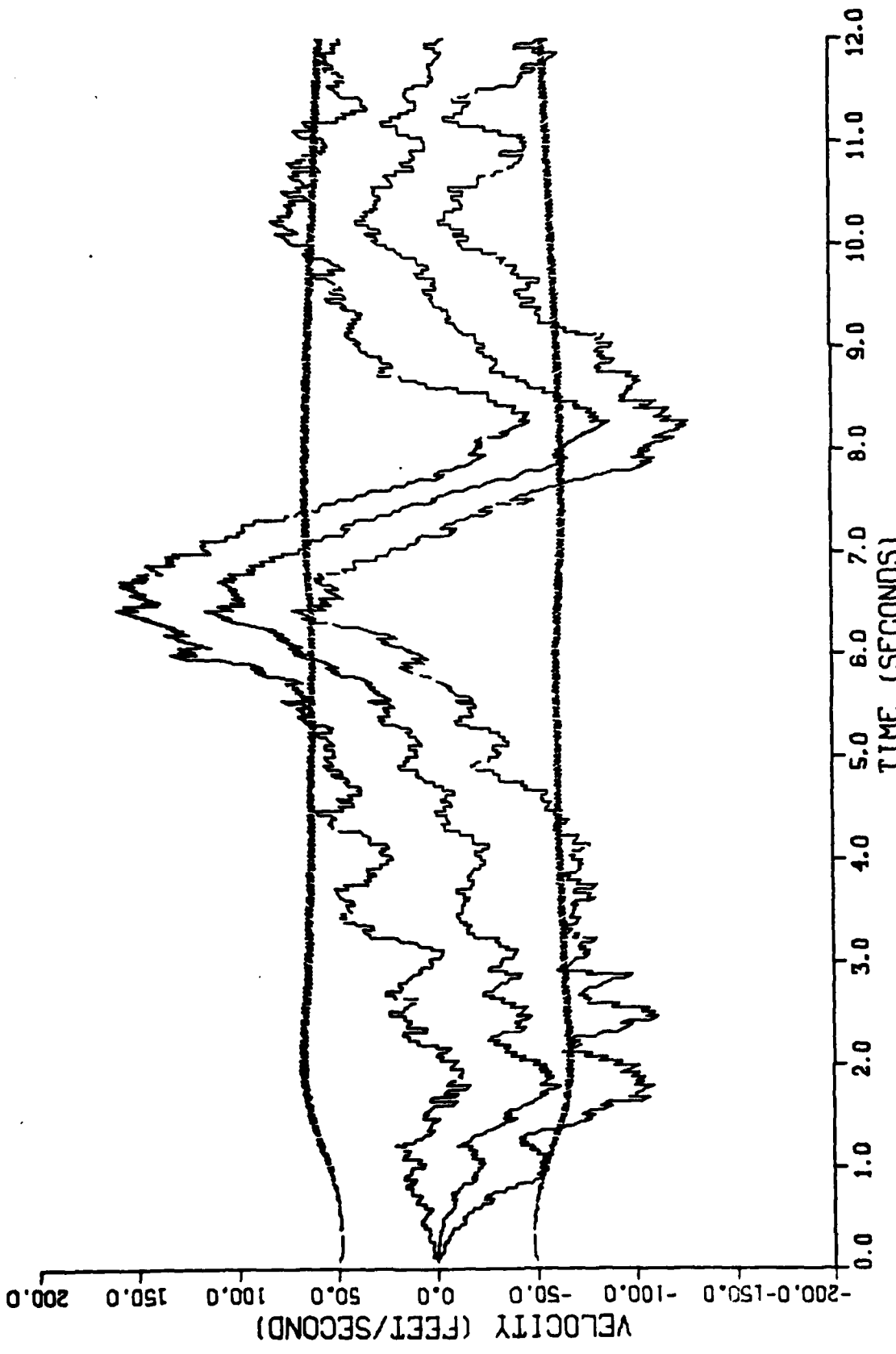


Figure I-5. Performance of the Constant Turn Rate Inertial Coordinate Filter Along the East-Axis for Trajectory 2 with a Range Rate Measurement Noise Variance of 62.5 Feet²/Second²

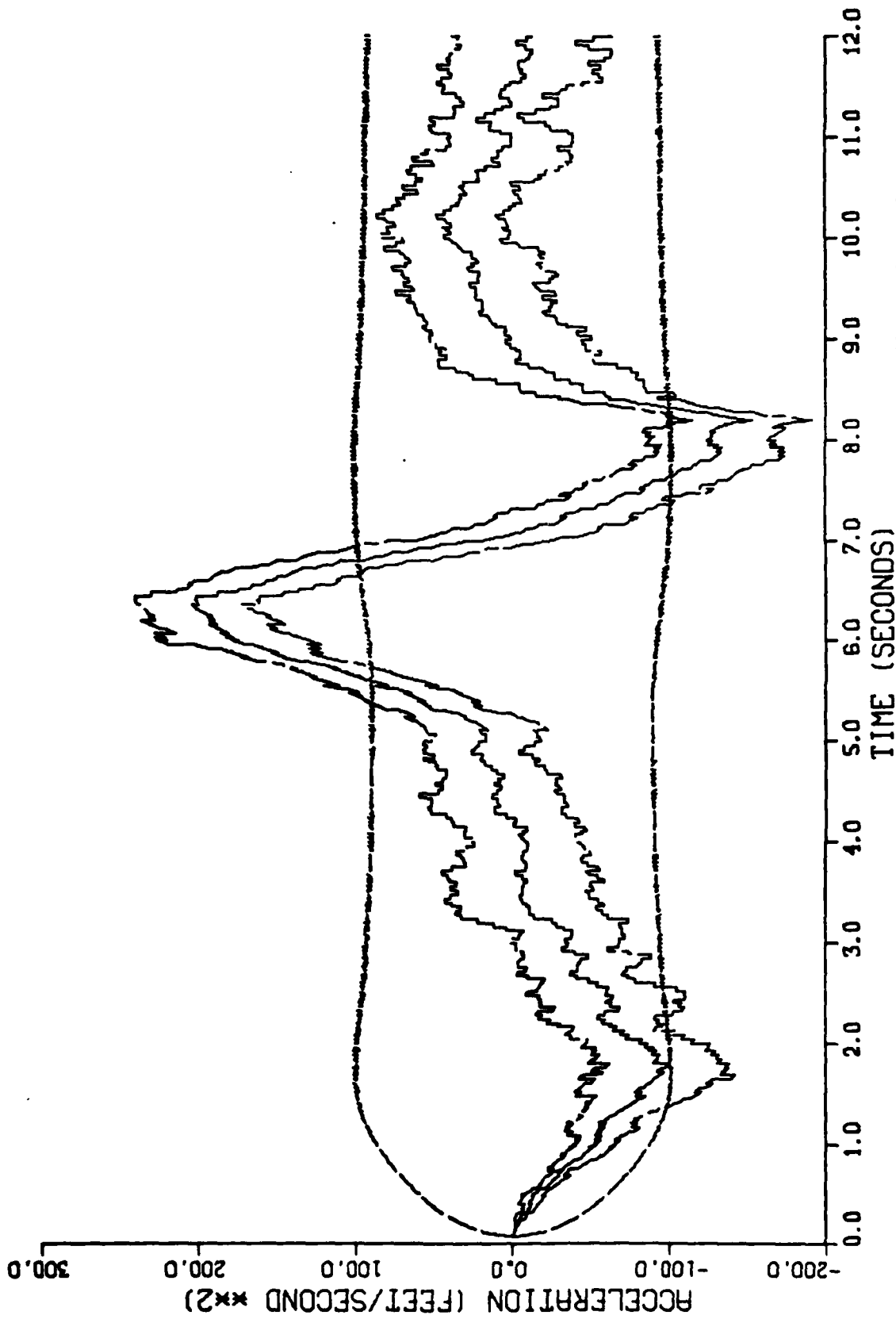


Figure I-6. Performance of the Constant Turn Rate Inertial Coordinate Filter Along the East-Axis for Trajectory 2 with a Range Rate Measurement Noise Variance of 62.5 Feet²/Second²

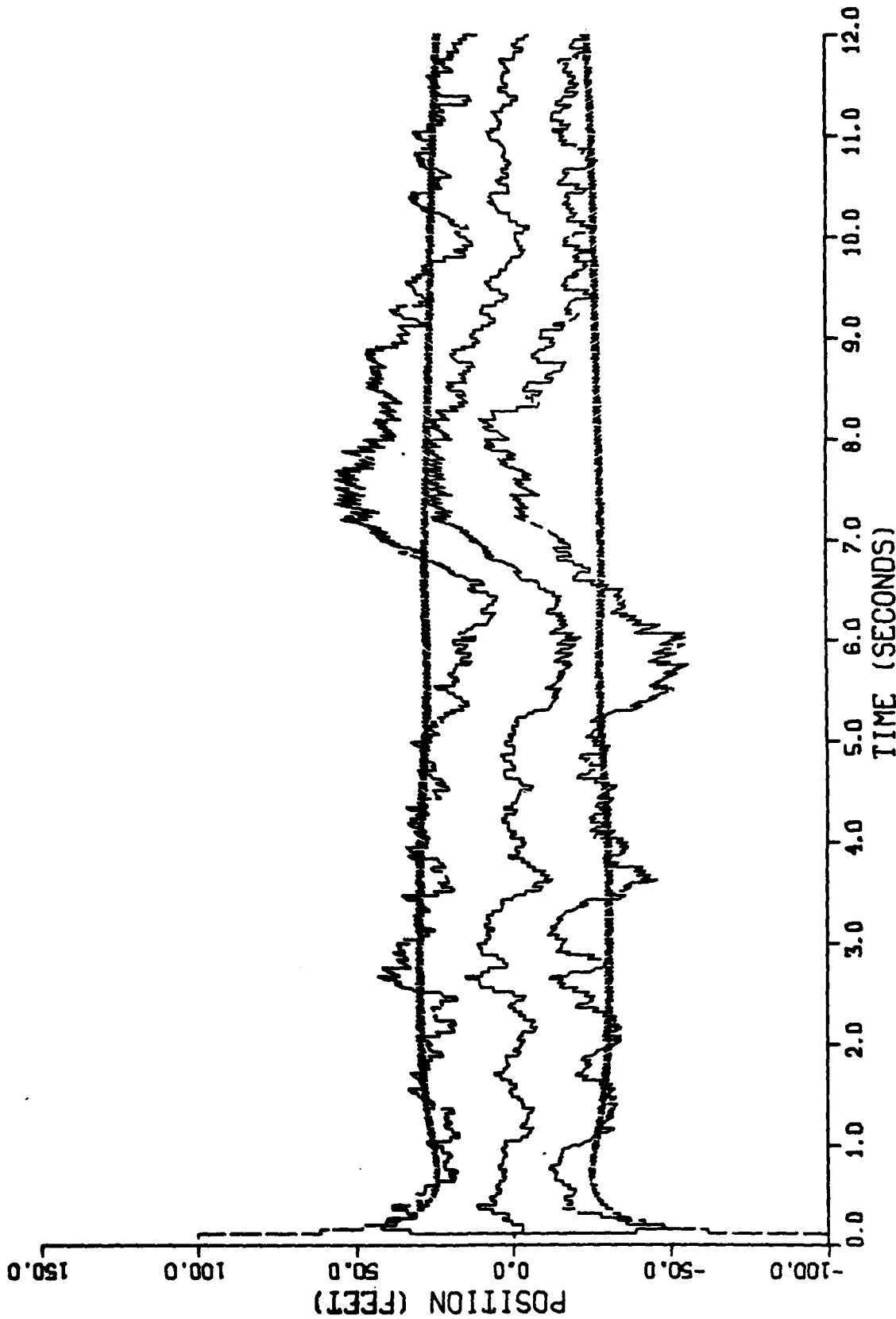


Figure I-7. Performance of the Constant Turn Rate Inertial Coordinate Filter Along the Down-Axis for Trajectory 2 with a Range Rate Measurement Noise Variance of $62.5 \text{ Feet}^2/\text{Second}^2$

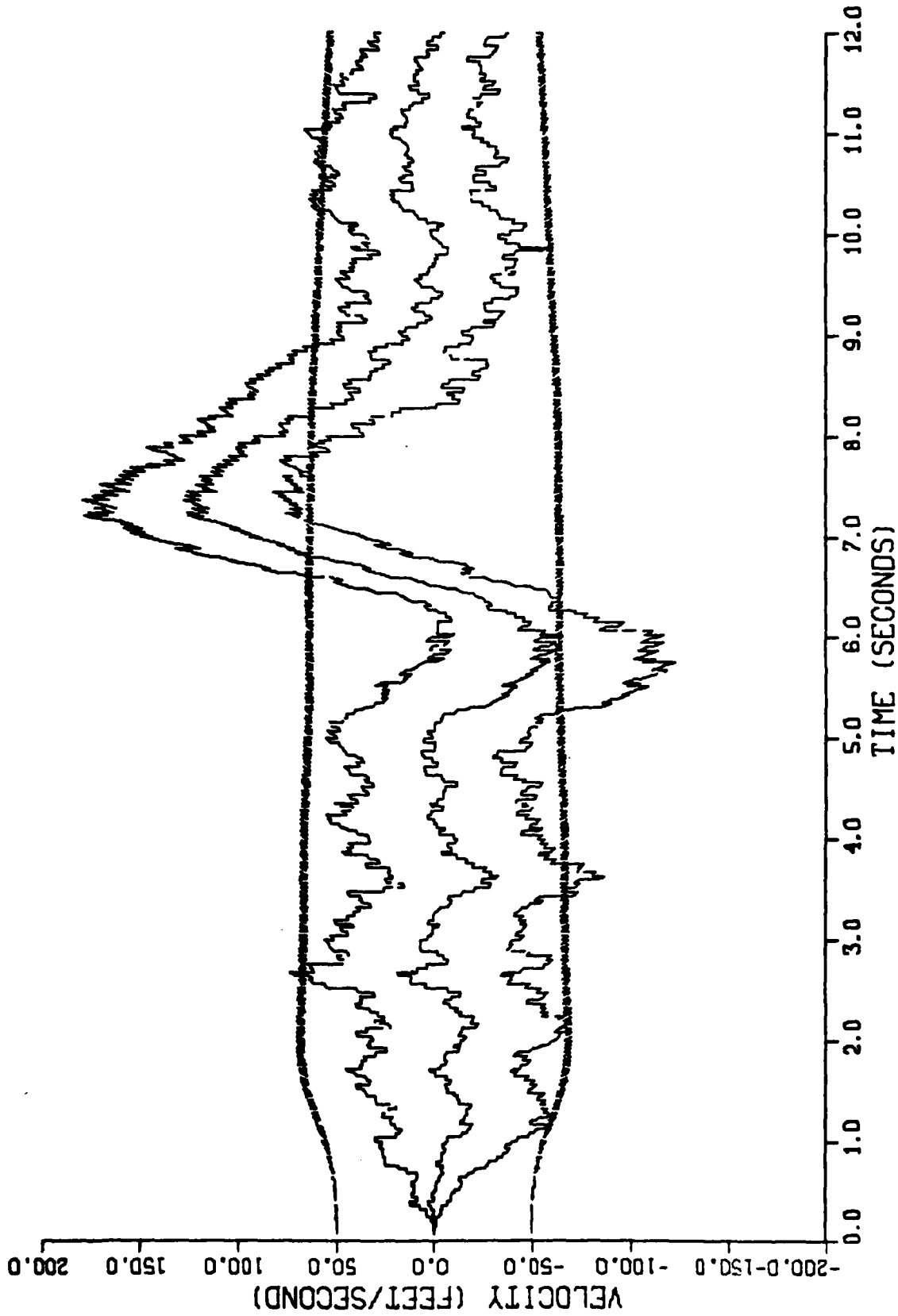


Figure I-8. Performance of the Constant Turn Rate Inertial Coordinate Filter Along the Down-Axis for Trajectory 2 with a Range Rate Measurement Noise Variance of 62.5 Feet²/Second²

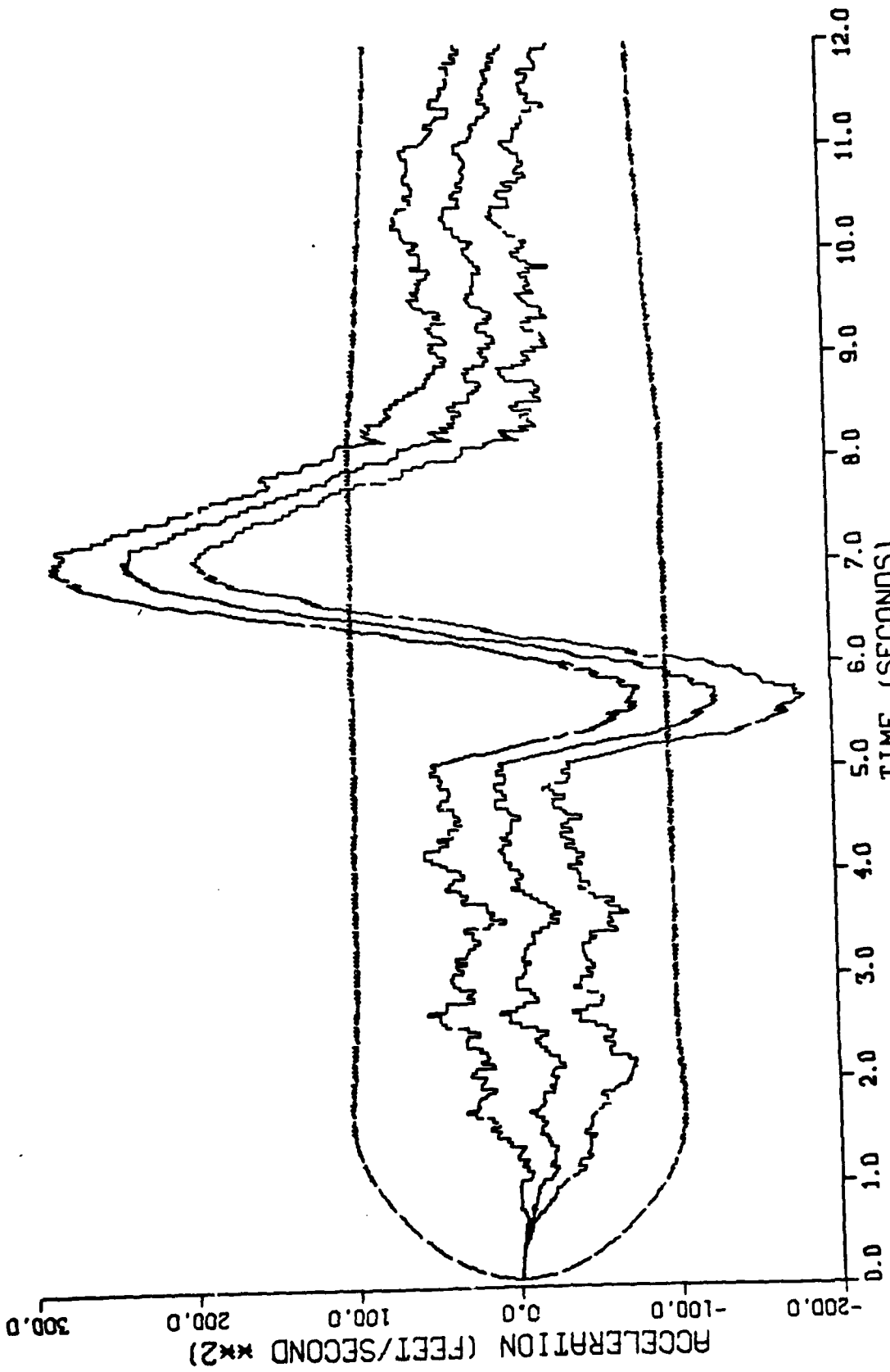


Figure I-9. Performance of the Constant Turn Rate Inertial Coordinate Filter Along the Down² Axis for Trajectory 2 with a Range Rate Measurement Noise Variance of 62.5 Feet²/Second²

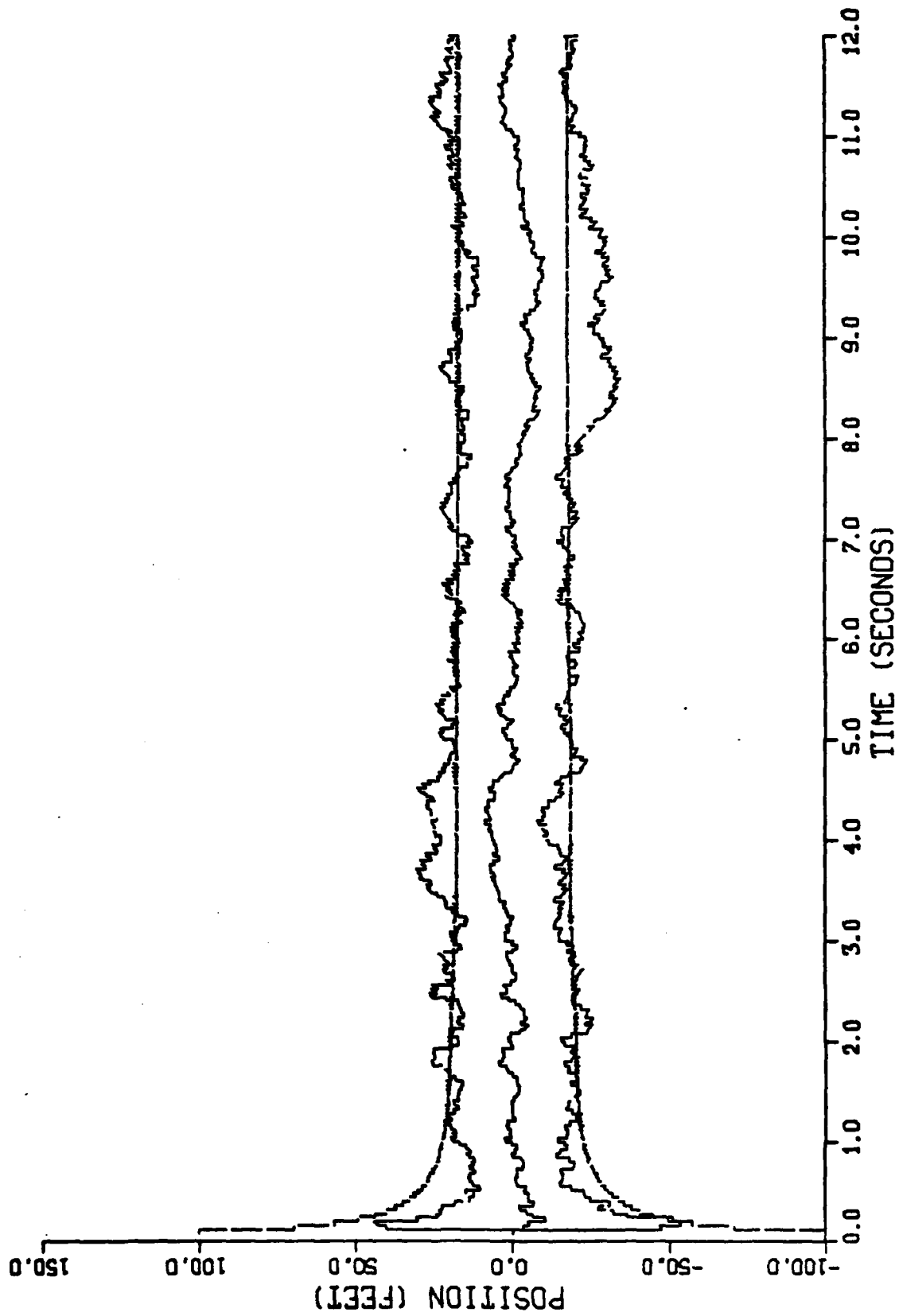


Figure I-10. Performance of the Constant Turn Rate Inertial Coordinate Filter Along the North-
 Axis for Trajectory 2 with a Range Rate Measurement Noise Variance of $6250 \text{ Feet}^2/\text{Second}^2$

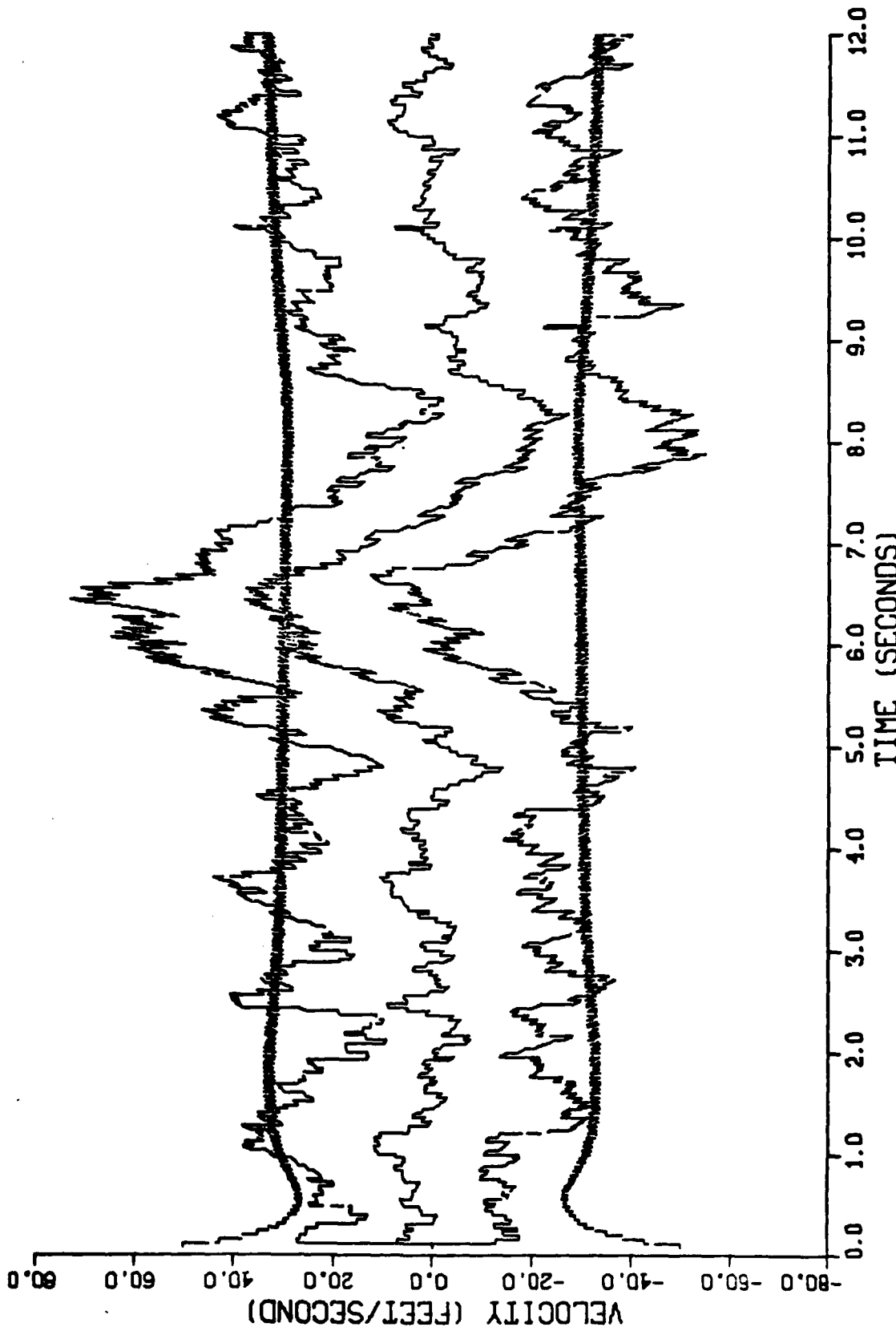


Figure I-11. Performance of the Constant Turn Rate Inertial Coordinate Filter Along the North Axis for Trajectory 2 with a Range Rate Measurement Noise Variance of 6250 Feet²/Second²

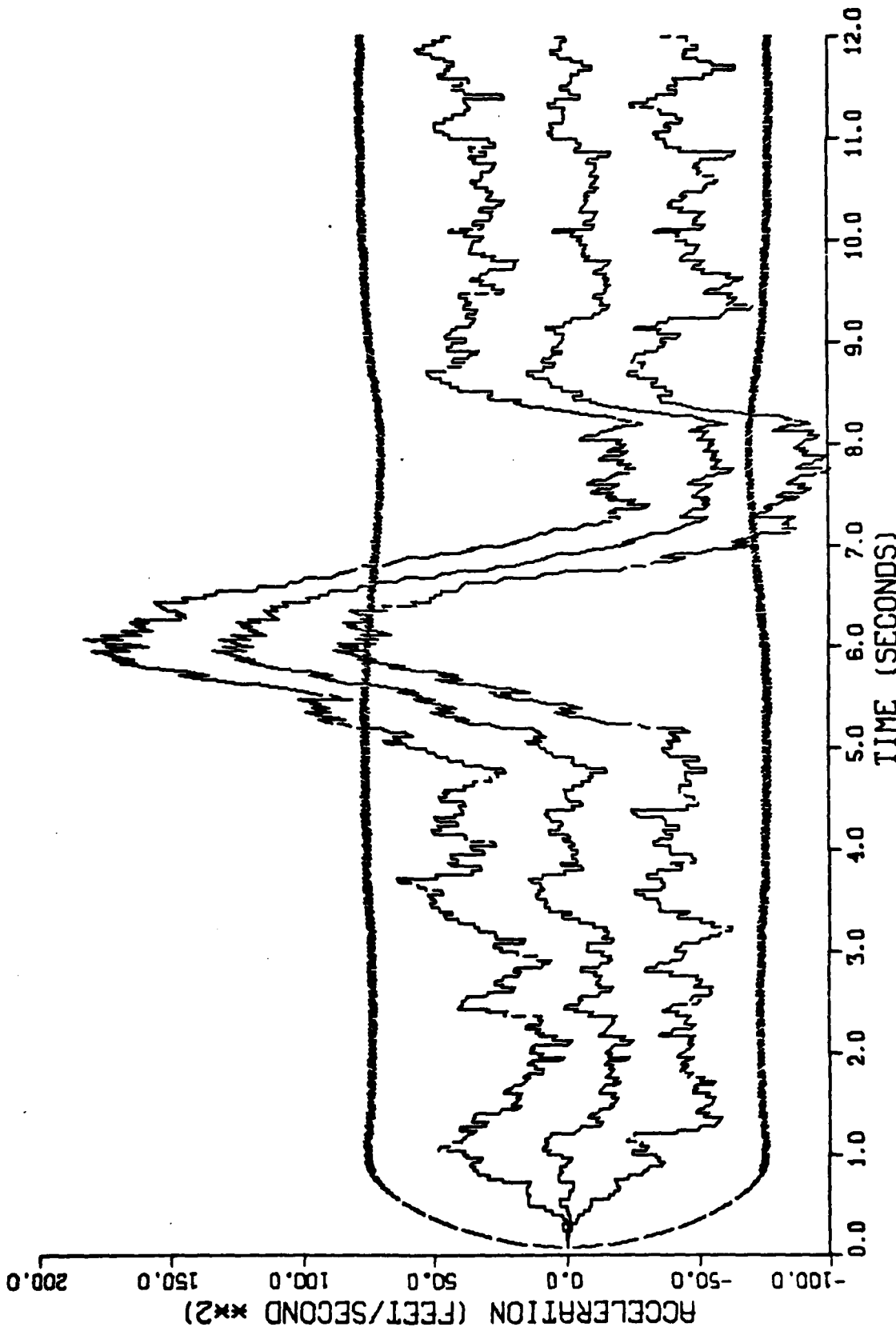


Figure I-12. Performance of the Constant Turn Rate Inertial Coordinate Filter Along the North-Axis for Trajectory 2 with a Range Rate Measurement Noise Variance of 6250 Feet²/Second²

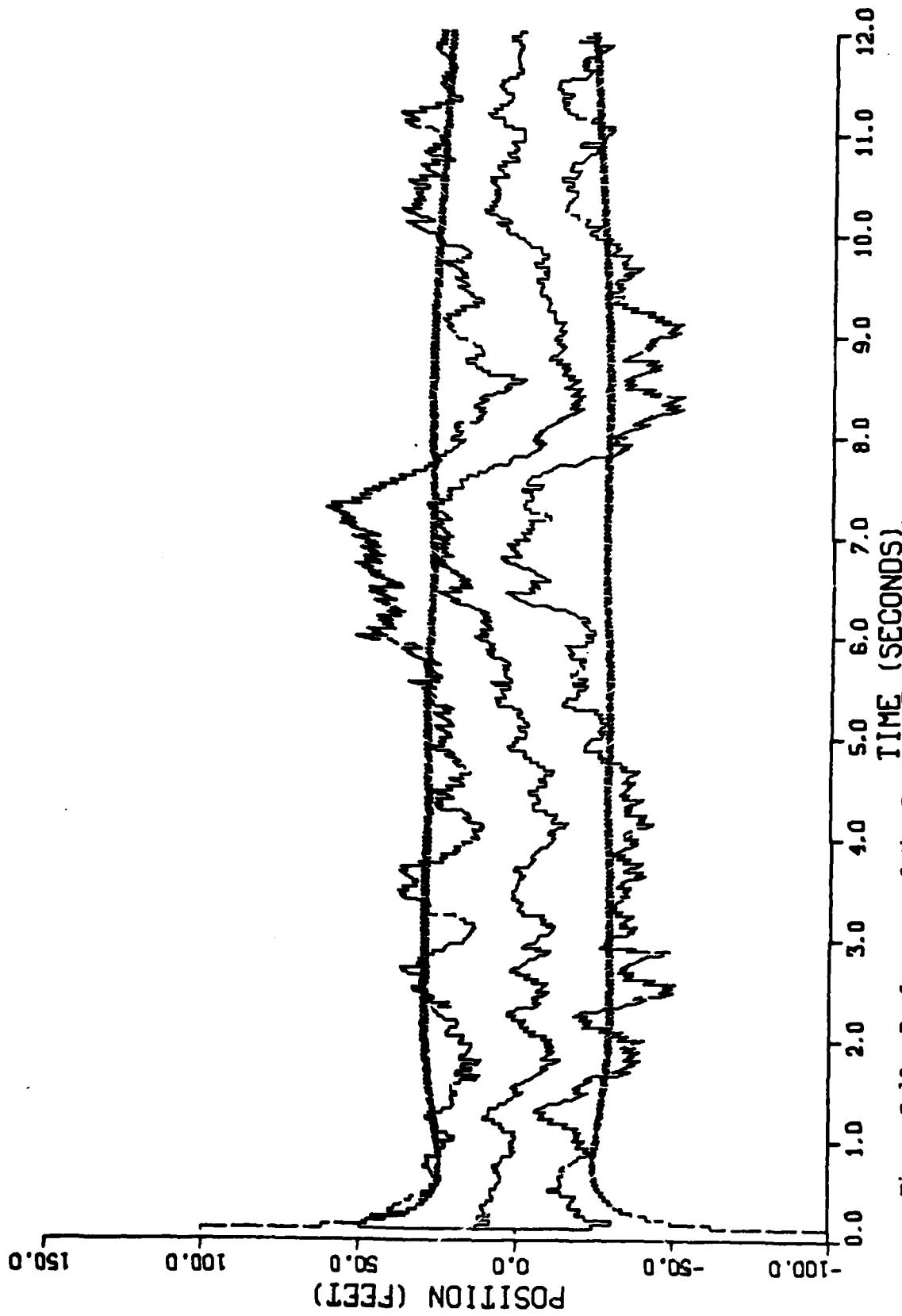


Figure I-13. Performance of the Constant Turn Rate Inertial Coordinate Filter Along the East-² Axis for Trajectory 2 with a Range Rate Measurement Noise Variance of 6250 Feet²/Second²

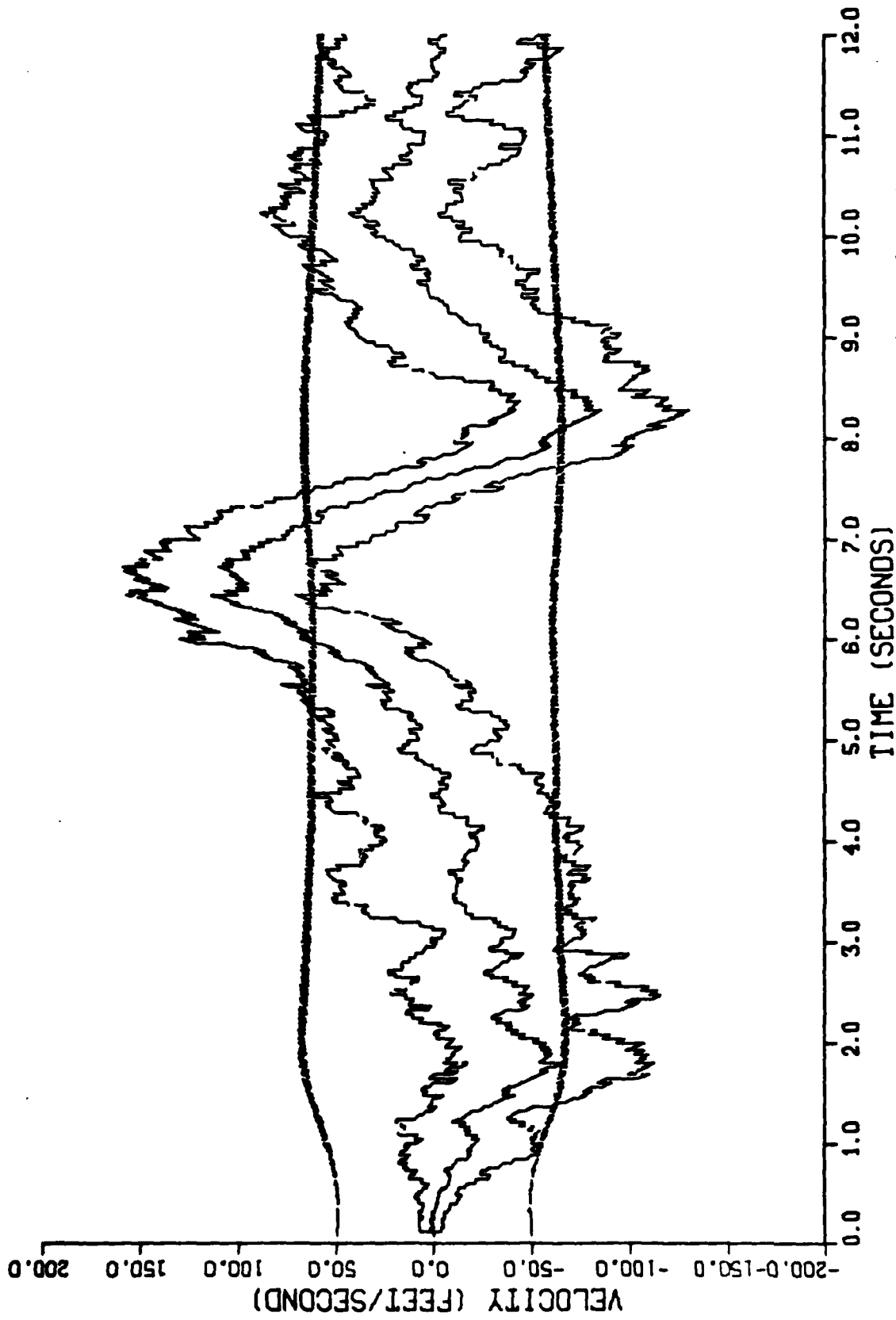


Figure I-14. Performance of the Constant Turn Rate Inertial Coordinate Filter Along the East-Axis for Trajectory 2 with a Range Rate Measurement Noise Variance of 6250 Feet²/Second²

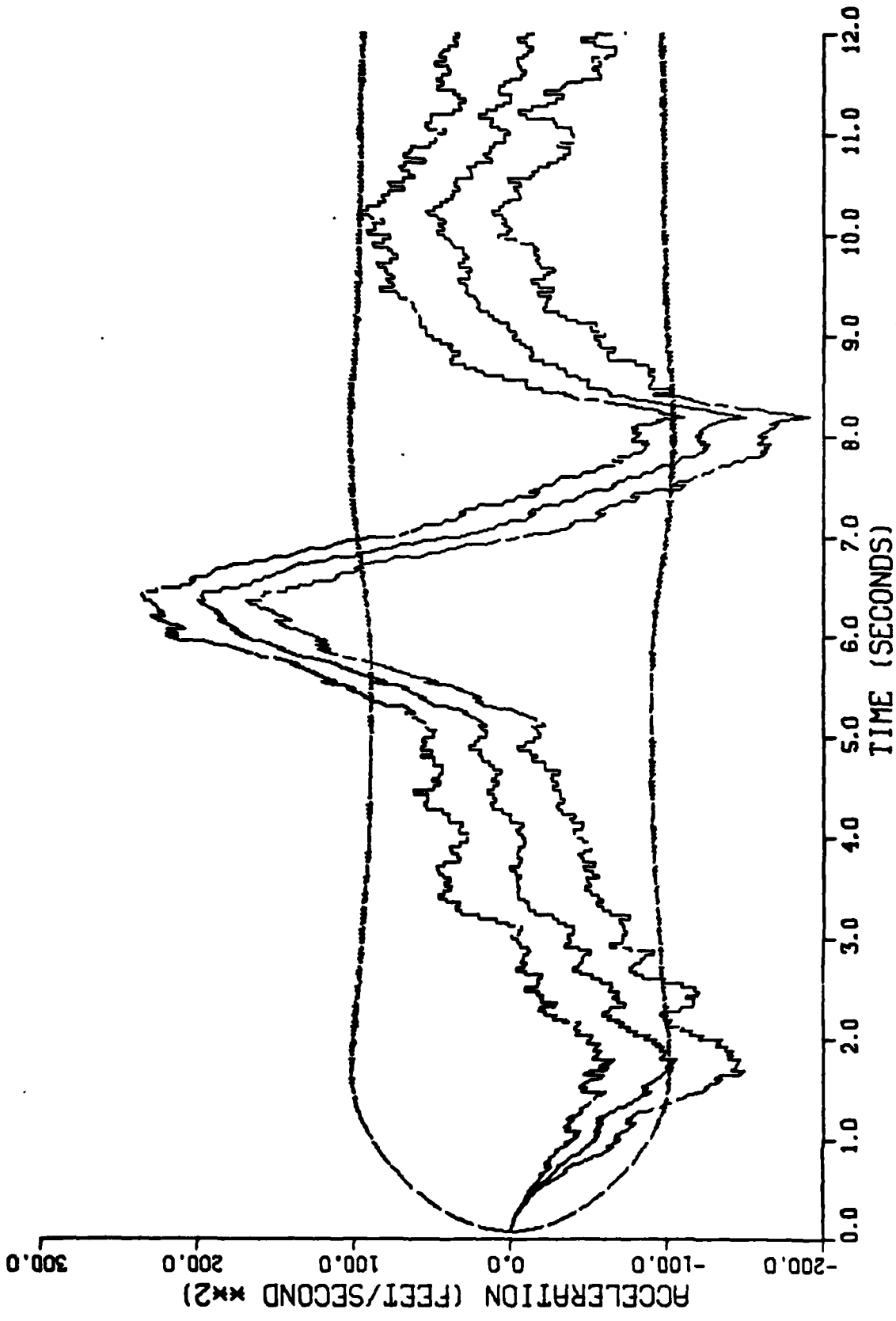


Figure I-15. Performance of the Constant Turn Rate Inertial Coordinate Filter Along the East Axis for Trajectory 2 with a Range Rate Measurement Noise Variance of 6250 Feet²/Second²

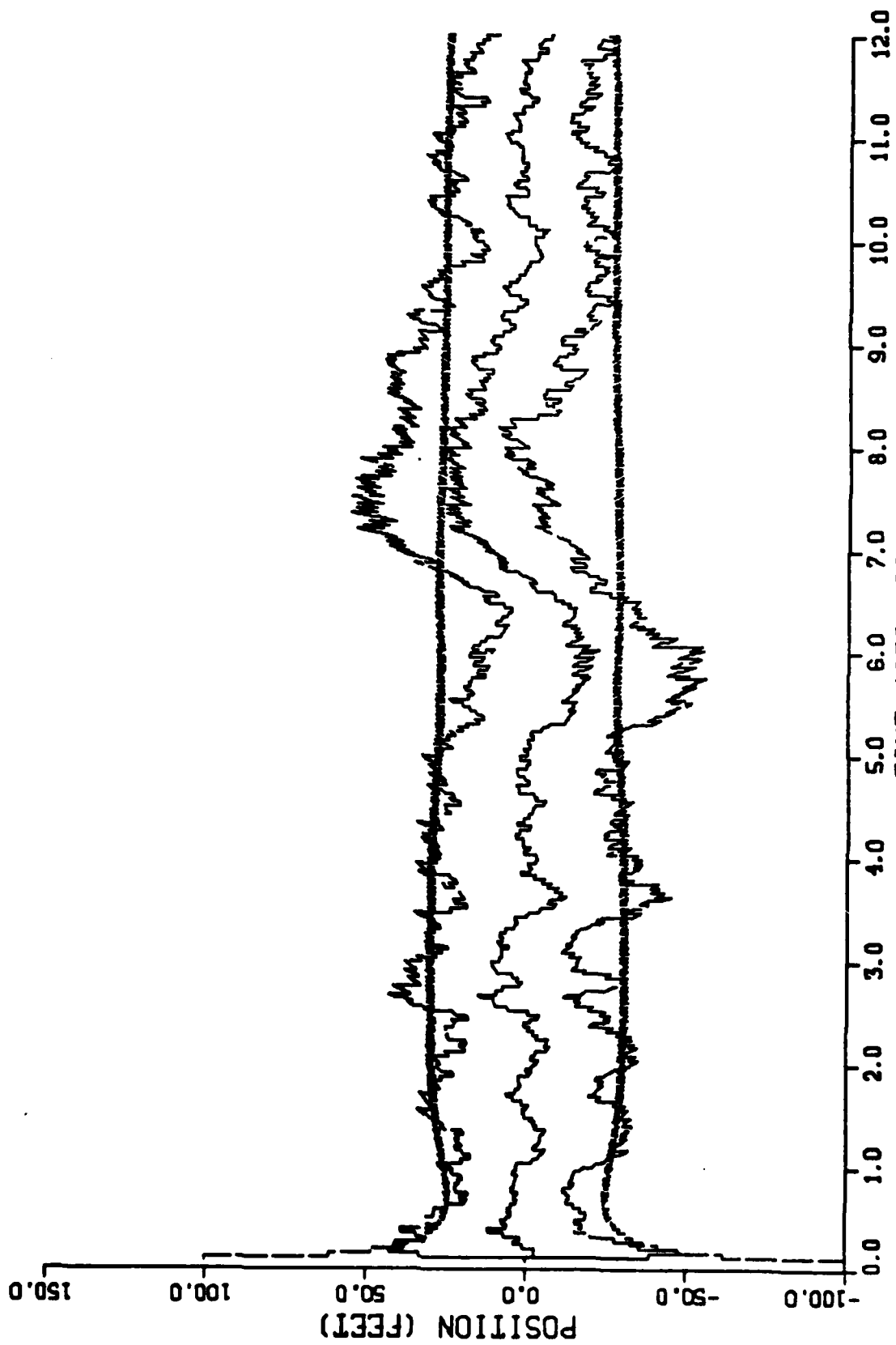


Figure I-16. Performance of the Constant Turn Rate Inertial Coordinate Filter Along the Down₂ Axis for Trajectory 2 with a Range Rate Measurement Noise Variance of 6250 Feet²/Second²

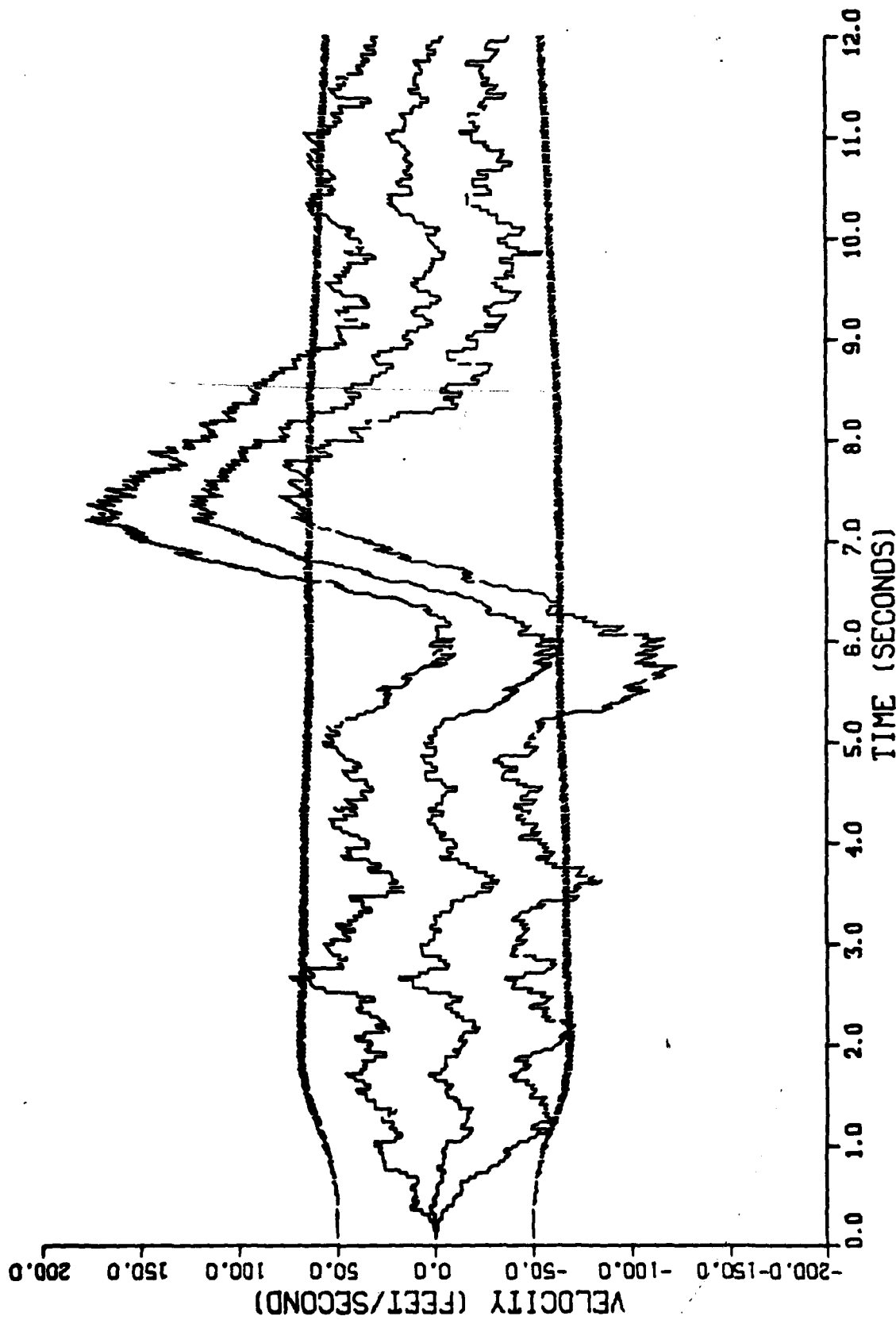


Figure I-17. Performance of the Constant Turn Rate Inertial Coordinate Filter Along the Down-Axis for Trajectory 2 with a Range Rate Measurement Noise Variance of 6250 Feet²/Second²

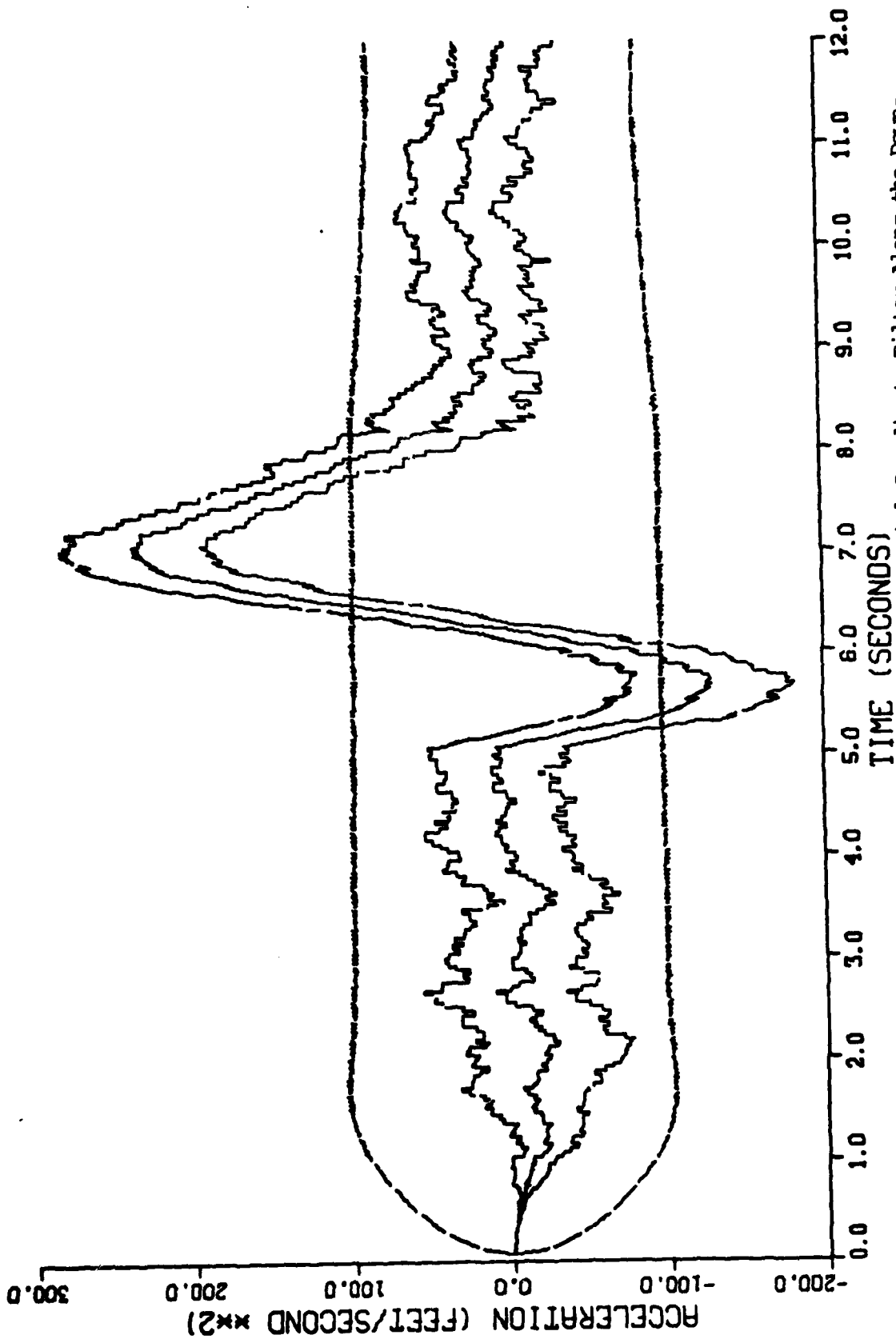


Figure I-18. Performance of the Constant Turn Rate Inertial Coordinate Filter Along the Down-Axis for Trajectory 2 with a Range Rate Measurement Noise Variance of 6250 Feet²/Second²

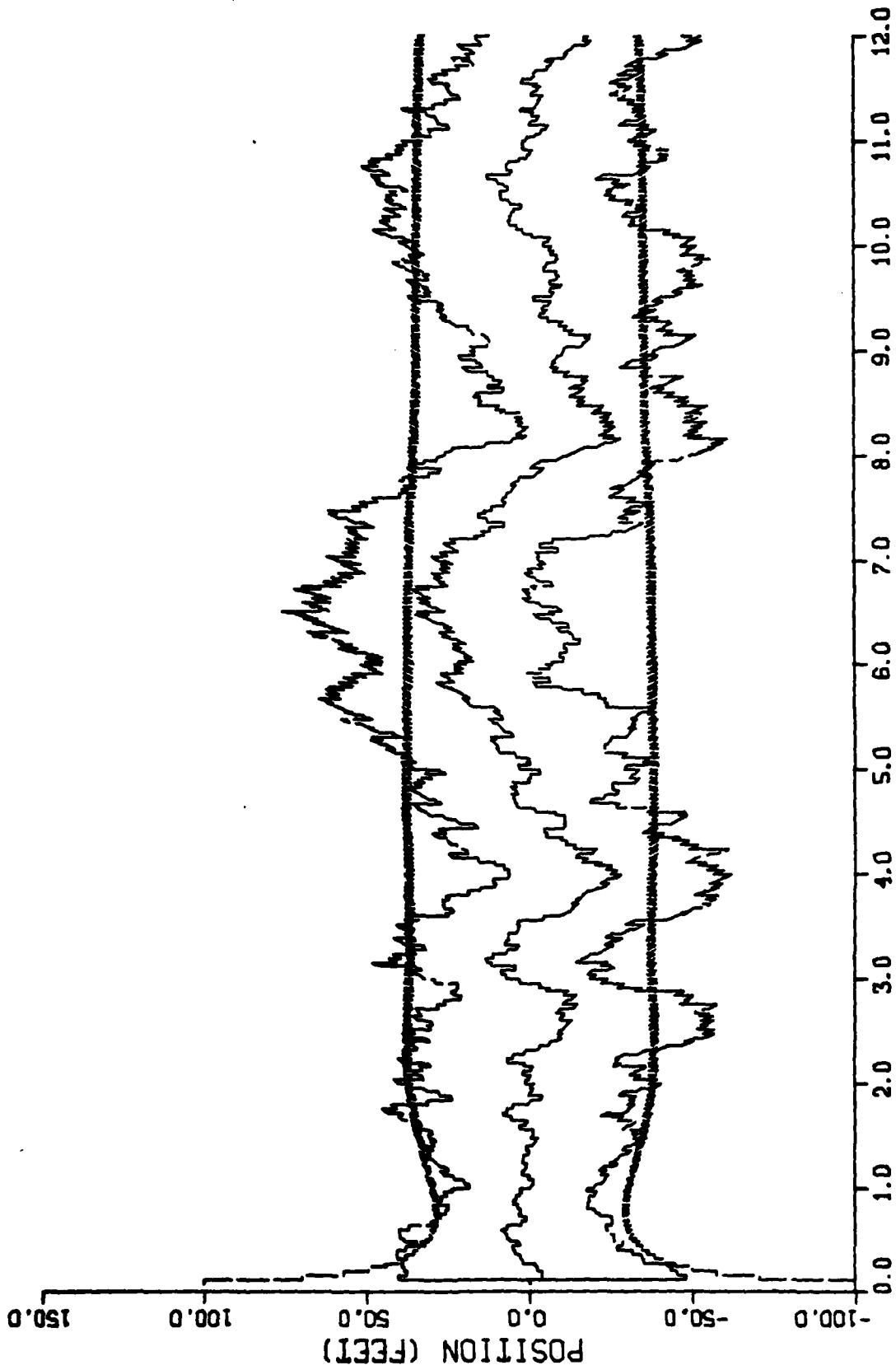


Figure I-19. Performance of the Constant Turn Rate Inertial Coordinate Filter Along the North-Axis for Trajectory 2 with No Range Rate Measurements

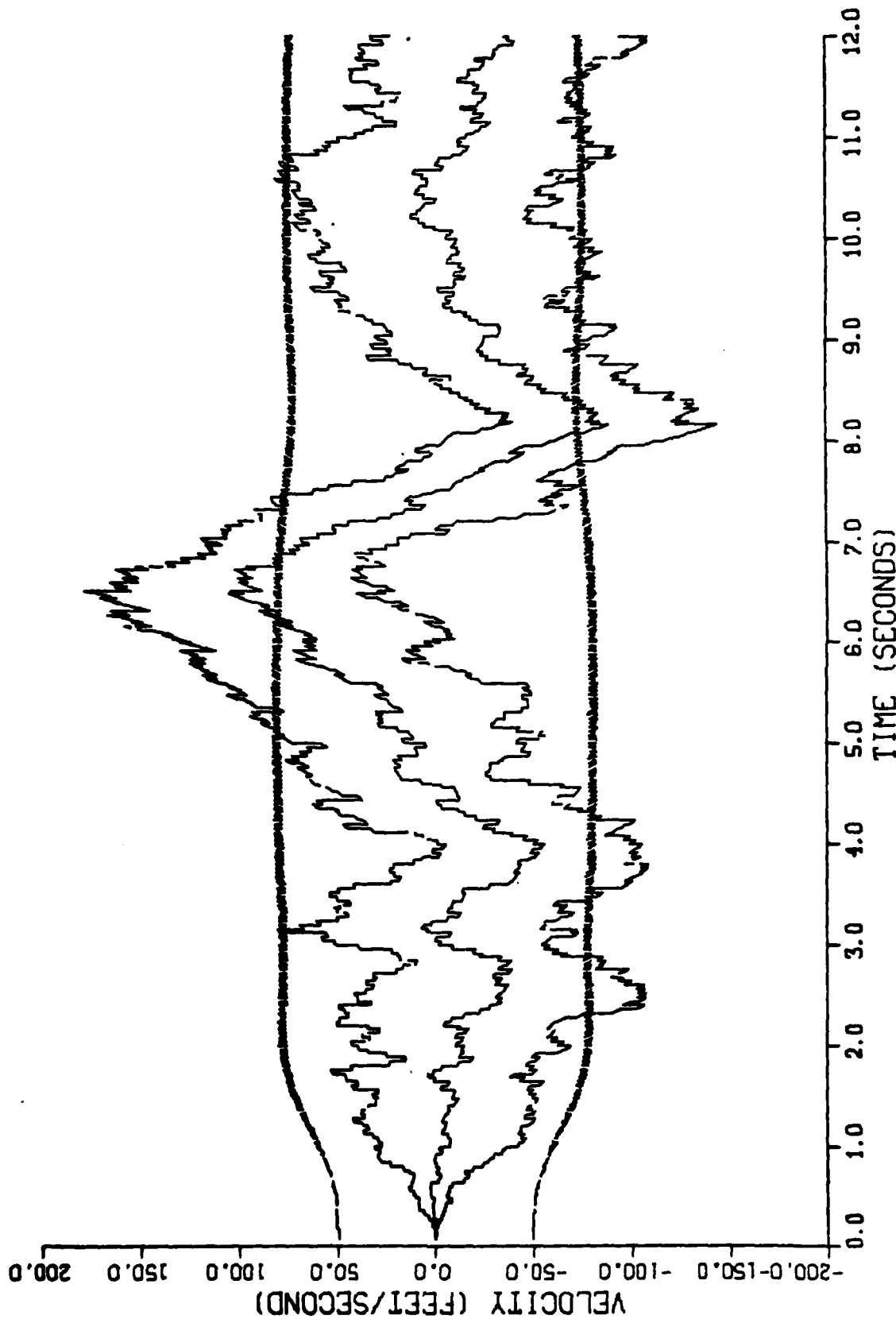


Figure I-20. Performance of the Constant Turn Rate Inertial Coordinate Filter Along the North-Axis for Trajectory 2 with No Range Rate Measurements

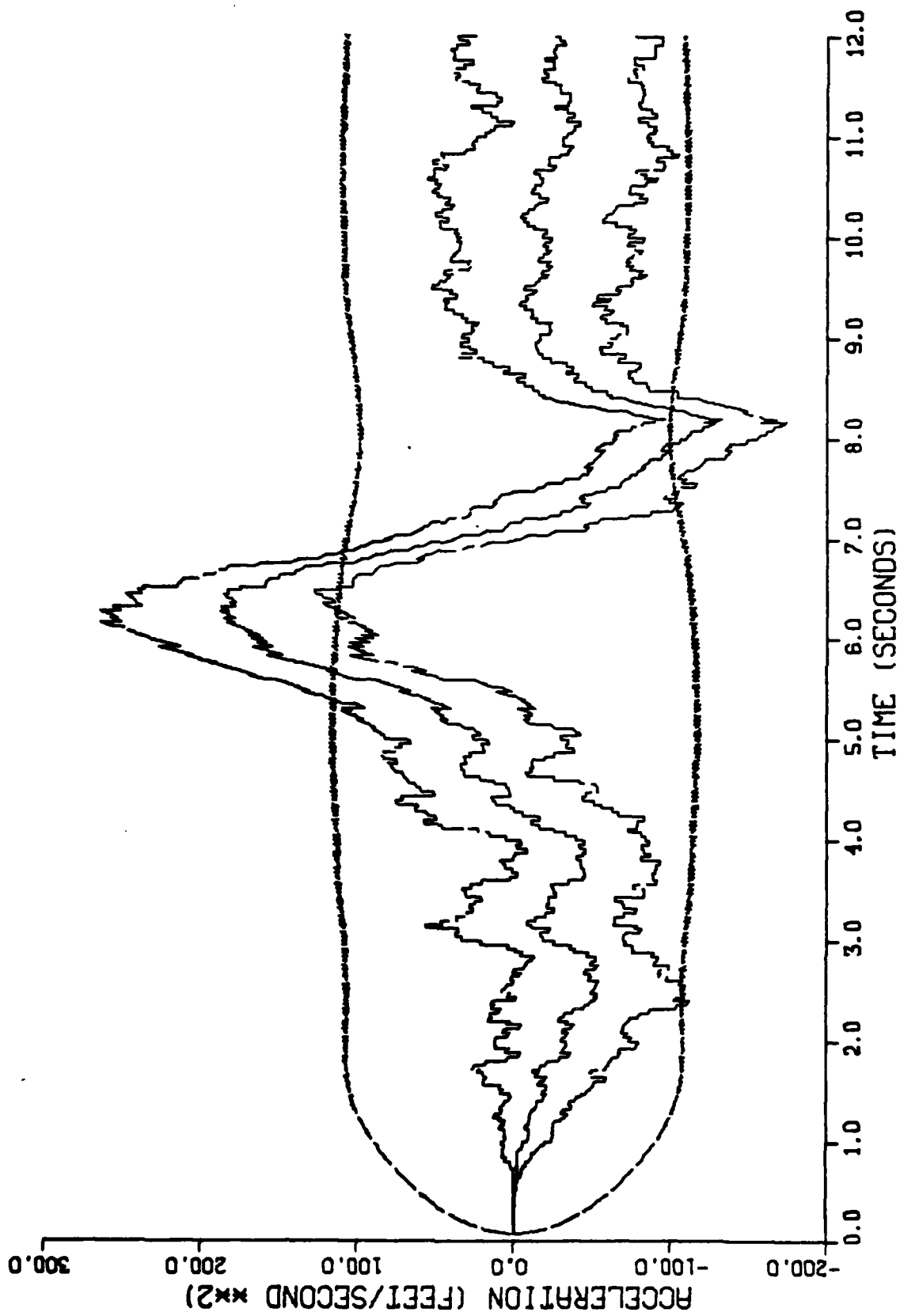


Figure I-21. Performance of the Constant Turn Rate Inertial Coordinate Filter Along the North-Axis for Trajectory 2 with No Range Rate Measurements

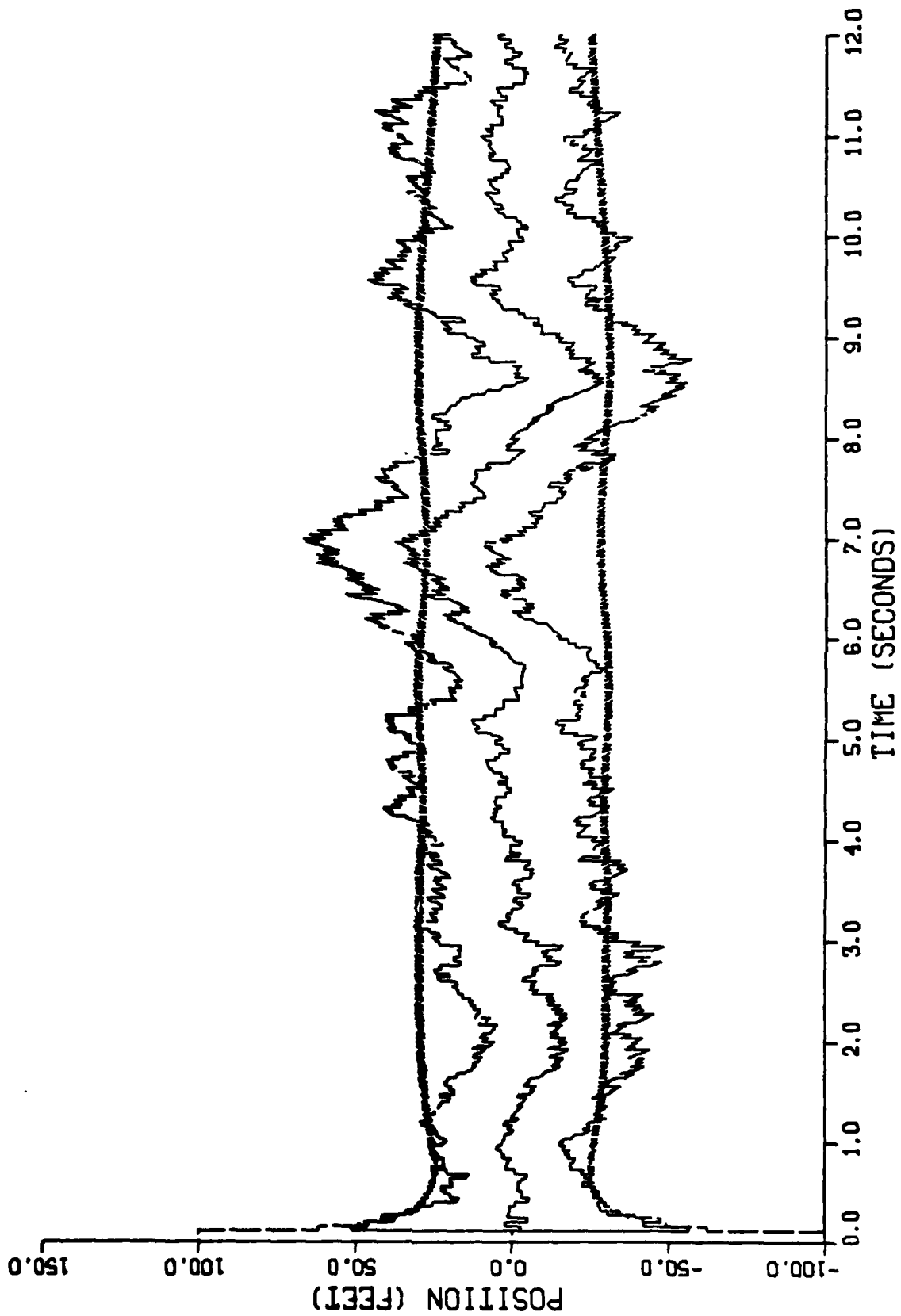


Figure I-22. Performance of the Constant Turn Rate Inertial Coordinate Filter Along the East-Axis for Trajectory 2 with No Range Rate Measurements

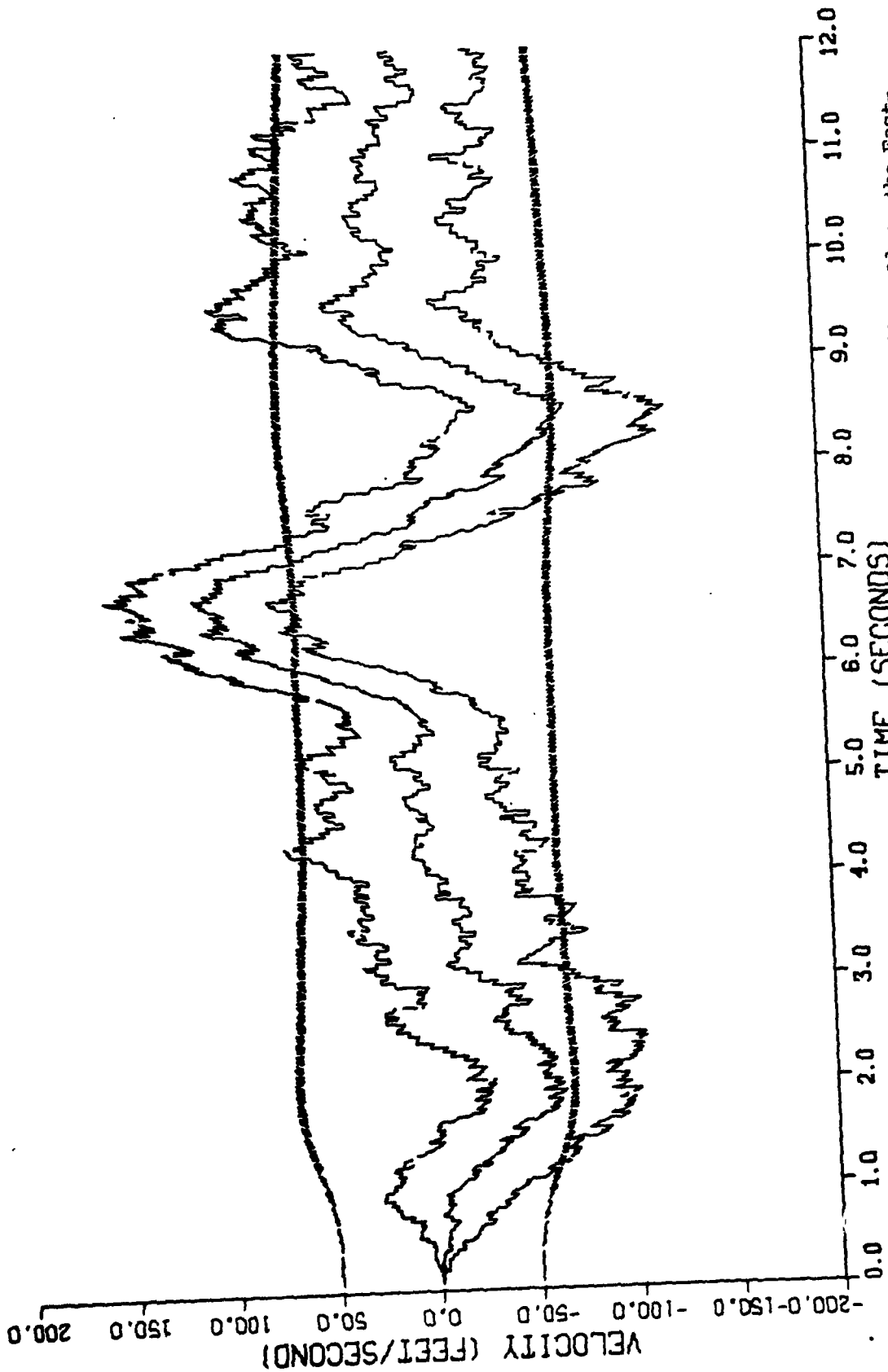


Figure I-23. Performance of the Constant Turn Rate Inertial Coordinate Filter Along the East-Axis for Trajectory 2 with No Range Rate Measurements

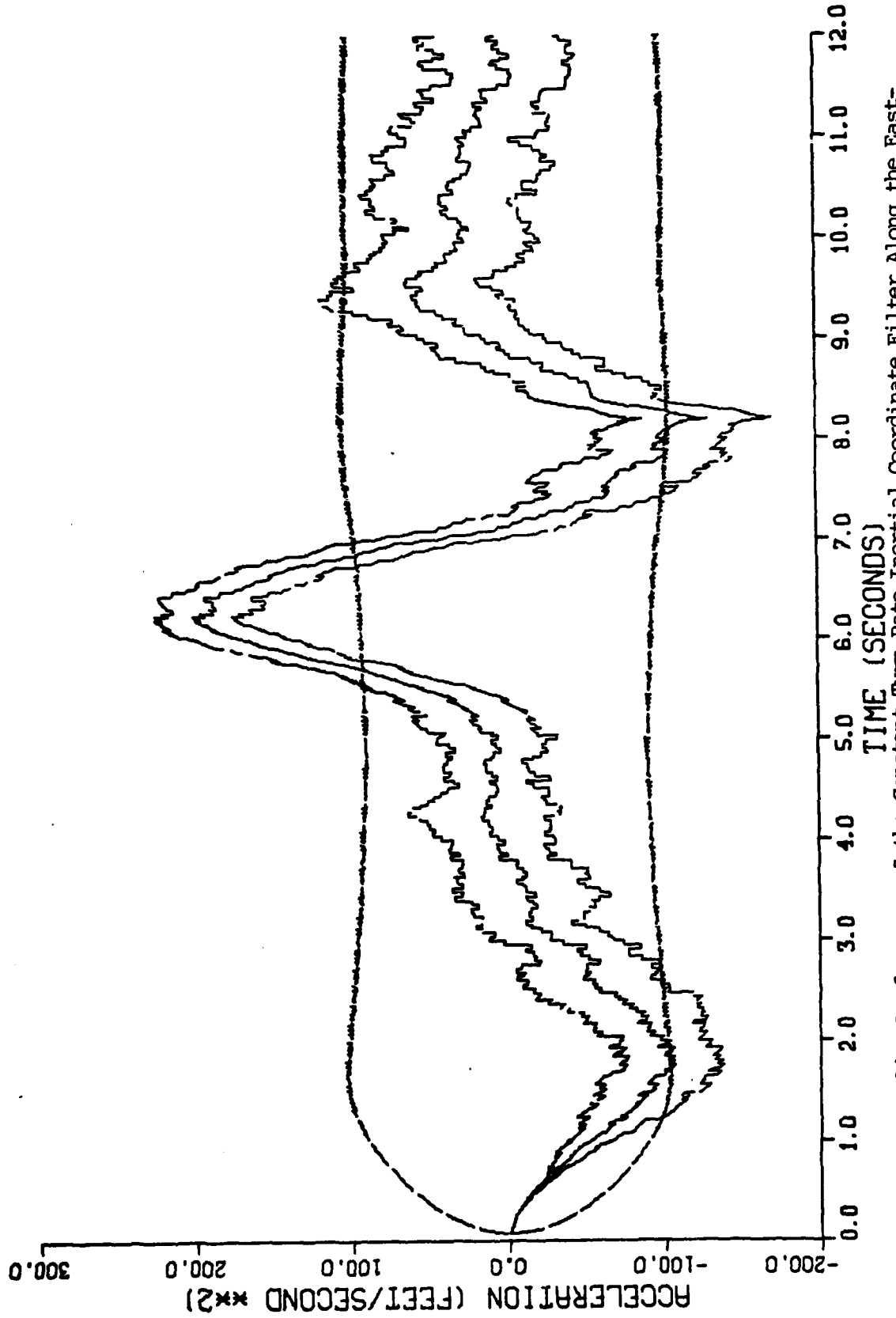


Figure I-24. Performance of the Constant Turn Rate Inertial Coordinate Filter Along the East-Axis for Trajectory 2 with No Range Rate Measurements

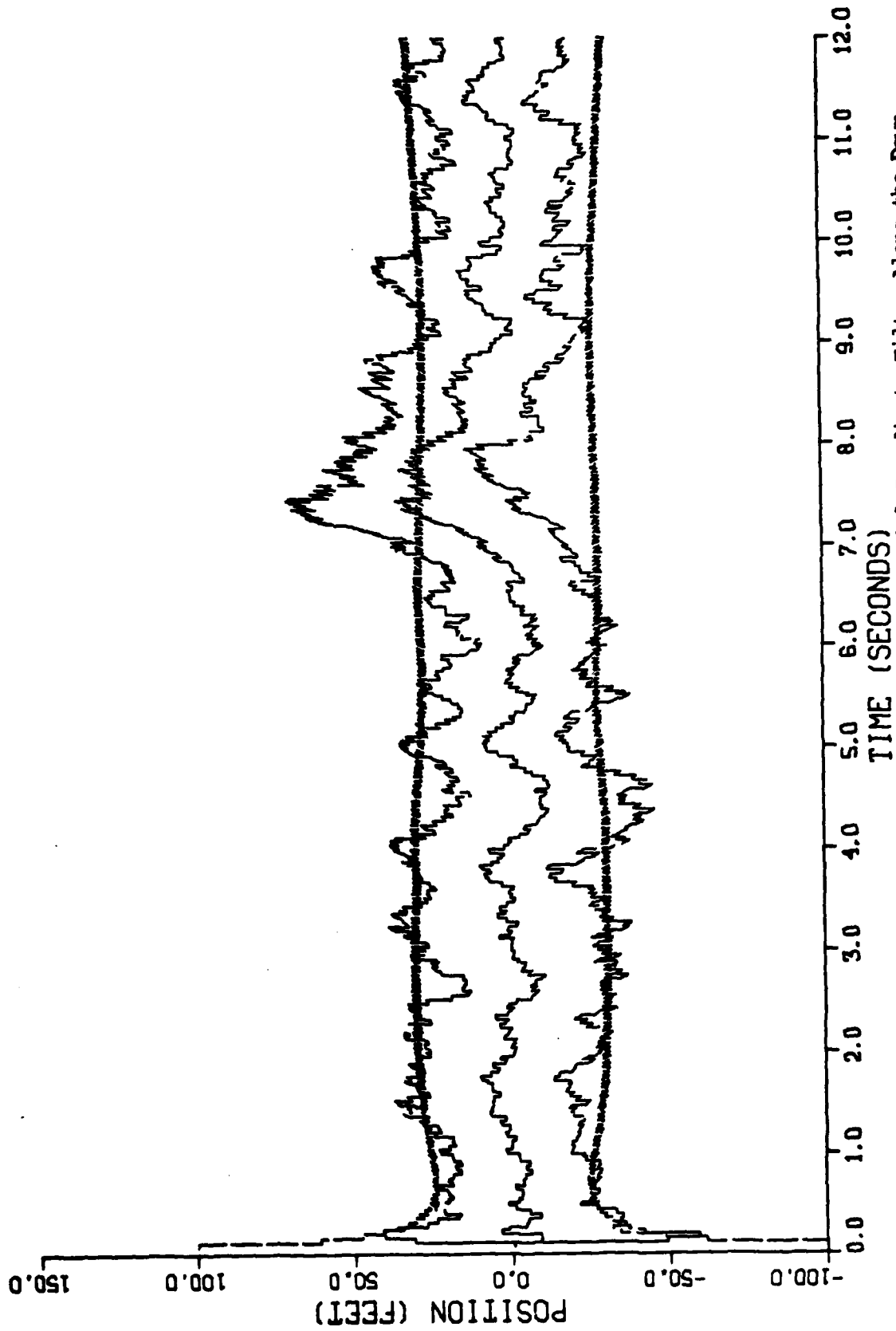


Figure I-25. Performance of the Constant Turn Rate Inertial Coordinate Filter Along the Down-Axis for Trajectory 2 with No Range Rate Measurements

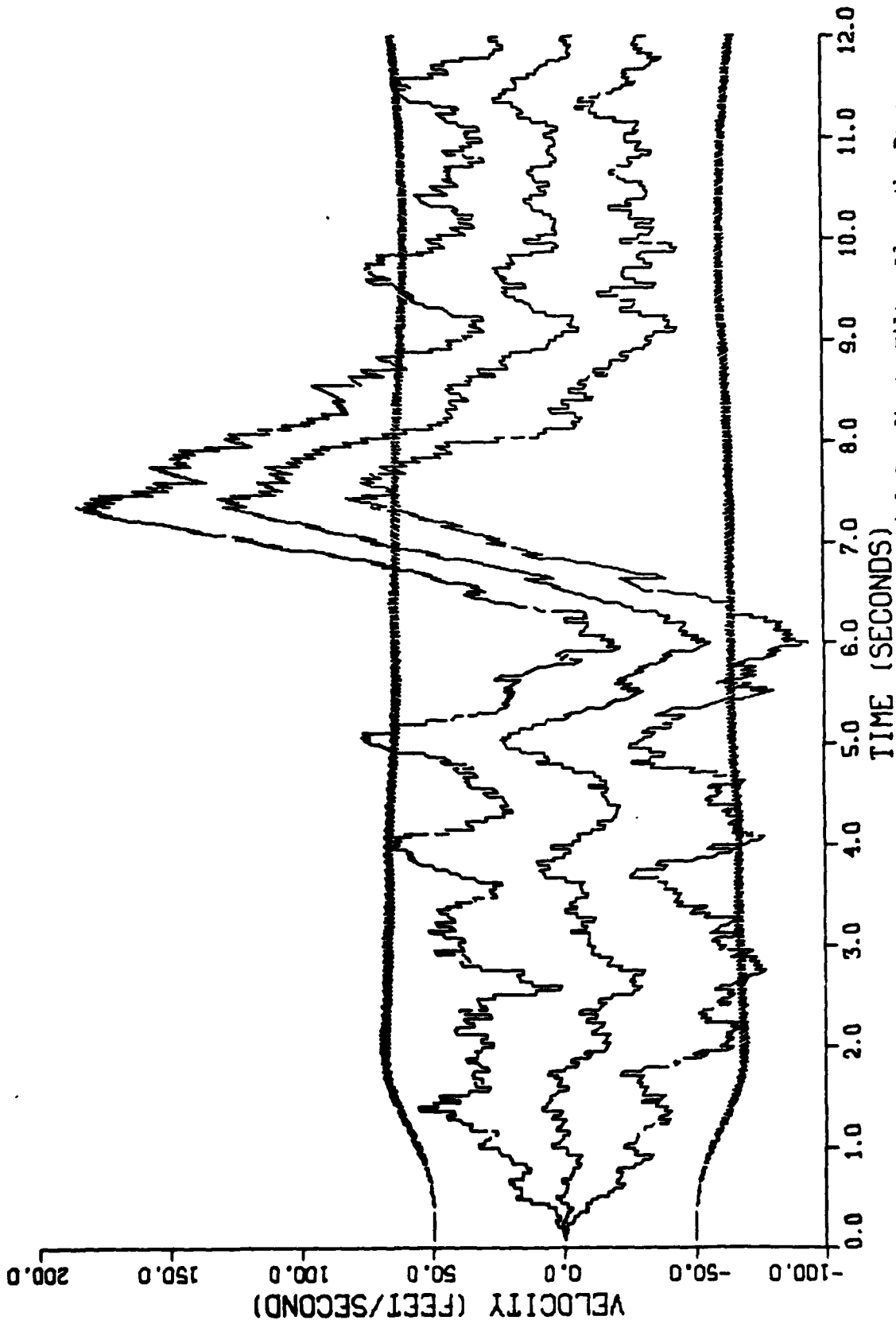


Figure I-26. Performance of the Constant Turn Rate Inertial Coordinate Filter Along the Down-Axis for Trajectory 2 with No Range Rate Measurements

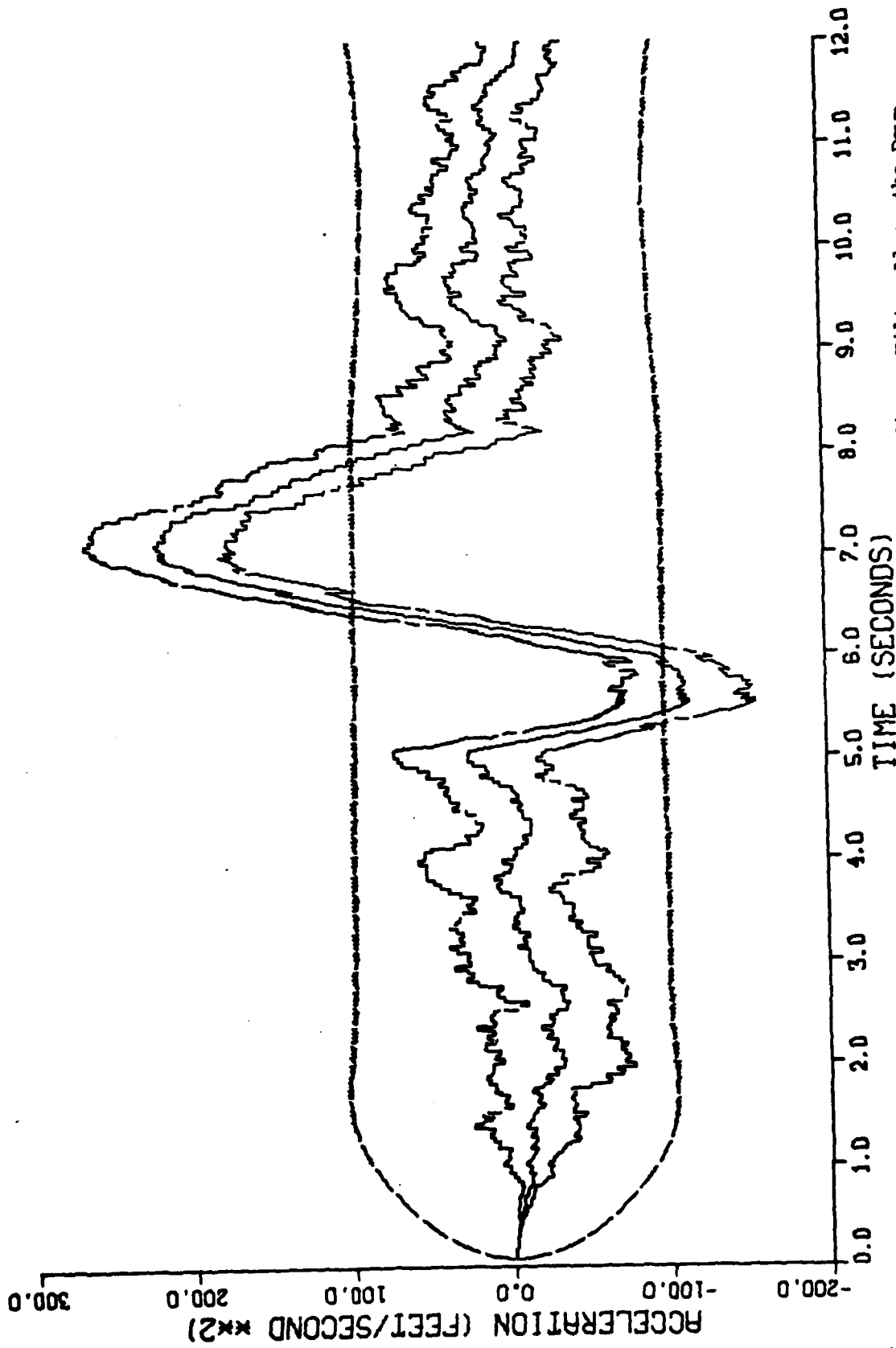


Figure I-27. Performance of the Constant Turn Rate Inertial Coordinate Filter Along the Down-Axis for Trajectory 2 with No Range Rate Measurements

VITA

William H. Worsley was born on 22 September 1948 in Greenville, North Carolina. He graduated from Junus H. Rose High School in Greenville in 1966 and attended North Carolina State University at Raleigh, North Carolina. He received his Bachelor of Science in Aerospace Engineering in 1970, graduating from the honors program. While at North Carolina State University, he was elected to membership in Tau Beta Pi, Sigma Gamma Tau, Pi Tau Sigma, and Phi Kappa Phi honor societies. He was commissioned a second lieutenant in the United States Air Force in May, 1972 and was assigned as a project engineer in the Missile Branch of the Service Engineering Division at Warner Robins AFB, Georgia, where he worked on AIM-4 and AIM-9 air-to-air missiles. In 1975, he was selected to attend the USAF Test Pilot School in the Flight Test Engineer's Course which he completed in July, 1976. His next assignment was to the 475th Test Squadron at Tyndall AFB, Florida, where he worked as a test director/engineer on the gunsight for the F-106 aircraft. In 1979, he was selected to attend the Air Force Institute of Technology which he entered in June, 1979.

Permanent address: 1412 N. Overlook Dr.
Greenville, North Carolina
27834

UNCLASSIFIED

SECURITY CLASSIFICATION OF THIS PAGE (When Data Entered)

REPORT DOCUMENTATION PAGE		READ INSTRUCTIONS BEFORE COMPLETING FORM
1. REPORT NUMBER AFIT/GAE/AA/80S-2	2. GOVT ACCESSION NO. AD-A094767	3. RECIPIENT'S CATALOG NUMBER
4. TITLE (and Subtitle) COMPARISON OF THREE EXTENDED KALMAN FILTERS FOR AIR-TO-AIR TRACKING	5. TYPE OF REPORT & PERIOD COVERED MS Thesis	
	6. PERFORMING ORG. REPORT NUMBER	
7. AUTHOR(s) William H. Worsley Capt USAF	8. CONTRACT OR GRANT NUMBER(s)	
9. PERFORMING ORGANIZATION NAME AND ADDRESS Air Force Institute of Technology (AFIT-EN) Wright Patterson AFB, Ohio 45433	10. PROGRAM ELEMENT, PROJECT, TASK AREA & WORK UNIT NUMBERS	
11. CONTROLLING OFFICE NAME AND ADDRESS	12. REPORT DATE December 1980	
	13. NUMBER OF PAGES 346	
14. MONITORING AGENCY NAME & ADDRESS (if different from Controlling Office)	15. SECURITY CLASS. (of this report) Unclassified	
	15a. DECLASSIFICATION/DOWNGRADING SCHEDULE	
16. DISTRIBUTION STATEMENT (of this Report) Approved for public release; distribution unlimited		
17. DISTRIBUTION STATEMENT (of the abstract entered in Block 20, if different from Report)		
18. SUPPLEMENTARY NOTES Approved for public release; IAW AFR 190-17 FREDRIC C. LYNCH, Major, USAF Director of Public Affairs 50 DEC 1980		
19. KEY WORDS (Continue on reverse side if necessary and identify by block number) Extended Kalman Filter Air-to-Air Tracking Gauss-Markov Target Acceleration Model Constant Turn Rate Target Acceleration Model		
20. ABSTRACT (Continue on reverse side if necessary and identify by block number) The performances of the extended Kalman filter implementations for three different target acceleration models that estimate target position, velocity, and acceleration states for air-to-air gunnery were compared. The models included 1) a first order zero-mean Gauss-Markov relative target acceleration model, 2) a first order zero-mean Gauss-Markov total target acceleration model, and 3) a constant turn rate target acceleration model. Measurements available to the extended Kalman filter at update were the range, range rate,		

DD FORM 1 JAN 73 1473

EDITION OF 1 NOV 65 IS OBSOLETE

UNCLASSIFIED

SECURITY CLASSIFICATION OF THIS PAGE (When Data Entered)

UNCLASSIFIED

SECURITY CLASSIFICATION OF THIS PAGE(When Data Entered)

and the error angles between the true line of sight and the estimated line of sight. Additional evaluations of the effect of variations in the length of the sample period and the effect of variations in the variances of the measurement noises were conducted for the extended Kalman filter using the constant turn rate target acceleration model. All evaluations were accomplished using Monte Carlo simulation techniques.

UNCLASSIFIED

SECURITY CLASSIFICATION OF THIS PAGE(When Data Entered)

LMED
-8-